Fermilab Library
0 1160 0086861 6

E-744/770

Nevis 292

COLUMBIA UNIVERSITY

Department of Physics

A Next-to-Leading-Order QCD Analysis of Neutrino-Iron Structure Functions at the Tevatron

William Glenn Seligman

NEVIS LABORATORIES

Irvington-on-Hudson, New York

Wednesday, April 06, 2005.jpg

E-744/770

R-1257
CU-398
Nevis-292

Columbia University
Department of Physics
New York, New York 10027

A NEXT-TO-LEADING-ORDER QCD ANALYSIS OF NEUTRINO-IRON STRUCTURE FUNCTIONS AT THE TEVATRON

William Glenn Seligman

Reproduction in whole or in part
is permitted for any purpose by the
United States Government.

Submitted in partial fulfillment of the
requirements for the degree
of Doctor of Philosophy
in the Gradauate School of Arts and Sciences
COLUMBIA UNIVERSITY

National Science Foundation
NSF PHY 92-15987

1997

Second Edition

A NEXT-TO-LEADING-ORDER QCD ANALYSIS OF NEUTRINO-IRON STRUCTURE FUNCTIONS AT THE TEVATRON

William Glenn Seligman
Columbia University, New York, NY

* Research supported by the National Science Foundation.
† Submitted in partial fulfillment of the requirement for the degree of Doctor of Philosophy in the Graduate School of Arts and Sciences, Columbia University.

Abstract

Nucleon structure functions measured in neutrino-iron and antineutrino-iron charged-current interactions are presented. The data were taken in two high-energy high-statistics runs by the LAB-E detector at the Fermilab Tevatron. Structure functions are extracted from a sample of 950,000 neutrino and 170,000 antineutrino events with neutrino energies from 30 to 360 GeV. The structure functions F_2 and xF_3 are compared with the the predictions of perturbative Quantum Chromodynamics (PQCD). The combined non-singlet and singlet evolution in the context of PQCD gives value of $\Lambda_{\overline{\mathrm{MS}}}^{\mathrm{NLO},(4)} = 337 \pm 28$ (exp.) MeV, which corresponds to $\alpha_S(M_Z^2)$ = 0.119 ± 0.002 (exp.) ± 0.004 (theory), and with a gluon distribution given by $xG\left(x, Q_0^2 = 5GeV^2\right) = (2.22 \pm 0.34) \times (1-x)^{4.65 \pm 0.68}$.

Neutrinos, they are very small
They have no charge and have no mass
And hardly interact at all.
The earth is just a silly ball
To them, through which they simply pass,
Like dustmaids down a drafty hall
Or photons through a sheet of glass.
They snub the most exquisite gas,
Ignore the most substantial wall,
Cold shoulder steel and sounding brass,
Insult the stallion in his stall,
And scorning barriers of class,
Infiltrate you and me! Like tall
And painless guillotines, they fall
Down through our heads into the grass.
At night, they enter at Nepal
And pierce the lover and his lass
From underneath the bed—you call
It wonderful; I call it crass.

John Updike

Acknowledgments

What a long, strange trip it has been. The time I've spent working on my doctorate has been a period of great mental, physical, and spiritual change for me. With the deposit of this thesis, I've completed one major goal of my life: to become the third-generation Dr. Seligman in my family (the first two were MD's, whereas I am a PhD). As I stand at the end of my journey as a student of physics, I want to thank the friends and teachers who guided me to this point in my life. If you're bored by lengthy expressions of sentimentality, turn to the Table of Contents on page vii and start reading the thesis. If you're offended when such expressions are spiced with a dash of humor, again go to page vii. Otherwise, please read on.

Michael Shaevitz was my thesis advisor. He is well-suited to the job of advisor, because his advice was always excellent. At the first meeting we had as advisor and grad student, he told me, "To be a good physicist, physics should not only be your job, but your hobby." Not a day has gone by that I haven't recalled those words. The analysis described in this thesis turned out to be more complex than either of us expected it to be, which partly explains why this thesis is more than 400 pages long. (The rest of the explanation is our desire to share all the details of the analysis, our wish to include all the results, my natural prolixity, and my use of double-spaced paragraphs.) Throughout it all, Mike remained a good teacher, patient, understanding, and exhibiting a true love of physics. I shall be forever grateful that he made the time I spent at Nevis a positive and educational experience. A few years ago, Mike and I played a game of pool at the Fermilab User's Center. To make the game more interesting, we bet my thesis: if I won, Mike would write my thesis for me. So, if you like this thesis, please remember that Mike is a dedicated physicist and academician who would never allow the outcome of a pool game to affect his ethical standards. If you don't like this thesis, well… Mike lost the game.

When Janet Conrad first came to Nevis Labs to interview for the job of post-doc, I told her, "As you look around Nevis, remember that you're making an important decision. You can work with the finest physicists in the world, do work on the leading edge of scientific study, achieve world-wide recognition for the research that you do… or you can work here." Fortunately for me, Janet laughed at my feeble attempt at humor. She came to work at Nevis, became an assistant professor, and proved my joke to be the lie that it was. Janet didn't take my joke seriously, but she took me seriously. On her own initiative, she reviewed my thesis, pointed out errors and gaps in logic, indicated those places where I should mention the work of others and helped me to locate the references, and aided me in obtaining data for plots. Basically, she made Mike Shaevitz's life easier by making me fix the mistakes before he read the thesis. She also helped to prepare me for the rigors of the thesis defense. I am grateful to Janet, the Pheobe Fingerlilly of high-energy physics, for all the assistance she provided.[†]

The closest connections one forms in graduate school are with one's fellow grad students. Let's begin with the denizens of the infamous Room 116, the social center of Nevis Labs:

Walter Lefmann was my best friend during my time as a graduate student. I enjoyed the time I spent at Fermilab during the run of E770, and Walter was the most important reason why. Afterwards, as we both analyzed the data, Walter was always available to offer advice when asked: how to repair a car, how to fix a snapped-off shower head, or how to dress in costume for the Renaissance Faire. We also shared many interests: science fiction, D&D, martial arts, and Macintoshes. Unfortunately, Walter and I are now

[†] Pheobe Fingerlilly was the "real" name of Nanny in the 1970's TV series *Nanny and the Professor*. In the series, when Nanny was around, everything would come out for the best. It was never made clear whether this was due to coincidence, magic, or a lot of off-stage work on Nanny's part. In Janet's case, I suspect it's hard work.

separated by 800 miles and we communicate mostly by e-mail. I will always remember what his friendship meant to me. I shall also remember the Lefmann-Seligman Treaty: if one of us wins the Lottery, he must buy the other one the most powerful Macintosh available at the time. May the fulfillment of that treaty come soon!

Of all my office mates, Steve Rabinowitz was the most educational. He'd listen to WBAI, an ultra-liberal radio station, until 12 noon. Then he'd switch channels to Rush Limbaugh. The dramatic political shift from left to right always made us dizzy. A political discussion with Steve was often frustrating, but it was never dull. He also had the ability to send me into fits of uncontrollable laughter. Good luck, Steve, wherever you are.

Andrew Bazarko could not abide the long-standing Room 116 practice of reversing the gears on the office clock so that it ran backwards, and set the time to move forwards again. (The interior decorators of Room 116 have since reset the clock to its natural spin -1 state). Andrew was the epicure of the office. What little I know of good food, good wine, and QCD factorization comes from conversations with him. Andrew also supplied the right words when words failed me. I wish him the best of luck as he pursues his career in high-energy physics.

Carlos Arroyo does not like attention. In fact, he probably wishes I didn't mention him here. His expertise in statistics was invaluable, and I could always turn around and bounce ideas off him. Thanks for the help, Carlos.

Cindy McNulty came to Room 116 while waiting for her X-terminal to be installed in her own office, but it turned out she came to stay. She has the toughest job of anyone I know: she's both a grad student and a single mother. Cindy has my thanks for providing transportation when my car, the Talamobile, was in the shop. She also has my thanks for proving that my high-x results were right after all.

Now let's meet some of the graduate students outside of Room 116.

When I was living at Fermilab, I woke up one night with chest pains. I couldn't drive, so I asked Bruce King if he could drive me to the Fermilab medical center. It was closed. He drove me around for an hour, as I clutched my chest and tried to breathe, and we went from one closed clinic to another. Finally he brought me to the emergency room of DuPage Hospital, where I was diagnosed with a bad case of indigestion. So, since I can't thank Bruce for saving my life, I'll thank him instead for the muon calibration.

Since I've mentioned Walter and Bruce, I must also mention the remaining member of the Nevis Cold Fusion Team: Paul Stankus. When I grew discouraged with physics, Paul reminded me of the joys of science, in part through his instigation of our own private cold-fusion experiment. (I wish I could tell you the results of our study, but the patents have not yet been accepted.) Paul also renewed my faith in science education when he told me that any student in his celestial mechanics class could calculate the Deimos-Venus ballistic-trajectory problem posed in Robert Heinlein's novel *Space Cadet*. Wherever Paul is now, I hope his co-workers can keep up with him.

Sanjib Mishra, Paul Quintas, and Wing Cheong Leung were responsible for the previous analysis of the E744/E770 charged-current data. Ed Oltman performed the charged-current analysis on the E616/E701 data. I tried to maintain their traditions of quality in my own work, and I hope they find the analysis in this thesis to be up to their standards. Frank Sciulli was the thesis advisor for all these students, and was always available when I had questions on the work they'd done.

The Nevis staff provided me with an excellent environment in which to work. Ann Therrien kept my feet on the ground, Dorothy Palmer made sure the ground was stable, Bob Peters and Gail Smith made sure I had shoes on my feet, and Don Bunch kept

pulling my leg. Have I overworked the foot metaphor, or can I thank Dave Leon, who kept the Nevis computers running? I also wish to thank the Nevis machine-shop personnel: Lubo Kral, Ed Anderson, Dave Thomas, Paul Betts, Ralph Gardner, and the late John Perticare; they taught me that precision is important, whether building the SLD Endcap Calorimeter or a wizard's staff.

I must also give thanks to members of the CCFR collaboration from institutions other than Columbia. Wesley Smith was the project spokesman for E770, and provided the co-ordination that allowed me to work with the others on the project. Tim Bolton's expertise in statistics led to the global systematic fit technique that allowed for a precision measurement. I could tell more stories about the individual members of the CCFR collaboration and those of the new experiment, NuTeV. Instead I'll give a general thanks to Kurt Bachmann, Bob Bernstein, Arie Bodek, Fred Borcherding, Howard Budd, Pawel de Barbaro, Costas Foudas, Debbie Harris, Drasko Jovanovic, John Kim, Tim Kinnel, Mike Lamm, Bill Marsh, Frank Merritt, Donna Naples, Mark Oreglia, Alex Romosan, Willis Sakumoto, Pamela Sandler, Heidi Schellman, Panagliotis Spentzouris, Eric Stern, and Masoud Valiki.

The help I received was not restricted to the mundane world of physics. My folks, Stephen and Hannelore Seligman and Beatrice and Robert Prentice, gave me support during these years of work. Don Buskard and Bill Brady gave me support of quite another kind. I introduced Dan Holzman to high-energy physics, and he introduced me to Wicca; we both think it was a fair trade. I also received aid and comfort from a special circle of friends: Rosie, Tom, Kenny, Nancy, Isaac, Connie, Vann, Dave, Michele, Deborah, Roberta, Jennifer, Lisa, and Dan; and to this list I can now happily add beloved Susan. There's a warm place in my heart, and an icy spell on my lips, for the men,

women, elves, dwarves, and trolls of Boy Scout Explorer Post #510, the Live-Action Role-Playing Explorers—Winston Waterston sends his greetings from Wainscoting.

On the spiritual level I dedicate this thesis to Brigid, the Celtic Goddess of inspiration and intellect. On the mundane level, I wish to acknowledge the contributions of three of my Columbia physics teachers who, unfortunately, passed away during the time I was a graduate student. (A fourth Columbia physicist and teacher, Professor Gerald Feinberg, also passed away during this time, but I never had the fortune to be in a class he taught; I never met the late Professor I. I. Rabi.)

Professor James Rainwater was a Nobel Laureate, but I knew him as the teacher of the advanced physics lab course on the sixth floor of Pupin. I can still hear his admonition to use the $\hat{T}-\hat{H}-\hat{I}-\hat{N}-\hat{K}$ operator. His desire to teach exceeded his physical limits, but he never let that stop him. He remains an inspiration for me to this day.

When Paul, Walter, Bruce, and I decided to attempt the Nevis Cold Fusion Project, we went to **Professor Alan Sachs** for approval. He made sure we understood what we were doing, what electronics and materials were available at Nevis, what the physics of the phenomenon were, and why we couldn't expect to see any result at all with the equipment at our disposal. Then he authorized the expenditure of a small amount of money to buy D_2O and palladium. He let us play our game, as long we acted like scientists.

If it wasn't for **Professor Jacob Shaham**, I would never have made it through my first year of graduate school. When I had difficulty in advanced quantum mechanics, he made time to sit down with me and work through problems. Whatever skills I've acquired as a physicist I owe to him.

It is to these physicists and teachers that this thesis is dedicated.

Table of Contents

Acknowledgments i

Table of Contents vii

List of Figures xiii

List of Tables xx

1 Introduction 1

1.1 The Standard Model 2

1.2 Neutrino-Nucleon Scattering 5

1.2.1 The Kinematics of a Charged-Current Neutrino Event 6

1.2.2 The Formalism of Deep-Inelastic Scattering 9

1.2.3 The Parton Model 13

1.2.4 The Theory of QCD 21

1.2.4.1 Renormalization 21

1.2.4.2 Factorization 23

1.2.4.3 Evolution Equations 25

1.2.4.4 Hard-Scattering Integrals 27

1.2.4.5 QCD Scales 27

1.3 Analysis Overview 28

1.3.1 The Data Sample 28

1.3.2 Synopsis of This Thesis 29

1.3.3 Prior Analyses 30

2 The Neutrino Beam and Detector 33

2.1 Neutrinos at the Fermilab Tevatron 34

2.2 Neutrino Beam 37

2.3 Detector and Trigger 40

2.3.1 Target Calorimeter 40
2.3.1.1 Scintillator Counters 41
2.3.1.2 Drift Chambers 46
2.3.2 Muon Spectrometer 49
2.4 Data Acquisition 52
2.4.1 Event Triggers 53
2.4.2 Data Collection 55
3 Calibration and Data Analysis **57**
3.1 Hadron Energy Measurement 57
3.1.1 Counter Gain Calibration 58
3.1.2 Map and Time Variation Corrections 61
3.1.3 Calorimeter Energy Calibration 64
3.1.4 Hadron Energy Calculation 71
3.2 Muon Angle and Momentum Measurement 75
3.2.1 Muon Tracking Procedure 76
3.2.2 Muon Angle Measurement 77
3.2.3 Muon Momentum Measurement 79
3.2.4 Muon Energy Calculation 82
3.3 Analysis Cuts 84
3.3.1 Fiducial-Volume Cuts 84
3.3.2 Geometric Cuts 85
3.3.3 Cross-section Cuts 86
3.3.4 Structure-Function Cuts 86
4 Correcting the Data **89**
4.1 Monte Carlo Corrections 90
4.1.1 Event Generation 91

4.1.2 Resolution Smearing 93
4.1.3 Muon Energy Loss 94
4.1.4 Event Re-weighting 96
4.1.4.1 Flux Re-weighting Correction 96
4.1.4.2 Dimuon Correction 96
4.1.5 Smearing, Acceptance, and Dimuon Correction 98
4.2 Physics Model Corrections 98
4.2.1 The Buras-Gaemers Model 99
4.2.1.1 Valence Densities 100
4.2.1.2 Sea Densities 102
4.2.1.3 R 104
4.2.1.4 Structure Functions and Buras-Gaemers Fits 105
4.2.1.5 Systematic Error in the Buras-Gaemers Model 108
4.2.2 Corrections to the Physical Cross-section 109
4.2.2.1 Isoscalar Correction 109
4.2.2.2 Radiative Correction 110
4.2.2.3 Charm Production Threshold 113
4.2.2.4 Propagator Correction 116
4.3 Bin-center Correction 116

5 Flux and Cross-Sections **118**

5.1 Flux Versus Energy: the Fixed-ν Method 118
5.1.1 Flux Extraction 121
5.1.2 Systematic Errors 134
5.1.2.1 Experimental Systematics 134
5.1.2.2 Model Systematics 141
5.1.2.3 Theoretical Systematics 141
5.2 Flux Versus Detector Vertex 143

5.3 Cross-Section Analysis 144
5.3.1 Results and Comparisons 144
5.3.2 The Partonic-Level Cross-Section 153
5.3.3 Deviations in the Cross-Section Measurement 155

6 Structure Functions **157**

6.1 Method of Structure-Function Extraction 157
6.1.1 Error Calculation 159
6.1.2 Strange Sea Correction 161
6.1.3 Large-*x* Events and the Monte Carlo 162
6.1.4 Alternate Extraction Methods 163
6.2 Implementing the Method 169
6.2.1 Structure-Function Cuts 170
6.2.2 Structure-Function Calculation 170
6.2.3 Combining Experiments 185
6.3 Iteration 186
6.4 Systematic Errors 188
6.4.1 Experimental Systematics 189
6.4.2 Flux-Extraction Systematics 190
6.4.3 Cross-section Systematics 191
6.4.4 Model Systematics 192
6.5 Results 193

7 QCD Comparisons **202**

7.1 The QCD Model 203
7.1.1 Initial Parton Distributions 204
7.1.2 Comments on Parton Sum Rules 205
7.1.2.1 The Fermion Conservation Rule 206

7.1.2.2 The Momentum Sum Rule 208
7.1.3 Evolution Equations 209
7.1.4 Hard-Scattering Integrals 211
7.1.5 Target Mass Correction 211
7.1.6 Higher-Twist Effects 212
7.1.7 Forming the χ^2 216
7.2 Tests of QCD 217
7.2.1 Fit Results 217
7.2.2 Logarithmic Slopes 227
7.2.3 Systematic Errors 229
7.3 Global Systematic Fits 235
8 Comparisons and Conclusions **245**
8.1 Structure-Function Comparisons 245
8.1.1 Comparison with CDHSW 245
8.1.2 Charged-Lepton Experiments 250
8.1.2.1 Heavy Target Correction 250
8.1.2.2 Quark-Charge Correction 251
8.1.2.3 Comparison Plots 252
8.1.2.4 Explaining the CCFR-NMC Discrepancy 261
8.2 QCD Comparisons 265
8.2.1 Comparing α_S From Different Experiments 265
8.2.2 Comparing $xG(x)$ From Different Experiments 270
8.3 Conclusions 272
Bibliography **274**
Appendix A: The CCFR/NuTeV Collaboration **286**

Appendix B: Accessing Analysis Results via the Internet **287**

B.1 Accessing the site via FTP 287

B.2 Accessing the site via a WWW browser 289

Appendix C: Program Source Code **290**

C.1 The Buras-Gaemers Code 290

C.2 The Structure-Function Extraction Code 295

C.3 The QCD Evolution Code 299

C.4 Higher-Twist Calculation 314

Appendix D: Structure-Function Tables **321**

D.1 Statistical and Systematic Errors 321

D.2 Separate E744 and E770 Results 322

D.3 Removing Physics-Model Corrections 322

D.4 Notes on the Use of the Structure-Function Tables 324

D.4.1 Using the Physics-Model Correction Tables 324

D.4.2 Correlated Errors 324

D.4.3 Correlations Between Point-to-Point Systematic Errors 325

Appendix E: Data versus Monte Carlo Plots **395**

Appendix F: Small Corrections to the Energy Calibration **426**

F.1 Corrections to the Hadron Energy Calibration 426

F.2 Relative Gain Correction 433

Appendix G: Parton Distribution Functions **437**

Appendix H: Article Submitted to *Physical Review Letters* **441**

Colophon **448**

List of Figures

Figure 1.1: Kinematic variables of deep-inelastic scattering 7

Figure 1.2: Possible helicity configurations for high-energy neutrinos and anti-neutrinos scattering from quarks and anti-quarks 15

Figure 1.3: The leading-order splitting function diagrams 26

Figure 1.4: The next-to-leading-order splitting function diagrams 26

Figure 2.1: Fermilab neutrino beamline layout 36

Figure 2.2: Tevatron magnet current versus time during fixed-target operation 37

Figure 2.3: Neutrino Center beamline 39

Figure 2.4: Schematic representation of the CCFR detector 40

Figure 2.5: A typical charged-current event as seen by the elements of the CCFR detector 41

Figure 2.6: Stack layout of a CCFR target cart 42

Figure 2.7: CCFR scintillation counter 43

Figure 2.8: Readout electronics for a single scintillation counter 45

Figure 2.9: Sketch of CCFR target drift chamber section 48

Figure 2.10: Schematic drawing of a CCFR toroid cart, showing overhead and transverse views 50

Figure 3.1: Muon energy loss distribution in a scintillation counter 59

Figure 3.2: Contours of the relative muon response for counter 37 63

Figure 3.3: Energy response of the CCFR calorimeter, relating MIPs to *GeV* 66

Figure 3.4: Energy distributions of 25 and 200 *GeV* hadrons from the 1987 calibration 67

Figure 3.5: The hadron shower energy resolution of the CCFR calorimeter from 25 to 240 *GeV* test beam calibrations 68

Figure 3.6: The *E/p* distribution for E744 range-out muons 70

Figure 3.7: A sketch of the expected generated versus measured *EHAD* distributions 73

Figure 3.8: Data versus Monte Carlo distributions for low *ENEU* and low *EHAD* 74

Figure 3.9: Muon momentum resolution function for 120 GeV muons 81

Figure 4.1: Radiative-correction diagram included in both the Bardin and the de Rujula calculations 111

Figure 4.2: Radiative-correction diagram included in the Bardin calculation 111

Figure 4.3: Radiative corrections due to Bardin and de Rujula vs. y 112

Figure 5.1: Effects of Monte-Carlo corrections in flux extraction 126

Figure 5.2: Effects of physics-model corrections in flux extraction 128

Figure 5.3: Kinematic map showing the region where quasi-elastic processes dominate the cross-section 129

Figure 5.4: The differential cross-section $d\sigma/d\nu$ in the low-y region for $E_\nu = 60\ GeV$ 129

Figure 5.5: A typical fit for B/A to the $dN/d\nu$ distribution 130

Figure 5.6: A typical fit for B/A to the $dN/d\bar{\nu}$ distribution 130

Figure 5.7: B/A as a function of energy for experiment E744 131

Figure 5.8: The correction due to B/A 132

Figure 5.9: The fully-corrected flux × energy spectra for E744 and E770 133

Figure 5.10: Effects of ±1% shift in E_μ 136

Figure 5.11: Effects of ±1% shift in E_{HAD} 137

Figure 5.12: Effects of $\pm 1\sigma$ shift in B/A 138

Figure 5.13: Effects of $\pm 1\sigma$ shift in m_c 139

Figure 5.14: Effects of the alternate model parameterization 140

Figure 5.15: Monte-Carlo corrections applied to the cross-section data 146

Figure 5.16: Physics-model corrections applied to the cross-section data 147

Figure 5.17: Results from the cross-section analysis 149

Figure 5.18: World status of neutrino-iron cross-section measurements 150

Figure 5.19: Partonic-level cross-sections, including all physics-model corrections 154

Figure 5.20: Flux adjustment factor $A(1+B)E_\nu \big/ \sigma^{\nu N}_{partonic}(E_\nu)$ 156

Figure 6.1: x_{GEN} for $0 < x_{SMR} < 0.02$ 164

Figure 6.2: x_{GEN} for $0.02 < x_{SMR} < 0.08$ 165

Figure 6.3: x_{GEN} for $0.08 < x_{SMR} < 0.20$ 166

Figure 6.4: x_{GEN} for $0.20 < x_{SMR} < 0.50$ 167

Figure 6.5: x_{GEN} for $0.5 < x_{SMR} < 0.9$ 168

Figure 6.6: The total corrections applied to neutrino events in the structure-function analysis 175

Figure 6.7: The total corrections applied to anti-neutrino events in the structure-function analysis 176

Figure 6.8: The acceptance corrections for neutrino events in the structure-function analysis 177

Figure 6.9: The acceptance corrections for anti-neutrino events in the structure-function analysis 178

Figure 6.10: The smearing corrections for neutrino events in the structure-function analysis 179

Figure 6.11: The smearing corrections for anti-neutrino events in the structure-function analysis 180

Figure 6.12: The physics-model corrections for neutrino events in the structure-function analysis 181

Figure 6.13: The physics-model corrections for anti-neutrino events in the structure-function analysis 182

Figure 6.14: The bin-center corrections for neutrino events in the structure-function analysis 183

Figure 6.15: The bin-center corrections for anti-neutrino events in the structure-function analysis 184

Figure 6.16: Diagram of the iterative analysis procedure 187

Figure 6.17: Structure function F_2 194

Figure 6.18: Structure function xF_3 195

Figure 6.19: Structure function F_2, displaying as many x-bins as possible on a common axis 196

Figure 6.20: The high-x bins of structure function F_2 197

Figure 6.21: Structure function xF_3, displaying as many x-bins as possible on a common axis 198

Figure 6.22: The high-x bins of structure function xF_3, ... 199

Figure 6.23: The high-x bins of structure functions F_2 and xF_3 superimposed to show $F_2(x>0.5) \approx xF_3(x>0.5)$ 200

Figure 6.24: F_2 and xF_3 averaged at $Q^2 = 12.6\,GeV^2$ 201

Figure 6.25: $(F_2 + xF_3)/2$ and $(F_2 - xF_3)/2$ averaged at $Q^2 = 12.6\,GeV^2$ 201

Figure 7.1: D_2 higher-twist term 214

Figure 7.2: D_4 higher-twist term 214

Figure 7.3: xF_3 D_2 higher-twist term 215

Figure 7.4: F_2 versus x in Q^2 bins 225

Figure 7.5: xF_3 versus x in Q^2 bins 226

Figure 7.6: QCD prediction of logarithmic slopes of xF_3 for various values of Λ 228

Figure 7.7: The logarithmic slopes of xF_3 228

Figure 7.8: The logarithmic slopes of F_2 229

Figure 8.1: A comparison of the values of xF_3 from the present analysis with those from the CDHSW experiment 247

Figure 8.2: A comparison of the values of F_2 from the present analysis with those from the CDHSW experiment 248

Figure 8.3: The xF_3 logarithmic slopes from the CCFR and CDHSW experiments 249

Figure 8.4: The F_2 logarithmic slopes from the CCFR and CDHSW experiments 249

Figure 8.5: Ratio of F_2 from heavy nuclear targets to deuterium from charged-lepton experiments 251

Figure 8.6: F_2 from the CCFR ν-Fe result compared to the F_2 from charged-lepton experiments for $x = 0.0075$, 0.0125, and 0.0175 254

Figure 8.7: F_2 from the CCFR ν-Fe result compared to the F_2 from charged-lepton experiments for $x = 0.025$, 0.035, and 0.050 255

Figure 8.8: F_2 from the CCFR ν-Fe result compared to the F_2 from charged-lepton experiments for $x = 0.070$, 0.090, and 0.110 256

Figure 8.9: F_2 from the CCFR ν-Fe result compared to the F_2 from charged-lepton experiments for $x = 0.140$, 0.180, and 0.225 257

Figure 8.10: F_2 from the CCFR ν-Fe result compared to the F_2 from charged-lepton experiments for $x = 0.275$, 0.350, and 0.450 258

Figure 8.11: F_2 from the CCFR ν-Fe result compared to the F_2 from charged-lepton experiments for $x = 0.550$, 0.650, and 0.750 259

Figure 8.12: F_2 logarithmic slopes from charged-lepton data and CCFR neutrino-iron data 260

Figure 8.13: Ratio of fits from charged-lepton data to CCFR neutrino-iron data 260

Figure 8.14: The strange sea from the CCFR NLO dimuon analysis compared with the strange sea from global fits 263

Figure 8.15: $\alpha_S(Q^2)$ for three different values of $\Lambda_{\overline{MS}}$ 266

Figure 8.16: $\alpha_S(M_Z^2)$ for several experiments, along with the average of the experiments shown 267

Figure 8.17: A comparison of gluon distributions to the CCFR result 271

Figure E.1: Data and Monte-Carlo hadron shower length distributions for $-1 < E_{HAD} < 40\ GeV$ 396

Figure E.2: Data and Monte-Carlo hadron shower length distributions for $E_{HAD} > 40\ GeV$ 397

Figure E.3: Resolution functions $\mathcal{F} = \left(1/p_{meas} - 1/p_{gen}\right)/\left(1/p_{gen}\right)$ for $0 < E_\mu < 60\ GeV$ 398

Figure E.4: Resolution functions $\mathcal{F} = \left(1/p_{meas} - 1/p_{gen}\right)/\left(1/p_{gen}\right)$ for $60 < E_\mu < 100\ GeV$ 399

Figure E.5: Resolution functions $\mathcal{F} = \left(1/p_{meas} - 1/p_{gen}\right)/\left(1/p_{gen}\right)$ for $100 < E_\mu < 180\ GeV$ 400

Figure E.6: Resolution functions $\mathcal{F} = \left(1/p_{meas} - 1/p_{gen}\right)/\left(1/p_{gen}\right)$ for $180 < E_\mu < 290\ GeV$ 401

Figure E.7: Resolution function $\mathcal{F} = \left(1/p_{meas} - 1/p_{gen}\right)/\left(1/p_{gen}\right)$ for $290 < E_\mu < 450\ GeV$ 402

Figure E.8: Resolution functions $\mathcal{F} = \left(1/p_{meas} - 1/p_{gen}\right)/\left(1/p_{gen}\right)$ for $E_\mu > 450\ GeV$ 403

Figure E.9: E744 data versus Monte Carlo for the variables E_ν and E_{HAD} 404

Figure E.10: E744 data versus Monte Carlo for the variables E_μ and θ_μ 405

Figure E.11: E744 data versus Monte Carlo for the variables x_{BJ} and y_{BJ} 406

Figure E.12: E744 data versus Monte Carlo for the variables $\log\left(Q^2\right)$ and the x-vertex 407

Figure E.13: E744 data versus Monte Carlo for the y-vertex and the vertex radius 408

Figure E.14: E744 data versus Monte Carlo for *PLACE* and ϕ 409

Figure E.15: E744 data versus Monte Carlo for x- and y-vertex at the T2 counter 410

Figure E.16: E744 data versus Monte Carlo for E_μ^{FF} and the hadron shower length (*PLACE–SHEND*) 411

Figure E.17: E744 data versus Monte Carlo for E_ν in the radial bins 0-10 *in* and 10-20 *in* 412

Figure E.18: E744 data versus Monte Carlo for E_ν in the radial bins 20-30 *in* and 30-40 *in* 413

Figure E.19: E744 data versus Monte Carlo for E_ν in the radial bins 40-50 *in* and 50-99 *in* 414

Figure E.20: E770 data versus Monte Carlo for the variables E_ν and E_{HAD} 415

Figure E.21: E770 data versus Monte Carlo for the variables E_μ and θ_μ 416

Figure E.22: E770 data versus Monte Carlo for the variables x_{BJ} and y_{BJ} 417

Figure E.23: E770 data versus Monte Carlo for the variables $\log\left(Q^2\right)$ and the x-vertex 418

Figure E.24: E770 data versus Monte Carlo for the y-vertex and the vertex radius 419

Figure E.25: E770 data versus Monte Carlo for *PLACE* and ϕ 420

Figure E.26: E770 data versus Monte Carlo for x- and y-vertex at the T2 counter 421

Figure E.27: E770 data versus Monte Carlo for E_μ^{FF} and the hadron shower length (*PLACE–SHEND*) 422

Figure E.28: E770 data versus Monte Carlo for E_ν in the radial bins 0-10 *in* and 10-20 *in* 423

Figure E.29: E770 data versus Monte Carlo for E_ν in the radial bins 20-30 *in* and 30-40 *in* 424

Figure E.30: E770 data versus Monte Carlo for E_ν in the radial bins 40-50 *in* and 50-99 *in* 425

Figure F.1: Relative gain versus counter number 436

Figure G.1: A comparison of the valence distributions from leading-order, next-to-leading-order, and global fits 438

Figure G.2: A comparison of the sea distributions from leading-order, next-to-leading-order, and global fits 439

Figure G.3: A comparison of the gluon distributions from next-to-leading-order and global fits 439

Figure G.4: A comparison of the strange distributions from next-to-leading-order and leading-order analyses, and from global fits 440

Figure G.5: A comparison of the charm distributions from global fits 440

List of Tables

Table 1.1: The quarks and leptons, constituents of matter 3

Table 1.2: Interactions in the Standard Model 4

Table 1.3: The number of parameters in the minimal Standard Model 5

Table 2.1: Triggers written to tape in E744 and E770 56

Table 3.1: CCFR calorimeter calibration constants 71

Table 3.2: Muon Angular Resolution 78

Table 3.3: Number of events passing each of the analysis cuts 88

Table 4.1: Set of parameters for parton densities used as input to the Monte Carlo 106

Table 4.2: Set of parameters for parton densities from fit to final structure functions ... 107

Table 4.3: Error matrix from MINUIT fit to final structure functions using the Buras-Gaemers parameterization 107

Table 5.1: Number of events passing the cross-section cuts as a function of E_{HAD} 122

Table 5.2: Number of events passing flux cuts 123

Table 5.3: Number of flux events in each energy bin 125

Table 5.4: $\langle B/A \rangle$ from the flux analysis 131

Table 5.5: Results from the cross-section analysis 148

Table 5.6: The ratio $\sigma^{\bar{\nu}}/\sigma^{\nu}$ measured in two energy ranges 151

Table 5.7: World average values of isoscalar-corrected $\sigma^{\nu N}/E$, $\sigma^{\bar{\nu}N}/E$, and $\sigma^{\bar{\nu}}/\sigma^{\nu}$ (including this experiment) for the energy range 30-200 GeV 153

Table 6.1: Number of events passing structure-function cuts 171

Table 7.1: Results of QCD fits to the structure functions 219

Table 7.2: Error matrix σ_{ij} from the xF_3-only fit 219

Table 7.3: Correlation coefficients $(\sigma_{ij})/(\sigma_{ii}\sigma_{jj})^{1/2}$ from the xF_3-only fit 220

Table 7.4: Error matrix σ_{ij} from the combined F_2 and xF_3 fit 220

Table 7.5: Correlation coefficients $(\sigma_{ij})/(\sigma_{ii}\sigma_{jj})^{1/2}$ from the combined F_2 and xF_3 fit 220

Table 7.6: QCD fit results as a function of the Q^2 cut on the data and the Q_0^2 of the evolution 221

Table 7.7: QCD fit results as a function of the x cut on the data 221

Table 7.8: QCD fit results for xF_3-only fits for different functional forms of q_{NS} 223

Table 7.9: The values for one alternate parameterization of the parton distributions..... 224

Table 7.10: Systematic quantities and their $+1\delta$ variations 231

Table 7.11: Variations in QCD fit results due to positive and negative systematic shifts 232

Table 7.12: Statistical and average systematic errors in QCD fit results 233

Table 7.13: Results from separate QCD fits to experiments E744 and E770 234

Table 7.14: Results of the global systematic QCD fit 238

Table 7.15: The error matrix σ_{ij} from the xF_3-only global systematic fit 239

Table 7.16: Correlation coefficients $\left(\sigma_{ij}\right)\Big/\left(\sigma_{ii}\sigma_{jj}\right)^{1/2}$ for the xF_3-only global systematic fit 240

Table 7.17: The error matrix σ_{ij} from the combined F_2 and xF_3 global systematic fit 241

Table 7.18: Correlation coefficients $\left(\sigma_{ij}\right)\Big/\left(\sigma_{ii}\sigma_{jj}\right)^{1/2}$ for the combined F_2 and xF_3 global systematic fit 242

Table 7.18: Comparison of $\Lambda_{\overline{\mathrm{MS}}}^{\mathrm{NLO}}$ from the basic fit and the global systematic fit 244

Table D.1: F_2, xF_3, and their associated statistical errors 327

Table D.2: F_2 energy-calibration systematic errors 331

Table D.3: xF_3 energy-calibration systematic errors 335

Table D.4: F_2 flux-extraction systematic errors 339

Table D.5: xF_3 flux-extraction systematic errors 343

Table D.6: F_2 cross-section systematic errors 347

Table D.7: xF_3 cross-section systematic errors 351

Table D.8: F_2 physics-model systematic errors 355

Table D.9: xF_3 physics-model systematic errors 359

Table D.10: F_2, xF_3, and the associated statistical errors from E744 only 363

Table D.11: F_2, xF_3, and the associated statistical errors from E770 only 367

Table D.12: Systematic errors for E744 F_2 371

Table D.13: Systematic errors for E770 F_2 375

Table D.14: Systematic errors for E744 xF_3 379

Table D.15: Systematic errors for E770 xF_3 383

Table D.16: F_2(without model correction) / F_2(with correction) 387

Table D.17: xF_3(without model correction) / xF_3(with correction) 391

Table F.1: Relative gain averaged over calorimeter carts 435

1 Introduction

The science of physics is the study of matter in the universe. Broadly speaking, this study is divided into two tasks: identifying what kinds of matter exist, and understanding the properties of the different types of matter. This thesis presents a study of one of the most common particles of matter in the visible universe: the proton. Specifically, it addresses an important relationship between the components of matter that make up the proton: the quarks and the gluons.

The physical process on which this analysis is based is called "neutrino-nucleon deep-inelastic scattering." In a scattering experiment, a target composed of one type of particle is exposed to a beam. The particles in the beam are said to "scatter" off of the particles that make up the target. The formula that describes this interaction is

$$\nu_\mu + N \rightarrow \mu + X \tag{1.1}$$

The symbol ν refers to the neutrino, which is a light, neutral, weakly-interacting particle; the subscript μ implies that the neutrino is of a particular type: the muon neutrino. The symbol N represents a nucleon, either a proton or a neutron, in the nucleus of an atom. One product of this interaction is a muon, designated by the symbol μ. It is the transformation of the neutral neutrino to a charged muon that labels the event as a "charged-current" event; if the charge of the neutrino remained unchanged as a result of the interaction, it would be a "neutral-current" event. The other result of the interaction is a shower of particles known as hadrons, which result from the break-up of the proton due to the energy transferred to the proton by the incoming neutrino. It is the "hadron shower" that labels the event as "deep-inelastic scattering," since in elastic scattering the proton remains intact.

This introductory chapter provides the context for the rest of the thesis. The Standard Model of particle physics is described, introducing the quarks and leptons—the constituents of all matter—and the forces by which they interact. The kinematic variables that define the interaction of Equation 1.1 are described. Next, the formalism of deep-inelastic scattering is discussed, starting with the definition of the structure functions in terms of the Standard Model of electroweak interactions, and then connecting the measured structure functions with the theory of Quantum Chromodynamics. The chapter concludes with an overview of the structure-function analysis and this thesis.

1.1 The Standard Model

Over the last three decades, experimental and theoretical efforts in the field of particle physics developed a paradigm known as the Standard Model, which includes the unified theory of electroweak interactions [Wei67, Sal68] along with Quantum Chromodynamics (QCD) [Ynd93], the theory of strong interactions. The sample of charged-current events presented in this thesis are analyzed using the Standard Model, and the theory is shown to be consistent with the data. A fundamental parameter of the Standard Model, the strong coupling constant α_S, is measured in this analysis.

In the Standard Model, all fundamental interactions occur between quarks and leptons, which are fermions, through the exchange of gauge particles, which are bosons. This theoretical edifice has been successful in explaining the ever-growing number of experiments that have been performed to study it. A complete introduction to the Standard Model may be found in textbooks [Per82, Hal84] and only a brief description of the Standard Model follows.

Table 1.1: The quarks and leptons, constituents of matter.

	Charge (units of electron charge)	First Generation	Second Generation	Third Generation
Quarks	+2/3	up (u)	charm (c)	top (t)
	–1/3	down (d)	strange (s)	bottom (b)
Leptons	–1	electron (e)	muon (μ)	tau (τ)
	0	e-neutrino (ν_e)	μ-neutrino (ν_μ)	τ-neutrino (ν_τ)

The fermions of the Standard Model are listed in Table 1.1, where they are grouped into three generations. Each entry in Table 1.1 represents a different "flavor" of particle. Ordinary terrestrial matter is made of particles from the first generation: protons and neutrons carry net up and down quantum numbers, electrons orbit the nuclei of atoms, and electron-(anti)-neutrinos are emitted in nuclear beta decay. The higher-mass fermions of the second and third generations are present in the high-energy environments produced by cosmic rays and particle accelerators. All of the fermions have antimatter partners, which have the same mass but opposite quantum numbers. Of the particles listed, only the ν_τ has not yet been directly observed through their interaction with other matter.

The fermions interact through the exchange of gauge bosons. The mediators of each of the four forces are listed in Table 1.2. All the fermions interact weakly, through the exchange of the Z^0 and $W^\pm$ bosons, known as the intermediate gauge bosons. Electrically-charged particles—that is, all fermions other than the neutrinos—interact electromagnetically, through the exchange of photons. Finally, quarks alone interact strongly and therefore they alone are the fermions that carry strong (or color) charge. Quarks interact strongly by exchanging gluons. Gravity affects all particles, and its carrier is assumed to be the graviton. However, when considering interactions of elementary particles, the effects of gravity are negligible, and gravity is not discussed further.

Table 1.2: Interactions in the Standard Model. The relative strengths of the forces are roughly indicated, for short distance scales of a few *GeV*.

Interaction	Relative strength	Mediator	Participating fermions
strong	1	gluon (g)	quarks
electromagnetic	10^{-2}	photon (γ)	quarks and charged leptons
weak	10^{-5}	Z^0 and $W^{\pm}$	all
gravitational	10^{-42}	graviton (G)	all

The ultimate validity of the Standard Model rests in its ongoing confirmation by experimental data. Up to now, the confirmation has been excellent, and there is no compelling evidence for physics beyond the Standard Model. However, the Standard Model leaves some questions unanswered. For example, the Standard Model has 19 input parameters, which are listed in Table 1.3. Precise measurements of these parameters check the self-consistency of the theory, but offer no insight into the parameters themselves. Physicists expect that an elegant theory beyond the Standard Model would not require such a large number of parameters. Furthermore, the Standard Model does not explain the number of fermions or the generational hierarchy of the quarks and leptons, nor offers any reason for the symmetry that seems to exist between the quark and lepton sectors. And although the Standard Model accommodates CP (charge-conjugation and parity) violating interactions, it offers no explanation of them.

A few mandatory empirical tests of the Standard Model are yet to be completed, most notably the detection of the Higgs particle. Precise measurements of Standard Model parameters may uncover the first discrepancy between the model and observation. However well-established our current Standard Model, there is a need to go beyond it, to explain the questions it cannot answer. New physics may emerge as new generations of

Table 1.3: The number of parameters in the minimal Standard Model. The neutrinos, photons, and gluons are massless.

Type of parameter	Number of parameters
quark masses	6
charged lepton masses	3
CKM mixings	4
Z^0 and $W^{\pm}$ masses	2
Higgs particle mass	1
α_{em} electromagnetic coupling	1
G_F weak coupling	1
α_S strong coupling	1
TOTAL	19

accelerators probe shorter distances and higher energies, or as experiments push existing limits with more precise measurements.

1.2 Neutrino-Nucleon Scattering

Neutrinos make excellent probes for studying the structure of hadrons. They are structureless particles and their electroweak interactions are well understood. Neutrinos are always polarized, and are therefore uniquely suited for studies of the helicity-dependent dynamics of the nucleon constituents.

The Standard Model describes the phenomenology of deep-inelastic scattering well. At high energy, deep-inelastic neutrino-nucleon scattering is interpreted as elastic neutrino-parton scattering. Nucleon structure at high momentum transfers is characterized by parton distribution functions, which describe the nucleon in terms of quarks and gluons using the factorization theorems of Quantum Chromodynamics (QCD) [Sop89]. This

Section introduces the formalism used to describe nucleon structure in terms of parton distributions.

The process of probing the nucleon with neutrinos begins by using the inclusive charged-current data sample to measure the nucleon's structure functions. The structure functions are a complete set of Lorentz scalars that parameterize the unknown structure of the proton. The properties of the structure functions lead to the parton model, which proposes that the nucleon is composed of point-like constituents, partons, that scatter elastically with the neutrino. Finally, the partons are identified with the quarks and gluons of QCD, and QCD describes the parton dynamics. A QCD analysis of the structure function measurements provides a determination of the nucleon's valence and sea quark distributions and gluon distribution, along with a determination of α_S.

1.2.1 The Kinematics of a Charged-Current Neutrino Event

Three kinematic parameters provide a full description of a deep-inelastic scattering event. In this experiment, the three measured parameters of a charged-current event are the muon momentum, p_μ, the angle of the outgoing muon, θ_μ, and the observed energy of the outgoing hadrons, E_{HAD}. From these measured parameters it follows that the neutrino energy is $E = E_\nu = E_{HAD} + E_{\mu^-} + M$.

The kinematic variables of deep-inelastic scattering are shown in Figure 1.1. The lepton is designated by four-momentum k, the hadron system by momentum p, and after scattering their four-momenta are designated by k' and p', respectively. In terms of the experimental quantities each of these four-momenta in the lab system are (M is the mass of the nucleon):

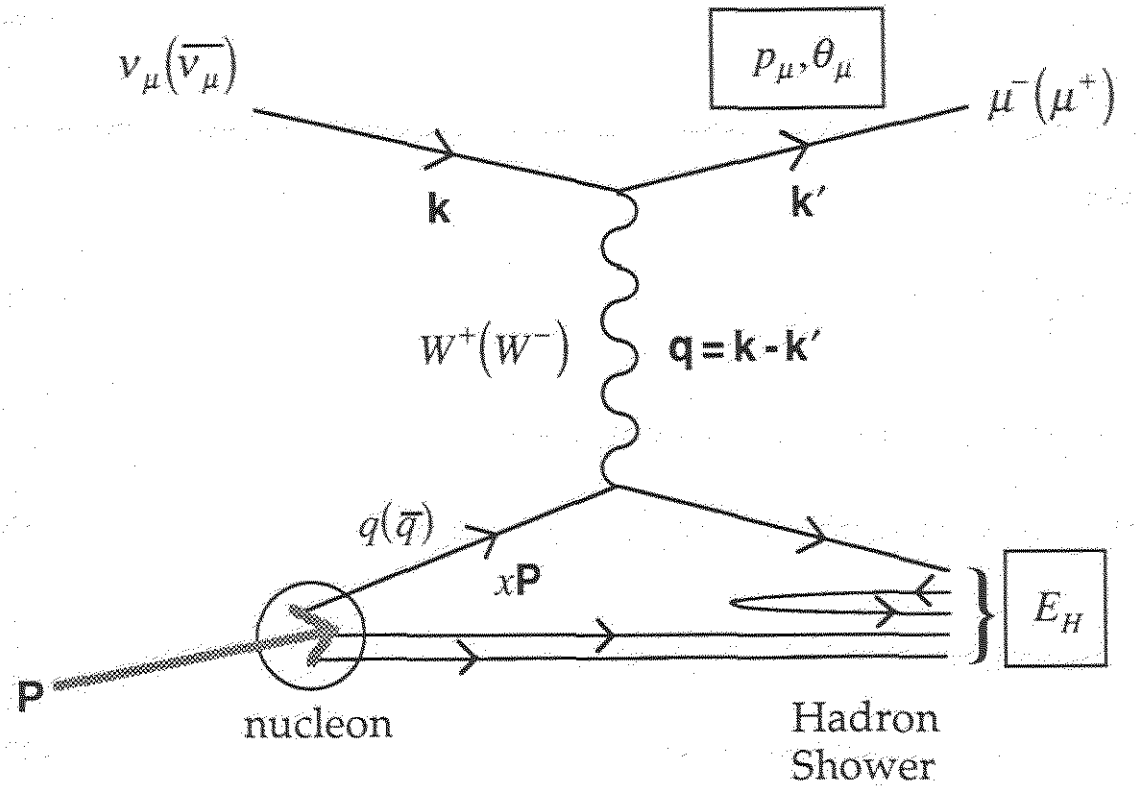

Figure 1.1: Kinematic variables of deep-inelastic scattering. A point-like constituent of the nucleon, a parton, carries a fraction x of the nucleon's momentum p. The measured experimental quantities are enclosed in rectangles.

$$k = \left(E_\nu, 0, 0, E_\nu\right) \tag{1.2}$$

$$k' = \left(E_\mu, p_\mu \sin\theta_\mu \cos\phi_\mu, p_\mu \sin\theta_\mu \sin\phi_\mu, p_\mu \cos\theta_\mu\right) \tag{1.3}$$

$$p = (M, 0, 0, 0) \tag{1.4}$$

$$p' = p + q = p + (k + k') \tag{1.5}$$

Lorentz-invariant variables commonly used to describe deep-inelastic scattering are derived as follows.

The square of the center of mass energy:

$$s = (p+k)^2 = M^2 + 2ME \tag{1.6}$$

The energy transferred to the hadronic system (the mass of the unobserved baryon is neglected):

$$\nu = \frac{p \cdot q}{M} = E_\nu - E_\mu = E_{HAD} \tag{1.7}$$

The negative square of the four-momentum transfer:

$$Q^2 = -q^2 = -(k-k')^2 = m_\mu^2 + 2E_\nu\left(E_\mu - p_\mu \cos\theta_\mu\right) \tag{1.8}$$

The invariant mass of the hadronic system:

$$W^2 = (p')^2 = (p+q)^2 = M^2 + 2M\nu - Q^2 \tag{1.9}$$

The Bjorken scaling variable, which represent the fractional momentum of the struck parton within the nucleon:

$$x = \frac{-q^2}{2p \cdot q} = \frac{Q^2}{2M\nu} \tag{1.10}$$

The inelasticity:

$$y = \frac{p \cdot q}{p \cdot k} = \frac{E_{HAD}}{E_\nu} \tag{1.11}$$

The inelasticity y is directly related to the lepton scattering angle θ^* in the center-of-mass frame:

$$y \approx 1 - \frac{1}{2}\left(1 + \cos\theta^*\right) \tag{1.12}$$

1.2.2 The Formalism of Deep-Inelastic Scattering

In this section the relationship between the structure functions and the neutrino-hadron cross-section is derived. The matrix element for the neutrino-hadron interaction can be written as [Rob90]:

$$\mathcal{M} = \frac{G_F}{\sqrt{2}} \frac{1}{1+Q^2/M_W^2} \underbrace{\bar{u}_\mu(k',s')\gamma_\alpha\left(1-\gamma_5\right)u_{\bar{\nu}}(k,s)}_{\text{lepton}} \underbrace{\left\langle X \middle| J_{CC} \middle| N;p,s \right\rangle}_{\text{hadron}} \tag{1.13}$$

where G_F is the weak coupling constant, M_W is the mass of the W-boson, (k,s) is the four-momentum and helicity of the incoming neutrino, (k',s') is the four-momentum and helicity of the outgoing muon, (p,s) is the four-momentum and helicity of the target nucleon, and $\bar{u}_\mu$ and $u_{\bar{\nu}}$ are the lepton spinors. The inclusive, spin-averaged cross-section proportional to $|\mathcal{M}|^2$ takes the form

$$\frac{d^2\sigma^{\nu N}}{d\Omega_\mu dE_\mu} = \frac{1}{\left(1+Q^2/M_W^2\right)^2} \frac{G_F^2}{2} \frac{m_\nu}{E_\nu} \frac{m_\mu}{E_\mu} \frac{E_\mu^2}{(2\pi)^2} L_{\alpha\beta} W^{\alpha\beta} \tag{1.14}$$

where E_ν and E_μ are the energies of the incident neutrino and final-state muon in the lab frame (nucleon at rest), and Ω is the solid angle into which the scattered muon lies. The leptonic tensor $L_{\alpha\beta}$ is given by

$$\begin{aligned} L_{\alpha\beta} &= \sum_{s,s'} \bar{u}_\mu(k',s')\gamma_\alpha(1-\gamma_5)u_\nu(k,s)\bar{u}_\nu(k,s)\gamma_\beta(1-\gamma_5)u_\mu(k',s') \\ &= \frac{2}{m_\nu m_\mu}\left[k'_\alpha k_\beta + k'_\beta k_\alpha - k\cdot k' g_{\alpha\beta} \mp i k^\gamma k'^\delta \varepsilon_{\gamma\delta\alpha\beta}\right] \end{aligned} \tag{1.15}$$

where the –(+) term applies to incident neutrinos (anti-neutrinos). The hadronic tensor $W^{\alpha\beta}$ is a second-rank tensor that parameterizes the unknown structure of the boson-

nucleon vertex. There are only two independent vectors upon which $W^{\alpha\beta}$ can depend: p and q. Therefore the most general rank-2 tensor that can be constructed out of these two vectors is

$$\begin{aligned} W^{\alpha\beta} = & -g^{\alpha\beta}W_1 + \frac{p^\alpha p^\beta}{M^2}W_2 - \frac{i\varepsilon^{\alpha\beta\gamma\delta}p_\gamma q_\delta}{2M^2}W_3 \\ & + \frac{q^\alpha q^\beta}{M^2}W_4 + \frac{\left(p^\alpha q^\beta + p^\beta q^\alpha\right)}{M^2}W_5 \\ & + \frac{i\left(p^\alpha q^\beta - p^\beta q^\alpha\right)}{2M^2}W_6 \end{aligned} \tag{1.16}$$

where the *structure functions* W_i are real functions that depend only on q^2 and $p \cdot q$. In the limit of negligible quark masses,

$$q^\alpha L_{\alpha\beta} = q^\beta L_{\alpha\beta} = 0 \tag{1.17}$$

so that terms proportional to q^α or q^β in $W^{\alpha\beta}$ can be ignored; these are the coefficients of W_4, W_5, and W_6. After contracting the lepton and hadron tensors, Equation 1.14 becomes (neglecting Q^2/M_W^2 and lepton masses):

$$\frac{d^2\sigma^{\nu(\bar{\nu})N}}{d\Omega\, dE_\mu} = \frac{G_F^2}{2\pi^2}E_\mu^2\begin{bmatrix} \cos^2\frac{\theta}{2}W_2^{\nu(\bar{\nu})N} + 2\sin^2\frac{\theta}{2}W_1^{\nu(\bar{\nu})N} \\ \pm\frac{E_\nu + E_\mu}{M}\sin^2\frac{\theta}{2}W_3^{\nu(\bar{\nu})N} \end{bmatrix} \tag{1.18}$$

where the +(–) term corresponds to neutrino (anti-neutrino) scattering. In general, the structure functions $W_i\left(q^2, p\cdot q\right)$ depend on the target and may depend as well on the neutrino helicity. In terms of the absorption cross-sections for left-handed, right-handed, and scalar W bosons (σ_L, σ_R, σ_S) the structure functions can be written as:

$$W_1 = \frac{K}{\pi G_F \sqrt{2}}\left(\sigma_R + \sigma_L\right) \tag{1.19}$$

$$W_2 = \frac{K}{\pi G_F \sqrt{2}} \frac{Q^2}{Q^2 + \nu^2}\left(\sigma_R + \sigma_L + 2\sigma_S\right) \tag{1.20}$$

$$W_3 = \frac{K}{\pi G_F \sqrt{2}} \frac{2M}{\sqrt{Q^2 + \nu^2}}\left(\sigma_R - \sigma_L\right) \tag{1.21}$$

where K represents the flux of virtual Ws. While there is some arbitrariness in the definition of K, the ratio of absorption cross-sections for longitudinally- to transversely-polarized bosons is well-defined:

$$R(\nu, Q^2) \equiv \frac{\sigma_S}{\sigma_T} = \frac{W_2}{W_1}\left(1 - \frac{\nu^2}{Q^2}\right) - 1 \tag{1.22}$$

In terms of the scaling variables x, y, and Q^2, Equation (1.18) becomes

$$\frac{d^2\sigma^{\nu(\bar{\nu})}}{dx\,dQ^2} = \frac{G_F^2}{2\pi x} E_\mu^2 \left[\left(1 - y - \frac{Mxy}{2E}\right) W_2^{\nu(\bar{\nu})} + y^2 x W_1^{\nu(\bar{\nu})} \pm y\left(1 - \frac{y^2}{2}\right) x\nu W_3^{\nu(\bar{\nu})}\right] \tag{1.23}$$

In the modern structure-function notation,

$$2xMW_1(\nu, Q^2) = 2xF_1(x, Q^2) \tag{1.24}$$

$$\nu W_2(\nu, Q^2) = F_2(x, Q^2) \tag{1.25}$$

$$x\nu W_3(\nu, Q^2) = xF_3(x, Q^2) \tag{1.26}$$

and so the differential cross-section takes the form

$$\frac{d^2\sigma^{\nu(\bar{\nu})}}{dx\,dy} = \frac{G_F^2 ME}{\pi}\left[\left(1-y-\frac{Mxy}{2E}\right)F_2^{\nu(\bar{\nu})} + \frac{y^2}{2}2xF_1^{\nu(\bar{\nu})} \pm y\left(1-\frac{y^2}{2}\right)\nu F_3^{\nu(\bar{\nu})}\right] \quad (1.27)$$

and

$$R(x,Q^2) = \frac{F_2}{2xF_1}\left(1-\frac{Q^2}{(2Mx)^2}\right)-1 \quad (1.28)$$

Equation 1.27 is the master equation of deep-inelastic neutrino and anti-neutrino scattering. It is the point where theory and experiment meet. That is, measurement of the deep inelastic differential cross-section is equivalent to a measurement of the structure functions. The structure functions contain all that can be known about the structure of the nucleon from deep-inelastic scattering.

R has been measured by other experiments and, in this analysis, the value of R used comes from a parameterization of the world's available data [Whi90b]. Hence Equation 1.27 can be expressed in terms of two unknown, measurable structure functions F_2 and xF_3:

$$\frac{d^2\sigma^{\nu(\bar{\nu})}}{dx\,dy} = \frac{G_F^2 ME}{\pi}\left[\begin{array}{l}\left(1-y-\frac{Mxy}{2E}+\frac{y^2}{2}\frac{1+4M^2x^2/Q^2}{1+R(x,Q^2)}\right)F_2^{\nu(\bar{\nu})} \\ \pm y\left(1-\frac{y^2}{2}\right)\nu F_3^{\nu(\bar{\nu})}\end{array}\right] \quad (1.29)$$

This is the form of the differential cross-section used to extract the structure functions.

1.2.3 The Parton Model

The first experimental evidence that the proton is made of point-like constituents came from the large-Q^2 behavior of the structure functions. If two structureless particles scatter, the point "structure functions" are

$$2MW_1^{\text{point}}(\nu,Q^2)=\frac{Q^2}{2M\nu}\delta\left(1-\frac{Q^2}{2M\nu}\right) \tag{1.30}$$

$$\nu W_2^{\text{point}}(\nu,Q^2)=\delta\left(1-\frac{Q^2}{2M\nu}\right) \tag{1.31}$$

which have the property of being functions of a single dimensionless quantity, $Q^2/2M\nu$. Therefore, if large-Q^2 scattering begins to resolve point-like constituents inside the nucleon, the structure functions will begin to depend on a single dimensionless variable:

$$\lim_{\substack{Q^2\to\infty \\ x \text{ fixed}}} F_i(x,Q^2)=F_i(x) \tag{1.32}$$

This phenomenon is known as Bjorken scaling [Bjo69]. Early deep-inelastic scattering data verified that the structure functions become roughly independent of Q^2 above Q^2 = 1 GeV^2, in sharp contrast to the elastic form factors, which are strongly Q^2 dependent, falling like $1/Q^2$ below $Q^2=0.7\ GeV^2$.

Scaling of structure functions at high Q^2 is explained by the parton model. In this model, the nucleon is assumed to consist of point-like constituent partons. The deep-inelastic scattering environment is described by a highly relativistic frame, the "infinite momentum frame." In this highly-boosted frame, quarks interact among themselves on a

time scale much longer than that of the collision, so the scattering is incoherent. Inelastic neutrino-nucleon scattering reduces to elastic scattering from free, individual partons. The partons are on-shell, the travel collinearly with the nucleon, and carry a fraction x of its momentum.

Elastic scattering of point particles depends only on the center-of-mass energy and the net angular momentum of the system. Neutrinos are left-handed and anti-neutrinos are right-handed. Considering spin-1/2 and spin-0 constituents in the nucleon, the possible helicity-dependent cross-sections for elastic neutrino-parton scattering are given by

$$\text{total spin } 0: \frac{d\sigma^{\nu q}}{d\cos\theta^*} = \frac{d\sigma^{\bar{\nu}\bar{q}}}{d\cos\theta^*} = \frac{G^2 ME_\nu}{\pi\left(1+Q^2/M_W^2\right)^2} \tag{1.33}$$

$$\text{total spin } 1: \frac{d\sigma^{\nu\bar{q}}}{d\cos\theta^*} = \frac{d\sigma^{\bar{\nu}q}}{d\cos\theta^*} = \frac{G^2 ME_\nu}{\pi\left(1+Q^2/M_W^2\right)^2}\left(\frac{1+\cos\theta^*}{2}\right)^2 \tag{1.34}$$

$$\text{total spin } \frac{1}{2}: \frac{d\sigma^{\nu k}}{d\cos\theta^*} = \frac{d\sigma^{\bar{\nu}k}}{d\cos\theta^*} = \frac{2G^2 ME_\nu}{\pi\left(1+Q^2/M_W^2\right)^2}\left(\frac{\cos\theta^*}{2}\right)^2 \tag{1.35}$$

where θ^* is the muon's center-of-mass scattering angle. The superscripts identify the spin-1/2 partons with the quarks and anti-quarks. In principle, a spin-0 constituent may also be present, which is identified by the superscript k. As shall be seen, while the neutrino does not directly interact with a spin-0 component, the $p_\perp$ of the quark gives rise to an effective spin-0 component of the cross-section. The V–A structure of the weak interaction causes parity to maximally violated, so for massless partons only left-handed particles and right-handed anti-particles participate. Therefore, the four possible helicity configurations for high-energy neutrino-quark scattering are shown in Figure 1.2.

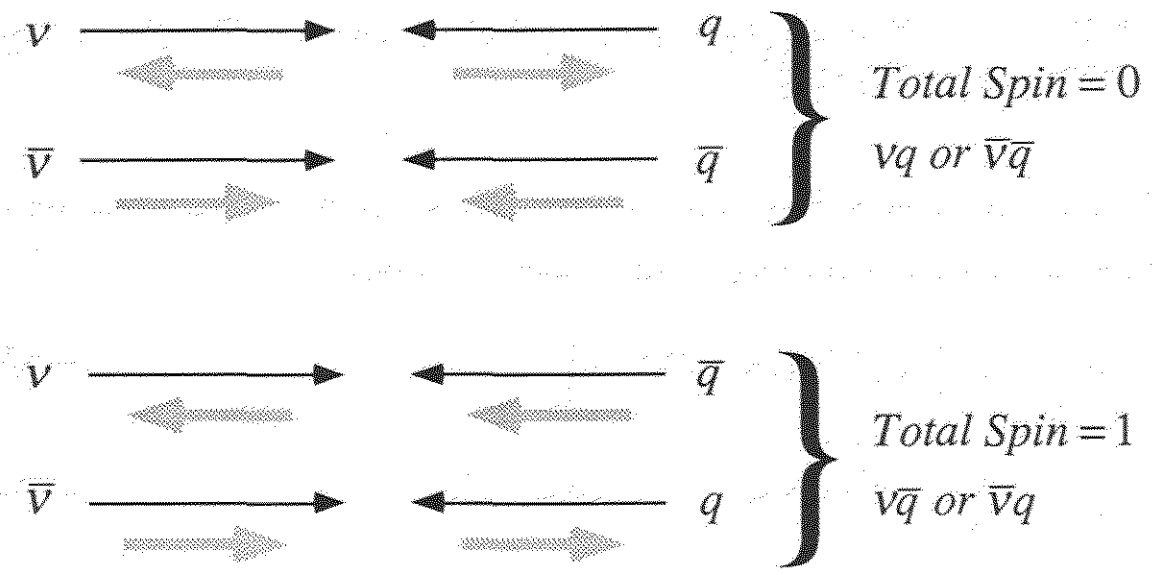

Figure 1.2: Possible helicity configurations for high-energy neutrinos and anti-neutrinos scattering from quarks and anti-quarks.

The probability of scattering from a particular type of parton is introduced with a parton distribution function $p(x)$. The quantity $p(x)dx$ is interpreted as the probability of finding a parton of type p in a hadron carrying a fraction x to $x + dx$ of the hadron's momentum. Then using the parton momentum distribution function $xp(x)$, the differential cross-section for scattering off one parton is

$$\frac{d^2\sigma}{dx\,dy} \propto \frac{G^2\,2ME}{\pi\left(1+Q^2/M_W^2\right)^2}xp(x) \tag{1.36}$$

and gathering all contributions from the constituents of a target T, the cross-sections for neutrino and anti-neutrino scattering are

$$\frac{d^2\sigma^{\nu T}}{dx\,dy} = \frac{G^2xs}{\pi\left(1+Q^2/M_W^2\right)^2}\left[q^{\nu T}(x)+(1-y)^2\bar{q}^{\nu T}(x)+2(1-y)k^{\nu T}(x)\right] \tag{1.37}$$

$$\frac{d^2\sigma^{\overline{\nu}T}}{dx\,dy} = \frac{G^2 xs}{\pi\left(1+Q^2/M_W^2\right)^2}\left[\overline{q}^{\overline{\nu}T}(x)+(1-y)^2 q^{\overline{\nu}T}(x)+2(1-y)k^{\overline{\nu}T}(x)\right] \tag{1.38}$$

The parton distributions are associated with the structure functions by comparing the y dependencies of the above formulas with Equation 1.27, yielding

$$2xF_1^{\nu(\overline{\nu})T} = 2\left[xq^{\nu(\overline{\nu})T}(x)+x\overline{q}^{\nu(\overline{\nu})T}(x)\right] \tag{1.39}$$

$$F_2^{\nu(\overline{\nu})T} = 2\left[xq^{\nu(\overline{\nu})T}(x)+x\overline{q}^{\nu(\overline{\nu})T}(x)+2xk^{\nu(\overline{\nu})T}\right] \tag{1.40}$$

$$xF_3^{\nu(\overline{\nu})T} = 2\left[xq^{\nu(\overline{\nu})T}(x)-x\overline{q}^{\nu(\overline{\nu})T}(x)\right] \tag{1.41}$$

where the Q^2/M_W^2 and $Mxy/2E$ terms have been neglected. Thus, in the parton model, deep-inelastic structure functions are simply related to the momentum fractions of the partons in the target.

If the scattering were to take place exclusively from free spin-1/2 constituents, the Callan-Gross relation

$$2xF_1 = F_2 \tag{1.42}$$

would be satisfied. However, at available energies, partons have non-negligible transverse momenta, which gives them apparent spin-0 behavior in the infinite-momentum-frame formalism. This leads to a difference between F_2 and $2xF_1$ that diminishes at higher Q^2.

The analogous expressions for electromagnetic charged-lepton scattering follow from the pure vector nature of the electromagnetic current. While neutrino scattering measures the helicity content of the nucleon, electromagnetic scattering measures the charge content:

$$2xF_1^{\ell T} = \sum_i e_i^2 \left[xq_i^{\ell T} + x\bar{q}_i^{\ell T} \right] \tag{1.43}$$

$$F_2^{\ell T} = \sum_i e_i^2 \left[xq_i^{\ell T} + x\bar{q}_i^{\ell T} + xk_i^{\ell T} \right] \tag{1.44}$$

where e_i is parton i's electric charge. There is no equivalent to the xF_3 term in electromagnetic interactions.

Neutrino scattering has the ability to resolve the flavor of the nucleon's constituents. The charge-current interaction changes the flavor of the struck quark, and conservation of charge at the quark vertex limits neutrinos to scatter from d, s, $\bar{u}$, and $\bar{c}$ quarks, and anti-neutrinos to scatter from $\bar{d}$, $\bar{s}$, u, and c quarks. Considering a parton target, the quark densities that contribute to the structure functions are

$$q^{\nu p}(x) = d^p(x) + s^p(x) \tag{1.45}$$

$$\bar{q}^{\nu p}(x) = \bar{u}^p(x) + \bar{c}^p(x) \tag{1.46}$$

$$q^{\bar{\nu} p}(x) = u^p(x) + c^p(x) \tag{1.47}$$

$$\bar{q}^{\bar{\nu} p}(x) = \bar{d}^p(x) + s^p(x) \tag{1.48}$$

Strong isospin invariance demands a symmetry between the proton and the neutron light quark densities:

$$d(x) \equiv d^p(x) = u^n(x) \tag{1.49}$$

$$\bar{d}(x) \equiv \bar{d}^p(x) = \bar{u}^n(x) \tag{1.50}$$

$$u(x) \equiv u^p(x) = d^n(x) \tag{1.51}$$

$$\bar{u}(x) \equiv \bar{u}^p(x) = \bar{d}^n(x) \tag{1.52}$$

Nucleons exhibit no net strangeness or charm, and these heavier flavors have isospin of zero. For this analysis, the following symmetries are assumed:

$$s(x) \equiv s^p(x) = s^n(x) \tag{1.53}$$

$$\bar{s}(x) \equiv \bar{s}^p(x) = \bar{s}^n(x) \tag{1.54}$$

$$c(x) \equiv c^p(x) = c^n(x) \tag{1.55}$$

$$\bar{c}(x) \equiv \bar{c}^p(x) = \bar{c}^n(x) \tag{1.56}$$

$$s(x) \equiv \bar{s}(x) \tag{1.57}$$

$$c(x) \equiv \bar{c}(x) \tag{1.58}$$

Using these symmetries, the quark distributions of the neutrino and the proton are described in terms of the proton quark distributions. All the parton distributions that follow are those for the proton.

$$q^{\nu n}(x) = u(x) + s(x) \tag{1.59}$$

$$\bar{q}^{\nu n}(x) = \bar{d}(x) + \bar{c}(x) \tag{1.60}$$

$$q^{\bar{\nu} n}(x) = d(x) + c(x) \tag{1.61}$$

$$\bar{q}^{\bar{\nu} n}(x) = \bar{u}(x) + \bar{s}(x) \tag{1.62}$$

Finally, the parton densities for an isoscalar nucleon, $N = 1/2 \times$ (proton + neutron), are

$$q^{\nu N}(x) = \frac{1}{2}[u(x) + d(x) + 2s(x)] \tag{1.63}$$

$$q^{\bar{\nu} N}(x) = \frac{1}{2}[u(x) + d(x) + 2c(x)] \tag{1.64}$$

$$\bar{q}^{\nu N}(x) = \frac{1}{2}\left[\bar{u}(x) + \bar{d}(x) + 2\bar{c}(x)\right] \tag{1.65}$$

$$\bar{q}^{\bar{\nu} N}(x) = \frac{1}{2}\left[\bar{u}(x) + \bar{d}(x) + 2\bar{s}(x)\right] \tag{1.66}$$

The quark content of the isoscalar structure function $2xF_1$ for neutrino scattering is obtained by substituting these densities into Equation 1.39:

$$\begin{aligned} 2xF_1^{\nu N}(x) &= 2xF_1^{\bar{\nu} N}(x) \\ &= xu(x) + x\bar{u}(x) + xd(x) + x\bar{d}(x) \\ &+ xs(x) + x\bar{s}(x) + xc(x) + x\bar{c}(x) \end{aligned} \tag{1.67}$$

The electromagnetic structure functions $2xF_1^{\ell p}$ and $2xF_1^{\ell n}$ are constructed from Equation 1.43 using the same parton densities as above and including the quark charges:

$$\begin{aligned} 2xF_1^{\ell p} &= \left(\frac{1}{3}\right)^2 \left[xd(x) + x\bar{d}(x) + xs(x) + x\bar{s}(x)\right] \\ &+ \left(\frac{2}{3}\right)^2 \left[xu(x) + x\bar{u}(x) + xc(x) + x\bar{c}(x)\right] \end{aligned} \tag{1.68}$$

$$\begin{aligned} 2xF_1^{\ell n} &= \left(\frac{1}{3}\right)^2 \left[xu(x) + x\bar{u}(x) + xs(x) + x\bar{s}(x)\right] \\ &+ \left(\frac{2}{3}\right)^2 \left[xd(x) + x\bar{d}(x) + xc(x) + x\bar{c}(x)\right] \end{aligned} \tag{1.69}$$

Thus $2xF_1^{\ell N}$ is given by

$$
\begin{aligned}
2xF_1^{\ell N} &= \left(2xF_1^{\ell p} + 2xF_1^{\ell n}\right)/2 \\
&= \frac{5}{18}\left(xu + x\bar{u} + xd + x\bar{d}\right) \\
&+ \frac{1}{9}(xs + x\bar{s}) + \frac{4}{9}(xc + x\bar{c})
\end{aligned}
\tag{1.70}
$$

Assuming that the value of $R = \sigma_L / \sigma_T$ is the same for the electromagnetic neutral-current and weak charged-current structure functions, the ratio of $2xF_1^{\ell N} / 2xF_1^{\nu N}$ is equal to $F_2^{\ell N} / F_2^{\nu N}$:

$$
\frac{F_2^{\ell N}}{F_2^{\nu N}} = \frac{5}{18}\left(1 - \frac{3}{5}\frac{xs + x\bar{s} - xc - x\bar{c}}{q + \bar{q}}\right)
\tag{1.71}
$$

This relationship is known as the "5/18ths rule," and will be used in Chapter 8 to compare the charged-lepton structure functions to the results of this analysis.

The structure function xF_3, associated with the parity-violating weak interaction, represents the momentum density of valence quarks. Substituting the parton densities into Equation 1.41 yields

$$
xF_3^{\nu N} = xu_V(x) + xd_V(x) + 2xs(x) - 2xc(x)
\tag{1.72}
$$

$$
xF_3^{\bar{\nu} N} = xu_V(x) + xd_V(x) - 2xs(x) + 2xc(x)
\tag{1.73}
$$

where $u_V \equiv u - \bar{u}$ and $d_V \equiv d - \bar{d}$ are the proton's valence densities. The asymmetry of the s–c doublet results in $xF_3^{\nu N} \neq xF_3^{\bar{\nu} N}$. The method of extracting xF_3, described in Chapter 6, extracts the average of the neutrino and anti-neutrino distributions, so that

$$
xF_3(x) = \left(xF_3^{\nu N}(x) + xF_3^{\bar{\nu} N}(x)\right)/2 = xu_V(x) + xd_V(x)
\tag{1.74}
$$

1.2.4 The Theory of QCD

The parton model explains the scaling of the structure functions in terms of point-like constituents, but by itself offers no explanation for the dynamics between these constituents. If nucleons are made of quarks then how does one reconcile that quarks are never observed in isolation, yet when quarks participate in high-Q^2 scattering they behave like free particles? The need to refine the parton model was also apparent from detailed studies of structure functions, which found that scaling is only an approximation, and that logarithmic scaling violations are observed. QCD provides a consistent theory of quark dynamics, explains the scaling violations of the structure functions, and provides the detailed phenomenology of deep-inelastic scattering.

The behavior of quarks as quasi-free particles in high-Q^2 processes is accommodated by QCD's property of asymptotic freedom. Asymptotic freedom is a direct consequence of the non-Abelian structure of QCD. In a non-Abelian theory the gauge particles self-interact; that is, both the quarks and the gluon carry a color charge. Quarks are confined to hadrons because the self-interactions of the gluons tend to anti-screen a color charge, so that the strong force between two quarks increases as the distance between the two quarks gets larger. However, at shorter distances (equivalent to high Q^2), the strong coupling α_S decreases, so that as $Q^2 \to \infty$, $\alpha_S \to 0$.

1.2.4.1 Renormalization

When perturbatively calculating a cross-sections, the inclusion of higher-order diagrams leads to terms that are ultraviolet divergent. The purpose of renormalization is to remove these infinities in a systematic way. Renormalization [Alt82] involves introducing a free parameter μ^2, the renormalization scale, where μ has dimensions of mass. This scale is completely arbitrary, and different choices of μ^2 in the perturbative expansion are

possible. The set of rules that specify the value of μ^2 for each divergent diagram describes the renormalization scheme that is used. The most commonly-used scheme is the modified minimum-subtraction ($\overline{\text{MS}}$) scheme, and in a minimal-subtraction scheme μ is chosen to be the same for every divergent integral.

A calculation of an observable quantity, like a cross-section, must be independent of these arbitrarily-chosen renormalization schemes and scales. This requirement is contained in the renormalization group equation

$$\mu \frac{d\mathcal{M}}{d\mu} = 0 \tag{1.75}$$

the renormalization group being the set of all rescalings of μ^2. To next-to-leading-order, the renormalization scale dependence of the strong coupling α_S is given by the beta function

$$\mu \frac{d\alpha_S\left(\mu^2\right)}{d\mu} = -\frac{\beta_0}{2\pi}\alpha_S^2\left(\mu^2\right) - \frac{\beta_1}{8\pi^2}\alpha_S^3\left(\mu^2\right) \tag{1.76}$$

where the coefficients are given by

$$\beta_0 = 11 - 2n_f/3 \tag{1.77}$$

$$\beta_1 = 102 - 38n_f/3 \tag{1.78}$$

and n_f is the number of quark flavors.

Solving Equation 1.76 for $\alpha_S(\mu^2)$ introduces one constant of integration, which may be denoted by $\alpha_S(\mu_0^2)$. This constant is the one fundamental constant of QCD, and it is determined by experiment: by measuring the strong coupling at one reference momentum

scale μ_0^2. QCD then predicts how the coupling runs to any other scale according to Equation 1.76.

It is conventional to introduce the dimensional parameter Λ, and give the solution to Equation 1.76 in terms of it:

$$\alpha_S(\mu^2) = \frac{4\pi}{\beta_0 \ln\left(\mu^2/\Lambda^2\right)} \times \left[1 - \frac{\beta_1}{\beta_0^2} \frac{\ln\left[\ln\left(\mu^2/\Lambda^2\right)\right]}{\ln\left(\mu^2/\Lambda^2\right)}\right] \tag{1.79}$$

Therefore, the measurement of Λ is equivalent to measuring $\alpha_S(\mu_0^2)$. Λ effectively sets the scale of the running coupling constant, and so it marks the boundary between quasi-free quarks and gluons and the hadronic bound states. Only for Q^2 values much larger than Λ, where the effective coupling is small, do perturbative techniques with quasi-free partons apply. If renormalization is carried out according to the $\overline{\text{MS}}$ scheme, then Λ is referred to as $\Lambda_{\overline{\text{MS}}}$.

1.2.4.2 Factorization

The connection between the quarks and the gluons and the physically-observed hadrons is established by the factorization theorem of QCD [Sop89]. The factorization theorem states that the structure functions can be decomposed into two parts, a parton distribution and a hard-scattering coefficient. The statement of the theorem is given by

$$W^{\alpha\beta}(q,p) = \sum_i \int_x^1 \frac{dz}{z} q_i^N(z,M)\hat{\omega}_i^{\alpha\beta}\left(q, zp, M, \alpha_S(\mu)\right) \tag{1.80}$$

The sum is over all partons i. The parton-level hard-scattering coefficient $\hat{\omega}_i^{\alpha\beta}$ is a calculable function describing the probability for scattering to take place. The parton

distribution function $q_i^N(z,M)$ is defined as before, where the index i indicates an individual type of parton, N refers to a given hadronic target, z is the fraction of the nucleon's momentum carried by parton i, and M is the factorization scale. The factorization scale M is distinguished from the renormalization scale μ because in principle they can be different.

The factorization theorem relies on QCD's property of asymptotic freedom, which permits high-energy scattering to be calculated using perturbation theory. The parton distribution function includes all the incalculable phenomena that occur at low energy scales—the infra-red dominated contributions. These are the interactions that bind the quarks and gluons into hadrons and are not amenable to perturbative calculations. The hard-scattering coefficient is sensitive only to momenta of order Q^2 and is ultraviolet dominated. The hard-scattering coefficients are calculable using QCD's Feynman rules. The scale M^2, therefore, sets the separation between the long-distance and short-distance parts of the process. A propagator that is off-shell by M^2 or more will contribute to the hard-scattering coefficient, and below the scale will contribute to the parton distribution. The factorization M^2 appears in the definition of the parton distributions in a similar way to the appearance of the renormalization scale μ^2 in the renormalization scheme.

Using the factorization theorem, the parton distributions can be determined experimentally. The structure functions in the hadronic tensor $W^{\alpha\beta}$ on the left-hand side of Equation 1.80 are measured and the hard-scattering coefficients on the right-hand side are calculated to a chosen order in perturbation theory, after making a choice of renormalization scheme. This way, the remaining unknown parton distributions are isolated. The parton distributions thus depend on the order and scheme used to determine them.

1.2.4.3 Evolution Equations

The parton distributions are infra-red dominated and perturbative QCD is unable to predict them outright. However, once the parton distributions are measured at one momentum scale, QCD predicts how they revolve to any other scale. The evolution of parton distributions is governed by the Dokshitzer-Gribov-Lipatov-Altarelli-Parisi evolution equations [Alt77, Dok78, Dok80, Gri72]:

$$\frac{dq^{NS}(x,M^2)}{d\ln M^2} = \frac{\alpha_S(\mu^2)}{2\pi}\int_x^1 \frac{dy}{y} q^{NS}(y,M^2)\, P_{qq}\left(\frac{x}{y}\right) \tag{1.81}$$

$$\frac{dq^{S}(x,M^2)}{d\ln M^2} = \frac{\alpha_S(\mu^2)}{2\pi}\int_x^1 \frac{dy}{y}\left[q^{S}(y,M^2)\, P^{S}_{qq}\left(\frac{x}{y}\right) + G(y,M^2)\, P_{qG}\left(\frac{x}{y}\right)\right] \tag{1.82}$$

$$\frac{dG(x,M^2)}{d\ln M^2} = \frac{\alpha_S(\mu^2)}{2\pi}\int_x^1 \frac{dy}{y}\left[q^{S}(y,M^2)\, P_{Gq}\left(\frac{x}{y}\right) + G(y,M^2)\, P_{GG}\left(\frac{x}{y}\right)\right] \tag{1.83}$$

where

$$q^{NS} = \sum_i q^i - \bar{q}^i = u_V + d_V \tag{1.84}$$

$$q^{S} = \sum_i q^i + \bar{q}^i \tag{1.85}$$

G is the gluon distribution, and the "splitting functions" $P_{ij}(x/y)$ are the probability that parton j with momentum y will be resolved as parton i with momentum $x < y$. Thus the parton distributions evolve according to the radiative processes available to them. Note that the evolution of the non-singlet quark distribution q^{NS} does not depend on the gluon distribution. The diagrams for the leading-order splitting functions are shown in Figure

1.3, and the diagrams for the next-to-leading-order splitting functions are shown in Figure 1.4.

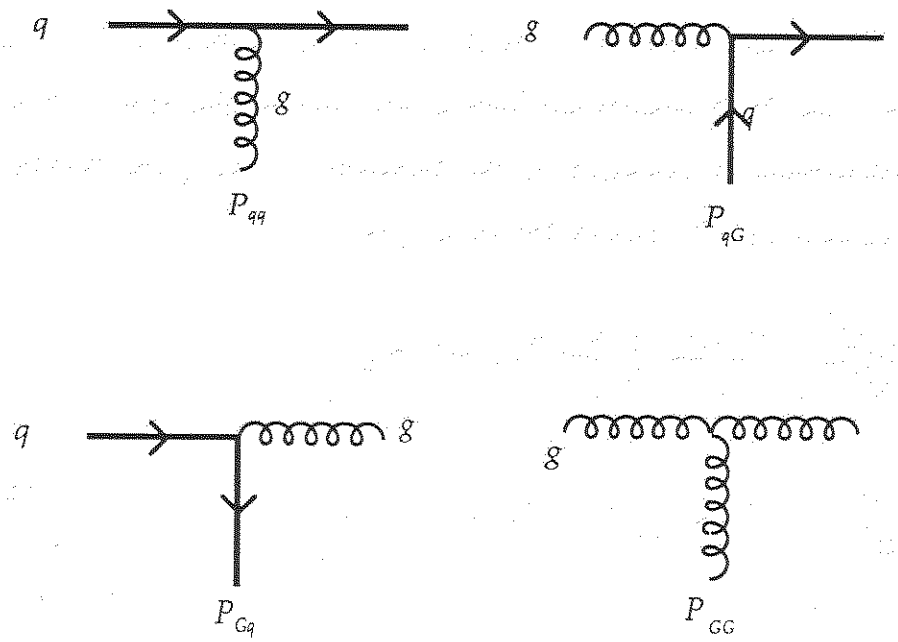

Figure 1.3: The leading-order splitting function diagrams.

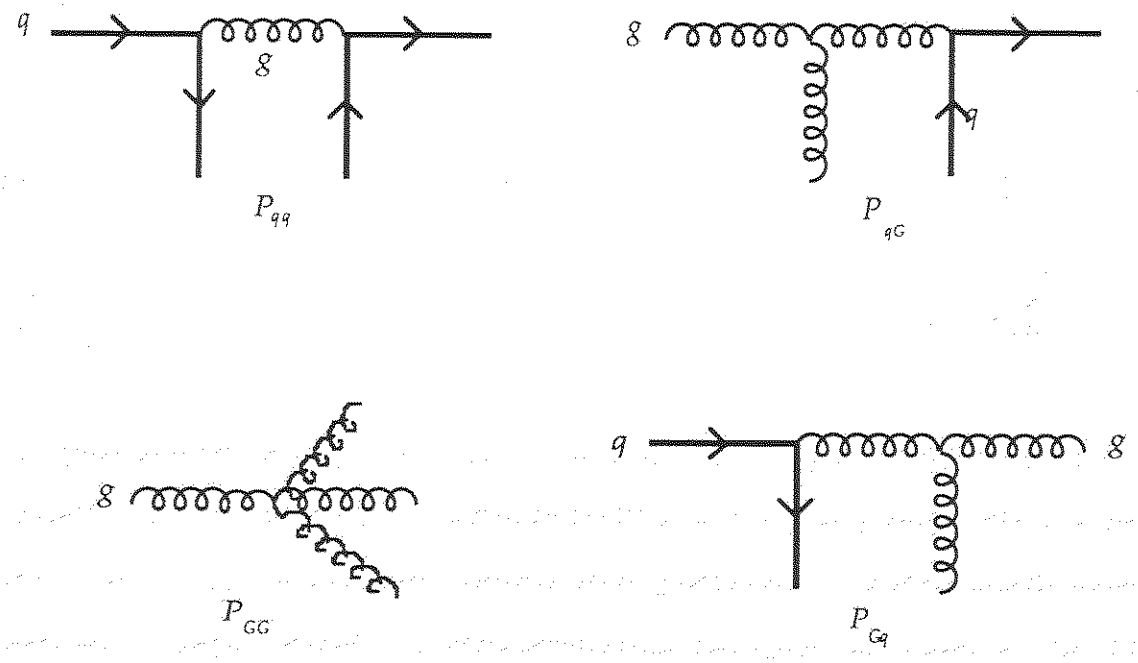

Figure 1.4: The next-to-leading-order splitting function diagrams.

1.2.4.4 Hard-Scattering Integrals

Using the factorization theorem of Equation 1.80, the measured structure functions are related to parton distributions, which evolve according to the evolution equations. The structure functions are found by convoluting the parton distributions with the hard-scattering coefficients:

$$F_3(x,Q^2) = \int_x^1 dy \left[C_3^q\left(\frac{x}{y}, M^2\right) q^{NS}(x,M^2) \right] \tag{1.86}$$

$$x^{-1}F_2(x,Q^2) = \int_x^1 dy \left[C_2^q\left(\frac{x}{y}, M^2\right) q^S(x,M^2) + C_2^G\left(\frac{x}{y}, M^2\right) G(x,M^2) \right] \tag{1.87}$$

where the C_i are the hard-scattering coefficients. The QCD behavior of the parton distributions—their evolution with scale—leads to the logarithmic scaling violations observed in the measurements of the structure functions.

The general relations between the partons and the structure functions given above simplify considerably at leading order. At leading order, the hard-scattering coefficients of the quark terms are proportional to $\delta(1-x/y)$ and the coefficient of the gluon term vanishes. Hence, the leading-order quark assignments are simply $F_2 = q^S$ and $xF_3 = q^{NS}$. At NLO the parton assignments for the structure functions become more complicated and gluons are also involved.

1.2.4.5 QCD Scales

As with all applications of perturbative QCD, a theoretical uncertainty is associated with the choice of factorization and renormalization scales. A cross-section calculation done to

all orders in α_S would be independent of scale. However, some scale dependence is unavoidable for any calculation done to finite order in α_S.

The choice of a scale when performing a calculation must be similar to a physical scale present in the process. In the case of deep-inelastic scattering, the μ^2 scale should be of order Q^2, the momentum transferred in the hard scattering. This is necessary because higher-order terms include logarithms proportional to $\ln(Q/\mu)$, and an unsuitably small choice of scale will mean that truncating these terms from the perturbative expansion is invalid. The convention is to choose $Q = \mu$ so that the $\ln(Q/\mu)$ terms vanish in all orders. It is also conventional to choose the factorization scale $M = \mu = Q$.

The error in the measurement of α_S due to the choice of the renormalization and factorization scales in deep-inelastic scattering has been investigated [Vir92, Mar91]. The results of those studies are included as a theoretical error in the measurement of α_S by this experiment (see Chapter 7).

1.3 Analysis Overview

1.3.1 The Data Sample

The CCFR collaboration performed two neutrino deep-inelastic scattering experiments at the Fermilab Tevatron. High-energy muon-type neutrinos and anti-neutrinos were provided using the Fermilab Quadrupole Triplet beamline, which focused pion and kaon secondaries produced in collisions of 800 *GeV* protons on a BeO target, before allowing them to decay in flight. Neutrino interactions were detected in the CCFR steel-scintillator target calorimeter, which was separated from the neutrino source by approximately one kilometer of earth and steel.

The unmagnetized CCFR target calorimeter is instrumented with liquid scintillator counters and drift chambers. In charged-current events, the angle of the muon and the total hadronic energy are measured in the target. The target is followed by a toroidal magnetic spectrometer, which includes drift chambers and provides the muon momentum measurement.

Approximately 3.7 million charged-current event triggers were analyzed. Since the flux of the neutrino beam cannot be directly measured, the flux is derived from a sample of events with low hadronic energy. From the flux and the number of observed events, the structure functions can be determined; about 950,000 neutrino-induced and 170,000 anti-neutrino-induced events were selected for inclusive nucleon structure-function measurements.

Once the structure functions are known, their Q^2 evolution can be compared against the theory of perturbative quantum chromodynamics. This yields a measurement of the QCD scale parameter Λ and hence the value of the strong coupling, α_S. The coupled evolution of the non-singlet and singlet quark distributions also yields a measurement of the gluon distribution.

1.3.2 Synopsis of This Thesis

The chapters of this thesis are organized as follows: The experimental setup, including the accelerator facilities at Fermilab and the CCFR detector, is described in Chapter 2. The calibration of the detector and the principles of event reconstruction are described in Chapter 3. Chapter 4 describes the corrections made to the data, including the corrections for detector acceptance and resolution. The flux extraction procedure is discussed in Chapter 5. The procedure for extracting structure functions, including the statistical and

systematic errors, is described in Chapter 6. In Chapter 7 the structure functions are compared against the theory of QCD, and a precise measurement of $\alpha_S(M_Z^2)$ is made in the context of that theory. The structure functions and the QCD measurements are compared against measurements from other experiments in Chapter 8, which also presents the final conclusions of this thesis.

1.3.3 Prior Analyses

The structure-function analysis presented in this thesis is the latest in a series of analyses performed on neutrino data collected by the detector in Lab E at Fermilab. FNAL Experiment E616 [Mac84a, Pur84] used a narrow-band neutrino beam with a maximum incident proton energy of 400 *GeV*. The statistics of the experiment were limited by the low flux of the beam and the use of spark chambers, which could only record one neutrino event per "ping" in the accelerator cycle. E701 used the same beamline as E616, but added a second upstream detector to search for neutrino oscillations [Sto85]; a structure-function analysis on the combined E616/E701 data sample was also performed [Olt89].

In contrast, FNAL Experiments E744 and E770 were performed using the Tevatron, which provided an 800 *GeV* incident proton energy. The Quadrupole Triplet beamline provided a wide-band high-intensity beam of mixed neutrinos and anti-neutrinos. The statistics were further increased by replacing the spark chambers with drift chambers in the Lab E detector, which can record multiple events per ping.

A structure-function analysis on the combined E744/E770 data sample has previously been presented [Leu91, Qui92, Qui93]. The analysis in this thesis improves upon the previous analysis in several respects:

- The hadronic energy and muon energy calibrations now come directly from test beam data accumulated during the E744 and E770 neutrino runs. In the previous analysis, a technique called "relative calibration" was used to adjust the measured test beam calibrations. This technique was dropped for this analysis, since the results were shown to have large systematic uncertainties.

- The event analysis has been improved. In particular, the energy loss of the muon in the calorimeter is now more accurately modeled.

- The previous analysis used the radiative corrections due to de Rujula [Ruj79], which only included the effects of energy loss due to electromagnetic radiation by the outgoing muon. The present analysis uses the radiative corrections due to Bardin [Bar86], which includes the effects of electromagnetic interactions with the struck quark.

- In the previous analysis, the value of R used was that from a parameterization of data taken only at SLAC. The current analysis uses a value of R determined from a global fit the world's available measured data on R [Whi90b].

- The previous analysis used the strange sea determined from the E744 data only [Fou90]. The current analysis uses the strange sea determined from the combined E744 and E770 data sample [Rab93].

- The earlier analysis only presented the results of a non-singlet QCD evolution. This thesis also presents the results of a simultaneous QCD fit to the non-singlet and singlet structure functions, which not only reduces the statistical error on $\Lambda_{\overline{MS}}$, but also provides information on the gluon content of the proton.

- The previous analysis did not include higher-twist effects in the QCD fits, apart from correction for target mass. These effects are accounted for in the present analysis.

- The systematic error study has been expanded from the study presented in the previous analysis. In addition, the systematic errors have been incorporated into the QCD fits to produce a precise measurement of $\alpha_S(M_Z^2)$ from deep-inelastic scattering.

2 The Neutrino Beam and Detector

A high-energy, accelerator-based neutrino experiment has two requirements: a beam of neutrinos and anti-neutrinos, and a detector capable of measuring the properties of neutrino interactions. Complicating both of these requirements is how rarely neutrinos interact. These particles do not interact electromagnetically, so it is not possible to accelerate or steer a neutrino beam. Because the weak interaction is very weak, the neutrinos' mean free path in any material is very large, making their detection a challenge.

Therefore, in general, neutrino detectors are massive—hundreds of tons—and neutrino beams are intense, in order to raise the probability of a neutrino interaction to something appreciable. The detector is both the target in which the neutrinos scatter and the instrument that measures the properties of the neutrino events. The neutrino beam is a tertiary beam, produced when a secondary beam of mesons is allowed to decay in flight. The meson beam is produced by a primary proton beam. Since protons are readily available, and are stable, charged, and strongly interacting, this produces a large number of mesons. Since neutrino experiments are so large in scale, they require the collaborative effort of many people. There are several large accelerator laboratories where high-energy neutrino experiments have been performed: Fermilab, in Batavia, Illinois; Argonne, in Argonne, Illinois; Brookhaven, in Upton, New York; and CERN, located in Geneva, Switzerland.

The experiment presented in this thesis was performed at the Fermi National Accelerator Laboratory. Fermilab's 800 *GeV* proton beam was used to produce a wide-band beam of neutrinos and anti-neutrinos, which remains the highest-energy neutrino beam yet produced. The experiment was done with the CCFR detector, located in Lab E, one of

several experimental areas in the Fermilab neutrino beam line. The detector consists of a 690-ton sampling calorimeter and a muon spectrometer. The data were gathered in two runs: E744 ran from February to August 1985 and E770 started in June 1987 and concluded in February 1988.

This chapter describes the experimental apparatus: the accelerator facilities at Fermilab, the neutrino beam, and the CCFR detector. The final section of this chapter describes the triggering criteria and the data processing.

2.1 Neutrinos at the Fermilab Tevatron

The experiment benefited from taking place at the Fermilab Tevatron, the highest-energy accelerator in the world at the time of this writing. During the experiment, 800-*GeV* protons produced a beam of neutrinos and anti-neutrinos with an average energy of about 140 *GeV*, with maximum neutrino energies going as high as 600 *GeV*. A schematic diagram of the Fermilab accelerator complex is shown in Figure 2.1. Below is a description of the various stages used to accelerate the proton beam:

- ION SOURCE: H^- ions are produced by a cesium cathode immersed in hydrogen gas.

- COCKROFT-WALTON ACCELERATOR: The Cockroft-Walton is an electrostatic machine which begins the proton acceleration process. By employing multiple electrostatically-induced potential drops, the ions are collected from the source and accelerated to 750 *keV*.

- LINAC: A linear accelerator, consisting of a chain of radio-frequency cavities, increased the energy of the H^- ions to 200 *MeV*. As the ions exit the LINAC they pass through a carbon foil, which strips them of their two electrons.

- BOOSTER: The Booster is a 140 *m* diameter synchrotron. A synchrotron is a ring-shaped machine in which an applied magnetic field maintains the protons in the proper orbit while an accelerating RF electric field is provided at gaps along the ring. As the particles gain energy, the magnetic field is increased to preserve the orbit while the frequency of the accelerating electric field also increases. The Booster accelerates the protons to 8 *GeV* and injects them into the main ring.

- MAIN RING: The main ring is a 2 *km* diameter synchrotron that accelerates the protons to 150 *GeV*. It contains 1000 conventional, copper-coiled magnets to bend and focus the protons. Prior to construction of the Tevatron ring, the main ring served as Fermilab's primary accelerator.

- TEVATRON RING: The Tevatron is a superconducting proton synchrotron. It shares the tunnel with the main ring and is positioned immediately below it. The Tevatron's superconducting magnets operate in the temperature range of liquid helium and provide a 40 *kG* field. The accelerator was designed to accelerate particles to 1 *TeV*. During this experiment, the protons were accelerated to 800 *GeV*, a choice of energy that optimized the machine performance.

When operating in fixed-target mode (as opposed to collider mode) the Tevatron operates on a 60-second cycle. During each cycle the Tevatron is filled with approximately 10^{13} protons. The protons are held at their maximum energy for about a third of the cycle and extracted in fast and slow spills. The fast spills are called pings and are of millisecond duration while the slow spills last two seconds. Protons from slow spill are directed to other experiments, while the pings are used to create the neutrino beam.

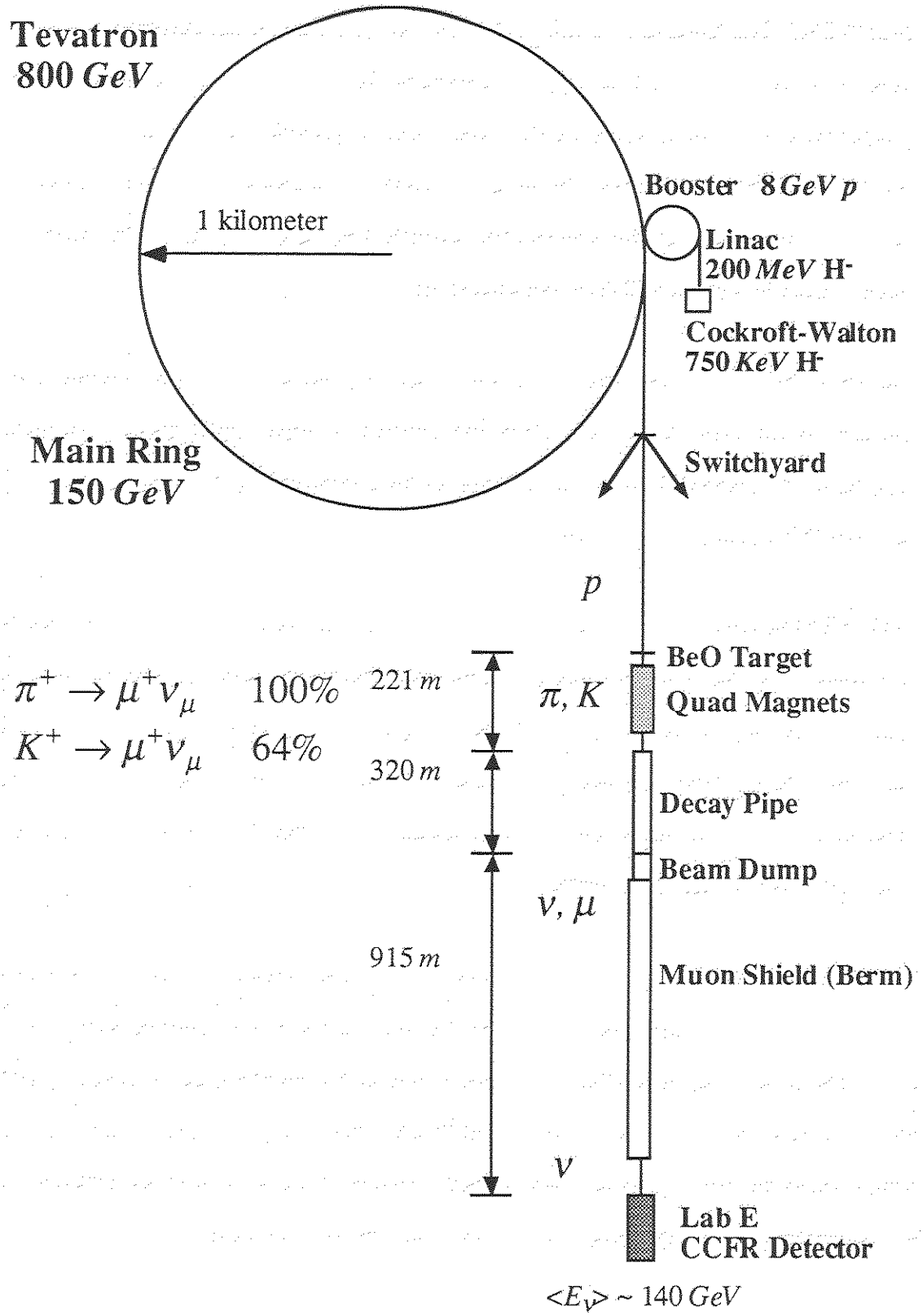

Figure 2.1: Fermilab neutrino beamline layout.

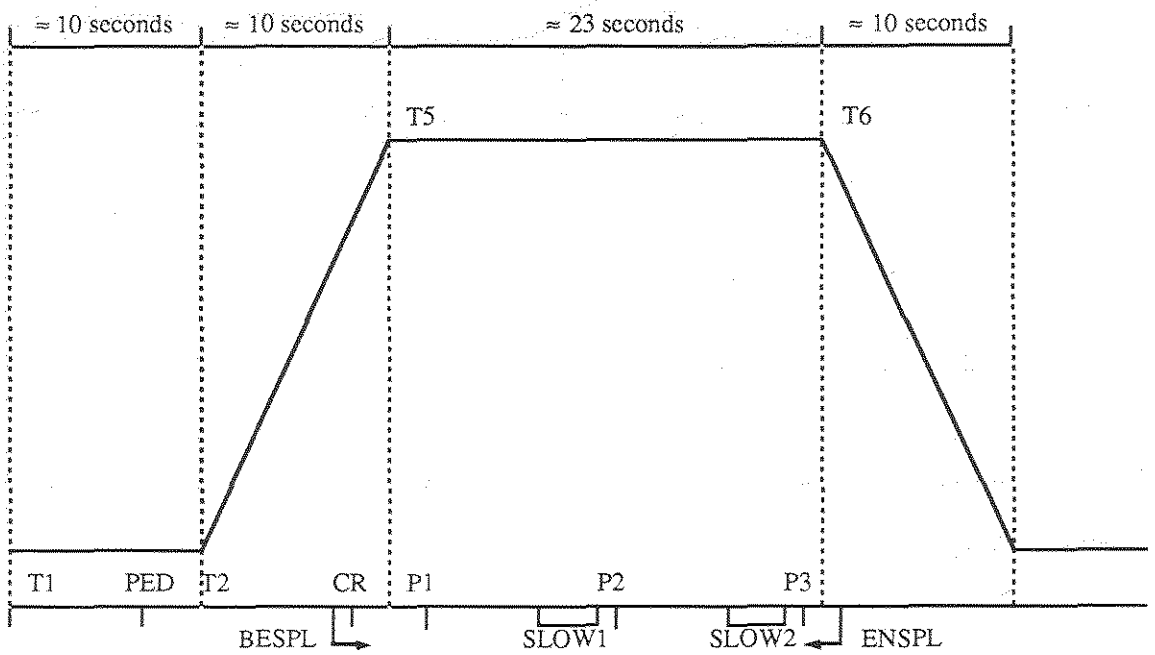

Figure 2.2: Tevatron magnet current versus time during fixed-target operation. The magnet cycle is described in the text.

The timing structure of the Tevatron magnets is shown in Figure 2.2. The cycle begins at time T1. The Tevatron is filled with protons that have been stored in the main ring and after ten seconds, at time T2, the current in the Tevatron magnets begins to ramp up, and the protons are accelerated. The increase in the magnetic field is synchronous with the increasing RF frequency. After 10 seconds and approximately 10^{13} revolutions, the protons reach 800 *GeV*. The beam is stored at this energy for 23 seconds, between T5 and T6, while the protons are extracted. P1, P2, and P3 indicate the fast spills, while two slow spills are extracted between them. At T6 the magnets being to ramp down and the cycle repeats.

2.2 Neutrino Beam

For neutrino production, the proton beam was directed onto a 33 *cm* long (1 interaction length) beryllium-oxide target in the Neutrino Center beamline. A secondary beam of

mesons emerges from the target and is focused by a triplet of quadrupole magnets. The secondaries enter a 320 m decay region 221 meters beyond the target. Pions and kaons decay in flight, with dominate decay modes:

$$\pi^+ \rightarrow \mu^+ \nu_\mu,\ \pi^- \rightarrow \mu^- \overline{\nu}_\mu \qquad \text{BR} = 99.99\% \tag{2.1}$$

$$K^+ \rightarrow \mu^+ \nu_\mu, K^- \rightarrow \mu^- \overline{\nu}_\mu \qquad \text{BR} = 63.5\% \tag{2.2}$$

The maximum neutrino energy is governed by the mass ratio of the muon and the decaying particle:

$$E_\nu^{\max} = E_{\pi,K}\left[1 - \left(\frac{m_\mu}{m_{\pi,K}}\right)^2\right] \tag{2.3}$$

so that the neutrino beam exhibits a dichromatic spectrum, with the more energetic muons coming from the kaon decays:

$$\left(E_\nu^{\max}\right)_K = 0.95 E_K \tag{2.4}$$

$$\left(E_\nu^{\max}\right)_\pi = 0.43 E_\pi \tag{2.5}$$

The Fermilab Neutrino Center beamline is shown in Figure 2.3. Event timing is initiated by a signal pulse as the proton bunch passes through a toroid (NC1TOR) upstream of the target. After the BeO target, the focusing of pions, kaons, and other charged particles is done by a triplet of quadrupole magnets, NC1Q4 through NC1Q6. The triplet serves to gather the mesons off the target and collimate them into a parallel beam in the decay region. To gain maximum acceptance, no sign or momentum selection is done, and the beamline is configured as a *wide-band beam* with large momentum acceptance.

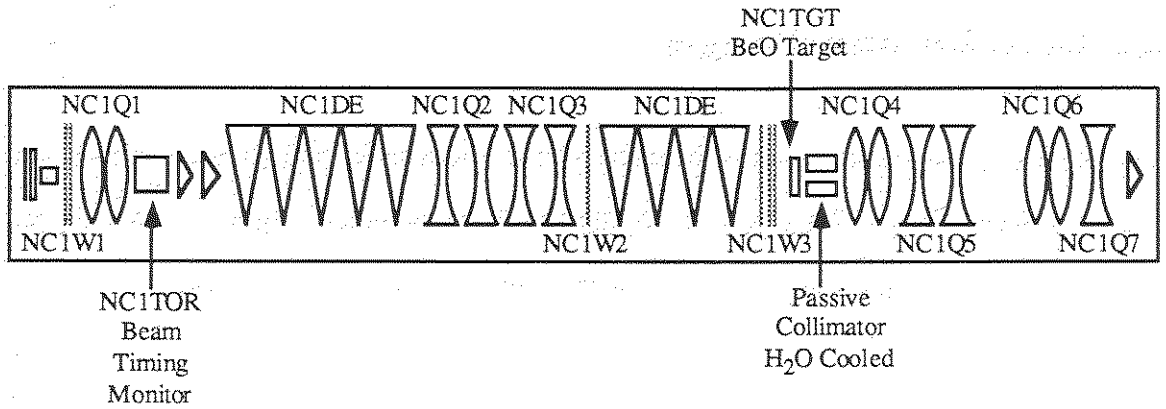

Figure 2.3: Neutrino Center beamline. Dipole magnet are indicated by prisms (triangles), and quadrupole magnets are indicated by concave and convex lenses.

Approximately one-tenth of the mesons decay in the decay region and the remainder of the beam is dumped into a 6 *m* block of aluminum followed by steel shielding. The CCFR detector is positioned 915 *m* beyond the dump. The muons and neutrinos that penetrate the aluminum beam dump encounter approximately 241 *m* of steel shielding and 582 *m* of earth berm before reaching the detector. The amount of material in front of the detector is sufficient for the muons from the meson decays to range out, so that of all the particles entering the berm, only the neutrinos penetrate into the experimental areas. However, neutrinos may interact inside the berm, and a small number of berms muons also enter the experimental hall. Events due to muons are identified and discarded by their interaction in the veto wall, a set of scintillation counters positioned upstream of the target calorimeter. The front face of the CCFR detector is 915 *m* from the end of the decay region, and neutrinos strike the detector within about a one meter radius around the beam axis. Therefore, the neutrinos have an incident angle no larger than about 1 *mrad*, allowing the good approximation that neutrinos strike the target at normal incidence. The procedure used to determine the neutrino flux is described in Chapter 5 and the relative neutrino and anti-neutrino flux is shown in Figure 5.9.

2.3 Detector and Trigger

The following sub-sections describe each of the elements of the CCFR detector and trigger system. Figure 2.4 shows a schematic of the detector. Figure 2.5 shows the appearance of a charged-current event as seen by the elements of the apparatus.

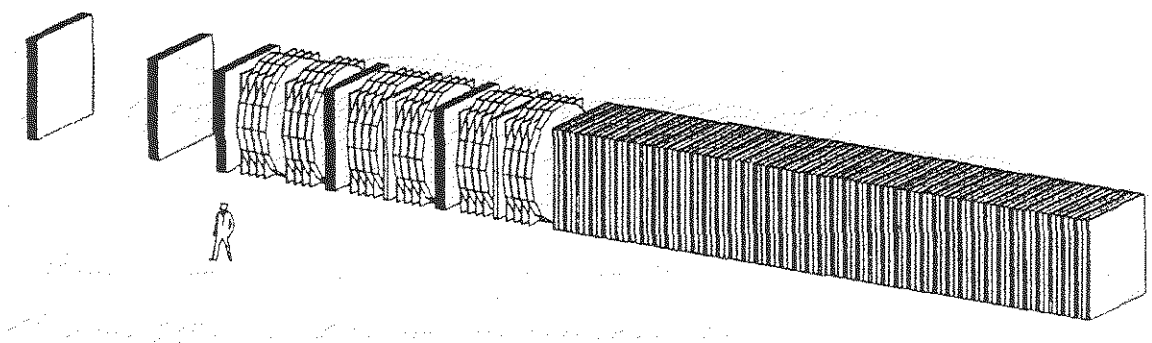

Figure 2.4: Schematic representation of the CCFR detector. The neutrino beam enters from the right. The target calorimeter is on the right and muon spectrometer is on the left. The two leftmost banks of drift chambers are known as the blue cart.

2.3.1 Target Calorimeter

The target calorimeter is a steel-scintillator large-area calorimeter that also includes drift chambers for charged-particle tracking. It has a mass of 690 tons, is 17.7 *m* long and measures 10 feet by 10 feet transversely. It is made up of six identical modules called carts. Each cart contains 28 steel plates, seven drift chamber stations, and fourteen scintillation counters. Each steel plate is 5.15 *cm* thick. A liquid scintillation counter is positioned between every two plates and a drift chamber is placed between every four plates. Each scintillation counter occupies 6.48 *cm* along the beam axis, and each drift chamber station occupies 8.87 *cm*. A schematic view of one cart is shown in Figure 2.6.

The carts are numbered so that cart 6 is the most upstream and cart 1 is the most downstream. The counters are numbered so that counter 84 is the most upstream.

2.3.1.1 Scintillator Counters

The energy sampling fraction of the calorimeter is approximately 11%. The measurement is made by scintillation counters, which are acrylic tanks measuring 10 × 10 feet by 1 inch filled with mineral oil doped with scintillating fluors. A photomultiplier tube (PMT) at each corner of the square counter is used for readout. Each counter is enveloped in opaque material to prevent external light from reaching the phototubes, and plastic bags filled with water occupy the space between the counters and the steel plates to balance the pressure on the acrylic walls. Figure 2.7 shows a sketch of a scintillation counter.

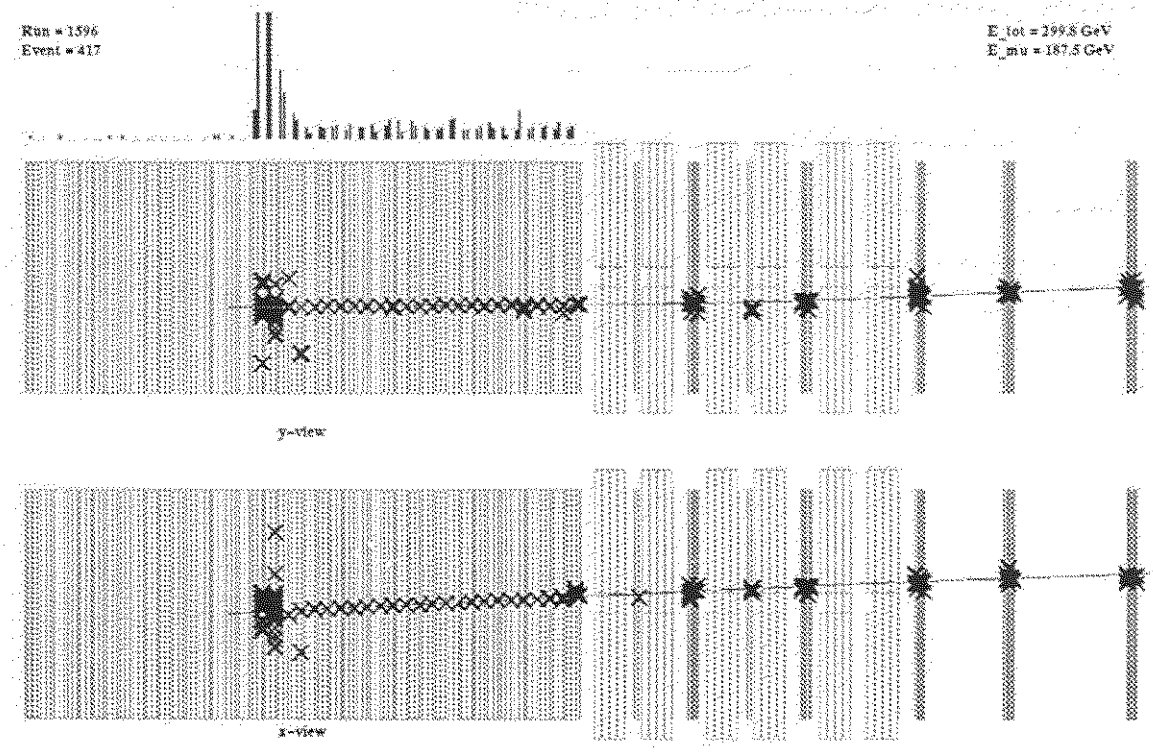

Figure 2.5: A typical charged-current event as seen by the elements of the CCFR detector. Hits in the drift chambers are shown as "X". Pulse heights in the calorimeter scintillators are shown in a logarithmic scale above the target. The line linking the hits in the target and the toroid is derived by the tracking software as described in Chapter 3.

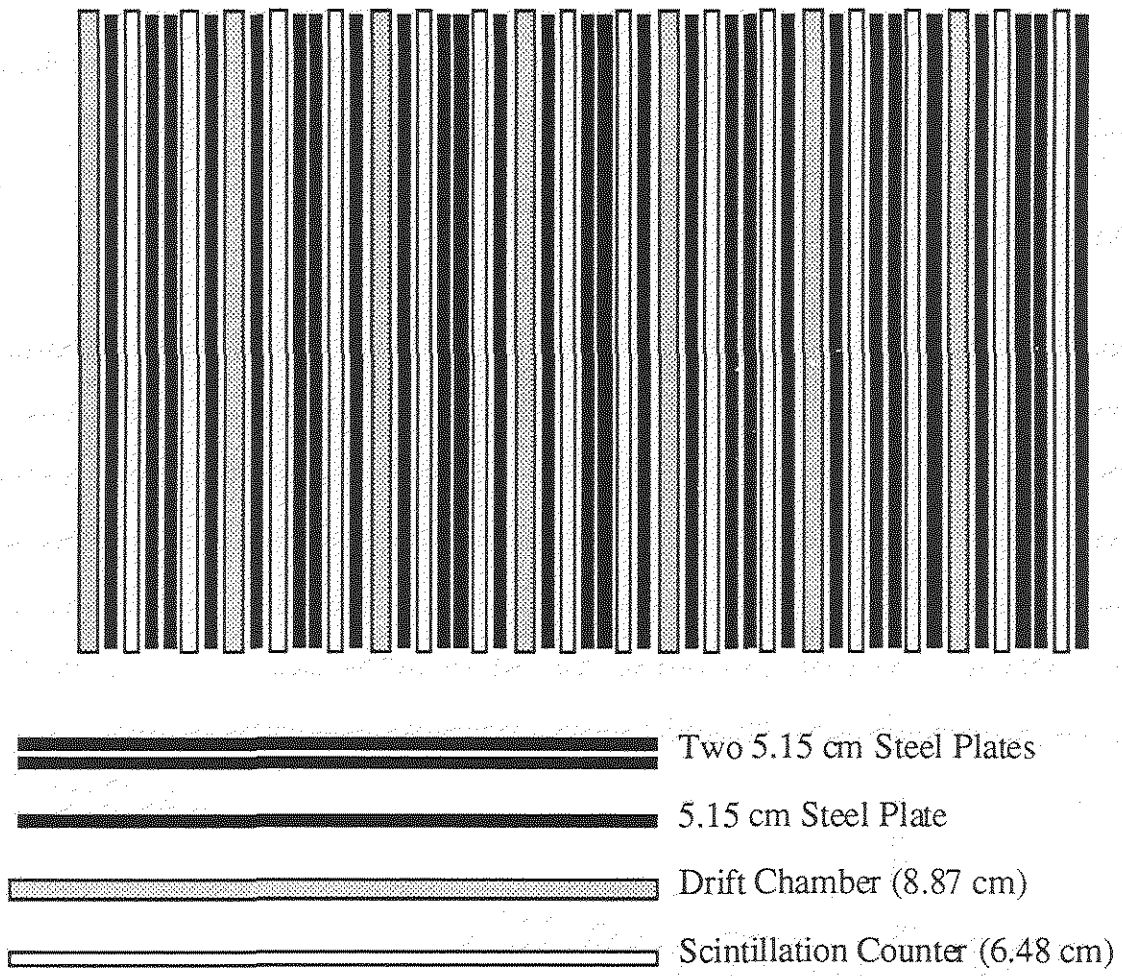

Figure 2.6: Stack layout of a CCFR target cart. A drift chamber is positioned after every two steel plates and a scintillation counter is found after every four.

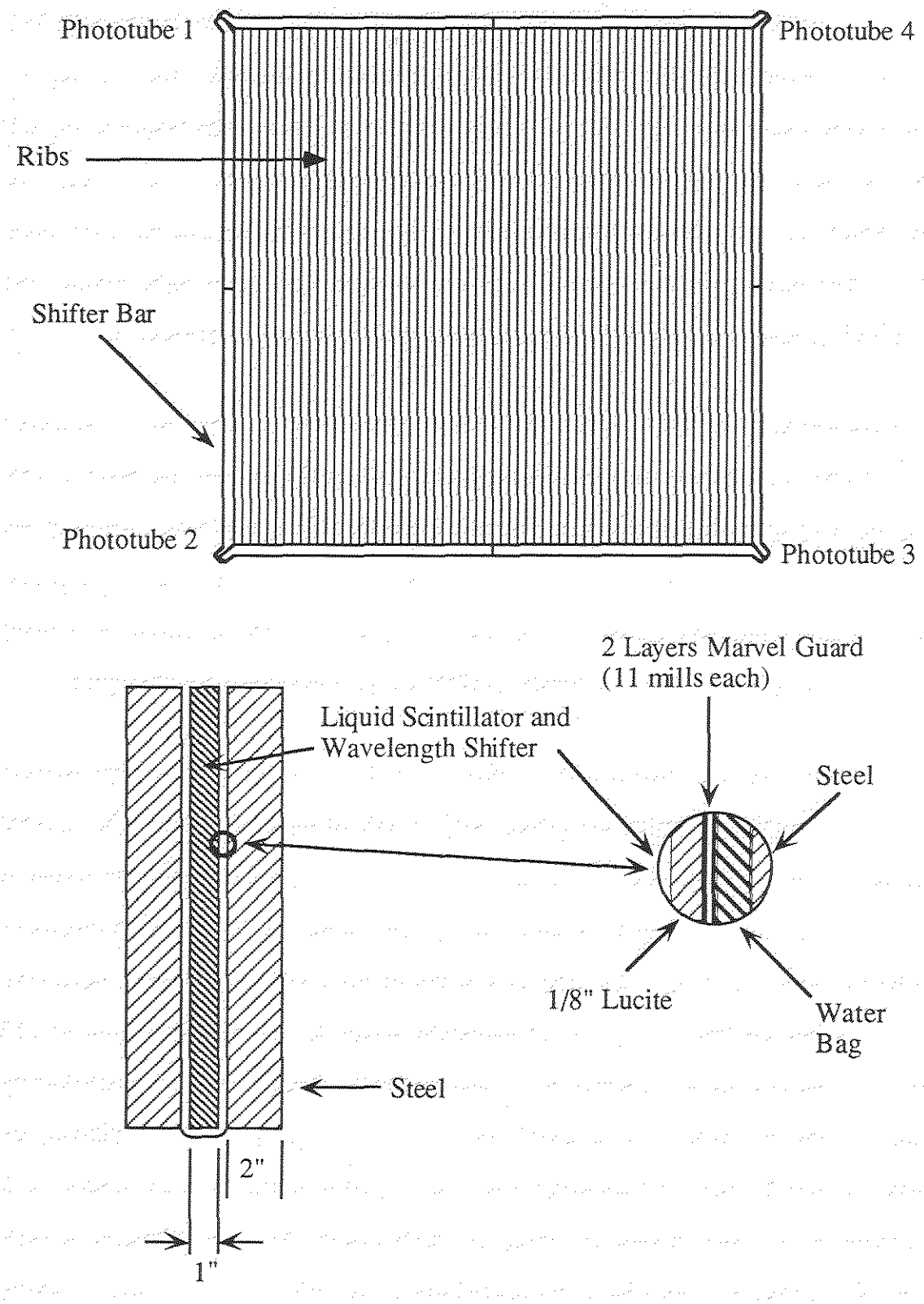

Figure 2.7: CCFR scintillation counter.

A charged particle passing through the counter excites primary fluors in the oil, which radiate ultraviolet light. The ultraviolet light is absorbed by secondary fluors in the oil, which emit visible blue light. The blue light has a longer attenuation length in the oil, about 40 inches, and light emerging below the critical angle is transmitted to the edges of the counter through total internal reflection. At the edges there are one-half-inch-thick BBQ-doped plastic bars that absorb the blue light and re-emit green light. Finally, the green light is guided to the ends of the bars where the phototubes are positioned.

Each counter has four RCA 6342A phototubes, which were operated with a potential drop of 1400 volts across the cathode. A photon striking the cathode has about a 20% probability of liberating an electron. The tube multiplies this signal with a series of ten dynodes, each dynode emitting four electrons for each one absorbed. A single initial photoelectron produces a signal of about 0.25 picoCoulombs. The sensitivity to a muon traversing through the center of a counter is about 2.5 photoelectrons per phototube.

The phototube signal is digitized by a LeCroy 4300 FERA, a fast and buffered readout system with analog-to-digital converters with 11 bits of dynamic range. The counter readout has seven ADC channels of differing sensitivity and the phototube signal is fanned out, giving the system an effective dynamic range of 19 bits. One counter's readout is shown in Figure 2.8. The gate width of the ADCs is 244 *nsec*, beginning 30 *nsec* before the leading edge of the phototube signal, for an integration time of 215 *nsec*. The charge collected is stored on a capacitor and the digitization is accomplished by measuring the time required to discharge the capacitor through a resistor. Digitizing the signal requires 8.5 μsec and another 3.2 μsec is needed to buffer the data, leading to a dead time of 11.7 μsec. A pedestal voltage of approximately 50 counts is applied to each ADC. This pedestal is recorded every accelerator cycle, before the first ping, by taking twenty fake events, so that it can be subtracted from the data readings.

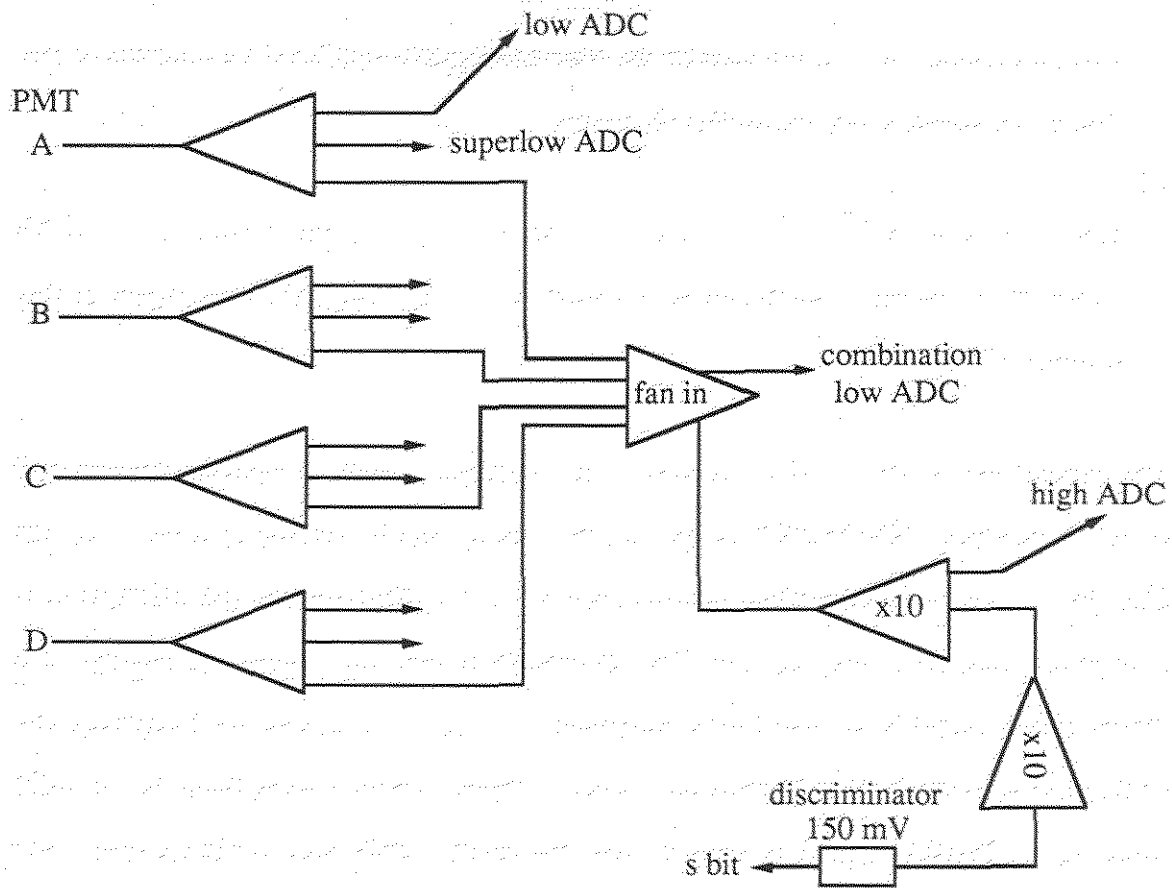

Figure 2.8: Readout electronics for a single scintillation counter. Each counter's signal is digitized by seven ADC channels, as described in the text. The threshold of the s-bit discriminator is set at one-quarter of minimum-ionizing level.

The analog phototube outputs from each counter are fanned out and digitized by seven ADC channels of differing sensitivity:

- There are four LO channels A_j^{LO}, one for each of the j phototubes in a counter. A muon passing through the center of a counter will typically produce 2 ADC counts at each LO channel.

- The combination-low (or COMBLO) channel A^{COMBLO} is the analog sum of the four LO signals. A muon yields 8 ADC counts at this channel.

- The HI channel A^{HI} is the sum of the four LO signals amplified by a factor of ten. The muon signal at this channel is 80 counts.

- The super-low $A_j^{SUPERLO}$ is a sum of LOs from phototube j from every tenth consecutive counter, attenuated by a factor of ten. The typical muon signal at this channel is 0.2 counts.

The signals are so digitized to maximize the dynamic range. A hadron shower will typically produce 1000 to 2000 counts in one counter and be measured directly by the LOs. In the event of an overflow (greater than $2^{11} - 1 = 2047$ counts) the SUPERLO is used to measure the energy deposit. The HI channel is used to measure the passage of a muon, whose signal is too small to be measured by the LOs. Important for triggering, the COMBLO channel is used to produce a logical signal known a scintillator-bit or s-bit, when the COMBLO signal is greater than one-quarter minimum-ionizing level (see Figure 2.8).

At the Tevatron, the accelerator rf buckets arrive in intervals of 18.6 *ns*. Event timing is measured at each counter using the same time-to-digital converters (TDCs) that are used for the drift chambers (see the next Section). Each counter's s-bit pulse is fed to the TDC, providing a time resolution of 4 *nsec*. When information from all active counters is combined, the overall event time resolution has an rms of 2.4 *nsec*.

2.3.1.2 Drift Chambers

Muons emerging from the neutrino interaction are tracked inside the calorimeter target by drift chamber stations. A drift chamber records the passage of a charged particle by detecting the liberation of ionization electrons. Each drift chamber station has an active area of 10 square feet and is comprised of 24 horizontal and 24 vertical cells. Each cell is

5 inches across and 0.75 inches thick and contains three wires. Figure 2.9 shows a sketch of a drift chamber cell.

Each chamber is constructed of Hexcel-covered aluminum walls. Parallel aluminum I-beams spaced every five inches support G-10 cover plates and define the drift chamber cells. Within each cell, a 127 μm diameter copper-beryllium central field wire is held at +350 volts. Two 30 μm diameter gold-plated tungsten wires run on either side of the field wire and are held at +1750 volts. Nylon spacers placed every 12 inches maintain 2 mm spacing between each sense wire and the field wire. The I-beams are maintained at –4500 volts. Finally, the inside of the G-10 cover within each cell is clad with 19 copper cathode strips, each of which is held at a particular voltage so that a uniform electric field of 690 volts/cm is created.

The chambers are filled with an equal mix of argon and ethane. A noble gas, argon does not form molecules and so lacks vibrational or rotational modes of excitation. Therefore, argon readily ionizes when excited by a passing energetic charged particle. After the primary ionization, the electrons and ions separate due to the applied electric field. The electrons drift toward the anode sense wires and accelerate, producing secondary ionizations. Ethane, an organic compound, is included to render the chamber self-quenching. That is, the ethane absorbs the ultraviolet photons liberated in the argon as the electrons drift towards the sense wires. This limits the avalanche of charge that would otherwise smear the signal pulse.

The drift velocity of electrons in the drift chamber is 50 $\mu m/nsec$, so that the total drift time to cross 2.5 in inside a cell is 1.3 μsec. The arrival time of the drift chamber pulse on one wire relative to the event time allows the determination of the particle's position in one dimension, up to the ambiguity of knowing on which side of the wire the particle

passed. Having two sense wires per cell resolves this ambiguity, as the wire closer to the particle received the ionization first. Combining the hit information from two adjacent orthogonal cells proved the determination of the particles' position in the *x-y* plane.

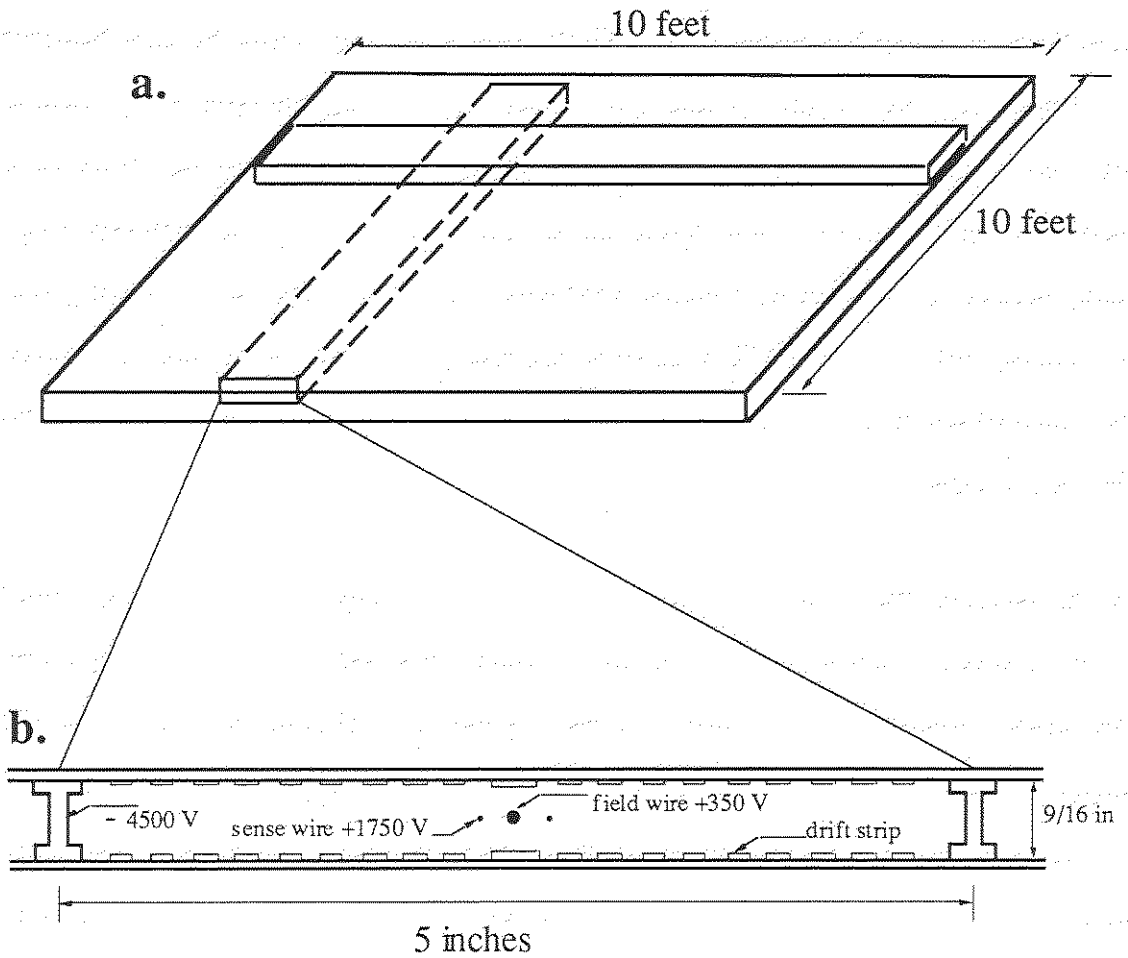

Figure 2.9: Sketch of CCFR target drift chamber section. **a.** Diagram of one chamber. There are two orthogonally-oriented planes per station, consisting of three-wire cells. **b.** A three-wire drift-chamber cell.

The signal from the sense wires is amplified and sent to two coupled TDCs, which have their 8 *nsec* time bins staggered by 4 *nsec*. Thus the coupled TDC digitizes the time of the pulse in 4 *nsec* bins. The TDC is capable of buffering hits in 512 bins, so its live time is slightly in excess of 2 μsec and so can buffer the full drift range of the cell. The TDC

then takes 8 *nsec* to transfer its information into a first-in-first-out (FIFO) buffer. The FIFO buffer can store 32 events per spill.

The overall position resolution of the drift chambers depends on the time resolution of the TDCs, variations in the electric field, and misalignment of the chambers. All elements of the detector were aligned with an optical survey, and precise alignment of the chambers was accomplished by using high-energy straight-through muons with $p_\mu > 125\ GeV$. The alignment procedure iteratively varied the chamber coordinates to provide the best fit to the sample of straight-through muons. In the target, such an alignment procedure was straightforward because the target is unmagnetized, and the effects of multiple Coulomb scattering (described in the next Chapter) diminish with energy. The intrinsic position resolution of the target drift chambers is 225 μm.

2.3.2 Muon Spectrometer

Downstream of the target calorimeter lies a muon spectrometer consisting of three large toroidal iron magnets instrumented with acrylic counters and with arrays of 10-square-foot- drift chambers. Each of the three instrumented magnets is referred to as a toroid cart. A sketch of a typical toroid cart is shown in Figure 2.10. Each toroid cart is segmented into eight 8-inch-thick cylinders, called washers, each with a 70-inch outer radius and a 5-inch inner radius. Each washer is divided horizontally into semicircles separated by 0.95 *cm* with aluminum spaces to allow insertion of a Hall probe. The bottom of each washer includes two iron legs that support the magnets on movable platforms.

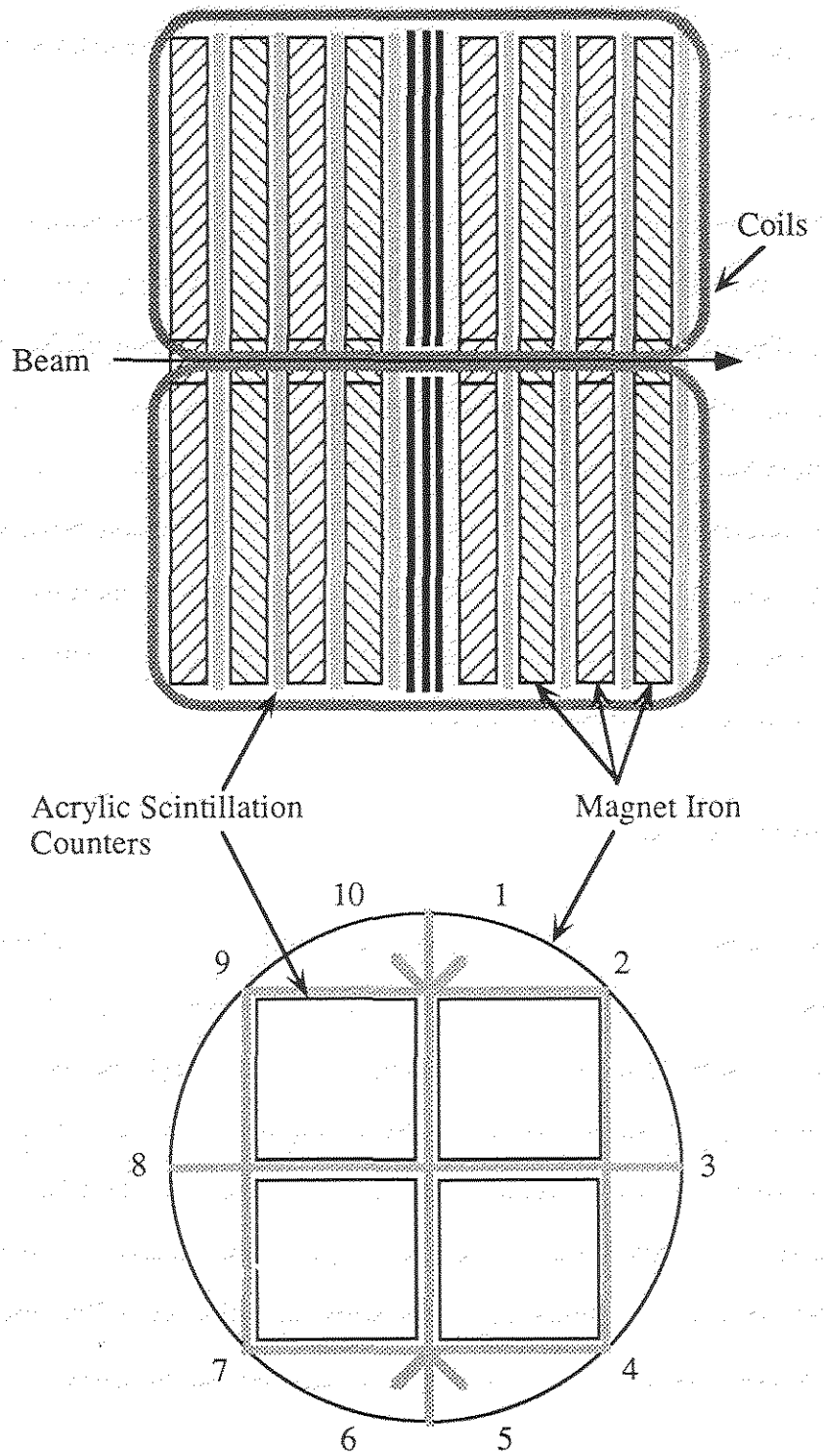

Figure 2.10: Schematic drawing of a CCFR toroid cart, showing overhead and transverse views. In the transverse view, the shaded liens indicate the wave shifter bars along the outer edges of the scintillators, and the numerals indicate the positions of phototubes.

Four copper coils of 12 turns each encircle the magnets at 90° intervals. A current of 1200 A produces a magnetic field ranging from 1.9 T near the center of the toroid to 1.55 T near the outer edge. The field was found to be azimuthal throughout the magnets except for a small radial component at the iron legs [Kin91]. A muon traveling the length of the spectrometer receives a 2.4 GeV transverse momentum component from the magnetic field.

Tracking muons through the spectrometer is accomplished by five sets of the five drift chambers, positioned immediately downstream of each toroid cart and 3 m and 7 m behind the last toroid. The two most downstream sets of drift chambers are referred to as the blue cart. The drift chambers in the muon system contain one-wire cells. To resolve the left-right ambiguity, the chambers are staggered by 1/4 of a cell width. This staggering method is possible in the muon spectrometer because successive drift chambers are not separated by steel, as they are in the target, making the effects of multiple Coulomb scattering between chamber planes negligible. Muons are tracked cleanly through the set of five drift chambers, allowing the five to be treated as a unit.

In addition, there are two u-v drift chambers, whose orientation is rotated 5° about the beam axis. One is located immediately downstream of the target and the other included in the set of five chambers on the upstream side of the blue cart.

Alignment of the drift chambers in the toroid spectrometer using straight-through muons was more complicated than in the case of the target calorimeter because of the bending of tracks in the spectrometer's magnetic field. A description of the alignment procedure can be found in Ref. [Rab92]. The alignment of the toroid drift chambers was accomplished to within 380 μm, and the overall position resolution of these drift chambers is 0.5 mm.

The muon spectrometer is instrumented with acrylic scintillation counters, and for fast detection of muons for triggering. One set of counters, called T2, is located just after the first toroid cart (in gap 1), and another set, T3, is after the second cart (in gap 2). T2 is composed of a total of 10 counters, organized into three planes, and T3 is made up of six counters, organized into two planes. These counters are equipped with 56AVP phototubes. The first two T2 planes and both T3 planes are composed of two narrow counters, referred to as hodoscopes, and one large counter. The final T2 plane is composed of four hodoscopes. Usually, the term "hodoscope" refers to a counter system capable of making a good determination of particle position. In this case, no measurement of position is made. The trigger condition for the gap is satisfied if any counter in the gap fires its s-bit.

There is an acrylic counter plane positioned after every washer. Each of these planes is divided into four separate counters, so that the quadrant through which the muon traveled is determined. The four planes in one half-cart are grouped together. These counters, forming 24 planes in all, are used to define the PTOR trigger condition, which is described below.

2.4 Data Acquisition

The CCFR detector (the target calorimeter and muon spectrometer) records the raw data of a neutrino event. These raw signals—the pulse heights from the scintillation counters, the drift chamber hits, the timing pulses—must be converted to physical quantities like muon energy, muon angle, and hadronic energy. In the process, the data is reduced to select the events of interest, while discarding events due to background or noise.

2.4.1 Event Triggers

The first step in concentrating on events of interest is to record only those that satisfy basic requirements or *triggers*. The satisfaction of a trigger causes the data acquisition system to accept the event and record the full detector response. A subset of the detector is used to define the trigger, using scintillator signals that can be processed quickly. Each trigger rigorously defines an event signature that can be used to discriminate between different types of events. The triggers are designed to accept charged-current and neutral-current neutrino events and other specific events of interest while rejecting cosmic ray and beam-related backgrounds.

The beam-related backgrounds are caused by charged particles emanating from the berm, due to neutrino interactions in the berm. Two $17.5 \times 4.5\ m$ scintillation counter arrays are positioned immediately upstream of the first calorimeter cart to form a veto wall. The veto wall counters are shielded from an upstream flux of low-energy hadrons and photons by a one-meter-thick concrete wall, and lead sheets are mounted between the two scintillators of the veto wall. During beam running, secondary particles from the berm interact with the air above the detector and illuminate the detector with low-energy photons. A layer of lead bricks is stacked above the toroid gaps to shield the trigger counters.

The muon trigger hardware consists of scintillators located in the muon spectrometer. The T2 and T3 counters, located in the gaps between toroid carts, are used to define the charged-current event trigger. The acrylic counters positioned after each of the spectrometer's 24 magnetic washers are used to define the PTOR condition, used for Triggers 4 and 6. Six separate triggers were used during the runs:

- **Trigger 1** (Charged Current): This trigger is designed to selected charged-current events. It attempts to select events in which a muon originates in the target and penetrates into the toroid for momentum analysis. This trigger requires the presence of a charged particle in the last target cart and in the first toroid cart, while requiring no activity in the veto wall. Either of two topologies must be satisfied: In the first, at least two out of the last four counters (counters 1 through 4) fire their s-bits, and a minimum-ionizing signal is record in both T2 (toroid gap 1) and T3 (gap 2). The second trigger definition does not require the muon to penetrate to T3 but demands the firing of two s-bits out of target counters 9 through 12.

- **Trigger 2** (Neutral Current): This trigger is designed to select neutral-current events, which are events in which a Z^0 is exchanged to create a hadronic shower without a muon track. It demands that there be at least 8 *GeV* of energy in 8 adjacent counters, coincident with 2 MIPs deposited in two counters out of a set of four consecutive counters, and no signal in the veto wall. No muon requirement is made.

- **Trigger 3** (Penetrating Muon): This trigger is used to study muons ranging out in the calorimeter. It requires that 16 counters in the target (not necessarily consecutive) fire their s-bits with no veto, along with 4 *GeV* of hadronic energy deposited in a set of 8 consecutive counters (not necessarily those that fired their s-bits).

- **Trigger 4** (Redundant Charged Current): This trigger was used to measure the Trigger 1 inefficiency, and found it to be $< 10^{-4}$. It is similar to Trigger 1; instead of counters 1 through 4 and counters 9 through 12, it uses counters 5 through 8 and 13 though 16. Instead of using T2 and T3, Trigger 4 requires that PTOR be satisfied, which is that two out of four acrylic counters in the same quadrant in each of the half-

carts fire their s-bits. Since Trigger 4 makes this stricter requirement than Trigger 1, all of the Trigger 4s should be included in the Trigger 1 sample.

- **Trigger 5** (Test Beam): The use of this trigger is reserved for test beam running, when muon and hadron beams are directly incident on the target.

- **Trigger 6** (Straight-Through Muon): This trigger is designed to select muons produced upstream of Lab E that pass through the entire detector. One s-bit out of a set of four in each of the target carts must fire, along with the veto, and the muon must penetrate the toroid system and satisfy the PTOR requirement. The stiff muon tracks passing this trigger are used for calibration and drift-chamber alignment. In E744 this trigger was prescaled down by a factor of 8. In E770 the trigger was generally not prescaled in order to accumulate additional events for counter energy calibration.

2.4.2 Data Collection

The raw data collected in both runs of the experiment fill about 1000 open-reel tapes, comprising approximately 300 gigabytes of information. The number of events recorded according to trigger type is listing in Table 2.1.

Once written on tape, the data passed through several stages of offline processing, which ultimately reduced it to data summary tape (DST) format. The raw data's first pass was through a process called stripping, which unpacked ADC pulse heights and subtracted their pedestal values, and otherwise rewrote the data in a modified format. The second-pass data analysis passed the stripped data through a program called the cruncher, which did the bulk of the processing to extract the events' characteristics: pulse heights were converted to hadron energies, TDC times to hit positions. A pattern-recognition algorithm

fit muon tracks to the hit positions, leading to a determination of the muon angle and energy. The final event observables—the hadron energy, the muon angles and energies, and secondary variables like x and y—were written to a DST. The DST file contains the basic set of data used for physics analysis.

Event reconstruction, writing DSTs, and the final physics results are all predicated on the ability to measure the absolute hadron shower and muon angles and energies, the parameters that define a charged-current deep inelastic scattering event. The next chapter describes the detector calibration: the process that determines the precise number of ADC counts that correspond to 1 GeV of hadronic energy, and the precise bend of a muon's trajectory that corresponds to a measurement of 1 GeV of muon momentum.

Table 2.1: Triggers written to tape in E744 and E770. An event can satisfy more than one trigger.

Trigger Type	E744	E770
1	1740427	1981136
2	2267724	2915707
3	1611230	2001988
4	696664	806985
5	16447	64627
6	166682	1406410
Total	3235717	5095487

3 Calibration and Data Analysis

Neutrino and antineutrino deep inelastic scattering events are specified by three parameters: the energy of the outgoing muon E_μ, the angle of the muon θ_μ, and the total energy of the hadronic shower E_{HAD}. This Chapter describes how each of these three quantities are measured and calibrated.

3.1 Hadron Energy Measurement

When a neutrino scatters inelastically with a nucleon, the nucleon is broken apart and its constituents emerge in the form of hadrons, primarily pions, kaons, protons, and neutrons. In the detector, these hadrons decay and interact, producing a hadron shower that propagates until its energy is totally absorbed by the calorimeter. In the calorimeter, the shower propagates through active detector elements, the scintillation counters and drift chambers, and passive elements, primarily the steel plates. The fraction of shower energy deposited in the counters provides a sample of the total shower energy.

The energy deposited in any material by a high-energy particle is largely independent of particle type and energy, and is referred to as the minimum-ionizing energy. As the hadrons pass through the detector, they interact producing showers of secondary particles. The interactions are energy-dependent, hence the number of particles in the shower is a function of the energy of the original particle. As each secondary particle passes through a scintillator, it deposits the same minimum-ionizing energy, and so by dividing the amount of energy measured in a single scintillator by the amount of minimum-ionizing energy, one measures the number of "minimum-ionizing particles," or MIPs. This is why the layers of scintillator in the detector are called scintillation "counters," because they effectively count the number of particles passing through them: the pulse heights

registered by the phototubes in the corner of each counter are proportional to the number of MIPs that pass through the counter.

Although the counters are of identical design, slight variations in their construction, the phototube gain, and the counter electronics causes their response to vary. Therefore, each counter is calibrated separately. In practice the response of each counter is determined by a set of calibration coefficients and phototube gains, which provide the conversion between ADC counts and MIPs for each counter. An overall energy calibration specifies the number of MIPs that corresponds to 1 *GeV* of energy. This calibration is determined for hadronic showers, electromagnetic showers, and minimum-ionizing muons separately.

3.1.1 Counter Gain Calibration

The muon energy loss distribution as measured for one of the counter is plotted in Figure 3.1. A muon's energy deposit provides the standard measure of minimum-ionizing energy. Muon energy loss is well-understood. It is described by a Landau distribution, with a pronounced peak due to ionization and a long high energy tail. The tail is due to stochastic energy losses from bremsstrahlung, pair production, and delta-ray production. Each counter's response is calibrated to the standard muon signal by analysis of the sample of Trigger 1 and Trigger 6 data. The muons in this sample are momentum-analyzed by the toroid spectrometer, and small muon-energy dependent corrections are also included in determining the counters' response.

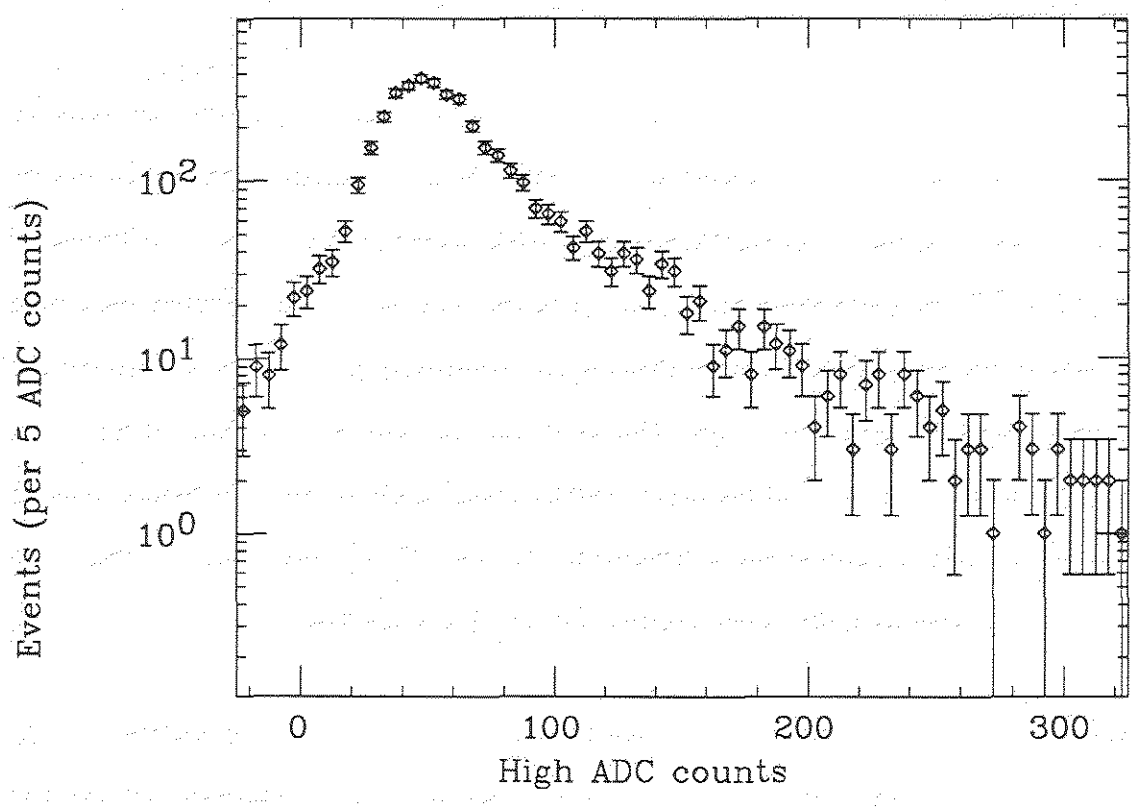

Figure 3.1: Muon energy loss distribution in a scintillation counter.

In order to find each counter's response to a minimum-ionizing particle, an iterative procedure called the "truncated mean" is used. First, the mean energy deposited by muons in a scintillation counter is measured in units of ADC counts. The distribution is truncated from 0.2 to 2.0 times this mean and a mean is found. This process is repeated, each time returning to the original ADC count distribution, truncating from 0.2 to 2.0 around the new mean, until the mean converges. This procedure minimizes the effects of the muon energy on the determination of the mean. The truncated mean of the distribution is taken to be one MIP in that counter and is denoted by $\Delta E_i\left(V_x, V_y, t\right)$, indicating that this mean depends on the counter i, the vertex position $\left(V_x, V_y\right)$, and the time t.

Muon energy loss is measured with the HI ADC channels, but the hadron energy measurement is made with the LO channels or the SUPERLO channels (if the LO channels are saturated). To convert the muon energy loss measured by the HIs to that measured by the LOs and the COMBLOs, a set of interchannel calibration coefficients are used. The relationships between the channels for each counter in terms of the counter's calibration coefficients:

$$A_i^{COMBLO} = \sum_{j=1}^{4} a_{ij} A_{ij}^{LO} \tag{3.1}$$

$$A_i^{HI} = \beta_i A_i^{COMBLO} \tag{3.2}$$

where A_i refers to the response of counter i in a particular channel, β_i is each counter's HI-to-LO calibration coefficient, and a_{ij} are calibration coefficients for each phototube j in counter i. The calibration coefficients are determined by minimizing the quantities

$$\sum_{events} \sum_{i=counters} \left(A_i^{COMBLO} - \sum_{j=1}^{4} a_{ij} A_{ij}^{LO} \right)^2 \tag{3.3}$$

and

$$\sum_{events} \sum_{i=counters} \left(A_i^{HI} - \beta_i A_i^{COMBLO} \right)^2 \tag{3.4}$$

and are determined to better than 1% because of good overlap in the dynamic range of the channels (small nonlinearities in the electronics were also measured and included). Typical values are $a \sim 0.8$ and $\beta \sim 12$.

Assuming no variation in response over time or position within a counter, the LO energy in MIPs for each counter is given by

$$\Delta E_i = \beta_i \sum_{j=1}^{4} a_{ij} A_{ij}^{LO} \tag{3.5}$$

3.1.2 Map and Time Variation Corrections

A counter's energy response is not uniform over the active area nor does it stay constant with time. The counter response differs according with the position in the counter where the particle passed, due to the attenuation of light within the scintillator oil and wave-shifter bars and differences in phototube response. Counter response is also time-dependent, primarily because phototube gains tend to drift, and because of a slight degradation of the scintillator oil. Frequent measurements of phototubes gains were made to account for detector changes over time. Differences in detector response due to position are handled with map corrections. All counter measurements are corrected so that they can be interpreted as having occurred at $t = 0$ and $\left(V_x, V_y\right) = (0,0)$.

The map corrections are determined by dividing the active area of each counter into nine-by-nine inch squares, and measuring the counter's response to muons in each of these

position bins separately. The most probable value of the energy distribution for each square bin is determined using the truncated mean algorithm, and a bin-center correction is made because the energy response varies slightly within each bin. The final map correction is given by

$$R_i^{map}\left(V_x, V_y, 0\right) = \frac{\Delta E_i\left(V_x, V_y, t=0\right)}{\Delta E_i\left(0,0,t=0\right)} \tag{3.6}$$

Figure 3.2 shows a counter map, which displays contours of the muon response relative to the center of the counter.

The time variations in counter response are measured at the center of a counter, where the event population is highest. To account for drift in phototube gains, the gain for each tube relative to the four in the counter is determined by the quantity

$$G_{ij}\left(0,0,t\right) = \frac{4a_{ij}\left(t\right)A_{ij}^{LO}\left(0,0,t\right)}{\sum_{k=1}^{4} a_{ik}\left(t\right)A_{ik}^{LO}\left(0,0,t\right)} \tag{3.7}$$

Measurements of the relative phototube gains were made frequently. At the start of E744 and again at the start of E770, the phototube base voltages were adjusted to equalize the relative gains of a counter's four tubes. In this procedure, known as balancing, a 1 mCi ^{137}Cs source is positioned at the center of a counter and the voltage at each phototube base is set to make the tubes' anode currents equal to within ±25%. The muon data were used to better determine the relative gain throughout the running. From time to time during the run, counters that fell severely out of balance were readjusted with the source.

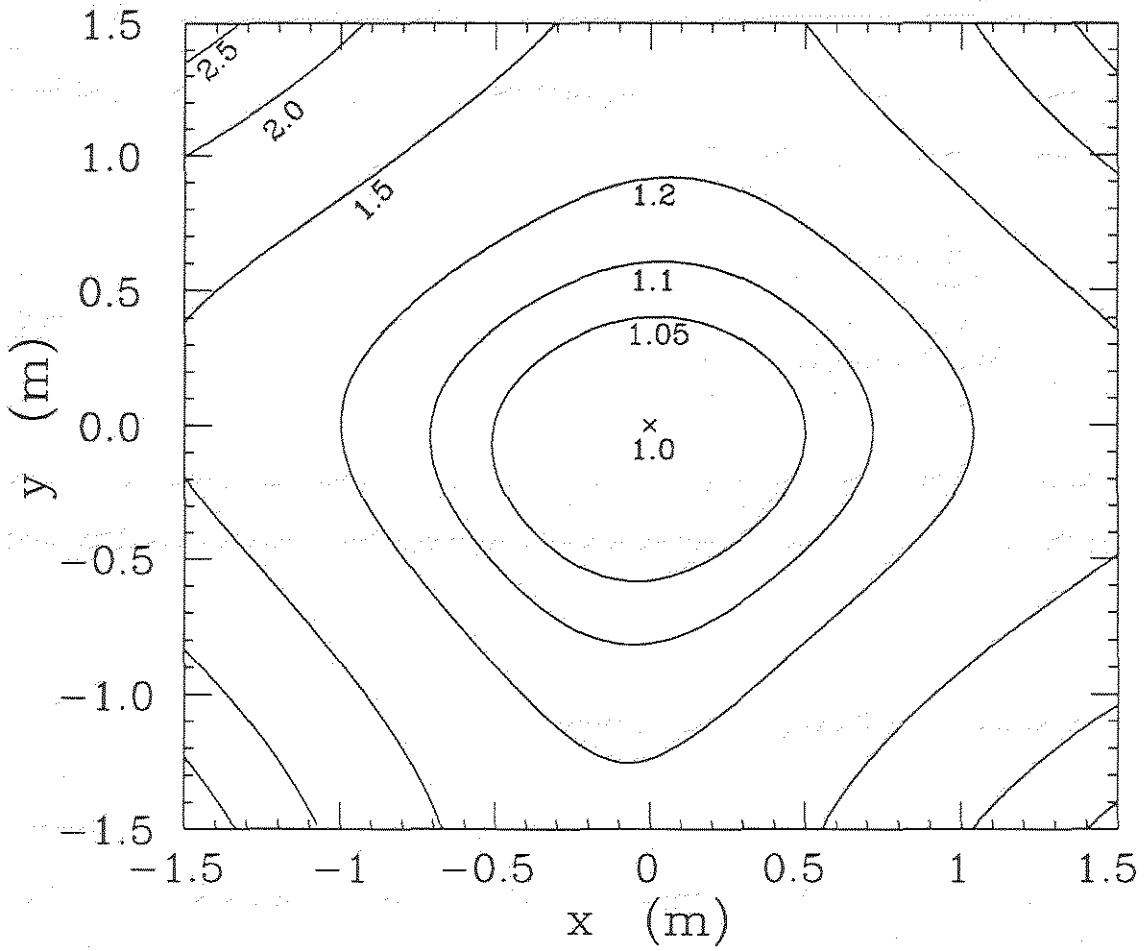

Figure 3.2: Contours of the relative muon response for counter 37.

Combining the map and time variations together, the energy loss in MIPs measured by a scintillation counter is given by

$$\Delta E_i = \frac{\beta_i(t)\sum_{j=1}^{4} A_{ij}^{LO}(t) G_j(0)/G_j(t)}{\Delta E_i(0,0,t) R_i\left(V_x, V_y, 0\right)} \tag{3.8}$$

with all position and time-dependent corrections included. A small adjustment is made to assure that the counter response is the same for all counters; this is described in Appendix F.

3.1.3 Calorimeter Energy Calibration

The target calorimeter was absolutely calibrated twice with hadron test beams [Sak90]. These calibration runs took place before E744 in 1984, and in the middle and end of E770, at the end of 1987 and early 1988. The neutrino test west (NTW) beamline at Fermilab transported beams into the CCFR experimental hall (Lab E) and various target carts were moved into the test beam for calibration. The NTW beam contained secondary particles produced by the primary Tevatron proton beam, which were charge- and momentum-selected. Pions were the dominant component of the test beam. For positively-charged test beams, the proton fraction was about 20% at 100 GeV, increased to about 50% at 300 GeV. The electron component was about 10% at 50 GeV and increased at lower momenta; the kaon component was about 5%, and the muon component was about one percent.

The total energy response of the calorimeter is obtained from runs where the test beam is centered on the target. Figure 3.3 plots $\langle E/p \rangle$ versus $\langle p \rangle$, where $\langle\ \rangle$ indicates the mean of a distribution from various test beam runs, where p being the momentum of the test

beam and E the total energy measured by the calorimeter in units of MIPs. $\langle E/p \rangle$ is constant to within 1%, 4.74 MIPs/GeV, indicating that the response of the calorimeter is linear to better than 1%. Furthermore, there is no difference in the response of the identical target carts at the 1% level and the calibration between the E744 and E770 calibration runs is different by 0.3%.

The calorimeter's resolution function for hadrons is Poisson-like and is parameterized by the function

$$f(x,\bar{x}) = \frac{\bar{x}^{x} e^{-\bar{x}}}{\Gamma(x+1)} \tag{3.9}$$

where $\bar{x} = E/s$, s is a scaling parameter, and $\bar{x}$ is the mean. The energy distributions of 25 and 200 GeV hadrons from the E770 test beam are shown in Figure 3.4. By fitting for s and $\bar{x}$, the values of $\sigma = s\sqrt{\bar{x}}$ and $\langle E \rangle = s\bar{x}$ give the fractional sampling resolution $\sigma/\langle E \rangle$. This resolution is characterized by the statistical fluctuations of the N particles sampled in the shower, therefore the resolution is dominated by sampling fluctuations.

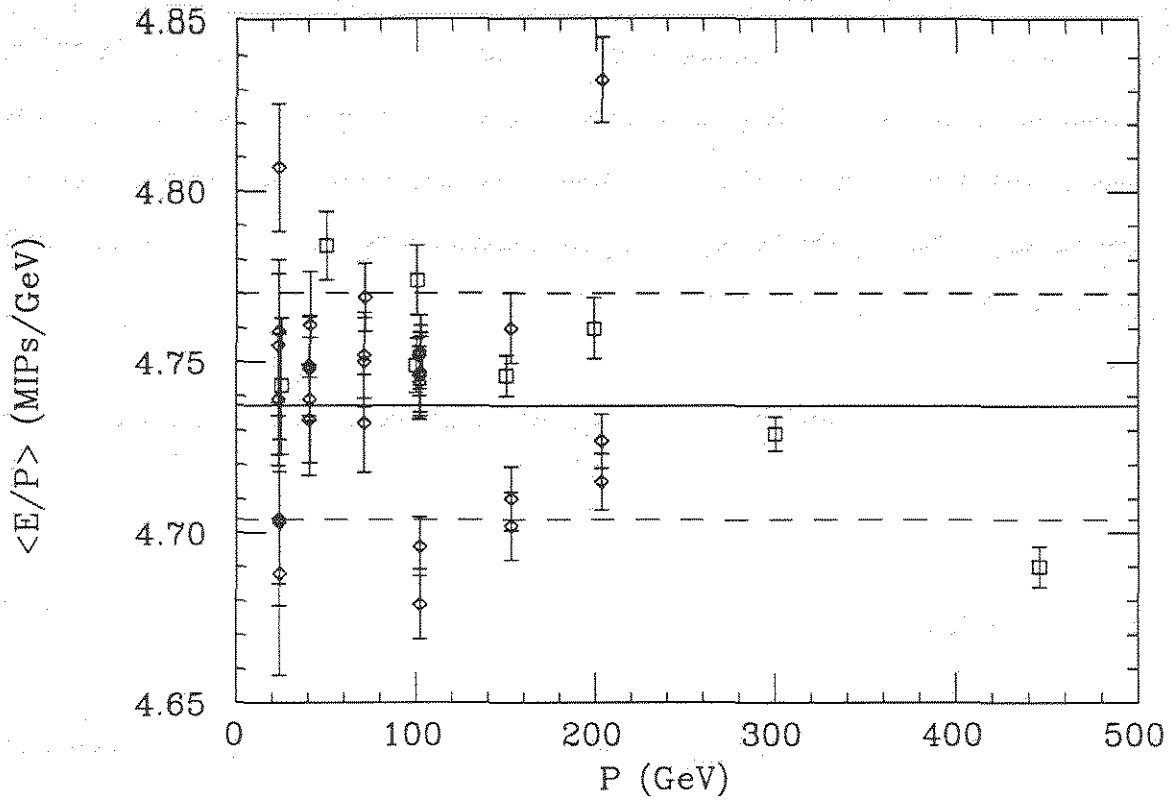

Figure 3.3: Energy response of the CCFR calorimeter, relating MIPs to *GeV*. Hadronic test beam data are for E744 (squares) and E770 (diamonds). The horizontal line is a weighted mean of the E770 points, 4.737 MIPs/*GeV*. The fractional rms dispersion about the mean for the E770 (e744) point is 0.7% (0.8%), and is shown for the E770 points by the dashed lines. The weighted mean of the E744 points is 4.724 MIPs/*GeV*.

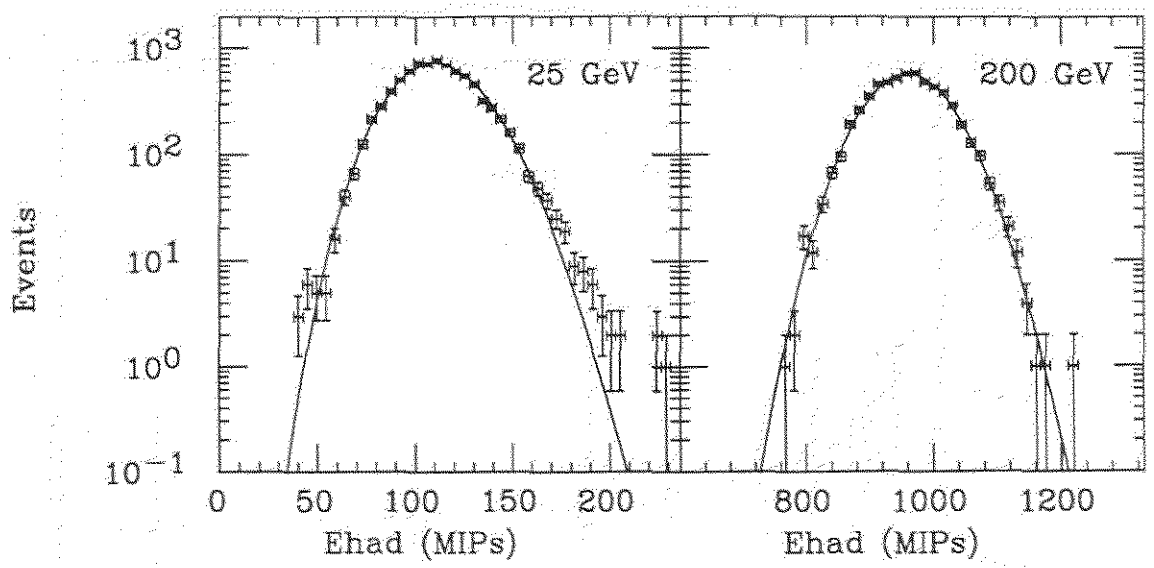

Figure 3.4: Energy distributions of 25 and 200 *GeV* hadrons from the 1987 calibration. The Poisson-like parameterizations of the resolution functions are shown by the solid curves.

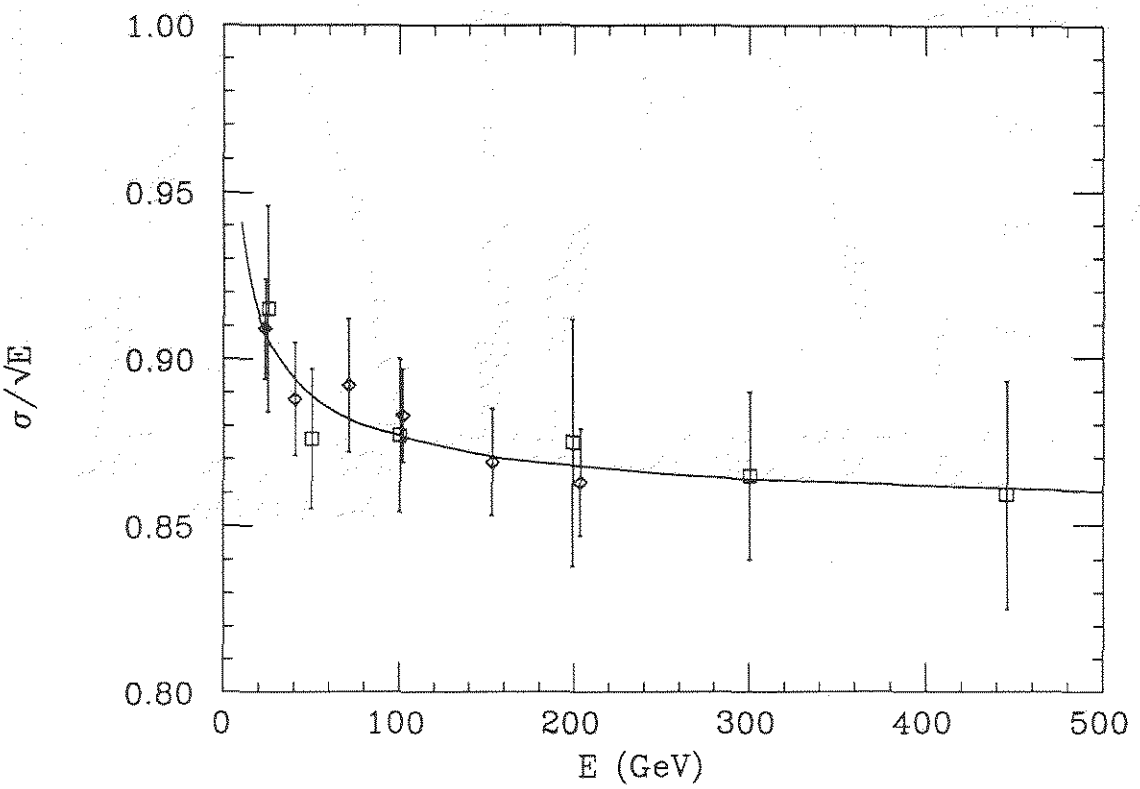

Figure 3.5: The hadron shower energy resolution of the CCFR calorimeter from 25 to 240 *GeV* test beam calibrations. The curve is the value of Equation 3.10.

From these data, the energy resolution is found to be

$$\frac{\sigma}{E} = \frac{0.847 \pm 0.015}{\sqrt{E}} + \frac{0.30 \pm 0.12}{E} \tag{3.10}$$

where E is in GeV. The values of $\sigma/\sqrt{\langle E \rangle}$ are shown in Figure 3.5 for various test beam energies. The term proportional to $1/\sqrt{E}$ measures the sampling fluctuations, and the term proportional to $1/E$ is characteristic of detector-related noise.

The calorimeter response to electromagnetic showers was calibrated using the electron component of the 25 and 50 GeV test beams. The electromagnetic resolution was found to be $\sigma_e / E = 0.60/\sqrt{E}$.

As a final study of the calorimeter response, the calibration for minimum-ionizing muons was determined using the E744 sample of neutrino-induced charged-current events in which the muons ranged out inside the calorimeter. Muons emerging far from the end of the hadron shower were selected in order to measure the response to muons alone. Using this sample, the muon energy in GeV, denoted by p, is determined by comparing the track length to entries in range-energy tables [Koi78]. The distribution of E/p for the range-out muons, where E is the total energy deposited by the muon in the counters, is shown in Figure 3.6. The resolution for these range-out muons is $\sigma_\mu / E = 0.17$.

The energy calibration of the CCFR calorimeter is summarized in Table 3.1, for hadronic showers (π), electromagnetic shower (e), and minimum-ionizing muons (μ). The errors given include both statistical and dominant systematic errors. As shown in the Table, the calorimeter response to π's and e's is very close: the ratio of the electromagnetic to hadronic response of the calorimeter, denoted by e/π, is 1.1.

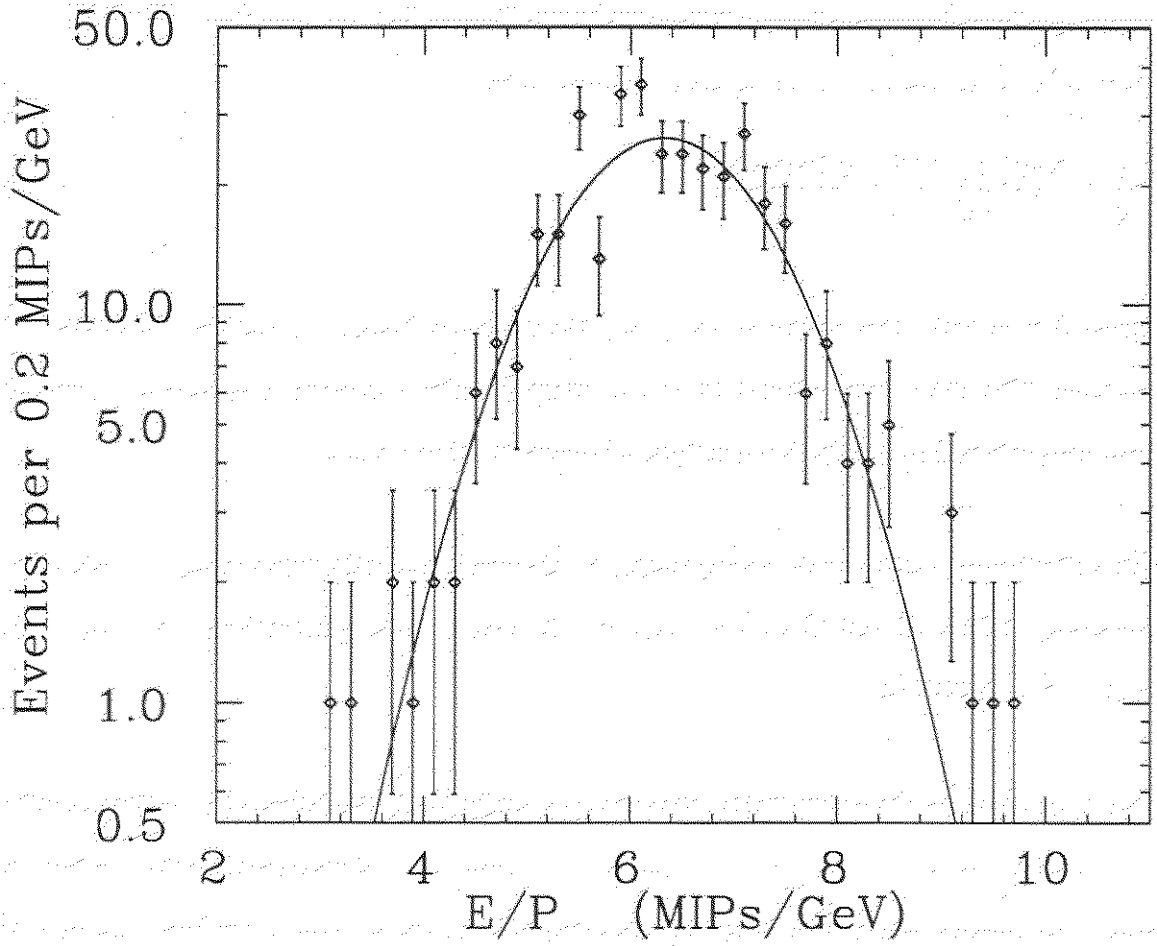

Figure 3.6: The *E/p* distribution for E744 range-out muons. *E* is the energy measured along the track length in the counters in *MIPs*; *p* is the muon energy in *GeV* obtained from the path length and the range-energy tables.

Table 3.1: CCFR calorimeter calibration constants.

Type of signal	calibration	σ/E
π	4.73 ± 0.02 MIPs/GeV	$0.847/\sqrt{E} + 0.30/E$
e	5.25 ± 0.10 MIPs/GeV	$0.60/\sqrt{E}$
μ	6.33 ± 0.17 MIPs/GeV	0.17

3.1.4 Hadron Energy Calculation

The detector region over which the counter response is summed in order to contain a hadronic shower (or electromagnetic shower) is rigorously defined. The origin of a shower, called *PLACE*, is the more upstream of the most upstream pair of counters than each contain more than 4 MIPs of energy. The shower end, called *SHEND*, is defined as the first counter downstream from *PLACE* that is followed by three consecutive counters with less than 4 MIPs. The total shower energy is defined as the sum of the energy measurement from all counters from *PLACE* to (*SHEND* – 5), so as to include the lowest energy particles at the end of a shower.

A determination of hadronic energy exclusive of muon energy deposition requires the subtraction of 1 MIP from each counter for each muon track in the event. The same approximation to the muon restricted energy loss in the hadron shower region, *RLOSSH*, is subtracted from the hadron shower energy as is added to the muon energy in Equations 3.23-3.24. There is an important exception: since the MIPs in the hadron shower region are interpreted as hadronic interactions in the calorimeter, the hadron energy calibration constant C_{HAD} = 0.211 GeV/MIP is used in the calculation (see Table 3.1). Thus the hadron energy is given by:

$$EHAD = C_{HAD} \times \left(\frac{\beta_i(t) \sum_{j=1}^{4} A_{ij}^{LO}(t) G_j(0) / G_j(t)}{\Delta E_i(0,0,t) R_i\left(V_x, V_y, 0\right)} - RLOSSH \right) \tag{3.11}$$

The MIPs are measured in the calorimeter, but *RLOSSH* is a function. Therefore, if a hadron shower stochastically deposits a small number of MIPs, the value of *EHAD* may be negative.

The "true" or "generated" value of *EHAD* must always be positive, but the measured value can be negative. Figure 3.7 shows a sketch of the anticipated relationship between the generated and measured *EHAD* distributions: the generated *EHAD* cuts off at $EHAD = 0$, but the measured *EHAD* distribution will have a component below zero. Even though the data will have a peak of events at $EHAD = 0$ due to quasi-elastic processes that are not modeled in the Monte Carlo, the relationship pictured in Figure 3.7 is expected to hold: the area delimited by the measured distribution for $EHAD < 0$ will equal the area subtracted from the $EHAD > 0$ distribution, and the point at which the measured distributions reach half-maximum should be the same for the data and the Monte Carlo.

However, when the distributions of low *EHAD* events for the data and the Monte Carlo (see Chapter 4) were compared, it was observed that the data was offset by -150 *MeV* from the expected shape. This was attributed to small errors in the ADC LO pedestal subtraction. To correct for this, 150 *MeV* is added to the value of *EHAD* calculated from Equation 3.11. A systematic error of 100 *MeV* is assigned to this procedure from the error in determining the *EHAD* shift from the plot. Figure 3.12 shows the reconstructed *EHAD* distributions after this correction is applied.

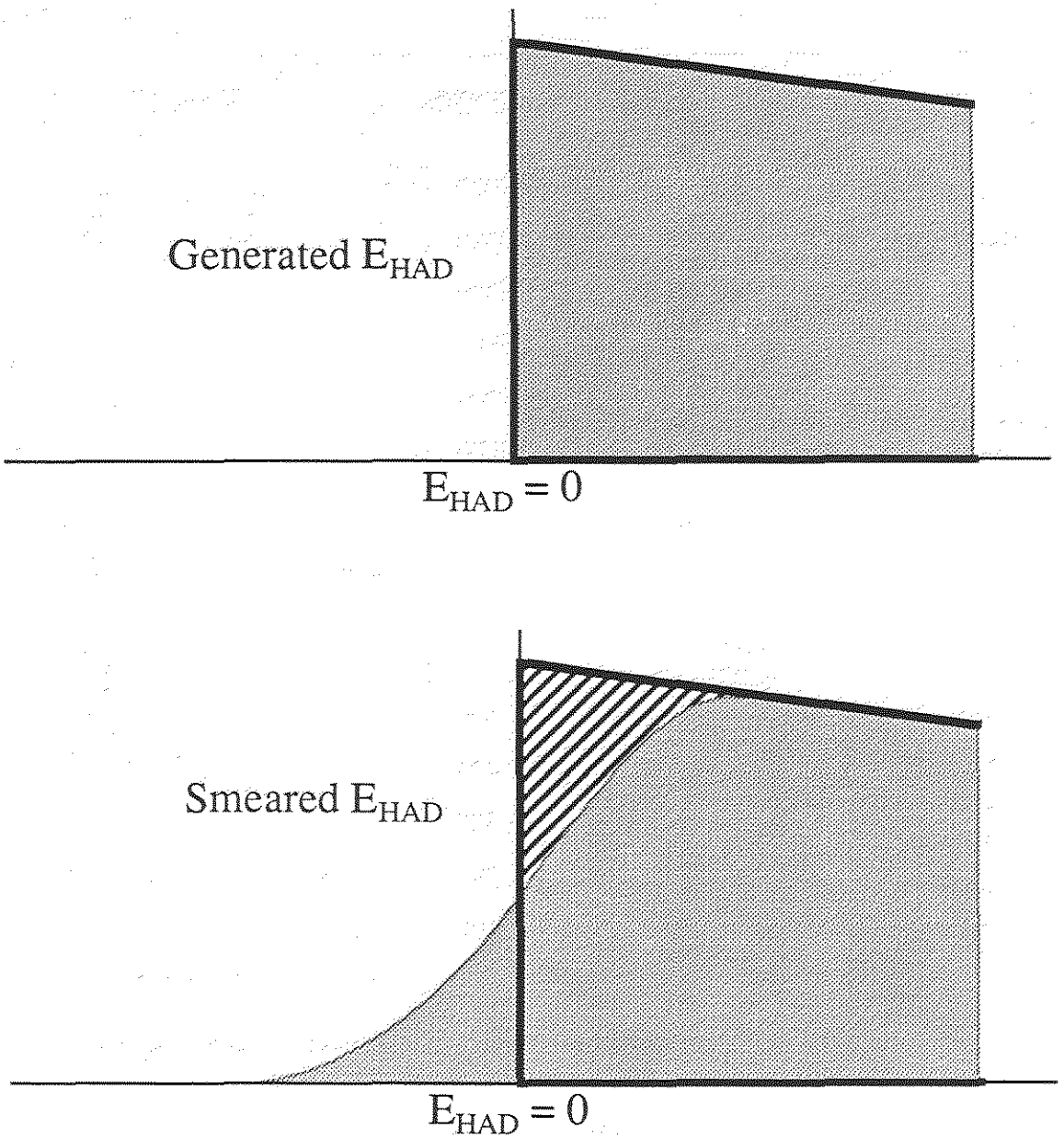

Figure 3.7: A sketch of the expected generated versus measured *EHAD* distributions. Note that the number of events with *EHAD* < 0 is equal to the area marked out by diagonal lines in the Figure. The sketch shows the expected cross-section for deep-inelastic scattering only.

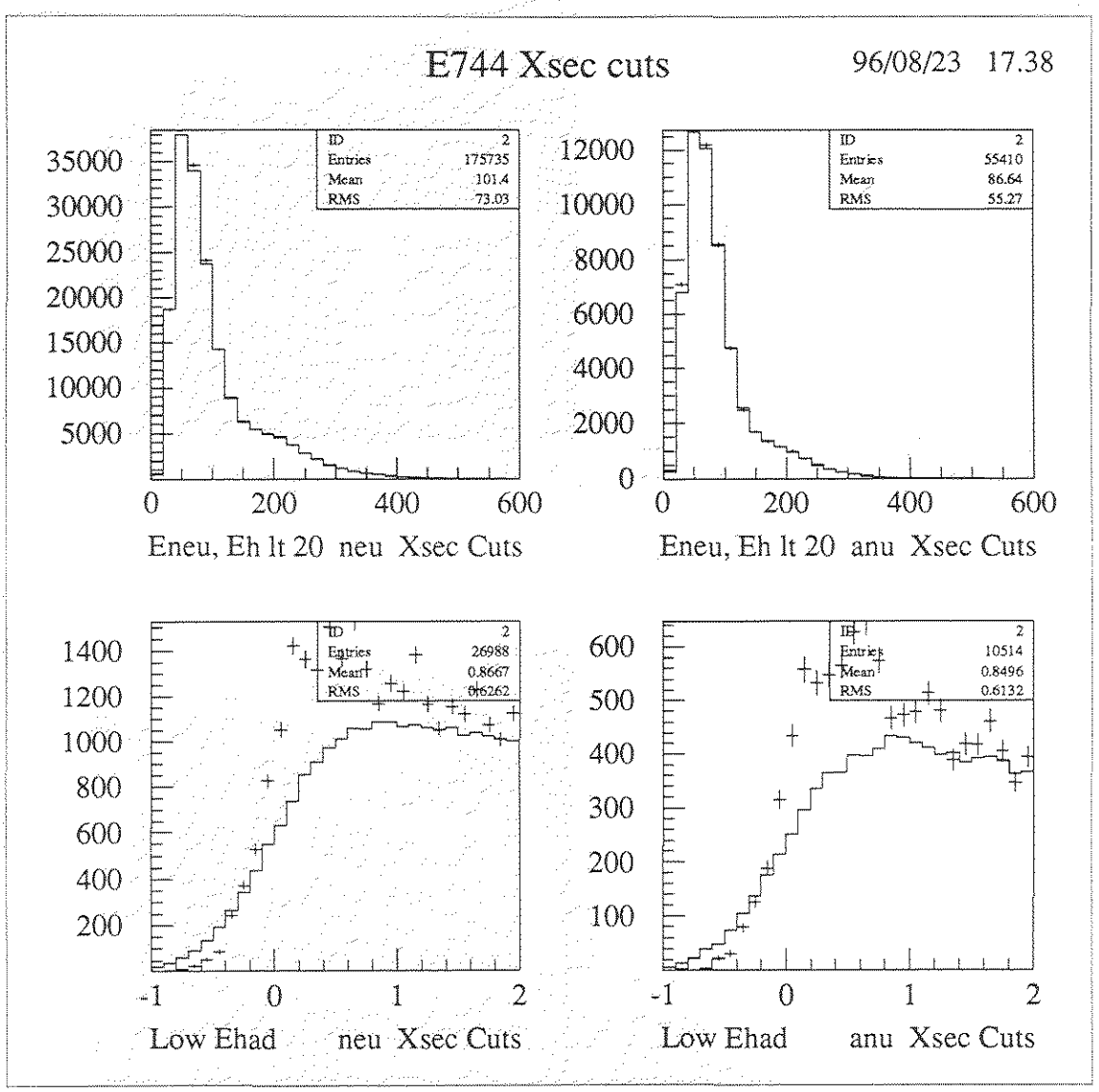

Figure 3.8: Data versus Monte Carlo distributions for low *ENEU* and low *EHAD*. The data are crosses, the solid lines are Monte Carlo events. The low *ENEU* distributions are relevant for the flux extraction (see Chapter 5). The excess data events in the low *EHAD* plots come from quasi-elastic scattering that is not modeled in the Monte Carlo.

When the need for the above correction was recognized, the hadron-energy calibration analysis described in Ref. [Sak90] was re-evaluated. It was determined that the same issues with pedestal subtraction discussed above were potential sources of miscalibration for the calorimeter (see Appendix F). Hence, the measured hadron energy is adjusted for $EHAD > 5\ GeV$:

$$EHAD_{meas}^{E744} = EHAD^{E744} \times 0.9887 \frac{1}{1 + 0.071/EHAD^{E744}} \tag{3.12}$$

$$EHAD_{meas}^{E770} = EHAD^{E770} \times 1.0039 \frac{1}{1 + 0.130/EHAD^{E770}} \tag{3.13}$$

3.2 Muon Angle and Momentum Measurement

Muons are penetrating particles, so their presence may be unambiguously detected by their long trajectories through the target calorimeter and muon spectrometer. The path followed by the muon is called a track, and points along the track are indicated by drift chamber hits. A tracking algorithm fits the hits and determines the muon track. In the target, where there is no magnetic field, a muon travels in an approximately straight line, allowing for a precise measurement of its angle. The bend of a muon's path in the toroid system provides a measurement of its momentum. Complicating both measurements, however, is the effect of multiple Coulomb scattering (MCS)—a muon traversing a medium is deflected by many small angle scatters in the target and toroid steel. Due to MCS θ_μ and p_μ are correlated, necessitating that they be determined together using an iterative procedure.

3.2.1 Muon Tracking Procedure

The z-position of the vertex V_z is assigned to be halfway between $PLACE$ and the adjacent upstream counter. V_x and V_y are initially assigned by taking the centroid of the drift chamber hit positions within the hadron shower region. If a muon track is found the x- and y- positions are revised by extrapolating the track to V_z.

At the start of the iterative track-fitting procedure, a line segment is chosen in the calorimeter to fit the hits in the eight-most downstream chambers. This line segment is extended upstream to V_x, and in the first pass MCS effects are neglected. In the toroid spectrometer, line segments are fit to the hits in each set of five chambers following each toroid cart. A crude initial estimate of the muon momentum is made by using the track deflection $\Delta\theta_{bend}$ in the first toroid gap:

$$p_\mu = \frac{0.3\langle B\rangle L_k}{\Delta\theta_{bend}} \tag{3.14}$$

where $L_k = \rho\Delta\theta_{bend}$ is the distance traversed in the magnetic field in centimeters (ρ is the track's radius of curvature) and $\langle B\rangle$ is the mean magnetic field strength is kilogauss ($\langle B\rangle \approx 17\ kG$).

In the next iteration, the initial determination of p_μ is used to include MCS effects. A particle with momentum p_μ traversing a distance L_k in a material with radiation length X_0 will undergo MCS deflections with a distribution whose width is

$$\sigma_k = \frac{0.015}{p_\mu}\sqrt{L_k / X_0} \tag{3.15}$$

The mean MCS deflection over each discrete track segment was used to form a χ^2 function, which is minimized to fit the track:

$$\chi^2 = \sum_i \sum_j \left(x_i - x_i^p\right) M_{ij}^{-1} \left(x_j - x_j^p\right) \tag{3.16}$$

where x_i are the measured chamber hit positions and x_i^p are the predicted track positions in the i-th plane. The full error matrix M_{ij} is defined by

$$M_{ij} = \left\langle \left(x_i - x_i^p\right)\left(x_j - x_j^p\right) \right\rangle = \sum_{k=1}^{i} \sigma_k^2 \left[\frac{L_k^2}{3} + \frac{L_k}{2}\left(z_{kj} + z_{ki}\right) + z_{kj} z_{ki} \right] + \sigma_0^2 \delta_{ij} \tag{3.17}$$

where L_k is the distance in inches between the k-th and $(k+1)$-st chamber planes and $z_{ki} = \sum_{m=k+1}^{i} L_m$ is the distance from the k-th to the i-th plane. The track fit through the toroid includes the full error matrix and the fit in the target omits the off-diagonal (z_{ki}) terms. The intrinsic drift chamber resolution is $\sigma_0 = 225\,\mu m$.

3.2.2 Muon Angle Measurement

The vertex angle is determined by fitting the track near the vertex at position V_z. However, the large number of hits near the vertex from particles in the hadron shower limits the tracking ability. As a result, the few chambers nearest the vertex are not used for tracking. The number of drift chambers nearest the vertex position that are omitted from tracking is known as the tracking vertex offset. A study of Trigger 1 (charged-current) events determined the magnitude of the offset as a function of hadron energy and track length [Rab92]. To include a chamber in the track fit, the probability for choosing a good hit had to be twice that of selecting a bad one. Using this criterion, the study found that events with $E_{HAD} < 25\ GeV$ require no offset, those with $25 < E_{HAD} < 50\ GeV$ should be offset by one chamber, and those with $E_{HAD} > 50\ GeV$ should be offset by two

chambers. Including the E_{HAD} offset, hits in the six chambers closest to the vertex are fit to a line which determines the angle θ_μ with respect to the beam axis.

The resolution of the muon angle at the event vertex is limited by the muon momentum and the hadron energy. MCS effects are most severe at low muon momenta, as seen from Equation 3.15, whereas large hadron energies lead to high hit multiplicities that make tracking near the vertex difficult. The angular resolution was determined by studying the Trigger 6 sample of stiff muon tracks ($75 < \theta_\mu < 200\ GeV$) in which the track angle determined by upstream and downstream track segments was compared on either side of a simulated "vertex" chosen at the center of the track. The angular resolution was found to be [Rab92]:

$$\sigma_\theta = a + \frac{b}{P_\mu}\,(\text{mrad}) \tag{3.18}$$

with parameters a and b given in Table 3.2

Table 3.2: Muon Angular Resolution.

Track Length	$E_{HAD} < 25GeV$		$25GeV < E_{HAD} < 50GeV$		$E_{HAD} > 50GeV$	
(chambers)	a	b	a	b	a	b
4	0.535	35.4	0.547	46.0	0.407	75.0
5	0.366	49.5	0.393	57.3	0.343	77.8
6	0.294	56.6	0.361	59.4	0.260	84.9
7	0.235	61.5	0.337	62.2	0.235	87.0
8	0.235	61.5	0.337	65.8	0.235	87.7

Since the muon angle measurement depends on the magnitude of the muon momentum, the θ_μ measurement procedure is repeated, using the more precise measurement of p_μ from fitting the muon track through the toroidal spectrometer.

3.2.3 Muon Momentum Measurement

The muon momentum measurement required a detailed map of the muon spectrometer's toroidal magnetic field. Such a map was prepared from Hall probe measurements of the field strength at numerous points along the *z-x* plane of the magnets and from measurement of the current in the magnet windings, up to a single overall normalization, N_{field}. The value of N_{field} was determined using momentum-analyzed muon test beams.

The muon momentum measurement is made via an iterative procedure, using the same algorithm used to track the muon in the target. Using the initial determination of the muon angle and position at the front face of the spectrometer, the predicted muon trajectory is extrapolated through the steel of the magnets in 4 *in* steps, and the energy loss due to ionization is accounted for in each step. The predicted muon track is compared to the hits in the drift chambers located between the toroids, and a χ^2 function comparing the predicted and measured hit positions, Equation 3.16, is minimized by varying the momentum. After each new minimization the full error matrix, Equation 3.17, is recalculated. This procedure continues until the momentum differs by less than 0.5% from the previous iteration.

The resolution of the muon momentum measurement is limited by the effects of multiple Coulomb scattering in the solid-steel toroids. The resolution can therefore be simply estimated by considering a track that traverses the entire spectrometer, or 500 *cm* of steel.

Having received a 2.4 GeV transverse momentum kick, the track is magnetically deflected by

$$\theta_{bend} = \frac{p_{\perp}}{p_{\mu}} = \frac{2.4}{p_{\mu}} \tag{3.19}$$

The typical sigma for an angular deflection of this track due to MCS is

$$\sigma_{\theta_{mcs}} = \frac{0.015}{p_{\mu}}\sqrt{500/1.76} = \frac{0.25}{p_{\mu}} \tag{3.20}$$

Therefore the spectrometer resolution is estimated by

$$\frac{\sigma}{p} = \frac{\sigma_{\theta_{mcs}}}{\theta_{bend}} \approx 10\% \tag{3.21}$$

and should be independent of momentum.

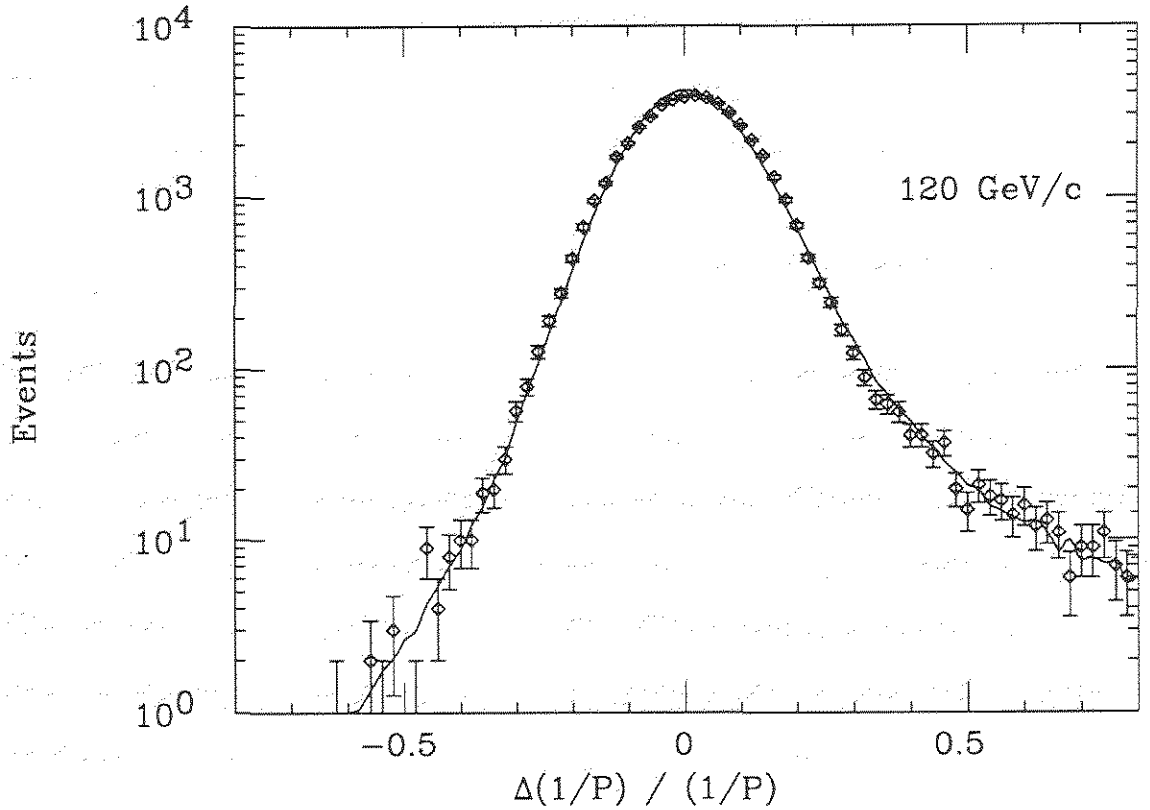

Figure 3.9: Muon momentum resolution function for 120 *GeV* muons. The points are measurements of test beam muons, the solid line is an independent Monte Carlo prediction. The tail of the negative side is due to hard single scatters and the tail of the positive side is due to catastrophic energy losses.

The spectrometer resolution was measured using a 120 GeV muon test beam. Figure 3.9 shows the experimental resolution function obtained. The central region is well approximated by a Gaussian distribution with an rms width of 10.1%, as expected.

3.2.4 Muon Energy Calculation

The toroid fit determines the muon momentum at the start of the spectrometer, *EMUFF* (meaning the muon energy at the front face of the toroid). The muon momentum at the event vertex is determined by adding the amount of energy the muon lost as it traversed the target calorimeter, E_{μ}^{loss}, to the toroid momentum measurement. As it traverses the target, a muon loses energy primarily through ionization, and typically deposits one MIP of energy in each counter. Occasionally, a high-energy muon may deposit a larger amount of energy, due to processes such a pair production and bremsstrahlung, which are known as catastrophic losses.

The energy lost by the muon outside the hadron shower region is determined by looking at the number of MIPs deposited in each counter from ($SHEND - 6$) to counter 1. If the amount of energy deposited in a counter is 3 MIPs or less, the entire amount is attributed to muon ionization losses and multiplied by the muon-ionization-loss calibration constant of $C_{\mu} = 0.158$ GeV/MIP (see Table 3.1). If the amount of counter energy is more than 3 MIPs, the first 3 MIPs attributed to muon ionization and the excess over 3 MIPs is attributed to catastrophic loss, which is multiplied by the electromagnetic calibration constant of $C_e = 0.190$ GeV/MIP. Hence the energy loss of a muon outside the hadron shower is given by

$$ELOSS = \sum_{i=SHEND-6}^{1} \left[MIN(3, \mathrm{MIP}_i) \times C_{\mu} + MAX(0, \mathrm{MIP}_i - 3) \times C_e \right] \tag{3.22}$$

Comparisons with the muon energy loss seen by the data versus that predicted by a Monte Carlo simulation (described in Chapter 4) indicated that the calorimeter had a slightly different muon energy calibration constant during the E744 and E770 runs. The most likely explanation for this is an error in the ADC pedestal subtraction for the HI channels. The value of C_μ for E770 was increased by 0.5% to cause the energy-loss distributions for the two experiments and the Monte Carlo simulation to agree.

Inside the hadron shower region, the energy loss of the muon cannot be directly observed. Instead, an approximation to the average restricted loss is used:

$$RLOSSH = \sum_{i=PLACE}^{SHEND-5} \left(.9315 + .02359 \ln E_i^{EST} \right) \Big/ \cos\theta_\mu \tag{3.23}$$

where E_i^{EST}, the estimated energy in GeV of the muon at counter i, is given by:

$$E_i^{EST} = EMUFF + 0.15952 \times SHEND \tag{3.24}$$

and the energy loss of muon for each counter is given by 0.15952 GeV/counter. Note that while E_i^{EST} is measured in GeV, the units of $RLOSSH$ are MIPs. Equation 3.23 parameterizes the characteristic "relativistic rise" of the ionization loss, making $RLOSSH$ a weak function of the particle energy.

Hence the energy of the muon is taken to be the muon momentum measured at the front face of the toroid, plus the measured energy loss outside the hadron shower, plus the estimated restricted energy loss inside the hadron shower:

$$EMU = EMUFF + ELOSS + C_\mu \times RLOSSH \tag{3.25}$$

3.3 Analysis Cuts

After reconstruction, the data events are cut according to criteria that ensure good efficiency and small acceptance corrections. The criteria are grouped together into sets defined in the following sub-sections.

3.3.1 Fiducial-Volume Cuts

The following cuts ensure that the event takes place within the active area of the detector. The one exception is the dimuon cut, which is not strictly a "fiducial-volume" cut, but is included that set to correspond to the Monte Carlo procedure for eliminating the dimuon cross-section from the event sample.

- *RUN/IGATE/NSTIME:* This cut eliminates runs for which the quality of the neutrino beam was poor or the detector was not functioning properly. It also eliminates all events detected during the non-neutrino "pings" of the accelerator cycle (see Section 2.1). Finally, this cut eliminates all Triggers with more than one neutrino interaction in the same detector event.

- *NO DIMUONS:* This cut eliminates events with a second track that either enters the toroid spectrometer, or penetrates more than 19 counters. The latter condition implies that the second particle had an energy greater than 3 GeV. The reason for this cut is the neutrino species of a charged-current event is determined from the higher-energy muon. For low values of x, especially at high y, there is a significant contribution of neutrino events in the anti-neutrino event sample, and this would affect the low-x value of xF_3. Also, if the secondary muon enters the toroid but the primary muon does not, the kinematics of the event will not be properly reconstructed. Hence the potential dimuon events are removed from the data sample. These events are removed

from the Monte Carlo sample using by re-weighting the cross-section as described in Chapter 4.

- $20 < PLACE < 80$: This cut assures good longitudinal containment of the hadron shower in the calorimeter.

- $-50 < V_x < 50\ in$, $-50 < V_y < 50\ in$: This cut assures good transverse containment of the hadron shower in the calorimeter.

3.3.2 Geometric Cuts

The following cuts assure good momentum resolution in the toroid spectrometer.

- *Trigger 1:* This cut assures that a muon entered the spectrometer.

- *Target Track:* Enough hits must be detected in the target drift chambers for a muon track to be identified in the calorimeter. This assures that the muon angle can be measured in the target.

- *Toroid Containment:* The muon track in the target is extrapolated from the event vertex through the toroid, without assuming any deflection due to multiple scattering or the magnetic field. Tne extrapolated track must have a radius < 64 *in* at the front face of the toroid, and must have a radius at the T2 counter of less than 55 *in*.

- *Toroid Track:* Enough hits must be detected in the toroid drift chambers for a muon track to be identified in the toroid.

- *Good Fit:* The muon track must be fit in the toroid.

- *Fit Quality:* The χ^2 of the fit must be less than 10. Note that the number of degrees of freedom is the number of chambers that the muons passed through in the toroid, and the following cut assures that the muon will pass through at least 10 chambers.

- *Two Gaps:* The muon track must pass through both the first and second toroid carts. This is to assure good reconstruction efficiency of the muon momentum.

3.3.3 Cross-section Cuts

The following cuts are used in the cross-section analysis described in Chapter 5.

- $\theta_\mu < 150 mr$ and $R_{FF} > 8\ in$— The muon angle cut assures good acceptance of the muon track as it passes through the muon spectrometer. R_{FF} is the radius of the muon track at the front face of toroid; this radial cut assures that the muon does not pass through the hole in the center of the spectrometer.

- $E_\mu > 15 GeV$ — 15 GeV is the lower limit of the acceptance of the muon spectrometer.

3.3.4 Structure-Function Cuts

The following additional cuts are applied for the structure-function analysis described in Chapter 6.

- $E_{HAD} > 10 GeV$ — This lower limit on E_{HAD} was picked to minimize the correlations between the flux and structure-function data sample (see Chapter 5).

- $Q^2 > 1 GeV^2$ — This eliminates the quasi-elastic events from the data sample, which are not modeled in our Monte Carlo.

- $30\,GeV < E_\nu < 360\,GeV$ — The lower limit of 30 GeV was chosen because below that energy a large acceptance correction is required. The upper limit of 360 GeV was chosen because above that energy the error on the Monte-Carlo smearing corrections becomes greater than 10%; also, the number of anti-neutrino events above 360 GeV is small and hence would not make a significant impact on the analysis.

Table 3.3 lists the number of events passing each of the cuts described above. Note that the events are listed in independent categories. The categories are defined by data run (experiment E744 or E770), neutrino species (ν or $\bar{\nu}$), and whether the toroid spectrometer was set to focus positively- or negatively-charged muons. Thus there are eight categories of events: two data runs × two neutrino species × two toroid polarities. Each of these categories have different fluxes and different acceptance corrections, and hence must be separately corrected using a Monte Carlo. The calculation of these corrections is described in the next Chapter.

Table 3.3: Number of events passing each of the analysis cuts.

	E744				E770			
Neutrino Type	ν	ν	$\bar{\nu}$	$\bar{\nu}$	ν	ν	$\bar{\nu}$	$\bar{\nu}$
Toroid Pol	Foc μ^-	Foc μ^+	Foc μ^-	Foc μ^+	Foc μ^-	Foc μ^+	Foc μ^-	Foc μ^+
Raw Events	700579	682503	97111	101451	798445	845644	116657	133188
RUN/GATE/TIME	596544	682503	79777	101451	789445	845644	116657	133188
No Dimuons	589538	674839	78550	99668	789464	836500	115037	131076
PLACE	516764	591114	67949	86483	691338	731878	99969	113824
Vertex	442935	508164	59459	73880	592267	625309	88821	99825
Trigger 1	326395	369124	59344	73099	434564	447517	88712	98799
Target Track	326152	368988	59331	73077	434342	447266	88697	98766
Toroid Contain.	298201	335404	54938	65612	387869	207746	82162	88891
Toroid Track	289195	330076	54938	65612	386296	401160	82162	88891
Good Fit	289127	329945	54900	65519	386139	401004	82107	88768
Fit Quality	277752	329428	54784	65364	385642	400196	81942	88509
Two Gaps	282796	284111	48150	64182	377318	345351	71986	86957
$\theta_\mu < 150 mr$	280262	283833	48134	64018	373955	345062	71961	86735
$E_\mu > 15 GeV$	276420	283205	48002	63077	368889	344366	71807	85383
$E_{HAD} > 10$	227607	230696	32766	43444	305657	282161	48421	58285
$Q^2 > 1 GeV^2$	219772	222444	30624	40751	295495	272179	45177	54607
$30 < E < 360$	207630	209050	30226	40276	278552	255330	44637	53975

4 Correcting the Data

The data events, after the analysis described in the previous chapter, must be corrected for the effects of detector geometry, detector resolution, kinematic cuts, and various physics effects such as the mass of charm quark. The data will be grouped into bins defined by kinematic variables: $\left(E_{\nu(\bar{\nu})}, E_{HAD}\right)$ bins for the flux analysis (described in Chapter 5) and (x, Q^2) bins for the structure-function analysis (described in Chapter 6). Let K denote a given kinematic bin; conceptually, the corrections applied to the data in a bin K can be described as follows:

$$DATA^{corrected} = DATA^{reconstructed} \times \underbrace{\frac{MC^{GEN}_{No\,cuts}(\text{with}\,2\mu\,\sigma)}{MC^{SMR}_{CUTS}(\text{w/o}\,2\mu\,\sigma)} \times \frac{\Phi_{NEW}}{\Phi_{EST}}}_{\text{Monte Carlo Corrections}}$$

$$\times \underbrace{\frac{\sigma(\text{isoscalar target})}{\sigma(\text{Fe target})} \times \frac{\sigma(\text{no Rad. Corr.})}{\sigma(\text{Rad. Corr.})} \times \frac{\sigma(m_c = 0)}{\sigma(m_c = 1.31\,GeV)} \times \frac{\sigma(m_W = 0)}{\sigma(m_W = 80\,GeV)}}_{\text{physics model corrections}} \tag{4.1}$$

$$\times \underbrace{\frac{\sigma(K_{bin-center})}{\sigma(K)}}_{\text{bin-center correction}}$$

Only the flux re-weighting and dimuon corrections are calculated on an event-by-event basis (see Section 4.1.4). For the other corrections an average is determined for each bin K and the correction applied to the sum of the reconstructed data events in that bin. The Monte-Carlo corrections, the physics-model corrections, and the bin-center correction are described in the following sections. Figures 5.1-5.2 and 6.6-6.15 display the values of these corrections for the flux and structure-function analyses respectively.

4.1 Monte Carlo Corrections

The flux-extraction and structure-function analyses require a model of the complicated effects of energy resolution smearing and acceptance in the data sample. This is done by using a computer simulation of the physics events in the CCFR detector, using a high-statistics, detailed Monte Carlo calculation.

The Monte-Carlo correction is defined by:

$$\begin{aligned} corr^{MC} &= corr^{acceptance,\, resolution, dimuon} \times corr^{flux} \\ &= \frac{MC^{GEN}_{Nocuts}(\text{with}\, 2\mu\, \sigma)}{MC^{SMR}_{CUTS}(\text{w/o}\, 2\mu\, \sigma)} \times \frac{\Phi_{NEW}}{\Phi_{EST}} \end{aligned} \tag{4.2}$$

The data events are divided into sets with different flux and acceptance criteria: the two experiments E744 and E770 had different fluxes and slightly different detector calibrations; neutrinos and anti-neutrinos have different flux spectra; events taken with the muon spectrometer set to focus positively- or negatively-charged muons have different acceptance corrections. Each of these eight different categories (two experiments × two neutrino species × two toroid polarities) has a separate Monte-Carlo correction calculated for it. The different categories of data events are not summed together until after they have been corrected by the Monte Carlo.

To minimize the effects of statistical variations in the Monte Carlo event sample for the corrections, 27 million Monte Carlo events are generated (roughly ten times the number of data events). This assures that the statistical error in the Monte Carlo correction for a given bin K is approximately a factor of three smaller than the statistical error due to the number of data events in the bin.

The details of each individual correction are described below. First, the method of generating Monte Carlo events is discussed.

4.1.1 Event Generation

The procedure for generating a charged-current event in the structure-function Monte Carlo is as follows:

- Randomly choose the neutrino type: neutrino vs. anti-neutrino, for toroid focusing vs. de-focusing negatively-charged muons. The ratio of different neutrino types generated by the Monte Carlo is approximately the same as that of the data. Since the ratio of $\bar{\nu}$-induced to ν-induced Monte Carlo events is renormalized to agree with the data, there is no need for this ratio to be accurate in the Monte Carlo.

- Randomly "throw" *ENEUG*, the generated neutrino energy, from the input flux distribution Φ_{EST}. Throw *VERTX* and *VERTY*, the (x,y) vertex of the event, from the vertex flux distribution $\Phi(E_i, V_x, V_y)$ (see Section 5.1).

- From estimated parton distributions q_{EST} and the physics model defined in Section 4.2, throw *XG* (the generated x) and *YG* (the generated y).† From *ENEUG*, *XG*, and

---

† *XG* and *YG* are generated randomly using the rejection method [Pre92] from the $d^2\sigma(E,x,y)/dx\,dy$ distribution implied by the parton distribution q_{EST}. If *XG* and *YG* are rejected, the event-generation process begins again with the random throwing of *ENEUG* in the previous step. This guarantees that the energy dependence of the cross-section in the Monte Carlo is the same as that of the Buras-Gaemers parameterization.

YG, the variables *EHADG* (the generated hadron energy), *EMUG* (the generated muon energy), and *THETAG* (the generated muon angle) are calculated. *PHIG* (the azimuthal angle of the muon) is thrown uniformly between 0 and 2π.

- Throw *PLACE* (see Chapter 3) uniformly along the z-axis of the calorimeter. The hadron shower length *(PLACE–SHEND+5)* is thrown randomly from a set of *EHADG*-dependent shower-length distributions determined from a study of the data; The length distributions generated by the structure-function Monte Carlo are shown in Appendix E.

- The muon track is propagated through the calorimeter using a standard energy-loss algorithm. Simulated energy losses for muons with more than 5 *GeV* at the vertex include ionization, bremsstrahlung, pair production, and δ-ray production. Muons with less than 5 *GeV* have their ionization losses simulated according to range-energy tables. The multiple Coulomb scattering of the muon is modeled as well.

- For each drift chamber through which the muon passed, the Monte Carlo keeps track of the restricted energy loss, *RESLOS*,‡ and the catastrophic energy loss, *CATLOS*.

---

‡ A study was performed comparing the results of the standard energy-loss calculation with the GEANT simulation program. The study indicated that the restricted energy loss calculated by the standard calculation was 1.5% too low, presumably because the standard calculation (as adapted by our collaboration) did not include the non-iron elements of the CCFR detector. Hence *RESLOS* is multiplied by 1.5% in the structure function Monte Carlo.

- When the modeled track reaches the front face of the toroid spectrometer, the total dE/dx loss of the muon ($RESLOS$ + $CATLOS$) is subtracted from $EMUG$, giving $EMUFFG$; the position of the muon at this point is given by $VXFF$ and $VYFF$.

4.1.2 Resolution Smearing

As detailed in the previous section, the Monte Carlo generates the quantities *ENEUG*, *EHADG*, *EMUG*, *THETAG*, *PHIG*, *RESLOS*, *CATLOS*, *EMUFFG*, *VERTX*, *VERTY*, *VXFF*, and *VYFF*. The first eight variables in this list are smeared to simulate detector resolution effects as described below. The position resolution of the muon track is less than 0.1 *in* (see Chapter 2), small enough that the smearing of the last four variables is not significant for the charged-current analysis.

EHADG, the generated hadron energy, is smeared according to the resolution function given by Equation 3.10. *THETAG* and *PHIG*, the generated muon angle parameters, are projected onto the x- and y- axes and separately smeared according to the angular resolution given by Equation 3.18.

As described in Section 3.2.3, the muon momentum resolution function was measured at $E_\mu = 120\ GeV$. A detailed simulation of the muon path in the toroid spectrometer (not included in the regular structure function Monte Carlo) was used to extrapolate the muon momentum resolution function to other energies. This detailed simulation included multiple scattering, energy loss, and variations in the magnetic field of the spectrometer as a function of position [Kin91]. The reconstructed momentum of the muon was then calculated using the same momentum-fitting procedure used in the analysis of the data events (see Section 3.2.3).

The fractional muon momentum measurement error

$$\mathcal{F} \equiv \frac{1/p_{meas} - 1/p_{gen}}{1/p_{gen}} = \frac{p_{gen}}{p_{meas}} - 1 \tag{4.3}$$

was histogrammed in bins of p_{gen} after cross-section cuts were applied (see Section 3.3.3). In the structure-function Monte Carlo, these resolution histograms were used to smear the generated muon momentum *EMUFFG* to give *EMUFF*. The muon momentum resolution functions are shown in Appendix E.

4.1.3 Muon Energy Loss

As described above, the restricted energy loss (due to ionization) and the catastrophic energy loss (due to bremsstrahlung, pair production, and δ-ray production) is calculated for the muon as it passes from one drift chamber to the next in the calorimeter. This energy loss must be interpreted in the same way by both the data analysis and the Monte Carlo. The following transformations to *RESLOS* and *CATLOS* assure that this is the case.

• The sum (*RESLOS* + *CATLOS*) is smeared according to an electromagnetic energy resolution function determined in the test beam analysis [Sak90].

• Inside the region of the hadron shower (between *PLACE* and *SHEND*–5), the energy loss is multiplied by the ratio 0.211/0.158, the ratio of the hadronic to the muonic *MIPs/GeV* (see Section 3.1.3). This is done because, in the data analysis, all the *MIPs* seen in the hadron shower region are interpreted as being hadrons. The sum of the smeared muonic energy loss in the hadron shower is thus given by:

$$ELOSSH = \frac{0.211}{0.158} \times \sum_{i=PLACE}^{SHEND-5} (RESLOS + CATLOS)_i^{smeared} \tag{4.4}$$

• Outside the region of the hadron shower (between *SHEND–6* and counter 1), the energy loss is interpreted in the same way as in the data: the portion of the energy loss less than 3 *MIPs* is multiplied by the muon calibration constant, while the portion of the energy loss greater than 3 *MIPs* is multiplied by the electromagnetic calibration constant (see Section 3.2.4).

$$ELOSS = \sum_{i=SHEND-6}^{1} \begin{bmatrix} MIN(3,(RESLOS+CATLOS)_i/0.158)\times 0.158 \\ +\,MAX(0,\left((RESLOS+CATLOS)_i/0.158\right)-3)\times 0.190 \end{bmatrix} \tag{4.5}$$

Therefore, the reconstructed muon energy from the Monte Carlo is given by

$$EMU^{MC}_{reconstructed} = EMUFF + ELOSS + RLOSSH \tag{4.6}$$

and the reconstructed hadron energy is given by

$$EHAD^{MC}_{reconstructed} = EHADG_{smeared} + ELOSSH - \left(RLOSSH \times \frac{0.211}{0.158} \right) \tag{4.7}$$

where *RLOSSH* is defined by Equation 3.23. Note that *RLOSSH* in Equation 4.7 must be multiplied by the ratio of the hadronic to muonic calibration constants, because in the hadron shower region the *MIPs* are interpreted hadronically in the data.

Appendix E contains the Figures that compare the distributions of kinematic quantities observed in the data and simulated by the Monte Carlo after structure-function cuts.

4.1.4 Event Re-weighting

The flux re-weighting and dimuon corrections are applied on an event-by-event basis. These two corrections are assigned to the variables *HISTWT* and *GENWT* as follows and are used to re-weight the events summed into histograms:

$$HISTWT = corr^{dimuon} \times corr^{flux} \tag{4.8}$$

$$GENWT = corr^{flux} \tag{4.9}$$

Therefore, the actual sum of Monte-Carlo events in an analysis bin K is the sum of *HISTWT* or *GENWT* for those events that fall within the bin limits.

4.1.4.1 Flux Re-weighting Correction

The iterative procedure required to extract the structure functions is discussed in Section 6.3. As part of the procedure, the Monte Carlo is generated with an estimated flux Φ_{EST}. This Monte Carlo is used to correct the data for the flux extraction described in Chapter 4, resulting in a new flux Φ_{NEW}. It would be possible to generate a new Monte Carlo with Φ_{NEW}, but this is not necessary. Instead, the individual events in the existing Monte Carlo are each re-weighted by

$$corr^{flux} = \frac{\Phi_{NEW}}{\Phi_{EST}} \tag{4.10}$$

4.1.4.2 Dimuon Correction

The dimuon events are removed from the data sample, as discussed in Section 3.3.1. These events must also be removed from the Monte Carlo sample of reconstructed events in order to correspond with the data sample. However, the structure-function Monte Carlo

does not model the production of a second muon, either from charm production or from a π/K decay in the hadron shower. The cross-section for producing dimuon events is therefore removed from the Monte Carlo event sample by re-weighting the reconstructed events.

The dimuon correction is calculated by

$$
\begin{aligned}
corr^{dimuon} &= \frac{\sigma(\text{without } 2\mu \text{ cross-section})}{\sigma(\text{with } 2\mu \text{ cross-section})} \\
&= \frac{\left[\begin{array}{l} \sigma_{total}\left(E_\nu, x, y\right) \\ -\left(B_c \times \sigma_{2\mu}\left(E_{vis}, x_{vis}, y_{vis}\right)\right) \\ -\left(P_{\pi/K}\left(E_{HAD}, p_{\mu_2} > 3GeV\right) \times \sigma_{total}\left(E_\nu, x, y\right)\right) \end{array}\right]}{\sigma_{total}\left(E_\nu, x, y\right)}
\end{aligned}
\tag{4.11}
$$

where

$\sigma_{total}\left(E_\nu, x, y\right)$ is the cross-section for an event with kinematics $\left(E_\nu, x, y\right)$ as calculated by our physics model (see Section 4.2);

$\sigma_{2\mu}\left(E_{vis}, x_{vis}, y_{vis}\right)$ is the cross-section for producing a dimuon event with kinematics $\left(E_{vis}, x_{vis}, y_{vis}\right)$ (this is fully discussed in Ref. [Rab92], which describes the leading-order dimuon analysis);

B_c is the branching ratio for a charm quark to decay into a muon (= 0.105, as given in Ref. [Rab92]);

$P_{\pi/K}\left(E_{HAD}, p_{\mu_2} > 3GeV\right)$ is the probability of producing a second muon with momentum $p_{\mu_2} > 3GeV$ from π/K decay in a hadron shower with energy E_{HAD} [San93].

4.1.5 Smearing, Acceptance, and Dimuon Correction

Let K denote a bin in some kinematic variables, such as $\left(E_{\nu(\bar{\nu})}, E_{HAD}\right)$ or (x, Q^2). Then K_{GEN} will be the bin defined in terms of the generated variables, and K_{REC} will be the same bin defined in terms of the reconstructed variables. The combined smearing, acceptance, and dimuon correction is then given by

$$corr^{MC} = \frac{MC^{GEN}_{Nocuts}(\text{with}\, 2\mu\,\sigma)}{MC^{SMR}_{CUTS}(\text{w/o}\, 2\mu\,\sigma)} \times \frac{\Phi_{NEW}}{\Phi_{EST}} = \frac{\sum_{i}^{\text{event in } K_{GEN}} GENWT_i}{\sum_{j}^{\substack{\text{event in } K_{REC} \\ \text{after cuts}}} HISTWT_j} \tag{4.12}$$

4.2 Physics Model Corrections

The physics-model correction is defined by:

$$\begin{aligned} corr^{model} &= corr^{isoscalar} \times corr^{radiative} \times corr^{charm-mass} \times corr^{propagator} \\ &= \frac{\sigma(\text{isoscalar target})}{\sigma(\text{Fe target})} \times \frac{\sigma(\text{no Rad. Corr.})}{\sigma(\text{Rad. Corr.})} \\ &\times \frac{\sigma(m_c = 0)}{\sigma(m_c = 1.31GeV)} \times \frac{\sigma(M_W = 0)}{\sigma(M_W = 80GeV)} \end{aligned} \tag{4.13}$$

The details of each individual correction are described below. Each of these corrections depends on a model of the physical cross-sections in terms of parton distributions, which is discussed in the following section. The parameters of this model are determined by a fit

to the structure functions extracted as described in Chapter 6. Since the physics-model correction is required to extract the structure functions, and the model depends on the as-yet-unknown structure functions to be extracted, one of two approaches must be chosen:

1) The model can use one of the available parton distributions extracted from global fits to the world's deep-inelastic scattering data [Mar96, Glu95, Lai96]. The disadvantage of this approach is that most of the currently-accepted global fits incorporate data from previous analyses of data from this and other experiments. Using these global fits would then introduce unknown correlations between the model assumed and the previous analysis, and would complicate any comparisons between these results and others (see Chapter 8).

2) The model can use an iterative approach, where the structure functions F_{NEW} are extracted from the model using an assumed initial parton distribution q_{EST}. The parameters of the model are then determined from a fit to F_{NEW} giving a new distribution q_{NEW}. As this procedure is iterated the difference between the structure functions extracted from q_{EST} and q_{NEW} becomes small. This is the approach used in this analysis.

4.2.1 The Buras-Gaemers Model

The physics-model corrections are applied assuming the model suggested by Buras and Gaemers [Bur78] for the quark distributions that are then used in a leading-order calculation of the ν-nucleon cross-section. The question arises: if the remaining analysis, in particular the QCD studies described in Chapter 7, are calculated in next-to-leading QCD, why use a leading-order model to correct the data? The answer is that, while the difference in the *models* may be large, the difference in the *corrections* due to the models is small:

$$\frac{\sigma_{LO}(\text{bare proton target})}{\sigma_{LO}(\text{physical Fe target})} \approx \frac{\sigma_{NLO}(\text{bare proton target})}{\sigma_{NLO}(\text{physical Fe target})} \tag{4.14}$$

In the Buras-Gaemers model, differential cross-sections are constructed from a set of parton densities representing the momentum densities of the valence and sea quarks inside a nucleon. The following sections detail how the quark densities are parameterized. The FORTRAN code to generate these parton densities is listed in Appendix C.

4.2.1.1 Valence Densities

The valence quark momentum densities are parameterized as:

$$xV(x,Q^2) = A_V(s)x^{\eta_1(s)}(1-x)^{\eta_2(s)} \tag{4.15}$$

where

$$\eta_1(s) = \eta_{10} + \eta_{11} \cdot s \tag{4.16}$$

$$\eta_2(s) = \eta_{20} + \eta_{21} \cdot s \tag{4.17}$$

$$s = \log\left(\frac{\log\left(Q^2/\Lambda^2\right)}{\log\left(Q_0^2/\Lambda^2\right)}\right) \tag{4.18}$$

$$Q_0^2 = 12.6 GeV^2 \tag{4.19}$$

This value for Q_0^2 has no effect on the final results and was picked for historical reasons; it was the mean Q^2 of experiments E616/E701. $A_V(s)$ is defined below in Eq. (4.25).

We have chosen to separate the valence quark distribution into u_V and d_V quark distributions, parameterized as

$$xu_V(x,Q^2) = c_u(s)x^{\eta_1(s)}(1-x)^{\eta_2(s)} \tag{4.20}$$

$$xd_V(x,Q^2) = c_d(s)x^{\eta_1(s)}(1-x)^{\eta_2(s)+1} \tag{4.21}$$

where the d_V quark distribution is a more rapidly falling function as $x \to 1$. This is in accordance with results from deep-inelastic electron-scattering experiments using hydrogen and deuterium targets [Blo73, Bod74]. The experiments found that F_2^{en} / F_2^{ep} = 1/4 as $x \to 1$, suggesting that the valence quarks are dominated by u_V quarks at large x. The relative normalizations of u_V to d_V quark densities is supplied by the proton quark counting rule:

$$\int_0^1 \frac{dx}{x} xu_V(x,Q^2) = 2\int_0^1 \frac{dx}{x} xd_V(x,Q^2) \tag{4.22}$$

which states that there are two valence u quarks and one valence d quark in the proton. Thus, the valence density of a nucleon is

$$xu_V + xd_V = A_V(s)x^{\eta_1(s)}(1-x)^{\eta_2(s)}\left[1+\frac{1}{2}\frac{\eta_1(s)+\eta_2(s)+1}{\eta_2(s)+1}(1-x)\right] \tag{4.23}$$

The normalization of the valence quark distribution is allowed to vary while retaining the Q^2 dependence as predicted by next-to-leading-order QCD:

$$\int_0^1 \frac{dx}{x}\left[xu_V(x,Q^2) + xd_V(x,Q^2)\right] = A_1\left(1-\frac{4}{\left(11-\frac{2}{3}n_f\right)\log\left(Q^2/\Lambda^2\right)}\right) \tag{4.24}$$

or

$$A_V(s) = \frac{2/3}{\beta\left(\eta_1(s), \eta_2(s)+1\right)} A_1 \left(1 - \frac{4}{\left(11 - \frac{2}{3} n_f\right) \log\left(Q^2/\Lambda^2\right)} \right) \tag{4.25}$$

where $n_f = 4$ is the number of quark flavors contributing to the cross sections. The β-function is defined to be the usual:

$$\beta(a,b) = \frac{\Gamma(a)\Gamma(b)}{\Gamma(a+b)} = \int_0^1 t^{a-1}(1-t)^{b-1}\, dt \tag{4.26}$$

4.2.1.2 Sea Densities

Two sea densities, an SU(3)-symmetric piece and a charmed piece, were considered by Buras and Gaemers. We have assumed the charmed component to be zero [Mis89]. In the leading-order dimuon analysis [Rab93], the strange sea $xS_s(x,Q^2)$ was found to possess a different shape than the non-strange sea $xS(x,Q^2) = xq(x,Q^2) + x\bar{q}(x,Q^2)$:

$$xS(x,Q^2) = A_S(s)(1-x)^{\eta_s(s)} \tag{4.27}$$

$$\begin{aligned} xS_S(x,Q^2) &= \frac{A_S(s)}{\eta_s(s)+1}\left(\beta_s(s)+1\right)(1-x)^{\eta_s(s)+\alpha} \\ &= xS(x,Q^2)\frac{\left(\beta_s(s)+1\right)}{\eta_s(s)+1}(1-x)^{\alpha} \end{aligned} \tag{4.28}$$

where

$$\beta_S(s) = \eta_S(s) + \alpha \tag{4.29}$$

quantifies the shape difference between strange and non-strange sea. These distributions are normalized such that

$$\int xS(x,Q^2)dx = \int xS_S(x,Q^2)dx \tag{4.30}$$

The amount of strange relative to non-strange quarks in the sea is then parameterized by the variable κ,

$$\kappa = \frac{2S}{\left(\overline{U}+\overline{D}\right)} \tag{4.31}$$

where

$$S = \int_0^1 dx\, xS_S(x,Q^2) \tag{4.32}$$

$$\overline{U} = \int_0^1 dx\, x\overline{u}(x,Q^2) \tag{4.33}$$

$$\overline{D} = \int_0^1 dx\, x\overline{d}(x,Q^2) \tag{4.34}$$

The κ variable is assumed to be independent of Q^2 which is consistent with previous analyses [Rab93]. With these definitions, the various flavor densities of the sea are then expressed as

$$2xu_S = 2x\overline{u} = 2xd_S = 2x\overline{d} = \frac{1}{2+\kappa}xS(x,Q^2) \tag{4.35}$$

and

$$2xs = 2x\overline{s} = \frac{\kappa}{2+\kappa}xS_S(x,Q^2) \tag{4.36}$$

For this analysis, the values $\alpha = 2.50$ and $\kappa = 0.373$ [Rab92] are used in the fit to the measured structure functions. However, the value of the strange sea $S_S(x,Q^2)$ is taken

to be the exact value determined by the analysis of Ref. [Rab92]. The Q^2-dependence of $xS(x,Q^2)$ can be expressed in terms of its first two (Q^2-dependent) moments:

$$A_S(Q^2) = \left\langle xS(Q^2)\right\rangle_2 \left(\frac{\left\langle xS(Q^2)\right\rangle_2}{\left\langle xS(Q^2)\right\rangle_3} - 1 \right) \tag{4.37}$$

$$\eta_S(Q^2) = \frac{\left\langle xS(Q^2)\right\rangle_2}{\left\langle xS(Q^2)\right\rangle_3} - 2 \tag{4.38}$$

where

$$\left\langle xS(Q^2)\right\rangle_n = \int_0^1 dx\, x^{n-2} xS(x,Q^2) \tag{4.39}$$

The Q^2 evolution of the moments $\left\langle xS(Q^2)\right\rangle_n$ is specified by leading-order QCD and is given in Ref. [Bur78]. Since this evolution is coupled to that of the gluon density $xG(x,Q^2)$, it is necessary to parameterize $xG(x,Q^2)$. The gluon density parameterization is of the same form as the sea, and evolves in a similar way with Q^2:

$$xG(x,Q^2) = A_G (1-x)^{\eta_G} \tag{4.40}$$

4.2.1.3 R

The value of $R = \sigma_L / \sigma_T$ used in the Buras-Gamers fits (see the following section) comes from an empirical parameterization of the world's available data on R [Whi90b]. The formula used is:

$$\theta = 1 + \frac{12Q^2}{Q^2+1} \times \frac{c^2}{c^2+x^2} \tag{4.41}$$

$$R = \frac{b_1}{s}\theta + \frac{b_2}{Q^2} + \frac{b_3}{Q^4 + 0.09} \tag{4.42}$$

with $c = 0.125$, $b_1 = 0.0635$, $b_2 = 0.5747$, $b_3 = -0.3534$, $s = \ln(Q^2/0.04)$. At the time Ref. [Whi90b] was published, the world's available data on R was restricted to the region $x > 0.1$ and $Q^2 < 75\ GeV^2$. For this analysis, it is assumed that the above parameterization of R is good over the kinematic region of the CCFR data: $x > 0.005$ and $Q^2 < 125\ GeV^2$.

4.2.1.4 Structure Functions and Buras-Gaemers Fits

The differential cross-section is expressed in terms of the structure functions by

$$\frac{d^2\sigma^{\nu,\bar{\nu}}}{dx\,dQ^2} = \frac{G^2 M}{\pi}\frac{E}{2MEx}\left[\left(1 - y - \frac{Mxy}{2E} + \frac{y^2}{2}\frac{1+4M^2x^2}{1+R(x,Q^2)}\right)F_2(x,Q^2) \pm y\left(1-\frac{y}{2}\right)xF_3(x,Q^2)\right] \tag{4.43}$$

In leading order, the extracted structure functions (Chapter 6) can be parameterized in terms of the parton densities described in the previous sections as

$$F_2(x,Q^2) = \frac{1+R(x,Q^2)}{1+4M^2x^2/Q^2}\left[xu_v(x,Q^2) + xd_v(x,Q^2) + xS(x,Q^2)\right] \tag{4.44}$$

$$xF_3(x,Q^2) = xu_v(x,Q^2) + xd_v(x,Q^2) \tag{4.45}$$

The measured structure functions are compared to these parameterizations and a new sets of parameters are determined by minimizing the χ^2 of the difference. The new parameters are then used as input to the next iteration of the Monte Carlo (Section 6.3). A total of nine free parameters are used to specify the valence and sea densities: η_{10}, η_{11},

η_{20}, η_{21}, and A_0 for the valence densities and $\langle xS(Q_0^2)\rangle_2$, $\langle xS(Q_0^2)\rangle_3$, and $\langle xG(Q_0^2)\rangle_3$ for the sea density, and Λ. Q_0^2 was fixed at 12.6 GeV^2/c^2. The first two moments of the valence density, required for the evolution of the sea, are computed from A_0, η_{10}, and η_{20}. The first moment of the gluon density, $\langle xG(Q_0^2)\rangle_2$, is also required for the evolution of the sea. It is not a free parameter, since it can be computed from the momentum sum rule

$$\int_0^1 dx\left[xS(x,Q_0^2)+xu_v(x,Q_0^2)+xd_v(x,Q_0^2)+xG(x,Q_0^2)\right]=1 \tag{4.46}$$

Table 4.1: Set of parameters for parton densities used as input to the Monte Carlo (with $\kappa = 0.373$ and $\alpha = 2.50$).

Number	Parameter	Value
1	Λ (GeV/c)	0.42687
2	A_1	0.93220
3	η_{10}	0.72428
4	η_{11}	-0.05049
5	η_{20}	3.11869
6	η_{21}	1.84026
7	$\langle xS(Q_0^2)\rangle_2$	0.14106
8	$\langle xS(Q_0^2)\rangle_3$	0.01394
9	$\langle xG(Q_0^2)\rangle_3$	0.05203

Table 4.2: Set of parameters for parton densities from fit to final structure functions (with $\kappa = 0.373$ and $\alpha = 2.50$).

Number	Parameter	Value
1	Λ (GeV/c)	0.55439
2	A_1	0.96908
3	η_{10}	0.68491
4	η_{11}	0.09575
5	η_{20}	2.97104
6	η_{21}	2.09762
7	$\langle xS(Q_0^2)\rangle_2$	0.14101
8	$\langle xS(Q_0^2)\rangle_3$	0.01417
9	$\langle xG(Q_0^2)\rangle_3$	0.04934

Table 4.3: Error matrix from MINUIT fit to final structure functions using the Buras-Gaemers parameterization. The correspondence between "No." and the Buras-Gaemers parameter is given in Table 4.2.

NO.	GLOBAL	1	2	3	4	5	6	7	8	9
1	0.97251	1.000	0.148	0.124	-0.106	0.081	-0.616	0.500	0.200	-0.516
2	0.98801	0.148	1.000	-0.841	0.133	-0.611	0.067	-0.411	-0.092	0.268
3	0.99266	0.124	-0.841	1.000	-0.389	0.873	-0.364	0.202	-0.267	-0.481
4	0.91642	-0.106	0.133	-0.389	1.000	-0.438	0.674	0.232	0.366	0.039
5	0.97197	0.081	-0.611	0.873	-0.438	1.000	-0.509	-0.054	-0.412	-0.345
6	0.95810	-0.616	0.067	-0.364	0.674	-0.509	1.000	-0.138	0.090	0.291
7	0.99134	0.500	-0.411	0.202	0.232	-0.054	-0.138	1.000	0.793	-0.392
8	0.98497	0.200	-0.092	-0.267	0.366	-0.412	0.090	0.793	1.000	0.175
9	0.94312	-0.516	0.268	-0.481	0.039	-0.345	0.291	-0.392	0.175	1.000

Table 4.1 shows the set of parameters for the parameterization of the parton distributions q_{EST} that were input to the final iteration of the structure-function Monte Carlo. Table 4.2 shows the set of parameters for the parameterization of the Buras-Gaemers parton distributions for the structure functions published in this thesis; Table 4.3 shows the error matrix from the MINUIT fit [Jam94] using the Buras-Gaemers parameterization of the structure functions. Although the values of the parameters are different between the two iterations, the actual difference in the values of the parton distributions is small.

4.2.1.5 Systematic Error in the Buras-Gaemers Model

The Buras-Gaemers model of the parton densities fits the structure-function data well in the region $x > 0.1$, but fits poorly at low x. In order to better fit the low-x data, an alternate parameterization was tested. Equations 4.15 and 4.27 were modified as follows:

$$xV(x,Q^2) = A_V(s)x^{\eta_1(s)}(1-x)^{\eta_2(s)} + A_2(1-x)^{\eta_3} \tag{4.47}$$

$$xS(x,Q^2) = A_S(s)(1-x)^{\eta_s(s)} + A_{S_2}(1-x)^{\eta_{S_2}} \tag{4.48}$$

Note that the new parameters A_2, η_3, A_{S_2}, and η_{S_2} are not functions of s, that is, they are not functions of Q^2. The normalization constraints of Equations 4.25 and 4.46 are not applied to these new terms. The resultant fit was better at low x, but was poor at high x.

For the purposes of this analysis, the difference in the results from using the two different models of the parton densities is treated as a systematic error. In the remainder of this thesis, this difference is referred to as the Buras-Gaemers model parameterization systematic error, or simply the model parameterization error.

4.2.2 Corrections to the Physical Cross-section

The preceding sections described the parameterization of the bare cross-section. Various physical effects must be applied to the bare cross-sections in order to accurately model the differential cross-sections for ν-N interactions in our iron-scintillator detector, as detailed in the following sections.

4.2.2.1 Isoscalar Correction

The calorimeter used in this experiment does not consist solely of isoscalar nuclei; it contains about 5.67% more neutrons than protons averaged over the entire fiducial volume [Kin94]. The effect of such an asymmetry on the differential cross-sections can be described by the parameter

$$v_f = \frac{N-Z}{A} = 0.0567 \tag{4.49}$$

where N, Z, and A are the number of neutrons, protons, and nucleons, respectively. The effective quark momentum density "seen" by neutrinos interacting in the calorimeter is then given by

$$\begin{aligned} xq^{\nu} &= 2\left\{\frac{Z}{A}\left(xd^{p}+xs^{p}\right)+\frac{A-Z}{A}\left(xd^{n}+xs^{n}\right)\right\} \\ &= 2\left\{\frac{Z}{A}(xd+xs)+\frac{A-Z}{A}(xu+xs)\right\} \\ &= \left(1-v_f\right)xd_v+\left(1+v_f\right)xu_v+xd_s+xs \\ &= \left(1-v_f\right)xd_v+\left(1+v_f\right)xu_v+\frac{1+\kappa}{2+\kappa}xS \end{aligned} \tag{4.50}$$

and the effective anti-quark density is

$$
\begin{aligned}
x\bar{q}^{\nu} &= 2\left\{\frac{Z}{A}x\bar{u}^{p} + \frac{A-Z}{A}x\bar{u}^{n}\right\} \\
&= 2\left\{\frac{Z}{A}x\bar{u} + \frac{A-Z}{A}x\bar{u}\right\} \\
&= \frac{1}{2+\kappa}xS
\end{aligned}
\tag{4.51}
$$

To derive Equation 4.50 and 4.51, we have made use of isospin conservation for the strong interaction, which leads to the relations $u^{p} = d^{n}$ and $u^{n} = d^{p}$. We also assume that $\bar{u}^{p} = \bar{u}^{n}$ and $\bar{d}^{p} = \bar{d}^{n}$. The effective momentum densities seen by anti-neutrinos are similarly given by

$$
xq^{\bar{\nu}} = \left(1+v_f\right)xd_v + \left(1-v_f\right)xu_v + \frac{1}{2+\kappa}xS \tag{4.52}
$$

$$
x\bar{q}^{\bar{\nu}} = \frac{1+\kappa}{2+\kappa}xS \tag{4.53}
$$

The isoscalar correction is therefore

$$
corr^{isoscalar} = \frac{\sigma(\text{isoscalar target})}{\sigma(\text{Fe target})} = \frac{\sigma(v_f = 0)}{\sigma(v_f = 5.67\%)} \tag{4.54}
$$

4.2.2.2 Radiative Correction

Radiative corrections to the total cross-section were calculated using the prescription of Bardin [Bar86]. Previous analyses of the CCFR charged-current data used the calculation of de Rujula [Ruj79], which only included the QED corrections involving the "upper half" of the neutrino-quark interactions; one example is the effects of the outgoing muon radiating a photon (see Figure 4.1). The Bardin calculation also includes the quark leg of

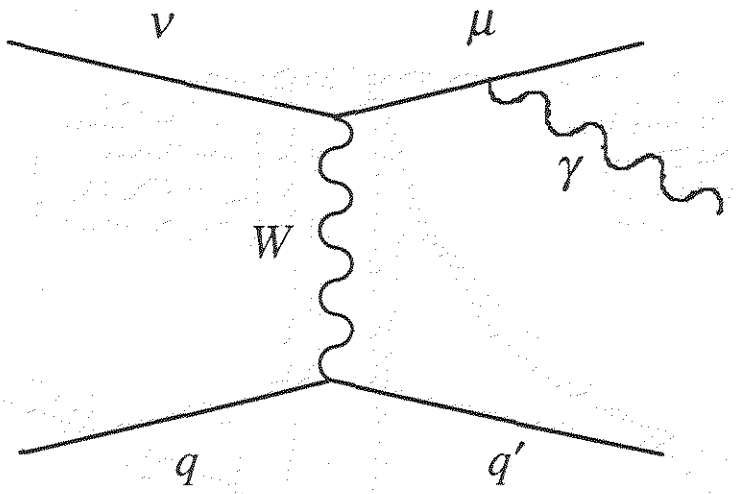

Figure 4.1: Radiative-correction diagram included in both the Bardin and the de Rujula calculations.

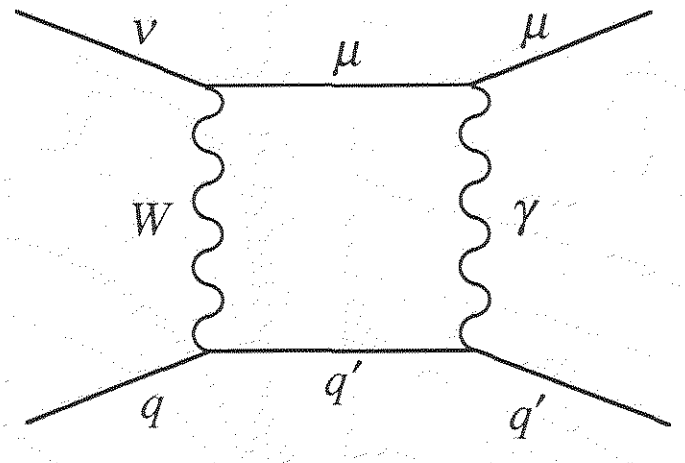

Figure 4.2: Radiative-correction diagram included in the Bardin calculation.

the diagram, including interaction between the outgoing muon and the quark (see Figure 4.2).

The Bardin calculation is too time-consuming to calculate on an event-by-event basis. Instead, tables of corrections were prepared for a range of values of E_ν, x, and y; the correction for a given bin was derived from the table by linear interpolation.

Figure 4.3 compares the values of the Bardin and de Rujula radiative correction calculations.

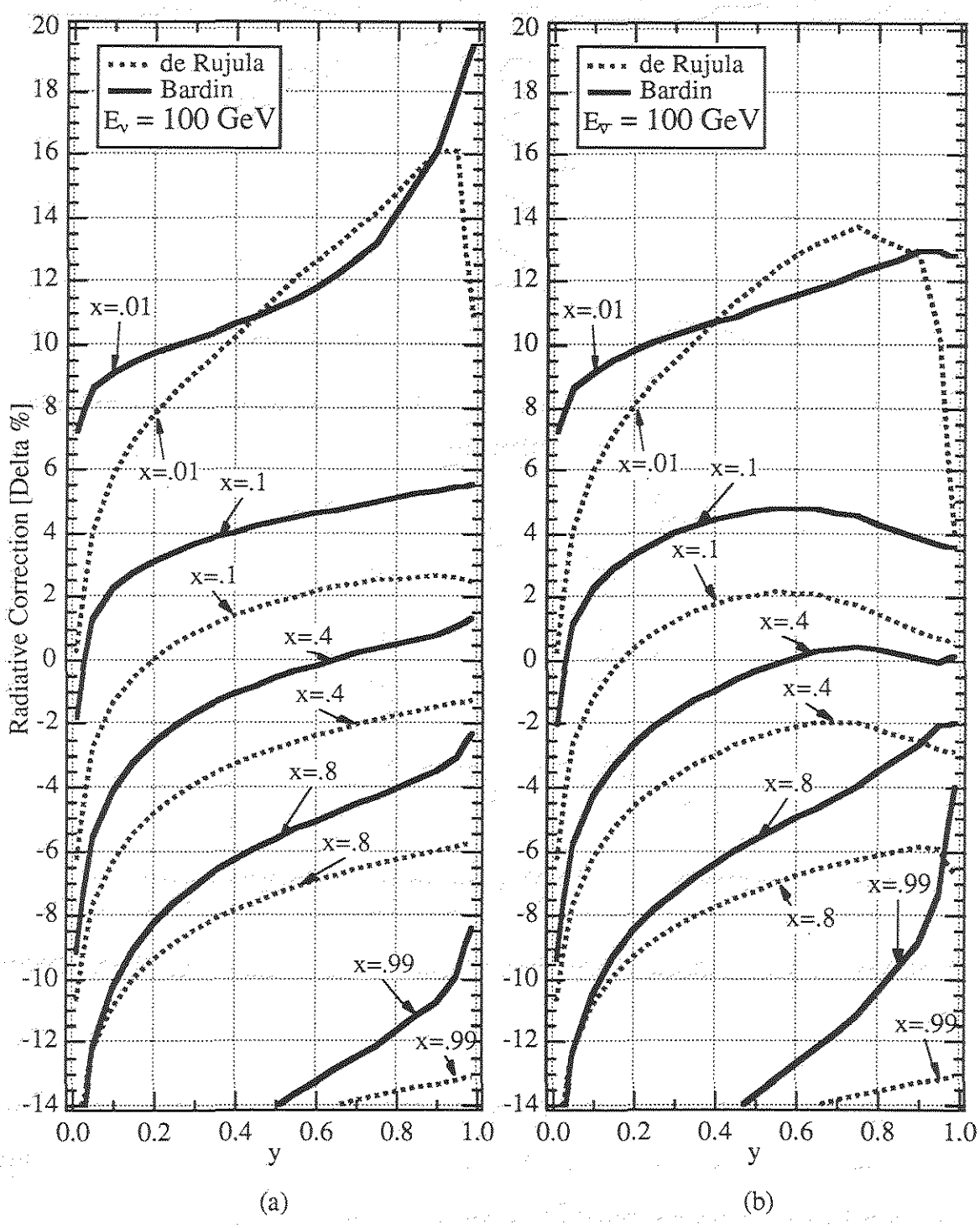

Figure 4.3: Radiative corrections due to Bardin and de Rujula vs. *y*. (a) Neutrino corrections; (b) Anti-neutrino corrections.

4.2.2.3 Charm Production Threshold

The slow-rescaling scheme [Bar76, Geo76] is used to account for the effects of charm production with a charm quark mass, m_c. In this scheme the normal scaling variable x no longer represents the momentum fraction carried by the struck quark. It is replaced by

$$\xi = x\left(1 - \frac{m_c^2}{Q^2}\right) \tag{4.55}$$

The inclusive cross-sections are modeled as a sum of two semi-inclusive cross-sections: charm-producing and non-charm-producing pieces. Correspondingly, the effective momentum densities were split into charm-producing and non-charm-producing pieces:

$$xq_{ncp}^{v} = \left(\left(1 - v_f\right)xd_v + \left(1 + v_f\right)xu_v + \frac{xS}{2+\kappa}\right)\cos^2\theta_c + \frac{\kappa}{2+\kappa}xS_S\sin^2\theta_c \tag{4.56}$$

$$xq_{cp}^{v} = \left(\left(1 - v_f\right)xd_v + \left(1 + v_f\right)xu_v + \frac{xS}{2+\kappa}\right)\sin^2\theta_c + \frac{\kappa}{2+\kappa}xS_S\cos^2\theta_c \tag{4.57}$$

$$x\overline{q}_{ncp}^{v} = \frac{1}{2+\kappa}xS \tag{4.58}$$

$$x\overline{q}_{cp}^{v} = 0 \tag{4.59}$$

$$xq_{ncp}^{\overline{v}} = \left(1 + v_f\right)xd_v + \left(1 - v_f\right)xu_v + \frac{xS}{2+\kappa} \tag{4.60}$$

$$xq_{cp}^{\overline{v}} = 0 \tag{4.61}$$

$$x\overline{q}_{ncp}^{\overline{v}} = \frac{1}{2+\kappa}xS\cos^2\theta_c + \frac{\kappa}{2+\kappa}xS_S\sin^2\theta_c \tag{4.62}$$

$$x\bar{q}_{cp}^{\bar{\nu}} = \frac{1}{2+\kappa} xS \sin^2\theta_c + \frac{\kappa}{2+\kappa} xS_S \cos^2\theta_c \tag{4.63}$$

where cp (ncp) indicates charm-producing (non-charm-producing) and $\theta_c = 13.2°$ is the Cabibbo angle and $m_c = 1.31\ GeV$ [Rab93].

Concentrating now on the charm-producing cross-sections, note that the transformation $x \to \xi$ preserves the differential area

$$\left|\frac{\partial(\xi, y)}{\partial(x, y)}\right| = 1 \tag{4.64}$$

Therefore, the charm-producing cross-section in the ξ-variable can be obtained by the transformation

$$2x\mathcal{F}_1^{\nu,\bar{\nu}cp}(x) \to \frac{x}{\xi} 2\xi\mathcal{F}_1^{\nu,\bar{\nu}cp}(\xi)\theta(1-\xi) \tag{4.65}$$

$$\mathcal{F}_2^{\nu,\bar{\nu}cp}(x) \to \mathcal{F}_2^{\nu,\bar{\nu}cp}(\xi)\theta(1-\xi) \tag{4.66}$$

$$x\mathcal{F}_3^{\nu,\bar{\nu}cp}(x) \to \frac{x}{\xi}\xi\mathcal{F}_3^{\nu,\bar{\nu}cp}(\xi)\theta(1-\xi) \tag{4.67}$$

The θ-function is used to insure sufficient energy transfer for charm production.

In order to preserve the identity

$$\mathcal{F}_2(x, Q^2) \equiv \frac{1+R(x,Q^2)}{1+4M^2x^2/Q^2} 2x\mathcal{F}_1(x, Q^2) \tag{4.68}$$

under the transformation $x \to \xi$ it is necessary to perform the transformation $R \to R'$:

$$R(x) \equiv \frac{\mathcal{F}_2^{cp}(x)}{2x\mathcal{F}_1^{cp}(x)}\left(1+\frac{4M^2x^2}{Q^2}\right)-1 \tag{4.69}$$

$$\begin{aligned} R'(x) &= \frac{\xi}{x}\frac{\mathcal{F}_2^{cp}(x)}{2\xi\mathcal{F}_1^{cp}(x)}\left(1+\frac{4M^2x^2}{Q^2}\right)-1 \\ &= \frac{\xi}{x}\frac{1+R(\xi)}{1+4M^2\xi^2/Q^2}\left(1+\frac{4M^2x^2}{Q^2}\right)-1 \end{aligned} \tag{4.70}$$

Note $R'(x) = R'([R(x)],\xi)$ and will, in general, be different for neutrinos and anti-neutrinos. Substituting for R' in Equation 4.70 yields

$$\mathcal{F}_2^{cp}(\xi) \to \frac{1+R(\xi)}{1+4M^2\xi^2/Q^2}2\xi\mathcal{F}_1^{cp}(\xi) \tag{4.71}$$

Combining the charm-producing and non-charm-producing contributions to the cross-sections results in the following physical structure functions:

$$2x\mathcal{F}_1^{\nu} = xq_{ncp}^{\nu}(x)+\bar{q}_{ncp}^{\nu}(x)+\frac{x}{\xi}q_{cp}^{\nu}(\xi) \tag{4.72}$$

$$2x\mathcal{F}_1^{\bar{\nu}} = xq_{ncp}^{\bar{\nu}}(x)+\bar{q}_{ncp}^{\bar{\nu}}(x)+\frac{x}{\xi}\bar{q}_{cp}^{\bar{\nu}}(\xi) \tag{4.73}$$

$$\mathcal{F}_2^{\nu} = \frac{1+R(x)}{1+4M^2x^2/Q^2}\left(q_{ncp}^{\nu}(x)+\bar{q}_{ncp}^{\nu}(x)\right)+\frac{1+R(x)}{1+4M^2\xi^2/Q^2}q_{cp}^{\nu}(\xi) \tag{4.74}$$

$$\mathcal{F}_2^{\bar{\nu}} = \frac{1+R(x)}{1+4M^2x^2/Q^2}\left(q_{ncp}^{\bar{\nu}}(x)+\bar{q}_{ncp}^{\bar{\nu}}(x)\right)+\frac{1+R(x)}{1+4M^2\xi^2/Q^2}\bar{q}_{cp}^{\bar{\nu}}(\xi) \tag{4.75}$$

$$x\mathcal{F}_3^{\nu} = xq_{ncp}^{\nu}(x)-\bar{q}_{ncp}^{\nu}(x)+\frac{x}{\xi}q_{cp}^{\nu}(\xi) \tag{4.76}$$

$$x\mathcal{F}_3^{\bar{\nu}} = xq_{ncp}^{\bar{\nu}}(x)-\bar{q}_{ncp}^{\bar{\nu}}(x)-\frac{x}{\xi}\bar{q}_{cp}^{\bar{\nu}}(\xi) \tag{4.77}$$

where the Q^2-dependence and the $\theta(1-\xi)$ terms multiplying the cp terms are suppressed. It can be observed that Equation 4.74 and 4.77 reduce to Equation 4.44 and 4.45 if m_c is set to zero. Therefore, the slow-rescaling correction to be applied to data is

$$corr^{charm-mass} = \frac{\sigma(m_c = 0)}{\sigma(m_c = 1.31GeV)} \tag{4.78}$$

4.2.2.4 Propagator Correction

The neutrino cross-section is slightly reduced at high Q^2 due to the W propagator. The effect of the massive W-boson propagator is accounted for by a re-definition of the Fermi-coupling constant:

$$G_F^2 \rightarrow \frac{G_F^2}{\left(1+\left(Q^2/m_W^2\right)^2\right)} \tag{4.79}$$

where the approximation $m_W = 80GeV/c$ [Abe89] suffices for this analysis. Therefore, the effects of the propagator are removed from the data by

$$corr^{propagator} = \frac{\sigma(m_W = 0)}{\sigma(m_W = 80GeV)} \tag{4.80}$$

4.3 Bin-center Correction

In a given analysis bin K, all the corrected events are assumed to have the kinematic values at the geometric center of the bin. The bin-center correction,

$$corr^{bin-center} = \frac{\sigma(K_{bin-center})}{\sigma(K_{average})} \tag{4.81}$$

corrects for the number of events at the average value of the kinematics in bin K versus the value at the bin center. For example, if for a given bin K the average x and Q^2 is (x_{avg}, Q^2_{avg}), and the geometric center of the bin is (x_{bc}, Q^2_{bc}), then $corr^{bin-center} = \sigma(x_{bc}, Q^2_{bc}) / \sigma(x_{avg}, Q^2_{avg})$. In the flux analysis, the bin widths are small enough so that the value of this correction less than 1%. Figures 6.14-6.15 show the values of the bin-center correction in the structure-function analyses. In the structure-function analysis, if a bin's center is kinematically forbidden, then that bin is not used.

5 Flux and Cross-Sections

The task of determining the differential cross-section depends on solving the following equation:

$$\frac{d^2N(E,x,y,V_x,V_y)}{dxdy} = \Phi(E,V_x,V_y)\frac{d^2\sigma(E,x,y)}{dxdy} \tag{5.1}$$

where N is the number of observed charged-current events in the detector at vertex position (V_x,V_y), and $\Phi(E,V_x,V_y)$ is the incident neutrino flux. Given the flux and event sums in a kinematic bin, the cross-section can be determined, and then the structure functions can be determined from Equation 1.29.

In principle, the neutrino flux could be deduced from the spectrum and intensity of secondary beam particles. However, the wide energy spectrum and intensity of the secondary beam preclude a direct method of measuring the flux in this experiment. For this reason, the flux is determined from a sub-class of the charged current events. This chapter describes the flux extraction; the procedure for extracting the structure functions is described in the next Chapter.

5.1 Flux Versus Energy: the Fixed-ν Method

The "fixed-ν" method of flux extraction relies on charged-current events with low ν (i.e., low hadronic energy) to determine the flux. As will be shown, the fixed-ν method cannot be used to determine the absolute normalization of the flux, but it can determine the relative flux between two energy bins $\Phi(E_i)/\Phi(E_j)$, and the relative flux between neutrinos and anti-neutrinos $\Phi^{\nu}/\Phi^{\bar{\nu}}$. This method is systematically more robust than an iterative procedure using all events because the data used to determine the flux comes

from charged-current events with low E_{HAD}, while the data used to determine the structure functions come from charged-current events with relatively large E_{HAD}.

The fixed-ν method is derived from the most general form of the charged-current neutrino-nucleon cross-section (Equation 1.27):

$$\frac{d^2\sigma^{\nu,\bar{\nu}}}{dx\,dy} = \frac{G^2 s}{2\pi}\left[\left(1-y-\frac{Mxy}{2E}\right)F_2(x,Q^2)+\frac{y^2}{2}2xF_1(x,Q^2) \pm y\left(1-\frac{y}{2}\right)xF_3(x,Q^2)\right] \tag{5.2}$$

where the +(–) sign in the last term is for neutrino(antineutrino) interactions. This equation can be transformed using $2xF_1 = \left[\left(1+4M^2x^2/Q^2\right)\Big/\left(1+R(x,Q^2)\right)\right]F_2$, $s = 2ME$, and $y = \nu/E$ to get:

$$\frac{d^2\sigma^{\nu,\bar{\nu}}}{dx\,d\nu} = \frac{G^2 M}{\pi}\left[\left(1-\frac{\nu}{E}-\frac{Mx\nu}{2E^2}\right)F_2+\left(\frac{\nu^2}{2E^2}\frac{1+2Mx/\nu}{1+R}\right)F_2 \pm \frac{\nu}{E}\left(1-\frac{\nu}{2E}\right)xF_3\right] \tag{5.3}$$

Organizing Equation 5.3 in terms of ν/E gives:

$$\frac{d^2\sigma^{\nu,\bar{\nu}}}{dx\,d\nu} = \frac{G^2 M}{\pi}\left[F_2-\frac{\nu}{E}\left(F_2 \mp xF_3\right)+\frac{\nu^2}{2E^2}\left(\left(\frac{1+2Mx/\nu}{1+R}-\frac{Mx}{\nu}\right)F_2 \mp xF_3\right)\right] \tag{5.4}$$

Define $\tilde{R}(x,Q^2)$ such that:

$$1+\tilde{R} = \frac{1+2Mx/\nu}{1+R}-\frac{Mx}{\nu} \tag{5.5}$$

Then Equation 5.4 now takes the simple form:

$$\frac{d^2\sigma^{\nu,\bar{\nu}}}{dx\,d\nu} = \frac{G^2 M}{\pi}\left[F_2 - \frac{\nu}{E}\left(F_2 \mp xF_3\right) + \frac{\nu^2}{2E^2}\left(F_2 \mp xF_3 + \tilde{R}F_2\right)\right] \tag{5.6}$$

Integrating this over all x with ν and E fixed gives:

$$\frac{d\sigma^{\nu,\bar{\nu}}}{d\nu} = \frac{G^2 M}{\pi}\left[\int F_2 - \frac{\nu}{E}\left(\int F_2 \mp \int xF_3\right) + \frac{\nu^2}{2E^2}\left(\int F_2 \mp \int xF_3 + \int \tilde{R}F_2\right)\right] \tag{5.7}$$

where $\int F = \int_0^1 F(x,Q^2)\,dx$ for F_2 and xF_3. If we multiply both sides of Equation 5.7 by $\Phi(E)$, we get:

$$\frac{dN}{d\nu} = \Phi(E)\left(A + \frac{\nu}{E}B - \frac{\nu^2}{2E^2}C\right) \tag{5.8}$$

where:

$$A = \frac{G^2 M}{\pi}\int F_2 \tag{5.9}$$

$$B = -\frac{G^2 M}{\pi}\int\left(F_2 \mp xF_3\right) \tag{5.10}$$

$$C = B - \frac{G^2 M}{\pi}\int F_2\tilde{R} \tag{5.11}$$

Therefore, the derivative of the number of events with respect to ν is proportional to the flux times a function with a known energy dependence. The energy dependence comes in terms that are quadratic in ν/E, so if Equation 5.8 is integrated up to a small value of $\nu \equiv \nu_0$, the energy dependence of the parenthetical term will be small (see Figure 5.8). With the following definition:

$$\frac{B}{A} = -\left(1 \mp \frac{\int xF_3}{\int F_2}\right) \tag{5.12}$$

and integrating with respect to ν, Equation 5.8 becomes:

$$N(\nu < \nu_0) = \Phi(E)\int_0^{\nu_0} d\nu A\left(1 + \frac{\nu}{E}\left(\frac{B}{A}\right) - \frac{\nu^2}{2E^2}\left(\frac{B}{A} - \frac{\int F_2 \tilde{R}}{\int F_2}\right)\right) \tag{5.13}$$

$dN/d\nu$ can be determined empirically by binning events in $(E_\nu, E_{HAD} < \nu_0)$. This procedure is fully described in the next section.

5.1.1 Flux Extraction

For the flux analysis all events are accepted that pass the standard fiducial and geometric cuts (Section 3.3) and pass the following kinematic cuts:

- $\theta_\mu < 150\,mr$ — This cut assures good acceptance of the muon track as it passes through the muon spectrometer.

- $E_\mu > 15\,GeV$ — 15 GeV is the lower limit of acceptance of the muon spectrometer.

- $30\,GeV < E_\nu < 360\,GeV$ — The lower limit of 30 GeV was chosen because below that energy a large acceptance correction is required and the ν/E corrections become important. The upper limit of 360 GeV was chosen because above that energy the error on the Monte-Carlo smearing corrections becomes greater than 10%; also, the number of anti-neutrino events above 360 GeV is small and hence would not make a significant impact on the analysis.

• $E_{HAD} < \nu_0 = 20 GeV$ — The choice of 20 GeV was made so that there would be sufficient statistics in the higher energy bins, while minimizing the systematic correlations with the structure function data sample ($E_{HAD} > 10 GeV$); Table 5.1 lists the number of events as function of E_{HAD}. Also, the hadron energy resolution has been shown to be well understood down to 20 GeV [Sak90] so that mis-measuring the hadron energy near the region of the cut is not a concern.

A total of 389842 neutrino and 85910 anti-neutrino events pass the flux cuts. These events are binned into four categories: neutrino- or antineutrino-induced, toroid-focusing $\mu-$ or $\mu+$. Table 5.2 gives the number of events passing the flux cuts.

Table 5.1: Number of events passing the cross-section cuts (Section 3.3.3) as a function of E_{HAD} (in GeV). The region $10 < E_{HAD} < 20$ is the overlap between the structure-function event sample and the flux-extraction event sample.

	E744				E770			
Neutrino Type	ν	ν	$\bar{\nu}$	$\bar{\nu}$	ν	ν	$\bar{\nu}$	$\bar{\nu}$
Toroid Pol	Foc μ^-	Foc μ^+	Foc μ^-	Foc μ^+	Foc μ^-	Foc μ^+	Foc μ^-	Foc μ^+
$E_{HAD} < 10$	47447	51047	14857	19169	61598	60577	22881	26432
$10 < E_H < 20$	37017	38041	8863	11734	48139	45351	13542	15973
$E_{HAD} > 20$	189783	191940	23903	31705	256403	235949	34884	42315

Table 5.2: Number of events passing flux cuts.

	E744				E770			
Neutrino Type	ν	ν	$\bar{\nu}$	$\bar{\nu}$	ν	ν	$\bar{\nu}$	$\bar{\nu}$
Toroid Pol	Foc μ^-	Foc μ^+	Foc μ^-	Foc μ^+	Foc μ^-	Foc μ^+	Foc μ^-	Foc μ^+
Raw Events	700579	682503	97111	101451	798445	845644	116657	133188
Fid. Volume	442935	508164	59459	73880	592267	625309	88821	99825
Geometric	282796	284111	48150	64182	377318	345351	71986	86957
$\theta_\mu < 150 mr$	280262	283833	48134	64018	373955	345062	71961	86735
$E_\mu > 15 GeV$	276420	283205	48002	63077	368889	344366	71807	85383
$30 < E < 360$	265132	272703	46945	61031	353660	331360	70250	82519
$E_{HAD} < 20$	80830	86944	23179	29447	104890	103370	35521	40352

The events are further sub-divided into 17 energy bins with widths which vary to accommodate the change in the number of events as a function of energy and the energy resolution. Table 5.3 shows the number of flux events in each energy bin.

Within each E_ν bin the events are further divided into E_{HAD} bins; these E_{HAD} bins are limited by smearing and statistics to be 2 GeV wide, for a total of 10 bins with ν_0 = 20 GeV. The events in $\left(E_\nu, E_{HAD}\right)$ bins form a $dN/d\nu$ distribution which can be converted into the flux $\Phi(E)$ by inverting equation 5.13:

$$\Phi(E) \propto \int_0^{\nu_0} \frac{dN/d\nu}{\left[1+\frac{\nu}{E}\left(\langle B/A\rangle\right)-\frac{\nu^2}{2E^2}\left(\langle B/A\rangle-\int F_2\tilde{R}\Big/\int F_2\right)\right]} d\nu \tag{5.14}$$

where <B/A> is the average of B/A as defined in Eq. 5.12 averaged over all energy bins (to improve the statistical precision of measuring B/A which should be independent of energy).

The term $\int F_2 \tilde{R} / \int F_2$ is computed using the parton distributions q_{EST} in the Buras-Gaemers model as defined in section 4.2; that is, the structure functions from the previous iteration of the analysis loop (see section 6.3) are used to compute this term. The value of $\int F_2 \tilde{R} / \int F_2$ over the range $0 < E_{HAD} < 20 GeV$ is between –.12 and –.17.

These raw events must be corrected for detector acceptance and smearing before the flux can be extracted. Figure 5.1 shows the Monte-Carlo corrections as a function of energy. Overall, these corrections are less than 10% except at lower energies. In that region, the large acceptance correction reflects the fact that more muons are not momentum-reconstructed in those bins. The low-energy muons tend to be generated with wide angles, and thus more often escape the apparatus before reaching the toroid.

The procedure for determining <B/A> in Equation 5.13 for all E_ν bins is to fit for B/A in each individual energy bin and to compute the average over the different bins. The average can only be taken if $\int F$ in Equation 5.7 is a constant between different energy bins. Any variation in $\int F$ can be minimized by integrating to the same fixed ν_0 in each E_ν bin, and by correcting the number of events $dN/d\nu$ by the physics-model corrections to simulate interaction on a bare nuclear target. The effects of the physics-model corrections as defined in Equation 4.13 are shown in Figure 5.2.

Table 5.3: Number of flux events in each energy bin.

	E744				E770			
Neutrino Type	ν	ν	$\bar{\nu}$	$\bar{\nu}$	ν	ν	$\bar{\nu}$	$\bar{\nu}$
Toroid Pol	Foc μ^-	Foc μ^+	Foc μ^-	Foc μ^+	Foc μ^-	Foc μ^+	Foc μ^-	Foc μ^+
30–40 *GeV*	7336	5800	1765	2949	9398	6785	2813	4330
40–50 *GeV*	9430	9003	2540	3547	11932	10196	4467	5441
50–60 *GeV*	9842	10233	2963	3690	12510	11697	4965	5706
60–70 *GeV*	8782	9557	2829	3555	11472	11319	4508	4967
70–80 *GeV*	7581	8668	2668	3136	10181	10366	3869	4053
80–90 *GeV*	6251	7239	2180	2685	8310	8680	3120	3290
90–100 *GeV*	4947	5702	1680	2013	6467	6937	2327	2551
100–120 *GeV*	6623	7633	2140	2594	8294	9024	3015	3127
120–140 *GeV*	4118	4785	1087	1377	5000	5466	1732	1805
140–160 *GeV*	2958	3297	771	930	3788	4079	1157	1238
160–180 *GeV*	2492	2927	595	741	3282	3511	895	946
180–200 *GeV*	2256	2693	548	607	3142	3439	730	831
200–230 *GeV*	3049	3571	620	750	4227	4495	890	925
230–260 *GeV*	2143	2475	412	405	3011	3250	535	595
260–290 *GeV*	1440	1602	209	246	1906	2011	272	299
290–320 *GeV*	845	1044	109	136	1095	1213	144	159
320–360 *GeV*	737	715	63	86	875	902	82	89

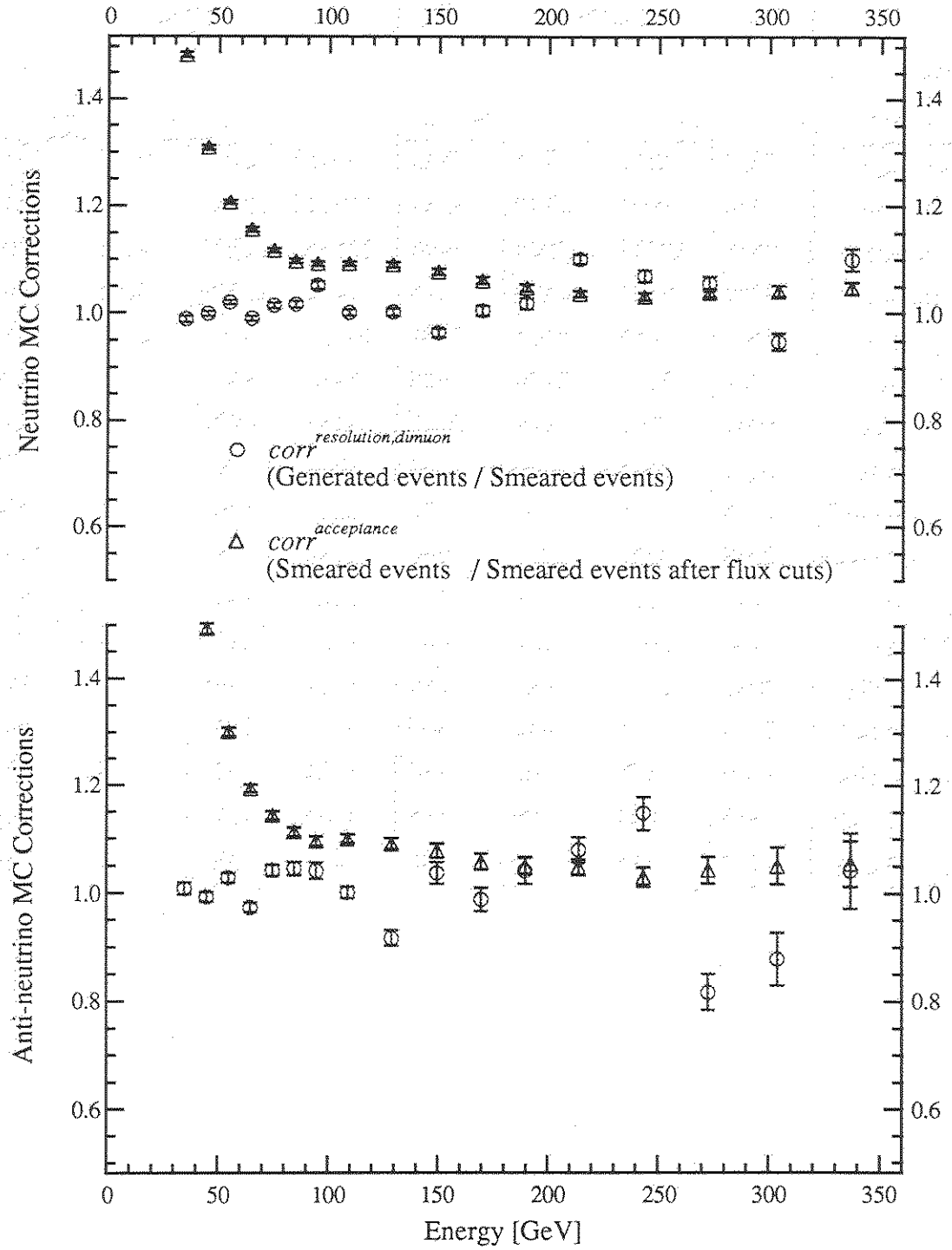

Figure 5.1: Effects of Monte-Carlo corrections in flux extraction. The "scatter" in the high-energy resolution corrections is due to the smearing of events between bins of varying widths.

After the physics-model corrections are applied, the $dN/d\nu$ distributions are fit to the form of Equation 5.13. However, there is an increase of events near zero hadron energy. These events are due to quasi-elastic scattering, resonance productions, and other quasi-elastic-like processes [Bel88, Bel92]. Figure 5.3 and 5.4 from Ref. [Bel88] show the kinematic region for which these processes are expected to contribute to the cross-section. Unlike the deep-inelastic interactions, whose cross-section is proportional to neutrino energy, these events have a cross-section which is constant at $0.9 \times 10^{-38}\ cm^2$ [Auc90].

These low-E_{HAD} processes are not included in the cross-section formalism of Equation 5.2. Therefore $dN/d\nu$ is only fit from $4\ GeV < E_{HAD} < 20\ GeV$ to determine the slope parameter B/A. The low-energy cut removes the quasi-elastic processes shown in Figure 5.4. Typical fits are shown in Figure 5.5 for neutrinos, and Figure 5.6 for anti-neutrinos.

Since B/A is first determined separately for each E_ν bin, the $\Phi(E)$ term in the Equation 5.13 is treated as a floating normalization in the fit. This normalization vanishes when B/A is calculated from Equation 5.12. The values of B/A from all the energy bins are averaged and are displayed in Figure 5.7. As the values do not show strong energy dependence they are averaged; Table 5.4 shows the results.

While the values of $\langle B/A \rangle^{\bar{\nu}}$ are reasonably consistent between the two experiments, there is a possible discrepancy between the experiments' values of $\langle B/A \rangle^{\nu}$. This difference is attributed to different systematic errors between the two experiments, and is dealt with in the systematic-error analysis, Section 5.1.2.

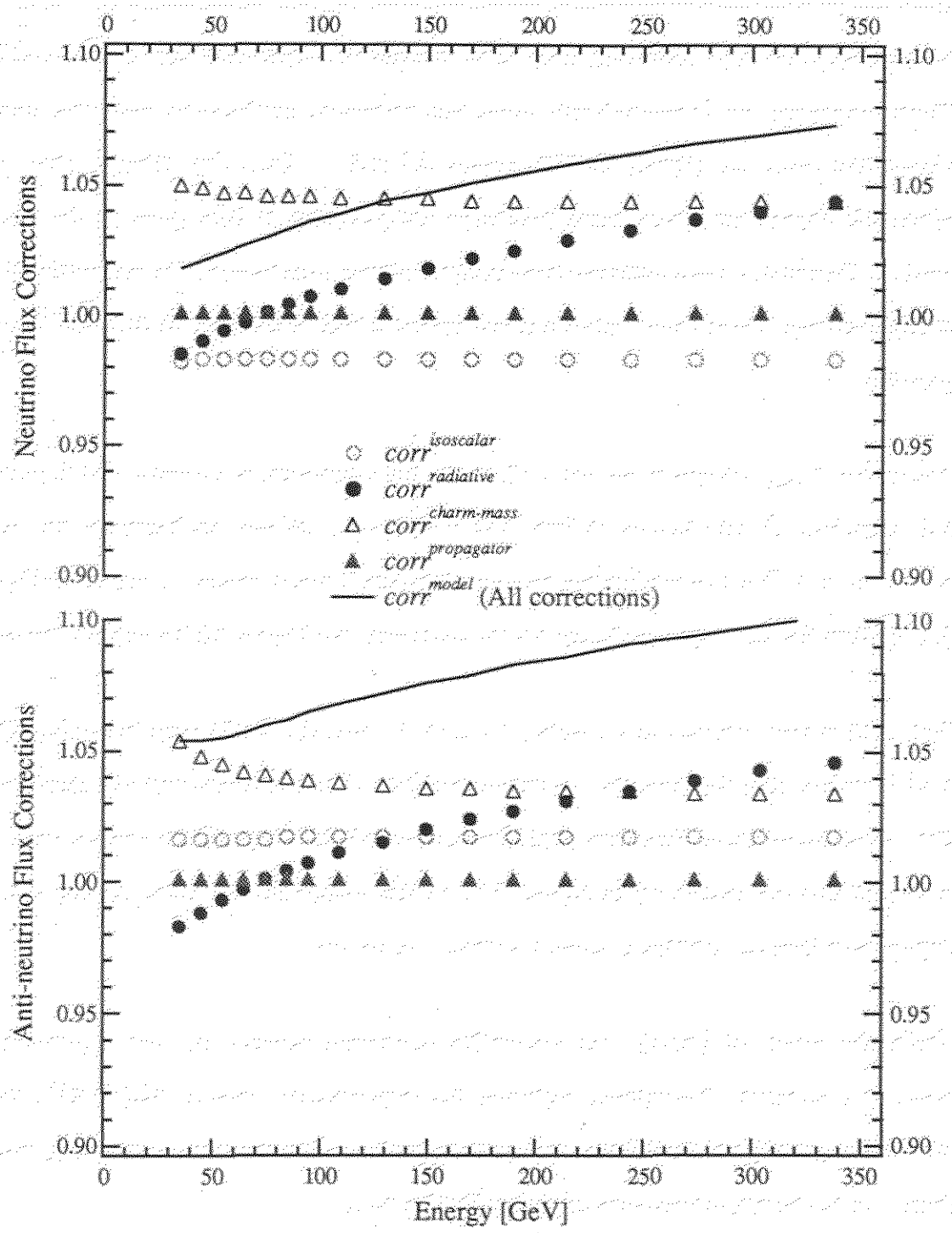

Figure 5.2: Effects of physics-model corrections in flux extraction.

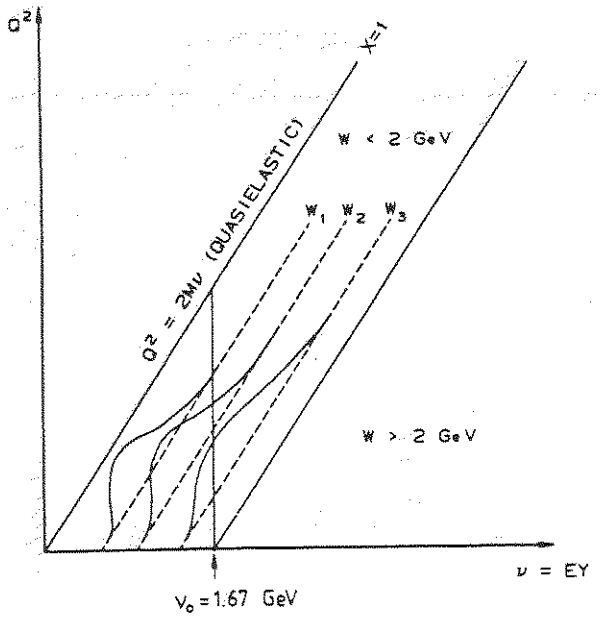

Figure 5.3: Kinematic map showing the region where quasi-elastic processes dominate the cross-section. This plot is FIG. 1 in Ref. [Bel88]. W is the invariant mass of the hadronic final state, $W^2 = 2M\nu + M^2 - Q^2$.

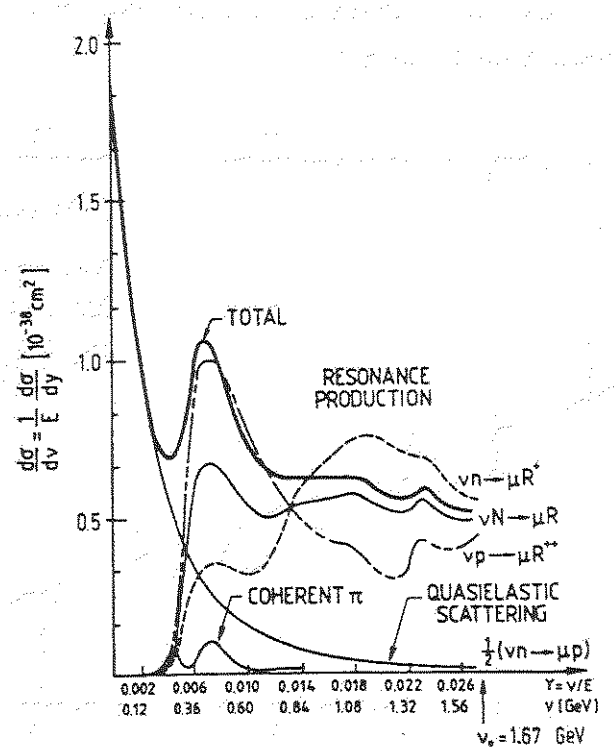

Figure 5.4: The differential cross-section $d\sigma/d\nu$ in the low-y region for $E_\nu = 60\ GeV$. This plot is FIG. 5 in Ref. [Bel88]. This plot shows that the conservative cut of $E_{HAD} = \nu > 4\ GeV$ will eliminate the quasi-elastic portion of the cross-section.

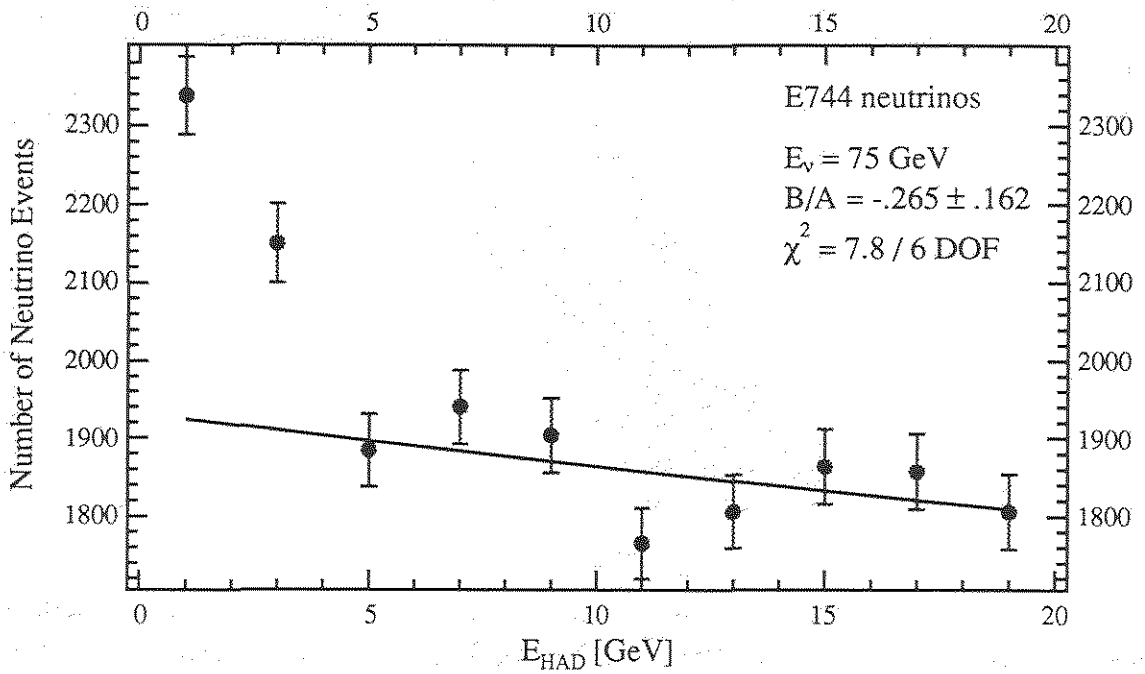

Figure 5.5: A typical fit for B/A to the $dN/d\nu$ distribution. The peak in events for $E_{HAD} < 4\ GeV$ is due to resonance production, as described in the text, and is not included in the fit for B/A.

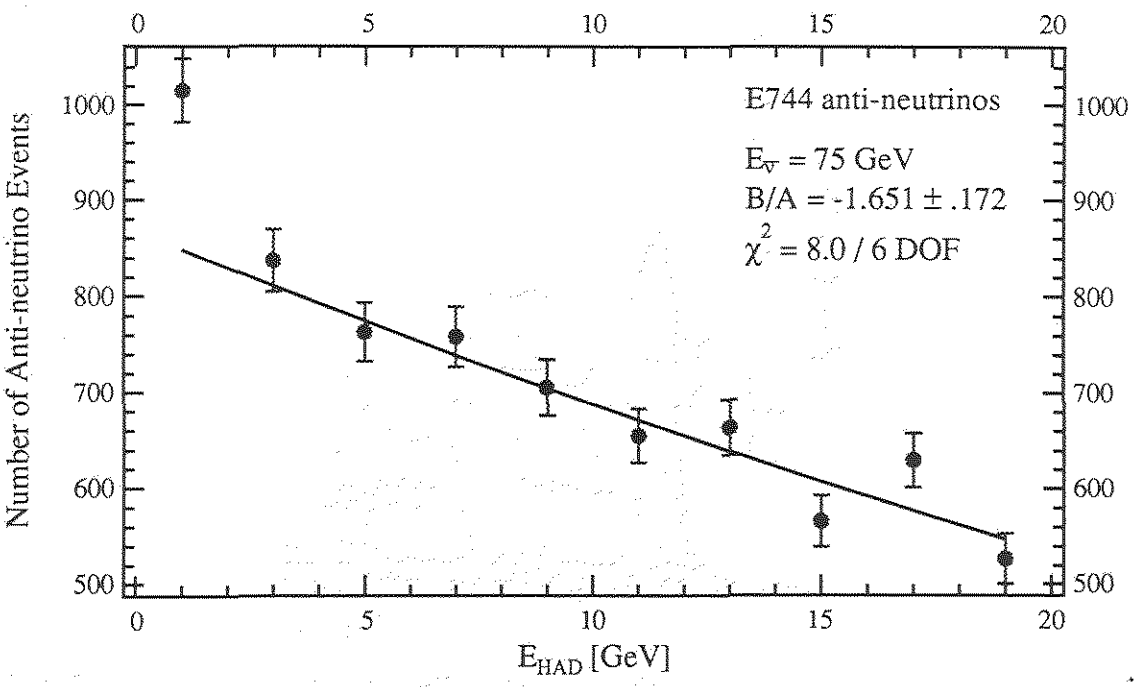

Figure 5.6: A typical fit for B/A to the $dN/d\bar{\nu}$ distribution. See the caption for Figure 5.5 for more information.

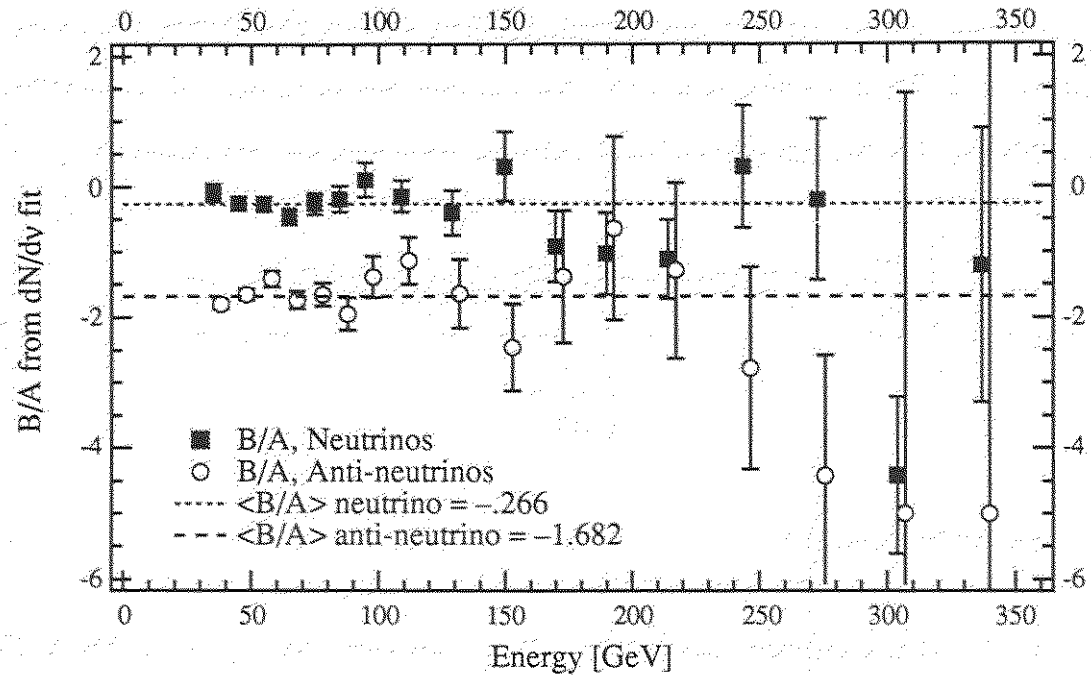

Figure 5.7: B/A as a function of energy for experiment E744. The anti-neutrino points have been offset by 3 GeV on the horizontal axis for clarity. The two lines indicate the average B/A from the points in the Figure. The χ^2 of the fit to the average neutrino (anti-neutrino) values is 25.0 (18.4) for 16 degrees of freedom.

Table 5.4: $\langle B/A \rangle$ from the flux analysis. The χ^2 is calculated for the difference between the E744 and E770 measurements. "Prob" is the integrated upper tail of the χ^2 distribution for 1 degree of freedom.

	ν	$\bar{\nu}$
$\langle B/A \rangle^{744}$	-0.266 ± 0.049	-1.682 ± 0.041
$\langle B/A \rangle^{770}$	-0.368 ± 0.043	-1.622 ± 0.037
$\langle B/A \rangle^{Combined}$	-0.324 ± 0.032	-1.649 ± 0.030
χ^2	2.5	1.2
Prob	12%	28%

Once the best values for B/A are known, the flux can be determined according to Equation 5.13. The correction implied by that equation can be substantial, especially for anti-neutrinos. The average value of the fixed-ν cut correction can be defined by

$$COR(E) = \frac{\int_0^{\nu_0} \frac{dN}{d\nu}\left[1 + \frac{\nu}{E}\left(\langle B/A\rangle\right) - \frac{\nu^2}{2E^2}\left(\langle B/A\rangle - \int F_2 \tilde{R} / \int F_2\right)\right]^{-1} d\nu}{\int_0^{\nu_0} \frac{dN}{d\nu} d\nu} \tag{5.15}$$

and is plotted in Figure 5.8.

Since σ/E is almost constant (see Section 5.3), it is conventional to plot the flux as $E\Phi$, which is approximately proportional to the number of events. Figure 5.9 shows the fully-corrected flux × energy spectra for experiments E744 and E770 as a function of energy.

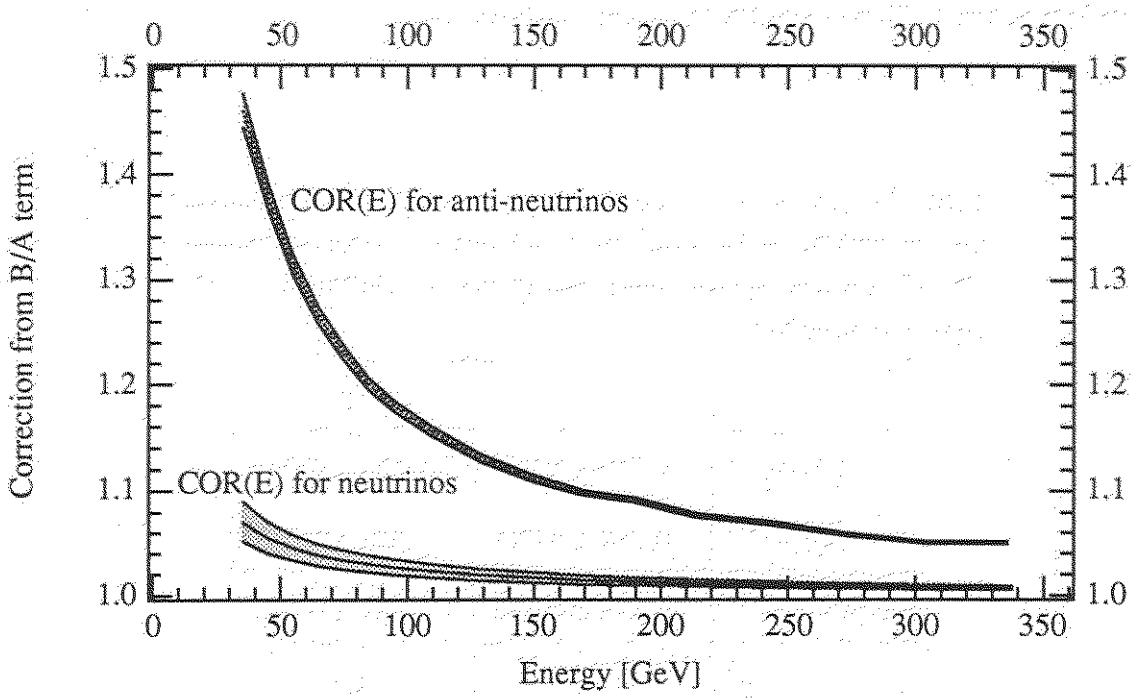

Figure 5.8: The correction due to B/A. $COR(E)$ is defined by Equation 5.15. The bands show the effect of a $\pm 1\sigma$ shift in B/A on the correction. The error on $\langle B/A\rangle^{\nu}$ has been multiplied by 1.5 as described in Section 5.1.2.1.

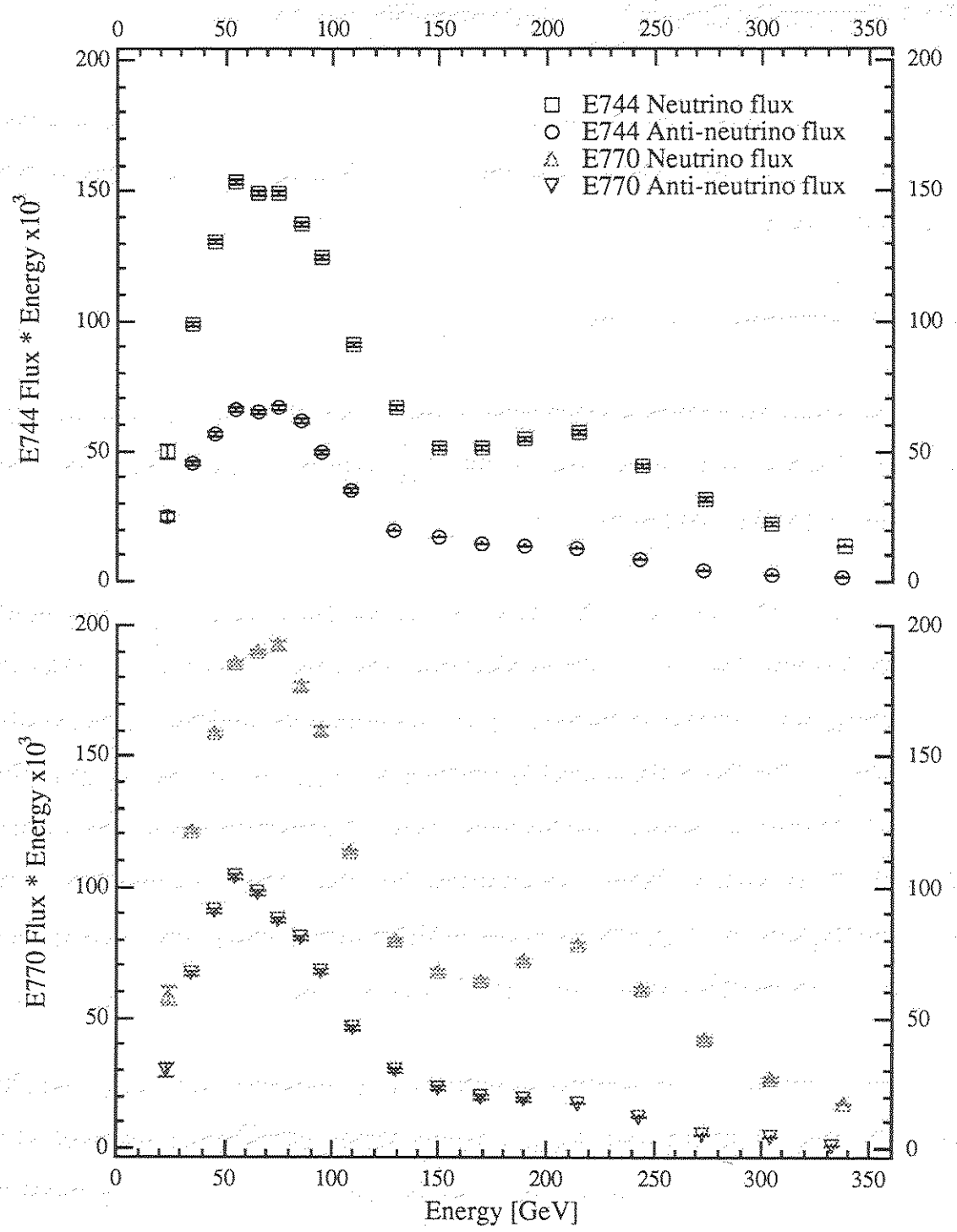

Figure 5.9: The fully-corrected flux × energy spectra for E744 and E770. The normalization along the left axes is arbitrary.

5.1.2 Systematic Errors

The systematic errors in the flux are included in the final results by propagating them through both the flux-extraction and the structure-function analyses. This is fully explained in Section 6.4.

5.1.2.1 Experimental Systematics

Of the experimental systematic errors listed in Section 6.4, the most important errors for the flux extraction are the uncertainties in the E_{HAD} calibration, the E_{μ} calibration, and the values of $\langle B/A \rangle^{\nu}$ and $\langle B/A \rangle^{\bar{\nu}}$.

Muon energy calibration was studied by comparing the flux extracted from three nearly identical data sets. The first was the standard data. The other two were sets in which the muon energy was increased or decreased by 1% (the error in the calibration determined in Ref. [Kin91]). The flux is determined by counting low E_{HAD} events, the energy of flux events is primarily determined from the muon energy. A systematic mis-measurement of E_{μ} will change the flux. Figure 5.10 illustrates this effect. Increasing (decreasing) the muon energy scale by 1% pushes the events to higher (lower) energy bins. This effect is less than 5% for neutrinos and less than 10% for anti-neutrinos.

By contrast, the flux is not sensitive to hadron energy miscalibrations. Since the flux events are counted up to a fixed E_{HAD}, a hadron energy miscalibration independent of muon energy should have the same effect on all flux energy bins. In effect, this would be a redefinition of ν_0. Since the energy bin is primarily determined by the muon energy, one expects a hadron energy calibration error of have little effect on the *relative* flux. Figure 5.11 shows the effect of ±1% E_{HAD} miscalibration (the error in the calibration determined in Ref. [Sak90]). The apparent level is shifted by about 1%, but the absolute

level is specified by other means. The shape is constant and the ratio of neutrinos to antineutrino fluxes is unaffected to within 2%.

The most important experimental systematic error is the value of $\langle B/A \rangle$. Equation 5.12 implies that the $\langle B/A \rangle$ should be an experimentally independent quantity, but Table 5.4 shows that the χ^2 between $\langle B/A \rangle$ from the E744 and E770 neutrino flux analyses is 2.5, with a probability of 12%. The only systematic effect that is different between the two experiments is a potential E_{HAD} miscalibration. However, a 1% miscalibration of E_{HAD} causes a shift of only 0.012 in $\langle B/A \rangle^{\nu}$.

This difference in $\langle B/A \rangle^{\nu}$ is not strongly significant, but to be conservative we choose to incorporate the difference between the measurements is our systematic errors. The difference between the E744 and E770 results is attributed to an unaccounted systematic error, and the difference is incorporated into the error quoted for the measurement. The statistical error in the average $\langle B/A \rangle^{\nu}$ is scaled up by the $\sqrt{\chi^2} = \sqrt{2.5} = 1.6$ between the values from the two experiments, with the error adjusted to account for the potential E_{HAD} calibration difference. Therefore, the statistical error in the measurement of $\langle B/A \rangle^{\nu,Combined}$ goes from 0.032 to 0.051, and this is the size of the error used in all subsequent systematic studies.

A similar calculation performed on the measurement of $\langle B/A \rangle^{\bar{\nu}}$ shows that any discrepancy between the values derived from the E744 and E770 analyses can be entirely explained by statistical and E_{HAD} calibration differences between the experiments. Therefore, the error on $\langle B/A \rangle^{\bar{\nu}}$ from Table 5.4 is not re-scaled.

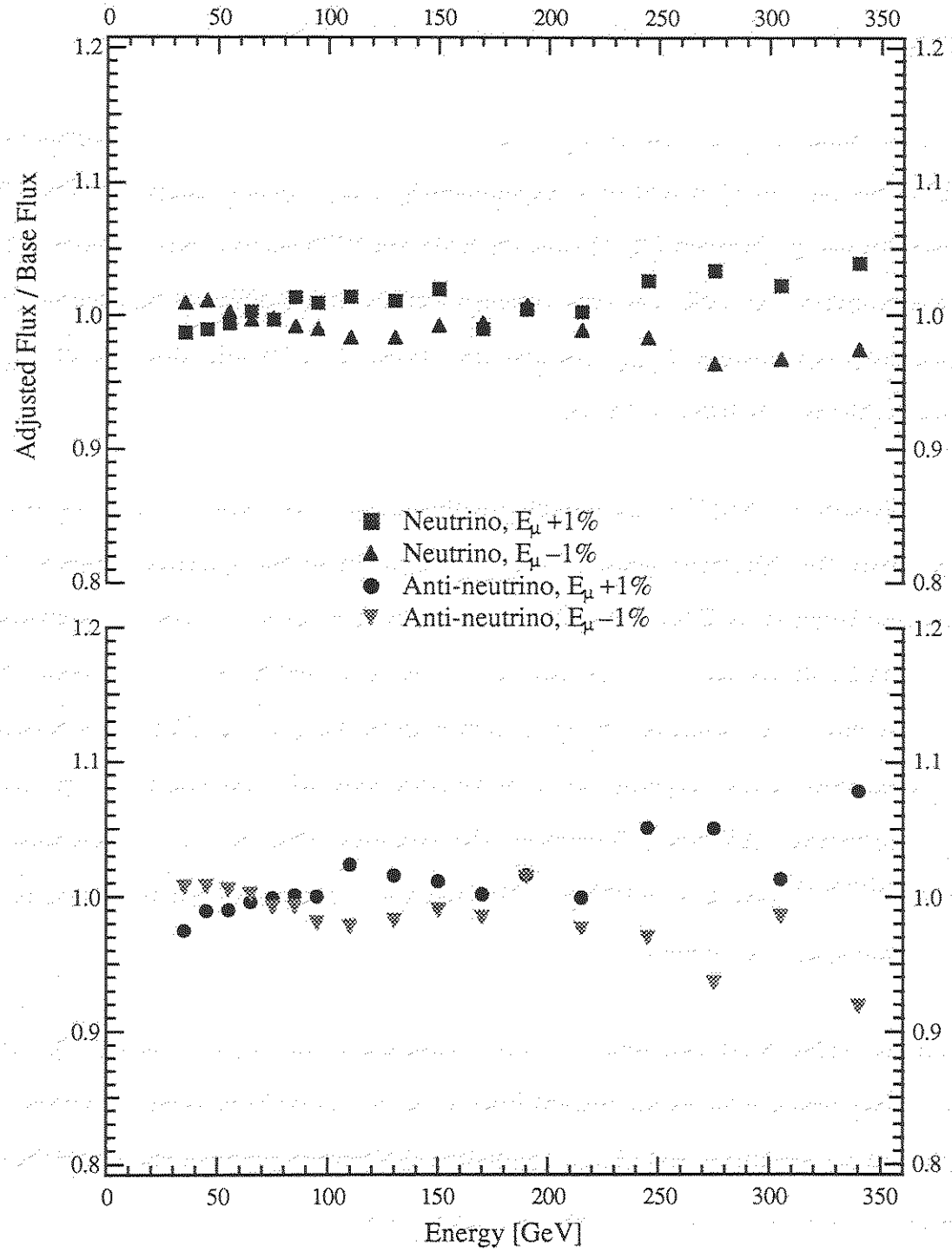

Figure 5.10: Effects of ±1% shift in E_μ.

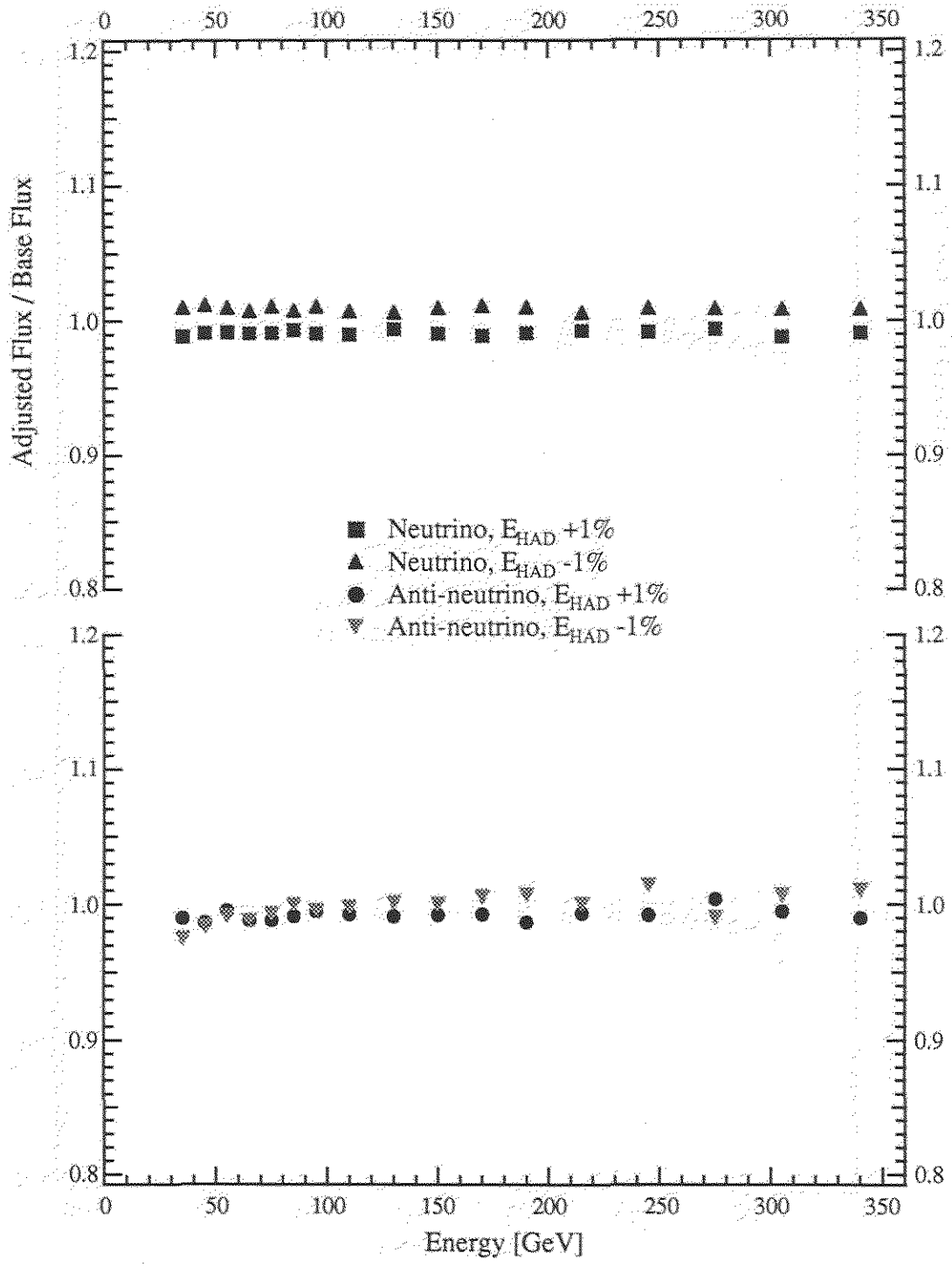

Figure 5.11: Effects of ±1% shift in E_{HAD}.

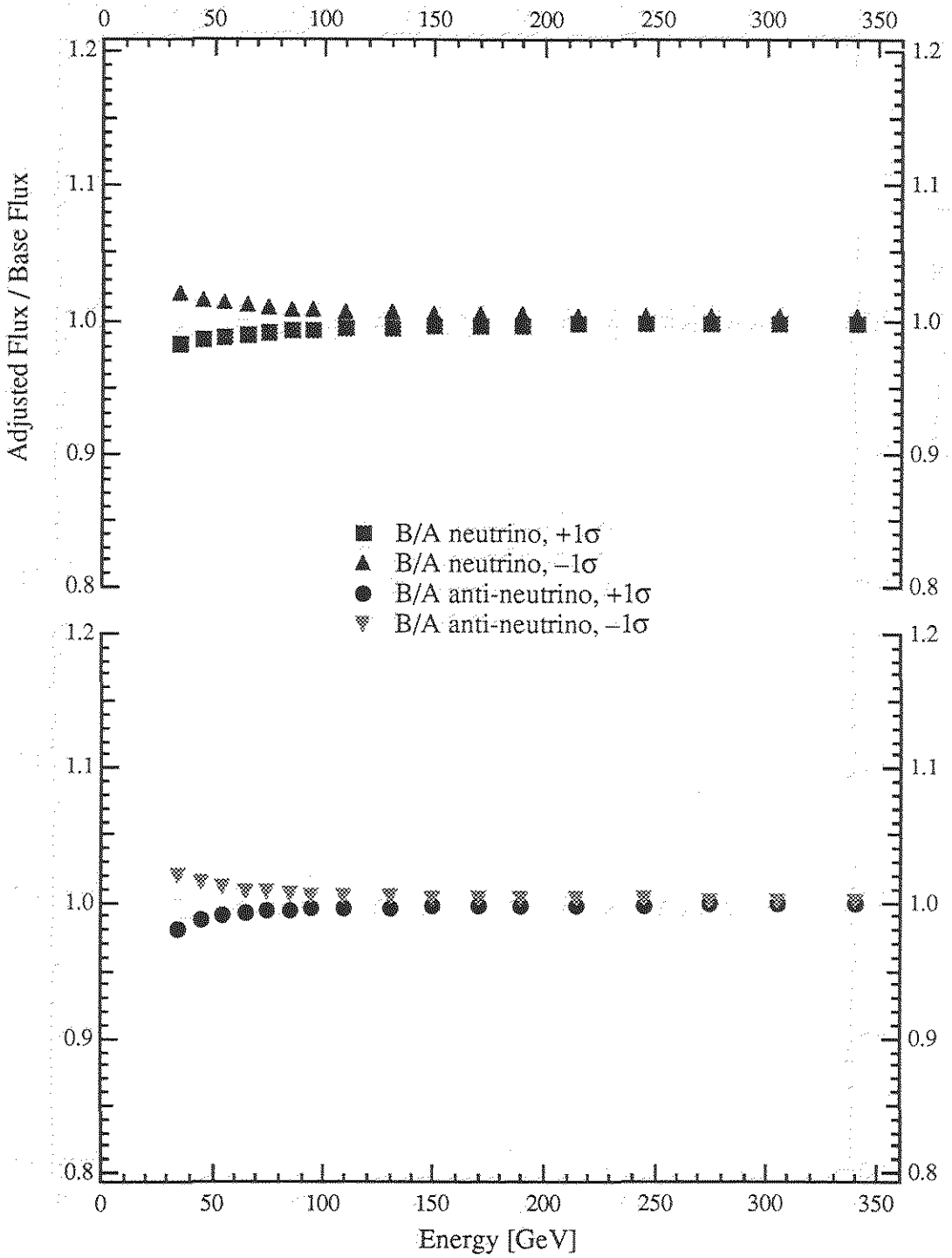

Figure 5.12: Effects of $\pm 1\,\sigma$ shift in B/A. The error in $\langle B/A \rangle^{\nu}$ has been scaled by a factor of 1.6 as described in the text.

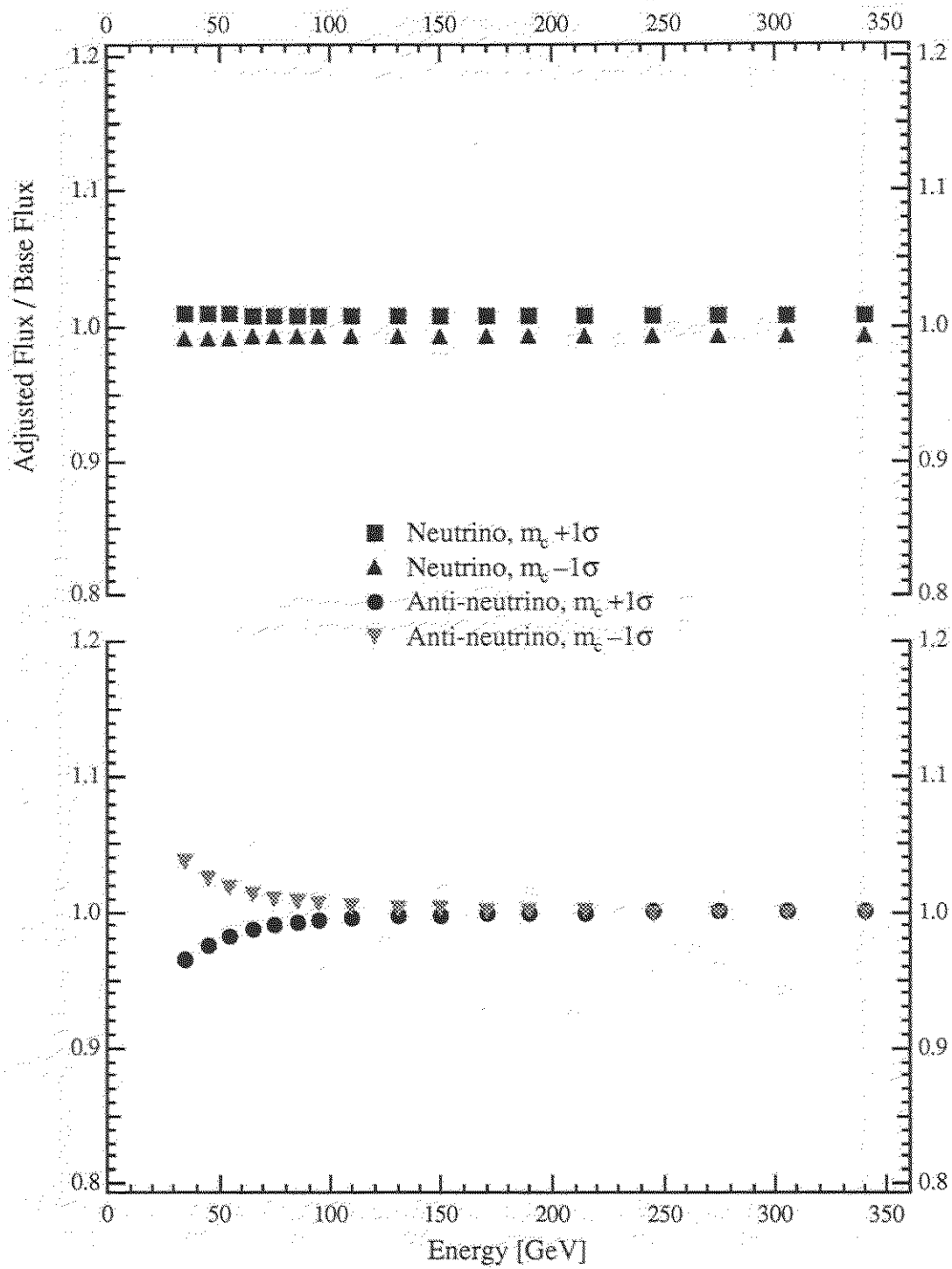

Figure 5.13: Effects of $\pm 1\sigma$ shift in m_c.

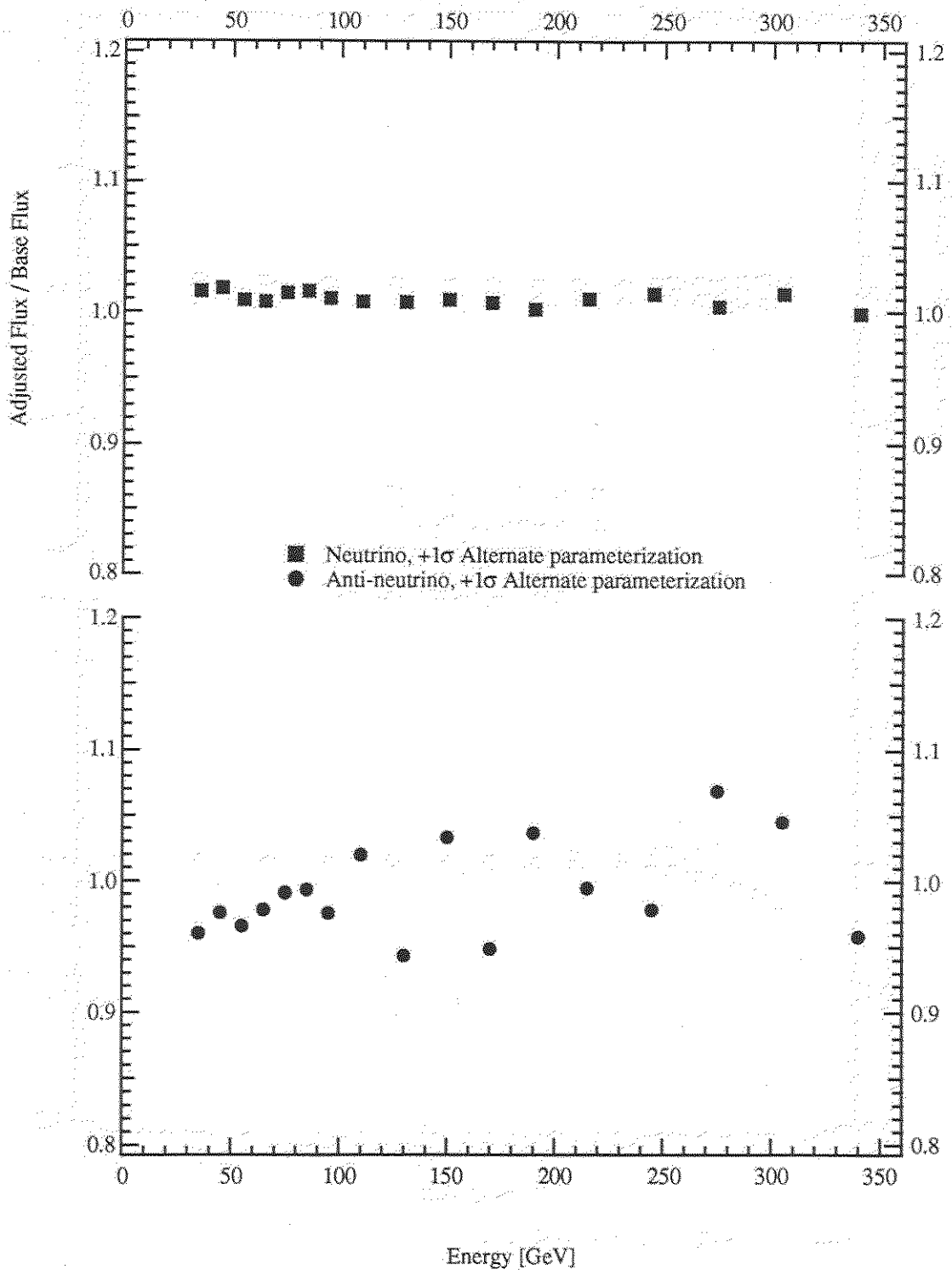

Figure 5.14: Effects of the alternate model parameterization.

Figure 5.12 shows the effects of varying $\langle B/A \rangle$ by $\pm 1\sigma$ (after the error rescaling described above). Since B/A is multiplied by terms proportional to ν/E the effect is largest at low energies. At 30 GeV the uncertainty is about 3%.

5.1.2.2 Model Systematics

The two most important systematic errors in the flux extraction due to the physics model of Section 4.2 are the slow-rescaling correction and the model systematic error.

The slow-rescaling correction is most sensitive to the charm quark mass parameter. The systematic error on the flux was determined by varying m_c within the limits set by the dimuon analysis [Rab93]. Shown in Figure 5.13 is the effect of $\pm 1\sigma$ changes (m_c = 1.55 and 1.07 GeV). The variation causes a constant $\pm 1\%$ shift in the level of the neutrino flux; however, there is a shift at low antineutrino energies of $\mp 4\%$, decreasing to 0% above 200 GeV.

The systematic error due to an alternate form of the Buras-Gaemers model of the parton densities is discussed in Section 4.2.1.5. Figure 5.14 shows the ratio of the flux extracted with data corrected by the alternate model to the flux extracted with the standard parameterization. The effect of the alternate model on the neutrino flux is less than 1%, but the the anti-neutrino flux is shifted by as much as 10%. As will be seen in Section 5.3.1 below, this will result in a large systematic error in the value of $\sigma^{\bar{\nu}} / \sigma^{\nu}$.

5.1.2.3 Theoretical Systematics

An assumption that was made between Equation 5.8 and 5.13 was that the structure functions were independent of ν for $\nu < \nu_0$. In particular, it was assumed that $\int F_2(\nu)dx$ is a constant with respect to ν. Since the structure functions depend on both x and Q^2,

and $Q^2 = 2Mx\nu$, this is not a strictly valid assumption [Hai94]. This experiment cannot reliably measure the structure functions at low ν, so the sensitivity of the flux extraction to this assumption is included as a systematic error. The assumption was tested by using the GRV 94 parton distributions† [Glu95] in place of the Buras-Gamers model; the differences in the resulting flux were small. A separate study tried to fit for any ν dependence in $\int F(\nu)dx$ from the data to the functional form $A + B\nu + C\nu^2$, but the statistics of the low-ν data are so poor that the values of B and C are consistent with zero with large errors. Based on the limits of these studies, we conservatively assign a 1% error to the flux extraction, which is incorporated into the structure-function analysis by including a 1% systematic error in $\sigma^{\bar{\nu}}/\sigma^{\nu}$ due to the low-ν extrapolation.

In the structure-function analysis, the (x, Q^2) bins of the structure-function extraction are the same as the (x, Q^2) bins in which the physics-model correction is applied. In the flux analysis, the events in the (E_ν, E_{HAD}) bins are corrected by the physics-model correction into all x and Q^2, including regions where the structure functions are not measured by the CCFR analysis. This raises the question of the accuracy of the Buras-Gaemers model in those regions. This issue was studied by comparing the results of extrapolating into those regions using Buras-Gaemers, using a NLO QCD parameterization, and using a simple logarithmic-slope fit to the structure functions. As a result of this study, we assign a 0.5% error to the flux extraction, which is incorporated into the structure-function analysis by including a 0.5% systematic error in $\sigma^{\bar{\nu}}/\sigma^{\nu}$ due to the acceptance correction.

---

† In this kinematic region the GRV parton distributions are not based on data, but on the theoretical assumptions made by the GRV group that went into their model of the parton distributions.

An additional flux-related systematic error, the error due to observed deviations in $\sigma^{\nu N}/E_\nu$ vs. E_ν, is discussed in the section on cross-sections below.

5.2 Flux Versus Detector Vertex

After the flux as a function of energy is determined using the fixed-ν technique, the relative vertex event rate, that is, the ratio of the number of events between different vertex positions within a given energy bin $\Phi(E_{BIN},V_{x,i},V_{y,j})/\Phi(E_{BIN},V_{x,k},V_{y,l})$, is determined by a simple iterative Monte Carlo procedure. This iterative method, as opposed to the fixed-ν method described above, must be used to determine the relative vertex flux because there are not enough events in most of the (E_ν,V_x,V_y) bins for the fixed-ν method to have any statistical usefulness. The number of events in a given (E_ν,V_x,V_y) bin is estimated by generating events according to $\Phi_{EST}(E,V_x,V_y)\times\sigma_0(E)$, where Φ_{EST} is an initial estimate to the (V_x,V_y) event distribution of the flux in square bins 5 *in* wide, and $\sigma_0(E)$ is the total cross-section assuming that σ/E is constant, a reasonable assumption given the relatively low statistics associated with the vertex flux. For each energy bin E_i the flux estimate Φ_{EST} is updated to a new estimate by:

$$\frac{\Phi_{NEW}(E_i,V_x,V_y)}{\Phi_{EST}(E_i,V_x,V_y)}=\frac{MC^{SMR}(E_i)}{DA^{OBS}_{SF-cuts}(E_i)}\frac{DA^{OBS}_{SF-cuts}(E_i,V_x,V_y)}{MC^{SMR}_{SF-cuts}(E_i,V_x,V_y)} \tag{5.16}$$

where $DA^{OBS}_{SF-cuts}(E_i,V_x,V_y)$ is the number of data events observed in the energy-vertex bin after standard structure-function cuts are applied (see section 6.2.1), $DA^{OBS}_{SF-cuts}(E_i)$ is the total number of events in the energy bin after cuts, $MC^{SMR}_{SF-cuts}(E_i,V_x,V_y)$ is the number of Monte Carlo events in the energy-vertex bin after smearing and structure-function cuts, and $MC^{SMR}(E_i)$ is the total number of smeared events in the energy bin

after cuts. The Monte Carlo is then run again with Φ_{NEW} replacing Φ_{EST}. This procedure is repeated until the corrections implied by Equation 5.16 are consistent with 1.0.

5.3 Cross-Section Analysis

The total cross-section of neutrinos and anti-neutrinos is an important result of this analysis. Although this analysis only measures *relative* flux, and hence *relative* cross-sections, a measurement of the linearity ($\sigma^{\nu N} \propto E_\nu$) can be made. In addition, the absolute level of $\sigma^{\bar{\nu}} / \sigma^{\nu}$ is measured since the same normalization is used for the neutrino and anti-neutrino flux.

The cross-section analysis proceeds in parallel to the flux analysis. The same cuts are used, except for the $\nu < \nu_0$ cut; all hadron energies are included in the total cross-section measurement. The Monte-Carlo corrections discussed in chapter 4 are applied to each E_ν bin; the neutrino-energy bins used in the cross-section analysis are the same as used in the flux analysis. Figure 5.15 shows the Monte-Carlo corrections applied to the cross-section data; Figure 5.16 shows the physics-model corrections applied to the cross-section data.

5.3.1 Results and Comparisons

The cross-sections are first extracted with only the isoscalar correction applied. This cross-section can be compared directly to other published measurements [Bla83, Ber87, Auc90]. The results of the analysis are shown in Table 5.5. Figure 5.17 shows the world status of neutrino-iron cross-section measurements and the new result from this analysis.

The cross-sections derived from experiments E744 and E770 are calculated separately, then summed statistically for the results shown. It should be noted that the value of

$\sigma^{\bar{\nu}}/\sigma^{\nu}$ (30-360 *GeV*) from E744 is 0.5024 ± 0.0032, and the value of $\sigma^{\bar{\nu}}/\sigma^{\nu}$ from E770 is 0.5135 ± 0.0028. The only accounted-for systematic differences between the two experiments that could cause a difference between the measurements are the difference in *B/A*, and (to a much smaller degree) the error due to a different E_{HAD} miscalibration. Including the *B/A* and E_{HAD} systematic errors, the χ^2 for the E744/E770 comparison is 2.38/1 DOF which has an acceptable probability of 12%. For the structure-function extraction, these systematic effects will propagate into the final results via the separate E744 and E770 flux files used to calculate the systematic variations in the structure functions (see Section 6.4).

The ratio of $\sigma^{\bar{\nu}}/\sigma^{\nu}$ can be compared directly against other experiments. This experiment can measure the ratio in the energy range 30-360 *GeV*; in contrast, previous experiments were only able to measure the ratio in the range 30-200 *GeV*. Therefore, we present here the ratios of $\sigma^{\bar{\nu}}/\sigma^{\nu}$ extracted for both 30-200 *GeV* and 30-360 *GeV;* the first value is the one that should be compared to other experiments. Table 5.6 lists the statistical and systematic errors in $\sigma^{\bar{\nu}}/\sigma^{\nu}$ both energy ranges.

As discussed in section 6.2, the structure-function extraction requires values of $\sigma^{\nu N}/E$ and $\sigma^{\bar{\nu}N}/E$ to normalize the result. Since the fixed-ν method cannot determine the absolute flux, the normalization due to the cross-section must come from other experiments. Since our experiment measures $\sigma^{\bar{\nu}}/\sigma^{\nu}$ to a precision that is roughly as good as any of the previous ν-Fe experiments, the value of $\sigma^{\bar{\nu}N}/E$ used in this analysis comes from multiplying the world average $\sigma^{\nu N}/E$ by the world average $\sigma^{\bar{\nu}}/\sigma^{\nu}$ *including* this experiment.

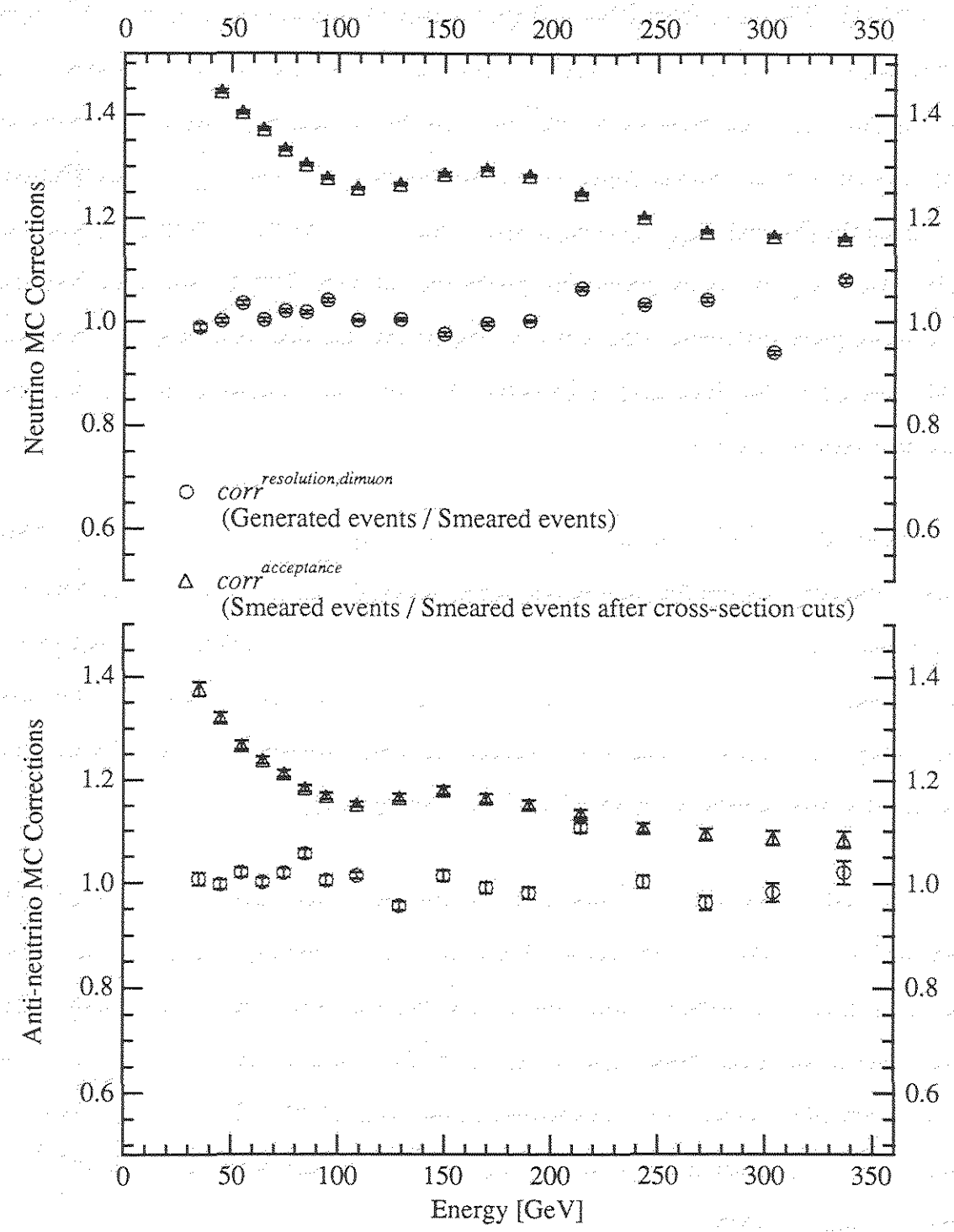

Figure 5.15: Monte-Carlo corrections applied to the cross-section data. The "scatter" in the high-energy resolution corrections is due to the smearing of events between bins of varying widths.

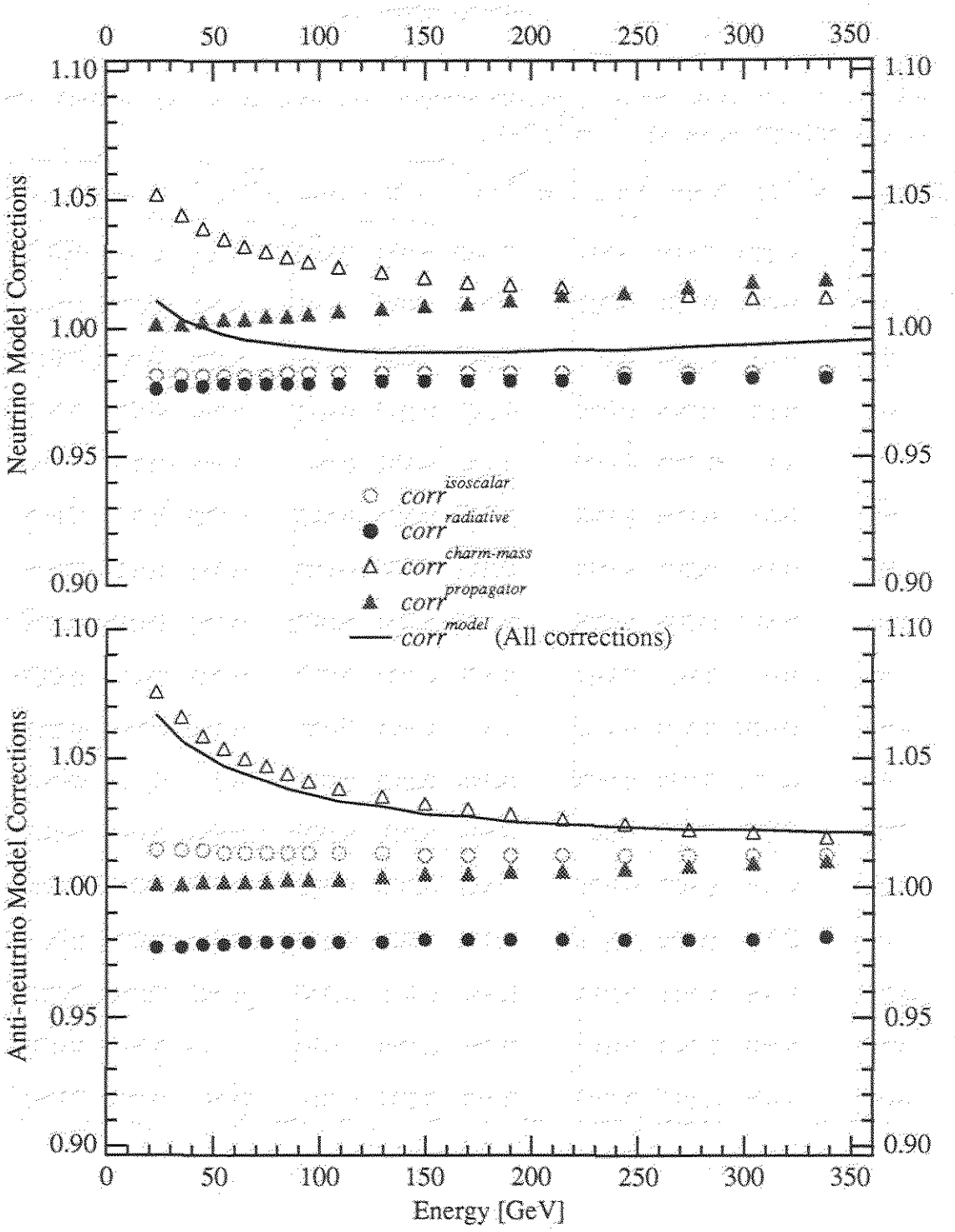

Figure 5.16: Physics-model corrections applied to the cross-section data.

Table 5.5: Results from the cross-section analysis. The units of energy are GeV; the units of cross-section are $10^{-38}\ cm^2/GeV$.

Energy	$\sigma^{\nu N}/E$	± stat	± syst	$\sigma^{\bar{\nu}N}/E$	± stat	± syst	$\sigma^{\bar{\nu}}/\sigma^{\nu}$	± stat	± syst
35	0.694	0.009	0.011	0.349	0.007	0.022	0.503	0.014	0.018
45	0.681	0.007	0.009	0.342	0.005	0.011	0.502	0.010	0.014
55	0.683	0.006	0.008	0.344	0.005	0.009	0.504	0.009	0.012
65	0.681	0.006	0.008	0.343	0.005	0.011	0.504	0.009	0.011
75	0.672	0.006	0.008	0.342	0.005	0.007	0.507	0.010	0.010
85	0.672	0.006	0.008	0.340	0.005	0.008	0.505	0.010	0.009
95	0.668	0.007	0.008	0.342	0.006	0.006	0.511	0.012	0.009
110	0.682	0.006	0.009	0.344	0.005	0.006	0.505	0.010	0.008
130	0.677	0.008	0.009	0.358	0.007	0.007	0.529	0.014	0.008
150	0.680	0.009	0.010	0.351	0.008	0.006	0.515	0.016	0.008
170	0.673	0.009	0.009	0.346	0.009	0.012	0.514	0.018	0.008
190	0.657	0.009	0.009	0.345	0.010	0.009	0.525	0.019	0.008
215	0.644	0.007	0.008	0.341	0.009	0.006	0.528	0.017	0.008
245	0.650	0.009	0.011	0.336	0.011	0.014	0.516	0.021	0.009
275	0.646	0.011	0.012	0.354	0.016	0.030	0.547	0.030	0.010
305	0.655	0.015	0.015	0.324	0.020	0.010	0.494	0.037	0.008
340	0.656	0.017	0.016	0.368	0.032	0.017	0.561	0.054	0.010

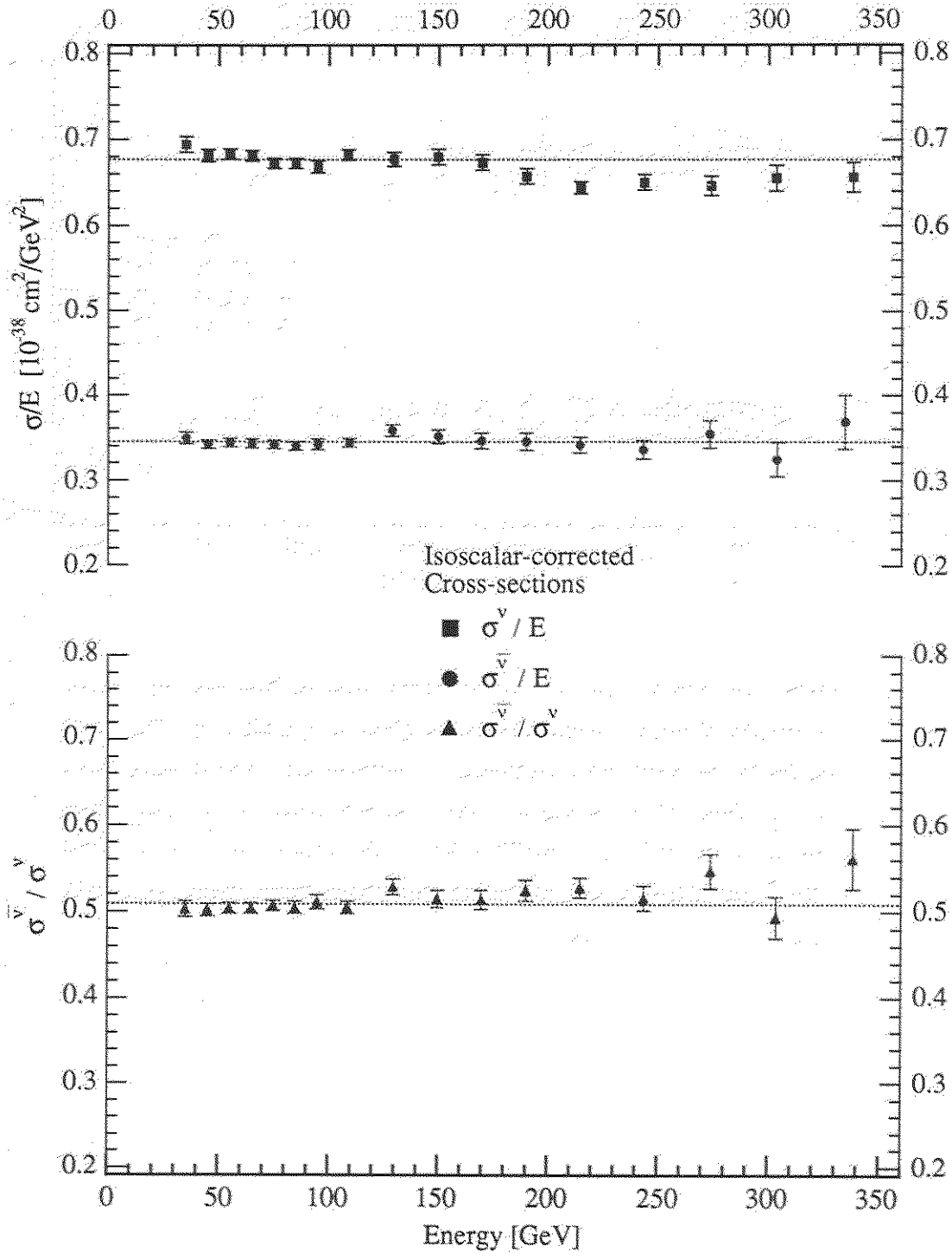

Figure 5.17: Results from the cross-section analysis. Error bars are statistical only. The dashed lines indicate the normalization values of the cross-sections measured between 30-200 GeV: $\sigma^{\nu N}/E = 0.677 \times 10^{-38}\, cm^2/GeV$, $\sigma^{\bar{\nu}N}/E = 0.345 \times 10^{-38}\, cm^2/GeV$, $\sigma^{\bar{\nu}}/\sigma^{\nu} = 0.509$. The slopes in $\sigma^{\nu N}/E$ and $\sigma^{\bar{\nu}N}/E$ as a function of energy are discussed in Section 5.3.2.

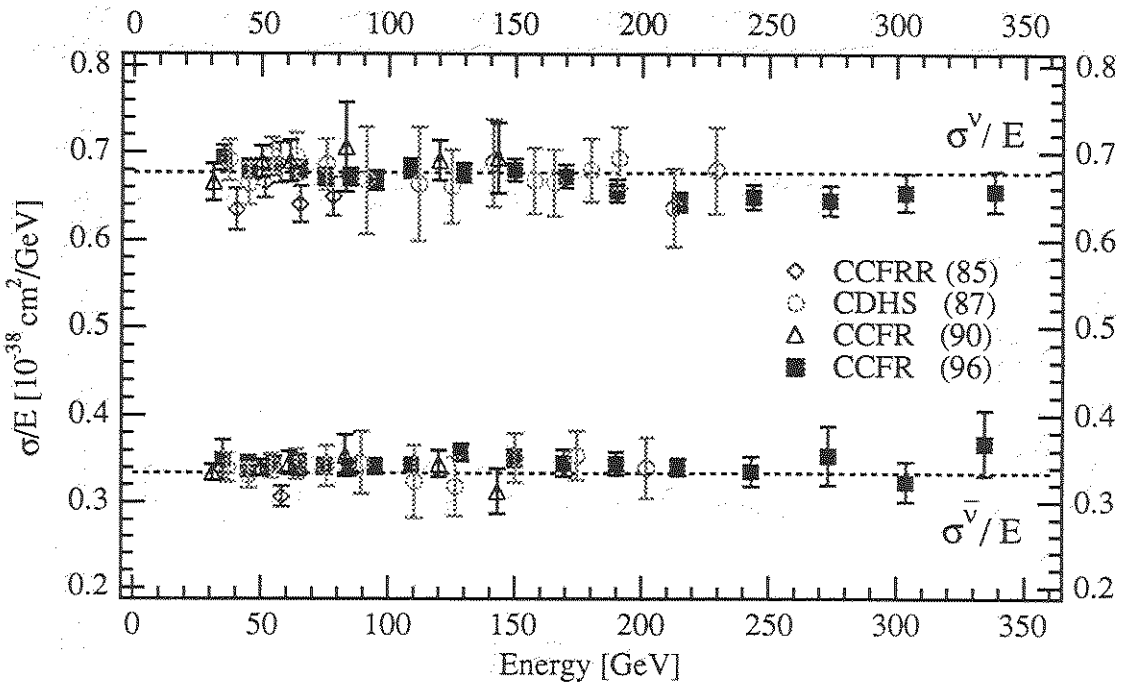

Figure 5.18: World status of neutrino-iron cross-section measurements. The results of the present analysis are given as CCFR (96). The error bars show the total error (statistical + systematic). The dashed lines show the level of the world average isoscalar-corrected neutrino-iron cross-sections ($\sigma^{\nu N}/E = 0.677 \times 10^{-38}\ cm^2/GeV$, $\sigma^{\bar{\nu}N}/E = 0.334 \times 10^{-38}\ cm^2/GeV$), not including this experiment which can only measure the relative cross-section.

Table 5.6: The ratio $\sigma^{\bar{\nu}}/\sigma^{\nu}$ measured in two energy ranges. The first energy range, 30-200 GeV, yields a result that can be compared to other experiments. For a complete description of the systematic effects described in this table, see Section 6.4. Systematic errors that were extracted separately for each experiment are added in quadrature.

	Energy range [GeV]:	30-200	30-360
	$\sigma^{\bar{\nu}}/\sigma^{\nu}$	**0.5089**	**0.5087**
	Statistical error	**±.0023**	**±.0020**
Systematic effect	*Systematic variation*		
E_{HAD} calibration	± 1%	±.0013	±.0013
ΔE_{HAD} shift	± 100 MeV	±.0008	±.0007
E_{μ} calibration	± 1%	±.0009	±.0009
ΔE_{μ} shift	± 100 MeV	±.0006	±.0006
$B/A\ \nu$	$\pm 1.5\ \delta(B/A\ \nu)$	±.0029	±.0031
$B/A\ \bar{\nu}$	$\pm\ \delta(B/A\ \bar{\nu})$	±.0026	±.0024
R_{World}	± 15%	±.0002	±.0002
charm mass m_c	$\pm\ \delta(m_c)$	±.0061	±.0059
strange sea normalization κ	$\pm\ \delta(\kappa)$	±.0010	±.0010
strange sea shape α	$\pm\ \delta(\alpha)$	±.0000	±.0001
charm branching ratio B_c	$\pm\ \delta(B_c)$	±.0005	±.0006
model parameterization error	new parameters	±.0075	±.0080
low-ν extrapolation	± 1.0%	±.0051	±.0051
acceptance correction	± 0.5%	±.0026	±.0026
	TOTAL (Systematic error)	**±.0121**	**±.0123**
	TOTAL (Statistical + systematic error)	**±.0123**	**±.0125**

The values of $\sigma^{\nu N}/E$ and $\sigma^{\bar{\nu}}/\sigma^{\nu}$ from other experiments are listed in Table 5.7, along with the resulting averages. It should be noted that the values listed in the table may not agree with the values given in the abstracts of the papers referenced, nor do the errors in $\sigma^{\nu N}/E$ and $\sigma^{\bar{\nu}}/\sigma^{\nu}$ add in quadrature to the error in $\sigma^{\bar{\nu}}/\sigma^{\nu}$. This is because:

- the values in Table 5.7 have all been corrected, where appropriate, to the isoscalar-corrected values;

- the values from within each experiment are averaged over the common energy range of all listed experiments, 30-200 *GeV;*

- according to the information contained in the individual papers, systematic errors that $\sigma^{\bar{\nu}N}/E$ and $\sigma^{\bar{\nu}N}/E$ have in common are not included in the ratio $\sigma^{\bar{\nu}}/\sigma^{\nu}$;

- additional systematic errors may have been included in $\sigma^{\bar{\nu}}/\sigma^{\nu}$ as specified within the individual papers.

Hence, the value of $\sigma^{\nu N}/E$ between 30-200 *GeV* used in the structure-function analysis is $0.677 \pm 0.014 \times 10^{-38}\ cm^2/GeV$, and the value of $\sigma^{\bar{\nu}}/\sigma^{\nu}$ used over the same energy range is 0.499 ± 0.007. Thus, the effective value of $\sigma^{\bar{\nu}N}/E$ used in this analysis is $\sigma^{\nu N}/E \times \sigma^{\bar{\nu}}/\sigma^{\nu} = 0.677 \times 0.499 = 0.338 \times 10^{-38}\ cm^2/GeV$.

Table 5.7: World average values of isoscalar-corrected $\sigma^{\nu N}/E$, $\sigma^{\bar{\nu}N}/E$, and $\sigma^{\bar{\nu}}/\sigma^{\nu}$ (including this experiment) for the energy range 30-200 GeV. Units are $10^{-38}\ cm^2/GeV$.

Experiment	$\sigma^{\bar{\nu}N}/E$	$\sigma^{\bar{\nu}N}/E$	$\sigma^{\bar{\nu}}/\sigma^{\nu}$
CCFRR [Bla83]	0.669 ± 0.024	0.340 ± 0.020	0.499 ± 0.025
CDHSW [Ber87]	0.686 ± 0.020	0.339 ± 0.022	0.495 ± 0.010
CCFR [Auc90]	0.659 ± 0.039	0.307 ± 0.020	0.467 ± 0.028
World Avg.	$\mathbf{0.677 \pm 0.014}$	0.334 ± 0.008	0.493 ± 0.009
This expt.			0.509 ± 0.012
World Avg. + this expt			$\mathbf{0.499 \pm 0.007}$

5.3.2 The Partonic-Level Cross-Section

In addition to the "isoscalar-only" cross-section discussed in the previous section, the "partonic-level" cross-section is also extracted with the full set of physics-model corrections described in 4.2 and plotted in Figure 5.16. After these corrections, $\sigma^{\nu N}/E_\nu$ should be a constant with energy, except for variations due to resonance production and QCD scaling violations. The partonic-level cross-sections are shown in Figure 5.19. The linearity of $\sigma^{\nu N}/E_\nu$ versus E_ν is determined by fitting to the form $A(1+BE)$; the results are:

$$\sigma^{\nu}_{partonic}/E = 0.699(1-[0.00022 \pm 0.00003 \pm 0.00007] \times E) \tag{5.17}$$

$$\sigma^{\bar{\nu}}_{partonic}/E = 0.350(1+[0.00002 \pm 0.00006 \pm 0.00015] \times E) \tag{5.18}$$

The first error in the slope is statistical, the second is systematic. The systematic error was determined by fitting the cross-sections extracted after varying each of the systematic quantities in Table 5.6, then summing the differences from the base slope in quadrature.

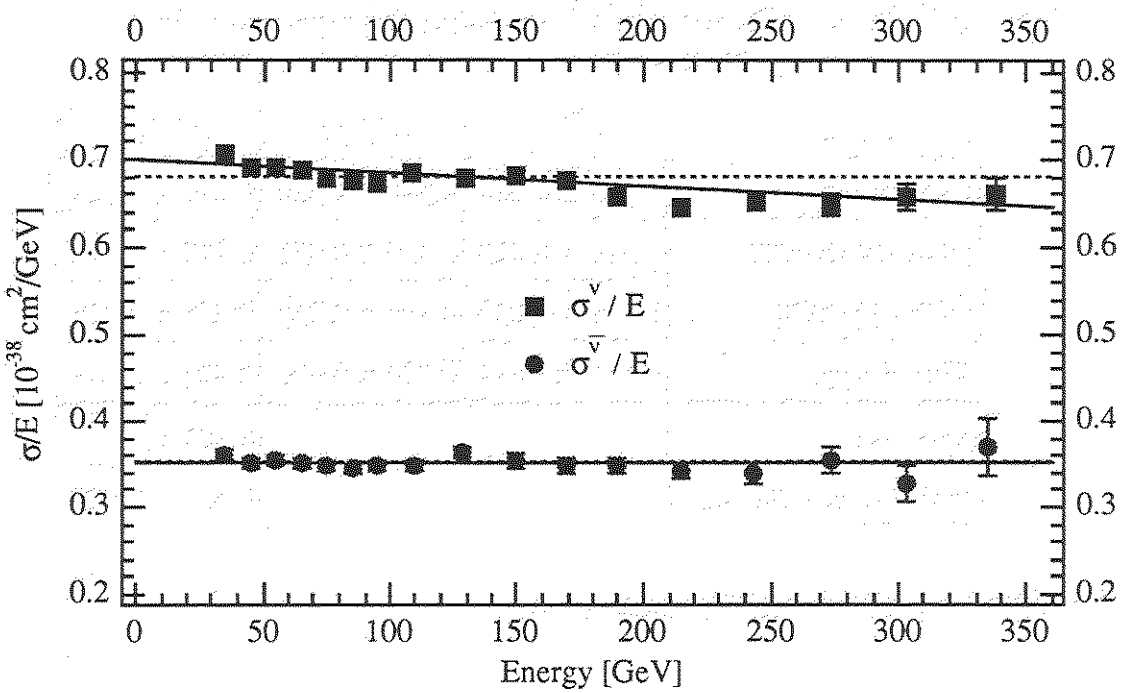

Figure 5.19: Partonic-level cross-sections, including all physics-model corrections. The dashed lines indicate the normalization values of the cross-sections measured between 30-200 GeV: $\sigma^{\nu N}/E = 0.677 \times 10^{-38}\, cm^2/GeV$, $\sigma^{\bar{\nu}N}/E = 0.345 \times 10^{-38}\, cm^2/GeV$. The solid lines indicate the linear fit to the cross-section.

Thus the slope in $\sigma^{\nu N}/E$ is given by $r^{\nu} = -(2.2 \pm 0.8)\%/100\, GeV$, and the slope in $\sigma^{\bar{\nu}N}/E$ is given by $r^{\bar{\nu}} = (0.2 \pm 1.6)\%/100\, GeV$. QCD predicts that $r^{\bar{\nu}} \approx 0$, while r^{ν} should be negative [Hin77]. To quote the reference, written in 1977: "...according to asymptotic freedom $\sigma^{\nu,\bar{\nu}}/E$ cannot vary by more than about 5% between 50 and 500 GeV unless there are more than four quarks or the W is unexpectedly light..." The value of r^{ν} is (9.9 ± 3.6)% between 50 and 500 GeV. It now known that the mass of the W is approximately 80 GeV and thus is not unexpectedly light. However, there are more than four quark flavors, and the Q^2 range of the data extends above the b-quark production threshold of $4.5^2 \approx 20\, GeV^2$ (see Figure E.12 or E.23).

5.3.3 Deviations in the Cross-Section Measurement

The cross-sections in Figure 5.19 display small deviations around the linear fit as a function of energy: a "wiggle" in the cross-section. There are several possible interpretations of this structure. One possible explanation is that the deviations are due to neutrino oscillations. This has been ruled out by experiment E701 [Sto85], which was performed specifically to search for any potential neutrino oscillations in the region of neutrino mass and mixing angle implied by the deviations in $\sigma^{\nu N}/E$.

Another interpretation are systematic errors in the present analysis. In particular, the shape of the deviations roughly corresponds to the deviations one would expect from an error in the E_μ calibration as shown in Figure 5.10. This hypothesis is consistent with the observation that the same muon spectrometer was used in Fermilab experiments E616, E701, E744, and E770, and that each of these experiments saw the same type of deviations. However, the naive approach of varying the E_μ calibration in an attempt to remove the deviations does not directly eliminate these effects.

FNAL experiment E815, the next generation of the experiment, will also use the same muon spectrometer. In addition to collecting neutrino data, a muon test beam will sweep the front face of the muon spectrometer to (a) calibrate the spectrometer more accurately than in the previous experiments, and (b) to test the hypothesis that variations in the E_μ calibration as a function of the position of the muon at the front face of the toroid might cause the deviations in $\sigma^{\nu N}/E$ versus E_ν.

In the present analysis, the deviations are treated as a separate systematic error in the structure-function extraction. The $\sigma^{\nu N}_{partonic}/E_\nu$ versus E_ν distributions are fit to a straight line; i.e., the functional form $A(1+B\,E_\nu)$. The flux is then "adjusted" so that the implied $\sigma^{\nu N}_{partonic}/E_\nu$ versus E_ν is a straight line:

$$\Phi^{adjusted}(E_\nu) = \Phi^{original}(E_\nu) \times \frac{A(1+B)E_\nu}{\sigma^{\nu N}_{partonic}(E_\nu)} \tag{5.19}$$

It is $\Phi^{adjusted}$ that is used to extract the structure functions as described in the next chapter. The structure functions are also extracted with $\Phi^{original}$, and the difference between the two structure functions is treated as the flux-adjustment systematic error. The adjustment factor $A(1+B)E_\nu \big/ \sigma^{\nu N}_{partonic}(E_\nu)$ is plotted in Figure 5.20.

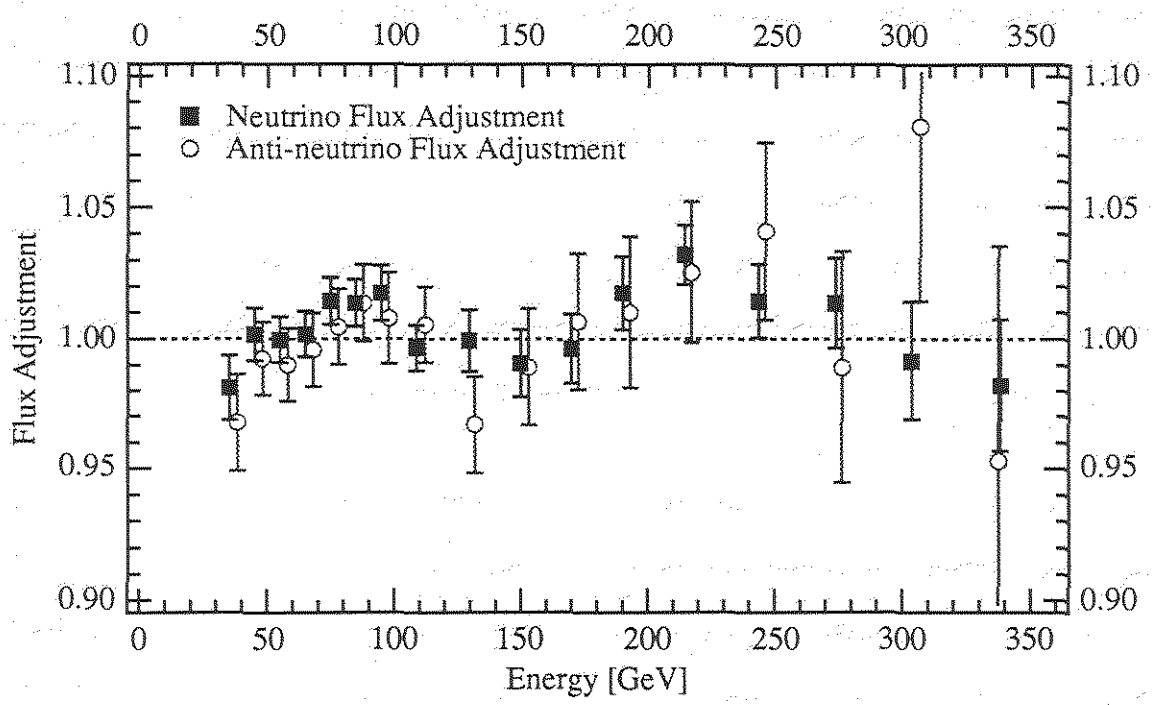

Figure 5.20: Flux adjustment factor $A(1+B)E_\nu \big/ \sigma^{\nu N}_{partonic}(E_\nu)$.

6 Structure Functions

The main goal of this analysis is to measure $F_2(x,Q^2)$ and $xF_3(x,Q^2)$ and correct them to the partonic level, which are most directly related to the bare quark distributions. This Chapter describes the method of extracting the structure functions, the actual implementation of the method, and the studies of the systematic uncertainties. The resultant tables of structure functions, statistical errors, point-to-point systematic errors, and the physics-model corrections are given in Appendix D.

6.1 Method of Structure-Function Extraction

The extraction method follows from the definition of a differential cross-section in terms of the cross-section. The number of events in any x and Q^2 bin is given by:

$$N^{\nu,\bar{\nu}}(x,Q^2) = \rho L N_A \int_{x-bin} dx \int_{Q^2-bin} dQ^2 \int_{all\,energies} dE \frac{d\sigma^{\nu,\bar{\nu}}}{dx\,dQ^2} \Phi^{\nu,\bar{\nu}}(E) \tag{6.1}$$

where $\rho L N_A$ is the number of scattering centers in the target. Since this constant will be absorbed into the normalization constant $k^{\nu,\bar{\nu}}_{\Phi,POL}$ (Equation 6.20), it will be omitted from later equations for simplicity. Note that the integration runs over the bin limits in x and Q^2, but over the entire available energy spectrum in the range of the flux. The differential cross-section can be replaced with the general expression in terms of the structure functions:

$$\frac{d^2\sigma^{\nu,\bar{\nu}}}{dx\,dQ^2} = \frac{G^2 M}{\pi} \frac{E}{2MEx}\left[\left(1 - y - \frac{Mxy}{2E}\right)F_2 + \frac{y^2}{2} 2xF_1 \pm y\left(1 - \frac{y}{2}\right)xF_3\right] \tag{6.2}$$

where the +(-) term corresponds to neutrinos(anti-neutrinos). (The factors in the first two fractions in Equation 6.2 have not been canceled because, within the analysis code, G^2M/π and $E\Phi$ are calculated separately.) The structure function $2xF_1$ is removed by using

$$2xF_1 = F_2 \frac{1+4M^2x^2/Q^2}{1+R} \tag{6.3}$$

where $R = \sigma_L/\sigma_T$, the ratio of the longitudinal to transverse cross-sections of the W-boson, is from a parameterization by Whitlow of the world's available data on the measurement of R [Whi90b]. This gives:

$$\begin{aligned} N^{\nu,\bar{\nu}}(x,Q^2) = {} & \frac{G^2M}{\pi}\int dx \int \frac{dQ^2}{2MEx}\int dE\, E\Phi^{\nu,\bar{\nu}}(E) \\ & \left[\left(1-y-\frac{Mxy}{2E}+\frac{y^2}{2}\frac{1+4M^2x^2/Q^2}{1+R(x,Q^2)}\right)F_2(x,Q^2) \pm y\left(1-\frac{y}{2}\right)xF_3(x,Q^2)\right] \end{aligned} \tag{6.4}$$

The x and Q^2 bins are small enough that the structure functions do not vary significantly within each bin, and so they may be brought outside the integral. For each x and Q^2 bin there is a system of two linear equations in two unknowns to be solved for the structure function values in that bin:

$$N^{\nu}(x,Q^2) = A^{\nu}\, F_2(x,Q^2) + B^{\nu}\, xF_3(x,Q^2) \tag{6.5}$$

$$N^{\bar{\nu}}(x,Q^2) = A^{\bar{\nu}}\, F_2(x,Q^2) - B^{\bar{\nu}}\, xF_3(x,Q^2) \tag{6.6}$$

where

$$A^{\nu,\bar{\nu}} = \frac{G^2M}{\pi}\iiint dx \frac{dQ^2}{2MEx} dE\, E\Phi^{\nu,\bar{\nu}}(E)\left(1-y-\frac{Mxy}{2E_\nu}+\frac{y^2}{2}\frac{1+4M^2x^2/Q^2}{1+R(x,Q^2)}\right) \tag{6.7}$$

$$B^{\nu,\bar{\nu}} = \frac{G^2 M}{\pi} \iiint dx \frac{dQ^2}{2MEx} dE\, E\Phi^{\nu,\bar{\nu}}(E) \left(y - \frac{y^2}{2} \right) \tag{6.8}$$

and $xF_3 = \left\langle xF_3^{\nu,\bar{\nu}} \right\rangle = \left(xF_3^{\nu} + xF_3^{\nu} \right) / 2$ (see Section 6.1.2). The solution of these equations is given by

$$\left.\begin{aligned} F_2(x,Q^2) &= \left(B^{\bar{\nu}} N^{\nu} + B^{\nu} N^{\bar{\nu}} \right) / \det \\ xF_3(x,Q^2) &= \left(A^{\bar{\nu}} N^{\nu} + A^{\nu} N^{\bar{\nu}} \right) / \det \\ \det &= A^{\nu} B^{\bar{\nu}} + B^{\nu} A^{\bar{\nu}} \end{aligned}\right\} \tag{6.9}$$

6.1.1 Error Calculation

Since the same event sums N^{ν} and $N^{\bar{\nu}}$ go into F_2 and xF_3, the two structure functions are correlated and there are three statistical errors: ΔF_2, ΔxF_3, and $\Delta F_2 \Delta xF_3$. The number of events that go into the calculation are corrected by the Monte Carlo as described in Section 4.1:

$$N_{corr}^{\nu,\bar{\nu}} = N_{meas}^{\nu,\bar{\nu}} \times \frac{MC_{GEN,nocuts}^{\nu,\bar{\nu}}(\text{with}\, 2\mu\sigma)}{MC_{SMR,SFcuts}^{\nu,\bar{\nu}}(\text{w/o}\, 2\mu\sigma)} \equiv N_{meas}^{\nu,\bar{\nu}} \times c_{MC}^{\nu,\bar{\nu}}(x,Q^2) \tag{6.10}$$

In calculating the statistical error on the structure functions, both the statistical error on the number of events and the statistical error in the Monte-Carlo correction must be considered. The error on the number of events $N_{meas}^{\nu,\bar{\nu}}$ is simple:

$$\left(\Delta N_{meas}^{\nu,\bar{\nu}} \right)^2 = N_{meas}^{\nu,\bar{\nu}} \tag{6.11}$$

However, the error on the Monte-Carlo correction has several components. Within a given (x,Q^2) bin the Monte Carlo events are being re-weighted and smeared; some

events leave the bin, others remain in the bin, and yet others enter the bin from other (x,Q^2) bins.

In order to calculate the statistical error on the Monte-Carlo correction $\Delta c_{MC}^{\nu,\bar{\nu}}(x,Q^2)$, the corrections were separately extracted for ten independent sets of Monte Carlo events. Each set of events was independently generated and smeared using a different random number seed. The statistical error was then taken to be the standard deviation of the resulting values of $c_{MC}^{\nu,\bar{\nu}}(x,Q^2)$.

The statistical errors ΔF_2, ΔxF_3, and $\Delta F_2 \Delta xF_3$ must then be calculated from Equations 6.9, 6.10, and the following:

$$\left(\Delta F_2\right)^2 = \sum_{i=\nu,\bar{\nu}} \left[\left(\frac{\partial F_2}{\partial N_{meas}^i} \right)^2 \left(\Delta N_{meas}^i \right)^2 + \left(\frac{\partial F_2}{\partial c_{MC}^i} \right)^2 \left(\Delta c_{MC}^i \right)^2 \right] \tag{6.12}$$

$$\left(\Delta xF_3\right)^2 = \sum_{i=\nu,\bar{\nu}} \left[\left(\frac{\partial xF_3}{\partial N_{meas}^i} \right)^2 \left(\Delta N_{meas}^i \right)^2 + \left(\frac{\partial xF_3}{\partial c_{MC}^i} \right)^2 \left(\Delta c_{MC}^i \right)^2 \right] \tag{6.13}$$

$$\Delta F_2 \Delta xF_3 = \sum_{i=\nu,\bar{\nu}} \left[\left(\frac{\partial F_2}{\partial N_{meas}^i} \right) \left(\frac{\partial xF_3}{\partial N_{meas}^i} \right) \left(\Delta N_{meas}^i \right)^2 + \left(\frac{\partial F_2}{\partial c_{MC}^i} \right) \left(\frac{\partial xF_3}{\partial c_{MC}^i} \right) \left(\Delta c_{MC}^i \right)^2 \right] \tag{6.14}$$

For simplicity, additional indices to represent the separate corrections required for focusing and defocusing events have been omitted from the above equations. The resulting expressions for the statistical errors are lengthy but straight-forward to calculate, and are incorporated into the structure-function extraction calculation.

6.1.2 Strange Sea Correction

In the leading-order parton model described in section 4.2, after the isoscalar corrections $F_2^{\nu} = F_2^{\bar{\nu}}$ but $xF_3^{\nu} \neq xF_3^{\bar{\nu}}$; that is, $xF_3^{\nu} - xF_3^{\bar{\nu}} = x(s-c)$, the difference between the strange- and charm-quark momentum sea densities in the proton. In the procedure derived from Equations 6.5-6.6, we extract $\langle xF_3 \rangle = \left(xF_3^{\nu} + xF_3^{\bar{\nu}}\right)/2 = x\left(u_v + d_v\right)$; that is, the effective xF_3 for both neutrinos and anti-neutrinos is the sum of the valence up- and down-quark momentum distributions in the proton. In order for the physics-model corrections to apply to this procedure, there must be an additional correction applied to the formula in Equation 4.13:

$$corr^{strange-sea} = \frac{\sigma\left(xF_3^{\nu} = xF_3^{\bar{\nu}} = \langle xF_3 \rangle\right)}{\sigma\left(xF_3^{\nu} - xF_3^{\bar{\nu}} = x(s-c)\right)} \tag{6.15}$$

The physics model of section 4.2 assumes the charm quark distribution is zero [Mis89]. The strange sea is measured in studies of dimuon production in neutrino interactions; in this analysis the leading-order result from the E744 and E770 data is used [Rab92].† The measurements find the level of the strange sea to be about 1/3rd that of the non-strange sea, and the x-distribution to be more sharply peaked. These differences are parameterized by κ and α defined by:

$$\int xs\,dx = \int x\bar{s}\,dx = \kappa \int \left(x\bar{u} + x\bar{d}\right)/2\,dx \tag{6.16}$$

$$xs = x\bar{s} \propto \frac{\left(x\bar{u} + x\bar{d}\right)}{2}(1-x)^{\alpha} \tag{6.17}$$

---

† The next-to-leading-order result of [Baz95] is not appropriate for the leading-order physics model.

with $\kappa = 0.373$ and $\alpha = 2.50$.

6.1.3 Large-x Events and the Monte Carlo

In the physics model described in section 4.2, the parton distributions used to generate the Monte Carlo approach zero as $x \to 1$. After the Monte-Carlo and physics-model corrections are applied to the data, the corrected data distributions are therefore forced to go to zero as $x \to 1$. Thus, with this model, a structure function measurement for $x \sim 1$ cannot be made.

On the other hand, the structure functions in iron should *not* vanish at $x = 1$. Effects such as Fermi motion give a non-zero contribution for $x > 1$. Studies of Fermi motion indicate that the corrections to the structure-functions are less than 5% for $x < 0.55$, about 20% at $x = 0.65$, and about 40% at $x = 0.75$ [Bod81]. No Fermi-motion corrections have been made in this structure-function extraction since, at the values of x for which they would be important, the statistical errors, systematic errors, and smearing corrections are so large that this large-x data would be excluded from this analysis by the standard analytic cuts.

A separate issue at large (and small) x is the amount of smearing between x-bins. The x-distributions are steeply falling at high x. This implies that the events from lower x-bins smear into higher ones leading to large smearing corrections. This issue is addressed by the histograms in Figures 6.1 through 6.5. These plots show the distribution of x-reconstructed, x_{REC}, in bins of x-generated, x_{GEN}, from the Monte Carlo. These distributions show that in the x-bins chosen for this analysis, enough reconstructed events remain in the bin in which they were generated for the measurement of the structure functions to be meaningful.

It is interesting to note that roughly twice as many uncorrected data events with $x > 1$ are observed in the data as are generated by our Monte Carlo after resolution-smearing effects have been applied. Others in the collaboration are studying the possibility of whether this is due to radiative corrections or Fermi-motion corrections for these events.

6.1.4 Alternate Extraction Methods

There are other methods of extracting F_2 and xF_3, and the collaboration is presently exploring such methods. One alternative is to go back to the expression for the differential cross-section:

$$\frac{d^2\sigma^{\nu,\bar{\nu}}}{dxdy} = \frac{G^2ME}{\pi}\left[\left(1-y-\frac{Mxy}{2E}\right)F_2 + \frac{y^2}{2}2xF_1 \pm y\left(1-\frac{y}{2}\right)xF_3\right] \tag{6.10}$$

If one extracted the cross-sections $d^2\sigma/dxdy$, the structure functions could be determined by fitting to the y-distribution of the cross-sections within each (x,Q^2) bin. In a related analysis, Un-Ki Yang is using a similar technique to determine R from the E744 and E770 neutrino data.

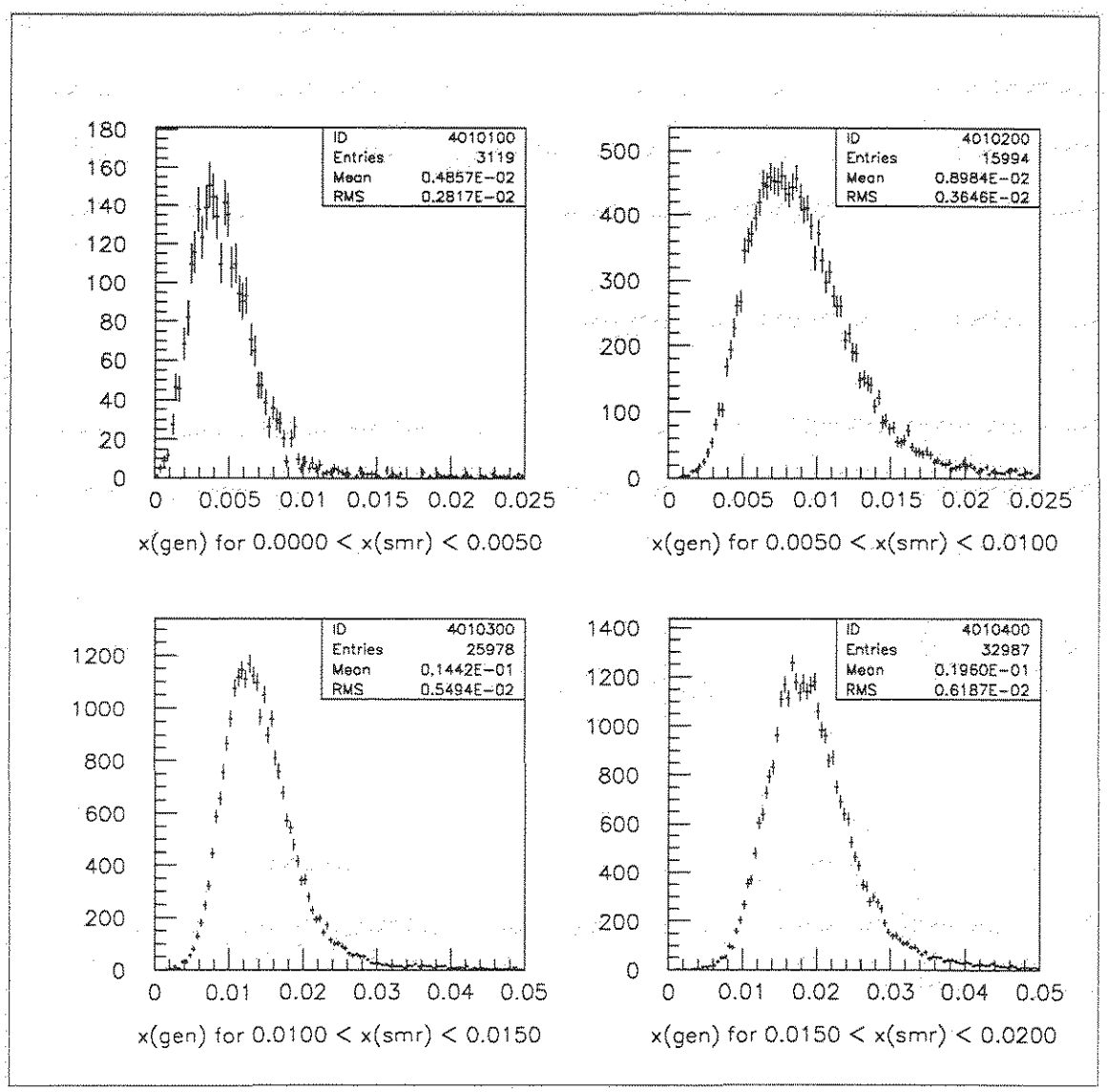

Figure 6.1: x_{GEN} for $0 < x_{SMR} < 0.02$. These plots show that for:

$.000 < x_{observed} < 0.005$, 54% of the events are generated within the bin;

$.005 < x_{observed} < 0.010$, 51% of the events are generated within the bin;

$.010 < x_{observed} < 0.015$, 41% of the events are generated within the bin;

$.015 < x_{observed} < 0.020$, 34% of the events are generated within the bin.

The first bin in this figure is not included in the structure-function analysis due to poor statistics and large systematic errors.

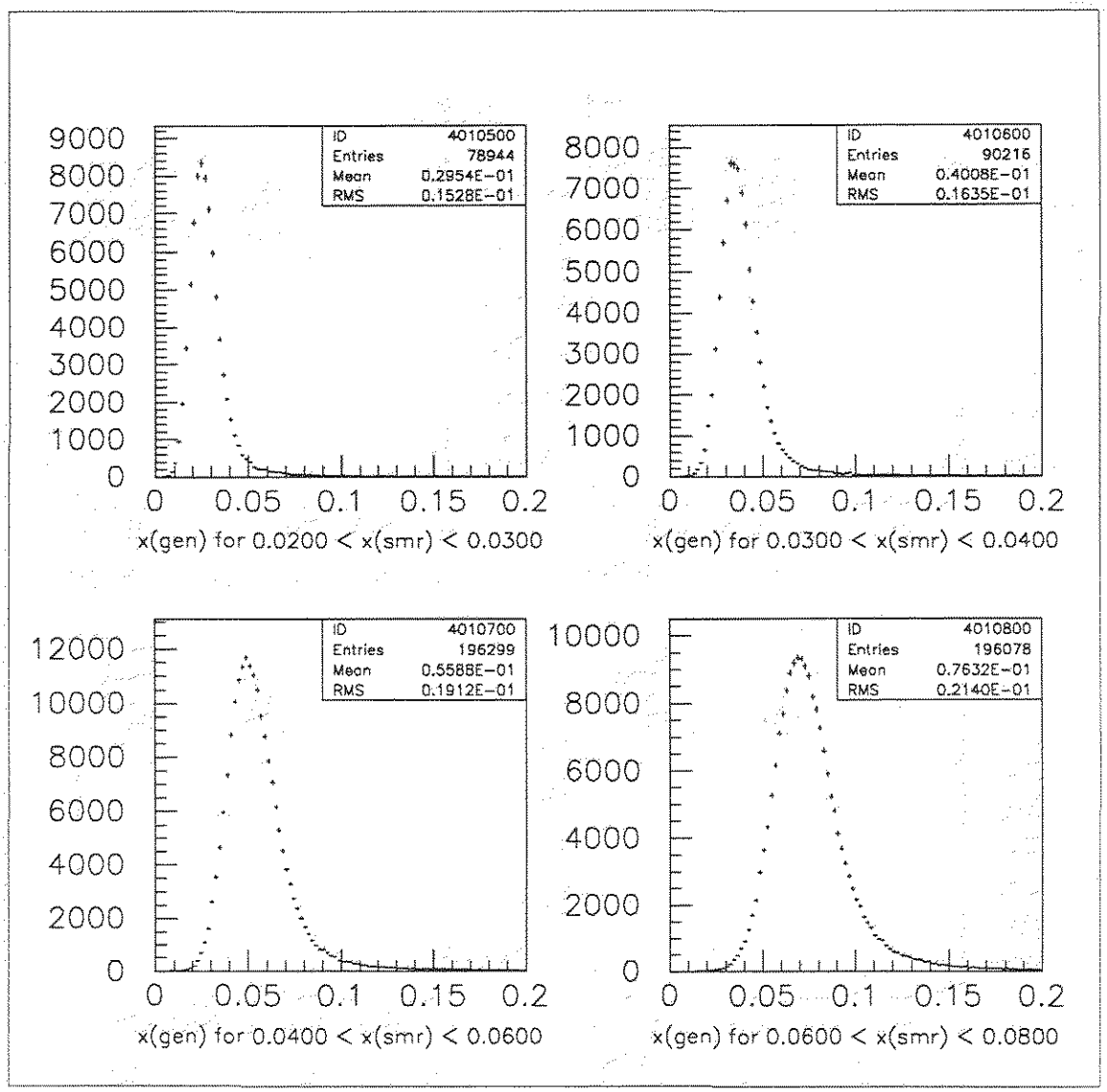

Figure 6.2: x_{GEN} for $0.02 < x_{SMR} < 0.08$. These plots show that for:

$.02 < x_{observed} < 0.03$, 48% of the events are generated within the bin;

$.03 < x_{observed} < 0.04$, 40% of the events are generated within the bin;

$.04 < x_{observed} < 0.06$, 54% of the events are generated within the bin;

$.06 < x_{observed} < 0.08$, 45% of the events are generated within the bin.

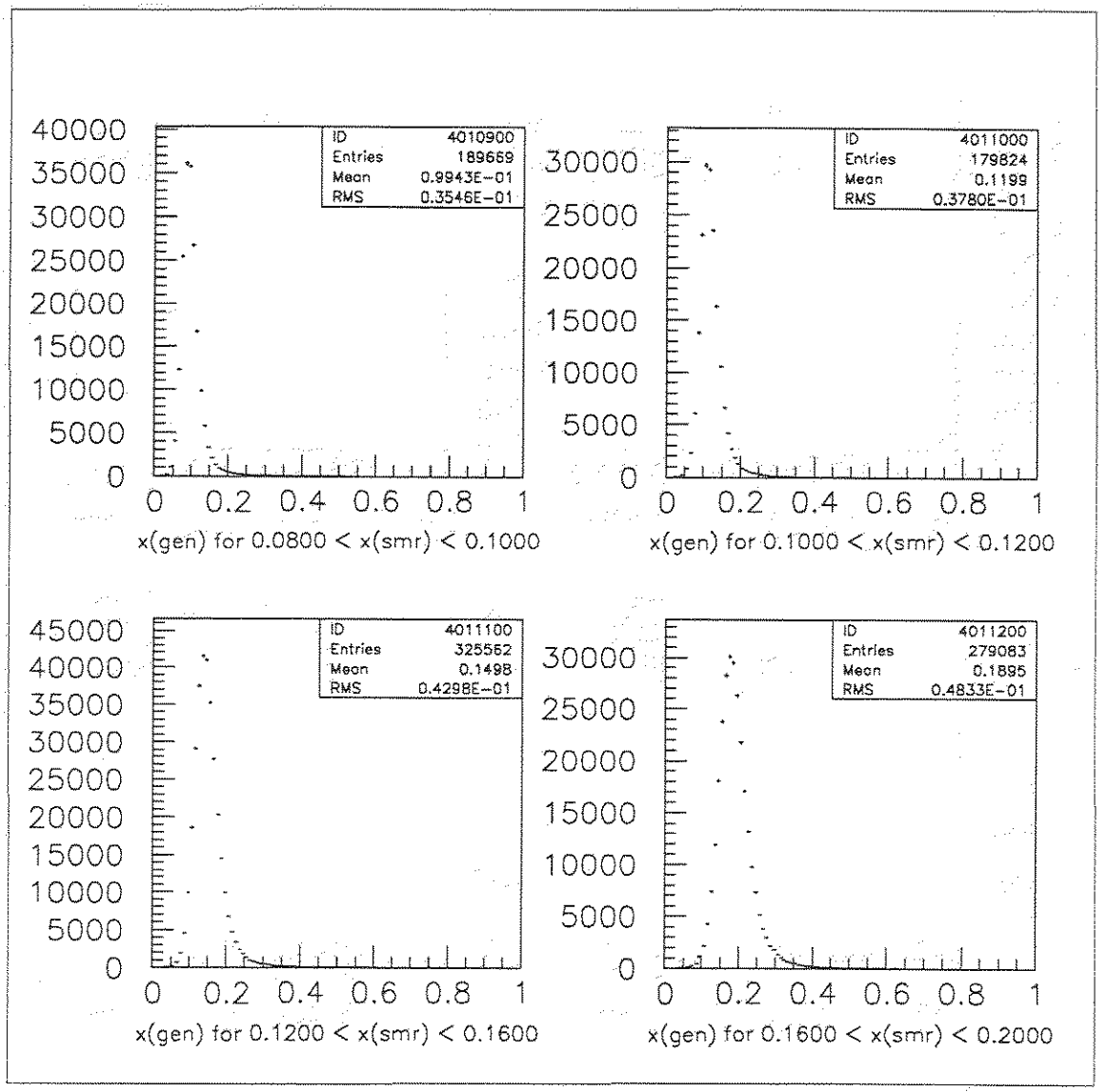

Figure 6.3: x_{GEN} for $0.08 < x_{SMR} < 0.20$. These plots show that for:

$.08 < x_{observed} < 0.10$, 38% of the events are generated within the bin;

$.10 < x_{observed} < 0.12$, 30% of the events are generated within the bin;

$.12 < x_{observed} < 0.16$, 48% of the events are generated within the bin;

$.16 < x_{observed} < 0.20$, 41% of the events are generated within the bin.

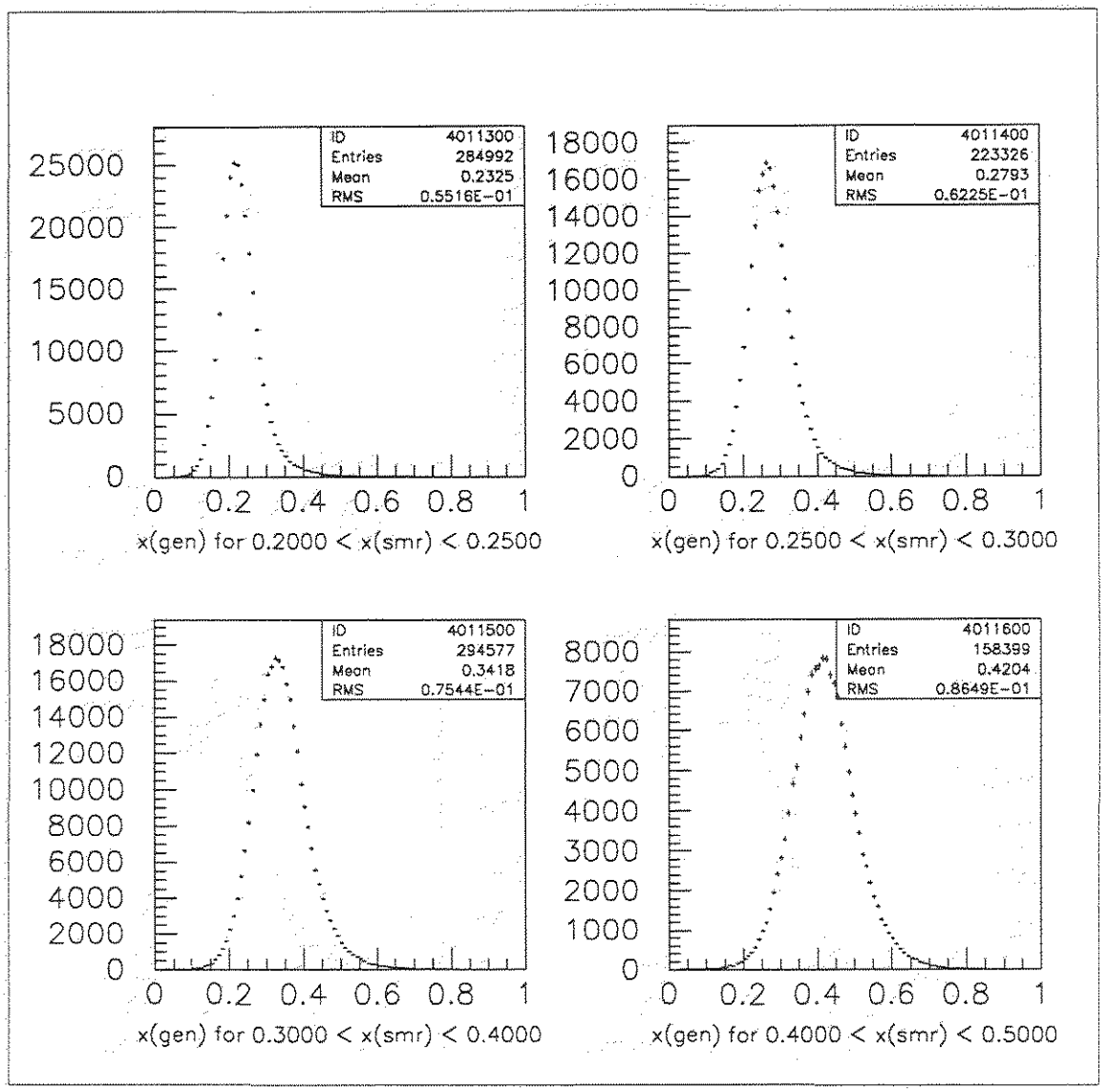

Figure 6.4: x_{GEN} for $0.20 < x_{SMR} < 0.50$. These plots show that for:

$.20 < x_{observed} < 0.25$, 42% of the events are generated within the bin;

$.25 < x_{observed} < 0.30$, 36% of the events are generated within the bin;

$.30 < x_{observed} < 0.40$, 52% of the events are generated within the bin;

$.40 < x_{observed} < 0.50$, 42% of the events are generated within the bin.

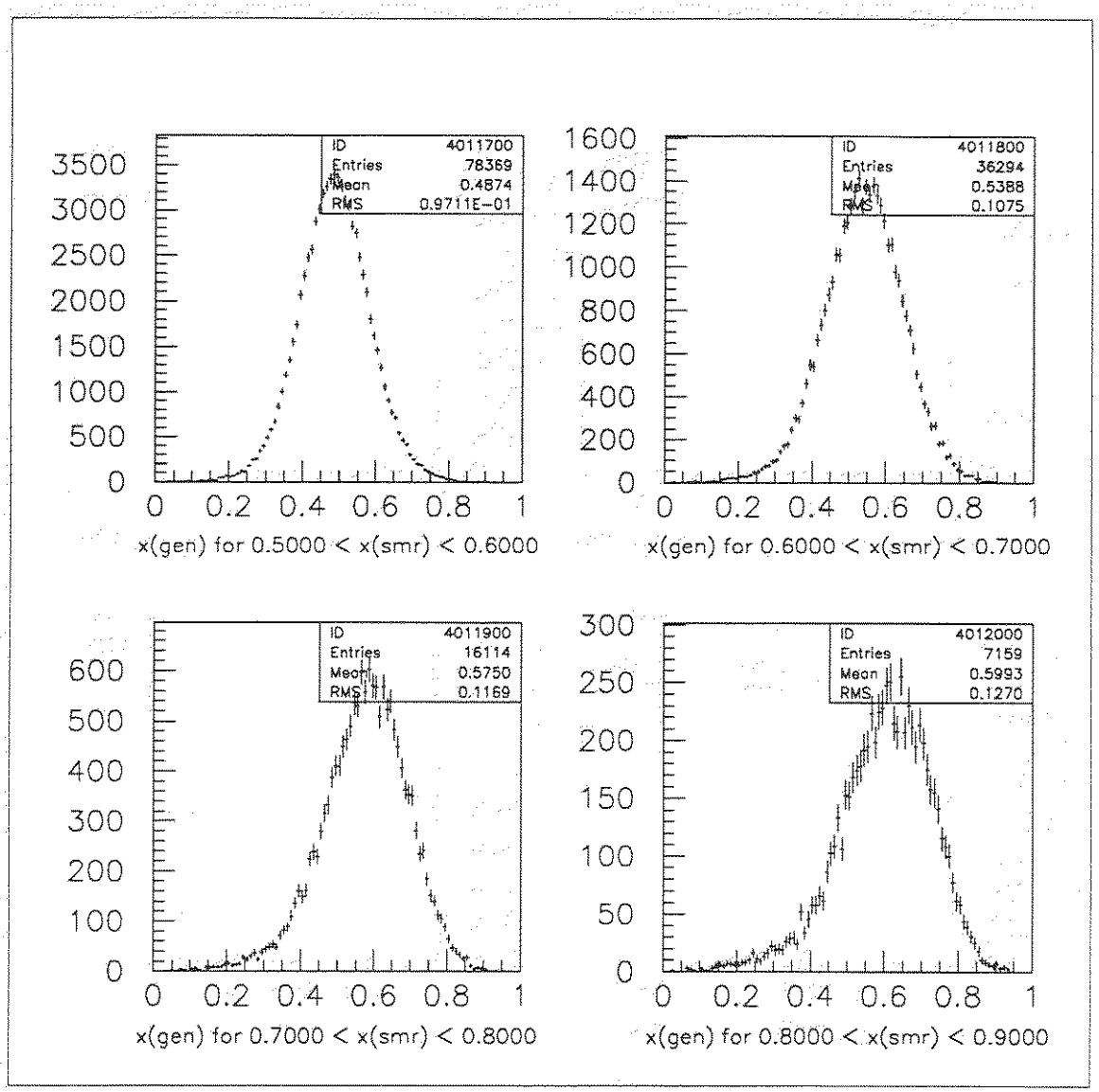

Figure 6.5: x_{GEN} for $0.5 < x_{SMR} < 0.9$. These plots show that for:

$.5 < x_{observed} < 0.6$, 32% of the events are generated within the bin;

$.6 < x_{observed} < 0.7$, 22% of the events are generated within the bin;

$.7 < x_{observed} < 0.8$, 12% of the events are generated within the bin;

$.8 < x_{observed} < 0.9$, 3% of the events are generated within the bin.

Due to the large amount of smearing for $x > 0.8$, these data are not included in the structure-function analysis. The structure functions for $0.7 < x < 0.8$ are reported in this thesis, but they are not included in the QCD fits of Chapter 7.

Another method is to multiply both sides of Equation 6.10 by the flux, integrate over the (x,Q^2) bin and over all energies, and to consider neutrinos and anti-neutrinos separately:

$$N^{\nu}(x,Q^2) \propto \iiint dx \frac{dQ^2}{2MEx} E\Phi^{\nu}(E)dE \left[\begin{array}{r} \left(1-y-\frac{Mxy}{2E}\right)F_2 + \frac{y^2}{2}2\,xF_1 \\ +y\left(1-\frac{y}{2}\right)xF_3^{\nu} \end{array} \right] \tag{6.11}$$

$$N^{\bar{\nu}}(x,Q^2) \propto \iiint dx \frac{dQ^2}{2MEx} EdE\Phi^{\bar{\nu}}(E) \left[\begin{array}{r} \left(1-y-\frac{Mxy}{2E}\right)F_2 + \frac{y^2}{2}2\,xF_1 \\ -y\left(1-\frac{y}{2}\right)xF_3^{\bar{\nu}} \end{array} \right] \tag{6.12}$$

Since $F_2^{\nu} = F_2^{\bar{\nu}}$ and $2xF_1^{\nu} = 2xF_1^{\bar{\nu}}$, only the difference between xF_3^{ν} and $xF_3^{\bar{\nu}}$ need be considered. By doing fits to the y-distributions within the (x,Q^2) bin, the values of F_2, $2xF_1$, xF_3^{ν}, and $xF_3^{\bar{\nu}}$ can be determined. From the relation in Equation 6.3 R can be determined; from the difference between xF_3^{ν} and $xF_3^{\bar{\nu}}$, one can determine s-c, the difference between the strange and charm quark distributions. Cindy McNulty is working on this analysis.

6.2 Implementing the Method

This section describes the implementation the structure-function calculation described above. The program code used to perform the calculation is in Appendix B.

6.2.1 Structure-Function Cuts

The data events are binned in 16 Q^2 bins and 18 x bins. The bins cover the entire x range from 0 to 1, and the Q^2 range from 1 to 600 GeV. In addition to fiducial volume and acceptance cuts discussed in chapter 3, the following cuts are applied:

- $30GeV < E_\nu < 360GeV$ — The lower limit of 30 GeV was selected because the lower energy bins in the flux analysis have a large systematic error. The upper limit of 360 GeV was picked because above that energy the error on the Monte-Carlo smearing corrections becomes large; also, the number of anti-neutrino events above 360 GeV is small and hence a coupled analysis with neutrino data cannot be made.

- $\theta_\mu < 150mr$ — This cut assures good acceptance of the muon track as it passes through the muon spectrometer.

- $E_{HAD} > 10GeV$ — This lower limit on E_{HAD} was picked to minimize the correlations between the flux and structure-function data sample (see Chapter 5).

- $E_\mu > 15GeV$ — 15 GeV is the lower limit of acceptance of the muon spectrometer.

- $Q^2 > 1GeV^2$ — This eliminates the quasi-elastic events from the data sample, which are not modeled in our Monte Carlo. An analysis is being prepared by the collaboration to determine the structure functions for $Q^2 < 1GeV^2$.

6.2.2 Structure-Function Calculation

As in the flux extraction, events and corrections must be binned in separate categories: the two experiments E744 and E770, neutrinos and anti-neutrinos, and the muon

Table 6.1: Number of events passing structure-function cuts.

	E744				E770			
Neutrino Type	ν	ν	$\bar{\nu}$	$\bar{\nu}$	ν	ν	$\bar{\nu}$	$\bar{\nu}$
Toroid Pol	Foc μ^-	Foc μ^+	Foc μ^-	Foc μ^+	Foc μ^-	Foc μ^+	Foc μ^-	Foc μ^+
Raw Events	700579	682503	97111	101451	798445	845644	116657	133188
Fid. Volume	442935	508164	59459	73880	592267	625309	88821	99825
Geometric	282796	284111	48150	64182	377318	345351	71986	86957
$\theta_\mu < 150 mr$	280262	283833	48134	64018	373955	345062	71961	86735
$E_\mu > 15 GeV$	276420	283205	48002	63077	368889	344366	71807	85383
$E_{HAD} > 10$	227607	230696	32766	43444	305657	282161	48421	58285
$Q^2 > 1\, GeV^2$	219772	222444	30624	40751	295495	272179	45177	54607
$30 < E < 360$	207630	209050	30226	40276	278552	255330	44637	53975

spectrometer set to focusing positively- or negatively-charged muons. This gives a total of eight categories (two experiments × two neutrino species × two spectrometer settings.) The number of events passing each of these cuts in each category is given in Table 6.1.

A total of 950562 neutrino and 169114 anti-neutrino events pass the structure-function cuts. The structure functions are determined separately for E744 and E770 as follows. For each (x, Q^2) bin, Equations 6.5 and 6.6 are implemented by:

$$\left(DA^{\nu,\bar{\nu}}_{ACC,FOC} \times allcorr^{\nu,\bar{\nu}}_{FOC} + DA^{\nu,\bar{\nu}}_{ACC,DEF} \times allcorr^{\nu,\bar{\nu}}_{DEF}\right)_{x,Q^2} = A^{\nu,\bar{\nu}} F_2(x,Q^2) \pm B^{\nu,\bar{\nu}} x F_3(x,Q^2) \tag{6.18}$$

where $DA^{\nu,\bar{\nu}}_{ACC,FOC}$ ($DA^{\nu,\bar{\nu}}_{ACC,DEF}$) are the *uncorrected* number of data events that pass all cuts for the spectrometer set to focus (defocus) negatively-charged muons, $A^{\nu,\bar{\nu}}$ and $B^{\nu,\bar{\nu}}$ are defined in Equations 6.7 and 6.8 above, and *allcorr* is the total correction that must be applied to the data events within each category, and for each (x,Q^2) bin. It is defined by

$$allcorr^{\nu,\bar{\nu}}_{POL}(x,Q^2) = \frac{corr^{\nu,\bar{\nu}}_{overall,POL}(x,Q^2)}{k^{\nu,\bar{\nu}}_{\Phi,POL}} \tag{6.19}$$

for $POL = FOC, DEF$ (that is, *allcorr* is calculated separately for toroid focusing (defocusing) negatively-charged muons), and for neutrinos and anti-neutrinos. $k^{\nu,\bar{\nu}}_{\Phi,POL}$ is the normalization between the flux extracted by the fixed-ν method and $\sigma^{\nu,\bar{\nu}}_{world}$, the world average ν-Fe isoscalar-corrected cross-section (as noted in Section 5.3, the fixed-ν method cannot determine the absolute normalization of the flux). $k^{\nu,\bar{\nu}}_{\Phi,POL}$ also absorbs ρLN_A from Equation 6.1 and is calculated from the following relation:

$$DA^{\nu,\bar{\nu}}_{cuts,POL} \times \frac{MC^{\nu,\bar{\nu}}_{GEN,POL}}{MC^{\nu,\bar{\nu}}_{SMR,cuts,POL}}$$

$$= \underbrace{k^{\nu,\bar{\nu}}_{\Phi,POL} \frac{\sigma^{\nu,\bar{\nu}}_{world}}{E} \int_{30}^{200} dE\, E\Phi^{\nu,\bar{\nu}}(E)}_{Factor\ 1} \times \underbrace{\frac{\left(\int dE \frac{\sigma^{\nu,\bar{\nu}}_{model,Fe}}{E} E\Phi^{\nu,\bar{\nu}} \Big/ \int dE\, E\Phi^{\nu,\bar{\nu}} \right)}{\left(\int dE \frac{\sigma^{\nu,\bar{\nu}}_{model,iso}}{E} \Big/ \int dE \right)}}_{Factor\ 2} \tag{6.20}$$

The left-hand side of Equation 6.20 computes the number of data events seen in the analysis and applies the Monte-Carlo correction, where "cuts" refers to the cross-section analysis cuts described in Section 3.3.3. Factor 1 of the right-hand side computes the number of events predicted in this experiment from the world-average isoscalar cross-

section. Factor 2 computes the correction from the number of events predicted for an isoscalar target to the number of events predicted for an Fe target, where the physics model used is the one described in Section 4.2. Note that the denominator of Factor 2 computes the energy-weighted average of the isoscalar cross-section predicted by the model which corresponds to the world-average cross-section in Factor 1, but the numerator of Factor 2 computes the flux×energy-weighted average of the model's Fe cross-section which corresponds to the quantity on the left-hand side of the equation. All energy integrals in Equation 6.20 are computed over the range 30-200 GeV, because the world-average cross-section was determined for that energy range.

Returning to the definition of $allcorr$ in Equation 6.19, the term $corr_{overall}$ is the bin-by-bin acceptance, smearing, model, and bin-center corrections applied to the data. It is calculated by

$$corr^{\nu,\bar{\nu}}_{overall,POL}(x,Q^2) = \frac{n^{\nu,\bar{\nu}}_{bin-center}(\text{with}\,2\mu)}{MC^{\nu,\bar{\nu}}_{SMR,SF-cuts,POL}(\text{no}\,2\mu)} \tag{6.21}$$

where $SF\text{-}cuts$ refers to the structure-function analysis cuts described above, and $n^{\nu,\bar{\nu}}_{bin-center}$ is the number of events predicted by the Monte Carlo, corrected for the physic-model corrections and the bin-center correction described in chapter 4, and the strange-sea correction described in section 6.1.2. Instead of applying an overall bin correction to determine $n^{\nu,\bar{\nu}}_{bin-center}$, as implied by Equation 4.1, $n^{\nu,\bar{\nu}}_{bin-center}$ is determined by re-weighting the Monte Carlo:

$$n^{\nu,\bar{\nu}}_{bin-center} = \sum_{\substack{Gen\,MC\,events \\ in(x,Q^2)bin}} \frac{\sigma^{\nu,\bar{\nu}}_{bare}(x_{BC},y_{BC},E_{gen})}{\sigma^{\nu,\bar{\nu}}_{phys}(x_{gen},y_{gen},E_{gen})} \tag{6.22}$$

where $\sigma_{bare}^{\nu,\bar{\nu}}$ is computed assuming an isoscalar target of bare quarks with no radiative, charm-mass, or W-boson propagator effects, and with $xF_3 = \left\langle xF_3^{\nu,\bar{\nu}} \right\rangle$. This method of calculating the physics-model corrections is more robust than the correction of Equation 4.1, since it properly averages the correction given the underlying kinematic distribution within the (x, Q^2) bin.

Figure 6.6 displays $corr_{overall}$ for neutrino events; Figure 6.7 displays $corr_{overall}$ for anti-neutrino events. The subsequent figures display some of the individual correction factors that are part of $corr_{overall}$: Figures 6.8-6.9 display the acceptance correction; Figures 6.10-6.11 display the smearing correction; Figure 6.12-6.13 display the physics-model correction; Figures 6.14-6.15 display the bin-center correction. As can be seen in the plots, the largest component of $corr_{overall}$ comes from the acceptance correction, which is the correction from applying the structure-function cuts to the reconstructed events.

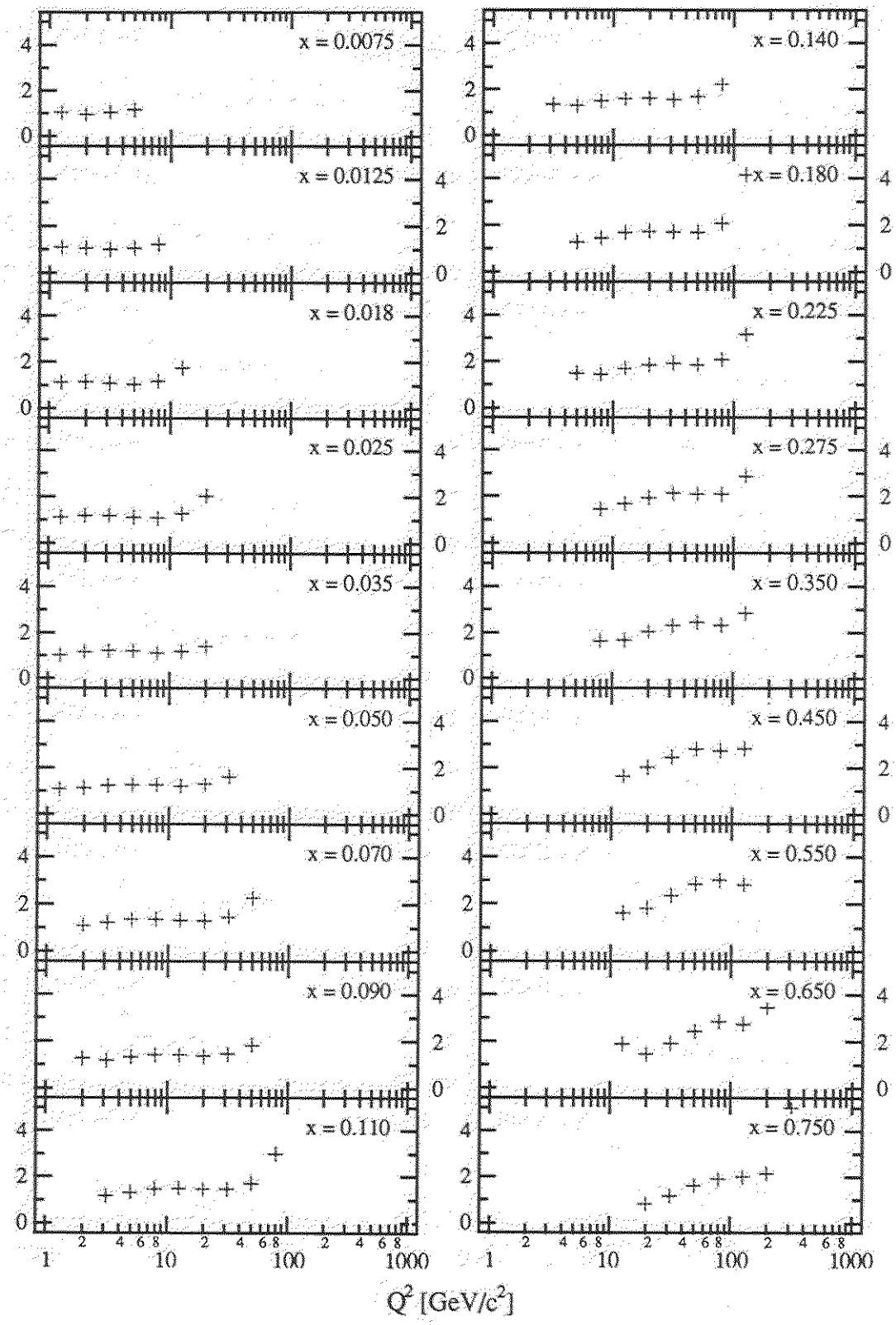

Figure 6.6: The total corrections applied to neutrino events in the structure-function analysis.

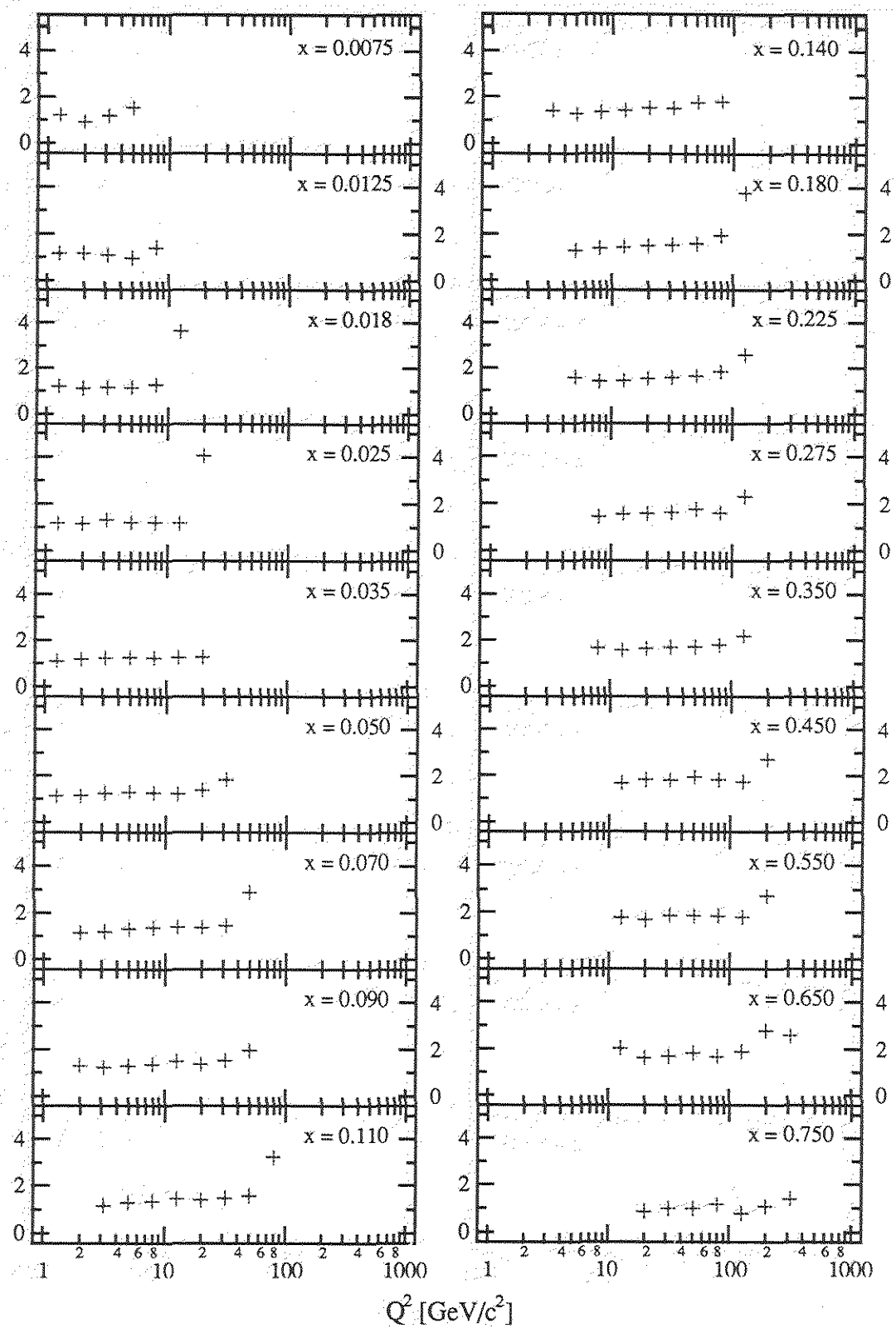

Figure 6.7: The total corrections applied to anti-neutrino events in the structure-function analysis.

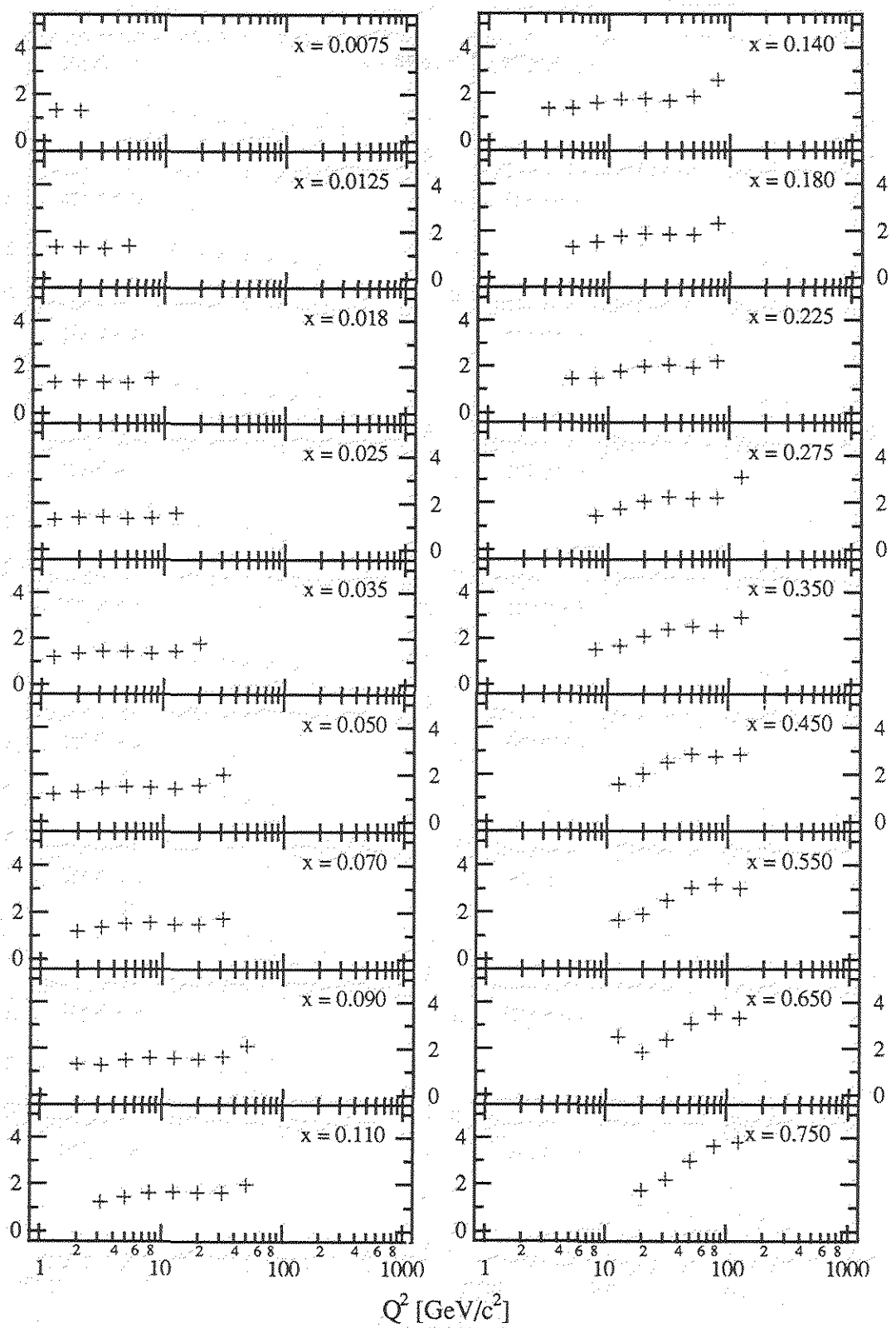

Figure 6.8: The acceptance corrections for neutrino events in the structure-function analysis.

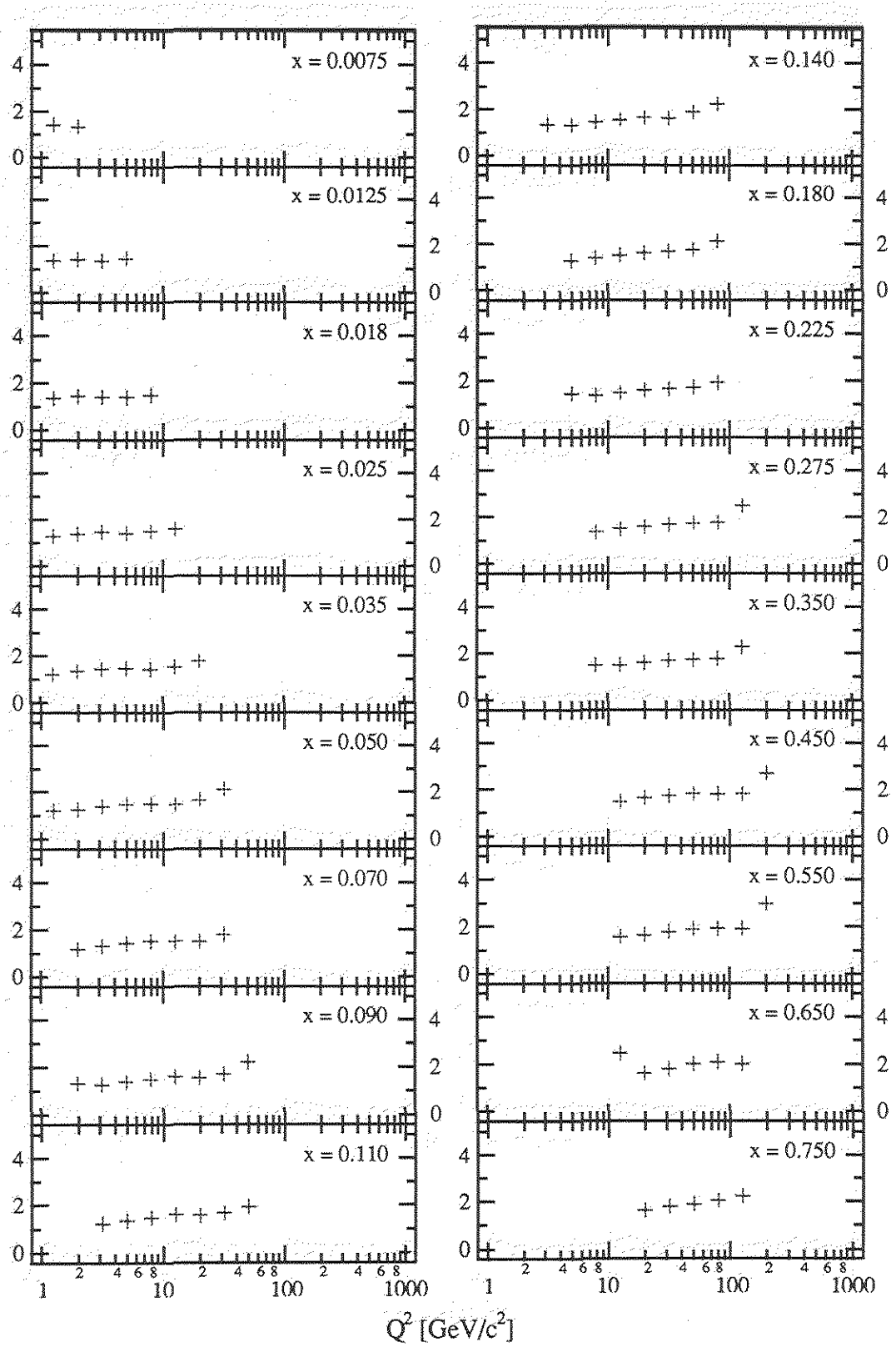

Figure 6.9: The acceptance corrections for anti-neutrino events in the structure-function analysis.

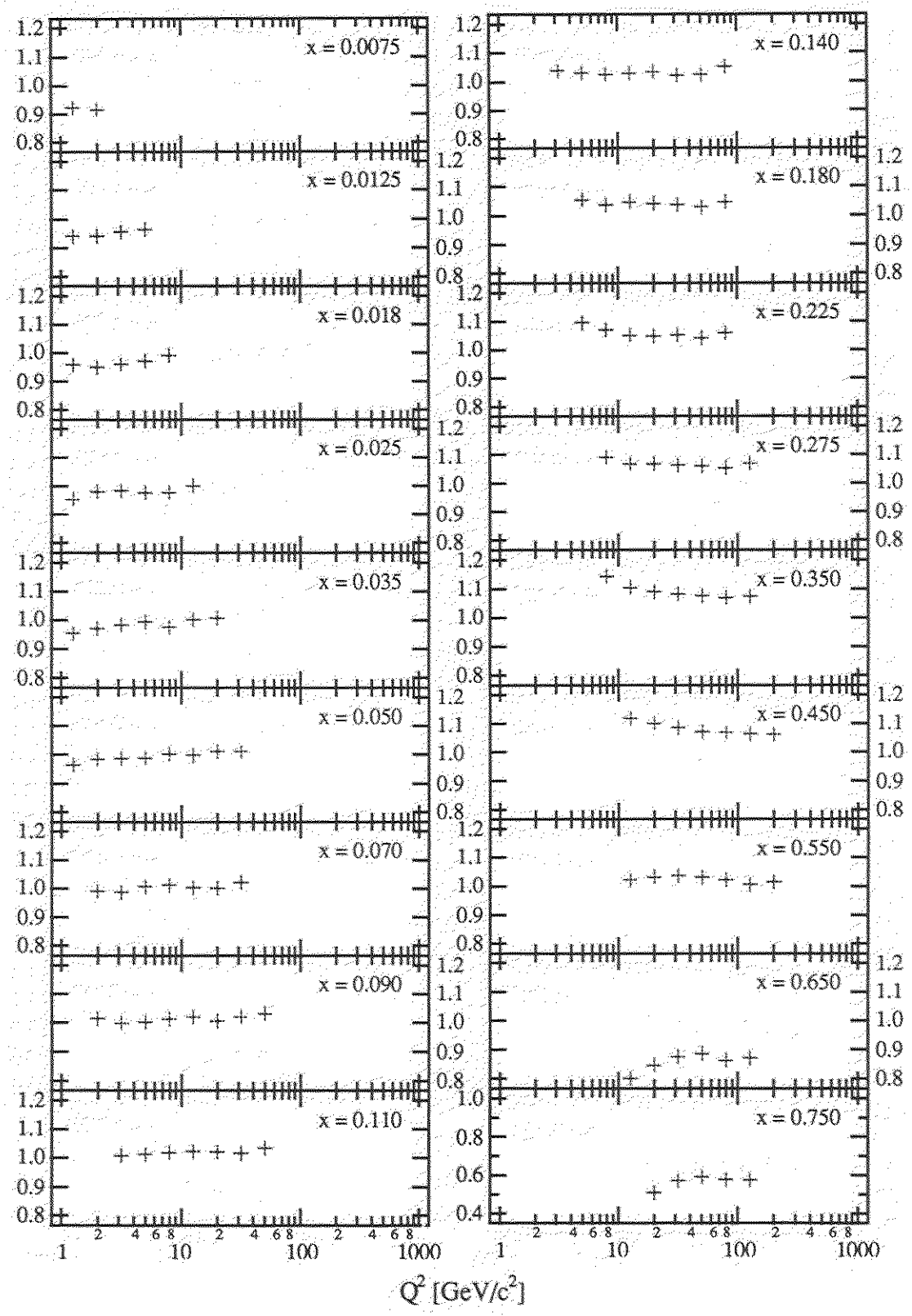

Figure 6.10: The smearing corrections for neutrino events in the structure-function analysis.

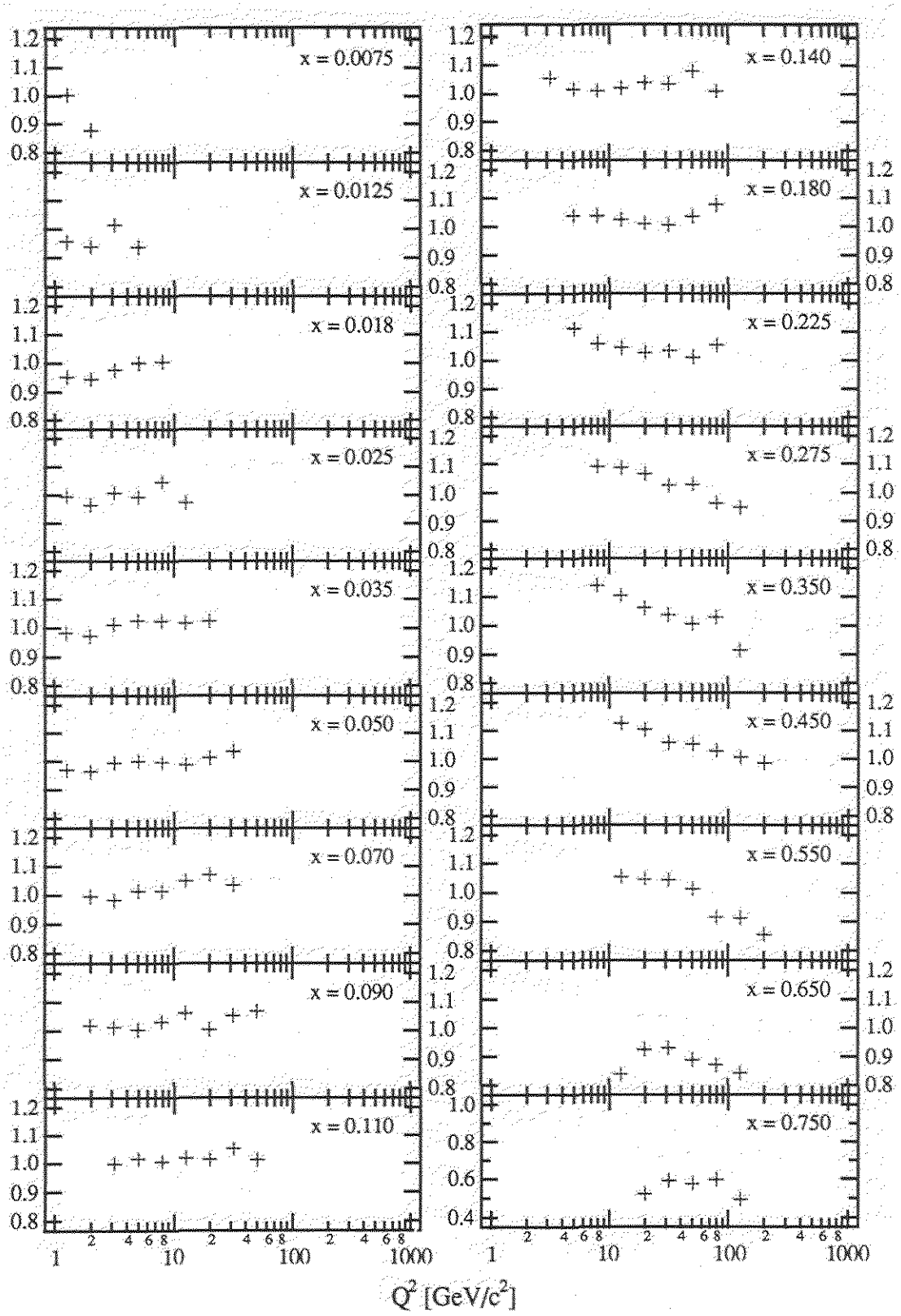

Figure 6.11: The smearing corrections for anti-neutrino events in the structure-function analysis.

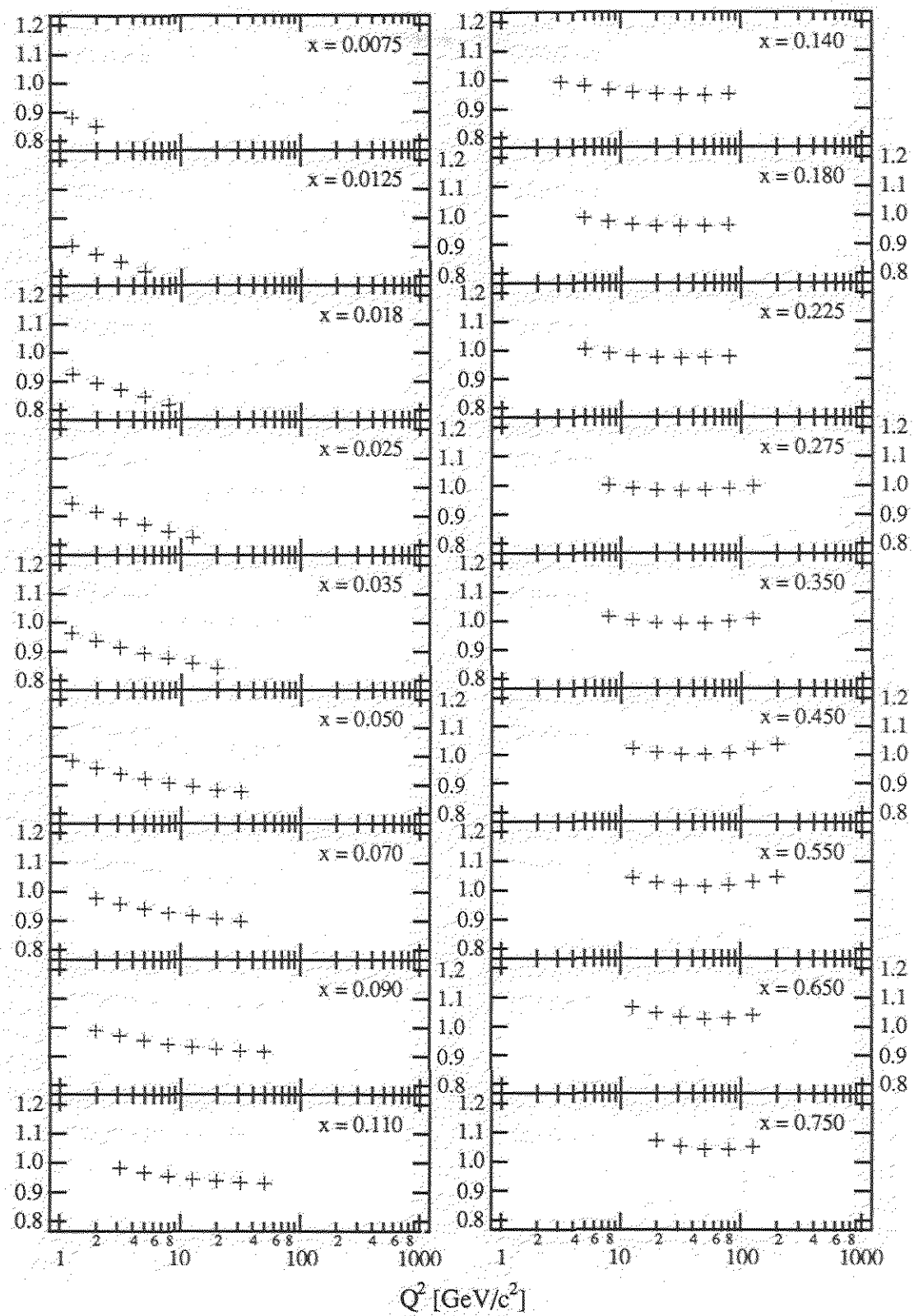

Figure 6.12: The physics-model corrections for neutrino events in the structure-function analysis.

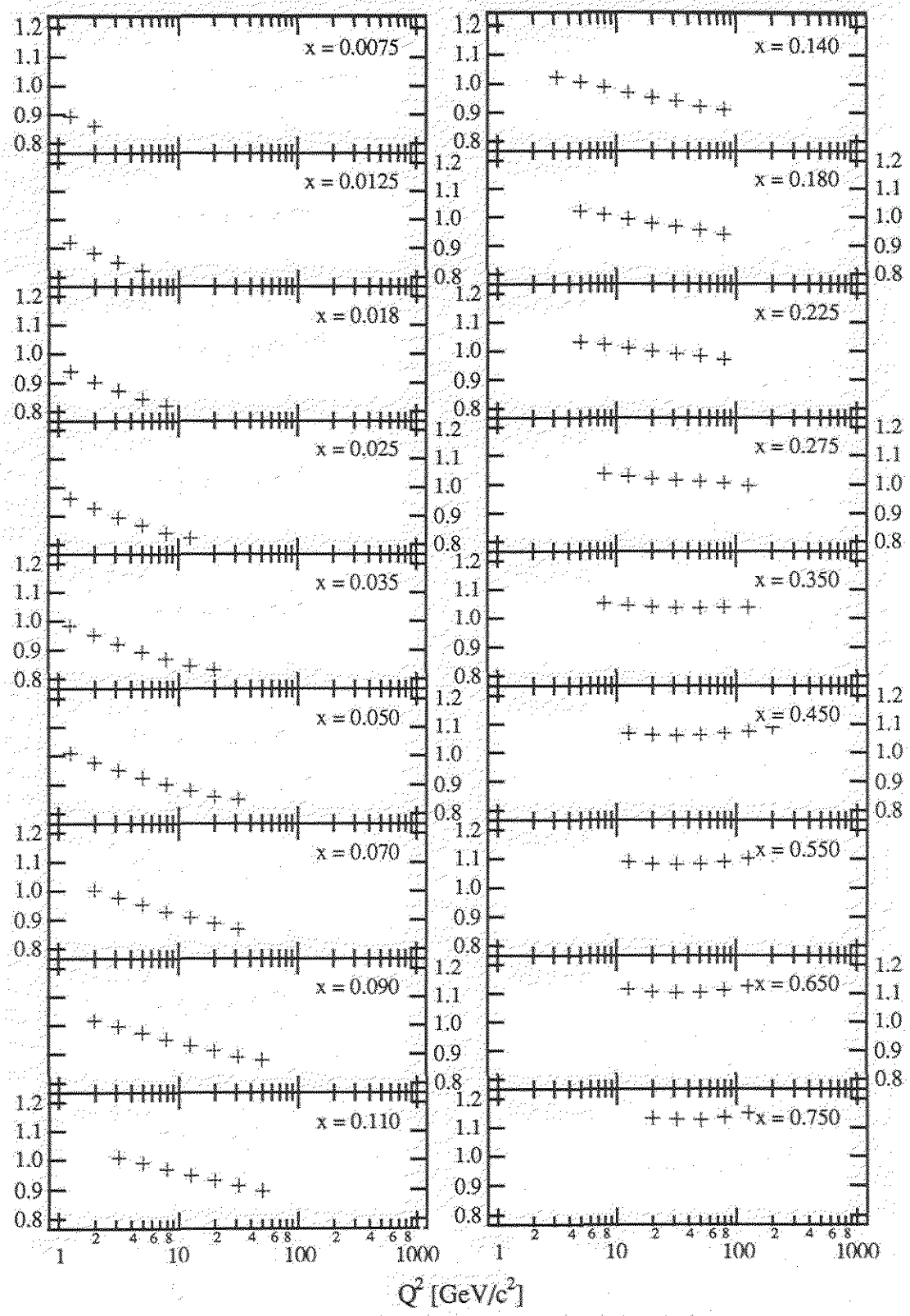

Figure 6.13: The physics-model corrections for anti-neutrino events in the structure-function analysis.

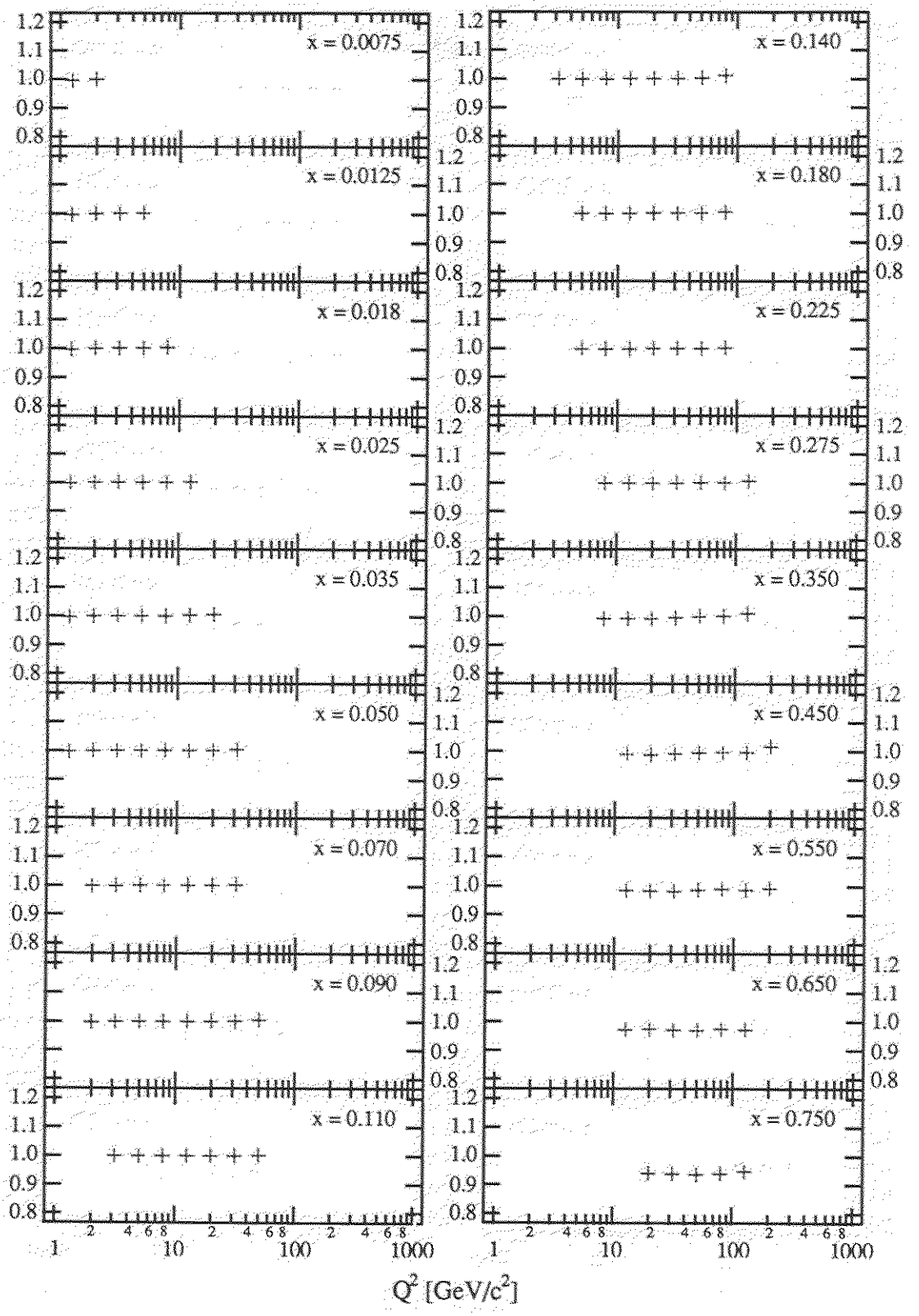

Figure 6.14: The bin-center corrections for neutrino events in the structure-function analysis.

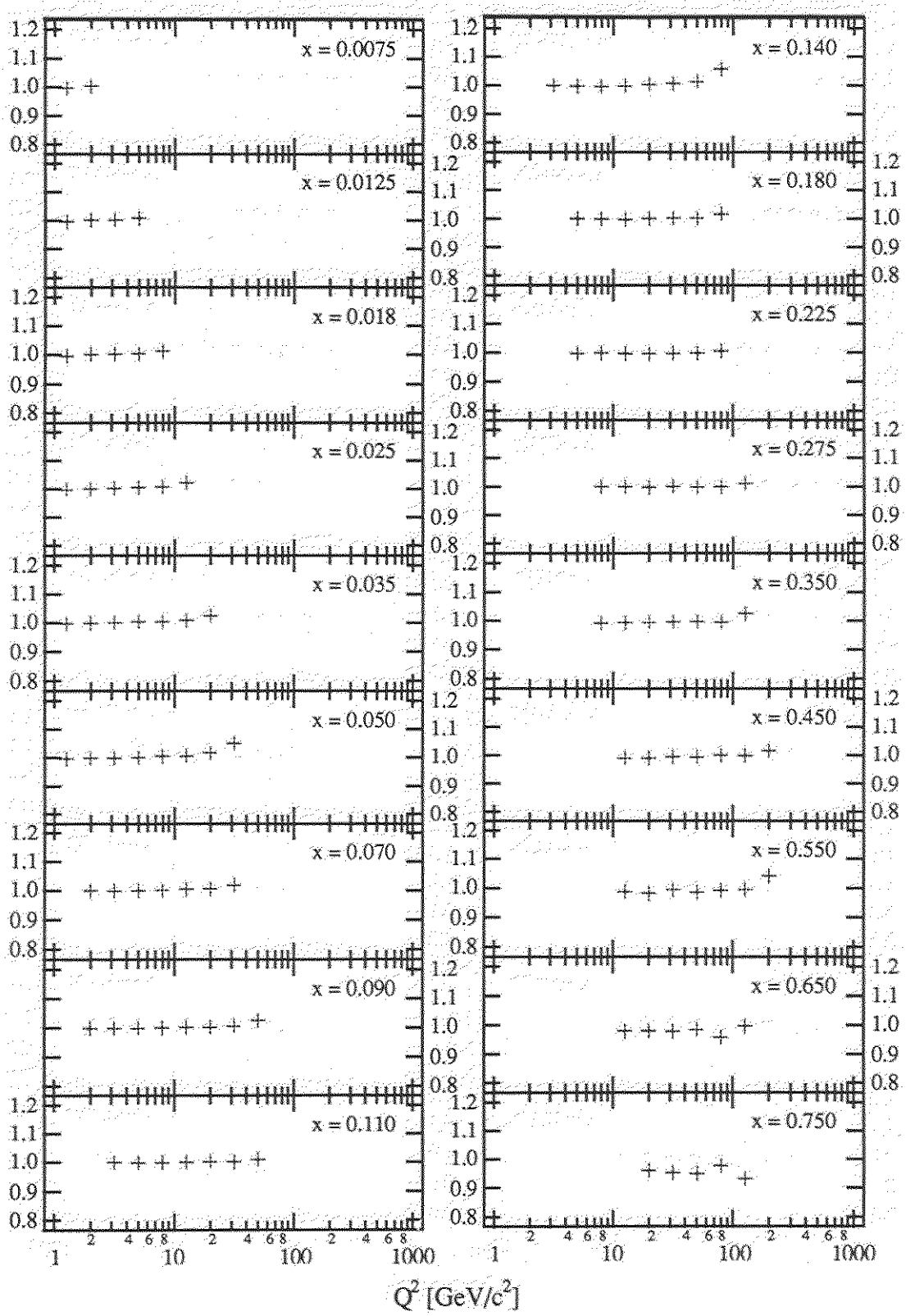

Figure 6.15: The bin-center corrections for anti-neutrino events in the structure-function analysis.

6.2.3 Combining Experiments

The structure functions F_2 and xF_3, and their associated statistical errors ΔF_2, ΔxF_3, and $\Delta F_2 \Delta xF_3$, are extracted separately for each experiment, E744 and E770, according to Equation 6.9. The structure functions are combined using the following procedure, which correctly incorporates the correlated statistical errors:

Define the structure-function vector

$$\vec{\mathbf{F}} = \begin{pmatrix} F_2 \\ xF_3 \end{pmatrix} \tag{6.23}$$

and the structure-function error matrix

$$\hat{\mathbf{V}} = \begin{pmatrix} (\Delta F_2)^2 & \Delta F_2 \Delta xF_3 \\ \Delta F_2 \Delta xF_3 & (\Delta xF_3)^2 \end{pmatrix} \tag{6.24}$$

Then to combine the vectors $\vec{\mathbf{F}}_{\mathrm{E744}}$ and $\vec{\mathbf{F}}_{\mathrm{E770}}$, and the matrices $\hat{\mathbf{V}}_{\mathrm{E744}}$ and $\hat{\mathbf{V}}_{\mathrm{E770}}$, the relations are:

$$\left(\hat{\mathbf{V}}_{\mathrm{Combined}}\right)^{-1} = \left(\hat{\mathbf{V}}_{\mathrm{E744}}\right)^{-1} + \left(\hat{\mathbf{V}}_{\mathrm{E770}}\right)^{-1} \tag{6.25}$$

$$\left(\hat{\mathbf{V}}_{\mathrm{Combined}}\right)^{-1} \vec{\mathbf{F}}_{\mathrm{Combined}} = \left(\hat{\mathbf{V}}_{\mathrm{E744}}\right)^{-1} \vec{\mathbf{F}}_{\mathrm{E744}} + \left(\hat{\mathbf{V}}_{\mathrm{E770}}\right)^{-1} \vec{\mathbf{F}}_{\mathrm{E770}} \tag{6.26}$$

As a check, it can be noted that if $\Delta F_2 \Delta xF_3 = 0$ for both experiments, Equations 6.25 and 6.26 reduce to

$$\sigma_{A+B}^2 = 1 \Big/ \left(1/\sigma_A^2 + 1/\sigma_B^2\right) \tag{6.27}$$

and

$$f_{A+B} = \left(f_A/\sigma_A^2 + f_B/\sigma_B^2\right)\Big/\left(1/\sigma_A^2 + 1/\sigma_B^2\right) \tag{6.28}$$

which are the familiar expressions for summing the results of two independent measurements.

6.3 Iteration

In both the flux and structure-function analysis, the physics-model correction requires a set of parton distributions based on some set of structure functions, and the Monte-Carlo correction requires a flux to calculate the smearing corrections. Since an input set of flux and structure functions is needed to extract a new output set of flux and structure functions, an iterative approach must be used. The steps of the "iterative loop" associated with this analysis are:

1) Assume a flux Φ_{EST} and a set of parton distributions q_{EST}.

2) Generate Monte Carlo events using q_{EST} and Φ_{EST}.

3) Apply the resolution smearing of section 4.1 to the events from step (2).

4) Use the Monte Carlo events from steps (2) and (3) to correct the low-E_{HAD} events and extract a flux Φ_{NEW} as discussed in chapter 5.

5) Use the events of step (2), but re-weight the events from Φ_{EST} to Φ_{NEW} as discussed in section 4.1.4.1, and apply the resolution smearing.

6) Use the Monte-Carlo events of step (5) to extract a set of structure functions F_{NEW}.

7) Fit a set of parton distributions q_{NEW} to the structure functions F_{NEW} using the physics-model parameterization described in section 4.2.

8) Replace $q_{NEW} \rightarrow q_{EST}$ and $\Phi_{NEW} \rightarrow \Phi_{EST}$ and repeat steps (1) through (7) until the difference between F_{NEW} and F_{EST} (from the previous iteration) is small.

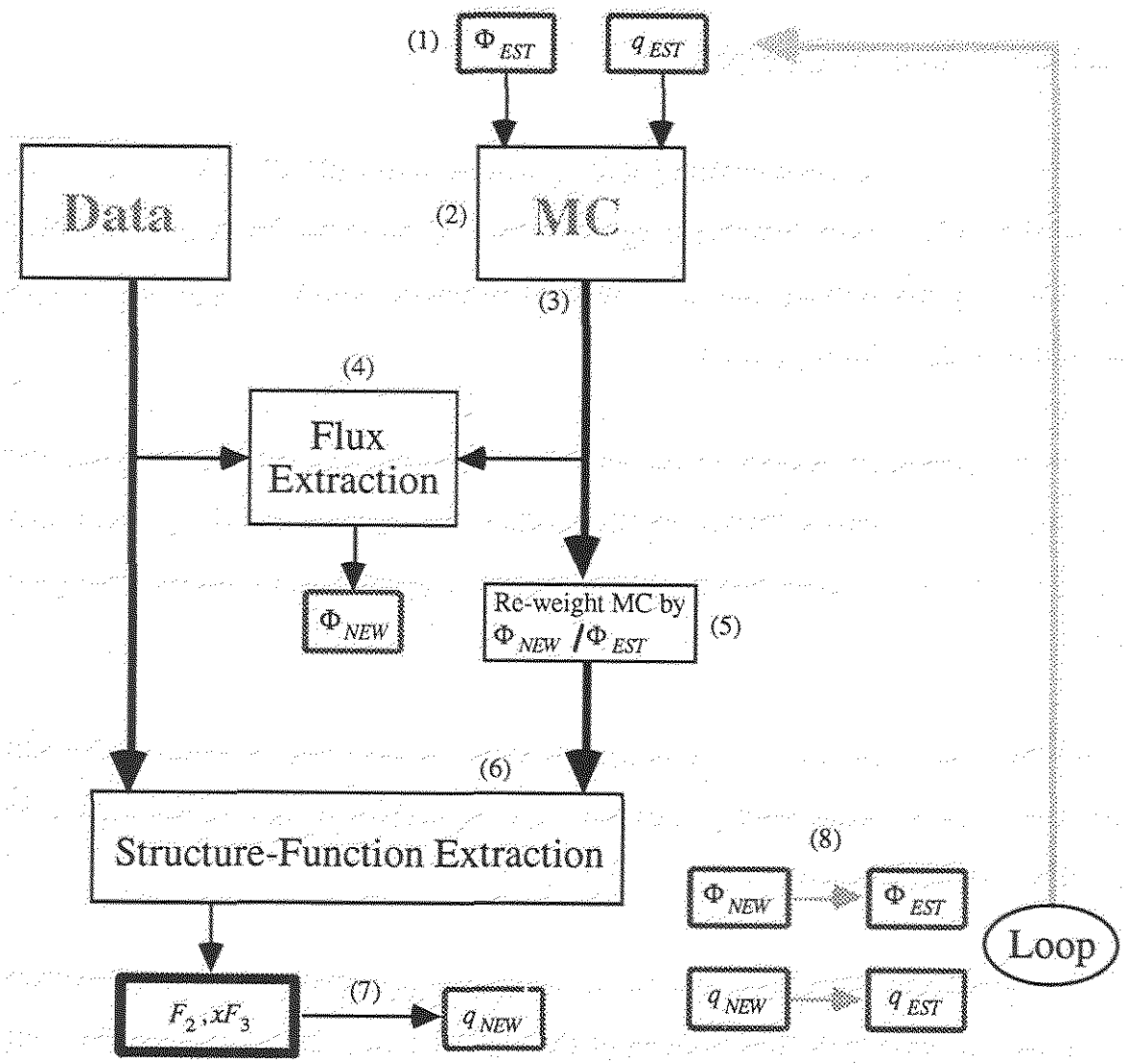

Figure 6.16: Diagram of the iterative analysis procedure. The numbers in parentheses correspond to the steps in the iteration described above.

In practice, the results converge after three iterations of steps (1) through (8). Figure 6.16 shows the iterative analysis loop in a diagrammatic form.

The structure-function extraction procedure was verified by generating a set of "fake data" events using the Monte Carlo, then using the "fake data" events in place of the data in the iterative loop. The resultant structure functions were identical to the structure functions used as input to the Monte Carlo.

6.4 Systematic Errors

This section contains the complete list of systematic errors identified in this analysis. Some of them have been described in earlier sections of this thesis, but all are included in the following sub-sections. The point-to-point systematic errors in Appendix D were generated by the following procedure:

• Vary the systematic quantity by the error listed (denoted as a shift of the systematic quantity by $1\delta_k$). With the exceptions noted below, each systematic quantity was varied by $\pm 1\ \delta_k$; that is, the error was calculated for both a positive and negative systematic shift.

• Use the Monte Carlo file created in step (2) of the iterative loop described in Section 6.3. The file used was the same as that used in the last iteration of the loop that resulted in the final structure functions.

• The parton distributions q_{EST} used for the systematic-error extraction were the same as were used as input to the last iteration of the final extraction loop; any exceptions are noted below.

• If was it was not necessary to extract a new flux, the same Φ as used in the last iteration for the final results was also used for the systematic variation.

• Steps (4) through (6) of the analysis described in Section 6.3 were performed, resulting in a flux Φ_k and associated structure functions F_k corresponding to this systematic variation.

• Within each (x, Q^2) bin, the systematic error reported in Tables D.2-D.9 is

$$\frac{\left(F_k(1\delta)-F\right)}{\left|\left(F_k(1\delta)-F\right)\right|}\times\frac{\left|\left(F_k(1\delta)-F\right)\right|+\left|\left(F_k(-1\delta)-F\right)\right|}{2} \tag{6.29}$$

That is, the shift in the table is the magnitude of average of the positive and negative shift, multiplied by the sign of the positive shift.

All of the systematic errors listed below are included in the "global systematic QCD fit" described in chapter 7.

6.4.1 Experimental Systematics

These errors are associated with systematic effects in the data analysis described in chapter 3.

Hadron energy calibration (C_{HAD}^{744}, C_{HAD}^{770}): As described in section 3.1.4, the hadron energy calibration for the experiment is known to within 1%. Due to the aging of the scintillator oil in the target counters, the re-adjustment of the photomultiplier-tube voltages, and changes made in the ADC readout electronics, the calibration of each of the two experiments E744 and E770 is allowed to be independently shifted by ±1%.

E_{HAD} shift (ΔE_{HAD}): As noted in section 3.1.4, there is a disagreement in the model of the hadron energy in the Monte Carlo and the data, and the data is corrected for this difference. The error in this correction is conservatively estimated to be $\pm 100\ MeV$.

Muon energy calibration (C_μ): As described in section 3.2, the muon energy calibration for the experiment is known to within 1%. Since the same toroid spectrometer was used for both experiments E744 and E770, the same muon calibration constant is assumed for both experiments.

E_μ shift (ΔE_μ): The model of the systematic error for the E_{HAD} calibration is $C_{HAD} \times E_{HAD} + \Delta E_{HAD}$. To be consistent, the model of the systematic error in the E_μ calibration is taken to be $C_\mu \times E_\mu + \Delta E_\mu$. The shift in E_μ is therefore zero, with an assumed error ΔE_μ of $\pm 100\ MeV$.‡

6.4.2 Flux-Extraction Systematics

B/A for neutrinos and anti-neutrinos ($(B/A)^{\nu,\bar{\nu}}_{\mathrm{E744,E770}}$): As discussed in section 5.1.2.1, there is a statistical error from the flux extraction in the value of B/A which affects the flux. The errors in $(B/A)^{\nu}$ and $(B/A)^{\bar{\nu}}$ from experiments E744 and E770 are treated as separate systematic errors.

---

‡ A study was done assuming a quadratic term in the energy calibration, i.e., $E_{meas} = \Delta E + CE(1 + C'E)$. The quadratic coefficient C' was allowed to vary by $\pm 2.5\%/(200\ GeV)$, the limit allowed by the hadron energy studies in [Sak90]. This study was performed separately for both the muon and hadron energy calibration, and the result in both cases was that the effect on the values of the structure functions was less than 10% of the shift due to ΔE.

Flux adjustment ($\Phi^{adjusted}$): As discussed in section 5.3.3, the difference between the actual flux extracted and the flux adjusted for a linear cross-section is treated as a systematic error. There is no "-1δ" shift for this error; the error in Tables D.4 and D.5 is the difference between the structure function extracted with $\Phi^{original}$ and the base structure function.

6.4.3 Cross-section Systematics

The following systematic errors come from errors in the ν-Fe cross-section.

Cross-section normalization (σ^{ν}/E): As discussed in section 5.3.1, there is an error of 2.1% in the world average of the neutrino-iron cross-sections. This systematic error results in a shift of ±2.1% in the level of the structure functions. There is no need to re-extract the flux for a shift in σ^{ν}/E since this does not change the relative flux.

Cross-section ratio ($\sigma^{\bar{\nu}}/\sigma^{\nu}$): As discussed in section 5.3.1, there is an error in the world average $\sigma^{\bar{\nu}}/\sigma^{\nu}$. However, the error quoted in Table 5.6 includes all the systematic effects for our experiment. In the systematic error analysis a new flux Φ_k and associated $\left(\sigma^{\bar{\nu}}/\sigma^{\nu}\right)_k$ are generated for all the systematic errors. Including the complete error from Table 5.6 in the variation of $1\delta_k$ would over-estimate the error due to the $\sigma^{\bar{\nu}}/\sigma^{\nu}$ error. Therefore, the only errors included in the shift of $\delta\left(\sigma^{\bar{\nu}}/\sigma^{\nu}\right)$ are the statistical, low-ν extrapolation, and acceptance-correction errors listed in Table 5.6. The resulting value of $\delta\left(\sigma^{\bar{\nu}}/\sigma^{\nu}\right)$ is 1.4%. There is no need to re-extract the flux for the shift in $\sigma^{\bar{\nu}}/\sigma^{\nu}$, since it does not change the relative flux.

6.4.4 Model Systematics

The following systematic errors come from errors in quantities measured from other analyses than the analysis described in this thesis. Aside from the error in R_{World}, the remaining errors come from the dimuon analysis [Rab92]. All of the model systematic errors apply to the physics model described in Section 4.2. To perform the systematic error study, a new $\left(q_{EST}\right)_k$ is derived by fitting to the F_{EST} from the next-to-the-last analysis iteration, varying the fixed parameters of the model only by the quantity listed. A new Monte Carlo file is not generated, nor are events re-weighted to the new cross-section; this is assumed to be unnecessary because these systematic shifts are small and because of the rapid convergence of the analysis iteration loop.

R_{World} error (δR): An error of $\pm 15\%$ is assumed for the parameterization of R given in Ref. [Whi90b].

Mass of the charm quark (m_c): As reported in Ref. [Rab93], the value of m_c is 1.31 ± 0.24. Thus the variation $\delta\left(m_c\right)$ is 18%.

Strange sea shape (α): As reported in Ref. [Rab93], the value of α (as defined in Equation 6.17) is 2.50 ± 0.65. Thus the variation $\delta(\alpha)$ is 26%.

Strange sea normalization (κ): As reported in Ref. [Rab93], the value of κ (as defined in Equation 6.16) is 0.373 ± 0.046. Thus the variation $\delta(\kappa)$ is 12%.

Charm branching ratio (B_c): As reported in Ref. [Rab93], the value of B_c is 0.105 ± 0.007. Thus the variation of $\delta\left(B_c\right)$ is 7%. Note: B_c enters into the analysis only indirectly via the small dimuon correction described in Section 4.1.4.2.

In addition to the above (relatively small) systematic errors, there is a systematic error due to the choice of the functional form of the physics model used in the Monte Carlo, as described in Section 4.2.1.5.

6.5 Results

Figures 6.17 and 6.18 display the values of F_2 and xF_3, respectively, with each x-bin shown separately. Figures 6.19-6.22 display as many x-bins on the same scale as possible, along with the QCD fits described in Chapter 7. Figure 6.19 displays F_2 extracted from this experiment and Figure 6.20 shows the values for $x > 0.3$. Similarly, Figures 6.21 and 6.22 display the values of xF_3 and the high-x values of xF_3. Only the statistical errors are shown. These Figures dramatically show the effects of scaling violations. True scaling would imply that the slopes of the lines connecting the data points be zero. Approximate scaling is only observed around $x = 0.14$.

Figure 6.24 shows F_2 and xF_3 at $Q^2 = 12.6\ GeV^2$, the average Q^2 of the data. Each structure function in this Figure was "averaged" over the Q^2 range of the experiment by fitting the data within each x-bin to a simple power-law form $F = A \times \left(Q^2\right)^C$, then evaluating the fit at $Q^2 = 12.6\ GeV^2$. Figure 6.25 shows the Q^2-averaged values for $\left(F_2 + xF_3\right)/2$ and $\left(F_2 - xF_3\right)/2$, which in the parton model are equivalent to $q(x)$ and $\overline{q}(x)$, the quark and anti-quark distributions respectively.

If the high-x structure functions are superimposed, as shown in Figures 6.23 and 6.24, it is clear that for $x > 0.5$ $F_2 \approx xF_3$. In Figure 6.25, it can be observed that $\overline{q}(x)$ is consistent with zero for $x > 0.5$. This observation will be addressed further in Chapter 7.

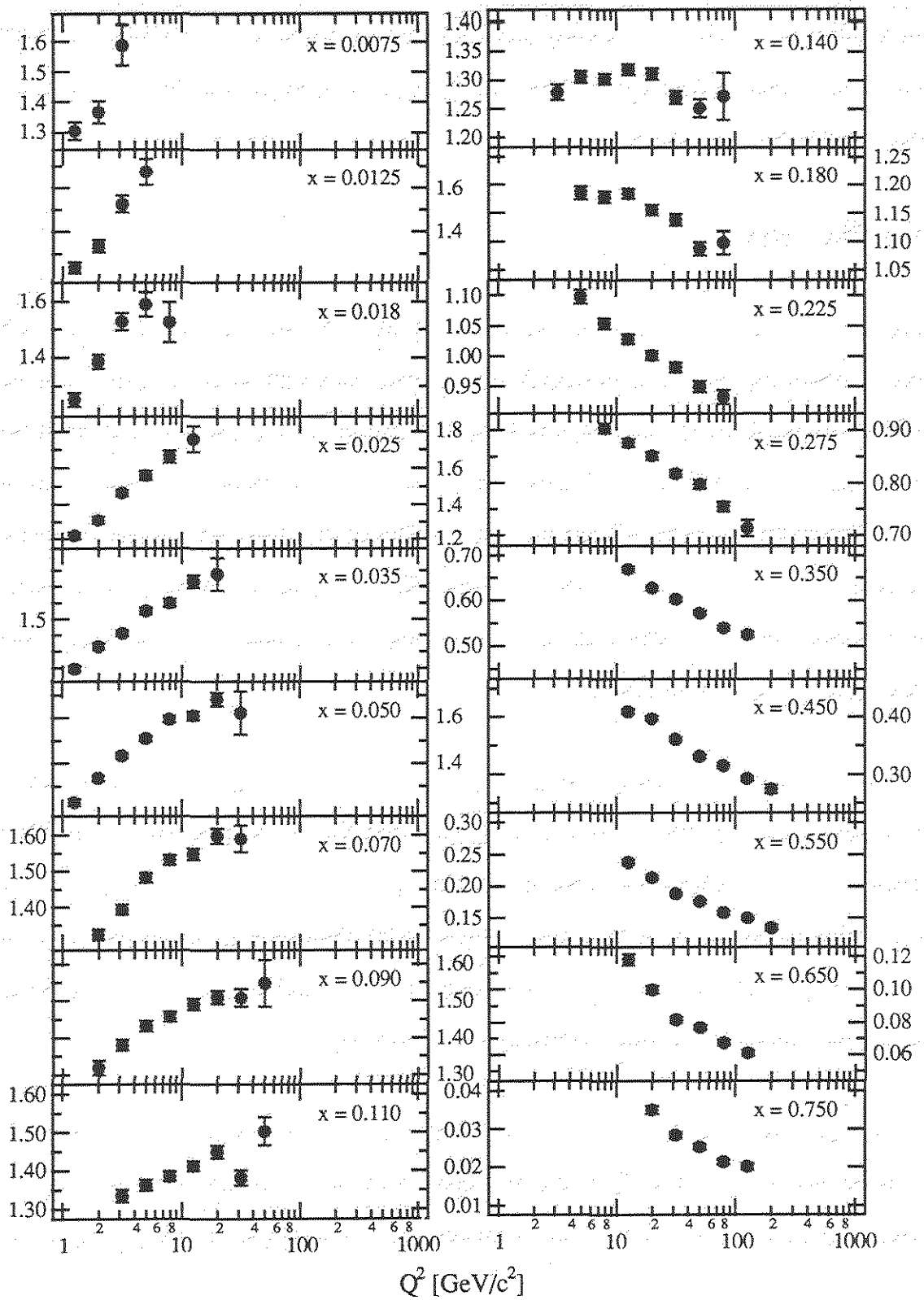

Figure 6.17: Structure function F_2. Each x-bin is displayed separately. Error bars are statistical only.

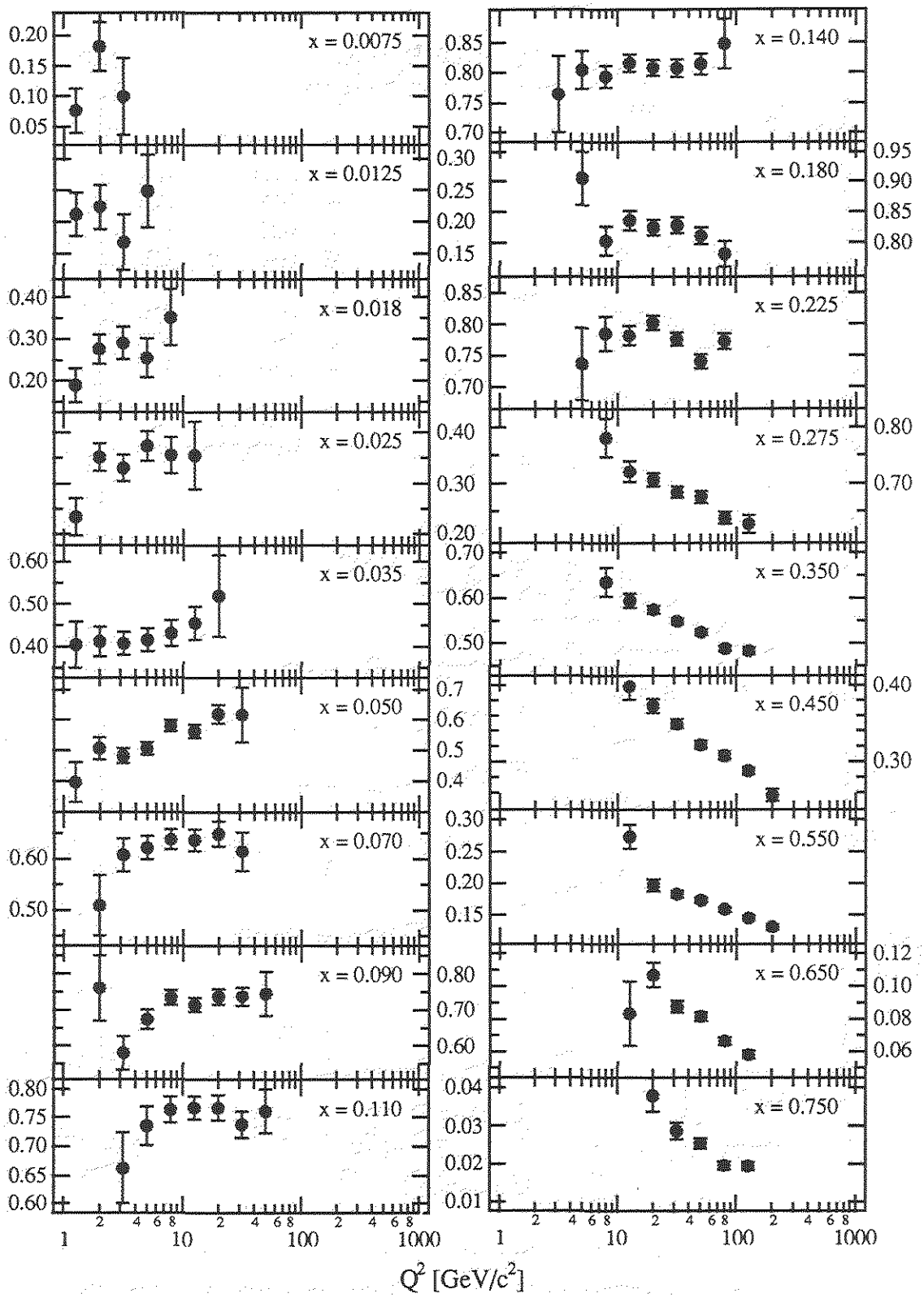

Figure 6.18: Structure function xF_3. Each x-bin is displayed separately. Error bars are statistical only.

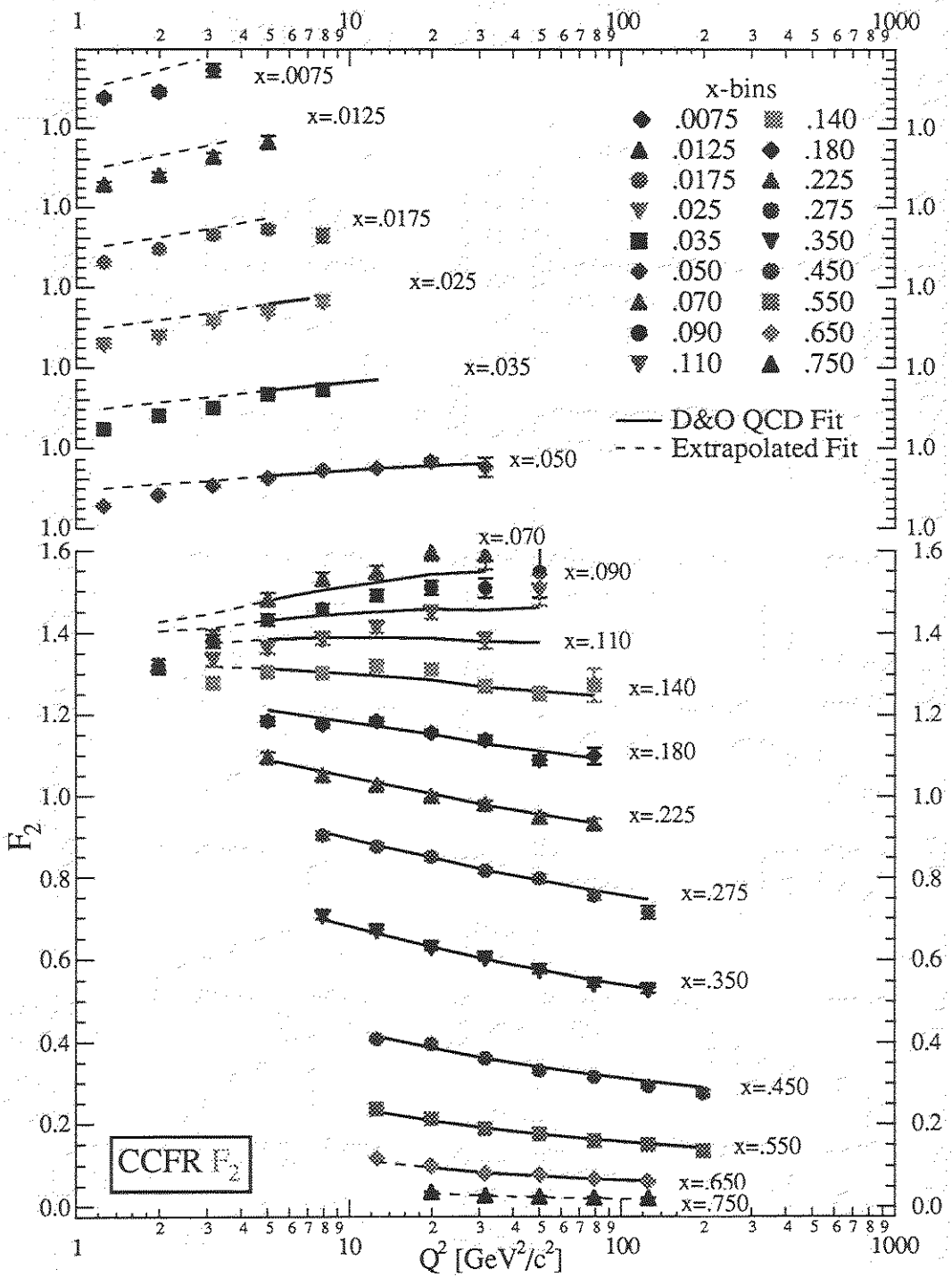

Figure 6.19: Structure function F_2, displaying as many x-bins as possible on a common axis. Error bars are statistical only. The solid lines are the QCD fit described in Chapter 7; the dashed lines extrapolate the fit to $Q^2 = 1 GeV^2$ and $x < 0.8$.

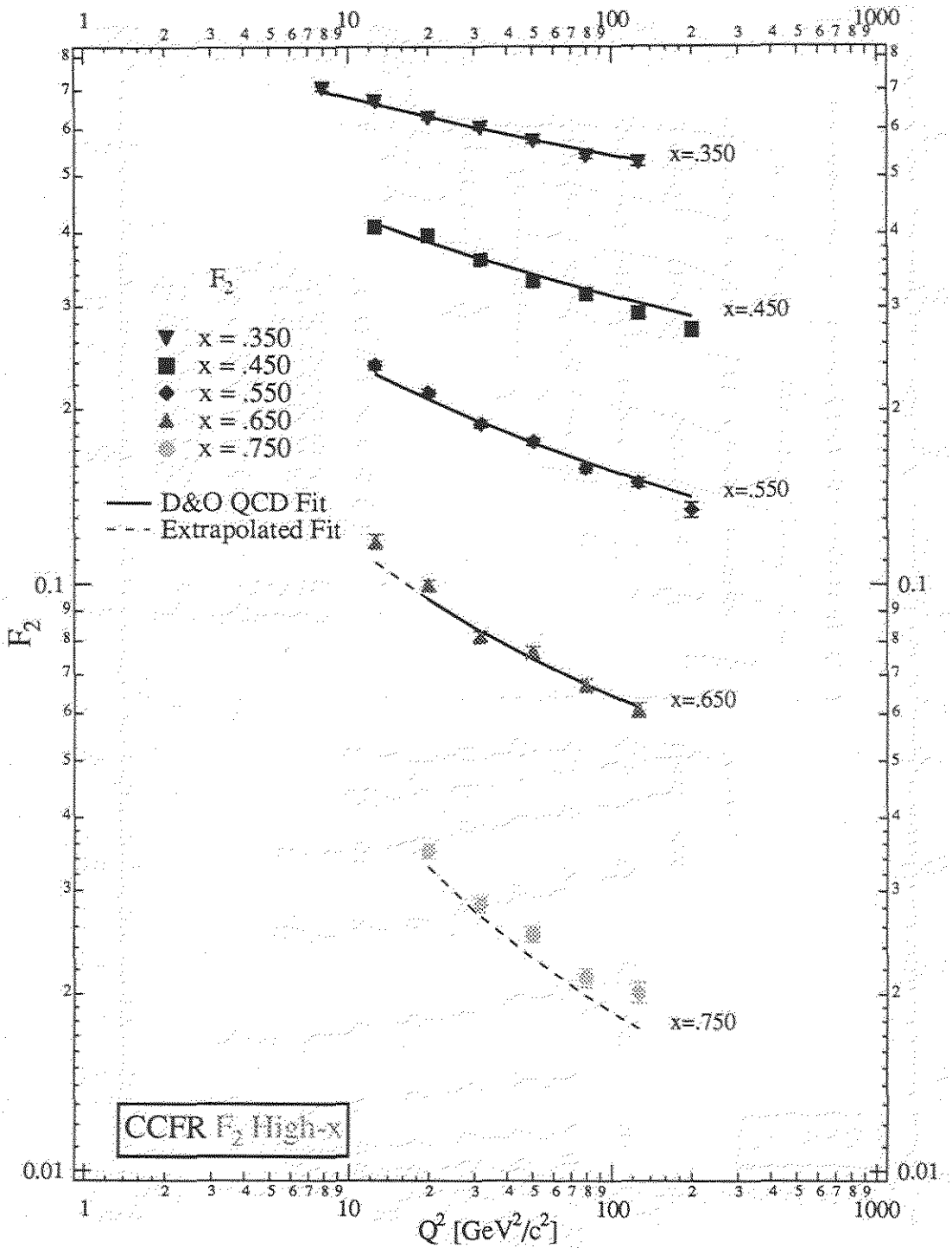

Figure 6.20: The high-x bins of structure function F_2. Error bars are statistical only. The solid lines are the QCD fit described in Chapter 7; the dashed lines extrapolate the fit to $Q^2 = 1GeV^2$ and $x < 0.8$.

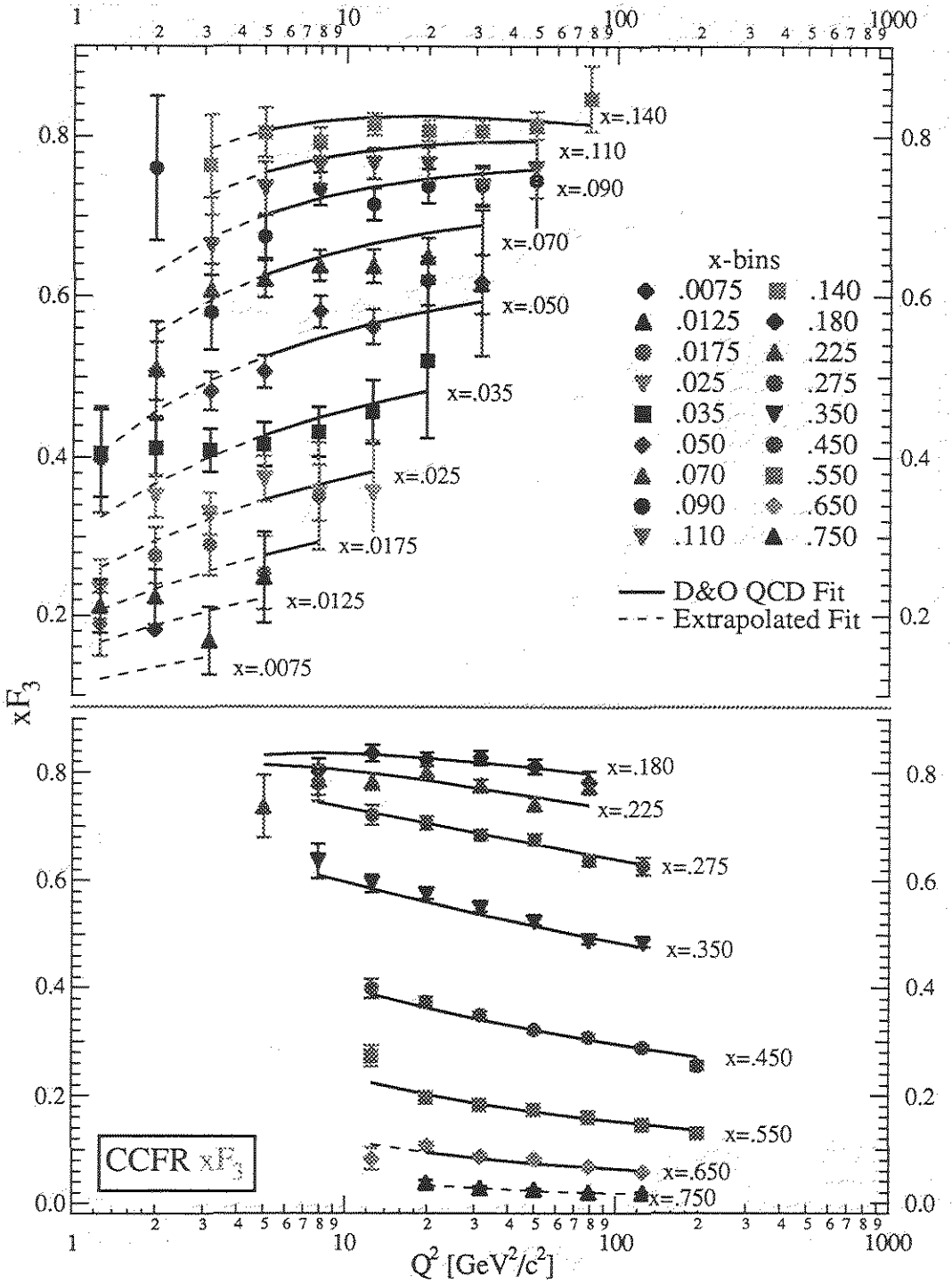

Figure 6.21: Structure function xF_3, displaying as many x-bins as possible on a common axis. Error bars are statistical only. The solid lines are the QCD fit described in Chapter 7; the dashed lines extrapolate the fit to $Q^2 = 1 GeV^2$ and $x < 0.8$.

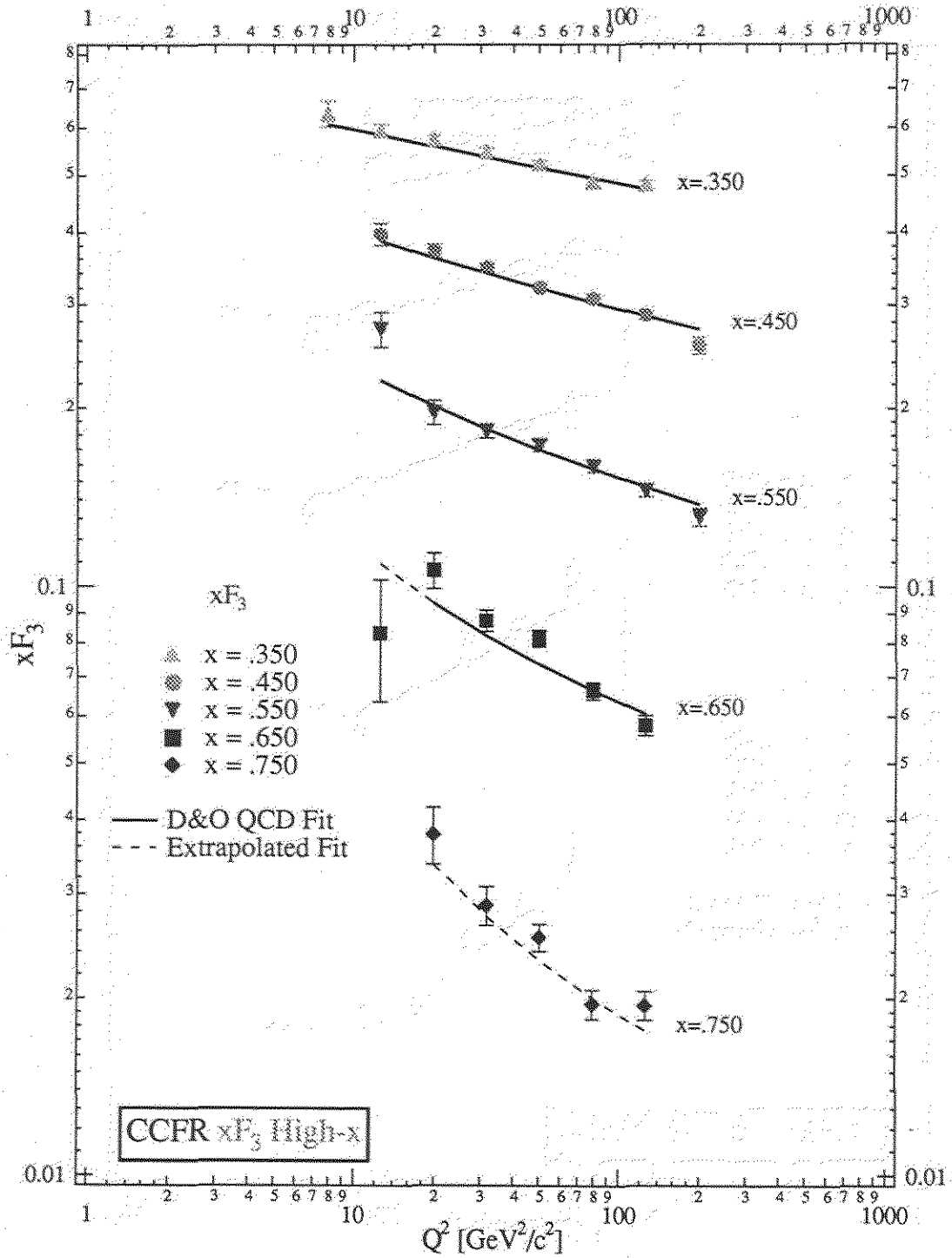

Figure 6.22: The high-x bins of structure function xF_3,. Error bars are statistical only. The solid lines are the QCD fit described in Chapter 7; the dashed lines extrapolate the fit to $Q^2 = 1GeV^2$ and $x < 0.8$.

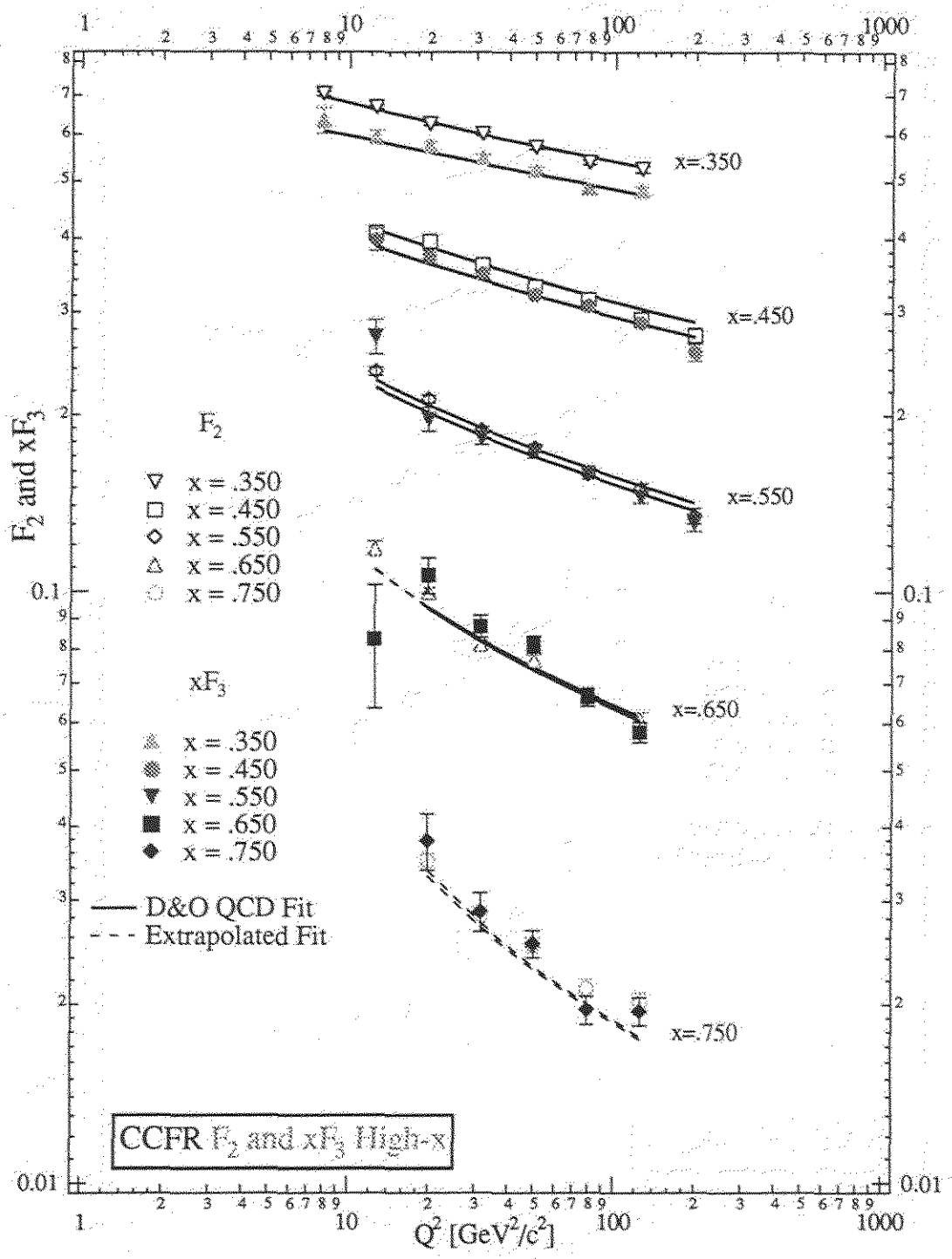

Figure 6.23: The high-x bins of structure functions F_2 and xF_3 superimposed to show $F_2(x>0.5) \approx xF_3(x>0.5)$. Error bars are statistical only. The solid lines are the QCD fit described in Chapter 7; the dashed lines extrapolate the fit to $Q^2 = 1GeV^2$ and $x < 0.8$.

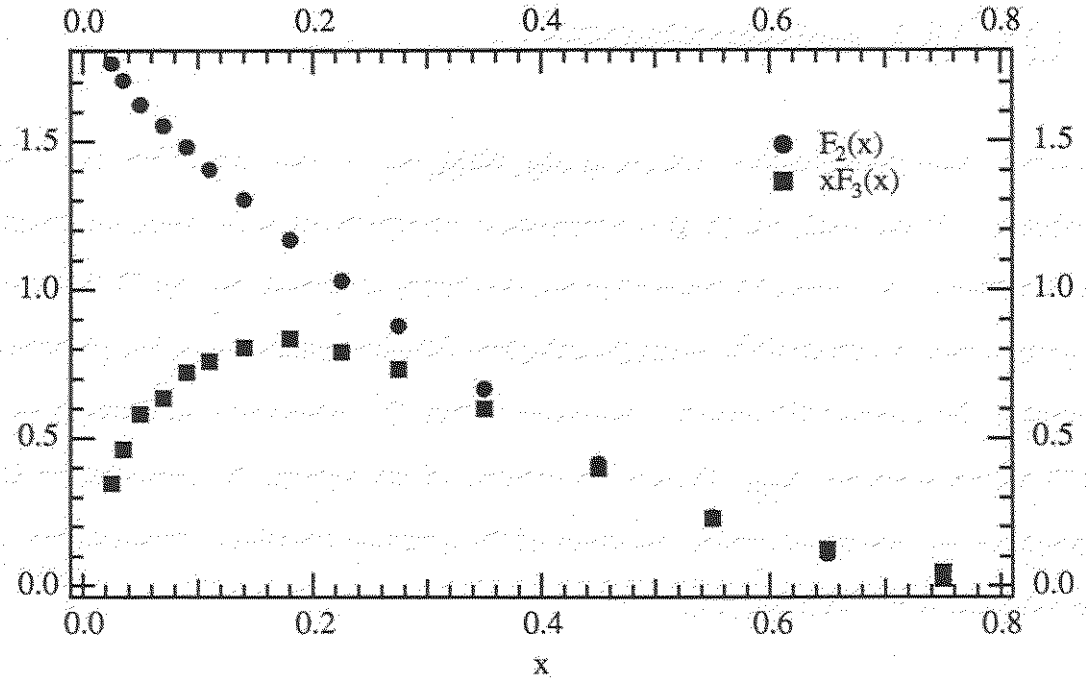

Figure 6.24: F_2 and xF_3 averaged at $Q^2 = 12.6\,GeV^2$.

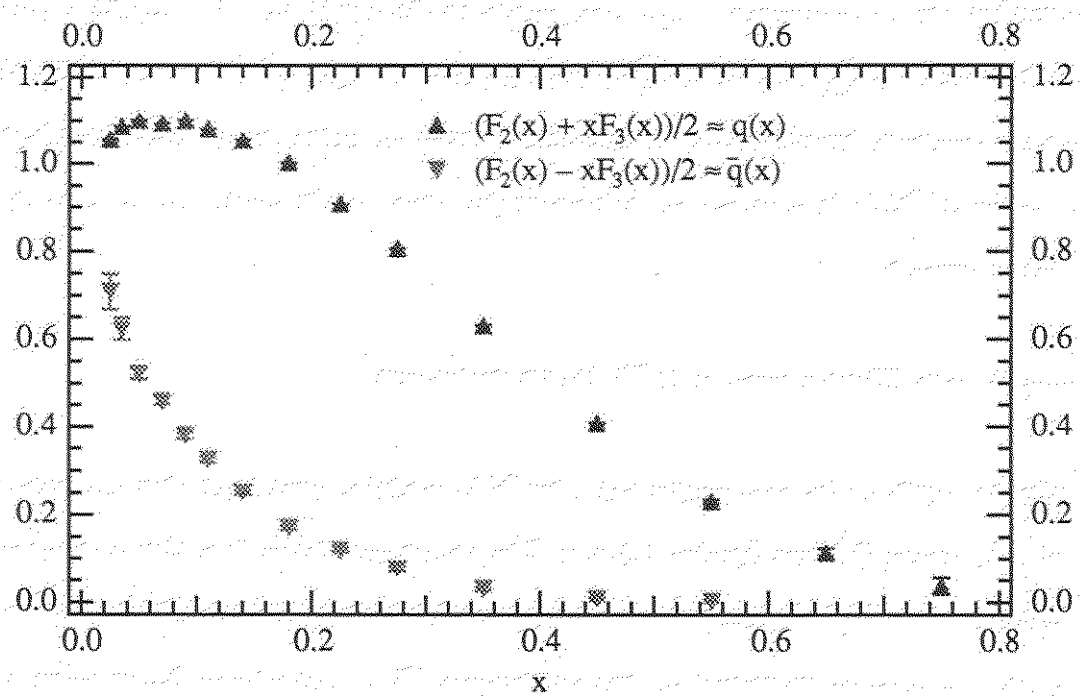

Figure 6.25: $\left(F_2 + xF_3\right)/2$ and $\left(F_2 - xF_3\right)/2$ averaged at $Q^2 = 12.6\,GeV^2$.

7 QCD Comparisons

Quantum Chromodynamics (QCD) is the field theory that describes the strong interactions. In this analysis, QCD is examined in two different ways. First, the structure functions shown in Chapter 6 are used to test the theory of perturbative QCD. The theory actually makes no predictions about the structure functions themselves, but predicts the change in the slope of the structure functions versus Q^2, which in turn depends on the QCD scale parameter $\Lambda_{\overline{\mathrm{MS}}}$. To test the validity of the theory, the perturbative QCD predictions are compared against the slope of the structure functions incorporating both the statistical and systematic errors.

The second way QCD is applied in this analysis is to assume that the theory is correct and incorporate the experimental systematic errors in the QCD fit. This yields a precise measurement of $\Lambda_{\overline{\mathrm{MS}}}$ and $\alpha_S(M_Z^2)$, the coupling strength of the strong interaction. Since the structure functions and the systematic errors are being interpreted in the context of a model of QCD, it is important to specify the exact model used. This is done in the following Section.

In general, two different types of QCD fits are performed:

- The xF_3-only fit (or non-singlet fit). The QCD model is used to predict the evolution of xF_3 versus Q^2 (see Section 1.2.4.3). The advantage of this fit is that the evolution equation for xF_3 (see Equation 7.12) does not involve the gluon distribution, which cannot be directly measured by this experiment. This approach to determining $\Lambda_{\overline{\mathrm{MS}}}$ is unique to a neutrino experiment, since the other available techniques all involve making some assumptions about the gluons.

- The F_2 and xF_3 fit (combined singlet and non-singlet fit). The QCD model is used to simultaneously predict the evolution of F_2 and xF_3 versus Q^2. Although this method requires some parameterization of the gluon distribution in the QCD fit, it has the advantage of including all the structure-function data. The result of this increase in statistics is that the statistical and systematic errors on $\Lambda_{\overline{MS}}$ are substantially reduced compared to the xF_3-only fit. In addition, this fit gives information on the shape and size of the gluon distribution.

7.1 The QCD Model

The procedure used to implement the theory of QCD is based on a computer program originally written by Dennis Duke and Jeff Owens [Dev83]. The χ^2 minimization was performed by using the function-minimization program MINUIT [Jam94]. After the Duke and Owens program was given to the CCFR collaboration, it was modified by Ed Oltman [Olt89] and William Seligman to suit the needs of the present analysis. Some of these changes were:

- performing a polynomial interpolation on the (x,s) grid (see Section 7.1.3; formerly the interpolation was linear);

- obtaining theoretical predictions for $2xF_1$, xF_3^{ν}, and $xF_3^{\bar{\nu}}$, in addition to the values of F_2^{ν}, F_2^{ℓ}, and $\langle xF_3 \rangle$ that the program originally provided;

- testing alternative parameterizations for the parton distributions (see Section 7.2.1);

- modifying the χ^2 calculation for the global systematic error analysis (see Section 7.3).

The following sub-sections describe the overall operation of the program. The FORTRAN source code for the QCD evolution is included in Appendix C.

7.1.1 Initial Parton Distributions

The QCD model starts with parameterizations of the parton distributions at a given Q_0^2. For this analysis, the typical value assigned is $Q_0^2 = 5GeV^2$, which according to Ref. [Dev83] is the lower limit of the validity of the target mass correction (see Section 7.1.5).

For the xF_3-only fit, only the non-singlet quark distribution, q_{NS}, need be specified:

$$xq_{NS}(x,Q_0^2) = A_{NS}x^{\eta_1}(1-x)^{\eta_2} \tag{7.1}$$

The parameters in Equation 7.1, namely η_1, η_2, and A_{NS}, are variables whose values are determined by the MINUIT χ^2 minimization.

For the F_2 and xF_3 fit, two additional parton distributions are needed: the singlet quark distribution and the gluon distribution, q_S and G. These are parameterized by

$$xq_S(x,Q_0^2) = xq_{NS}(x,Q_0^2) + A_S(1-x)^{\eta_S} \tag{7.2}$$

$$xG(x,Q_0^2) = A_G(1-x)^{\eta_G} \tag{7.3}$$

which leads to additional parameters included in the fit: A_S, η_S, A_G, and η_G. The functional forms for q_{NS}, q_S, and G come from theoretical predictions on the behavior of the parton distributions at small and large x [Rob90].

The remaining parameter to be varied by MINUIT, $\Lambda_{\overline{MS}}$, enters into the fit via the evolution equations (see section 7.1.3). It affects these equations via the value of $\alpha_S(Q^2)$, which is determined in next-to-leading-order from

$$\ln\left(\frac{Q^2}{\Lambda^2_{\overline{MS}}}\right)=\frac{4\pi}{\beta_0\alpha_S\left(Q^2\right)}-\frac{\beta_1}{\beta_0^2}\ln\left[\frac{4\pi}{\beta_0\alpha_S\left(Q^2\right)}+\frac{\beta_1}{\beta_0^2}\right] \tag{7.4}$$

with

$$\beta_0=11-\frac{2}{3}N_f \tag{7.5}$$

and

$$\beta_1=102-\frac{38}{3}N_f \tag{7.6}$$

where N_f = number of quark flavors. In these QCD fits, N_f was allowed to vary as a function of Q^2, with thresholds set at N_f = 3 for $Q^2<(1.5\,GeV)^2$, N_f = 4 for $(1.5\,GeV)^2<Q^2<(4.5\,GeV)^2$, and $N_f=5$ for $Q^2>(4.5\,GeV)^2$. For this analysis, the value of $\Lambda_{\overline{MS}}$ is always the value for 4 quark flavors, denoted by $\Lambda^{(4)}_{\overline{MS}}$, which was chosen to simplify comparison of this result from those of previous deep-inelastic scattering experiments. The mean Q^2 of the data used in the QCD fit is 30 GeV^2, just above the threshold of *b*-quark production.

7.1.2 Comments on Parton Sum Rules

In previous QCD analyses performed by this collaboration [Olt89, Leu91, Qui92] the parameters A_{NS} and A_G were not fit parameters, but were constrained by the "Fermion

Conservation Rule" and the "Momentum Sum Rule" respectively. This section describes the reasons why these sum-rule constraints were removed for the present analysis.

7.1.2.1 The Fermion Conservation Rule

The Fermion Conservation Rule sets the number of valence quarks in the proton to 3:

$$\int_0^1 \frac{xq_{NS}}{x} dx = 3 \tag{7.7}$$

However, when this constraint was imposed on the non-singlet parameterization of Equation 7.1, the χ^2 of the fit was poor. In an attempt to improve the quality of the fit, alternate parameterizations were explored. The parameterization selected for the analysis reported in Ref. [Qui93] was

$$xq_{NS}(x,Q_0^2) = A_{NS}x^{\eta_1}(1-x)^{\eta_2} + B_{NS}x^{\eta_3} \tag{7.8}$$

With this parameterization, and with the constraint given in Equation 7.7, the value of A_{NS} is determined analytically by

$$A_{NS} = \frac{3-\left(B_{NS}/\eta_3\right)}{\beta\left(\eta_1,\eta_2+1\right)} \tag{7.9}$$

While the resulting fit had a good χ^2, the values of the parameters were odd: B_{NS} would be quite small (10^{-4} or less), too small to affect the shape of the parton distribution or the Q^2 evolution, but the value of B_{NS}/η_3 would be substantial (~ 0.3). The reason for this behavior is that the addition of the B_{NS}/η_3 term in Equation 7.9 allowed MINUIT to violate the Fermion Conservation Rule of Equation 7.7, without affecting the shape of the parton distribution themselves.

The question now is: why does the QCD fit not agree with the Fermion Conservation Rule? For the answer, it must be recalled that this constraint is related to the Gross-Llewellyn-Smith Sum Rule (GLS Sum Rule) constraint in QCD [Har95]:

$$\underbrace{\int_0^1 dx \frac{xq_{NS}}{x} = 3}_{\substack{\text{Fermion}\\ \text{Conservation}\\ \text{Rule}\\ \text{(parton model)}}} \xrightarrow[\text{QCD}]{}$$

$$\underbrace{\int_0^1 dx \frac{xF_3}{x}}_{\substack{\text{GLS Sum Rule}\\ \text{(measured)}}} = 3\left(\underbrace{1-\frac{\alpha_s}{\pi}}_{\substack{\text{In D\&O}\\ \text{program}}} - a(n_f)\left(\frac{\alpha_s}{\pi}\right)^2 - b(n_f)\left(\frac{\alpha_s}{\pi}\right)^3 - HO\right) - \Delta HT \tag{7.10}$$

where "HO" refers to higher-order terms in α_S, and "HT" refers to higher-twist terms. In the Duke and Owens program, the splitting functions and coefficient functions of Equations 7.12-7.20 are calculated only to next-to-leading-order (NLO) in α_s. The values of the NNLO and NNNLO coefficients for the GLS Sum Rule, $a(n_f)$ and $b(n_f)$, have been calculated. The higher-order calculable contributions subtract about 15% from the GLS Sum Rule at the Q_0^2 of this analysis [Har95]. Hence the Duke and Owens' program's apparent "violation" of the Fermion Conservation rule is most likely related to the higher-order corrections that are needed at low Q^2.

The need to remove the constraint of the Fermion Conservation Rule from the QCD analysis has two implications:

- The value of $\Lambda_{\overline{\text{MS}}}$ from this analysis is determined from a NLO QCD fit. When converting $\Lambda_{\overline{\text{MS}}}^{\text{NLO}}$ to $\alpha_S(Q^2)$, only the NLO expression of Equation 7.4 should be used.

- Although the NNLO and NNNLO splitting functions and hard-scattering coefficients are not yet available, the corresponding corrections to the GLS Sum Rule are. It should therefore be possible to independently determine $\alpha_S(Q^2)$ to NNNLO from this data by fitting the measured $\int dx\, xF_3/x$ to the form of Equation 7.10. Deborah Harris and Columbia student John Kim are preparing this analysis from the data presented in this thesis.

Another reason for difficulties in applying the Fermion Conservation Rule to a fit involving the CCFR data is the possible nuclear dependence of $\int dx\, xF_3/x$. However, theoretical predictions [Sid95] indicate that this effect should be less than 1% over the (x,Q^2) range of this data.

7.1.2.2 The Momentum Sum Rule

The Momentum Sum Rule states that the total momentum of the proton is carried by the quarks and the gluons:

$$\int_0^1 \left(xq_S(x,Q_0^2) + xG(x,Q_0^2) \right) dx = 1 \tag{7.11}$$

In the analyses of Refs. [Olt89, Leu91, Qui92], the Momentum Sum Rule was used to constrain the value of A_G.

Given the parameterizations of xq_S and xG shown in Equations 7.2 and 7.3, the values of the distributions at low x contribute the dominant part of this integral. However, the cut of $Q^2 > 5$ applied in the QCD fit implies an effective x cut in our data; Figures 6.19 and 6.21 illustrate this. The low-x data that would form the major constraint on the integral of Equation 7.11 is not included in the fit, and so the value of the Momentum Sum Rule

would depend mostly on the parameterizations chosen for q_S and G. Hence, the Momentum Sum Rule was removed as a constraint in the QCD fit.

It should be noted that this decision was based solely on the basis of maintaining the rigor of the analysis. The presence or absence of the Momentum Sum Rule constraint has a small effect on the QCD fit: removing the constraint reduces Λ by 15 MeV and reduces the χ^2 by 3 units for 164 degrees of freedom.

7.1.3 Evolution Equations

Given a set of parton distributions parameterized at Q_0^2, QCD predicts the parton distributions at any other Q^2. The evolution equations (1.81-1.83) are implemented in the Duke and Owens program by:

$$\frac{dq^{NS}(x,s)}{ds} = t\frac{\alpha_S(t)}{2\pi}\int_x^1 \frac{dy}{y} q^{NS}(y,s)\, P_{qq}\left(\frac{x}{y}\right) \tag{7.12}$$

$$\frac{dq^{S}(x,s)}{ds} = t\frac{\alpha_S(s)}{2\pi}\int_x^1 \frac{dy}{y}\left[q^{S}(y,s)\, P_{qq}^{S}\left(\frac{x}{y}\right) + G(y,s)\, P_{qG}\left(\frac{x}{y}\right)\right] \tag{7.13}$$

$$\frac{dG(x,s)}{ds} = t\frac{\alpha_S(s)}{2\pi}\int_x^1 \frac{dy}{y}\left[q^{S}(y,s)\, P_{Gq}\left(\frac{x}{y}\right) + G(y,s)\, P_{GG}\left(\frac{x}{y}\right)\right] \tag{7.14}$$

where

$$t = \ln\left(Q^2/\Lambda^2\right) \tag{7.15}$$

$$s = \ln\left[\ln\left(Q^2/\Lambda^2\right)\Big/\ln\left(Q_0^2/\Lambda^2\right)\right] = \ln\left(t/t_0\right) \tag{7.16}$$

$$q^{NS}(x,Q^2) = \sum_i \left(q^i - \bar{q}^i\right) = u_V + d_V \tag{7.17}$$

$$q^S(x,Q^2) = \sum_i \left(q^i + \bar{q}^i\right) \tag{7.18}$$

$G(x,Q^2)$ is the gluon distribution, and the P's are the splitting functions described in Section 1.2.4.3. The NLO splitting functions in the $\overline{\text{MS}}$ scheme are given in Refs. [Flo81, Her80].

Given the parton distributions of Equations 7.1-7.3, the QCD-evolution calculation proceeds as follows:

- Evaluate the slopes $\partial q(x,s)/\partial s$ from the right-hand side of Equation 7.12 (for an xF_3-only fit) or all three equations 7.12-7.14 (for a combined F_2 and xF_3 fit) at $Q^2 = Q_0^2$ (i.e., $s = 0$).

- Given the slopes $\partial q(x,s)/\partial s$ determined in the previous step, compute $q(x,s+\partial s)$ using a predictor-corrector method; also compute $G(x,s+\partial s)$ for combined fits.

- Let $s' = s + \partial s$. Compute the right-hand sides of Equations 7.12-7.14 for $q(x,s')$ and $G(x,s')$.

- Repeat the previous two steps until the entire Q^2 range of the experiment has been spanned in s.

The parton distributions q^{NS}, q^S, and G, are computed at discrete values of x and s and are stored in the program as a grid in (x_i, s_i). When the program requires a parton distribution at an arbitrary value of (x,s), it is obtained from the grid via a linear interpolation in s and a polynomial interpolation in x.

7.1.4 Hard-Scattering Integrals

To convert the parton distributions to the physically-measured structure functions, the hard-scattering integrals must be computed (see Section 1.2.4.4):

$$F_3(x,Q^2) = \int_x^1 dy \left[C_3^q\left(\frac{x}{y},Q^2\right) q^{NS}(x,Q^2) \right] \tag{7.19}$$

$$x^{-1}F_2(x,Q^2) = \int_x^1 dy \left[C_2^q\left(\frac{x}{y},Q^2\right) q^S(x,Q^2) + C_2^G\left(\frac{x}{y},Q^2\right) G(x,Q^2) \right] \tag{7.20}$$

The formulae for the hard-scattering coefficient functions C_i to NLO in the $\overline{\text{MS}}$ scheme are given in Ref. [Her80].

7.1.5 Target Mass Correction

In the derivation of the structure-function formalism in Section 1.2.2, the target and constituent quark masses were ignored in deriving the Q^2-dependence of the structure functions. In the non-perturbative regime of large x and small Q^2, the assumption of zero target mass is no longer valid. The target mass correction [Geo76] gives the correction of the structure-functions in Equation 1.27 relative to the observed structure functions. These corrections are:

$$F_2^{TMC} = \frac{x^2}{k^2}\frac{F_2^{QCD}(\xi,Q^2)}{\xi^2} + \frac{6M^2}{Q^2}\frac{x^3}{k^4}I_1 + \frac{12M^4}{Q^4}\frac{x^4}{k^5}I_2 \tag{7.21}$$

$$xF_3^{TMC} = \frac{x^2}{k^2}\frac{xF_3^{QCD}(\xi,Q^2)}{\xi^2} + \frac{2M^2}{Q^2}\frac{x^3}{k^3}I_3 \tag{7.22}$$

where

$$k = \left(1 + \frac{4x^2 M^2}{Q^2}\right)^{\frac{1}{2}} \tag{7.23}$$

$$\xi = \frac{2x}{1+k} \tag{7.24}$$

$$I_1 = \int_\xi^1 du \frac{F_2^{QCD}(u,Q^2)}{u^2} \tag{7.25}$$

$$I_2 = \int_\xi^1 du \int_u^1 dv \frac{F_2^{QCD}(v,Q^2)}{v^2} \tag{7.26}$$

$$I_3 = \int_\xi^1 du \frac{xF_3^{QCD}(u,Q^2)}{u^2} \tag{7.27}$$

7.1.6 Higher-Twist Effects

As the nucleon structure is probed to values below $Q^2 \sim 5\ GeV^2$, perturbative QCD begins to fail. The deviation of the observed structure-function evolution from the predicted evolution of Equations 7.12-7.14 is expressed in terms involving powers of $1/Q^2$. These terms are collectively known as "higher-twist" effects (HT). Some higher-twist effects have been calculated (e.g.; the target mass correction described in the previous Section), but a complete calculation of all higher-twist effects to all powers of Q^2 is not yet available. The higher-twist correction is expressed as

$$F^{\text{Measured}} = F^{\text{Perturbative QCD Prediction}} \left(1 + \frac{D_2(x)}{Q^2} + \frac{D_4(x)}{Q^4} + \ldots\right) \tag{7.28}$$

where $F = F_2$ or xF_3.

A measurement of the higher-twist effects in F_2 was performed using the combined electron scattering data at SLAC and the muon scattering data from BCDMS [Vir92]. In the referenced paper, the QCD prediction of $F_2^{\ell D}$ with the target mass effects applied was compared against the SLAC/BCDMS measurements; the deviation was attributed to the higher-twist effects. Similar analyses have been performed on neutrino deep-inelastic scattering data by Sidorov. One analysis was based on the previous CCFR analysis of data from E744 and E770 [Sid96a], and the other was based on all other neutrino scattering data available apart from CCFR [Sid96b]. As might be expected, the effects were most important in the region of high x and low Q^2, in the kinematic region where perturbative QCD is expected to fail.

Recently, a renormalon-based theoretical calculation of the higher-twist effects has become available [Das96, Dok95]; since the authors of the first referenced paper are Dasgupta and Webber, this collaboration denotes the calculation as the "D&W calculation." Figures 7.1 and 7.2 display the results of the D&W calculation for D_2 and D_4, along the F_2 higher-twist measurement from Ref. [Vir92]. Figure 7.3 displays the result of the D&W calculation for the xF_3 D_2 term only, along the with the NLO results from Refs. [Sid96a, Sid96b].

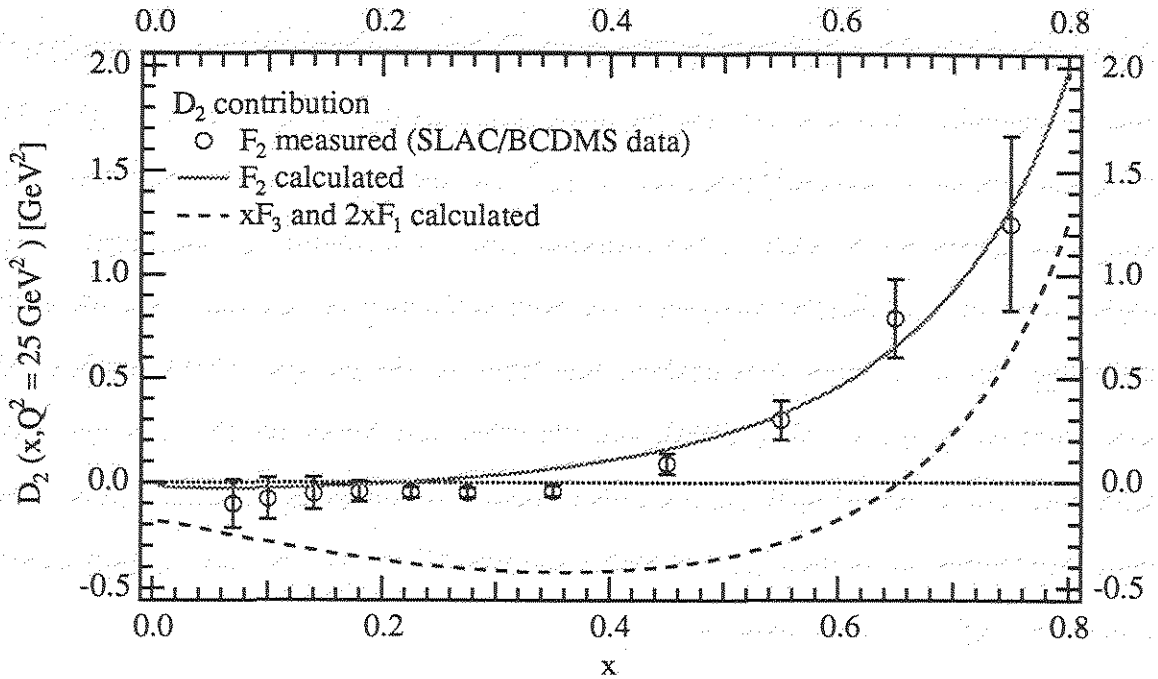

Figure 7.1: D_2 higher-twist term as calculated in Refs. [Das96, Dok95]. The measurement of the F_2 D_2 term from Ref. [Vir92] is included.

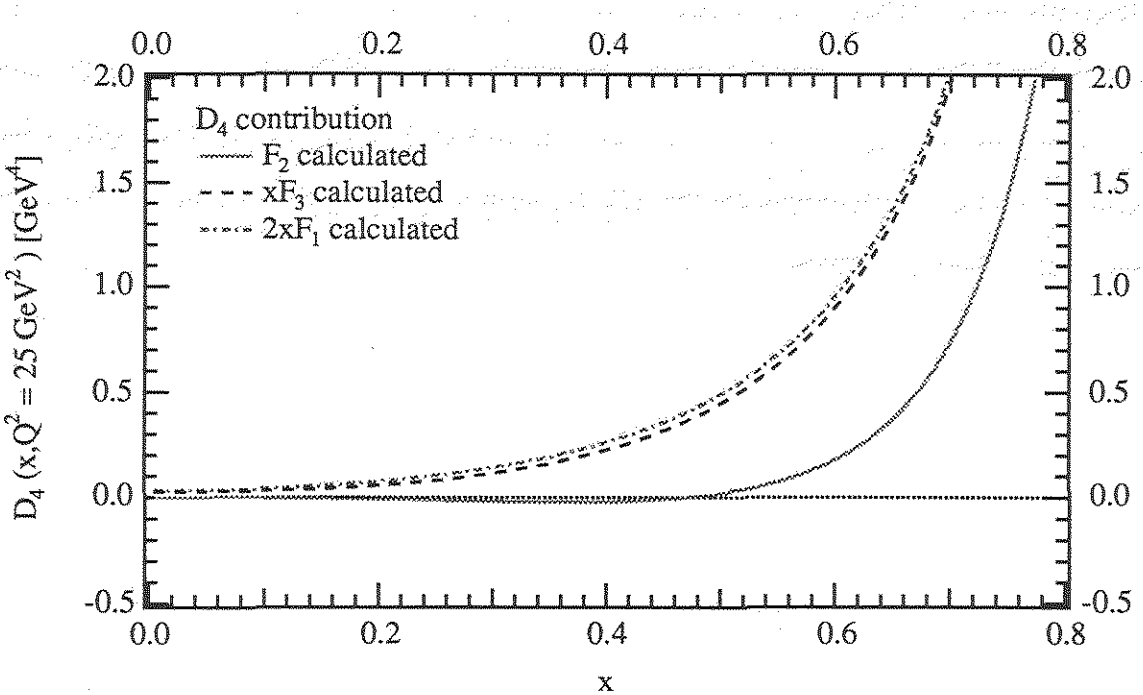

Figure 7.2: D_4 higher-twist term as calculated in Refs. [Das96, Dok95]. Bryan Webber is thanked for the program that generated these two Figures.

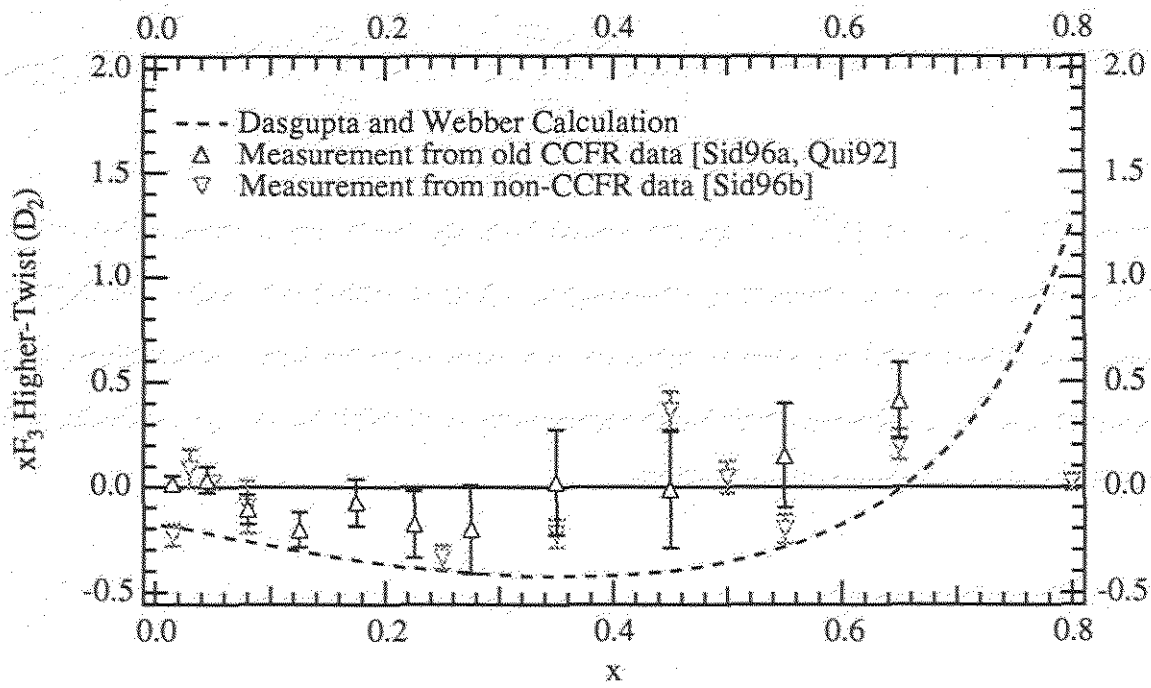

Figure 7.3: xF_3 D_2 higher-twist term as calculated in Refs. [Das96, Dok95]. The measurement of the xF_3 D_2 term from Refs. [Sid96a, Sid96b] is included.

The measurement of the xF_3 D_2 term in Figure 7.3 displays a smaller value for the higher-twist term than the D&W calculation, and this measurement is based in part on the previous CCFR data which is superseded by the present analysis. While the values of the D&W calculation agree with the F_2 D_2 measurement, the measurement was made assuming a value of $\alpha_S(M_Z^2) = 0.113$ which is lower than the present CCFR analysis indicates (see below); this would tend to increase the measured value of the higher-twist term.

Given the above uncertainties in the measurement and calculation of the higher-twist terms, this analysis makes a conservative estimate of the error due to higher-twist effects. The central value of the higher-twist applied to the QCD fit was taken to be

$$F^{\text{Theory}} = F^{\text{Perturbative QCD Prediction}} \left(1 + \frac{S \times D_2^{DW}(x)}{Q^2} + \frac{S \times D_4^{DW}(x)}{Q^4} \right) \tag{7.29}$$

where $D_2^{DW}(x)$ and $D_4^{DW}(x)$ are the values from the D&W calculation, and $S = 0.5$. The systematic error is obtained by repeating the QCD fit with $S = 0$ (that is, no higher-twist correction) and $S = 1$ (that is, using the full value from the D&W calculation). The result is that the systematic error due to higher-twist is 17 MeV for the xF_3-only fit, and 13 MeV for the combined F_2 and xF_3 fit.

7.1.7 Forming the χ^2

The previous sections described how the program calculates xF_3^{theory} and F_2^{theory}. The χ^2 calculation that compares the data with the theory in the combined F_2 and xF_3 fit must incorporate the statistical errors ΔF_2, ΔxF_3, and $\Delta F_2 \Delta xF_3$. Defining the structure-function vector as

$$\vec{\mathbf{F}} = \begin{pmatrix} F_2(x,Q^2) \\ xF_3(x,Q^2) \end{pmatrix} \tag{7.30}$$

and the structure-function error matrix

$$\hat{\mathbf{V}} = \begin{pmatrix} (\Delta F_2)^2 & \Delta F_2 \Delta xF_3 \\ \Delta F_2 \Delta xF_3 & (\Delta xF_3)^2 \end{pmatrix} \tag{7.31}$$

Then the χ^2 is calculated by summing over all the (x,Q^2) bins that pass the cuts:

$$\chi^2 = \sum_{(x,Q^2)\text{bins}} \left[\left(\vec{\mathbf{F}}^{data} - \vec{\mathbf{F}}^{theory} \right)^{\mathrm{T}} \hat{\mathbf{V}}^{-1} \left(\vec{\mathbf{F}}^{data} - \vec{\mathbf{F}}^{theory} \right) \right] \tag{7.32}$$

$$= \sum_{(x,Q^2)\text{bins}} \begin{bmatrix} \left(F_2^{theory} - F_2^{data}\right)^2 v_{22} \\ + \left(xF_3^{theory} - xF_3^{data}\right)^2 v_{33} \\ +2\left(F_2^{theory} - F_2^{data}\right)\left(xF_3^{theory} - xF_3^{data}\right) v_{23} \end{bmatrix} \tag{7.33}$$

where

$$\hat{\mathbf{V}}^{-1} = \begin{bmatrix} v_{22} & v_{32} \\ v_{23} & v_{33} \end{bmatrix} = \frac{1}{\det \hat{\mathbf{V}}} \begin{bmatrix} \left(\Delta xF_3\right)^2 & -\Delta F_2 \Delta xF_3 \\ -\Delta F_2 \Delta xF_3 & \left(\Delta F_2\right)^2 \end{bmatrix} \tag{7.34}$$

and $v_{23} = v_{32}$. As a check, it can be noted that if $\Delta F_2 \Delta xF_3 = 0$, Equation 7.32 becomes (independently for F_2 and xF_3) $\chi^2 = \sum_{(x,Q^2)\text{bins}} \left(f^{data} - f^{theory}\right)^2 / \Delta f^2$, the familiar expression for calculating a χ^2.

7.2 Tests of QCD

7.2.1 Fit Results

As described above, the parameters $\Lambda_{\overline{\text{MS}}}$, η_1, η_2, A_{NS} and, for combined F_2 and xF_3 fits, A_S, η_S, A_G, η_G, are varied by MINUIT to minimize the χ^2 between NLO QCD and the data. The following cuts are applied to the structure-function data:

- $Q^2 > 5GeV^2$ and $W^2 > 10GeV^2$ – to eliminate the non-perturbative region [Bel88, Bel92], and to minimize the effects of any higher-twist corrections to the QCD fit (see Section 7.1.6).

- $x < 0.7$ – to eliminate the region with large Fermi-motion and Monte-Carlo corrections (see Section 6.1.3).

- The relative statistical error (both $\Delta xF_3 / xF_3$ and $\Delta F_2 / F_2$) must be less than 0.5. This cut was chosen to eliminate bins with poor statistics.

The results of the fits are given in Table 7.1; Tables 7.2 and 7.3 give the error matrix and correlation matrix for the xF_3-only fit; Table 7.4 and 7.5 give the error matrix and correlation matrix for the combined F_2 and xF_3 fit. Figures 6.19 through 6.22 show the results of the QCD fit graphically, in x bins as a function of Q^2; Figures 7.4 and 7.5 show the same fit in Q^2 bins as a function of x.

The statistical error on $\Lambda_{\overline{\text{MS}}}$ from the combined F_2 and xF_3 fit is roughly half that of the xF_3-only fit; this is the result of including the additional F_2 data in the fit. Even though the values of $F_2 \approx xF_3$ for $x > 0.5$ (see Section 6.5), the statistical error on F_2 is smaller, and hence the statistical error on $\Lambda_{\overline{\text{MS}}}$ is smaller, because xF_3 is determined by the *difference* between the number of neutrino and anti-neutrino events, but F_2 is determined by the *sum* of neutrino and anti-neutrino events.

The χ^2/DOF from the combined fit indicates a lower probability than that from the xF_3 fit. The increase in χ^2 is uniformly distributed over the kinematic region of the fit. This increase is caused by the smaller F_2 statistical errors, which make the χ^2 of the fit more sensitive to systematic effects. The global systematic fits described in the next section deal with the effects of the systematic errors on the χ^2 and greatly improve the quality of the fit.

Table 7.1: Results of QCD fits to the structure functions. "Prob" is the integrated upper tail of the χ^2 distribution for the given number of degrees of freedom (DOF). "FSR" is the value of the left-hand side of the integral in the Fermion Sum Rule in Equation 7.7. "MSR" is the value of the left-hand side of the integral of the Momentum Sum Rule in Equation 7.11.

Number		xF_3-only fit	F_2 and xF_3 fit
1	$\Lambda_{\overline{MS}}$ $[MeV]$	387 ± 42	381 ± 24
2	η_1	0.801 ± 0.010	0.804 ± 0.008
3	η_2	3.88 ± 0.03	3.91 ± 0.02
4	A_{NS}	8.57 ± 0.20	8.65 ± 0.16
5	A_S		1.52 ± 0.02
6	η_S		7.82 ± 0.09
7	A_G		1.94 ± 0.24
8	η_G		4.44 ± 0.65
	χ^2 / DOF	81.4 / 82	190.6 / 164
	Prob	50%	8%
	FSR	2.84	2.85
	MSR		0.93

Table 7.2: Error matrix σ_{ij} from the xF_3-only fit. The parameter numbers are defined in Table 7.1.

Number	1	2	3	4
1	0.152E-02	0.102E-04	0.654E-03	-0.167E-02
2	0.102E-04	0.941E-04	0.224E-03	0.180E-02
3	0.654E-03	0.224E-03	0.931E-03	0.393E-02
4	-0.167E-02	0.180E-02	0.393E-02	0.385E-01

Table 7.3: Correlation coefficients $\left(\sigma_{ij}\right)/\left(\sigma_{ii}\sigma_{jj}\right)^{1/2}$ from the xF_3-only fit. The parameter numbers are defined in Table 7.1.

Number	GLOBAL	1	2	3	4
1	0.97748	1.000	0.027	0.550	-0.218
2	0.98502	0.027	1.000	0.757	0.946
3	0.97957	0.550	0.757	1.000	0.657
4	0.99372	-0.218	0.946	0.657	1.000

Table 7.4: Error matrix σ_{ij} from the combined F_2 and xF_3 fit. The parameter numbers are defined in Table 7.3.

#	1	2	3	4	5	6	7	8
1	0.484E-03	0.963E-06	-0.160E-03	0.670E-03	-0.125E-03	0.458E-03	-0.341E-02	-0.866E-02
2	0.963E-06	0.698E-04	0.145E-03	0.131E-02	0.993E-04	0.405E-03	-0.767E-04	-0.331E-03
3	-0.160E-03	0.145E-03	0.420E-03	0.276E-02	0.225E-03	0.779E-03	0.106E-02	0.239E-02
4	0.670E-03	0.131E-02	0.276E-02	0.269E-01	0.161E-02	0.950E-02	-0.629E-02	-0.186E-01
5	-0.125E-03	0.993E-04	0.225E-03	0.161E-02	0.319E-03	0.774E-03	0.162E-02	0.457E-02
6	0.458E-03	0.405E-03	0.779E-03	0.950E-02	0.774E-03	0.776E-02	-0.675E-02	-0.163E-01
7	-0.341E-02	-0.767E-04	0.106E-02	-0.629E-02	0.162E-02	-0.675E-02	0.556E-01	0.125E+00
8	-0.866E-02	-0.331E-03	0.239E-02	-0.186E-01	0.457E-02	-0.163E-01	0.125E+00	0.336E+00

Table 7.5: Correlation coefficients $\left(\sigma_{ij}\right)/\left(\sigma_{ii}\sigma_{jj}\right)^{1/2}$ from the combined F_2 and xF_3 fit. The parameter numbers are defined in Table 7.3.

#	GLOBAL	1	2	3	4	7	8	9	10
1	0.97237	1.000	0.005	-0.354	0.186	-0.318	0.236	-0.658	-0.680
2	0.99472	0.005	1.000	0.849	0.958	0.665	0.550	-0.039	-0.068
3	0.98531	-0.354	0.849	1.000	0.821	0.616	0.432	0.219	0.202
4	0.99737	0.186	0.958	0.821	1.000	0.549	0.658	-0.163	-0.196
7	0.95228	-0.318	0.665	0.616	0.549	1.000	0.492	0.385	0.442
8	0.94226	0.236	0.550	0.432	0.658	0.492	1.000	-0.325	-0.320
9	0.92182	-0.658	-0.039	0.219	-0.163	0.385	-0.325	1.000	0.918
10	0.95600	-0.680	-0.068	0.202	-0.196	0.442	-0.320	0.918	1.000

Table 7.6: QCD fit results as a function of the Q^2 cut on the data and the Q_0^2 of the evolution. "Prob" is the integrated upper tail of the χ^2 distribution for the given number of degrees of freedom (DOF). The $x < 0.7$ cut was applied to all the fits in this Table.

		xF_3-only fit			Combined F_2 and xF_3 fit			
Q_0^2	$Q^2_{\min}$	$\Lambda_{\overline{MS}}$	χ^2/DOF	Prob	$\Lambda_{\overline{MS}}$	η_G	χ^2/DOF	Prob
1	1	313 ± 39	124/106	11%	281 ± 12	2.83 ± 0.18	557/212	0%
1	5	390 ± 45	82/82	47%	272 ± 13	2.81 ± 0.33	366/164	0%
1	10	381 ± 47	59/59	49%	353 ± 28	3.17 ± 0.54	158/118	1%
1	15	392 ± 58	49/46	34%	392 ± 29	3.59 ± 0.64	107/ 92	13%
5	5	387 ± 42	81/82	50%	381 ± 24	4.44 ± 0.65	191/164	8%
5	10	422 ± 47	58/59	51%	381 ± 27	4.21 ± 1.55	138/118	10%
5	15	433 ± 53	50/46	31%	411 ± 37	4.00 ± 2.45	107/ 92	14%

Table 7.7: QCD fit results as a function of the x cut on the data. "Prob" is the integrated upper tail of the χ^2 distribution for the given number of degrees of freedom (DOF). $Q^2 = 5$ and $Q_0^2 = 5$ for all the fits in this Table.

	xF_3-only fit			Combined F_2 and xF_3 fit			
$x_{\max}$	$\Lambda_{\overline{MS}}$	χ^2/DOF	Prob	$\Lambda_{\overline{MS}}$	η_G	χ^2/DOF	Prob
.5	348 ± 49	62/70	74%	352 ± 27	4.99 ± 0.72	159/170	13%
.6	355 ± 43	72/77	65%	373 ± 23	4.62 ± 0.64	172/154	15%
.7	387 ± 42	81/82	50%	381 ± 24	4.44 ± 0.65	191/164	8%
.8	391 ± 40	86/86	48%	372 ± 20	4.61 ± 0.53	218/172	1%

The values of $\Lambda_{\overline{\text{MS}}}$ from both fits are consistent with one another. This is an important check on the values of A_G and η_G, since the gluon distribution can only be determined indirectly by the co-evolution of the singlet and gluon distributions from Equation 7.13 and 7.14. The value of $\Lambda_{\overline{\text{MS}}}$ and the shape of the gluon distribution are correlated: the correlation coefficient between $\Lambda_{\overline{\text{MS}}}$ and η_G is 68%. If $\Lambda_{\overline{\text{MS}}}$ from the non-singlet and combined fits had *not* agreed with each other, it might be concluded that the assumptions being made about the gluon shape and evolution were biasing the fit somehow. Since the values of $\Lambda_{\overline{\text{MS}}}$ from the fits agree, it can be assumed that the values of A_G and η_G represent a valid measurement of the gluon distribution.

It is possible that the cuts made on the data have biased the QCD fit in some way. As a check, the QCD fits were repeated for different values of the x and Q^2 cut. Tables 7.6 and 7.7 show the results of this study. For the fits that evolve from $Q_0^2 = 1$, the poor χ^2 of the combined fit indicates that the predictions of perturbative QCD are not suitable for this kinematic region. For the fits that evolve from $Q_0^2 = 5$, the χ^2 of the combined fit does not lead to a "preferred" Q^2 cut, and so the fit with the greatest number of data points was chosen. For the fits for different x cuts, only the fit for $x < 0.8$ is poor, but the smearing corrections on the data at $x = 0.75$ are large, as noted in Section 6.1.3. The fit for $x < 0.7$ is chosen since the χ^2 is good and it includes the most data points.

Another possibility is that the choice of the functional form of the parameterization in Equation 7.1 may bias the fit to a particular value for $\Lambda_{\overline{\text{MS}}}$. Table 7.8 shows the values of $\Lambda_{\overline{\text{MS}}}$ determined from fits using different functional forms for q_{NS}. The results show that the value of $\Lambda_{\overline{\text{MS}}}$ does not depend on the particular parameterization used in the fit. Table 7.9 shows the values for one set of alternate parameterizations.

Table 7.8: QCD fit results for xF_3-only fits for different functional forms of q_{NS}. "Prob" is the integrated upper tail of the χ^2 distribution for the given number of degrees of freedom (DOF). The $x < 0.7$ cut was applied, and $Q^2 = 5$ and $Q_0^2 = 5$ for all the fits in this Table. Functional form (1) was used for the results presented in this thesis; form (2) was used for the E616/E701 results reported in Ref. [Olt89]; form (3) was used in the preliminary QCD fits to the E744/E770 data [Qui92, Leu91]; form (4) was suggested [Zhi93] to look for two-nucleon correlations using QCD fits. The values of $\Lambda_{\overline{MS}}$ obtained from using any of these functional forms are consistent with one another, and the χ^2 of the fits do not suggest that any of these forms should be preferred.

Number	xq_{NS}	$\Lambda_{\overline{MS}}$	χ^2/DOF	Prob
1	$Ax^{\eta_1}(1-x)^{\eta_2}$	387 ± 42	81/82	50%
2	$Ax^{\eta_1}(1-x)^{\eta_2}(1+\gamma x)$	394 ± 41	80/81	50%
3	$Ax^{\eta_1}(1-x)^{\eta_2} + Bx^{\eta_3}$	387 ± 36	81/80	44%
4	$Ax^{\eta_1}(1-x)^{\eta_2} + Bx^{\eta_1}(1-x/2)^{\eta_3}$	390 ± 61	81/82	50%

Table 7.9: The values for one alternate parameterization of the parton distributions. "Prob" is the integrated upper tail of the χ^2 distribution for the given number of degrees of freedom (DOF). "FSR" is the value of the left-hand side of the integral in the Fermion Sum Rule in Equation 7.7. "MSR" is the value of the left-hand side of the integral of the Momentum Sum Rule in Equation 7.11. The values of $\Lambda_{\overline{MS}}$ from both the xF_3-only and combined F_2 and xF_3 fit are consistent with one another. The alternate parameterizations used for this fit at $Q_0^2 = 5GeV^2$ are

$$xq_{NS} = A_{NS} x^{\eta_1} (1-x)^{\eta_2} (1+\gamma x)$$
$$xq_S = xq_{NS} + A_S x^{\eta_R} (1-x)^{\eta_S} (1+\gamma_S x)$$
$$xG = A_G x^{\eta_F} (1-x)^{\eta_G} (1+\gamma_G x)$$

	xF_3-only fit	F_2 and xF_3 fit
$\Lambda_{\overline{MS}}$ $[MeV]$	394 ± 41	368 ± 25
η_1	0.78 ± 0.03	0.78 ± 0.02
η_2	4.01 ± 0.12	3.99 ± 0.08
A_{NS}	8.00 ± 0.64	8.04 ± 0.52
γ	0.31 ± 0.33	0.25 ± 0.24
A_S		1.61 ± 0.13
η_R		0.02 ± 0.02
η_S		5.74 ± 0.36
γ_S		-1.79 ± 0.15
A_G		5.51 ± 3.61
η_F		0.33 ± 0.20
η_G		4.91 ± 1.29
γ_G		-1.44 ± 0.76
χ^2 / DOF	80 / 81	181 / 159
Prob	49%	11%
FSR	2.87	2.85
MSR		0.90

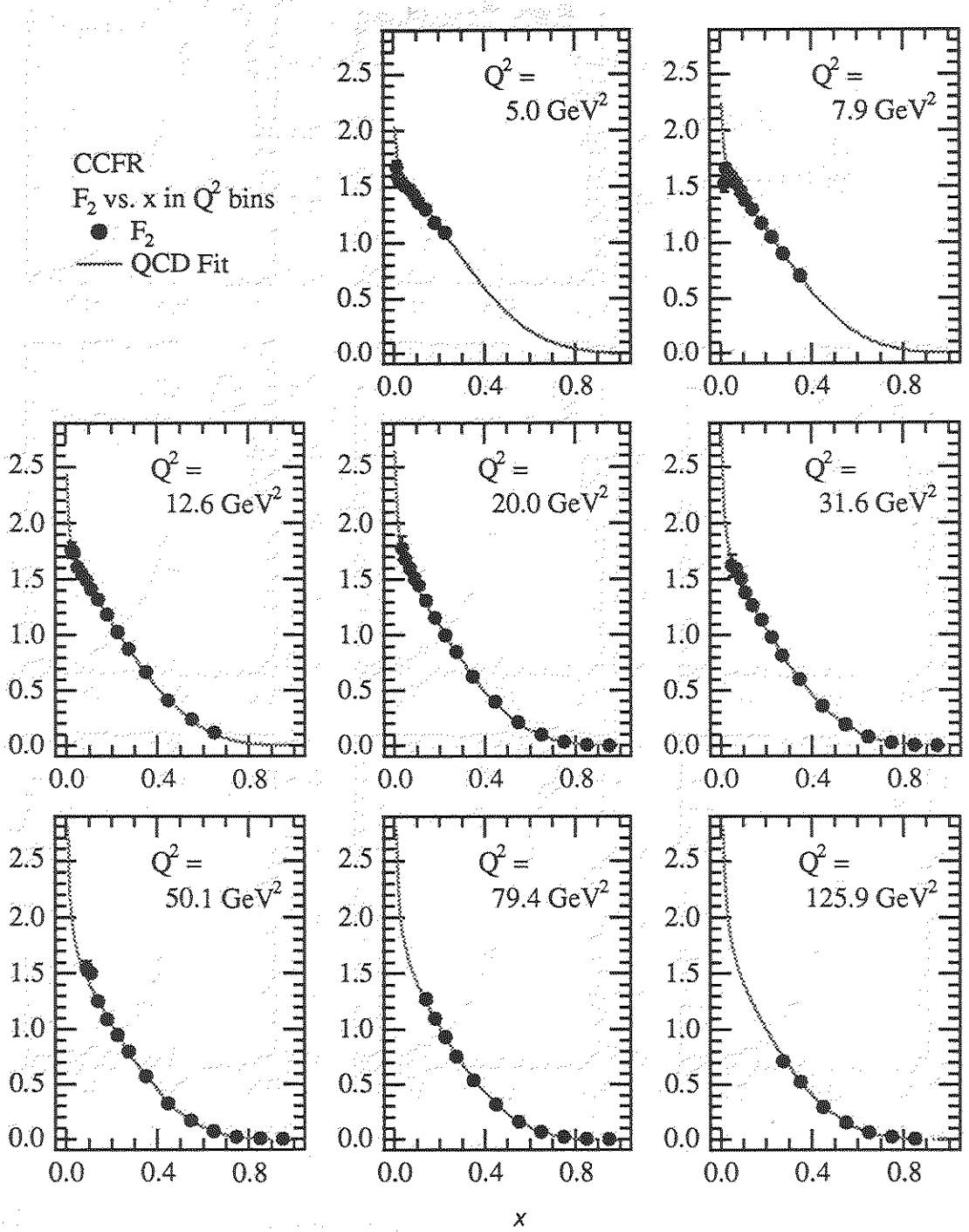

Figure 7.4: F_2 versus x in Q^2 bins. The line is the QCD fit to the data.

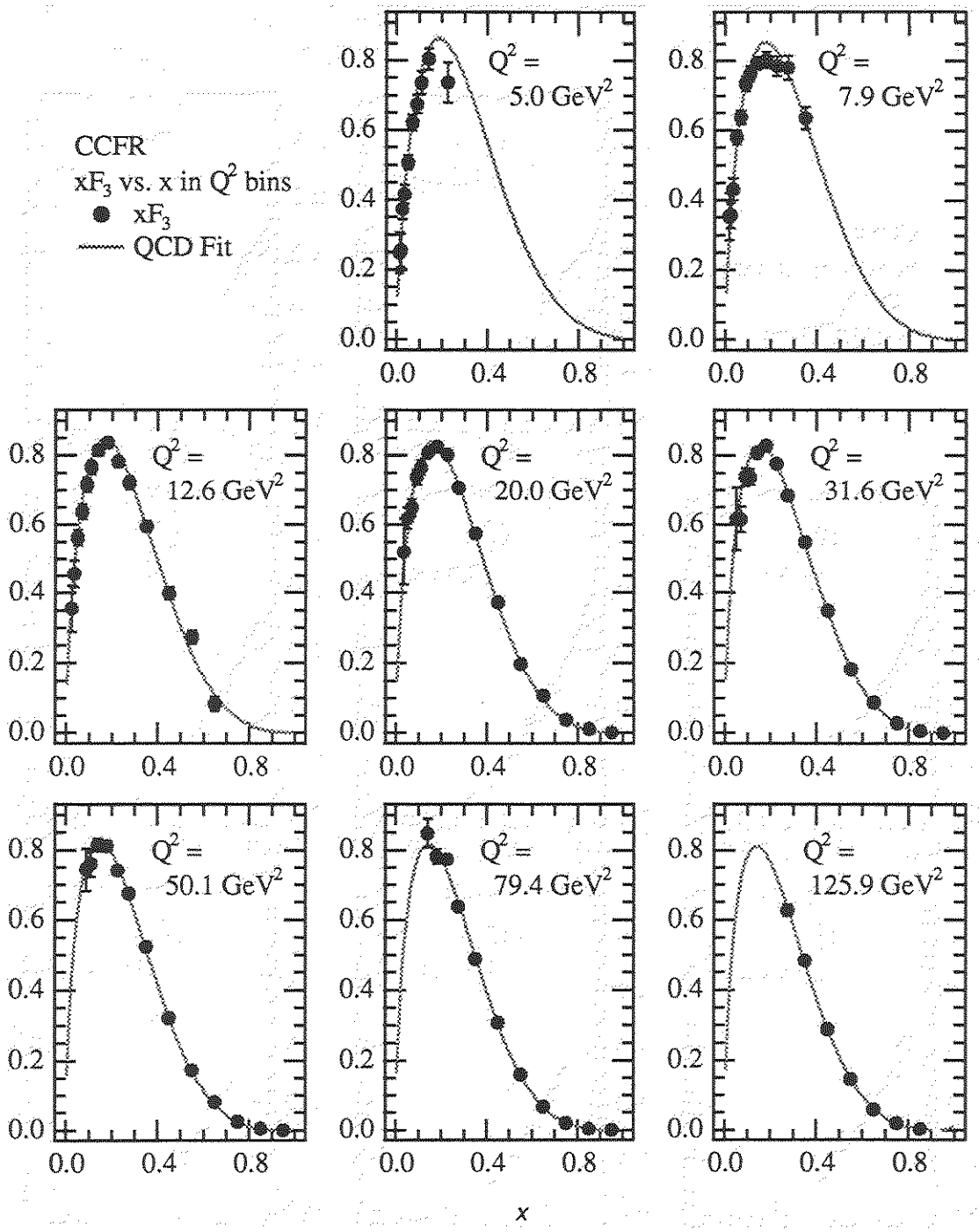

Figure 7.5: xF_3 versus x in Q^2 bins. The line is the QCD fit to the data.

7.2.2 Logarithmic Slopes

Plots of the logarithmic slopes provide a visual summary of the comparison between structure functions and QCD predictions, and verify that the data is consistent with the theory. These plots are also of historical significance, since the CCFR collaboration was the first to show agreement between the Q^2 evolution of both F_2 and xF_3 and the theory of QCD [Qui92].

The logarithmic slope of xF_3, $\left(d\ln xF_3\right)/\left(d\ln Q^2\right)$, is determined by fitting the xF_3 data separately within each x-bin to a power-law form:

$$xF_3\left(Q^2\right) = A \times \left(Q^2\right)^C \Rightarrow \frac{d\ln xF_3}{d\ln Q^2} = C \tag{7.35}$$

The relationship between $\Lambda_{\overline{\mathrm{MS}}}$ and the logarithmic slopes is illustrated in Figure 7.6, which shows the slopes for xF_3 for different values of $\Lambda_{\overline{\mathrm{MS}}}$. This family of curves shows that the value of $\Lambda_{\overline{\mathrm{MS}}}$ is primarily determined by the high-x data. Since $F_2 \approx xF_3$ at $x >$ 0.5 (see Section 6.5), this implies that the value of $\Lambda_{\overline{\mathrm{MS}}}$ from either the xF_3-only fit or the combined F_2 and xF_3 fit should be the same. Indeed, Table 7.1 shows that this is the case. Another consequence of the QCD theory is that the point in x at which the xF_3 slopes vanish should be almost independent of $\Lambda_{\overline{\mathrm{MS}}}$ [Dev83]; this is seen in Figure 7.6. In leading-order QCD the "cross-over point" of the family of logarithmic slopes is exactly at $\left(d\ln xF_3\right)/\left(d\ln Q^2\right) = 0$, but this is shifted in NLO due to weak dependence of the splitting functions on α_S.

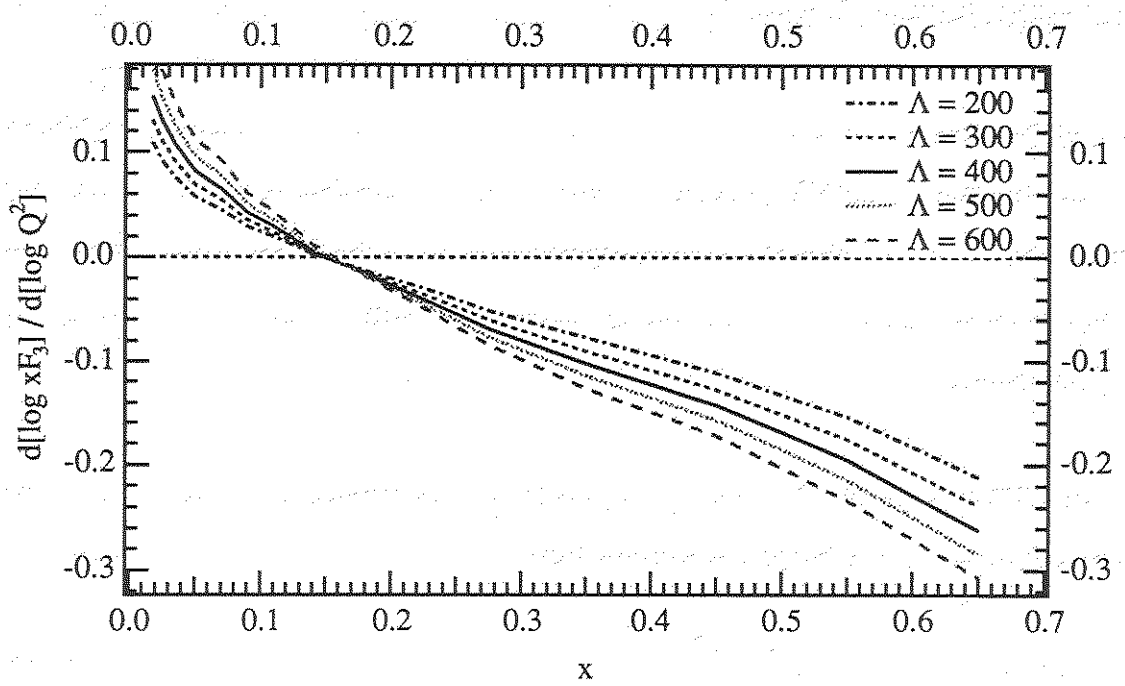

Figure 7.6: QCD prediction of logarithmic slopes of xF_3 for various values of Λ.

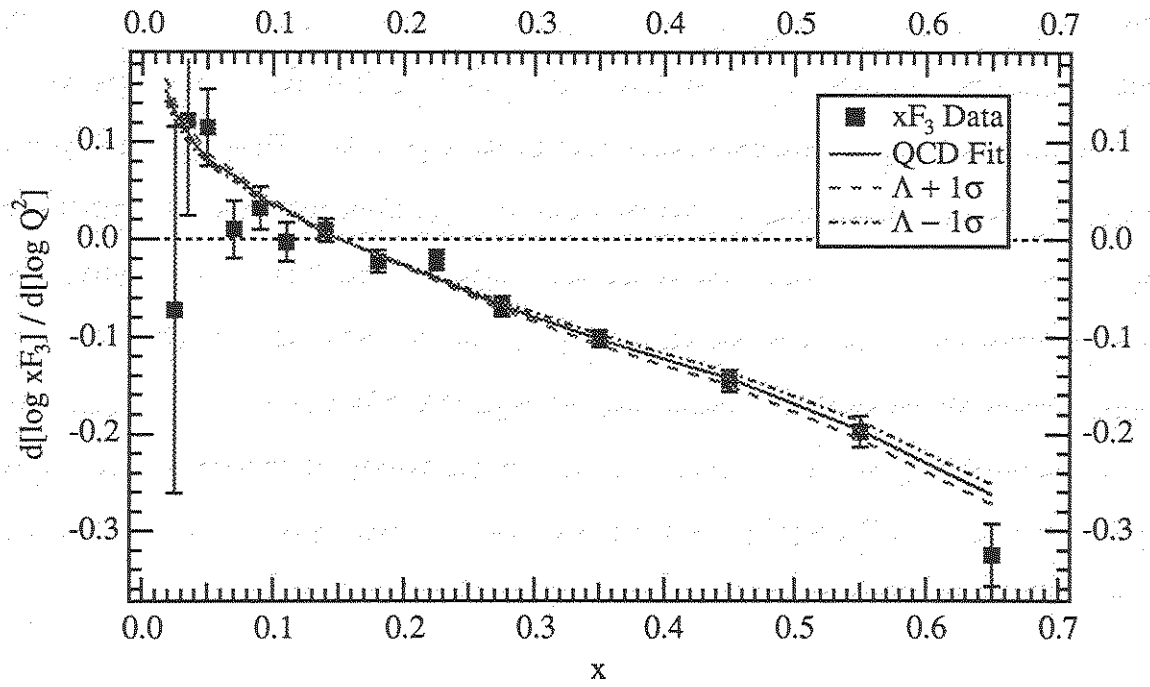

Figure 7.7: The logarithmic slopes of xF_3. The slopes from the QCD fit are plotted as a solid line. The $\pm 1\sigma$ variations in $\Lambda_{\overline{MS}} = 387 \pm 42\ MeV$ from the xF_3-only fit (dashed lines) are plotted to show the sensitivity of $\Lambda_{\overline{MS}}$ to the data.

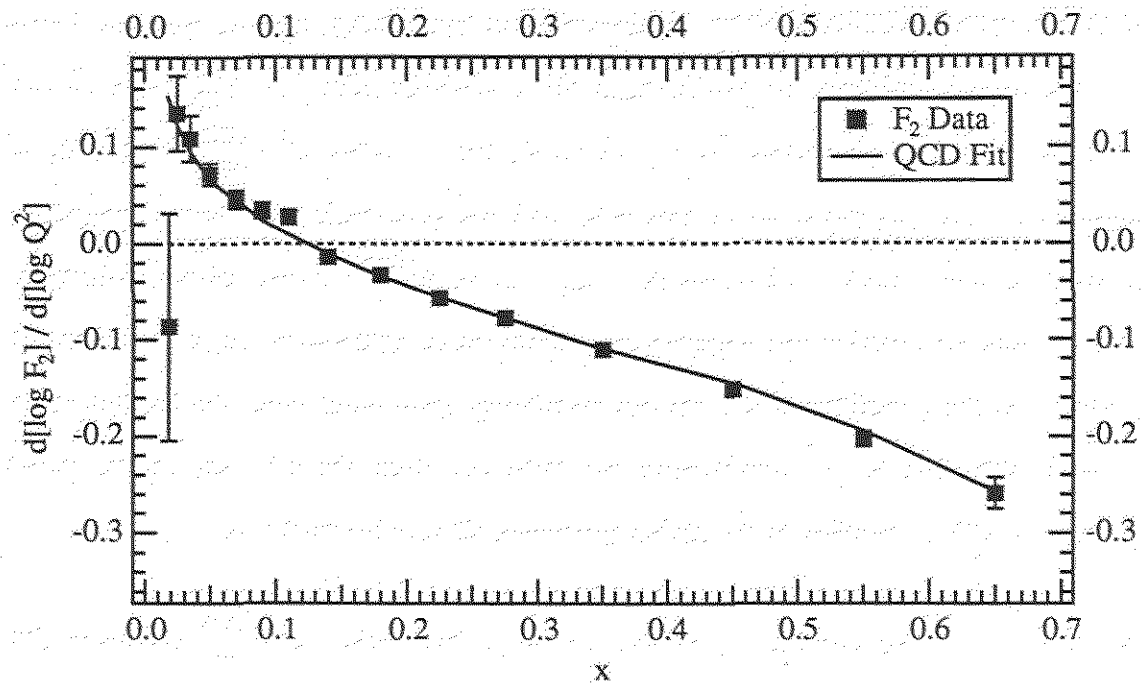

Figure 7.8: The logarithmic slopes of F_2. The slopes from the QCD fit are plotted as a solid line.

Figure 7.7 shows the comparison between the logarithmic slopes of xF_3 with the slopes from the xF_3-only QCD fit; the slopes for the $\pm 1\sigma$ variation in $\Lambda_{\overline{MS}}$ are also plotted. Figure 7.8 shows the corresponding plot for the slopes of F_2, with the QCD from the combined F_2 and xF_3 fit; the slopes for a $\pm 1\sigma$ $\Lambda_{\overline{MS}}$ variation are not included because on the scale of the plot a ± 20 *MeV* shift would be barely visible.

7.2.3 Systematic Errors

This section discusses a basic approach to determining the systematic errors in the measurement of $\Lambda_{\overline{MS}}^{NLO}$. This approach is appropriate for *testing* QCD in the context of the systematic errors on the structure functions. Section 7.3 discusses another approach that *assumes* QCD and improves upon the measurement of $\Lambda_{\overline{MS}}^{NLO}$ in that context.

The experimental systematic errors are described in Section 6.4, and are listed in Table 7.10. The basic approach for determining the systematic error in $\Lambda_{\overline{\mathrm{MS}}}^{\mathrm{NLO}}$ due to the systematic error in a given quantity k is to fit F_k for the value of $\Lambda_{\overline{\mathrm{MS}}}^{\mathrm{NLO}}$, where F_k is obtained by extracting the structure functions with the systematic parameter changed by one standard error. Table 7.11 shows the variations in $\Lambda_{\overline{\mathrm{MS}}}^{\mathrm{NLO}}$ for each of the systematic errors for both the positive and negative systematic shifts, along with the χ^2 of the fit to F_k. Note that the variations of Λ_k are not necessarily symmetric about the central value Λ, nor is the shift in χ^2 necessarily the same for both the $\pm 1\delta$ variations; these asymmetries will be handled in the global systematic fit (see Section 7.3).

Table 7.12 shows the average systematic variation. The value of $\Lambda_{\overline{\mathrm{MS}}}^{\mathrm{NLO}}$ shown is the average of that obtained from a shift of $\pm 1\delta$ in the systematic quantity:

$$\frac{\left(\Lambda_k(1\delta)-\Lambda\right)}{\left|\left(\Lambda_k(1\delta)-\Lambda\right)\right|}\times\frac{\left|\left(\Lambda_k(1\delta)-\Lambda\right)\right|+\left|\left(\Lambda_k(-1\delta)-\Lambda\right)\right|}{2} \tag{7.36}$$

The total systematic error at the end of Table 7.12 is the sum of the individual systematic errors added in quadrature; the statistical and systematic errors in $\Lambda_{\overline{\mathrm{MS}}}^{\mathrm{NLO}}$ and η_G are summed in quadrature in the last line of the Table.

From Table 7.12, it can be seen that the largest source of systematic error in $\Lambda_{\overline{\mathrm{MS}}}^{\mathrm{NLO}}$ are the energy-calibration systematic errors, the muon-calibration error in particular, and the model parameterization error. The combined F_2 and xF_3 fit is, in general, less sensitive to systematic effects than the xF_3-only fit; the greatest reduction is in the systematic error due to $\sigma^{\bar{\nu}}/\sigma^{\nu}$.

Table 7.10: Systematic quantities and their $+1\delta$ variations as defined in Chapter 6. The percentage variation is given where appropriate.

Systematic Quantity	Central Value	$+1\delta$ Variation	Percentage Variation
C_{HAD}^{744}	Test Beam		1%
C_{HAD}^{770}	Test Beam		1%
ΔE_{HAD}	+150 MeV	100 MeV	
C_{μ}	Test Beam		1%
ΔE_{μ}	0	100 MeV	
$(B/A)_{744}^{\nu}$	-0.266	0.078	29%
$(B/A)_{744}^{\bar{\nu}}$	-1.682	0.041	2.4%
$(B/A)_{770}^{\nu}$	-0.324	0.069	21%
$(B/A)_{770}^{\bar{\nu}}$	--1.622	0.037	2.3%
σ^{ν}/E	0.677	0.014	2.1%
$\sigma^{\bar{\nu}}/\sigma^{\nu}$	0.499	0.007	1.4%
No Φ Adj		Adj. On/Off	
R_{World}	[Whi90b]		15%
m_c	1.31	0.24	18%
κ	0.373	0.046	12%
α	2.50	0.65	26%
B_c	0.105	0.007	7%
Model parameterization		On/Off	

Table 7.11: Variations in QCD fit results due to positive and negative systematic shifts. The values of $\Lambda = \Lambda_{\overline{MS}}^{NLO}$ and η_G for each systematic quantity varied by a positive and, if available, negative shift are listed. The units of $\Lambda_{\overline{MS}}^{NLO}$ are MeV. Note that not all systematic quantities have a negative variation defined. There were 82 degrees of freedom in the xF_3-only fit, and 164 DOF in the combined F_2 and xF_3 fit. The asymmetry in some variations and the χ^2 values is handled in the global systematic fit of Section 7.3.

	xF_3-only fit				Combined F_2 and xF_3 fit					
	+ shift		– shift		+ shift			– shift		
Systematic Quantity	Λ	χ^2	Λ	χ^2	Λ	η_G	χ^2	Λ	η_G	χ^2
C_{HAD}^{744}	–35	79	+30	88	–22	–0.03	189	+19	± 0.05	207
C_{HAD}^{770}	–32	86	+31	85	–16	–0.24	190	+29	–0.12	194
ΔE_{HAD}	–24	85	+21	85	–20	+0.15	189	+26	–0.32	198
C_μ	+45	84	–54	83	+38	–0.04	201	–21	–0.28	199
ΔE_μ	–08	85	+08	84	+04	–0.09	190	+05	–0.09	194
$(B/A)_{744}^{\nu}$	+14	82	–12	81	+07	–0.03	193	–07	+0.04	189
$(B/A)_{744}^{\bar{\nu}}$	–02	81	+03	82	+00	+0.04	191	–00	–0.04	191
$(B/A)_{770}^{\nu}$	+17	84	–14	84	+14	–0.18	193	–02	–0.07	189
$(B/A)_{770}^{\bar{\nu}}$	–01	84	+06	83	+06	–0.07	191	+05	–0.16	190
σ^{ν}/E	+00	81	–00	82	+00	+0.00	191	–00	–0.00	191
$\sigma^{\bar{\nu}}/\sigma^{\nu}$	–32	82	+29	84	+01	+0.21	190	–00	–0.22	198
No Φ Adj	–09	85			+00	–0.05	199			
R	–08	85	–10	86	+00	–0.04	199	+01	–0.05	200
m_c	+06	86			+10	–0.06	201			
κ	–11	86			–02	–0.07	200			
α	–08	85			+01	–0.19	200			
B_c	–12	86			–02	–0.04	199			
Model parameterization	+41	81			–06	+0.38	200			

Table 7.12: Statistical and average systematic errors in QCD fit results. The units of $\Lambda_{\overline{MS}}^{NLO}$ are MeV. The shifts in $\Lambda_{\overline{MS}}^{NLO}$ and η_G from Table 7.11 are averaged. A "$\pm$" variation means that if the systematic quantity is varied by $+1\delta$ as given in Table 7.10, the value of $\Lambda_{\overline{MS}}^{NLO}$ increased; a "$\mp$" variation means that $\Lambda_{\overline{MS}}^{NLO}$ decreased.

	xF_3-only fit	Combined F_2 and xF_3 fit	
	$\Lambda_{\overline{MS}}^{NLO}$	$\Lambda_{\overline{MS}}^{NLO}$	η_G
Base ± Statistical Error	387 ± 42	381 ± 24	4.44 ± 0.65
Systematic Errors: C_{HAD}^{744}	∓ 32	∓ 21	± 0.04
C_{HAD}^{770}	∓ 32	∓ 23	∓ 0.18
ΔE_{HAD}	∓ 23	∓ 23	± 0.23
C_μ	± 49	± 30	∓ 0.16
ΔE_μ	∓ 08	± 04	± 0.09
$(B/A)_{744}^{\nu}$	± 13	± 07	∓ 0.04
$(B/A)_{744}^{\bar{\nu}}$	∓ 02	± 00	± 0.04
$(B/A)_{770}^{\nu}$	± 16	± 08	∓ 0.12
$(B/A)_{770}^{\bar{\nu}}$	∓ 03	± 06	∓ 0.12
σ^{ν}/E	± 00	± 00	± 0.00
$\sigma^{\bar{\nu}}/\sigma^{\nu}$	± 30	± 01	± 0.22
No Φ Adj	∓ 08	± 00	∓ 0.04
R	∓ 09	± 00	∓ 0.05
m_c	± 06	± 10	∓ 0.06
κ	∓ 11	∓ 02	∓ 0.07
α	∓ 08	± 01	∓ 0.19
B_c	∓ 12	∓ 02	∓ 0.04
Model parameterization	± 41	∓ 06	± 0.38
Total Systematic Error	± 93	± 51	± 0.63
Total Stat + Syst	± 102	± 56	± 0.91

Looking at the χ^2 of the different fits, it can be seen that none indicate a completely improbable fit. The poorest fit comes from the variation in m_c, which adds 5 units to the χ^2 of the xF_3-only fit, and 9 units to the χ^2 of the combined F_2 and xF_3 fit; however, the shift in $\Lambda_{\overline{\mathrm{MS}}}^{\mathrm{NLO}}$ due to the error in m_c is negligible. Overall, each individual systematically-varied fit is as consistent with QCD as the base fit, and so it is reasonable to conclude that the measurements of $\Lambda_{\overline{\mathrm{MS}}}^{\mathrm{NLO}}$ of $387 \pm 42 \pm 93$ MeV from the xF_3-only fit and $381 \pm 24 \pm 51$ MeV from the combined F_2 and xF_3 fit are both consistent with QCD. Since there is no reason not to select the result with the smaller statistical and systematic errors, the result of this basic approach to QCD fits is a value for $\Lambda_{\overline{\mathrm{MS}}}^{\mathrm{NLO}}$ of 381 ± 56 MeV (stat. + syst.) with a gluon distribution shape parameter η_G given by 4.44 ± 0.91 (stat. + syst.).

Given the systematic differences in $\sigma^{\bar{\nu}}/\sigma^{\nu}$ between E744 and E770 described in Section 5.3.1, it is worth examining the values of $\Lambda_{\overline{\mathrm{MS}}}^{\mathrm{NLO}}$ determined from each experiment separately. The results of separate QCD fits are shown in Table 7.13. The results of the individual experiments are consistent with each other and with the fits to both experiments combined.

Table 7.13: Results from separate QCD fits to experiments E744 and E770.

	xF_3-only fit		Combined F_2 and xF_3 fit		
	$\Lambda_{\overline{\mathrm{MS}}}^{\mathrm{NLO}}$	χ^2/DOF	$\Lambda_{\overline{\mathrm{MS}}}^{\mathrm{NLO}}$	η_G	χ^2/DOF
E744	398 ± 64	74/81	378 ± 25	3.80 ± 0.69	140/162
E770	391 ± 53	98/82	383 ± 30	5.15 ± 0.96	201/164
Both E744 + E770	387 ± 42	81/82	387 ± 24	4.44 ± 0.65	191/164

7.3 Global Systematic Fits

There are three approaches one can take when incorporating systematic errors in a fit of the structure functions to a theoretical model.

- The systematic errors can be together added in quadrature to the statistical error for each data point. This is the approach taken by most of the global fits that include the CCFR data [Lai96]. This approach ignores the point-to-point correlations between the systematic errors; for example, it assumes that one can vary $\sigma^{\bar{\nu}}/\sigma^{\nu}$ for one (x,Q^2) bin independently of $\sigma^{\bar{\nu}}/\sigma^{\nu}$ in an adjacent bin. This technique will overestimate the systematic errors, and it is not used in this thesis since the technique is patently wrong.

- Each structure function that has been varied by a systematic quantity k can be fit separately. The results of each of the fits can then be added in quadrature. This is the approach used in the previous section. This approach takes into account the point-to-point correlations of a systematic error, and can be used to test the agreement of the data with the QCD model. However, it ignores the possibility of correlations between the systematic errors. Also, Table 7.12 suggests that the effects of the systematic errors are being overestimated. For example, a 1δ shift in C_{HAD}^{770} adds 4 units to the χ^2 of the xF_3-only fit. This technique is not using the information in the structure-function data that could limit the C_{HAD}^{770} systematic uncertainty.

- The third approach, defined fully below, incorporates the systematic variations in the structure functions as part of the fit. As shown below, this approach tests to see if there are any correlations between the systematic errors, uses the data to test whether the limits assigned to the systematic variations are conservative, and reduces the size

of overall error due to systematic effects in comparison to the previous approach. However, this approach cannot test the theory of QCD. The theory is assumed to be true, and the fit is extracting the parameters of the theory with the best precision. This is appropriate because the quantity being measured by the fit, $\Lambda_{\overline{\mathrm{MS}}}^{NLO,(4)}$, *only* has meaning in the context of the theory of QCD.

The global systematic error fit incorporates the systematic errors described in Section 6.4 in the QCD fit. Each δ_k associated with a systematically-varied structure function becomes a MINUIT parameter. The χ^2 of Equations 7.32-7.33 is replaced by

$$\vec{\mathbf{F}}^{diff} = \vec{\mathbf{F}}^{data} - \vec{\mathbf{F}}^{theory} + \sum_k \delta_k \left(\vec{\mathbf{F}}^k - \vec{\mathbf{F}}^{data} \right) \tag{7.37}$$

$$\chi^2 = \sum_{(x,Q^2)\mathrm{bins}} \left(\vec{\mathbf{F}}^{diff} \right)^{\mathrm{T}} \hat{\mathbf{V}}^{-1} \left(\vec{\mathbf{F}}^{diff} \right) + \sum_k \delta_k^2 \tag{7.38}$$

With this definition, the value of δ_k determined by MINUIT is the fraction of the shift between the base structure function $\vec{\mathbf{F}}$ and the structure function varied by one unit of the systematic quantity, $\vec{\mathbf{F}}^k$. If, for example, the MINUIT fit reported that $\delta\left(\sigma^{\bar{\nu}}/\sigma^{\nu}\right) = 1.0$, then it would imply that the best fit to the data is found when $\sigma^{\bar{\nu}}/\sigma^{\nu}$ is varied by +14%, the definition of one unit of systematic variation defined in Chapter 6 and shown in Table 7.10. The inclusion of the $\sum \delta_k^2$ term in Equation 7.38 means that MINUIT must pay a χ^2 "penalty" for varying the data by any of the systematic quantities, and that δ_k typically varies between –1 and +1.

The one systematic error not included in the global systematic fit is that in the overall neutrino-iron cross-section, σ^{ν}/E. The reason is that, when used as a MINUIT parameter, it is highly correlated with A_{NS}, A_S, and A_G, the normalizations for the parton distributions. Since only one overall normalization parameter is necessary for the

fit, the parton distribution normalizations were picked as parameters so the results could be compared directly with the results in Table 7.1.

The results of the global systematic fit are shown in Table 7.14. The error matrix from the xF_3-only fit is shown in Table 7.15, and the correlation coefficients are shown in Table 7.16. The error matrix from the combined F_2 and xF_3 fit is shown in Table 7.17, and the correlation coefficients are shown in Table 7.18.

The error in δ_k reported by MINUIT reflects what improvement, if any, the given systematic error on that parameter can be reduced in context of the theory of QCD. If the error in δ_k is close to 1, then the global fit cannot improve upon the error defined in Section 6.4. For example, the error in $\delta(B_c)$ is 0.92 for the xF_3-only fit; this implies that the charged-current data in combination with the QCD model for the inclusive cross-section cannot improve upon the error of 7% determined for the charm branching ratio B_c from the dimuon analysis [Rab93].

In contrast, the error in $\delta(C_\mu)$ is 0.22 for the xF_3-only fit. The systematic error for C_μ from Table 7.10 is 1%. Therefore, the structure-function data in combination with QCD is able to reduce that systematic error to 0.22 × 1% = 0.22%. The reason for this reduction is that the value of $Q^2 \approx E_\nu E_\mu \theta_\mu^2$ is sensitive to the muon calibration. This changes the value of $d\ln xF_3 / d\ln Q^2$, which in turn affects the value of $\alpha_S(Q^2)$ and $\Lambda_{\overline{\mathrm{MS}}}$ according to Equation 7.12. Also, as shown in Figure 5.10, changing the muon energy calibration also changes the shape of the flux. Q^2 is also sensitive to the E_{HAD} calibration, since $E_\nu = E_{HAD} + E_\mu$, and so the systematic error in the hadron energy calibration is also reduced by the global fit. Note that though the error in C_μ is reduced its central value is not shifted. However, the error in C_{HAD}^{744} is reduced and its central value is shifted outside that reduced error.

Table 7.14: Results of the global systematic QCD fit. "Prob" is the integrated upper tail of the χ^2 distribution for the given number of degrees of freedom (DOF). "FSR" is the value of the left-hand side of the integral in the Fermion Sum Rule in Equation 7.7. "MSR" is the value of the left-hand side of the integral in Equation 7.11.

Number		xF_3-only fit	F_2 and xF_3 fit
1	$\Lambda_{\overline{MS}}$ $[MeV]$	381 ± 53	337 ± 28
2	η_1	0.794 ± 0.011	0.804 ± 0.009
3	η_2	3.88 ± 0.03	3.94 ± 0.03
4	A_{NS}	8.40 ± 0.21	8.60 ± 0.18
7	A_S		1.47 ± 0.04
8	η_S		7.67 ± 0.13
9	A_G		2.22 ± 0.34
10	η_G		4.66 ± 0.68
11	$\delta\left(C_{HAD}^{744}\right)$	1.01 ± 0.53	0.95 ± 0.42
12	$\delta\left(C_{HAD}^{770}\right)$	-0.10 ± 0.45	0.28 ± 0.27
20	$\delta\left(\Delta E_{HAD}\right)$	-0.03 ± 0.71	0.79 ± 0.44
21	$\delta\left(C_{\mu}\right)$	0.22 ± 0.25	0.21 ± 0.18
22	$\delta\left(\Delta E_{\mu}\right)$	0.11 ± 0.60	-0.15 ± 0.36
23	$\delta\left((B/A)_{744}^{\nu}\right)$	0.12 ± 0.94	-0.31 ± 0.91
24	$\delta\left((B/A)_{744}^{\bar{\nu}}\right)$	0.02 ± 0.99	-0.01 ± 0.98
25	$\delta\left((B/A)_{770}^{\nu}\right)$	-0.03 ± 0.71	0.18 ± 0.56
26	$\delta\left((B/A)_{770}^{\bar{\nu}}\right)$	0.13 ± 0.82	0.46 ± 0.70
30	$\delta\left(\sigma^{\bar{\nu}}/\sigma^{\nu}\right)$	-0.13 ± 0.64	0.04 ± 0.50
31	$\delta(\mathrm{No}\,\Phi\,\mathrm{Adj})$	0.08 ± 0.92	0.18 ± 0.73
32	$\delta(R)$	0.03 ± 0.91	-0.22 ± 0.42
33	$\delta\left(m_c\right)$	-0.34 ± 0.87	-1.22 ± 0.77
34	$\delta(\kappa)$	0.14 ± 0.92	0.37 ± 0.90
35	$\delta(\alpha)$	0.07 ± 0.92	-0.08 ± 0.88
36	$\delta\left(B_c\right)$	0.20 ± 0.92	0.09 ± 0.89
37	δ(model)	0.50 ± 0.20	0.44 ± 0.12
	χ^2 / DOF	69 / 82	157 / 164
	Prob	85%	62%
	FSR	2.84	2.80
	MSR		0.96

Table 7.15: The error matrix σ_{ij} from the xF_3-only global systematic fit. The elements above the diagonal are not printed. The parameter numbers are defined in Table 7.14. For space reasons, the column values "wrap around" to succeeding rows starting with parameter 25.

	1	2	3	4	11	12	20	21	22	23	24
1	0.203E-02										
2	-0.418E-04	0.131E-03									
3	-0.801E-03	0.238E-03	0.118E-02								
4	0.205E-02	0.202E-02	0.415E-02	0.424E-01							
11	-0.423E-02	-0.582E-03	0.723E-03	-0.139E-01	0.291E+00						
12	-0.140E-02	0.690E-03	0.300E-02	0.161E-01	-0.353E-01	0.198E+00					
20	-0.224E-02	0.293E-03	0.964E-03	0.874E-02	-0.854E-02	-0.364E-01	0.498E+00				
21	-0.107E-02	0.333E-03	-0.273E-02	-0.709E-02	0.365E-01	0.841E-02	0.121E-01	0.610E-01			
22	-0.295E-02	0.125E-03	0.138E-02	0.876E-02	-0.484E-01	-0.147E-01	-0.105E+00	-0.404E-01	0.365E+00		
23	0.418E-02	0.179E-02	0.193E-02	0.169E-01	0.606E-02	0.194E-01	-0.143E-02	-0.132E-01	0.217E-01	0.889E+00	
24	0.547E-03	-0.124E-02	-0.173E-02	-0.139E-01	-0.175E-02	0.346E-02	-0.228E-02	-0.553E-03	-0.563E-02	0.404E-01	0.977E+00
25	0.484E-02	-0.312E-03	-0.923E-03	-0.396E-02	0.507E-01	-0.317E-01	-0.111E+00	-0.222E-01	-0.349E-01	-0.653E-01	0.108E-01
	0.498E+00										
26	-0.935E-03	0.159E-03	0.116E-02	0.416E-02	0.566E-01	-0.406E-02	-0.139E+00	-0.249E-02	-0.455E-01	-0.401E-01	0.135E-01
	-0.237E+00	0.671E+00									
30	-0.568E-02	0.344E-02	0.370E-02	0.108E-01	-0.233E-01	-0.177E-01	-0.907E-02	0.346E-01	-0.605E-01	0.142E+00	-0.753E-01
	0.376E-01	-0.639E-02	0.405E+00								
31	-0.135E-02	-0.308E-04	0.544E-03	-0.708E-02	-0.919E-02	-0.157E-01	-0.163E-01	0.334E-02	-0.107E-01	-0.364E-02	0.586E-02
	-0.125E-01	-0.427E-01	0.383E-01	0.844E+00							
32	-0.113E-02	0.763E-04	0.708E-03	-0.514E-02	-0.144E-01	-0.166E-01	-0.898E-02	0.204E-02	-0.176E-01	-0.280E-02	0.335E-02
	-0.235E-01	-0.279E-01	0.228E-01	-0.153E+00	0.833E+00						
33	0.102E-01	0.780E-03	-0.537E-02	0.281E-01	0.785E-02	-0.161E-02	-0.107E-01	0.133E-02	-0.185E-01	0.624E-01	-0.294E-01
	0.993E-02	-0.239E-01	-0.569E-01	-0.140E+00	-0.140E+00	0.761E+00					
34	-0.243E-02	-0.107E-02	-0.358E-03	-0.205E-01	-0.838E-02	-0.152E-01	-0.200E-01	0.466E-02	-0.150E-01	0.137E-01	-0.459E-02
	-0.738E-02	-0.411E-01	-0.113E-01	-0.150E+00	-0.148E+00	-0.152E+00	0.848E+00				
35	-0.122E-02	-0.525E-04	0.389E-03	-0.900E-02	-0.825E-02	-0.160E-01	-0.145E-01	0.210E-02	-0.872E-02	-0.643E-02	0.709E-02
	-0.140E-01	-0.431E-01	0.493E-01	-0.157E+00	-0.153E+00	-0.139E+00	-0.150E+00	0.842E+00			
36	-0.241E-02	-0.514E-03	0.135E-03	-0.114E-01	-0.958E-02	-0.173E-01	-0.198E-01	0.636E-02	-0.166E-01	0.198E-01	-0.502E-02
	-0.385E-02	-0.394E-01	-0.170E-01	-0.152E+00	-0.150E+00	-0.152E+00	-0.152E+00	-0.151E+00	0.846E+00		
37	0.194E-02	-0.450E-03	-0.642E-03	-0.814E-02	0.228E-02	-0.119E-01	-0.156E-01	-0.152E-02	-0.194E-01	0.143E-02	-0.228E-02
	0.711E-02	-0.749E-02	0.999E-03	0.504E-02	0.523E-02	0.257E-02	0.287E-02	0.489E-02	0.393E-02	0.400E-01	

Table 7.16: Correlation coefficients $\left(\sigma_{ij}\right)\Big/\left(\sigma_{ii}\sigma_{jj}\right)^{1/2}$ for the xF_3-only global systematic fit. The parameter numbers are defined in Table 7.14. For space reasons, the column values "wrap around" to succeeding rows starting with parameter 33.

NO.	GLOBAL	1	2	3	4	11	12	20	21	22	23	24	25	26	30	31	32
1	0.98300	1.000	-0.081	-0.518	0.220	-0.174	-0.070	-0.071	-0.096	-0.108	0.098	0.012	0.152	-0.025	-0.198	-0.033	-0.028
2	0.98915	-0.081	1.000	0.608	0.857	-0.094	0.136	0.036	0.118	0.018	0.166	-0.109	-0.039	0.017	0.474	-0.003	0.007
3	0.98375	-0.518	0.608	1.000	0.588	0.039	0.197	0.040	-0.322	0.067	0.060	-0.051	-0.038	0.041	0.170	0.017	0.023
4	0.99445	0.220	0.857	0.588	1.000	-0.125	0.176	0.060	-0.139	0.070	0.087	-0.068	-0.027	0.025	0.082	-0.037	-0.027
11	0.63028	-0.174	-0.094	0.039	-0.125	1.000	-0.147	-0.022	0.273	-0.148	0.012	-0.003	0.133	0.128	-0.068	-0.019	-0.029
12	0.79387	-0.070	0.136	0.197	0.176	-0.147	1.000	-0.116	0.076	-0.055	0.046	0.008	-0.101	-0.011	-0.063	-0.038	-0.041
20	0.89843	-0.071	0.036	0.040	0.060	-0.022	-0.116	1.000	0.070	-0.246	-0.002	-0.003	-0.224	-0.240	-0.020	-0.025	-0.014
21	0.85322	-0.096	0.118	-0.322	-0.139	0.273	0.076	0.070	1.000	-0.271	-0.057	-0.002	-0.127	-0.012	0.220	0.015	0.009
22	0.86761	-0.108	0.018	0.067	0.070	-0.148	-0.055	-0.246	-0.271	1.000	0.038	-0.009	-0.082	-0.092	-0.158	-0.019	-0.032
23	0.64725	0.098	0.166	0.060	0.087	0.012	0.046	-0.002	-0.057	0.038	1.000	0.043	-0.098	-0.052	0.236	-0.004	-0.003
24	0.20852	0.012	-0.109	-0.051	-0.068	-0.003	0.008	-0.003	-0.002	-0.009	0.043	1.000	0.016	0.017	-0.120	0.006	0.004
25	0.89545	0.152	-0.039	-0.038	-0.027	0.133	-0.101	-0.224	-0.127	-0.082	-0.098	0.016	1.000	-0.411	0.084	-0.019	-0.036
26	0.91986	-0.025	0.017	0.041	0.025	0.128	-0.011	-0.240	-0.012	-0.092	-0.052	0.017	-0.411	1.000	-0.012	-0.057	-0.037
30	0.89713	-0.198	0.474	0.170	0.082	-0.068	-0.063	-0.020	0.220	-0.158	0.236	-0.120	0.084	-0.012	1.000	0.066	0.039
31	0.94920	-0.033	-0.003	0.017	-0.037	-0.019	-0.038	-0.025	0.015	-0.019	-0.004	0.006	-0.019	-0.057	0.066	1.000	-0.183
32	0.94873	-0.028	0.007	0.023	-0.027	-0.029	-0.041	-0.014	0.009	-0.032	-0.003	0.004	-0.036	-0.037	0.039	-0.183	1.000
33	0.94784	0.259	0.078	-0.179	0.157	0.017	-0.004	-0.017	0.006	-0.035	0.076	-0.034	0.016	-0.033	-0.103	-0.174	-0.176
		1.000	-0.189	-0.174	-0.190	0.015											
34	0.94963	-0.059	-0.102	-0.011	-0.108	-0.017	-0.037	-0.031	0.020	-0.027	0.016	-0.005	-0.011	-0.054	-0.019	-0.177	-0.176
		-0.189	1.000	-0.177	-0.179	0.016											
35	0.94901	-0.029	-0.005	0.012	-0.048	-0.017	-0.039	-0.022	0.009	-0.016	-0.007	0.008	-0.022	-0.057	0.084	-0.186	-0.183
		-0.174	-0.177	1.000	-0.180	0.027											
36	0.95019	-0.058	-0.049	0.004	-0.060	-0.019	-0.042	-0.030	0.028	-0.030	0.023	-0.006	-0.006	-0.052	-0.029	-0.180	-0.178
		-0.190	-0.179	-0.180	1.000	0.021											
37	0.79060	0.214	-0.197	-0.094	-0.198	0.021	-0.134	-0.111	-0.031	-0.161	0.008	-0.012	0.050	-0.046	0.008	0.027	0.029
		0.015	0.016	0.027	0.021	1.000											

Table 7.17: The error matrix σ_{ij} from the combined F_2 and xF_3 global systematic fit. The elements above the diagonal are not printed. The parameter numbers are defined in Table 7.14. For space reasons, the column values "wrap around" to succeeding rows starting with parameter 21.

	1	2	3	4	7	8	9	10	11	12	20
1	0.545E-03										
2	0.118E-04	0.878E-04									
3	-0.384E-03	0.156E-03	0.796E-03								
4	0.429E-04	0.147E-02	0.346E-02	0.289E-01							
7	0.347E-03	0.179E-03	0.224E-03	0.389E-02	0.103E-02						
8	-0.286E-03	0.158E-03	0.110E-02	0.854E-02	0.220E-02	0.154E-01					
9	-0.323E-02	-0.276E-05	0.339E-02	0.399E-02	-0.217E-02	0.291E-02	0.524E-01				
10	-0.258E-02	0.748E-04	0.308E-02	0.358E-02	-0.288E-02	-0.829E-03	0.569E-01	0.156E+00			
11	-0.166E-02	-0.126E-04	0.153E-02	0.255E-02	-0.300E-03	0.308E-02	0.120E-01	-0.446E-01	0.175E+00		
12	-0.691E-03	0.110E-03	0.122E-02	0.391E-02	-0.422E-03	0.384E-04	0.772E-02	-0.364E-02	-0.263E-02	0.710E-01	
20	-0.195E-02	0.158E-03	0.232E-02	0.541E-02	0.816E-04	-0.248E-02	-0.127E-03	0.501E-02	-0.416E-02	-0.216E-01	0.190E+00
21	0.946E-03	-0.955E-04	-0.261E-02	-0.620E-02	-0.122E-02	-0.344E-02	-0.117E-01	-0.110E-01	0.167E-01	0.270E-02	-0.512E-02
	0.312E-01										
22	-0.607E-03	-0.144E-03	-0.720E-04	-0.225E-03	0.601E-03	0.647E-02	0.571E-02	0.338E-02	-0.203E-02	-0.118E-01	-0.263E-01
	-0.137E-01	0.133E+00									
23	0.389E-02	0.102E-02	0.684E-03	0.568E-02	0.181E-02	-0.185E-01	-0.398E-01	0.747E-02	0.312E-01	0.113E-01	-0.174E-02
	-0.163E-01	0.194E-01	0.829E+00								
24	-0.642E-03	-0.100E-02	-0.616E-03	-0.128E-01	-0.198E-02	0.589E-02	0.223E-02	0.483E-01	0.570E-02	0.257E-02	-0.254E-02
	0.194E-02	-0.295E-02	0.469E-01	0.962E+00							
25	0.135E-02	0.695E-04	-0.565E-03	-0.936E-03	0.213E-02	-0.222E-02	-0.488E-02	-0.894E-02	0.200E-01	-0.113E-01	-0.174E-01
	-0.838E-02	-0.846E-02	-0.308E-01	0.589E-02	0.311E+00						
26	-0.277E-03	0.253E-04	0.927E-03	0.452E-02	-0.855E-03	0.178E-02	0.786E-02	-0.986E-02	0.416E-01	0.151E-01	-0.888E-01
	0.161E-03	-0.417E-01	-0.406E-01	0.525E-02	-0.225E+00	0.497E+00					
30	0.357E-02	0.178E-02	-0.151E-02	0.926E-02	0.834E-03	-0.394E-01	-0.287E-01	-0.158E-01	-0.273E-01	-0.108E-01	-0.250E-02
	0.484E-02	-0.219E-01	0.108E+00	-0.558E-01	0.282E-01	-0.251E-01	0.249E+00				
31	-0.326E-02	0.195E-05	0.480E-03	-0.102E-01	-0.244E-02	-0.152E-01	0.233E-01	0.107E+00	-0.321E-02	0.579E-02	0.471E-02
	0.591E-02	-0.101E-01	0.716E-02	-0.656E-02	-0.269E-01	-0.255E-01	0.434E-01	0.533E+00			
32	0.101E-02	0.360E-04	-0.380E-03	0.179E-02	0.405E-02	0.142E-01	0.629E-02	-0.145E-01	0.601E-02	-0.346E-01	-0.124E-01
	-0.622E-02	0.121E-01	-0.526E-02	0.471E-02	0.336E-01	-0.152E-01	-0.483E-02	-0.367E-01	0.174E+00		
33	0.114E-01	0.106E-02	-0.382E-02	0.370E-01	0.163E-01	0.297E-01	-0.104E+00	-0.116E+00	-0.216E-01	0.723E-03	-0.136E-01
	0.364E-02	-0.236E-02	0.435E-01	-0.281E-01	0.223E-02	-0.212E-01	-0.464E-01	-0.349E-01	-0.429E-01	0.586E+00	
34	-0.528E-02	-0.101E-02	0.760E-03	-0.256E-01	-0.781E-02	-0.130E-01	0.522E-01	0.878E-01	-0.206E-02	-0.130E-02	-0.345E-02
	-0.254E-02	-0.614E-03	-0.248E-01	0.123E-01	-0.103E-01	-0.257E-01	0.103E-01	0.157E+00	0.289E-02	-0.230E+00	0.175E+00
35	0.155E-03	0.677E-04	-0.261E-02	-0.120E-01	-0.646E-02	-0.172E-01	0.308E-02	-0.675E-02	-0.243E-01	-0.575E-02	-0.230E-01
	0.274E-01	-0.144E-01	0.167E-01	-0.148E-02	-0.162E-01	-0.260E-01	0.566E-01	-0.219E+00	-0.261E-01	-0.166E+00	0.192E-02
	0.277E+00										
36	-0.243E-02	-0.370E-03	0.289E-02	-0.464E-03	-0.418E-02	0.218E-02	0.106E-01	-0.450E-01	-0.715E-02	0.476E-02	0.149E-01
	-0.173E-01	-0.406E-02	0.142E-01	0.794E-02	-0.781E-02	-0.299E-01	-0.378E-01	-0.354E+00	-0.402E-01	-0.876E-01	-0.625E-01
	0.201E+00	0.369E+00									
37	-0.223E-04	0.393E-04	0.197E-03	-0.641E-03	-0.666E-03	-0.245E-02	-0.101E-02	0.474E-02	-0.310E-02	-0.133E-02	0.493E-02
	0.684E-03	-0.244E-02	0.202E-02	0.617E-03	-0.101E-01	0.145E-03	0.200E-02	0.229E-02	-0.579E-02	0.134E-02	-0.170E-02
	0.136E-02	0.346E-02	0.148E-01								

Table 7.18: Correlation coefficients $\left(\sigma_{ij}\right)\Big/\left(\sigma_{ii}\sigma_{jj}\right)^{1/2}$ for the combined F_2 and xF_3 global systematic fit. The parameter numbers are defined in Table 7.14. For space reasons, the column values "wrap around" to succeeding rows starting with parameter 26.

NO.	GLOBAL	1	2	3	4	7	8	9	10	11	12	20	21	22	23	24	25
1	0.97903	1.000	0.054	-0.584	0.011	0.464	-0.099	-0.604	-0.280	-0.170	-0.111	-0.192	0.229	-0.071	0.183	-0.028	0.104
2	0.99595	0.054	1.000	0.591	0.923	0.597	0.136	-0.001	0.020	-0.003	0.044	0.039	-0.058	-0.042	0.120	-0.109	0.013
3	0.99238	-0.584	0.591	1.000	0.721	0.248	0.313	0.525	0.276	0.130	0.162	0.189	-0.523	-0.007	0.027	-0.022	-0.036
4	0.99776	0.011	0.923	0.721	1.000	0.714	0.405	0.102	0.053	0.036	0.086	0.073	-0.207	-0.004	0.037	-0.077	-0.010
7	0.98834	0.464	0.597	0.248	0.714	1.000	0.554	-0.296	-0.227	-0.022	-0.049	0.006	-0.215	0.051	0.062	-0.063	0.119
8	0.97251	-0.099	0.136	0.313	0.405	0.554	1.000	0.103	-0.017	0.059	0.001	-0.046	-0.157	0.143	-0.163	0.048	-0.032
9	0.91376	-0.604	-0.001	0.525	0.102	-0.296	0.103	1.000	0.628	0.125	0.127	-0.001	-0.289	0.068	-0.191	0.010	-0.038
10	0.91506	-0.280	0.020	0.276	0.053	-0.227	-0.017	0.628	1.000	-0.270	-0.035	0.029	-0.158	0.023	0.021	0.125	-0.041
11	0.86603	-0.170	-0.003	0.130	0.036	-0.022	0.059	0.125	-0.270	1.000	-0.024	-0.023	0.226	-0.013	0.082	0.014	0.086
12	0.83339	-0.111	0.044	0.162	0.086	-0.049	0.001	0.127	-0.035	-0.024	1.000	-0.186	0.057	-0.121	0.047	0.010	-0.076
20	0.90640	-0.192	0.039	0.189	0.073	0.006	-0.046	-0.001	0.029	-0.023	-0.186	1.000	-0.067	-0.166	-0.004	-0.006	-0.072
21	0.93693	0.229	-0.058	-0.523	-0.207	-0.215	-0.157	-0.289	-0.158	0.226	0.057	-0.067	1.000	-0.212	-0.101	0.011	-0.085
22	0.85208	-0.071	-0.042	-0.007	-0.004	0.051	0.143	0.068	0.023	-0.013	-0.121	-0.166	-0.212	1.000	0.059	-0.008	-0.042
23	0.82669	0.183	0.120	0.027	0.037	0.062	-0.163	-0.191	0.021	0.082	0.047	-0.004	-0.101	0.059	1.000	0.052	-0.061
24	0.27136	-0.028	-0.109	-0.022	-0.077	-0.063	0.048	0.010	0.125	0.014	0.010	-0.006	0.011	-0.008	0.052	1.000	0.011
25	0.93063	0.104	0.013	-0.036	-0.010	0.119	-0.032	-0.038	-0.041	0.086	-0.076	-0.072	-0.085	-0.042	-0.061	0.011	1.000
26	0.95481	-0.017	0.004	0.047	0.038	-0.038	0.020	0.049	-0.035	0.141	0.080	-0.289	0.001	-0.163	-0.063	0.008	-0.571
		1.000	-0.071	-0.050	-0.052	-0.039	-0.087	-0.070	-0.070	0.002							
30	0.90764	0.306	0.380	-0.107	0.109	0.052	-0.637	-0.251	-0.080	-0.131	-0.081	-0.012	0.055	-0.120	0.237	-0.114	0.101
		-0.071	1.000	0.119	-0.023	-0.121	0.050	0.216	-0.124	0.033							
31	0.97478	-0.191	0.000	0.023	-0.082	-0.104	-0.167	0.139	0.369	-0.010	0.030	0.015	0.046	-0.038	0.011	-0.009	-0.066
		-0.050	0.119	1.000	-0.120	-0.062	0.513	-0.570	-0.799	0.026							
32	0.93358	0.104	0.009	-0.032	0.025	0.303	0.275	0.066	-0.088	0.034	-0.312	-0.068	-0.084	0.080	-0.014	0.011	0.144
		-0.052	-0.023	-0.120	1.000	-0.134	0.017	-0.119	-0.158	-0.114							
33	0.98465	0.635	0.147	-0.177	0.285	0.667	0.313	-0.594	-0.384	-0.068	0.004	-0.041	0.027	-0.008	0.062	-0.037	0.005
		-0.039	-0.121	-0.062	-0.134	1.000	-0.718	-0.412	-0.188	0.014							
34	0.94315	-0.541	-0.257	0.064	-0.360	-0.583	-0.250	0.546	0.531	-0.012	-0.012	-0.019	-0.034	-0.004	-0.065	0.030	-0.044
		-0.087	0.050	0.513	0.017	-0.718	1.000	0.009	-0.246	-0.033							
35	0.95845	0.013	0.014	-0.176	-0.135	-0.383	-0.263	0.026	-0.033	-0.110	-0.041	-0.100	0.295	-0.075	0.035	-0.003	-0.055
		-0.070	0.216	-0.570	-0.119	-0.412	0.009	1.000	0.628	0.021							
36	0.96737	-0.171	-0.065	0.168	-0.004	-0.215	0.029	0.077	-0.188	-0.028	0.029	0.056	-0.161	-0.018	0.026	0.013	-0.023
		-0.070	-0.124	-0.799	-0.158	-0.188	-0.246	0.628	1.000	0.047							
37	0.82074	-0.008	0.034	0.057	-0.031	-0.171	-0.162	-0.036	0.098	-0.061	-0.041	0.093	0.032	-0.055	0.018	0.005	-0.149
		0.002	0.033	0.026	-0.114	0.014	-0.033	0.021	0.047	1.000							

Of the central values of δ_k's themselves, most are shifted less than one unit of error from the central value of zero. The only quantity that is shifted significantly outside the original systematic error limits is m_c for the combined F_2 and xF_3 fit. The results of the $+1\,\delta(m_c)$ shift from Table 7.12 with the offset from Table 7.14 indicate that $\Lambda_{\overline{\mathrm{MS}}}^{\mathrm{NLO}}$ is shifted by $10\ MeV \times -1.22 = -12\ MeV$ due to m_c in the global systematic fit.

The following tests were made to confirm the results of the global systematic fit. The sensitivity of the fit to the starting values of all the MINUIT fit parameters, including the δ_k's, was tested by randomly setting the starting values of fit to plus or minus two standard error units from the final values found in previous fits. The final values of the fit did not depend on the starting values. The χ^2 variation of each δ_k variable was plotted to plus or minus five units of error from the central values found by the fit, and all were found to be parabolic with the minimum at the final value.

Table 7.18 compares the value of $\Lambda_{\overline{\mathrm{MS}}}^{\mathrm{NLO}}$ from the basic approach to the systematic errors to the results of the global QCD fit. The error on $\Lambda_{\overline{\mathrm{MS}}}^{\mathrm{NLO}}$ from the global systematic fit includes both the statistical and systematic error combined, and so the "systematic" error for the global fit was determined by subtracting in quadrature the statistical error from the basic fit. The Table shows that the global systematic fitting technique substantially reduces the χ^2 of the fit (12 units for the xF_3-only fit and 34 units for the combined F_2 and xF_3 fit). The size of the combined statistical and systematic error is also reduced in half. The value of $\Lambda_{\overline{\mathrm{MS}}}^{\mathrm{NLO}}$ is shifted by $-44\ MeV$ for the combined global systematic F_2 and xF_3 fit; Table 7.14 shows that this is due to larger shifts in the δ_k's in the combined fit compared to the xF_3-only fit.

Table 7.18: Comparison of $\Lambda_{\overline{MS}}^{NLO}$ from the basic fit and the global systematic fit. Units are MeV. The "systematic" error from the global fit is derived by subtracting the statistical error in quadrature from the combined error.

	$\Lambda_{\overline{MS}}^{NLO}$ from xF_3-only fit			$\Lambda_{\overline{MS}}^{NLO}$ from combined F_2 and xF_3 fit		
	Stat and Syst	Combined Error	χ^2/DOF	Stat and Syst	Combined Error	χ^2/DOF
Basic Fit	$387 \pm 42 \pm 93$	336 ± 102	81/82	$381 \pm 24 \pm 51$	346 ± 56	191/164
Global Fit	$381 \pm 41 \pm 34$	381 ± 53	69/82	$337 \pm 21 \pm 19$	337 ± 28	157/164

Overall, the values of $\Lambda_{\overline{MS}}^{NLO}$ from the different fits are consistent with one another. There is no reason not to choose the value with the smallest overall error. Therefore, the value of $\Lambda_{\overline{MS}}^{NLO}$ reported in this analysis is 337 ± 28 (stat + syst) MeV measured at an average value of $\langle Q^2 \rangle = 30\ GeV^2$. The exponent η_G of the shape of the gluon distribution for this fit is 4.65 ± 0.68.

As discussed in Chapter 8, the standard for comparing the strong coupling constants from different experiments is to quote $\alpha_S(M_Z^2)$. The coupling parameter Λ is converted to α_S using the relation of Equation 7.4, with corrections made at the quark-mass thresholds according to the prescription in Ref. [Bar96]. Thus the value for $\Lambda_{\overline{MS}}^{NLO,(4)}$ of 337 ± 28 MeV corresponds to $\alpha_S(M_Z^2) = 0.119 \pm 0.002$. An error of 13 MeV from the higher-twist systematic error corresponds to a shift in $\alpha_S(M_Z^2)$ of ± 0.001. From Refs. [Mar91, Vir92], a conservative scale error of 0.004 is assumed. Therefore, the value of $\alpha_S(M_Z^2)$ reported in this analysis is 0.119 ± 0.002 (stat + syst) ± 0.001 (HT) ± 0.004 (theory).

8 Comparisons and Conclusions

In this Chapter the results from this analysis are compared the results from other experiments. Section 8.1 compares the CCFR structure functions from those obtained by other deep-inelastic scattering experiments. Section 8.2 compares the value of $\alpha_S(M_Z^2)$ and the gluon distribution from this experiment against measurements by other experiments. Section 8.3 presents the final conclusions from this thesis.

8.1 Structure-Function Comparisons

8.1.1 Comparison with CDHSW

At the time of this writing, the only other neutrino deep-inelastic scattering experiment with comparable statistics and energy range of the CCFR data was performed by the CERN-Dortmund-Heidelberg-Saclay-Warsaw collaboration (CDHSW) [Ber91]. Their apparatus was a iron detector similar to the Lab E detector, but the entire target was magnetized. Their final event sample was roughly 640,000 neutrino and 550,000 anti-neutrino events, compared to the 950,000 neutrino and 170,000 anti-neutrino events in the CCFR sample. The energy range of their analysis was $20 < E_\nu < 212\ GeV$, compared to $30 < E_\nu < 360\ GeV$ for the CCFR analysis. Their analysis assumed $\sigma^\nu/E = 0.686 \times 10^{-38}\ cm^2$, $\sigma^{\bar{\nu}}/E = 0.339 \times 10^{-38}\ cm^2$, $\kappa = 0.22$, $R = R_{QCD}$, and no slow-rescaling corrections were made for the charm mass.

Figure 8.1 compares the values xF_3 from CCFR with the values from CDHSW. Figure 8.2 shows the corresponding plot for F_2. The CCFR data has been re-binned in x to agree with the x-bins used in the CDHSW analysis. The values of xF_3 from both experiments are in agreement, but the values of F_2 from CDHSW are lower than the CCFR values for

$x < 0.4$. The difference in the experiments is Q^2-dependent, that is, the two experiments exhibit different logarithmic slopes for the structure functions. Figure 8.3 compares the xF_3 logarithmic slopes from the two experiments, and Figure 8.4 compares the F_2 slopes. The difference in the slopes is larger for F_2 than for xF_3, but it's clear that the xF_3 slopes from CDHSW are inconsistent with the QCD prediction for non-singlet evolution shown in Figure 7.4.

The reason for the inconsistency between the two experiments is still not understood. One issue that remained unresolved until recently was whether the source of the discrepancy was the difference in structure-function extraction techniques between the two experiments, or whether the two experiments measured different differential cross-sections. This is an issue because of the way each experiment extracts its structure functions: CDHSW first extracts the differential cross-sections $d^2\sigma^{\nu,\bar{\nu}}/dx\,dy$, then extracts the structure functions from the y-distributions of the cross-sections; CCFR goes directly from the number of events to the structure functions, as described in Chapter 6. Recently this issue was resolved was by Un-Ki Yang, who showed [Yan96] that the difference between the experiments was also in the differential cross-sections. The most likely source of the difference is the energy-scale calibrations and resolution-smearing parameterizations used by the two experiments. The CCFR calibrations and resolutions are based on extensive test beam measurement in the actual detector and are well understood.

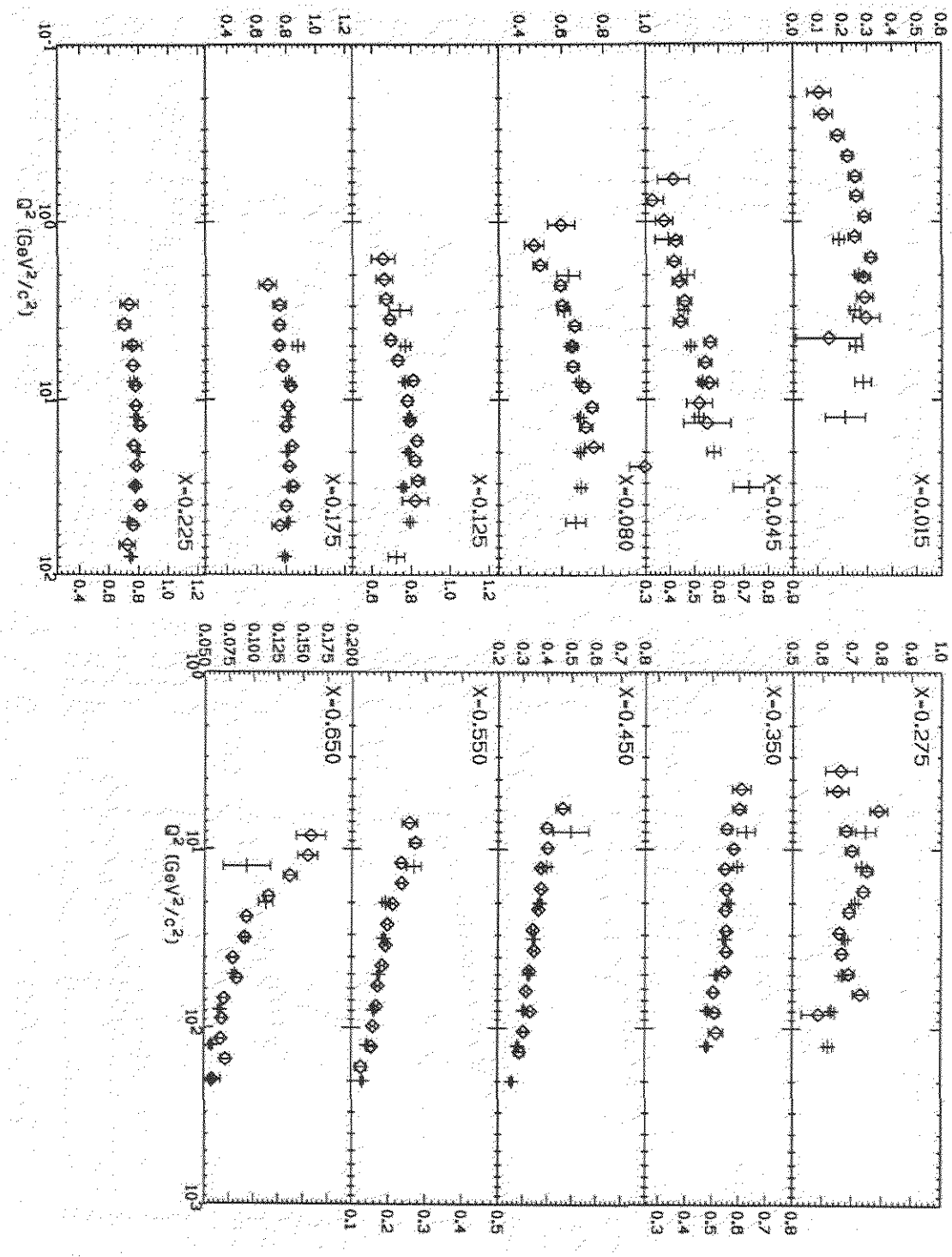

Figure 8.1: A comparison of the values of xF_3 from the present analysis with those from the CDHSW experiment. Error bars are statistical only.

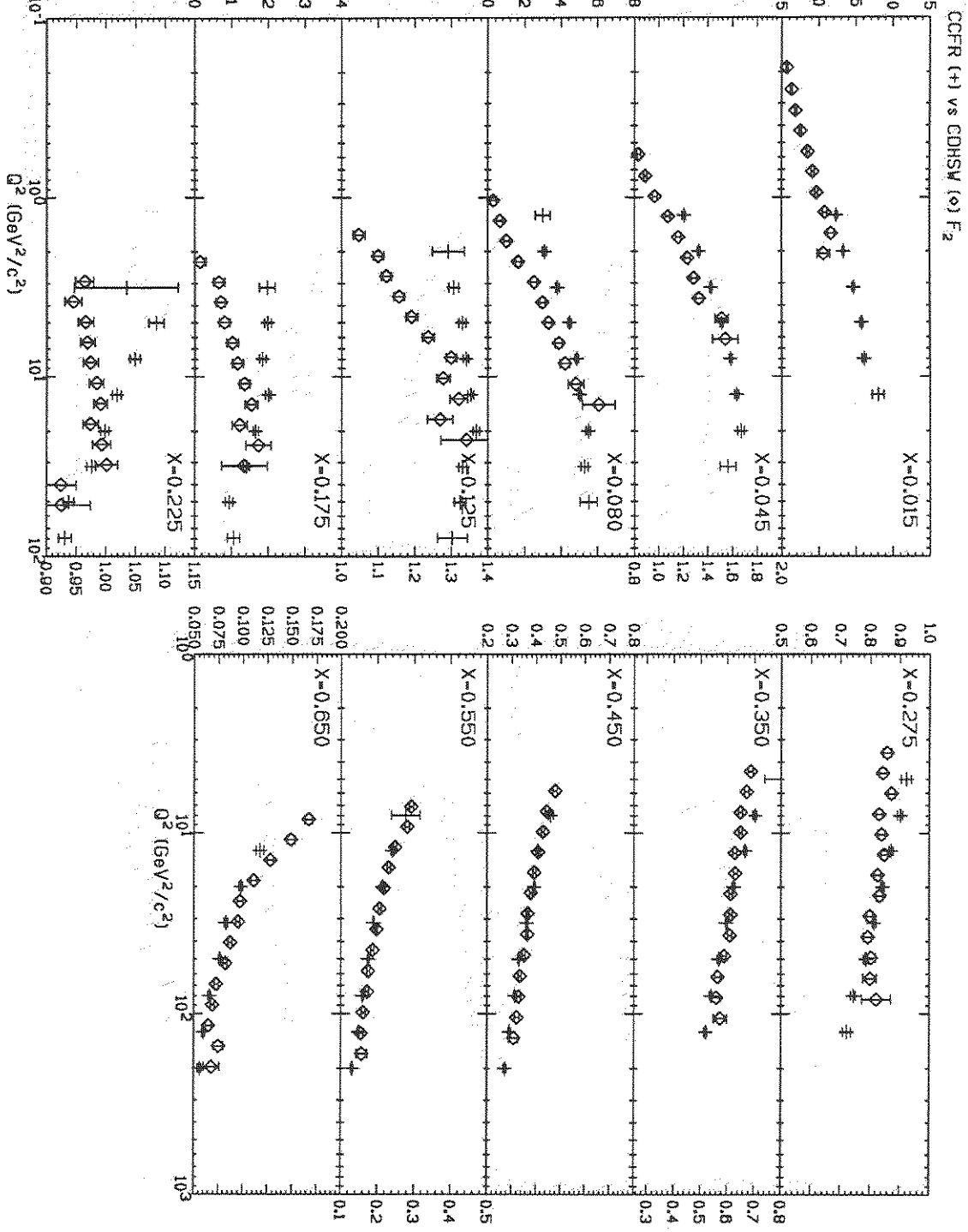

Figure 8.2: A comparison of the values of F_2 from the present analysis with those from the CDHSW experiment. Error bars are statistical only. Note that the slopes of F_2 are substantially different between the two experiments for $x < 0.4$.

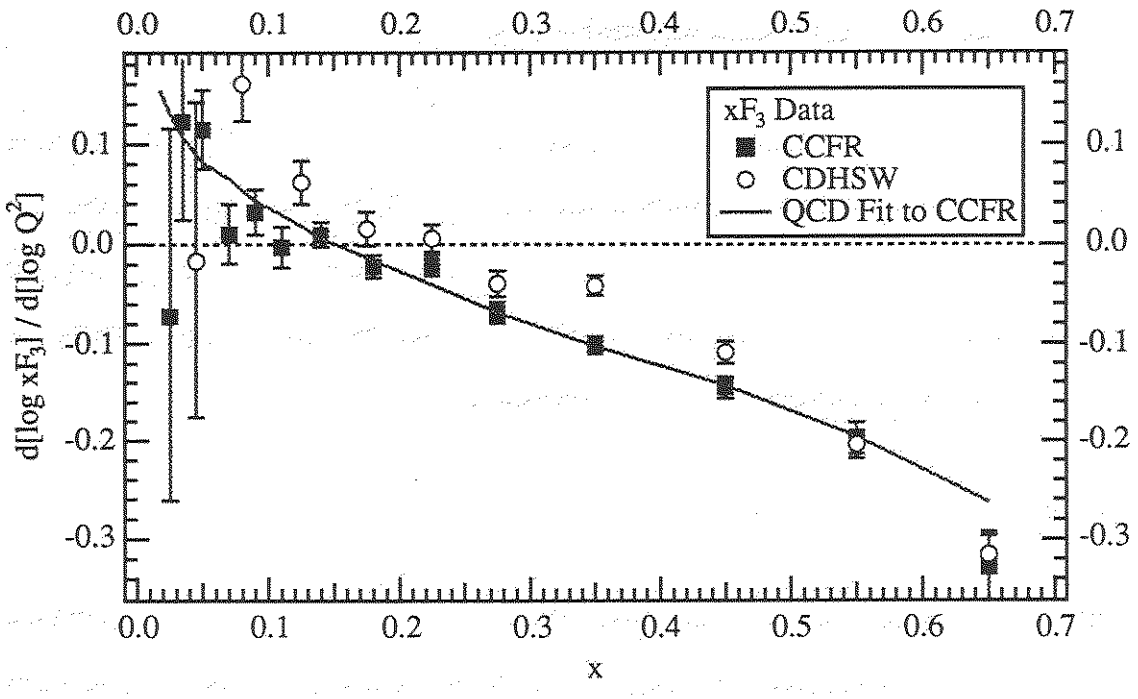

Figure 8.3: The xF_3 logarithmic slopes from the CCFR and CDHSW experiments. The solid line is from the QCD fit described in Chapter 7. Note that the values from CDHSW do not exhibit the behavior expected by QCD for the non-singlet evolution.

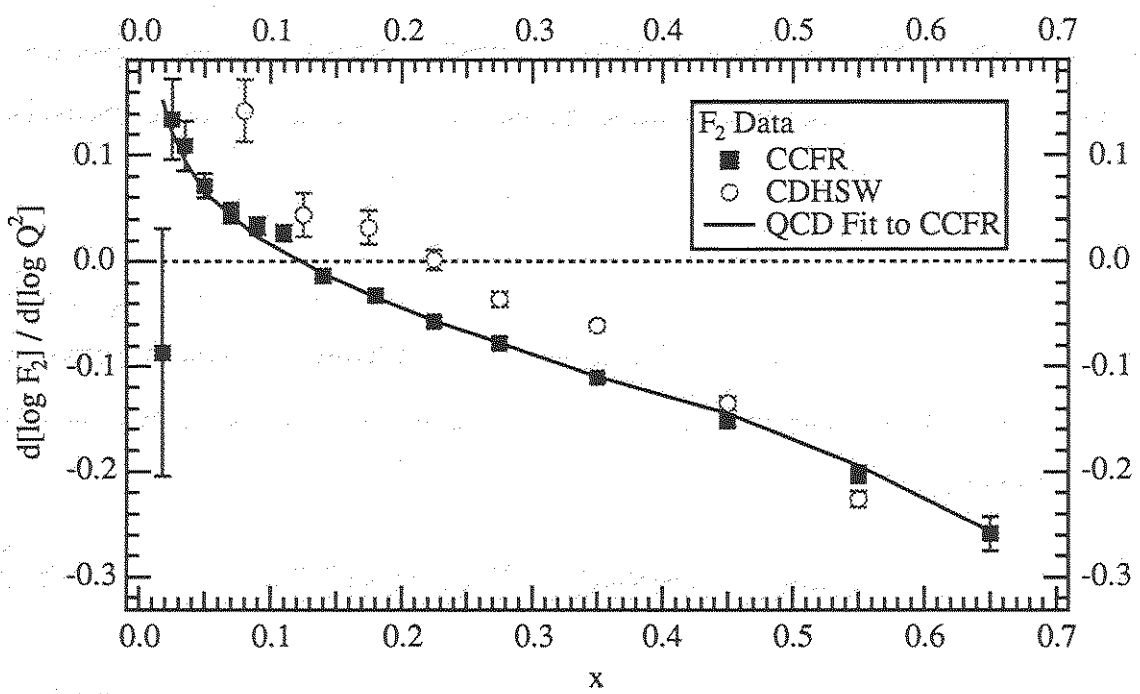

Figure 8.4: The F_2 logarithmic slopes from the CCFR and CDHSW experiments. The solid line is from the QCD fit described in Chapter 7.

8.1.2 Charged-Lepton Experiments

In order to compare F_2 from neutrino-iron deep-inelastic scattering, $F_2^{\nu N}$, to the F_2 from electron-deuterium or muon-deuterium scattering, $F_2^{\ell D}$, it is necessary to make two corrections. The first is a correction for the difference in light versus heavy nuclear targets. The second is the "5/18ths rule," which corrects for the quark charges seen by the electromagnetic interaction versus the weak interaction.

8.1.2.1 Heavy Target Correction

Several charged-lepton experiments have observed an x-dependent effect in which structure functions measured on heavy nuclei do not equal the structure functions measured in light nuclei [Ama95, Arn84, Gom94, Ada95a]. The ratio F_2^N / F_2^D displays the following features: for $x < 0.1$, the ratio falls below unity (the "shadowing" region); for $0.1 < x < 0.2$, the ratio is above 1 (the "anti-screening" region); for $0.2 < x < 0.7$, the ratio again falls below 1 (the "EMC effect"); and finally for $x > 0.7$ the ratio again rises due to Fermi motion of the nucleons within the nucleus. No significant Q^2 dependence has been observed in F_2^N / F_2^D.

Figure 8.5 shows the data from the references in the previous paragraph. The F_2^{Ca} / F_2^D is included in addition to the F_2^{Fe} / F_2^D data, because the difference between the calcium ratio (A = 40) and the iron ratio (A = 56) is less than 2%. The data on the plot is parameterized by:

$$F_2^N / F_2^D = 1.0963 - 0.36427x - 0.27805e^{-21.936x} + 2.7715x^{14.417} \tag{8.1}$$

The systematic error on the parameterization, shown by the gray lines in Figure 8.5, is included in the error bars of the charged-lepton data in Figures 8.6 through 8.11.

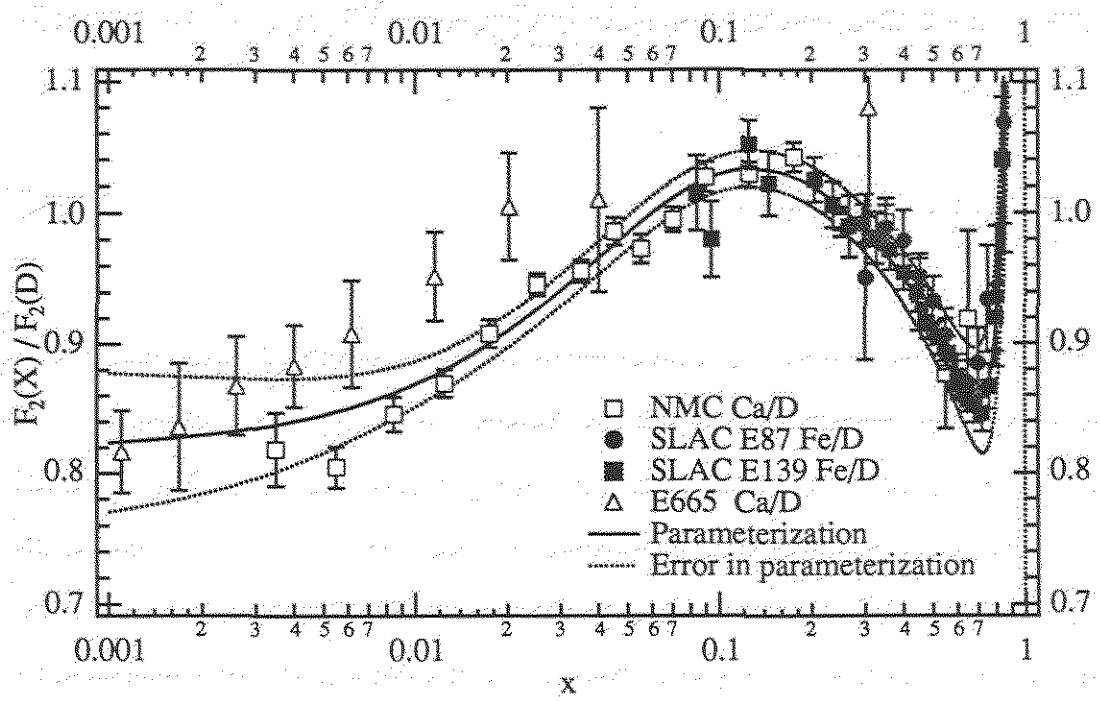

Figure 8.5: Ratio of F_2 from heavy nuclear targets to deuterium from charged-lepton experiments. The sources of the data are [Ama95] (NMC), [Arn84] (SLAC E87), [Gom94] (SLAC E139), [Ada95a] (E665). The dotted lines are the error in the parameterization due to the statistical and systematic errors in the experimental data.

8.1.2.2 Quark-Charge Correction

Electromagnetic charged-lepton scattering is proportional to the squared quark charge. Therefore comparing neutrino and charged-lepton structure functions is equivalent to measuring the mean squared charge of the nucleon's constituents. At leading order in the parton model, the structure functions measured by neutrinos and charged leptons for an isoscalar target are:

$$F_2^{\ell} = \frac{5}{18}\left(xu + x\bar{u} + xd + x\bar{d}\right) + \frac{4}{9}(xs + x\bar{s}) + \frac{1}{9}(c + \bar{c}) \tag{8.2}$$

$$F_2^{\nu} = xu + x\bar{u} + xd + x\bar{d} + xs + x\bar{s} + c + \bar{c} \tag{8.3}$$

If $q = u + d + s + c$, then the following is the leading-order "5/18ths rule" for the quark-charge correction:

$$\frac{F_2^{\ell}}{F_2^{\nu}} = \frac{5}{18}\left(1 - \frac{3}{5}\frac{(s+\bar{s}-c-\bar{c})}{q+\bar{q}}\right) \tag{8.4}$$

Equation 8.4 is correct in the leading-order parton model. In general, for higher orders in α_S and an arbitrary renormalization scheme, Equation 8.4 is *not* valid. However, it *is* valid in the DIS scheme, which is specifically defined such that $F_2 = \sum_i e_i^2 q_i$ to all orders, where e_i is quark charge appropriate for the interaction (1 for the weak interaction, $+2/3$ $(-1/3)$ for the electromagnetic interaction). Therefore, to compute the "5/18ths rule" the CTEQ4D set of parton distributions [Lai96] is used; these distributions were determined in the DIS scheme. For this correction, the charm sea $c+\bar{c}$ was *not* assumed to be zero, but was taken to be the value computed by CTEQ4D.

8.1.2.3 Comparison Plots

Figures 8.6 through 8.15 compare F_2 from the present CCFR analysis to the results from NMC [Arn96], E665 [Ada96], SLAC [Whi90a], BCDMS deuterium [Ben90], and BCDMS carbon [Ben87]. The error bars on the plots include both the statistical and systematic errors added in quadrature (see Section D.4.3). NMC, E665, and BCDMS are muon-deuterium scattering experiments; BCDMS data with both deuterium and carbon targets are included. SLAC is an electron scattering experiment. The data from the charged-lepton experiments have been converted to F_2^{ν} using Equation 8.4. The NMC, E665, SLAC, and BCDMS deuterium data have been corrected to F_2^{Fe} using the parameterization of Equation 8.1. The carbon data has not been corrected by a heavy-target correction, since the difference in the nuclear correction for Fe/C is smaller than the correction for C/D [Ama95]. Where the x values of the charged-lepton data did not

agree with the x-bin centers of the CCFR data, a bin-center correction was applied using the CTEQ4M parton distributions.

The NMC data in Ref. [Arn96] were presented as extracted with two different values of $R = \sigma_L / \sigma_T$. One set of data was extracted with the value of R from Ref. [Whi90b], the other using the value of R from the NMC data. Since the former value of R was used in the CCFR extraction, the corresponding set of NMC data is plotted below.

For comparison, the values for F_2 predicted by the CTEQ4M [Lai96], MRS R_2 [Mar96], and GRV 94 [Glu95] parton distribution functions are included in the Figures. The structure function F_2 is computed from the parton distributions using the NLO convolution integrals, target mass correction, and higher-twist correction described in Chapter 7.

At low x, there is a discrepancy between the CCFR and NMC result, as can be seen in Figure 8.6. The error bars on the E665 data are large enough that these data cannot resolve the discrepancy. As x increases, the discrepancy decreases. Above $x = 0.2$, the discrepancy vanishes. There is a small discrepancy between the CCFR and SLAC/BCDMS data at $x = 0.75$, but this can be readily explained by (1) a large smearing correction at $x = 0.75$ (see Chapter 6), (2) an uncertainty in the large heavy-target correction due to Fermi motion (see Figure 8.5).

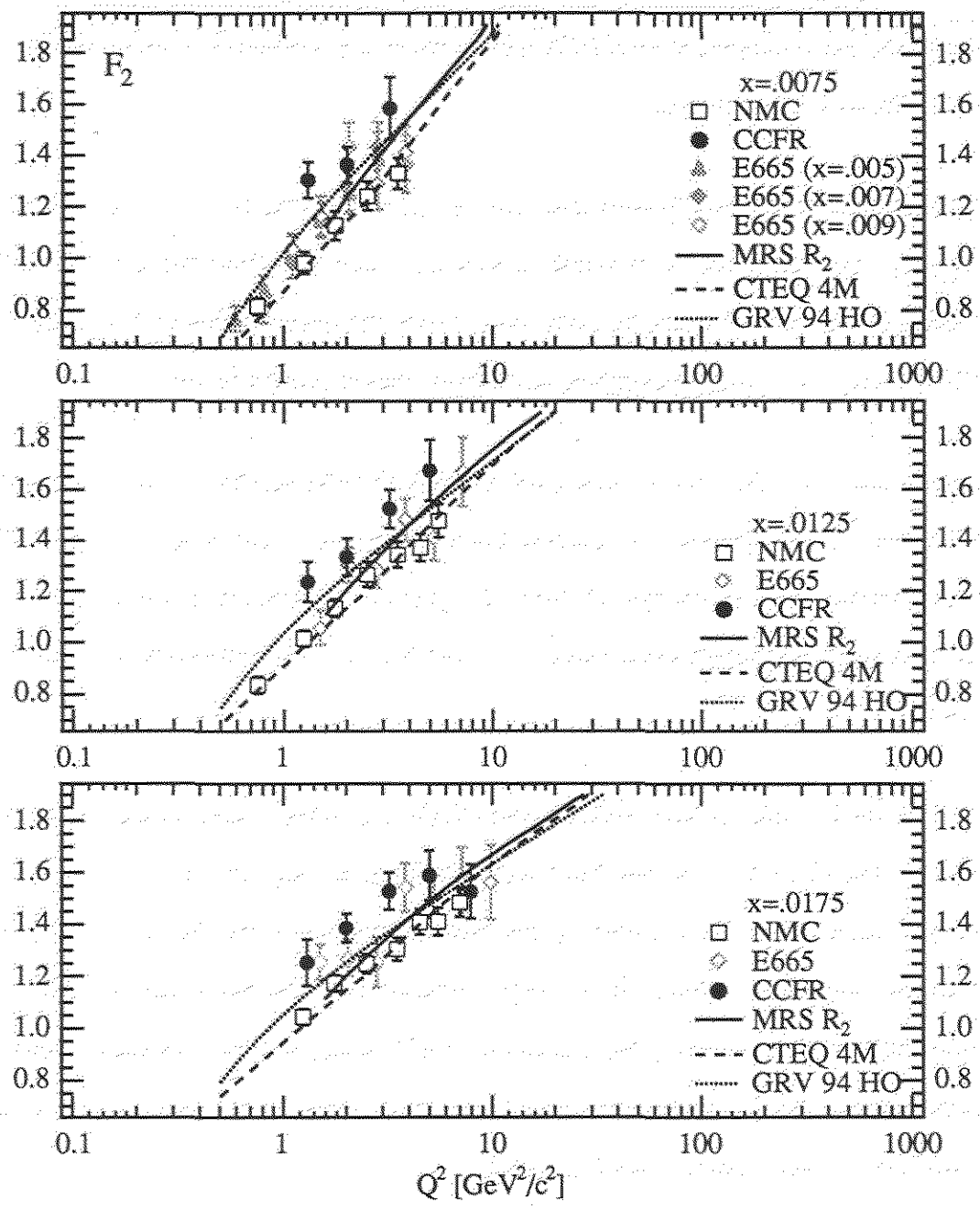

Figure 8.6: F_2 from the CCFR ν-Fe result compared to the F_2 from charged-lepton experiments for $x = 0.0075$, 0.0125, and 0.0175. Statistical and systematic errors are added in quadrature. All e-D and μ-D data have been corrected to ν-Fe by applying both a NLO F_2^{ℓ} / F_2^{ν} correction and the F_2^{N} / F_2^{D} ratio measured by SLAC and NMC. The global fits shown have also been corrected for target mass effects and the higher-twist corrections measured by SLAC/BCDMS data.

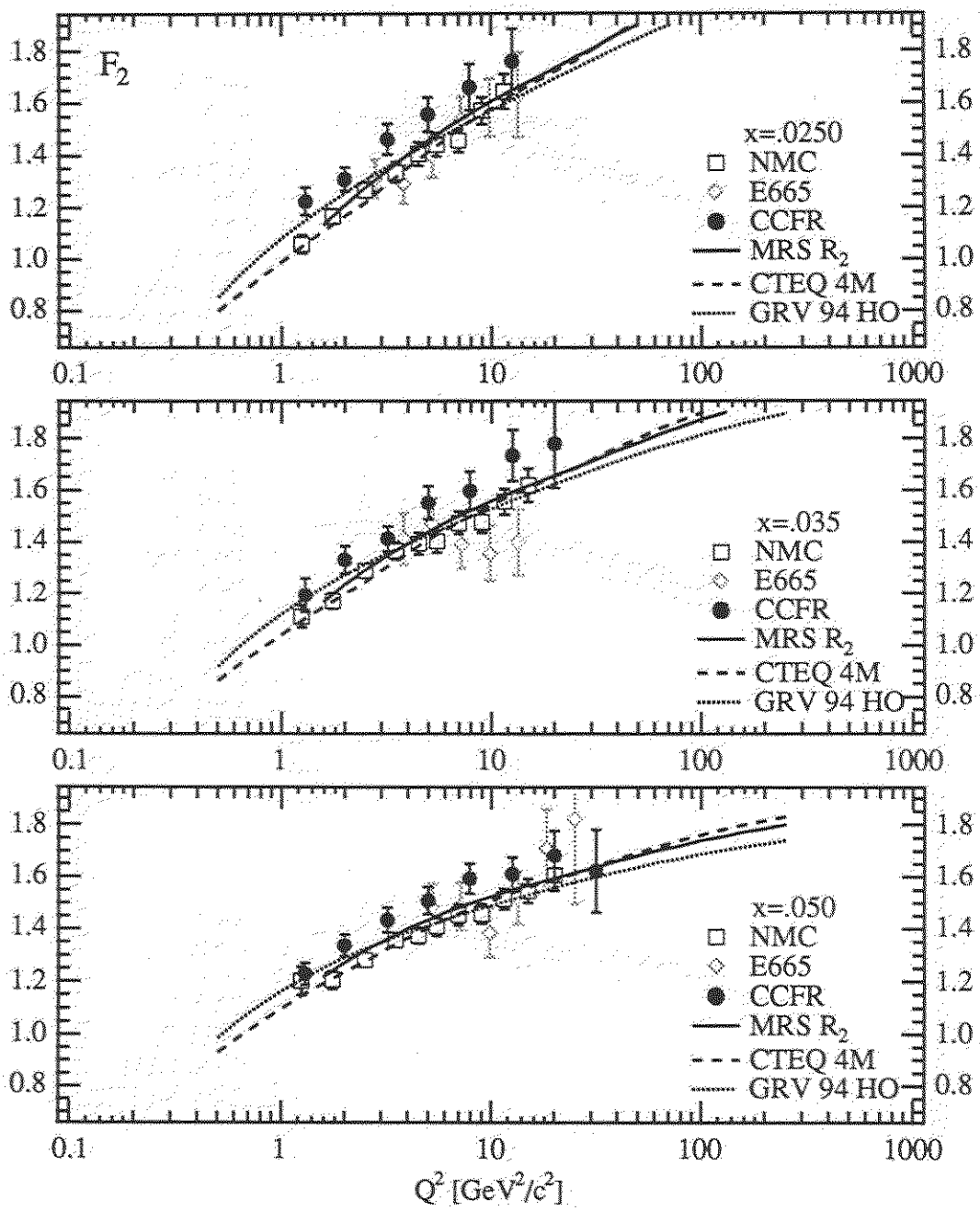

Figure 8.7: F_2 from the CCFR ν-Fe result compared to the F_2 from charged-lepton experiments for $x = 0.025$, 0.035, and 0.050. Statistical and systematic errors are added in quadrature. All e-D and μ-D data have been corrected to ν-Fe by applying both a NLO F_2^{ℓ} / F_2^{ν} correction and the F_2^{N} / F_2^{D} ratio measured by SLAC and NMC. The global fits shown have also been corrected for target mass effects and the higher-twist corrections measured by SLAC/BCDMS data.

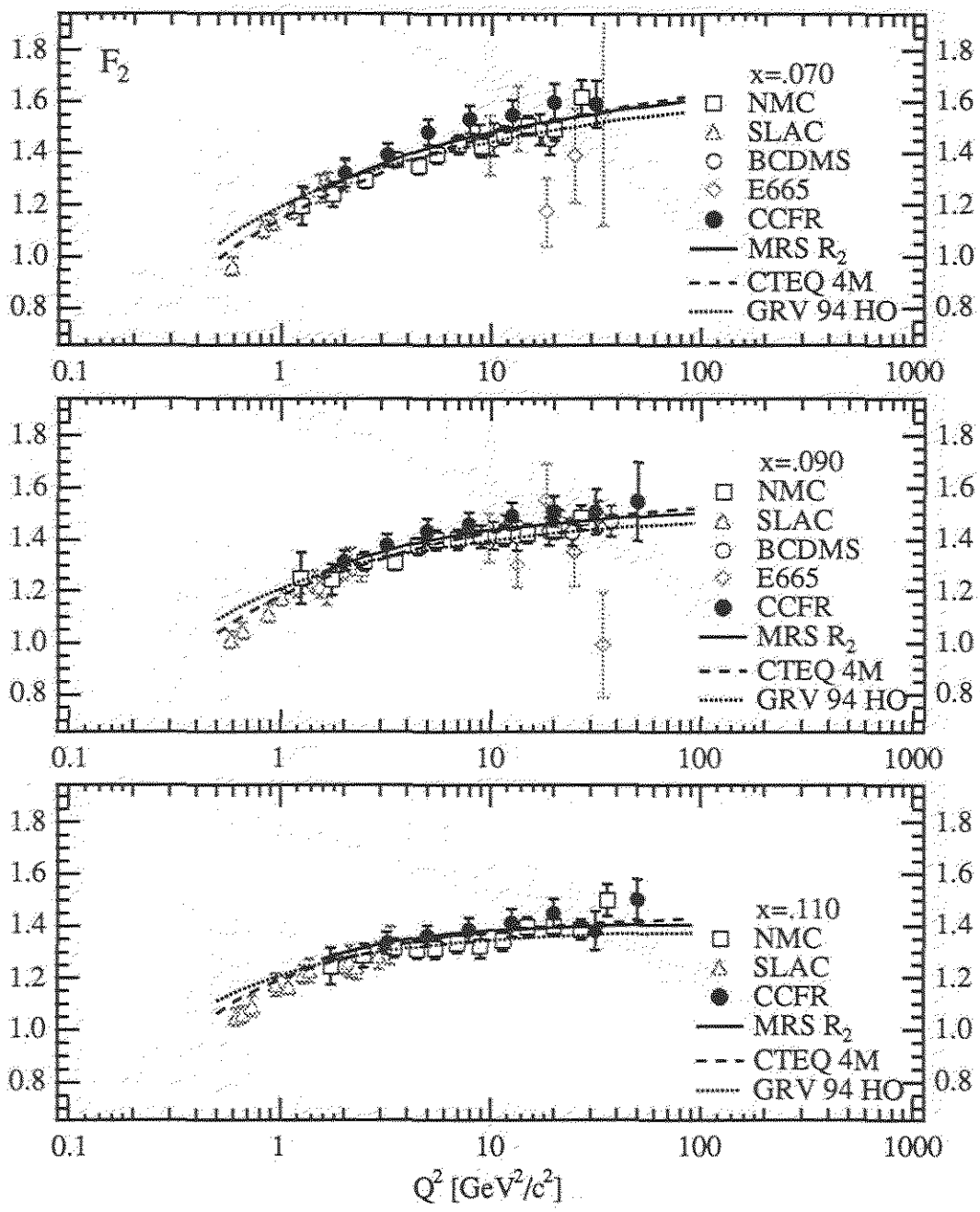

Figure 8.8: F_2 from the CCFR ν-Fe result compared to the F_2 from charged-lepton experiments for $x = 0.070$, 0.090, and 0.110. Statistical and systematic errors are added in quadrature. All e-D and μ-D data have been corrected to ν-Fe by applying both a NLO F_2^{ℓ} / F_2^{ν} correction and the F_2^{N} / F_2^{D} ratio measured by SLAC and NMC. The global fits shown have also been corrected for target mass effects and the higher-twist corrections measured by SLAC/BCDMS data.

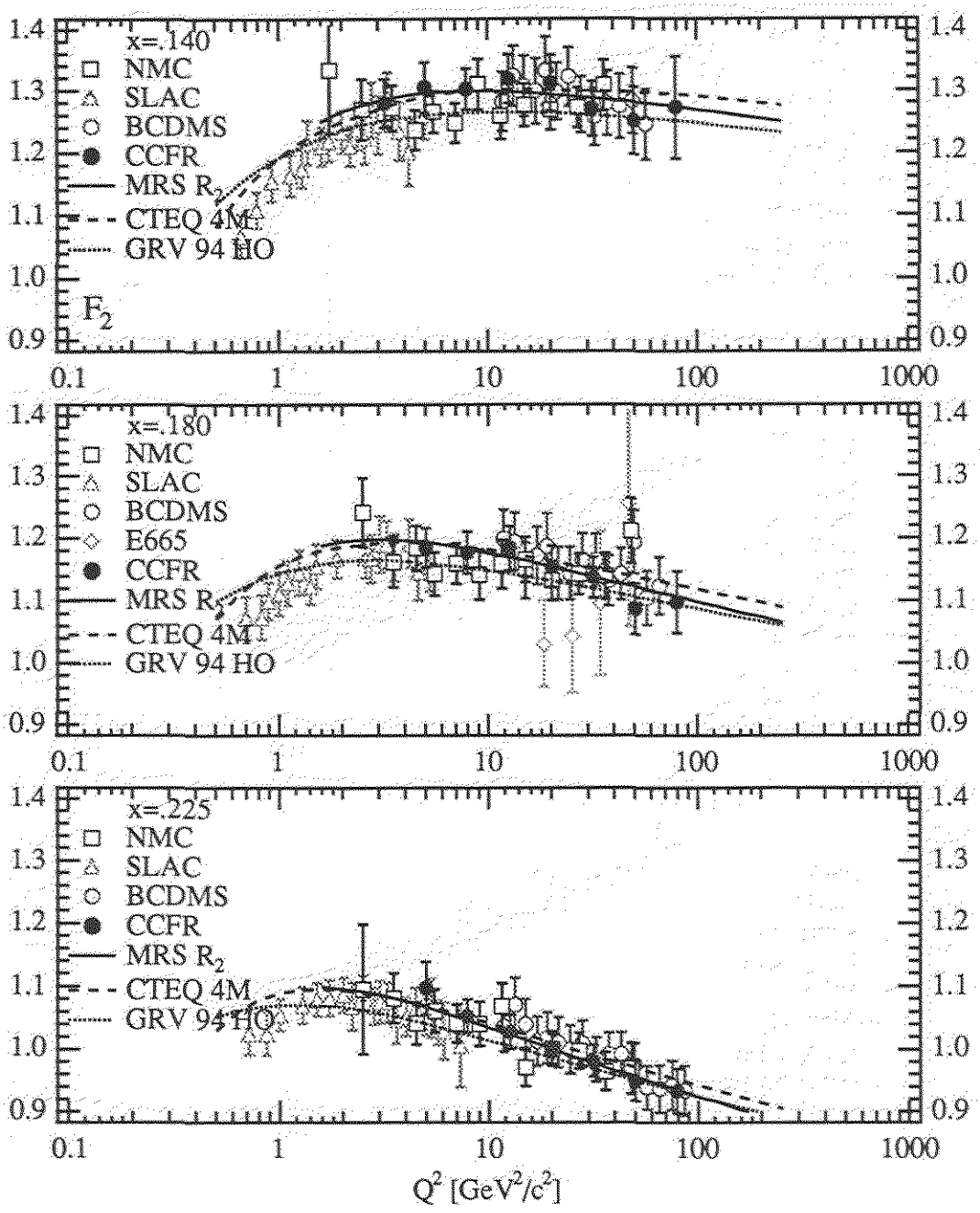

Figure 8.9: F_2 from the CCFR ν-Fe result compared to the F_2 from charged-lepton experiments for $x = 0.140$, 0.180, and 0.225. Statistical and systematic errors are added in quadrature. All e-D and μ-D data have been corrected to ν-Fe by applying both a NLO F_2^{ℓ} / F_2^{ν} correction and the F_2^{N} / F_2^{D} ratio measured by SLAC and NMC. The global fits shown have also been corrected for target mass effects and the higher-twist corrections measured by SLAC/BCDMS data.

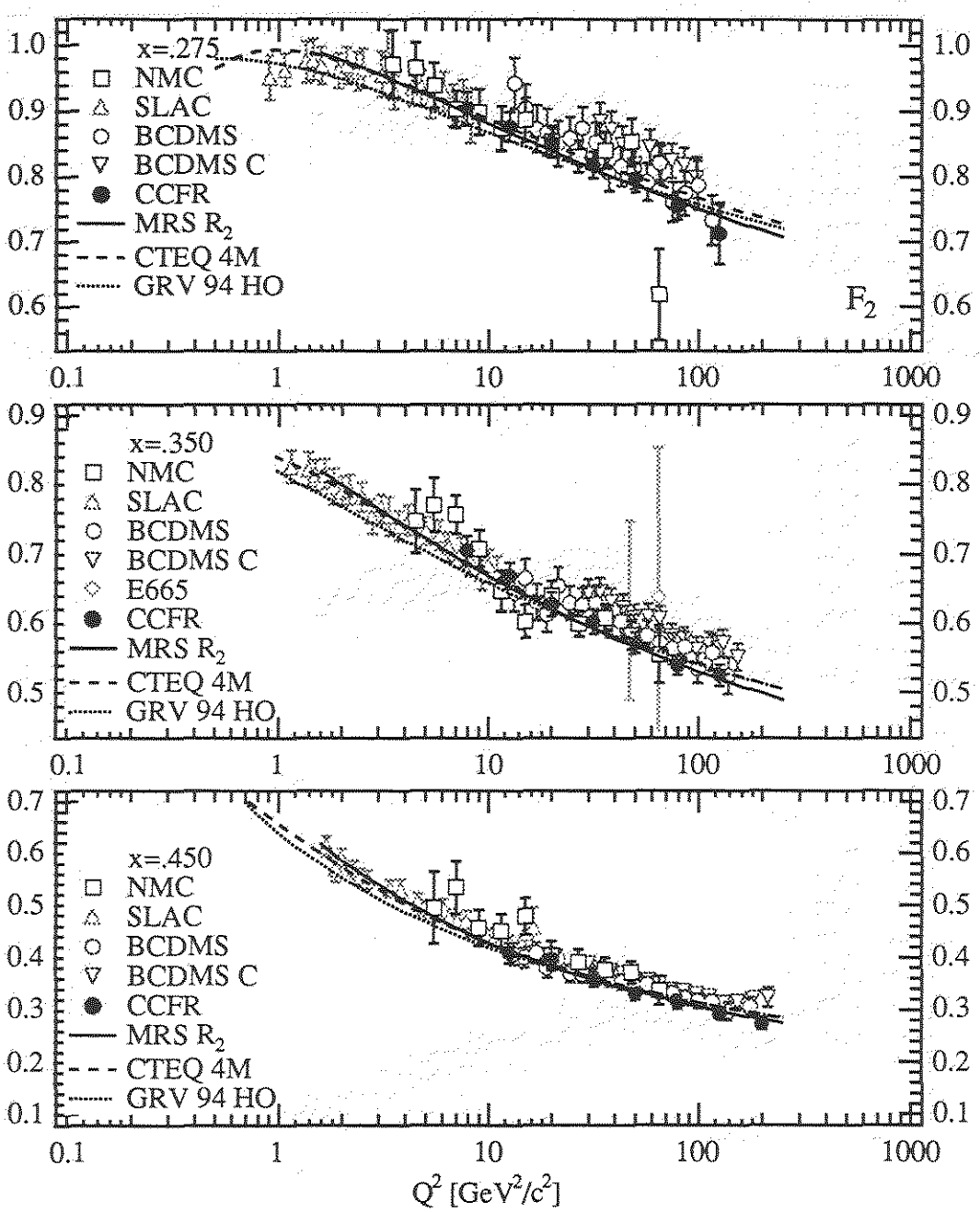

Figure 8.10: F_2 from the CCFR ν-Fe result compared to the F_2 from charged-lepton experiments for $x = 0.275$, 0.350, and 0.450. Statistical and systematic errors are added in quadrature. All e-D and μ-D data have been corrected to ν-Fe by applying both a NLO F_2^ℓ / F_2^ν correction and the F_2^N / F_2^D ratio measured by SLAC and NMC; the BCDMS Carbon data was only corrected by the F_2^ℓ / F_2^ν ratio. The global fits shown are corrected for target mass effects and the higher-twist corrections measured by SLAC/BCDMS data.

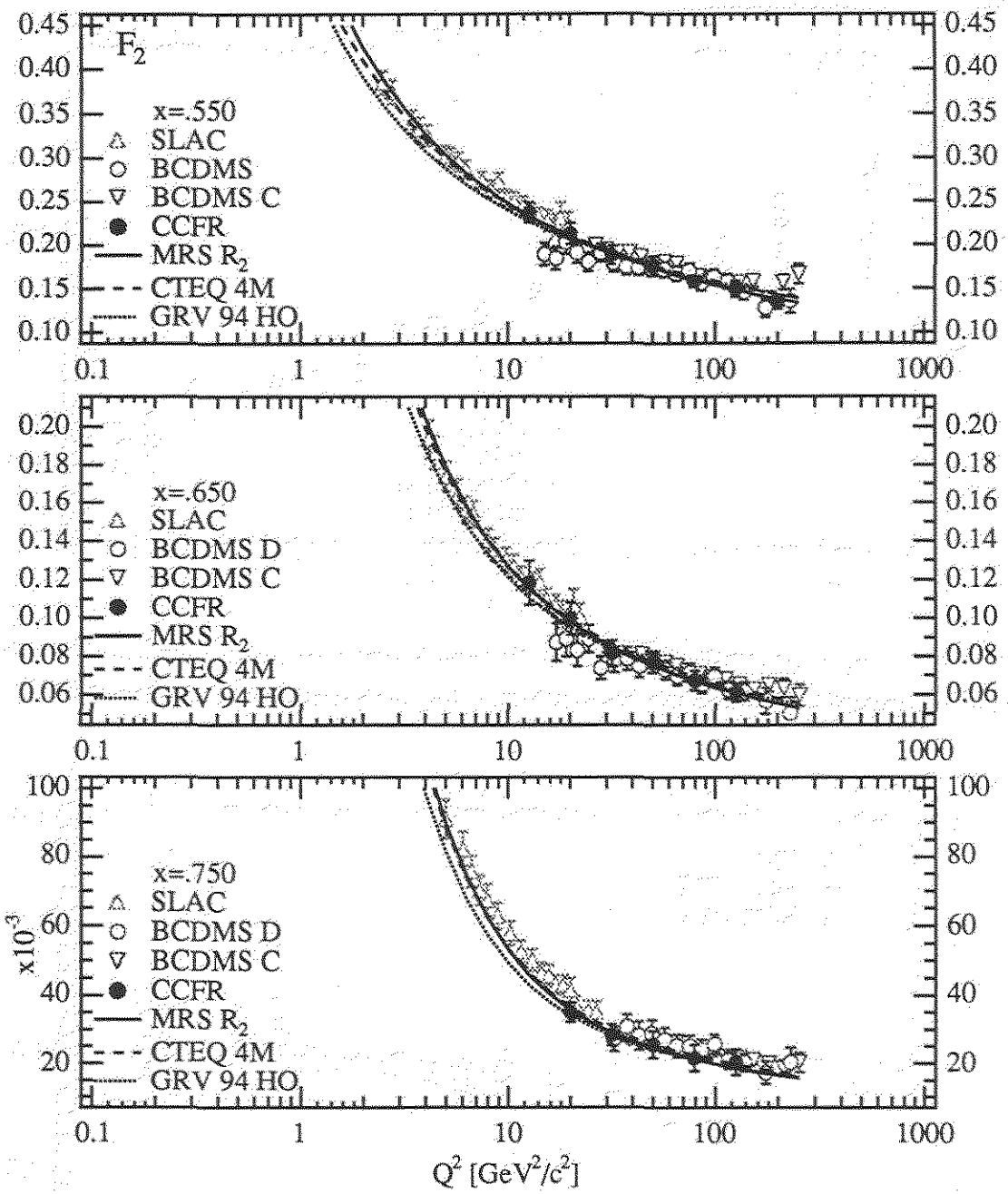

Figure 8.11: F_2 from the CCFR ν-Fe result compared to the F_2 from charged-lepton experiments for $x = 0.550$, 0.650, and 0.750. Statistical and systematic errors are added in quadrature. All e-D and μ-D data have been corrected to ν-Fe by applying both a NLO F_2^ℓ / F_2^ν correction and the F_2^N / F_2^D ratio measured by SLAC and NMC; the BCDMS Carbon data was only corrected by the F_2^ℓ / F_2^ν ratio. The global fits shown are corrected for target mass effects and the higher-twist corrections measured by SLAC/BCDMS data.

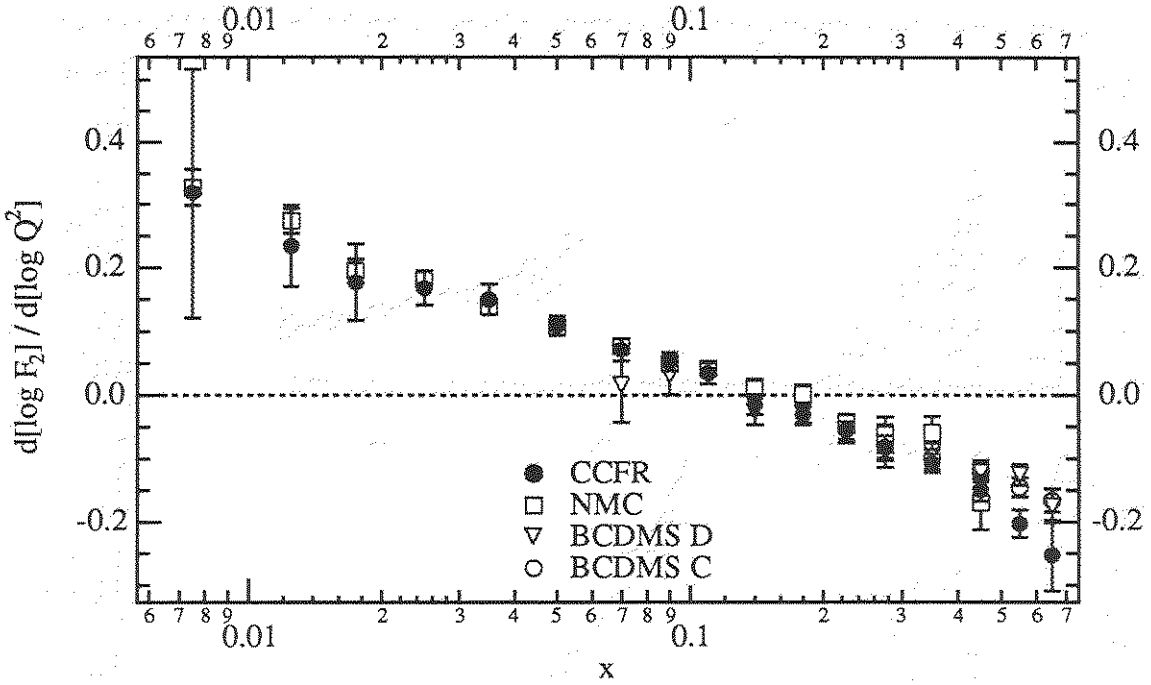

Figure 8.12: F_2 logarithmic slopes from charged-lepton data and CCFR neutrino-iron data. The charged lepton date has been corrected for quark-charge and nuclear effects.

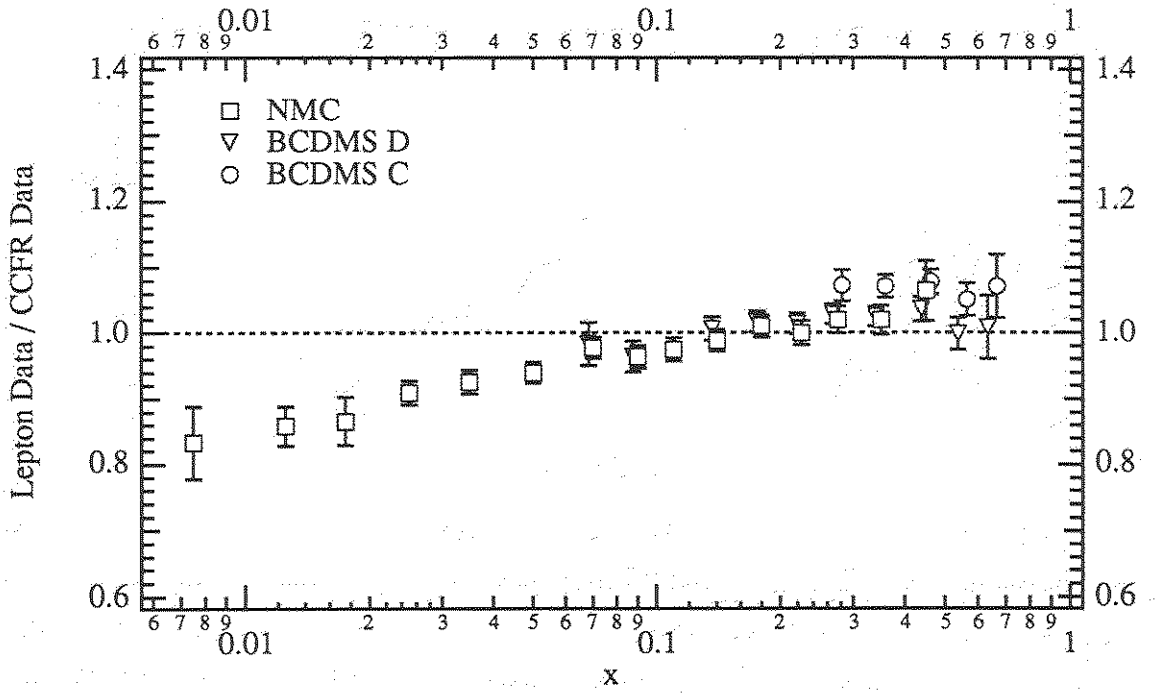

Figure 8.13: Ratio of fits from charged-lepton data to CCFR neutrino-iron data. The charged lepton date has been corrected for the "5/18ths rule" and for nuclear effects. The BCDMS D and BCDMS C ratios have been offset by $\pm.0005$ in x for clarity.

In order to quantify the discrepancy between CCFR and the charged-lepton experiments, the values of $F_2^{\nu Fe}$ were fit to a power-law form $F_2 = A \times \left(Q^2\right)^C$. A Q^2-dependent cut was applied to the data to eliminate the region affected by higher-twist terms. The E665 data is omitted due to large errors in the CCFR kinematic region. The SLAC data are omitted because it cannot be fit to a power-law form in the CCFR kinematic region. The slopes C_i from each x-bin are plotted in Figure 8.12. The error bars on the CCFR slopes are larger than those in Figure 7.7 and 8.3, since the systematic errors are included in the fit. For the purpose of comparing the normalization of the structure functions, the CCFR data points at (x,Q^2) = (.0075,1.3) and (.0175,7.9) are excluded from the power-law fit, since these points affected the slope of the power-law fit and made it difficult to use this technique to compare to the NMC results.

The slopes from the different experiments are generally in agreement. This allows a comparison of the normalizations A_i from the power-law fits. If the slopes had not agreed, the difference in normalization could have been attributed to the difference in the slopes. The ratio of the fits at a median Q^2 for each x-bin are plotted in Figure 8.13. The median Q^2 chosen was $70 \times 2Mx\ GeV^2$ for $x > 0.02$, and $130 \times 2Mx\ GeV^2$ for $x < 0.02$. The figure shows that the discrepancy between CCFR and NMC is ~10-15% for $x < 0.04$.

8.1.2.4 Explaining the CCFR-NMC Discrepancy

Although a number of suggestions have been proposed for the discrepancy between the NMC and CCFR data, no single explanation has been proven to be correct. This section describes some of the suggestions made so far.

One possibility is that one or both experiments have underestimated their systematic errors at the values of x where discrepancy exists. In the CCFR experiment, low-x events come from neutrino interactions with large E_{HAD}. It is possible, despite the test-beam

studies described in Ref. [Sak90] and the error analysis described in Chapter 6, that the error in the hadron energy calibration is under-estimated in this analysis. FNAL Experiment E815, the next generation of the experiment that uses the CCFR detector, is taking more extensive test beam data than in E744 and E770 combined. The scintillator oil in the counters has been replaced and the phototubes voltages have been re-adjusted for the new experiment, and so the hadron energy calibration between E815 and the earlier experiments is not expected to be the same. However, if non-linearities in the calibration are observed in E815, it would be reasonable to assume that similar non-linearities exist in the E744 and E770 data. This matter will be studied once the E815 test beam data is available.

Several groups, including CTEQ [Lai96], MRS [Mar96], and GRV [Glu95], consolidate the world's available data on nucleon structure, including the results of deep-inelastic scattering, direct photon experiments, jet production from $p\bar{p}$ colliders, etc. Each group performs fits on this data, making slightly different model assumptions and parameterizations of the parton distributions. As can be seen in Figure 8.6, the referenced global fits do not clearly select the CCFR data over the NMC data. This is not surprising, since each of the groups made difference decisions on which portions of the NMC or CCFR data to include in their fit. However, in a previous set of fits, the CTEQ group [Bot93] attributed the entirety of the CCFR-NMC discrepancy to the strange quark distribution. This approach can be illustrated using the leading-order parton model by observing that Equations 8.2 and 8.3 imply

$$\frac{5}{6}F_2^{\nu} - 3F_2^{\ell} = \frac{1}{2}x(s+\bar{s}) \tag{8.5}$$

assuming $c = \bar{c} = 0$. The CTEQ collaboration presented the strange sea from this approach in their CTEQ1 set of distributions.

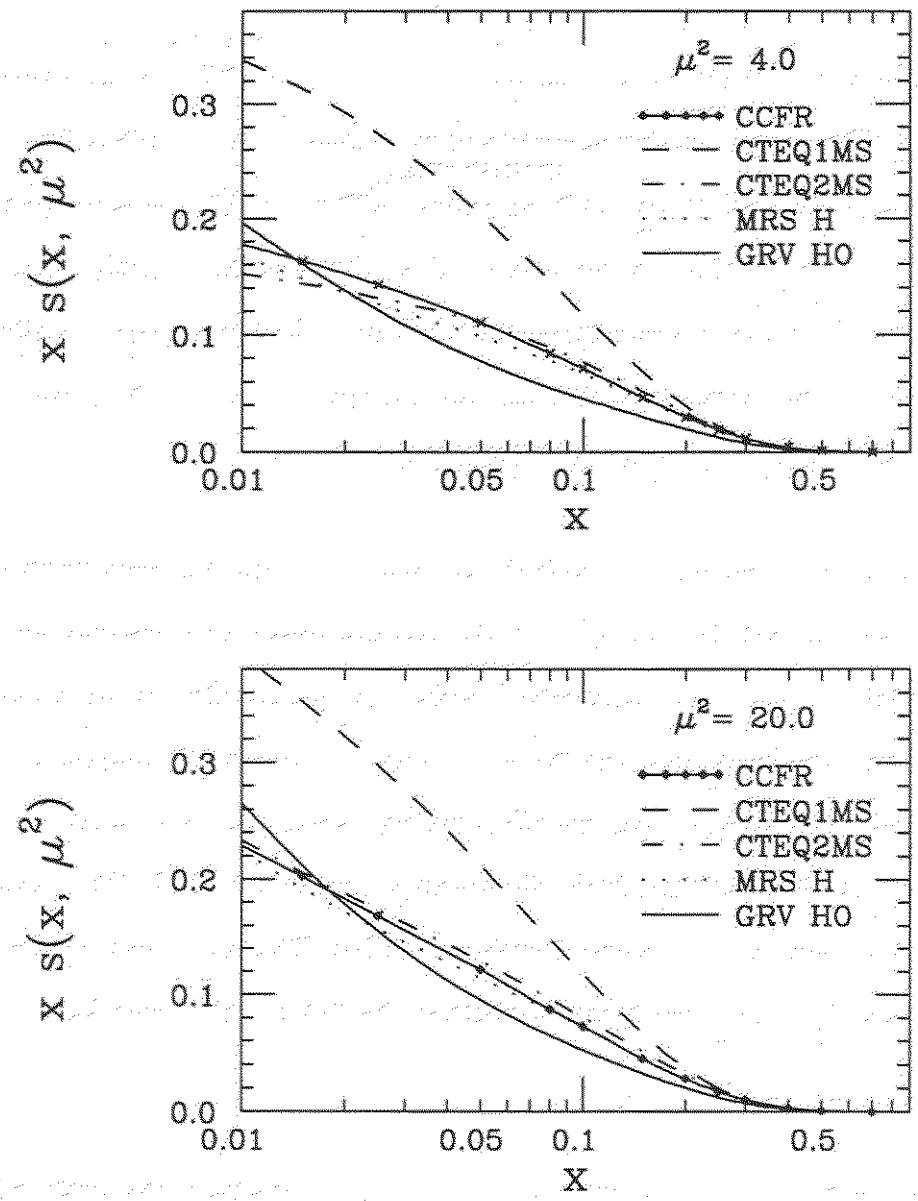

Figure 8.14: The strange sea from the CCFR NLO dimuon analysis compared with the strange sea from global fits. The CTEQ1 fit, which attributed the entirety of the CCFR-NMC discrepancy to the strange sea, differs by a factor of two from the directly-measured sea. The CTEQ2 and subsequent distributions from the CTEQ collaboration incorporated the CCFR measurement in their fits. This plot is from Ref. [Baz94].

However, the strange sea can be determined directly from CCFR data by examining dimuon events. The strange sea determined from the dimuon analysis differs by a factor of two from that of the CTEQ1 distributions, a factor of 5σ. CTEQ2 and subsequent sets of parton distributions incorporate the results of the CCFR dimuon analysis, and the strange sea from CTEQ is in close agreement with the CCFR measurement [Baz94]. Figure 8.14 shows the comparison between the strange sea measured by the CCFR dimuon data and the strange sea from the CTEQ1 distributions.

Another possible cause for the CCFR-NMC discrepancy is the expected form of the structure functions at low Q^2. At $Q^2 \sim 0$ the charged-lepton and neutrino structure functions are different due to the fundamental difference between the pure vector current of the electromagnetic interaction and the added axial vector current component of the weak interaction [Don94]. However, this effect has been show to be very small for $Q^2 >$ 1 and would not explain the CCFR-NMC discrepancy at the observed Q^2. This statement was recently confirmed by preliminary results at HERA [Zhu96], which showed that structure function F_2 exhibits the behavior predicted by Ref. [Don94] only for $Q^2 < 0.5$ GeV^2.

An interesting suggestion has been made in Ref. [Bro96]. The idea is that when a gluon splits into an s and $\bar{s}$ pair, the proton wave function fluctuates into a $K^+\Lambda$ configuration, that is, a combination of a $u\bar{s}$ meson and a uds hadron. The $\bar{s}$ quark then has the characteristic momentum distribution of a mesonic valence quark, while the s quark has the momentum distribution of a hadronic valence quark. The consequence of this is that $xs(x) \neq x\bar{s}(x)$, though the integrals $\int xs\,dx = \int x\bar{s}\,dx$ must be equal. The reason why this might explain the CCFR-NMC discrepancy is that the functional forms assumed for the xs and $x\bar{s}$ distributions by CCFR and the global-fitting groups would be incorrect, and thus both would arrive at an incorrect value for the "5/18ths rule."

If there is no problem in the derivation or calculation of the "5/18ths rule," then the immediate alternate possibility is that the nuclear shadowing correction parameterized in Equation 8.1 is incorrect, that is, nuclear shadowing is different for muon and neutrino scattering. If this is the case, it can only be proven by experiment. This would require a high-statistics neutrino-scattering experiment on a target with low A. Unfortunately, no such experiments are planned.

8.2 QCD Comparisons

In this section the results of the QCD fits of Chapter 7 are compared with the QCD results of other experiments.

8.2.1 Comparing α_S From Different Experiments

Comparing the values of α_S, the strong coupling constant, from different experiments is an important test of QCD, since α_S can be determined at several different energy scales from different physical processes. The different deep-inelastic scattering experiments, such as NMC [Arn93] and SLAC/BCDMS [Vir92], measure α_S from scaling violations. Other techniques, such as e^+e^- event topologies [Abe95] or τ decays [Coa95], do not involve the proton structure functions.

The search for differences between α_S from different physical processes can reveal new physics. The previous analysis of the same data [Qui93] quoted a value of $\alpha_S(M_Z^2)$ = 0.111 ± 0.005, a lower value than that seen in other physical processes. One hypothesis for the difference was the existence of a light gluino [Blu94]. If such a particle existed, the value of $\alpha_S(M_Z^2)$ measured at the typical Q^2 of DIS experiments would be lower than the value measured at the higher values of Q^2 accessible to LEP.

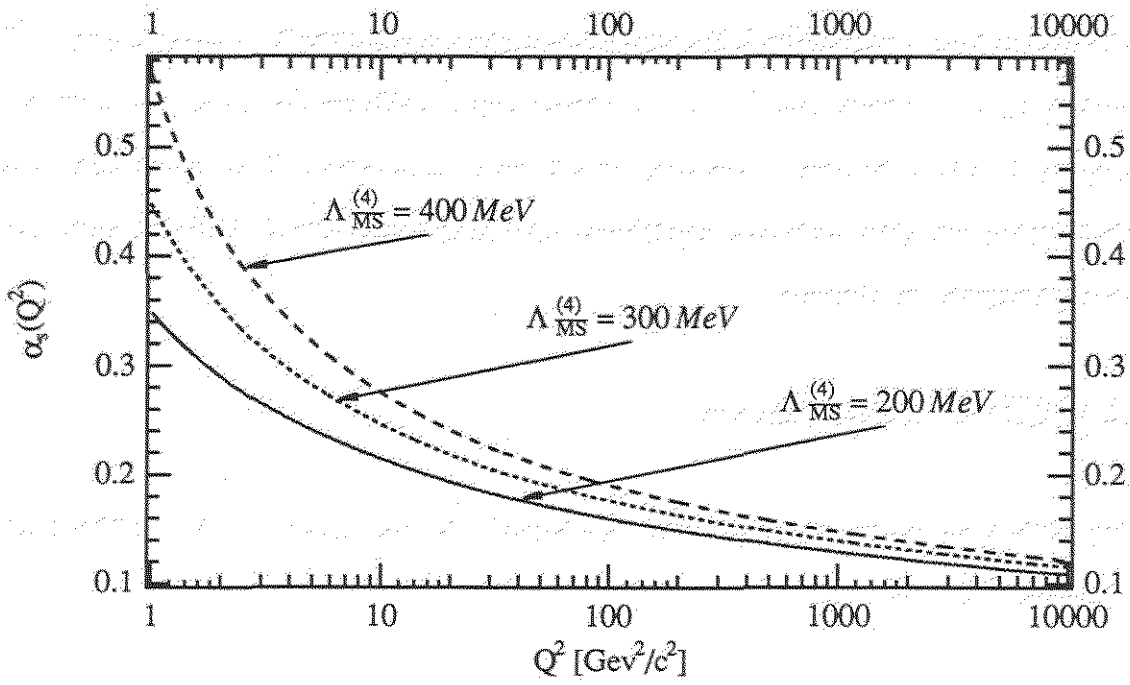

Figure 8.15: $\alpha_S(Q^2)$ for three different values of $\Lambda_{\overline{MS}}$.

α_S varies as a function of Q^2 as illustrated in Figure 8.15, which shows the variation in α_S for three different values of $\Lambda_{\overline{MS}}$ as computed from Equation 1.79. Therefore, to compare α_S between different experiments, the values must be evolved to the same value of Q^2. The standard Q^2 for such comparisons is now M_Z^2, since there are many physicists involved with the LEP and SLD programs.

Figure 8.16 shows the values of $\alpha_S(M_Z^2)$ from this analysis, 0.119 ± 0.004, along with the values from other experiments. The values from other fixed-target DIS experiment are also shown, namely EMC [Baz91], NMC [Arn93], and SLAC/BCDMS [Vir92]. The DIS average from these experiments is shown below the first dashed line. Note that the common QCD renormalization and factorization scale error of ±0.004 (discussed in Section 1.2.4.5) is removed from those results that include it, the average computed, and

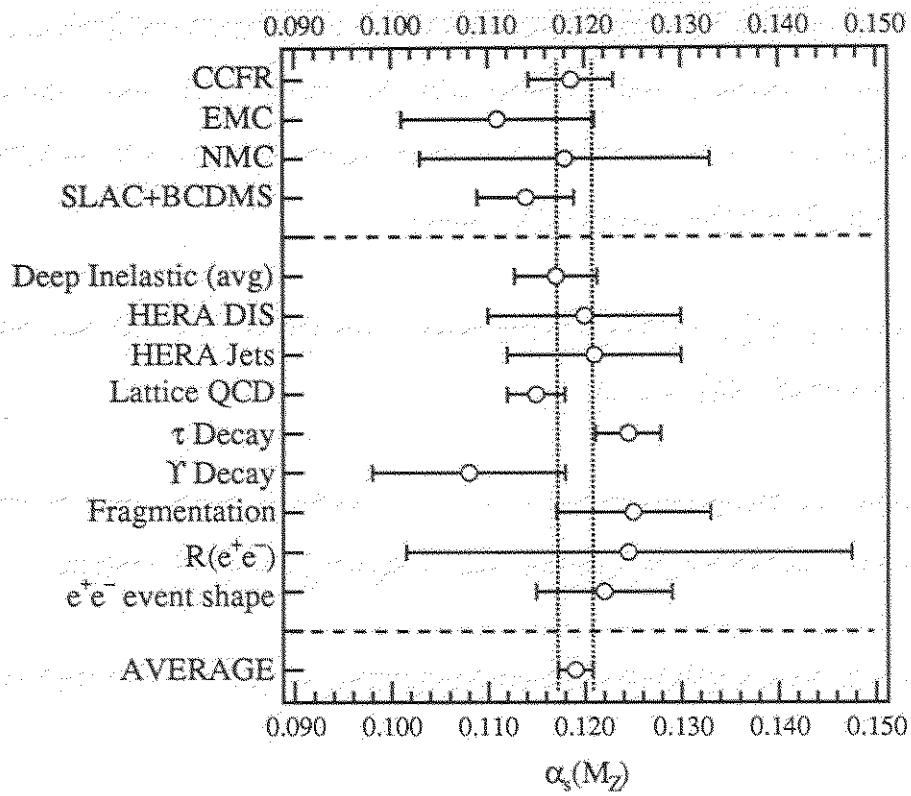

Figure 8.16: $\alpha_S(M_Z^2)$ for several experiments, along with the average of the experiments shown. The average values reported for the different physical processes (apart from the DIS experiments above the first dashed line) are from the Particle Data Group [Bar96]. The average DIS value, and the average from all experiments, are determined from the experiments shown.

then the scale error put back into the average. The resulting average for the DIS experiments is $\alpha_S(M_Z^2) = 0.117 \pm 0.004$.

The other values shown in Figure 8.16 are averages computed by the Particle Data Group [Bar96]. To summarize the physical processes used to derive these values:

- The HERA DIS result [Bal95] determines $\alpha_S(M_Z^2) = 0.120 \pm 0.005$ (exp.) $\pm$ 0.009 (theory) by including the x-dependence, rather than just the Q^2-dependence, of the structure functions at very small x and large Q^2.

- α_S can be determined from jets at HERA by comparing the rates for $e+q \rightarrow e+q$ to $e+q \rightarrow e+q+g$. The first process produces a (1 + 1) jet, since one jet is associated with the proton fragment and the other with the struck quark, while the second process produces a (2 + 1) jet. The result is shown is the average for H1 and ZEUS of $\alpha_S(M_Z^2) = 0.121 \pm 0.004$ (stat.) $\pm$ 0.008 (syst.).

- The result of $\alpha_S(M_Z^2) = 0.115 \pm 0.003$ comes from the lattice QCD calculation of the energy levels of a $Q\overline{Q}$ system.

- The hadronic branching ratio of the τ, $\tau \rightarrow \nu_\tau + hadrons$ can be used to compute $\alpha_S(M_\tau^2) = 0.370 \pm 0.033$. This corresponds to $\alpha_S(M_Z^2) = 0.115 \pm 0.003$.

- $\alpha_S(M_Z^2) = 0.108 \pm 0.010$ is determined from decays of $Q\overline{Q}$ systems such as the Υ by the ratio

$$R_\Upsilon = \frac{\Gamma(\Upsilon \rightarrow hadrons)}{\Gamma\left(\Upsilon \rightarrow \mu^+\mu^-\right)} \tag{8.6}$$

- The fragmentation function $d_i(x,E)$ is the probability that a hadron of type i is produced with energy zE in e^+e^- collisions at $\sqrt{s} = 2E$. QCD predicts the E dependence of the fragmentation function. Experiments at LEP have determined the value of $\alpha_S(M_Z^2) = 0.125 \pm 0.006$ (exp.) $\pm$ 0.006 (theory) from this technique.

- $R\left(e^+e^-\right)$ refers to the technique of measuring α_S from QCD corrections to the total cross-section for $e^+e^- \rightarrow hadrons$. This method yields $\alpha_S(34\,GeV) = 0.146 \pm 0.030$, which corresponds to $\alpha_S(M_Z^2) = 0.125 \pm 0.023$.

- α_S can be determined by looking at the rates for two-jet, three-jet, and four-jet events in e^+e^- collisions, and by looking for jet in special kinematic configurations. This technique yields an average $\alpha_S(M_Z^2) = 0.122 \pm 0.007$.

When the results from the different physical processes listed above are averaged, the final average is $\alpha_S(M_Z^2) = 0.119 \pm 0.002$.

The value of $\alpha_S(M_Z^2)$ from the CCFR analysis is the most accurate of the quoted values from the fixed-target DIS experiments, and one of the most accurate of all measurements. The CCFR value is also consistent with the average value from all experiments and significantly reduces the uncertainty in this fundamental constant. The only two measurements quoted in [Bar96] which are more accurate than the CCFR measurement are the averaged values from lattice QCD calculations and the averaged values from τ decay. The lattice QCD result [Dav94] is consistent with the value measured by this experiment. However, the τ decay measurement is not only inconsistent with the CCFR value, but is inconsistent with the world average. The procedure used in Ref. [Bar96] to average α_S from τ decays emphasizes the values from LEP data, which tends to produce values of $\alpha_S(M_Z^2)$ that are larger than those seen at other experiments; also, the theoretical error in the measurement may be underestimated [Bet95].

It should be noted that the value quoted from the previous analysis of the same data [Qui93] was $\alpha_S(M_Z^2) = 0.111 \pm 0.005$. The main reason for the change to $\alpha_S(M_Z^2) = 0.119 \pm 0.004$ was use of the test beam directly for the energy calibration (see Chapter 3), combined with improvements in the radiative correction and Monte Carlo muon energy-loss modeling.

The increased value and improved precision of the new CCFR α_S measurement eliminates any potential discrepancies between the value of $\alpha_S(M_Z^2)$ seen by deep-

inelastic scattering and the value seen in other types of experiments, and is thus an important confirmation of the Standard Model. In particular, the revised CCFR measurement rules out the light-gluino hypothesis mentioned above.

8.2.2 Comparing *xG(x)* From Different Experiments

There is little point in comparing the valence and sea distributions from this experiment to those from other experiments. Such comparisons would be made to the DIS experiments in overlapping the same kinematic region as CCFR, in other words, the NMC, SLAC, BCDMS, and E665 data. These comparisons are better made using the structure function data directly as done above in Section 8.1.2.

The remaining parton distribution that can be measured by this experiment is the gluon distribution *xG(x)*. The global parton distribution functions CTEQ4 [Lai96], MRS R_2 [Mar96], and GRV 94 [Glu95] already derive or include gluon distributions from the existing world data. For example, the CTEQ4 analysis includes Drell-Yan data from E605 [Mor91] and direct-photon data from UA6 [Soz93]. Therefore, comparing the CCFR gluon distribution against that from the global analyses is, in effect, comparing against the world-average gluon distributions.

Figure 8.17 shows the $\pm 1\sigma$ contour from CCFR gluon distribution of $xG\left(Q^2 = 5GeV^2\right)$ = $(2.22 \pm 0.34) \times (1-x)^{4.65 \pm 0.68}$., evolved to $Q^2 = 32GeV^2$. The gluon distribution from the global analyses at $Q^2 = 32GeV^2$ are also shown. Included are two gluon results that have not yet been incorporated into the global analyses: the gluon distribution from E665 [Ada96], and the gluon distribution from jets at H1 [Aid95]. The gluon distributions from the different experiments and analyses agree with one another for $x > 0.02$. The

CCFR gluon distribution is lower than the others at lower values of x, but the QCD fit does not include data at those values of x (see Figure 6.19).

Appendix G contains additional comparisons between the parton distributions from this analysis and the parton distributions from the global analyses.

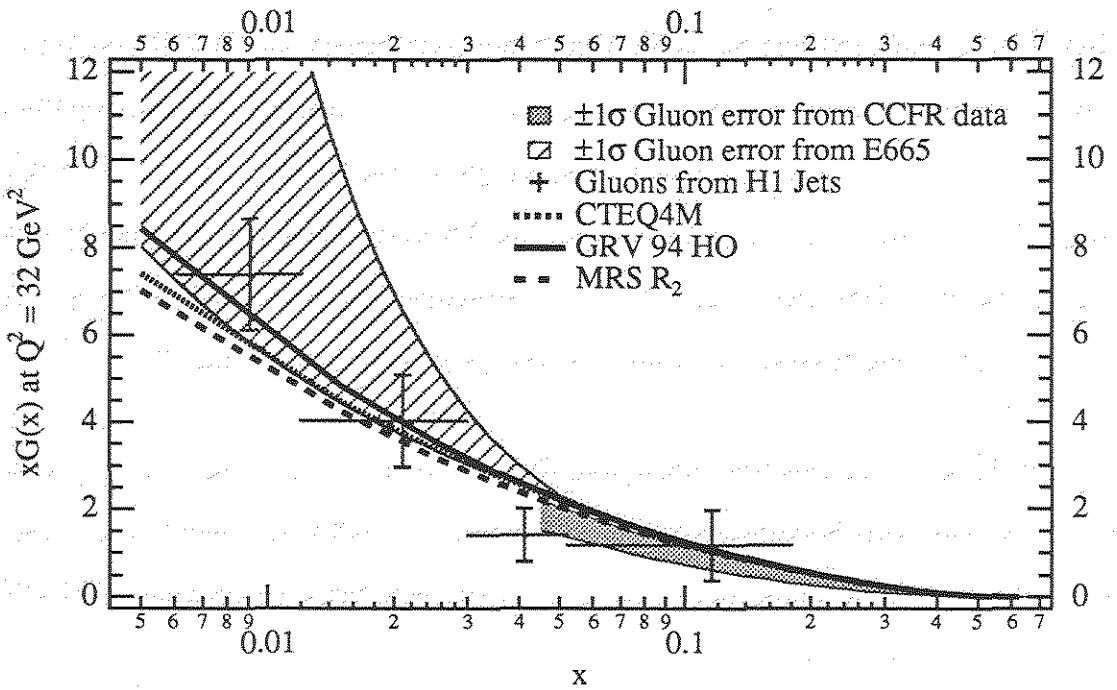

Figure 8.17: A comparison of gluon distributions to the CCFR result. The $\pm 1\sigma$ contour for the gluon results for CCFR and E665 are shown, as are the gluons from the H1 jet results. The CCFR result has an $x >$ 0.45 cut to include on that region where the data passed the QCD fit cuts. The solid, dashed, and dotted lines show the results from the global analyses. All results have been evolved or extracted at $Q^2 = 32 GeV^2$; in particular, the E665 result has been evolved from $Q^2 = 8 GeV^2$. Harsh Venkataramania is thanked for assistance in preparing this plot.

8.3 Conclusions

This thesis has presented a new determination of the structure functions F_2 and xF_3 from ν-Fe deep-inelastic scattering at the Tevatron. These structure functions are crucial inputs for determining the parton distributions inside the nucleon. These parton distributions are needed for tests of the Standard Model where various physical models are compared to the data. For example, recently the CDF collaboration reported an excess in the jet cross-section at high E_T [Abe96]. The observation that an excess existed came from comparing the observed cross-section to that predicted using global fits to the parton distributions determined from other data, including the structure functions previously reported by this experiment [Bot93]. Inclusion of the CCFR new structure-functions results in the global fits may thus affect the observation of the CDF excess cross-section at high E_T.

As part of the structure-function extraction, the ratio of the total neutrino-iron cross-section from anti-neutrino-induced to neutrino-induced events is measured. The value, corrected for the non-isoscalarity of iron, is $\sigma^{\bar{\nu}}/\sigma^{\nu}$ = 0.509 ± 0.002 (stat.) ± 0.012 (syst.) between 30 and 360 GeV.

A comparison of the values of F_2 from this experiment to the values of F_2 from charged-lepton DIS shows that the charged-lepton result is ~10-15% lower than the neutrino-iron data for $x < 0.04$. The discrepancy vanishes for $x > 0.2$. At present, the source of this discrepancy is unknown, but it may signal that further refinements in the model of deep-inelastic scattering are necessary.

The Q^2 evolution of the structure functions is found to be consistent with perturbative QCD. A QCD fit that incorporates the experimental systematic errors in context of the QCD model yields $\Lambda_{\overline{MS}}^{NLO,(4)}$ = 337 ± 28 (stat + syst) ± 13 (higher-twist) MeV measured at $\langle Q^2 \rangle = 30\,GeV^2$, with a gluon distribution given by $xG\left(x, Q_0^2 = 5GeV^2\right)$ =

$(2.22 \pm 0.34) \times (1-x)^{4.65 \pm 0.68}$. This corresponds to a measurement of $\alpha_S(M_Z^2) = 0.119 \pm 0.002$ (exp.) ± 0.001 (HT) ± 0.004 (theory), where the theoretical error comes from the QCD renormalization and factorization scale uncertainty. This result is one of the most precise measurements of $\alpha_S(M_Z^2)$, and is the most precise measurement from deep-inelastic scattering. The agreement of the α_S measurements between experiments using widely different processes is one of the most stringent tests of QCD. At present, the data support the Standard Model and limits any extensions such as those associated with supersymmetric theories.

Bibliography

[Abe89] "A Measurement of W-Boson Production in 1.8 TeV $p\bar{p}$ Collisions"; F. Abe, *et al.*; *Phys. Rev. Lett.* **62**:1005 (1989).

[Abe94] "Measurement Of $\alpha_S(M_Z^2)$From Hadronic Event Observables at the Z_0 Resonance"; K. Abe, *et al.* (SLD Collaboration); *Phys. Rev.* **D51**: 962-984 (1995); hep-ex/9501003.

[Abe96] "Inclusive jet cross section in $p\bar{p}$ collisions at $\sqrt{s} = 1.8\ TeV$"; F. Abe, *et al.*; (CDF Collaboration); *Phys. Rev. Lett.* **77**: 438-443 (1996); hep-ex/9601008

[Ada95a] "Shadowing in Inelastic Scattering of Muons on Carbon, Calcium and Lead at Low x_{BJ}"; M. R. Adams, *et al.* (E665 Collaboration); *Z. Phys.* **C67**: 403-410 (1995); hep-ex/9505006.

[Ada95b] "Determination of the Gluon Distribution Function of the Nucleon Using Energy-Energy Angular Pattern in Deep Inelastic Muon-Deuteron Scattering"; M. R. Adams, *et al.* (E665 Collaboration); FERMILAB-PUB-95-395-E (1995).

[Ada96] "Proton and Deuteron Structure Functions in Muon Scattering at 470-GeV"; M. R. Adams, *et al.* (E665 Collaboration); *Phys.Rev.* **D54**: 3006-3056 (1996).

[Aid95] "A Direct Determination of the Gluon Density in the Proton at Low x"; S. Aid, *et al.* (H1 Collaboration); *Nucl. Phys.* **B449**: 3-24 (1995); hep-ex/9505014.

[Alt77] "Asymptotic Freedom in Parton Language"; G. Altarelli (Ecole Normale Superieure), G. Parisi (IHES, Bures); *Nucl. Phys.* **B126**: 298 (1977).

[Alt82] "Partons in Quantum Chromodynamics"; G. Altarelli (Ecole Normale Superieure); *Phys. Rep.* **81**: 1-129 (1982); reprinted in *The Development of Perturbative QCD*, ed. G. Altarelli, World Scientific (1994).

[Ama95] "A Re-Evaluation of the Nuclear Structure Function Ratios for D, He, Li, C and Ca"; P. Amaudruz, *et al.* (New Muon Collaboration); *Nucl. Phys.* **B441**: 3-11 (1995); hep-ph/9503291.

[Arn84] "Measurements of the A-Dependence of Deep Inelastic Electron Scattering From Nuclei"; R. G. Arnold, *et al.*; *Phys. Rev. Lett.* **52**: 727 (1984).

[Arn93] "Quark and Gluon Distributions and α_S From Nucleon Structure Functions at Low x"; M. Arneodo et al. (New Muon Collaboration); *Phys.Lett.* **B309**: 222-230 (1993).

[Arn96] "Measurement of the Proton and the Deuteron Structure Functions, F_2^p and F_2^d, and of the Ratio σ_L/σ_T"; M. Arneodo, *et al.* (New Muon Collaboration); submitted to *Nucl. Phys.*; hep-ph/9610231.

[Auc90] "Measurement of the Inclusive Charged-Current Cross Section for Neutrino and Antineutrino Scattering on Isoscalar Nucleons"; P. S. Auchincloss, *et al.* (CCFR Collaboration); *Z. Phys.* **C48**: 411-432 (1990).

[Bac88] "A Study of Same Sign Dimuon Events in Neutrino-Nucleon Scattering"; K. T. Bachmann (Columbia University); Ph.D. Thesis, Nevis Reports 267 (1988).

[Bal95] "Determination Of α_S From F2(P) at HERA"; Richard D. Ball, Stefano Forte (CERN); *Phys. Lett.* **B358**: 365-378 (1995); hep-ph/9506233.

[Bar76] "Evidence For New Quarks and New Currents"; R. M. Barnett (Harvard University); *Phys. Rev. Lett.* **36**: 1163-1166 (1976).

[Bar86] "On the Radiative Corrections to the Neutrino Deep Inelastic Scattering"; D. Yu. Bardin and V. A. Dokuchaeva (Dubna, JINR); *JINR-E2-86-260* (1986).

[Bar96] "Review of Particle Physics"; R. M. Barnett, *et al.* (Particle Data Group); *Phys. Rev.* **D54** (1996).

[Baz91] "A Comparative Study of Structure Function Measurements from Hydrogen and Deuterium"; K. Bazizi and S. J. Wimpenny (UC, Riverside); UCR-DIS-91-02 (Jul 1991).

[Baz94] "Determination of the Strange Quark Distribution from a Next-to-Leading-Order QCD Analysis of Neutrino and Antineutrino Production of Charm"; Andrew Bazarko (Columbia University); Ph.D. Thesis, Nevis Reports 285 (1994).

[Baz95] "Determination of the Strange Quark Content of the Nucleon From a Next-To-Leading Order QCD Analysis of Neutrino Charm Production"; A.O. Bazarko, *et al.* (CCFR Collaboration); *Z. Phys.* **C65**: 189-198 (1995); hep-ex/9406007.

[Bel88] "Neutrino reactions in the low-y region"; R. Belusevic and D. Rein; *Phys. Rev.* **D38**: 2753-2757 (1988).

[Bel92] "Exclusive neutrino interactions on heavy nuclei"; R. Belusevic and D. Rein; *Phys. Rev.* **D46**: 3747-3750 (1992).

[Ben87] "A High Statistics Measurement of the Nucleon Structure Function $F_2(x,Q^2)$ From Deep Inelastic Muon - Carbon Scattering at High Q^2"; A. C. Benvenuti *et al.* (BCDMS Collaboration); *Phys. Lett.* **B195**: 91 (1987).

[Ben90] "A High Statistics Measurement of the Deuteron Structure Functions $F_2(x,Q^2)$ and R From Deep Inelastic Muon Scattering at High Q^2"; A. C. Benvenuti, *et al.* (BCDMS Collaboration); *Phys. Lett.* **B237**: 592 (1990).

[Ber87] "Total neutrino and antinuetrino charged current cross section measurement in 100, 160, and 200 GeV narrow band beams"; P. Berge, *et al.* (CDHS Collaboration); *Z. Phys.* **C35**: 443-452 (1987).

[Ber91] "A Measurement of Differential Cross-Sections and Nucleon Structure Functions in Charged-Current Neutrino Interactions On Iron"; P. Berge, *et al.* (CDHSW Collaboration); *Z. Phys.* **C49**: 187-223 (1991).

[Bet95] "Status of α_S Meeasurements"; S. Bethke; (Aachen, Tech. Hochsch.). PITHA-95-14, Jun 1995. Talk given at 30th Rencontres de Moriond: QCD and High Energy Hadronic Interactions, Meribel les Allues, France.

[Bjo69] "Asymptotic Sum Rules at Infinite Momentum"; J. D. Bjorken; *Phys. Rev.* **179**: 1547-1553 (1969).

[Bla83] "Measurement of the Rate of Increase of Neutrino Cross-Sections With Energy"; R. Blair, *et al.* (CCFRR Collaboration); *Phys. Rev. Lett.* **51**: 343-346 (1983).

[Blo76] "Recent Results Concerning the Electromagnetic Structure of the Nucleon"; E. D. Bloom (Cal Tech & SLAC); SLAC-PUB-1319, Oct 1973. Invited paper presented at International Symposium on Electron and Photon Interactions at High Energies (1973).

[Blu94] "Do Deep Inelastic Scattering Data Favor a Light Gluino?"; J. Blümlein and J. Botts (DESY); DESY-94-008 (Jan 1994); hep-ph/9401291.

[Bod74] "The Ratio of Deep-Inelastic eN to eP Cross-Sections in the Threshold Region"; A. Bodek, *et al.* (SLAC); *Phys. Lett.* **51B**: 417 (1974).

[Bod81] "Fermi Motion Effects in Deep Inelastic Lepton Scattering From Nuclear Targets"; A. Bodek, J. L. Ritchie (Rochester U.); *Phys. Rev.* **D23**: 1070 (1981).

[Bot93] "CTEQ Parton Distributions and Flavor Dependence of Sea Quarks"; J. Botts *et al.* (CTEQ Collaboration); *Phys. Lett.* **B304**: 159-166 (1993); hep-ph/9303255.

[Bro96] "The Quark/Antiquark Asymmetry of the Nucleon Sea"; S. Brodsky and B. Ma; *Phys. Lett.* **B381**: 317-324 (1996); hep-ph/9604393.

[Bur78] "Simple Parametrizations of Parton Distributions With Q**2 Dependence Given by Asymptotic Freedom"; A. J. Buras, K. J. F. Gaemers (CERN); *Nucl. Phys.* **B132**: 249 (1978).

[Coa95] "Measurement Of α_S From τ Decays"; T. Coan et al. (CLEO Collaboration); *Phys. Lett.* **B356**: 580-588 (1995).

[Dav94] "A Precise Determination of α_S From Lattice QCD"; C. T. H. Davies, *et al.*; *Phys. Lett.* **B345**: 42 (1995); hep-ph/9408328.

[Dev83] "Direct Analysis of Scaling Violations in Large Q**2 Deep Inelastic Neutrino and Muon Scattering";. A. Devoto, D. W. Duke, J. F. Owens (Florida State U.), R. G. Roberts (Rutherford); *Phys. Rev.* **D27**: 508-522 (1983).

[Das96] "Power Corrections and Renormalons in Deep Inelastic Structure Functions"; M. Dasgupta and B. R. Webber (Cambridge Univ.); *Phys. Lett.* **B382**: 273 (1996); hep-ph/9604388.

[Dok78] "Hard Semiinclusive Processes in QCD"; Yu. L. Dokshitser, D. I. Diakonov, S. I. Troyan (St. Petersburg, INP); *Phys. Lett.* **78B**: 290 (1978).

[Dok80] "Hard Processes in Quantum Chromodynamics"; Yu. L. Dokshitser, D. I. Diakonov, S. I. Troian; *Phys. Rep.* **58**: 269-395 (1980).

[Dok95] "Dispersive Approach to Power Behaved Contributions in QCD Hard Processes"; Yu. L. Dokshitser (CERN), G. Marchesini (Milan U. & INFN, Milan), B. R. Webber (Cambridge U., Cavendish Lab); CERN-TH-95-281, (Dec 1995); hep-ph/9512336.

[Don94] "Proton Structure Function at Small Q**2"; A. Donnachie (Manchester U.) and P.V. Landshoff (Cambridge U., DAMTP); *Z. Phys.* **C61**: 139-146 (1994); hep-ph/9305319.

[Flo81] "Higher-Order QCD Effects in Inclusive Annihilation and Deep-Inelastic Scattering"; E. G. Floratos, C. Kounnas (Ecole Normale Superieure), R. Lacaze (Saclay); *Nucl. Phys.* **B192**: 417 (1981).

[Fou90] "Neutrino Production of Opposite Sign Dimuons at Tevatron Energies"; C. Foudas, *et al.* (CCFR Collaboration); *Phys. Rev. Lett.* **64**: 1207 (1990).

[Geo76] "Freedom at Moderate Energies: Masses in Color Dynamics"; H. Georgi and H. D. Politzer (Harvard University); *Phys. Rev.* **D14**: 1829 (1976).

[Glu95] "Dynamical Parton Distributions of the Proton and Small x"; M. Glück, E. Reya (Dortmund U.), A. Vogt (DESY); *Z. Phys.* **C67**: 433-448 (1995).

[Gom94] "Measurement of the A-Dependence of Deep Inelastic Electron Scattering"; J. Gomez, *et al.*; *Phys. Rev.* **D49**: 4348-4372 (1994).

[Gri72] "Deep Inelastic e-P Scattering in Perturbation Theory"; V. N. Gribov, L. N. Lipatov (St. Petersburg, INP); *Sov. J. Nucl. Phys.* **15**: 438-450 (1972).

[Hai94] D. Haidt (DESY), private communication.

[Hal84] *Quarks and Leptons: An Introductory Course in Modern Particle Physics;* F. Halzen and A. D. Martin; John Wiley & Sons (1984).

[Har95] "A Measurement of Alpha-s (Q**2) From the Gross-Llewellyn-Smith Sum Rule"; D. A. Harris, *et al.* (CCFR-NUTEV Collaboration); *Moriond 1995: Hadronic:* 247-250; hep-ex/9506010.

[Her80] "Altarelli-Parisi Equation in the Next-To-Leading Order"; R. T. Herrod, S. Wada (Cambridge U., Cavendish Lab.); *Phys. Lett.* **96B**: 195 (1980).

[Hin77] "Scaling Violations and Neutrino Cross Sections"; I. Hinchcliffe and C. H. Llewellyn-Smith (Oxford Univ.); *Phys. Lett.* **70B**: 247-252 (1977).

[Jam94] *MINUIT – Function Minimization and Error Analysis;* F. James and M. Goosens (CERN); CERN Program Library entry **D506** (1994).

[Kin91] "Measuring Muon Momenta With the CCFR Neutrino Detector"; B. J. King, *et al.* (CCFR Collaboration); *Nucl. Instrum. Methods* **A302**: 254-260 (1991).

[Kin94] "A Precise Measurement of the Weak Mixing Angle in Neutrino-Nucleon Scattering"; B. J. King, Ph.D. Thesis (Columbia University); Nevis Reports 283 (1994).

[Koi78] G. Koizumi; FERMILAB-TM-0780 (1978).

[Lai96] "Improved Parton Distributions from Global Analysis of Recent Deep Inelastic Scattering and Inclusive Jet Data"; H. L. Lai, *et al.*; MSUHEP-60426; hep-ph/9606399.

[Leu91] "Nucleon Structure Functions from High-Energy ν-Iron Interactions at the Fermilab Tevatron"; W. C. Leung, Ph.D. Thesis (Columbia University); Nevis Reports 276 (1991).

[Mac84a] "Nucleon Structure from Neutrino Interactions in an Iron Target with a Study of the Singlet Quark Distribution"; D. MacFarlane (California Institute of Technology); Ph.D. Thesis (1984).

[Mac84b] "Nucleon Structure Functions From High-Energy Neutrino Interactions with Iron and QCD Results"; D. MacFarlane, *et al.* (CCFRR Collaboration); *Z. Phys.* **C26**: 1 (1984).

[Mar91] "Scale Dependence of $\Lambda_{\overline{\mathrm{MS}}}$ from Deep Inelastic Scattering"; A. D. Martin, W. J. Stirling (Durham Univ.), R. G. Roberts (Rutherford); *Phys. Lett.* **B266**: 173-177 (1991).

[Mar96] "Parton distributions: a study of the new HERA data, α_S, the gluon and $p\overline{p}$ jet production"; A. D. Martin (Durham Univ.), R. G. Roberts (Rutherford), W. J. Stirling (Durham Univ.); DTP/96/44, RAL-TR-96-037 (1996); hep-ph/9606345.

[Mis89] "A Study of Wrong Sign Single Muon Production in Muon-Neutrino–Nucleon Interaction"; S. R. Mishra, *et al.* (CCFR Collaboration); *Z. Phys.* **C44**: 187 (1989).

[Mor91] "Dimuon Production In Proton-Copper Collisions at $\sqrt{s}$ = 38.8 *GeV*"; G. Moreno, *et al.*; *Phys. Rev.* **D43**: 2815-2836 (1991).

[Olt89] "Nucleon Structure Functions from High Energy Neutrino and Antineutrino Interactions in Iron"; E. Oltman (Columbia University); Ph.D. Thesis, Nevis Reports 270 (1989).

[Per82] *Introduction to High Energy Physics*; D. H. Perkins; Addison-Wesley (1982).

[Pre92] *Numerical Recipes in FORTRAN – The Art of Scientific Computing, 2nd Edition;* W. H. Press, S. A. Teukolsky, W. T. Vetterling, B. P. Flannery; Cambridge University Press (1992).

[Pur84] "Nucleon Structure Functions from ν_μ-Fe Interactions and a Study of the Valence Quark Distribution"; M. Purohit (California Institute of Technology); Ph.D. Thesis (1984).

[Qui92] "Nucleon Structure Functions at the Fermilab Tevatron With a Measurement of $\Lambda_{\overline{MS}}$"; P. Z. Quintas (Columbia University); Ph.D. Thesis, Nevis Reports 277 (1992).

[Qui93] "Measurement of Λ_{QCD} from ν_μ-Fe Nonsinglet Structgure Functions at the Fermilab Tevatron"; P. Z. Quintas, *et al.* (CCFR Collaboration); *Phys. Rev. Lett.* **71**: 1307-1310 (1993).

[Rab92] "Opposite Sign Dimuon Production in Neutrino Interactions at the Fermilab Tevatron"; S. A. Rabinowitz (Columbia University); Ph. D. Thesis, Nevis Reports 279 (1992).

[Rab93] "Measurement of the Strange Sea Distribution Using Neutrino Charm Production"; S. A. Rabinowitz, *et al.* (CCFR Collaboration); *Phys. Rev. Lett.* **70**: 134-137 (1993).

[Rob90] *The Structure of the Proton;* R. G. Roberts; Cambridge University Press (1990).

[Ruj79] "Radiative Corrections to High-Energy Neutrino Scattering"; A. De Rujula, R. Petronzio (CERN), A. Savoy-Navarro (Saclay); *Nucl. Phys.* **B154**: 394 (1979).

[Sak90] "Calibration of the CCFR Target Calorimeter"; W. K. Sakumoto, *et al.* (CCFR Collaboration); *Nucl. Instrum. Meth.* **A294**: 179-192 (1990).

[Sal68] "Weak and Electromagnetic Interactions"; A. Salam (Imperial Coll., London & ICTP, Trieste); Originally printed in Svartholm: *Elementary Particle Theory, Proceedings Of The Nobel Symposium Held 1968 At Lerum, Sweden*, Stockholm 1968, 367-377; Reprinted in Lichtenberg, D. B. (ed.), Rosen, S. P. (ed.): *Developments In The Quark Theory Of Hadrons, Vol. 1*, 160-170; and in Lai, C. H. (ed.): *Gauge Theory Of Weak and Electromagnetic Interactions*, 188-198; Also in Rosner, J. L. (ed.): *New particles* 29-39.

[San93] "Neutrino Production of Same Sign Dimuons at the Fermilab Tevatron"; P. H. Sandler, *et al.* (CCFR Collaboration); *Z. Phys.* **C57**: 1-12 (1993).

[Sid95] "Nuclear effect in the deuteron, Q^2-evolution of the $xF_3^N(x,Q^2)$ structure function and the Gross-Llewellyn Smith sum rule"; A. V. Sidorov and M. V. Tokarev (JINR); *Phys. Lett.* **B358**: 353-359 (1995).

[Sid96a] "QCD analysis of the CCFR data for xF_3 and Higher-Twist Contribution"; A. V. Sidorov (JINR); *Phys. Lett.* **B389**: 379-382 (1996); hep-ph/9607275.

[Sid96b] "Next-to-next-to-leading order QCD analysis of combined data for xF_3 structure functions and higher-twist contribution"; A. V. Sidorov (JINR); hep-ph/9609345.

[Sop89] "Factorization of Hard Processes in QCD"; D. E. Soper, J. C. Collins, and G. Sterman; *Perturbative Quantum Chromodynamics*, ed. A. H. Mueller, World Scientific (1989).

[Soz93] "Direct Photon Production in $\bar{p}p$ and pp Interactions at $\sqrt{s} = 24.3\ GeV$"; G. Sozzi, et al. (UA6 Collaboration); Phys. Lett. B317: 243-249 (1993).

[Sto85] "Search For Muon Neutrino and Anti-Neutrinos Oscillations in the Mass Range 15 $eV^2/c^4 < \Delta m^{**}2 < 1000\ eV^2/c^4$"; I. E. Stockdale, *et al.* (CCFR collaboration); *Z. Phys.* **C27**: 53 (1985).

[Vir92] "A measurement of α_S and of higher twists from a QCD analysis of high statistics F_2 data on hydrogen and deuterium targets"; M. Virchaux and A. Milsztajn (Saclay); *Phys. Lett.* **B274**: 221-229 (1992).

[Wei67] "A Model of Leptons"; S. Weinberg (MIT, LNS) *Phys. Rev. Lett.* **19**: 1264-1266 (1967); Also in: Lichtenberg, D. B. (ed.), Rosen, S. P. (ed.): *Developments In The Quark Theory Of Hadrons, Vol. 1*, 157-159; in Lai, C. H. (ed.): *Gauge Theory Of Weak and Electromagnetic Interactions*, 185-187; in Rosner, J. L. (ed.): *New Particles*, 26-28.

[Whi90a] *Deep Inelastic Structure Functions from Electron Scattering on Hydrogen, Deuterium, and Iron at* $.56 < Q^2 < 30\ GeV^2$"; L. W. Whitlow (Stanford Univ.); Ph.D. Thesis, SLAC-REPORT-357 (1990).

[Whi90b] "A Precise Extraction of R = σ_L / σ_T From a Global Analysis of the SLAC Deep Inelastic eP and eD Scattering Cross-Sections"; L. W. Whitlow, *et al.*; *Phys. Lett.* **B250**: 193-198 (1990).

[Yan96] "A Measurement of R = Sigma-L / Sigma-T in Deep Inelastic Neutrino-Nucleon Scattering at the Tevatron"; U. K. Yang, *et al.* (CCFR/NuTeV Collaboration); *J. Phys.* **G22**: 775-780 (1996); hep-ex/9605005.

[Ynd93] *The Theory of Quark and Gluon Interactions*; F. J. Yndurain; Berlin: Springer-Verlag (1993).

[Zhi93] J. Zhitnitsky, private communication.

[Zhu96] "The first preliminary total cross section measurement at very low x and Q^2 at HERA"; Q. Zhu (for the ZEUS collaboration); Conference proceedings of the DIS96, Rome, Italy (1996).

Appendix A: The CCFR/NuTeV Collaboration

R. A. Johnson, M. Vakili

University of Cincinnati, Cincinnati, OH 45221

C. G. Arroyo, A. O. Bazarko, J. Conrad, J. H. Kim, B. J. King, W. C. Lefmann, C. McNulty, S. R. Mishra, P. Z. Quintas, A. Romosan, F. J. Sciulli, W. G. Seligman, M. H. Shaevitz, P. Spentzouris, E. G. Stern

Columbia University, New York, NY 10027

R. H. Bernstein, M. J. Lamm, W. Marsh, K. S. McFarland, Jae Yu

Fermi National Accelerator Laboratory, Batavia, IL 60510

T. Bolton, D. Naples

Kansas State University, Manhattan, KS 66506

L. de Barbaro, H. Schellman

Northwestern University, Evanston, IL 60208

P. de Barbaro, A. Bodek, H. Budd, D. Harris, W. K. Sakumoto, U. K. Yang

University of Rochester, Rochester, NY 14627

T. Kinnel, W. H. Smith

University of Wisconsin, Madison, WI 53706

Appendix B: Accessing Analysis Results via the Internet

The results of the analysis described in this thesis are available from a File Transfer Protocol (ftp) site on the Internet. This site can also be accessed via the World Wide Web (WWW). All of the structure-function files listed in Appendix D, the contents of this thesis (including Postscript files of important figures), program source code, and other files of analysis-related information are available at this site.

Every directory in this site contains a file named READ_ME (or READ_ME_FIRST) which describes the purpose of the directory, the files within the directory, and any sub-directories within that directory. When you explore the contents of this site, you should view the contents of the READ_ME file before you copy or view any of the other files within a directory.

The commands given below will connect you to the main ftp area for the results presented in this thesis: `/pub/ccfr/seligman`. The sub-directory of greatest interest to those wishing to access the tables in Appendix D is `/pub/ccfr/seligman/results`. In any given directory, consult the file READ_ME_FIRST (or READ_ME) for information about the contents of the directory.

B.1 Accessing the site via FTP

To access the site from computers running the UNIX or VAX operating systems, use anonymous ftp. The following is a sample session that connects a UNIX system to the ftp site. Characters in italics *like this* are typed by the user.

```
$ ftp nevis1.columbia.edu
Connected to nevis1.nevis.columbia.edu.
220 nevis1.nevis.columbia.edu FTP server ready.
Name: anonymous
331 Guest login ok, type your name as password.
Password:
230 Guest login ok, access restrictions apply.
Remote system type is UNIX.
```

```
Using binary mode to transfer files.
ftp> cd /pub/ccfr/seligman
250 CWD command successful.
ftp> dir
200 PORT command successful.
150 Opening ASCII mode data connection for '/bin/ls'.
total 43
-rw-r--r--    1 seligman ccfr        2466 Jan 21 13:17 READ_ME_FIRST
-rw-r--r--    1 seligman ccfr        5163 Jan 16 21:22 SYSTEMATICS
drwxr-xr-x    2 seligman ccfr        1024 Jan 17 11:03 bgpar
drwxr-xr-x    2 seligman ccfr        2048 Jan 15 15:06 flux
drwxr-xr-x    2 seligman ccfr         512 Jan 14 18:11 hbook
drwxr-xr-x    2 seligman ccfr         512 Jan 20 14:34 prl
drwxr-xr-x    4 seligman ccfr         512 Jan 21 13:21 ps
drwxr-xr-x    2 seligman ccfr        1024 Jan 17 22:24 results
drwxr-xr-x    2 seligman ccfr        2560 Jan 15 15:58 sftable
drwxr-xr-x    5 seligman ccfr         512 Jan 21 15:11 source
drwxr-xr-x    3 seligman ccfr         512 Jan 21 15:16 thesis
226 Transfer complete.
ftp>
```

The specific commands and responses depend on the type of the computer and its operating system. To list the contents of a directory, type *dir* as in the example above. In most versions of ftp, the command `get <filename>` will retrieve the given file. For example:

```
$ get READ_ME_FIRST
```

To change to a given directory, type `cd <directory>`. For example, these two commands:

```
$ cd /pub/ccfr/seligman
$ cd results
```

will first change the current directory to the main directory of the ftp site for these results, then move you to the `results` sub-directory.

B.2 Accessing the site via a WWW browser

An alternate method of accessing the ftp site is via a Web browser such as Netscape Navigator, NCSA Mosaic, or Microsoft Internet Explorer. The Uniform Resource Location (URL) of the ftp site is:

```
ftp://nevis1.columbia.edu/pub/ccfr/seligman
```

For the specifics of how to access and retrieve files using a Web browser, see the browser's documentation. In Netscape Navigator, option-click (on a Macintosh), ctrl-click (on an IBM-compatible), or alt-click (on UNIX machines) will retrieve a file onto your computer; double-click a directory name to move into a sub-directory; use the "BACK" button to move to a higher directory.

Appendix C: Program Source Code

This Appendix contains portions of the program source code that was used in the analysis described in this thesis. The complete FORTRAN source code for the analysis, including the routines given below, is available via the Internet as described in Appendix B. The routines listed below are included in this Appendix because they contain calculations that are not otherwise documented in this thesis:

- the model for the Buras-Gaemers leading-order Q^2-dependence of parton distributions [Bur78],
- the model used for the strange sea as measured in the leading-order dimuon analysis [Rab93],
- the calculation for extracting the structure functions, including the complete statistical-error calculation,
- the next-to-leading-order QCD evolution within the Duke and Owens program [Dev83, Flo81, Her80],
- the calculation of higher-twist effects [Das96].

C.1 The Buras-Gaemers Code

Subroutine `model.f` generates the parton distributions according to the Buras-Gaemers parameterization as described in Chapter 4. Subroutine `rabin_model.f`, called by `model.f`, returns the exact strange sea that was reported in Ref. [Rab92], and is based on the Buras-Gaemers parameters used in that analysis.

BGPARAM.CMN

```
C Buras-Gaemers parameters
C 25-Mar-92 Revised to include RCORFL  WGS
C 28-Dec-92 changed name of common block from /MUFF/ to /BGPARAM/  WGS
C 20-Nov-96 added new parameters according to CKM.   WGS
C  6-Dec-96 added switch that determines which "generation" of
C           parameters we're using: CKM or "old" version.  WGS
      INTEGER RCORFL,par_switch
      COMMON/BGPARAI/RCORFL,par_switch
      REAL A0,A1,E10,E11,E20,E21,S2,S3,G3
```

```
     $     ,          av2,e3,av3,e4,as2,es2
      COMMON/BGPARAM/A0,A1,E10,E11,E20,E21,S2,S3,G3
     $     ,          av2,e3,av3,e4,as2,es2
C-----------------------------------------------------------------
```

model.f

```
      SUBROUTINE MODEL(X,QSQ,UV,DV,SEA,SSEA,R)
      IMPLICIT DOUBLE PRECISION (A-H,O-Z)
      REAL X,QSQ,UV,DV,SEA,SSEA,R,RMODEL
      real rabin_model
C
C     CONVERTED 25-JUL-90  BILL SELIGMAN
C     20-Nov-96: Revised to include new parameters due to CKM
C                (that's Cindy Kay McNulty).   WGS
C     24-Dec-96: (Ho, Ho, Ho): put in (1-x) term into new
c                parameterization.             WGS
c     30-Dec-96: (New Year's Eve Eve): Now try my new parameterization
c                which only involves powers of (1-x).
c      2-Jan-97: For a brand-new year, avoid negative and irrational seas.
      DOUBLE PRECISION GN(2),GNP(2),GNN(2),AN(2),BN(2)
#include <SFCONST.CMN>
#include <BGPARAM.CMN>
      REAL PARAM(15)
      EQUIVALENCE(PARAM(1),A0)

      parameter (small=.002)     ! used to regulate new CKM parameterization
                                 ! at small x.

      LOGICAL INIT
#include <TWOMU.CMN>
      DATA GN,GNP,GNN,AN,BN/
     >0.427D0,0.667D0,
     >0.747D0,1.386D0,
     >0.D0   ,0.609D0,
     >0.429D0,0.925D0,
     >0.429D0,0.288D0/
      DATA INIT/.TRUE./
      DOUBLE PRECISION Q02/12.6D0/,XL/.250D0/
C
      integer icnt /0/, icntmx /30/
C
C   INLINE STUFF FOR F2 INTEGRATION
C
      F20(Y) =
     >       (A*Y**E10*(1D0-Y)**E20*(1D0+CD*(1.-Y)) + AS0*(1D0-Y)**ES0)
     >      *(1D0+RMODEL(SNGL(Y),SNGL(Q02)))/(1D0+(TWOMP*Y)**2/Q02)
      BETA(AA,BB) = DGAMMA(AA)*DGAMMA(BB)/DGAMMA(AA+BB)
C
C-----------------------------------------------------------------------------
C
      IF (INIT .OR. X .LT. 0.) THEN

C        THIS IS NEW..
         XL = A0
         CONST = 4D0/(11D0-8D0/3D0)
C
         XL2 = XL**2
         T0 = LOG(Q02/XL2)
         CD = .5*(1.+E10+E20)/(1.+E20)
         A = A1*(1.-CONST/T0)*2./BETA(E10,E20+1.)
         V82= A*(BETA(E10+1.,E20+1.)+CD*BETA(E10+1.,E20+2.))
         V83= A*(BETA(E10+2.,E20+1.)+CD*BETA(E10+2.,E20+2.))
         QS2= S2+V82
```

```
      QS3= S3+V83
      AS0= S2*(S2/S3-1.)
      ES0= S2/S3-2.
C     FIND INTEGRAL OF F2 AT QSQ = Q02
      F2INT = 0.
      H=.001
      Y=-H
      TWOH=2.*H
      DO 1 I=1,500
         Y=Y+TWOH
         F2INT=F2INT+4.*F20(Y)
 1    CONTINUE
      Y=0.
      DO 2 I=1,499
         Y=Y+TWOH
         F2INT=F2INT+2.*F20(Y)
 2    CONTINUE
      F2INT=F2INT+F20(0.)
      F2INT=H*F2INT/3.
      G2=1.-F2INT

c     print *,'model f2int:'
c     print *,' param=',param
c     print *,' xl,const,xl2,q02,t0,cd,e10,e20,a='
c     print *,  xl,const,xl2,q02,t0,cd,e10,e20,a
c     print *,' v82,v83,qs2,qs3,as0,es0,s2,s3='
c     print *,  v82,v83,qs2,qs3,as0,es0,s2,s3
c     print *,' twomp,f2int,g2='
c     print *,  twomp,f2int,g2

      INIT = .FALSE.
      QSQOLD = -999.
      IF (X .LT. 0.) RETURN

   ENDIF                        ! initialization

   IF (QSQ .NE. QSQOLD) THEN
      T = LOG(QSQ/XL2)
      S  = LOG(T/T0)
      EGN1 = EXP(-GN(1)*S)
      EGN2 = EXP(-GN(2)*S)
      D12=S2*EGN1
      D13=S3*EGN2
      D22=((1-AN(1))*QS2 - BN(1)*G2)*EXP(-GNP(1)*S)
A          + (AN(1)*QS2+BN(1)*G2)*EXP(-GNN(1)*S)
A          - V82*EGN1
      D23=((1.-AN(2))*QS3 - BN(2)*G3)*EXP(-GNP(2)*S)
A          + (AN(2)*QS3+BN(2)*G3)*EXP(-GNN(2)*S)
A          - V83*EGN2
      SQ2=0.75*D22 + 0.25*D12
      SQ3=0.75*D23 + 0.25*D13
      AS = max(SQ2*(SQ2/SQ3-1.), 0.) ! 2-Jan-97 Avoid negative and
      ES = max(SQ2/SQ3-2.       , 0.) !  irrational seas.
      E1 = E10 + E11*S
      E2 = E20 + E21*S
      AV = A1*(1.-CONST/T)*2./BETA(E1,E2+1.)
      CD = .5*(1.+E1+E2)/(E2+1.)
      QSQOLD = QSQ
   ENDIF                        ! qsqold .ne. qsq

   UV = AV*X**E1*(1.-X)**E2
$     + av2*(1.-x)**e3
$     + av3*(1.-x)**e4  ! 20-Nov-96 + 24-Dec-96 + 30-Dec-96
   DV = UV*CD*(1.-X)
```

```
      SEA = AS*(1.-X)**ES
     $     + as2*(1.-x)**es2 ! 20-Nov-96 + 24-Dec-96 + 30-Dec-96

c     6-Dec-96: new style gets the strange sea from Rabinowitz.
      if (par_switch .eq. 1) then
         ssea =  rabin_model(x,qsq,salpha)
      else
         SSEA = AS*(1./(ES+1.))*(ES+SALPHA+1.)*(1.-X)**(ES+SALPHA)
      end if

      R = RMODEL(X,QSQ)

c     if (icnt .lt. icntmx) then
c        icnt = icnt + 1
c        print *,'model: x,qsq,av,el,e2,cd,as,es='
c        print *,        x,qsq,av,el,e2,cd,as,es
c        print *,'       uv,dv,sea,ssea,r,salpha='
c        print *,        uv,dv,sea,ssea,r,salpha
c        print *,'       f2int,g2=',f2int,g2
c     end if

      RETURN
      END
```

rabin_model.f

```
      real function rabin_model(xx,qq,salpha)

*********************************************************************
* CKM 11/96: to fix the strange sea at the values rabinowitz measured  *
* i grabed this version of model.f from rabinowitz code                *
* which you can find in:                                               *
*     /usr7/ccfr2/usr6/ccfr/bazarko/amdahl/rabi_191/BGFITB.FORTRAN     *
* bg parameters are fixed at the values in rabinowitz thesis           *
*     (which are in bgpara)                                            *
* this is a stand alone program that doesn't need initialization       *
*********************************************************************
ckm...Declare all variables
      real xl,a,cd,es0,as0,aa,bb,beta,const
     +     ,xl2,v82,v83,qs2,qs3,f2int,t,s,egn1,egn2
     +     ,d12,d13,d22,d23,sq2,sq3,as,es,el,e2,ssea
     +     ,t0,g2,x,qsq,xx,qq,salpha
      data first /.true./

ckm...Explicitly assign values to the bg parameters (bgpara)
      real A0,A1,E10,E11,E20,E21,S2,S3,G3
      data A0,A1,E10,E11,E20,E21,S2,S3,G3 / .447269,1.000082,0.610119
     +     ,-0.028853,2.835008,1.426865,0.159240,0.018921,0.051486 /

ckm...The fixed Buras Gaemers variables
      REAL GN(2),GNP(2),GNN(2),AN(2),BN(2)
      DATA GN,GNP,GNN,AN,BN/
     A0.427,0.667,
     A0.747,1.386,
     A0.   ,0.609,
     A0.429,0.925,
     A0.429,0.288/

ckm...Rabinowitz code had to be called once to initialize certain
ckm...values.  since they will never change i've hard coded them
      data const / .48 /
      data xl    / 0.447269 /
      data xl2   / 0.200049 /
      data t0    / 4.142887 /
```

```
      data cd    / 0.579546 /
      data a     / 2.655745 /
      data v82   / 0.341807 /
      data v83   / 9.65246E-02 /
      data qs2   / 0.501041 /
      data qs3   / 0.115446 /
      data as0   / 1.180931 /
      data es0   / 6.416046 /
      data f2int / 0.548024 /
      data g2    / 0.451976 /

ckm...Gamma is a cernlib product
      BETA(AA,BB) = GAMMA(AA)*GAMMA(BB)/GAMMA(AA+BB)


ckm...To avoid any potential double precision problems
      x = sngl(xx)
      qsq = sngl(qq)


ckm...These values change with the given value of qsq
      T = LOG(QSQ/XL2)
      S  = LOG(T/T0)
      EGN1 = EXP(-GN(1)*S)
      EGN2 = EXP(-GN(2)*S)
      D12=S2*EGN1
      D13=S3*EGN2
      D22=((1-AN(1))*QS2 - BN(1)*G2)*EXP(-GNP(1)*S)
     A     + (AN(1)*QS2+BN(1)*G2)*EXP(-GNN(1)*S)
     A     - V82*EGN1
      D23=((1.-AN(2))*QS3 - BN(2)*G3)*EXP(-GNP(2)*S)
     A     + (AN(2)*QS3+BN(2)*G3)*EXP(-GNN(2)*S)
     A     - V83*EGN2
      SQ2=0.75*D22 + 0.25*D12
      SQ3=0.75*D23 + 0.25*D13
      AS = SQ2*(SQ2/SQ3-1.)
      ES = SQ2/SQ3-2.
      E1 = E10 + E11*S
      E2 = E20 + E21*S
      CD = .5*(1.+E1+E2)/(E2+1.)

ckm...take salpha from rabinowitz thesis
cwgs  salpha = 2.5
cwgs  for systematic studies, we need to get this from MODEL.F

      SSEA = AS*(1./(ES+1.))*(ES+SALPHA+1.)*(1.-X)**(ES+SALPHA)
      rabin_model = ssea

ckm...Debug
c      if(first) then
c      if (x.lt..0151.and.qsq.lt.2.01) then
c         write(6,*) 'rab: ssea=',ssea
c         write(6,*) 'rab: AS*(1./(ES+1.)),(ES+SALPHA+1.)'
c     +        ,' ,(1.-X)**(ES+SALPHA)'
c     +        ,AS*(1./(ES+1.)),(ES+SALPHA+1.)
c     +        ,(1.-X)**(ES+SALPHA)
c         write(6,*) 'rab: as,es,salpha,x=',as,es,salpha,x
c         write(6,*) 'rab: s2,s3,a1,a0,e10,e20,g3,qsq,r=',s2,s3
c     +        ,a1,a0,e10,e20,g3,qsq
c         first = .false.
c      endif
      RETURN
      END
```

C.2 The Structure-Function Extraction Code

The structure-function extraction is performed by a single program, `sfextr.f`. This program calculates the structure functions for experiments E744 and E770 in separate executions of the program. The structure functions from the two experiments are then combined as described in Chapter 6. The routine that actually calculates the structure functions is `calcsf`, and is listed below.

```
*DECK CALCSF
      SUBROUTINE CALCSF
C
C     CALCULATE F2 AND XF3
C
c     30-Apr-96: Let's take a different approach to make
c     it easier to calculate the errors.  Instead of
c     applying the acceptance and normalization corrections
c     to the A and B coefficients, apply them to the number
c     of data events (which is conceptually easier anyway).
#include <BINCOM.CMN>
#include <ACDDCOM.CMN>
#include <ACDFCOM.CMN>
#include <ACMDCOM.CMN>
#include <ACMFCOM.CMN>
#include <COEFCOM.CMN>
#include <CORDCOM.CMN>
#include <CORFCOM.CMN>
#include <BCMCCOM.CMN>
#include <SFCOM1.CMN>
#include <SFFUN.CMN>
      double precision aaaa,aaan,bbba,bbbn,f2,xf3
      double precision f2_err2, f3_err2, f23_err
      double precision cad,caf,cnd,cnf
      double precision rawa,rawn,rawaf,rawad,rawnf,rawnd
      double precision caderr2,caferr2,cnderr2,cnferr2
      double precision data_err2_nu, data_err2_anu
      double precision data_rel_err2_nu, data_rel_err2_anu
      double precision fake_events_nu, fake_events_anu
      double precision mc_rel_err2_nu, mc_rel_err2_anu
      double precision detf
      logical debug
C-----------------------------------------------------------------
C
C     *****  EXTRACT S.F.
C                                    MOD  11/11/92  LEUNG
C
C             N(ACC) = (COEA * F2 + COEB * XF3) * FLXNOR / CORF(D)
C            AN(ACC) = (COEA * F2 - COEB * XF3) * FLXNOR / CORF(D)
c
c     changed to:
C        (COEF(D)/FLXNOR) *  N(ACC) = COEA * F2 + COEB * XF3
C        (COEF(D)/FLXNOR) * AN(ACC) = COEA * F2 - COEB * XF3
c
C     I.E.
C             n(ACC) = COEA * F2 + COEB * XF3
C            an(ACC) = COEA * F2 - COEB * XF3
C
      RATNF = ACDFEVT(NQBIN,NXBIN,NESEL) / ACMFEVT(NQBIN,NXBIN,NESEL)
```

```
      RATND = ACDDEVT(NQBIN,NXBIN,NESEL) / ACMDEVT(NQBIN,NXBIN,NESEL)
      RATAF = ACDFEVT(NQBIN,NXBIN,NEBIN) / ACMFEVT(NQBIN,NXBIN,NEBIN)
      RATAD = ACDDEVT(NQBIN,NXBIN,NEBIN) / ACMDEVT(NQBIN,NXBIN,NEBIN)
C
      DO IE = 1, NESEL
         IE2 = IE + NESEL
         DO IX = 1, NXCUT - 2
            DO IQ = 1, NQCUT
C
               IF (XLIM(IX) .GT. .999) GOTO 3
C
C              *****  NEUTRINO - FOCUSING
C
               CNF = CORF(IQ,IX,IE) / FLXNOR(1,1)
               AANF = COEA(IQ,IX,IE)
               BBNF = COEB(IQ,IX,IE)
               rawnf = ACDFEVT(IQ,IX,IE)
               cornf = ACDFEVT(IQ,IX,IE) * CNF
               ACMNF = ACMFEVT(IQ,IX,IE) * RATNF
C
C              *****  NEUTRINO - DEFOCUSING
C
               CND = CORD(IQ,IX,IE) / FLXNOR(2,1)
               AAND = COEA(IQ,IX,IE)
               BBND = COEB(IQ,IX,IE)
               rawnd = ACDDEVT(IQ,IX,IE)
               cornd = ACDDEVT(IQ,IX,IE) * CND
               ACMND = ACMDEVT(IQ,IX,IE) * RATND
C
C              *****  ANTI-NEUTRINO - FOCUSING
C
               CAF = CORF(IQ,IX,IE2) / FLXNOR(4,1)
               AAAF = COEA(IQ,IX,IE2)
               BBAF = COEB(IQ,IX,IE2)
               rawaf = ACDFEVT(IQ,IX,IE2)
               coraf = ACDFEVT(IQ,IX,IE2) * CAF
               ACMAF = ACMFEVT(IQ,IX,IE2) * RATAF
C
C              *****  ANTI-NEUTRINO - DEFOCUSING
C
               CAD = CORD(IQ,IX,IE2) / FLXNOR(3,1)
               AAAD = COEA(IQ,IX,IE2)
               BBAD = COEB(IQ,IX,IE2)
               rawad = ACDDEVT(IQ,IX,IE2)
               corad = ACDDEVT(IQ,IX,IE2) * CAD
               ACMAD = ACMDEVT(IQ,IX,IE2) * RATAF
C
C              *****  SUM OF EVENTS AND COEFFICIENTS.
C
               rawn = rawnf + rawnd
               ACCN = cornf + cornd
               AAAN = AANF  + AAND
               BBBN = BBNF  + BBND
               rawa = rawaf + rawad
               ACCA = coraf + corad
               AAAA = AAAF  + AAAD
               BBBA = BBAF  + BBAD
C
               debug = ie .eq. nesel  .and.
     $                 ix .eq. 18     .and.
     $                (iq .eq. 7 .or. iq .eq. 11)

               if (debug) then
                  print *,' '
```

```
                PRINT *, ' IQ,IX,IE: ', IQ,IX,IE
                PRINT *,     ' RAWNF, RAWND, RAWAF, RAWAD, rawn, rawa'
                PRINT 8501,   RAWNF, RAWND, RAWAF, RAWAD, rawn, rawa
                PRINT *,     ' CORNF, CORND, CORAF, CORAD, ACCN, ACCA'
                PRINT 8501,   CORNF, CORND, CORAF, CORAD, ACCN, ACCA
                PRINT *,     ' AANF, AAND, AAAF, AAAD, AAAN, AAAA'
                PRINT 8501,   AANF, AAND, AAAF, AAAD, AAAN, AAAA
                PRINT *,     ' BBNF, BBND, BBAF, BBAD, BBBN, BBBA'
                PRINT 8501,   BBNF, BBND, BBAF, BBAD, BBBN, BBBA
                PRINT *, 'CORFN, CORDN, CORDA, CORFA'
                PRINT 8501, CORF(IQ,IX,IE), CORD(IQ,IX,IE)
     .                , CORD(IQ,IX,IE+NESEL), CORF(IQ,IX,IE+NESEL)
                PRINT *, 'CNF, CND, CAD, CAF'
                PRINT 8501, cnf, cnd, cad, caf
             ENDIF
 8501        FORMAT(6G15.6)
C
C            *****  S.F. EXTRACTION.
C
             F2  = 0.
             XF3 = 0.
             DETF = (AAAN * BBBA + AAAA * BBBN)

c            7-Mar-95 Make sure we have enough statistics to calculate
c            a reasonable value for the SF.

             IF (detf .GT. 0.d0
     $            .and. rawn .gt. 10. .and. rawa .gt. 10.) THEN
C
                F2   = (BBBA * ACCN + BBBN * ACCA) / DETF
                XF3  = (AAAA * ACCN - AAAN * ACCA) / DETF
C
                SF(IQ,IX,IE)  = F2
                SF(IQ,IX,IE2) = XF3
c
c               7-Mar-95: The error calculation has been completely
c               re-written (again), this time to determine the errors
c               explictly.  (See WGS notebook 9 page 136-137.)
C
c               26-Feb-96:
c               The statistical error due to the Monte Carlo was calculated
c               in stay-error.f and routine calcorr.
c
c               30-Apr-96: Here's the payoff: we can now include the error
c               due to the Monte Carlo correction in a relatively simple
c               expression. (See WGS notebook 10, pages 71-73).
c               Just to be accurate, separate calculate the focussing and
c               defocussing terms.

c               cxxerr2 = (CXX * CORF(D)ERR / CORF(D))
                cnferr2 = (corferr(iq,ix,ie )/flxnor(1,1))**2
                cnderr2 = (corderr(iq,ix,ie )/flxnor(2,1))**2
                caferr2 = (corferr(iq,ix,ie2)/flxnor(4,1))**2
                caderr2 = (corderr(iq,ix,ie2)/flxnor(3,1))**2

                f2_err2 =
     $               (rawnf*CNF**2 + rawnd*CND**2)*(bbba/detf)**2
     $             + (rawaf*CAF**2 + rawad*CAD**2)*(bbbn/detf)**2
     $             + cnferr2 * rawnf**2 * (bbba/detf)**2
     $             + cnderr2 * rawnd**2 * (bbba/detf)**2
     $             + caferr2 * rawaf**2 * (bbbn/detf)**2
     $             + caderr2 * rawad**2 * (bbbn/detf)**2

                f3_err2 =
```

```
     $                 (rawnf*CNF**2 + rawnd*CND**2)*(aaaa/detf)**2
     $               + (rawaf*CAF**2 + rawad*CAD**2)*(aaan/detf)**2
     $               + cnferr2 * rawnf**2 * (aaaa/detf)**2
     $               + cnderr2 * rawnd**2 * (aaaa/detf)**2
     $               + caferr2 * rawaf**2 * (aaan/detf)**2
     $               + caderr2 * rawad**2 * (aaan/detf)**2

                   f23_err =
     $                 (rawnf*CNF**2 + rawnd*CND**2)*aaaa*bbba/detf**2
     $               - (rawaf*CAF**2 + rawad*CAD**2)*aaan*bbbn/detf**2
     $               + cnferr2 * rawnf**2 * aaaa*bbba/detf**2
     $               + cnderr2 * rawnd**2 * aaaa*bbba/detf**2
     $               - caferr2 * rawaf**2 * aaan*bbbn/detf**2
     $               - caderr2 * rawad**2 * aaan*bbbn/detf**2

C
                   SFERR(IQ,IX,IE)  = SQRT(f2_err2)
                   SFERR(IQ,IX,IE2) = SQRT(f3_err2)
                   F23ERR(IQ,IX,IE) = f23_err
c
                   if (debug) then

                      print *,' '
                      print *,' Error Calc. Debug, iq=',iq,', ix=',ix
     $                     ,' ie=',ie
                      print *,' AAAN =',AAAN ,' AAAA =',AAAA
                      print *,' BBBN =',BBBN ,' BBBA =',BBBA
                      PRINT *,' ACCN=',ACCN,' ACCA=',ACCA,' DETF=',DETF
                      PRINT *,' F2=',F2,' XF3=',XF3
                      print *,' RATNF=',RATNF,' ACMNF=',ACMNF
                      print *,' RATND=',RATND,' ACMND=',ACMND
                      print *,' RATAF=',RATAF,' ACMAF=',ACMAF
                      print *,' RATAD=',RATAD,' ACMAD=',ACMAD
                      print *,' CORF (N,A)=',
     $                     corf(iq,ix,ie),corf(iq,ix,ie2)
                      print *,'  err (N,A)=',
     $                     corferr(iq,ix,ie),corferr(iq,ix,ie2)
                      print *,' CORD (N,A)=',
     $                     cord(iq,ix,ie),cord(iq,ix,ie2)
                      print *,'  err (N,A)=',
     $                     corderr(iq,ix,ie),corderr(iq,ix,ie2)
                      print *,' cnferr2=',cnferr2,
     $                        ' cnderr2=',cnderr2
                      print *,' caferr2=',caferr2,
     $                        ' caderr2=',caderr2
                      print *,' f2_err2=',f2_err2,
     $                        ' f3_err2=',f3_err2,
     $                        ' f23_err=',f23_err
                      PRINT *,' F2ERR=',SFERR(IQ,IX,IE)
                      PRINT *,' F3ERR=',SFERR(IQ,IX,IE2)
                      PRINT *,' F23ERR=',F23ERR(IQ,IX,IE)
                      print *,' '
                   END IF        ! ERROR DEBUG
C
                ENDIF
C
 3          end do ! ix loop
         end do ! iq loop
      end do ! ie loop
C
      RETURN
      END
```

C.3 The QCD Evolution Code

Within the Duke and Owens program, subroutine `theory.f` calls `intqcd.f`, which evolves the parton distributions in Q^2, calls `theorys.f` to determine the structure functions, calculates the target mass correction [Geo76], and calls `twist_factor.f` to calculate the higher-twist effect [Das96].

Subroutine `theorys.f` calculates the hard-scattering integrals that convert the parton distributions into structure functions. It calls `fetch.f` (not shown) to get the parton distributions from an (x,s) grid (see Chapter 7).

Subroutine `intqcd.f` calls `startv.f` and `starts.f` to initialize the QCD evolution at Q_0^2 for the valence and singlet/gluon distributions respectively. Subroutines `fintgs.f`, and `fintgg.f` calculate the convolution of the splitting functions with the parton distributions for the valence, singlet, and gluon distributions respectively. Subroutines `pqns.f`, `pqs.f`, and `pg.f` implement the splitting functions themselves.

Subroutine `twist_factor.f` is not shown, since it simply reads the calculation of Ref. [Das96] from a table (see Section C.4).

`theory.f`

```
      FUNCTION THEORY(IFUN,V)
      IMPLICIT DOUBLE PRECISION (A-H,O-Z)
C
C     CALCULATES THE VALUE OF A S.F. FOR THE CURRENT VALUES OF
C     THE PARAMETERS USING THE INDEPENDENT VARIABLES IN ARRAY V.
C     THE ACTUAL NITTY-GRITTY WORK IS PERFORMED BY THEORY2; THIS
C     ROUTINE DETERMINES WHEN TO RE-INITIALIZE THE CALC(X,S) GRID,
C     AND DOES THE TARGET MASS CORRECTIONS.
C
C     14-OCT-92 THE FIRST ARGUMENT TO THEORY HAS BEEN CHANGED. IT
C     NOW INDICATES THE STRUCTURE FUNCTIONS TO BE CALCULATED:
C     IFUN = 1 -> 2XF1 (neutrino)
C            2 ->   F2 (neutrino)
C            3 ->  XF3 (averaged neutrino + anti-neutrino)
C            4 ->   F2 (lepton)                 added 20-May-94 WGS
C            5 ->  XF3 (neutrinos only)         added 25-May-94
C            6 ->  XF3 (anti-neutrinos only)    added 25-May-94
C
C     22-DEC-92 WGS: ADDED EMC EFFECT.
C     05-JAN-93 WGS: ADDED FERMI-MOTION SMEARING.
C     03-Dec-96 WGS: Higher-twist calculation now in subroutine.
C                    then vary D2 for F2 HT by +- 1.

      DIMENSION V(4),VP(4)
      logical first /.true./
      integer icnt /0/, icntmx /0/
```

```
#include <GAUSS4.CMN>
#include <SIZES.CMN>
#include <PARAM.CMN>
#include <DODATA.CMN>
#include <INPUT.CMN>
#include <Q2STUF.CMN>
#include <GRPTHY.CMN>
#include <CONST.CMN>
C-----------------------------------------------------------------
C
C     WE RE-EVOLVE QCD IF THE EVOLUTION SWITCH IS SET.
C     28-Jun-96: We evolve in the factorization scale M2, not in Q2.
C
      IF (EVOLVE) THEN
        T0   = LOG(Q02/XP(1)**2)    + log(FSCALE)
        TMAX = LOG(Q2MAX/XP(1)**2) + log(FSCALE)
        SMAX = LOG(TMAX/T0)
        NMAX = SMAX/DELTA+1
        CALL INTQCD
      END IF
C
      X=V(1)
      Q2=V(2)
      ITYPE=V(4)
C
C     TARGET MASS CORRECTIONS?
      IF(ITMC .EQ. 0) THEN
C
C       DIS STRUCTURE FUNCTIONS CALCULATED HERE (NO TMC)
C
        CALL THEORYS(IFUN,V,ANS)
        THEORY=ANS
        go to 2465              ! Include emc, fermi, or higher-twist effects
      END IF
C
C     GEORGI-POLITZER TARGET MASS CORRECTIONS CALCULATED HERE
C     (SEE DASU'S THESIS, UNIV. ROCH. PUB. UR-1059, 1988, PG. 87).
C
      VP(2)=V(2)
      VP(4)=V(4)
C
C     FOR BOTH F2 AND 2XF1, WE INTEGRATE USING F2.
C
      IFUNI = IFUN
      IF (IFUN .EQ. 1) IFUNI = 2
C
      R=SQRT(1D0+4D0*.8836D0*X*X/Q2) ! THIS IS 'K' IN DASU'S THESIS
      XXI=2D0*X/(1D0+R)              ! THIS IS 'KSI' IN DASU'S THESIS
      VP(1)=XXI
      CALL THEORYS(IFUN,VP,FF)

      A1=0D0
      DO I=1,NTERMS
        XIP=.5D0*(1D0-XXI)*XI(I)+.5D0*(1D0+XXI)
        VP(1)=XIP
        CALL THEORYS(IFUNI,VP,FF_PRIME)
        A1=A1+.5D0*(1D0-XXI)*WI(I)*FF_PRIME/XIP**2
      END DO ! I LOOP
C
      IF(IFUN .eq. 1 .or. ifun .eq. 2 .or. ifun .eq. 4) THEN

        A2=0D0
        DO I=1,NTERMS
          XIP=.5D0*(1D0-XXI)*XI(I)+.5D0*(1D0+XXI)
```

```
          A3=0D0
          DO J=1,NTERMS
            XIPP=.5D0*(1D0-XIP)*XI(J)+.5D0*(1D0+XIP)
            VP(1)=XIPP
            CALL THEORYS(IFUNI,VP,FF_PRIME)
            A3=A3+.5D0*(1D0-XIP)*WI(J)*FF_PRIME/XIPP**2
          END DO ! J LOOP
          A2=A2+.5D0*(1D0-XXI)*WI(I)*A3
        END DO ! I LOOP

        IF (IFUN .EQ. 2 .or. ifun .eq. 4) THEN

          THEORY=(X/XXI)**2*FF/R**3+6D0*.8836D0/Q2*(X/R)**3/R*A1
     X           +12D0*(.8836D0/Q2)**2*(X/R)**4/R*A2

        ELSE ! IFUN = 1

          THEORY=(1D0/XXI)  *FF/R   +2D0*.8836D0/Q2*(X/R)**2  *A1
     X           + 4D0*(.8836D0/Q2)**2*(X/R)**3  *A2
          THEORY = THEORY * X ! THE ABOVE FORMULA ONLY GIVES US 2F1

        END IF

      ELSE ! IFUN = 3 or 5 or 6

        THEORY=(X/R/XXI)**2*FF+2D0*.8836D0/Q2*(X/R)**3*A1

      END IF

 2465 continue                    ! With or without TMC, we arrive here:
C
      IF (IEMC .EQ. 1) THEORY = THEORY * EMC(X,1)
      IF (IFERMI .EQ. 1) then
c        Fermi correction only calculated for IFUN = 1,2,3
         ifuni = ifun
         if (ifuni .eq. 5 .or. ifuni .eq. 6) ifuni = 3
         if (ifuni .eq. 4                  ) ifuni = 2
         THEORY = THEORY * FERMI(IFUNI,X,Q2)
      end if
      theory = theory * twist_factor(ifun,x,q2)

      RETURN
      END
```

theorys.f

```
      SUBROUTINE THEORYS(IFUN,V,THEORY)
C     Modified by $BASE/sf/qcd/include.sed   May-93 WGS
      IMPLICIT DOUBLE PRECISION (A-H,O-Z)
C     Modified by $BASE/sf/qcdfit/double.sed      12-May-93 WGS
C     CALCULATES THE VALUES OF THE STRUCTURE FUNCTIONS FOR THE
C     CURRENT VALUES OF THE FIT PARAMETERS GIVEN THE INDEPENDENT
C     VARIABLES IN ARRAY V.
C     V(1) = X
C     V(2) = Q**2
C     V(3) = W**2
C     V(4) = TYPE OF EXPERIMENT (SEE ROUTINE BLFIT)
C
C     IFUN SELECTS WHICH STRUCTURE FUNCTION IS RETURNED:
C     IFUN = 1 -> 2XF1 (neutrino)
C            2 ->   F2 (neutrino)
C            3 ->  XF3 (averaged neutrino + anti-neutrino)
C            4 ->   F2 (lepton)                added 20-May-94 WGS
C            5 ->  XF3 (neutrinos only)        added 25-May-94
```

```
C            6 ->  XF3 (anti-neutrinos only)  added 25-May-94
C
c     31-Jul-95: Factorization scale added to program -- Christina Rapp

      DIMENSION V(4),FTEMP(2)
#include <SIZES.CMN>
#include <PARAM.CMN>
#include <DODATA.CMN>
#include <GAUSS.CMN>
#include <GRPTHY.CMN>
#include <INPUT.CMN>
#include <Q2STUF.CMN>
#include <CONST.CMN>
C-----------------------------------------------------------------------
      X=V(1)
      Q2=V(2)
      ITYPE=V(4)
C
C     IFL, which determines which combination of parton
C     distributions is returned by subroutine FETCH,
C     is defined as follows:
C       IFL      FTEMP(1)              FTEMP(2)
C        1       XF3                   ZERO
C        2       F2 NEU-IRON           GLUON
C        3       F2 LEP-ISOSCALAR      GLUON
C        4       F2 LEP-PROTON         GLUON
C        5       xF3 (neutrino)        zero      ! added 25-May-94
C        6       xF3 (anti-neutrino)   zero      ! added 25-May-94
C
      if (ifun .eq. 1) ifl = 2
      if (ifun .eq. 2) ifl = 2
      if (ifun .eq. 3) ifl = 1
      if (ifun .eq. 4) ifl = 3
      if (ifun .eq. 5) ifl = 5
      if (ifun .eq. 6) ifl = 6
C
c     T0=LOG(Q02/XP(1)**2) + log(fscale) ! Defined in /Q2STUF/
      T =LOG(Q2 /XP(1)**2) + log(fscale)
      S = LOG(T/T0)

C     al_renom is the new value of alpha due to the renormalization scale.
C     Martin, Sterling, Roberts, Phys. Lett. B 266 (1991) 173-177

C     Establish number of quark flavors in ALPHA
      al_renom=ALPHA(T+log(rscale))/(4D0*PI)

      CALL FETCH(IFL,NDRV,X,S,FTEMP)
      THEORY=FTEMP(1)
C
C     HIGHER-ORDER CORRECTIONS.  THIS IS WHERE THE PARTON DISTRIBUTION
C     DISTRIBUTIONS ARE CONVOLUTED WITH THE COEFFICIENT FUNCTIONS.
C
      IF (IORD .GE. 1) THEN
C
C       FAC = FLAVOR -> NEUTRINO, FAC = 10/9 -> CHARGED LEPTON
C
        FAC=FLAVOR
        IF(ifl.EQ.3 .OR. ifl .EQ. 4) FAC=10D0/9D0
C
C       THE FOLLOWING 2ND-ORDER CORRECTION CAN BE FOUND ON PAGES
C       197 AND 199 OF HERROD & WADA, PHYS.LETT.96B:195 1980
C
        AL1=LOG(1D0-X)
C
```

```
      FX=THEORY
      fg=ftemp(2) ! see comment on factorization scale below
      THEORY=FX+FX*AL_RENOM*CF*(-9D0-2D0*PI2/3D0+AL1*(-3D0+2D0*AL1))
      DO I=1,NTERMS
        Y=0.5D0*(1D0-X)*XI(I)+0.5D0*(1D0+X)
        WT = .5D0*(1D0-X)*AL_RENOM*WI(I)
        XY=X/Y
        AL1=LOG(1D0-Y)
        CALL FETCH(IFL,NDRV,XY,S,FTEMP)
C
        IF (IFUN .EQ. 3 .or. ifun .eq. 5 .or. ifun .eq. 6) then
          C22 = CF*(4.5D0+2.5D0*Y-2D0*(1D0+Y*Y)*LOG(Y)/(1D0-Y)-2D0*(1D0+Y))
        ELSE IF (IFUN .EQ. 2 .or. ifun .eq. 4) THEN
          C22 = CF*(4.5D0+2.5D0*Y-2D0*(1D0+Y*Y)*LOG(Y)/(1D0-Y))
          ELSE IF (IFUN .EQ. 1) THEN
          C22 = CF*(4.5D0+2.5D0*Y-2D0*(1D0+Y*Y)*LOG(Y)/(1D0-Y)-4D0*Y)
        END IF
        C23 = CF*(-1.5D0+2D0*AL1)/(1D0-Y)
C
C        if the factorization scale is not equal to one, ln(f) will not be equal to
zero
C        and we must take this into account, both in our calculation of alpha and
C        in our equations.  See p227, Virchaux and Milsztajn:phys.lett.274B:221-229
1992.
C
        if (ifun .eq. 3 .or. ifun .eq. 5 .or. ifun .eq. 6) then
           ymi = 1d0/(1d0-y)
           fz=ftemp(1)
           pqns2 = cf*(1d0+y*y)
           p0 = (pqns2*fz-2d0*cf*fx)*ymi
        else
           ymi = 1d0/(1d0-y)
           fsz=ftemp(1)
           fgz=ftemp(2)
           pqs2 = cf*(1d0+y*y)
           pqg  = 2d0*tr*(y*y+(1d0-y)**2)
           p0 = ((pqs2*fsz-2d0*cf*fx)*ymi+pqg*fgz)
        endif

        THEORY=THEORY
     $          +WT*(C22*FTEMP(1)+C23*((1D0+Y*Y)*FTEMP(1)-2D0*FX))
     $          -wt*log(fscale)*p0
C
        IF (IFUN .eq. 1 .or. ifun .eq. 2 .or. ifun .eq. 4) THEN
         IF (IFUN .EQ. 2 .or. ifun .eq. 4) THEN
          CG2=2D0*FAC*(-1D0+8D0*Y*(1D0-Y)+(1D0-2D0*Y+2D0*Y*Y)*LOG(1D0/Y-1D0))
         ELSE ! ifun = 1
          CG2=2D0*FAC*(-1D0+4D0*Y*(1D0-Y)+(1D0-2D0*Y+2D0*Y*Y)*LOG(1D0/Y-1D0))
         END IF
c
         ymi = 1d0/(1d0-y)
         fgz=ftemp(2)
         fsz=ftemp(1)
         pgq = cf*(y*y-2d0*y+2d0)/y
         pgg1= 2d0*ca*(1d0-y+y*y-y*y*y)/y
         p0g = (pgq*fsz+pgg1*fgz+2d0*ca*(y*fgz-fx)*ymi)
c
         THEORY=THEORY+WT*CG2*FTEMP(2)-wt*log(fscale)*p0g
        END IF
C
      END DO ! I LOOP
C
    END IF
C
```

```
      RETURN
      END
```

intqcd.f

```
      SUBROUTINE INTQCD
      IMPLICIT DOUBLE PRECISION (A-H,O-Z)
C     Modified by $BASE/sf/qcdfit/double.sed      12-May-93 WGS
C     INITIALIZE THE CALC ARRAY WITH THE VALUE OF THE STRUCTURE
C     FUNCTIONS ON AN (X,S) GRID.  SEE THE COMMENTS IN COMMON
C     BLOCK GFUNC FOR A DESCRIPTION OF THE CALC ARRAY.
C     See comment in Q2STUF.CMN for relationship between S and T.

#include <SIZES.CMN>
#include <GRIDCM.CMN>
      DIMENSION FVL(NXGRID),FVL1(NXGRID),FVLSTO(NXGRID)
      DIMENSION PRD(NXGRID),PRD1(NXGRID),
     $ COR(NXGRID),COR1(NXGRID),FUDGE(NXGRID),PRDM(NXGRID)
      DIMENSION FS(NXGRID),FS1(NXGRID),FSSTO(NXGRID)
      DIMENSION PRDS(NXGRID),PRDS1(NXGRID),CORS(NXGRID),
     $ CORS1(NXGRID),FUDGES(NXGRID),PRDMS(NXGRID)
      DIMENSION FG(NXGRID),FG1(NXGRID),FGSTO(NXGRID)
      DIMENSION PRDG(NXGRID),PRDG1(NXGRID),CORG(NXGRID),
     $ CORG1(NXGRID),FUDGEG(NXGRID),PRDMG(NXGRID)
#include <ALQ2.CMN>
#include <GRPTHY.CMN>
#include <PARAM.CMN>
#include <INPUT.CMN>
#include <Q2STUF.CMN>
#include <GFUNC.CMN>
#include <CONST.CMN>
c-----------------------------------------------------------------
C
C     CLEAR CALC ARRAY. This array will contain the (x,s) grid
C     used by routines FETCH, GINTERP, and GETFV.
C
      DO 61 I=1,8
      DO 61 J=1,NSMAX
      DO 61 K=1,NXGRID
   61 CALC(I,J,K)=0D0

c     Calculate this immediately -- because calling ALPHA will
c     set the correct number of quark flavors at Q02 (T=T0, S=0)
c     which routines such as FCNVL, FINTGV, and PQNS require.
c     26-Jun-96: We evolve using the factorization energy M2, not in Q2
c     (see theory.f).

      S=0.0D0
      T=T0
      AL = ALPHA(T)/(2D0*PI)

C**   CALCULATE FS AND FG AT S=0.0D0
C     NOTE: BECAUSE OF THE FOLLOWING LINE, IF YOU'RE DOING A
C     SIMULTANEOUS FIT TO SINGLET & NON-SINGLET, YOU MUST EVOLVE
C     THE SINGLET PIECE FIRST.
C
      IF(INS .EQ. 1) GO TO 31
C
      DO I=1,NXGRID
        X=XGRID(I)
        FS(I)=FCNFS(X,S)
        FG(I)=FCNFG(X,S)
        CALC(7,1,I)=FS(I)     ! S.F. AT S = S0
        CALC(8,1,I)=FG(I)
```

```
      END DO
C**   CALCULATE D(FS,FG)/DS AT S=0.0D0
      DO I=1,NXGRID
        CALL FINTGS(I,FS,FG,FS1(I))  ! SLOPES OF S.F. AT S = S0
        CALL FINTGG(I,FG,FS,FG1(I))
      END DO
C**   CALCULATE FS AND FG AT S=0.0D0-DELTA
      T=T0*EXP(-DELTA)
      AL = ALPHA(T)/(2D0*PI)
      DLT=DELTA
      CALL STARTS(FS,FS1,FSSTO,FG,FG1,FGSTO,DLT)  ! S.F. AT S = S0-DELTA
C**   CALCULATE PREDICTOR AT S=0.0D0+DELTA
      DO I=1,NXGRID
        PRDS(I)=FSSTO(I)+2D0*DELTA*FS1(I)
        PRDG(I)=FGSTO(I)+2D0*DELTA*FG1(I)
      END DO
C**   CALCULATE D(PRD)/DS AT S=0.0D0+DELTA
      T=T0*EXP(DELTA)
      AL = ALPHA(T)/(2D0*PI)
      DO I=1,NXGRID
        CALL FINTGS(I,PRDS,PRDG,PRDS1(I))
        CALL FINTGG(I,PRDG,PRDS,PRDG1(I))
C**     CALCULATE CORRECTOR AT S=0.0D0+DELTA
        CORS(I)=FS(I)+0.5D0*DELTA*(FS1(I)+PRDS1(I))
        CORG(I)=FG(I)+0.5D0*DELTA*(FG1(I)+PRDG1(I))
        FUDGES(I)=PRDS(I)-CORS(I)
        FUDGEG(I)=PRDG(I)-CORG(I)
      END DO
      DO I=1,NXGRID
        CALL FINTGS(I,CORS,CORG,CORS1(I))
        CALL FINTGG(I,CORG,CORS,CORG1(I))
      END DO
C**   RESHUFFLE THE DECK
      DO I=1,NXGRID
        FSSTO(I)=FS(I)
        FGSTO(I)=FG(I)
        FS(I)=CORS(I)
        FG(I)=CORG(I)
        FS1(I)=CORS1(I)
        FG1(I)=CORG1(I)
        CALC(7,2,I)=FS(I)
        CALC(8,2,I)=FG(I)
      END DO
      DO NTIMES=2,NMAX
        NT1=NTIMES+1
        DO I=1,NXGRID
          PRDS(I)=FSSTO(I)+2D0*DELTA*FS1(I)
          PRDG(I)=FGSTO(I)+2D0*DELTA*FG1(I)
          PRDMS(I)=PRDS(I)-0.8D0*FUDGES(I)
          PRDMG(I)=PRDG(I)-0.8D0*FUDGEG(I)
        END DO
        T=T*EXP(DELTA)
        AL = ALPHA(T)/(2D0*PI)
        DO I=1,NXGRID
          FSSTO(I)=FS(I)
          FGSTO(I)=FG(I)
          CALL FINTGS(I,PRDMS,PRDMG,PRDS1(I))
          CALL FINTGG(I,PRDMG,PRDMS,PRDG1(I))
          CORS(I)=FS(I)+0.5D0*DELTA*(FS1(I)+PRDS1(I))
          CORG(I)=FG(I)+0.5D0*DELTA*(FG1(I)+PRDG1(I))
          FUDGES(I)=PRDS(I)-CORS(I)
          FUDGEG(I)=PRDG(I)-CORG(I)
          FS(I)=CORS(I)+0.2D0*FUDGES(I)
          FG(I)=CORG(I)+0.2D0*FUDGEG(I)
```

```
          CALC(7,NT1,I)=FS(I)
          CALC(8,NT1,I)=FG(I)
        END DO
        DO I=1,NXGRID
          CALL FINTGS(I,FS,FG,FS1(I))
          CALL FINTGG(I,FG,FS,FG1(I))
        END DO
        S=NTIMES*DELTA
      END DO ! NTIMES loop


C**   START THE NONSINGLET CALCULATION
C**   CALCULATE QVL AT S=0D0
   31 CONTINUE
      DO 100 IVL=1,NVL
        IPM=-1
        IF(IVL.GT.2) IPM=1
        S=0D0
        DO 41 I=1,NXGRID
          X=XGRID(I)
          FVL(I)=FCNVL(IVL,X,S)
          CALC(IVL,1,I)=FVL(I)
   41   CONTINUE
C**     CALCULATE D(FVL)/DS AT S=0D0
        T=T0
        AL = ALPHA(T)/(2D0*PI)
        DO 42 I=1,NXGRID
          CALL FINTGV(I,IPM,FVL,FVL1(I))
   42   CONTINUE
C**     CALCULATE FVL AT S=0D0-DELTA
        T=T0*EXP(-DELTA)
        AL = ALPHA(T)/(2D0*PI)
        DLT=DELTA
        CALL STARTV(FVLSTO,DLT,FVL,FVL1,IPM)
C**     CALCULATE PREDICTOR AT S=0D0+DELTA
        DO 43 I=1,NXGRID
          PRD(I)=FVLSTO(I)+2D0*DELTA*FVL1(I)
   43   CONTINUE
C**     CALCULATE D(PRD)/DS AT S=0D0+DELTA
        T=T0*EXP(DELTA)
        AL = ALPHA(T)/(2D0*PI)
        DO 44 I=1,NXGRID
          CALL FINTGV(I,IPM,PRD,PRD1(I))
          COR(I)=FVL(I)+0.5D0*DELTA*(FVL1(I)+PRD1(I))
          FUDGE(I)=PRD(I)-COR(I)
   44   CONTINUE
        DO 45 I=1,NXGRID
          CALL FINTGV(I,IPM,COR,COR1(I))
   45   CONTINUE
        DO 46 I=1,NXGRID
          FVLSTO(I)=FVL(I)
          FVL(I)=COR(I)
          FVL1(I)=COR1(I)
          CALC(IVL,2,I)=FVL(I)
   46   CONTINUE
C**     INITIALIZATION COMPLETE...ITERATE UNTIL S=SMAX
        DO 47 NTIMES=2,NMAX
          NT1=NTIMES+1
          DO 51 I=1,NXGRID
            PRD(I)=FVLSTO(I)+2D0*DELTA*FVL1(I)
            PRDM(I)=PRD(I)-0.8D0*FUDGE(I)
   51     CONTINUE
          T=T*EXP(DELTA)
          AL = ALPHA(T)/(2D0*PI)
```

```
          DO 52 I=1,NXGRID
            FVLSTO(I)=FVL(I)
            CALL FINTGV(I,IPM,PRDM,PRD1(I))
            COR(I)=FVL(I)+0.5D0*DELTA*(FVL1(I)+PRD1(I))
            FUDGE(I)=PRD(I)-COR(I)
            FVL(I)=COR(I)+0.2D0*FUDGE(I)
   52     CONTINUE
          DO 53 I=1,NXGRID
            CALL FINTGV(I,IPM,FVL,FVL1(I))
            CALC(IVL,NT1,I)=FVL(I)
   53     CONTINUE
          S=NTIMES*DELTA
 47     CONTINUE                  ! NTIMES loop
 100  CONTINUE                    ! IVL loop
      RETURN
      END
```

startv.f

```
*DECK STARTV
      SUBROUTINE STARTV(FVLSTO,DELTA,FVL,FVL1,IPM)
      IMPLICIT DOUBLE PRECISION (A-H,O-Z)
C     Modified by $BASE/sf/qcdfit/double.sed      12-May-93 WGS
C
C     THIS SUBROUTINES STARTS OFF THE Q2 EVOLUTION FOR THE
C     VALENCE STRUCTURE FUNCTIONS.  THE INPUTS ARE
C            FVL(I) = VALENCE S.F. AT XGRID(I) FOR S = S0
C            FVL1(I) = SLOPE OF SINGLET S.F. AT XGRID(I)
C            IPM = 1 FOR VALENCE, = 2 FOR STRANGE, CHARM, U+UBAR
C            DELTA = INTERVAL IN LOG(Q2/LAMBDA**2)
C     OUTPUTS:
C            FVLSTO = VALENCE S.F. FOR S = S0 - DELTA
C
#include <GRIDCM.CMN>
      DIMENSION FVLSTO(NXGRID),FVL(NXGRID),FVL1(NXGRID),TVLSTO(NXGRID)
C-----------------------------------------------------------------------
C
C     ESTIMATE THE STRUCTURE FUNCTIONS AT S = S0 - DELTA, USING
C     THE SLOPES AT S=S0.  IF THE EXTRAPOLATED STRUCTURE FUNCTIONS
C     ARE NEGATIVE, WE WON'T USE THEM TO DETERMINE SLOPES.
C
      NEG = 0
      DO I=1,NXGRID
        TVLSTO(I)=FVL(I)-DELTA*FVL1(I)
        IF (TVLSTO(I) .LT. 0D0) NEG = 1
      END DO
C
C     DETERMINE THE SLOPES OF THE STRUCTURE FUNCTIONS AT S=S0-DELTA,
C     THEN DETERMINE THE VALUES OF THE STUCTURE FUNCTIONS AT
C     S=S0-DELTA AGAIN, USING THE AVERAGE OF THE SLOPES AT S=S0
C     AND S=S0-DELTA.  HOWEVER, IF THE STRUCTURE FUNCTIONS EXTRAPOLATED
C     TO NEGATIVE VALUES AT S=S0-DELTA, DON'T USE THEM TO DETERMINE
C     SLOPES.
C
      IF (NEG .EQ. 0) THEN
        DO I=1,NXGRID
          CALL FINTGV(I,IPM,TVLSTO,FVLST1)
          FVLSTO(I)=FVL(I)-0.5D0*DELTA*(FVL1(I)+FVLST1)
        END DO
      ELSE
        DO I=1,NXGRID
          FVLSTO(I)=TVLSTO(I)
        END DO
      END IF
```

```
C
      RETURN
      END
```

starts.f

```
*DECK STARTS
      SUBROUTINE STARTS(FS,FS1,FSSTO,FG,FG1,FGSTO,DELTA)
      IMPLICIT DOUBLE PRECISION (A-H,O-Z)
C     Modified by $BASE/sf/qcdfit/double.sed      12-May-93 WGS
C
C     THIS SUBROUTINES STARTS OFF THE Q2 EVOLUTION FOR THE
C     SINGLET AND GLUON STRUCTURE FUNCTIONS.  THE INPUTS
C     ARE:
C            FS(I) = SINGLET S.F. AT XGRID(I) FOR S = S0
C            FS1(I) = SLOPE OF SINGLET S.F. AT XGRID(I) FOR S = S0
C            FG(I) = GLUON S.F. AT XGRID(I) FOR S = S0
C            FG1(I) = SLOPE OF GLUON S.F. AT XGRID(I) FOR S = S0
C            DELTA = INTERVAL IN LOG(Q2/LAMBDA**2)
C     OUTPUTS:
C            FSSTO = SINGLET S.F. FOR S = S0 - DELTA
C            FGSTO = GLUON S.F. FOR S = S0 - DELTA
C
#include <GRIDCM.CMN>
      DIMENSION FS(NXGRID),FS1(NXGRID),FSSTO(NXGRID),TSSTO(NXGRID),
     $          FG(NXGRID),FG1(NXGRID),FGSTO(NXGRID),TGSTO(NXGRID)
C-----------------------------------------------------------------------
C
C     ESTIMATE THE STRUCTURE FUNCTIONS AT S = S0 - DELTA, USING
C     THE SLOPES AT S=S0.  IF THE EXTRAPOLATED STRUCTURE FUNCTIONS
C     ARE NEGATIVE, WE WON'T USE THEM TO DETERMINE SLOPES.
C
      NEG = 0
      DO I=1,NXGRID
        TSSTO(I)=FS(I)-DELTA*FS1(I)
        TGSTO(I)=FG(I)-DELTA*FG1(I)
        IF (TSSTO(I) .LT. 0D0 .OR. TGSTO(I) .LT. 0D0) NEG = 1
      END DO
C
C     DETERMINE THE SLOPES OF THE STRUCTURE FUNCTIONS AT S=S0-DELTA,
C     THEN DETERMINE THE VALUES OF THE STUCTURE FUNCTIONS AT
C     S=S0-DELTA AGAIN, USING THE AVERAGE OF THE SLOPES AT S=S0
C     AND S=S0-DELTA.  HOWEVER, IF THE STRUCTURE FUNCTIONS EXTRAPOLATED
C     TO NEGATIVE VALUES AT S=S0-DELTA, DON'T USE THEM TO DETERMINE
C     SLOPES.
C
      IF (NEG .EQ. 0) THEN
        DO I=1,NXGRID
          CALL FINTGS(I,TSSTO,TGSTO,FSSTO1)
          CALL FINTGG(I,TGSTO,TSSTO,FGSTO1)
          FSSTO(I)=FS(I)-0.5D0*DELTA*(FS1(I)+FSSTO1)
          FGSTO(I)=FG(I)-0.5D0*DELTA*(FG1(I)+FGSTO1)
        END DO
      ELSE
        DO I=1,NXGRID
          FSSTO(I) = TSSTO(I)
          FGSTO(I) = TGSTO(I)
        END DO
      END IF
C
      RETURN
      END
```

fintgv.f

```
      SUBROUTINE FINTGV(I1,IPM,FVL,FINTG)
      IMPLICIT DOUBLE PRECISION (A-H,O-Z)
C     Modified by $BASE/sf/qcdfit/double.sed      12-May-93 WGS
C     CALCULATE RIGHT-HAND-SIDE OF ALTARELLI-PARISI EQUATION
C     (EXO THESIS 1.29)
C       INPUTS: I1  => DETERMINE SLOPE OF FVL AT XX(I1)
C               IPM = -1 FOR VALENCE, = 1 FOR CHARM, STRANGE, U+UBAR
C               FVL =  VALENCE STRUCTURE FUNCTION
C       OUTPUT: FINTG = SLOPE OF VALENCE STRUCTURE FUNCTION
C
c     31-Jul-95: Renormalization scale added to program -- Christina Rapp
C     21-Nov-95: Reorganized some statements to allow a change
c                in number of quark flavors vs. Q2.
C
#include <GAUSS.CMN>
#include <GRIDCM.CMN>
      DIMENSION FVL(NXGRID)
#include <GRPTHY.CMN>
#include <INPUT.CMN>
#include <CONST.CMN>
#include <ALQ2.CMN>
c-----------------------------------------------------------

      X = XGRID(I1)
      AL1X = LOG(1D0-X)
      T_renorm = t+log(rscale)
      AL_renorm=ALPHA(T_renorm)/(2D0*PI)
C
C     NOTE: THE DEL, PQNS0, AND PQNS2 TERMS ARE THOSE PARTS OF THE
C     SPLITTING FUNCTION THAT ARE PROPORTION TO DELTA(1-X) OR ARE
C     DEFINED LIKE (1-X)+ IN FLORATOS, LACAZE, KOUNNAS: PHYS.LETT.98B:
C     89 1981, EQ (17).
C
      PQNS0 = .5D0*CF*CA*(2D0*(67D0/9D0-PI2/3D0)) + CF*TR*(-20D0/9D0)
      DEL   = CF*CF*(3D0/8D0-PI2/2D0+ZET3-8D0*STWID)
     X      +.5D0*CF*CA*(17D0/12D0+11D0/9D0*PI2-ZET3+8D0*STWID)
     X      -CF*TR*(1D0/6D0+2D0/9D0*PI2)
      B0 = 11.D0 - 2.D0*flavor/3.d0
C
C     AL_renorm IS THE NEW VALUE OF AL, DUE TO THE RENORMALIZATION SCALE.
C     SEE VIRCHAUX AND MILSZTAJN: PHYS.LETT.274B:221-229 1992.
C     Note that we don't substitute T_renorm for T in the following integral,
C     because T comes from the left-hand (derivative side), not the right-hand
C     (integral) side, of the evolution equation.
C
      FX=GETFV(X,FVL)
      FINTG=T*AL_renorm*FX*CF*(3D0/2D0+2D0*AL1X)
      IF (IORD .GT. 0) FINTG=FINTG+T*AL_renorm**2*FX*(DEL+PQNS0*AL1X)
      DO I=1,NTERMS
        Z=0.5D0*(1D0-X)*XI(I)+0.5D0*(1D0+X)
        ZMI = 1D0/(1D0-Z)
        WT = .5D0*(1D0-X)*WI(I)*T*AL_renorm
        FZ=GETFV(X/Z,FVL)
        PQNS2 = CF*(1D0+Z*Z)
        P0 = (PQNS2*FZ-2D0*CF*FX)*ZMI
        FINTG=FINTG+WT*P0
        IF (IORD .GT. 0) THEN
          CALL PQNS(Z,I,I1,IPM,PQNS1,PQNS2)
          FINTG=FINTG +
     $          WT*AL_renorm*(PQNS1*FZ+(PQNS2*FZ-PQNS0*FX)*ZMI
     $          +LOG(RSCALE)*P0*B0/2d0)
        ENDIF
```

```
      END DO

      RETURN
      END
```

fintgs.f

```
      SUBROUTINE FINTGS(I1,FS,FG,FINTG)
      IMPLICIT DOUBLE PRECISION (A-H,O-Z)
C     Modified by $BASE/sf/qcdfit/double.sed        12-May-93 WGS
C     CALCULATE RIGHT-HAND-SIDE OF ALTARELLI-PARISI EQUATION
C     (EXO THESIS (1.80)
C       INPUTS: I1 => DETERMINE SLOPE OF FS AT XX(I1)
C               FS =  SINGLET STRUCTURE FUNCTION
C               FG =  GLUON STRUCTURE FUNCTION
C       OUTPUT: FINTG = SLOPE OF SINGLET STRUCTURE FUNCTION
c     31-Jul-95: Renormalization scale added to program -- Christina Rapp
C     21-Nov-95: Reorganized some statements to allow a change
c                in number of quark flavors vs. Q2.
C
#include <CONST.CMN>
#include <GAUSS.CMN>
#include <GRIDCM.CMN>
      DIMENSION FS(NXGRID),FG(NXGRID)
#include <GRPTHY.CMN>
#include <INPUT.CMN>
#include <ALQ2.CMN>
c-----------------------------------------------------

      X = XGRID(I1)
      AL1X = LOG(1D0-X)
      AL_renorm=ALPHA(T+LOG(RSCALE))/2D0/PI
C
C     NOTE: THE DEL, PQS0, AND PQS2 TERMS ARE THOSE PARTS OF THE
C     SPLITTING FUNCTION THAT ARE PROPORTION TO DELTA(1-X) OR ARE
C     DEFINED LIKE (1-X)+ IN HERROD & WADA, PHYS LETT 96B:195 1980
C
      DEL = CF*CF*(3D0/8D0-PI2/2+ZET3-8D0*STWID)
     X      +.5D0*CF*CA*(17D0/12D0+11D0/9D0*PI2-ZET3+8D0*STWID)
     X      -CF*TR*(1D0/6D0+2D0/9D0*PI2)
      PQS0 = .5D0*CF*CA*(2D0*(67D0/9D0-PI2/3D0))+CF*TR*(-20D0/9D0)
      B0 = 11.D0 - 2.D0*flavor/3.D0
C
C     AL_renorm IS THE NEW VALUE OF AL, DUE TO THE RENORMALIZATION SCALE.
C     $     SEE MARTIN, STIRLING, AND ROBERTS: PHYS. LETT. 266B:173-177 1991.
C     Note that we don't substitute T_renorm for T in the following integral,
C     because T comes from the left-hand (derivative side), not the right-hand
C     (integral) side, of the evolution equation.
C
      FX=GETFV(X,FS)
      FINTG=FX*T*AL_renorm*CF*(3D0/2D0+2D0*AL1X)
      IF(IORD .GT. 0) FINTG=FINTG + FX*T*AL_renorm**2*(DEL+PQS0*AL1X)
      DO 1 I=1,NTERMS
        Z=0.5D0*(1D0-X)*XI(I)+0.5D0*(1D0+X)
        ZMI = 1D0/(1D0-Z)
        WT = .5D0*(1D0-X)*WI(I)*T*AL_renorm
        FSZ=GETFV(X/Z,FS)
        FGZ=GETFV(X/Z,FG)
        PQS2 = CF*(1D0+Z*Z)
        PQG  = 2D0*TR*(Z*Z+(1D0-Z)**2)
        P0 = ((PQS2*FSZ-2D0*CF*FX)*ZMI+PQG*FGZ)
        FINTG=FINTG+WT*P0
        IF(IORD .GT. 0) THEN
          CALL PQS(Z,I,I1,PQS1,PQS2,PQG)
```

```
          FINTG=FINTG+
     $          WT*AL_renorm*(FSZ*PQS1+(PQS2*FSZ-PQS0*FX)*ZMI+PQG*FGZ
     $          +LOG(RSCALE)*P0*BO/2d0)
        ENDIF
    1 CONTINUE
      RETURN
      END
```

fintgg.f

```
      SUBROUTINE FINTGG(I1,FG,FS,FINTG)
      IMPLICIT DOUBLE PRECISION (A-H,O-Z)
C     Modified by $BASE/sf/qcdfit/double.sed      12-May-93 WGS
C     CALCULATE THE RIGHT-HAND SIDE OF ALTARELLI-PARISI EQUATION
C     (EXO THESIS 1.81)
C       INPUTS: I1 => DETERMINE SLOPE OF FG AT XX(I1)
C               FG =  GLUON STRUCTURE FUNCTION
C               FS =  SINGLET STRUCTURE FUNCTION
C       OUTPUT: FINTG = SLOPE OF GLUON STRUCTURE FUNCTION
c     31-Jul-95: Renormalization scale added to program -- Christina Rapp
C     21-Nov-95: Reorganized some statements to allow a change
c                in number of quark flavors vs. Q2.
#include <GAUSS.CMN>
#include <GRIDCM.CMN>
      DIMENSION FG(NXGRID),FS(NXGRID)
#include <GRPTHY.CMN>
#include <INPUT.CMN>
#include <CONST.CMN>
#include <ALQ2.CMN>
c-----------------------------------------------------------
      X = XGRID(I1)
      AL1X = LOG(1D0-X)
      AL_renorm=ALPHA(T+LOG(RSCALE))/2D0/PI
C
C     NOTE: THE DEL, PGG0, AND PGG1 TERMS ARE THOSE PARTS OF THE
C     SPLITTING FUNCTION THAT ARE PROPORTIONAL TO DELTA(1-X) OR ARE
C     DEFINED LIKE (1-X)+ IN HERROD & WADA, PHYS LETT 96B:195 1980
C
      DEL = CA*TR*(-4D0/3D0)+CF*TR*(-1D0) +
     X     CA*CA*(-4D0*STWID+.5D0*ZET3+8D0/3D0)
      PGG0 = CA*TR*(-20D0/9D0)+CA*CA*(67D0/9D0-PI2/3D0)
      B0 = 11.D0 - 2.D0*flavor/3.D0
C
C     AL_renorm IS THE NEW VALUE OF AL, DUE TO THE RENORMALIZATION SCALE.
C     $      SEE MARTAIN, STIRLING, AND ROBERTS: PHYS. LETT. 266B: 173-177 1991.
C     Note that we don't substitute T_renorm for T in the following integral,
C     because T comes from the left-hand (derivative side), not the right-hand
C     (integral) side, of the evolution equation.
C
      FX=GETFV(X,FG)
      FINTG=T*AL_renorm*FX*(11D0/6D0*CA-2D0/3D0*TR+2D0*CA*AL1X)
      IF(IORD.GT.0)FINTG=FINTG+T*AL_renorm**2*FX*(DEL+PGG0*AL1X)
      DO 1 I=1,NTERMS
        Z=0.5D0*(1D0-X)*XI(I)+0.5D0*(1D0+X)
        ZMI = 1D0/(1D0-Z)
        WT = .5D0*(1D0-X)*WI(I)*T*AL_renorm
        FGZ=GETFV(X/Z,FG)
        FSZ=GETFV(X/Z,FS)
        PGQ = CF*(Z*Z-2D0*Z+2D0)/Z
        PGG1= 2D0*CA*(1D0-Z+Z*Z-Z*Z*Z)/Z
        P0 = (PGQ*FSZ+PGG1*FGZ+2D0*CA*(Z*FGZ-FX)*ZMI)
        FINTG=FINTG+WT*P0
        IF(IORD.GT.0) THEN
          CALL PG(Z,I,I1,PGG1,PGQ)
```

```
          FINTG=FINTG+
     $          WT*AL_renorm*(PGQ*FSZ+PGG1*FGZ+PGG0*(FGZ-FX)*ZMI
     $          +LOG(RSCALE)*P0*B0/2d0)
        ENDIF
    1 CONTINUE
      RETURN
      END
```

pqns.f

```
      SUBROUTINE PQNS(Z,I,J,IPM,PQNS1,PQNS2)
      IMPLICIT DOUBLE PRECISION (A-H,O-Z)
C     Modified by $BASE/sf/qcdfit/double.sed      12-May-93 WGS
C
C  THIS ROUTINE CALCULATES THE NLO NONSINGLET SPLITTING FUNCTIONS
C
C   IPM = -1  MEANS Q-QBAR -- USED FOR XF3 ONLY
C   IPM = +1  MEANS Q+QBAR TYPE NONSINGLET PIECE - USED FOR F2
C
C   PQNS1 MULTIPLIES QNS(X/Z)
C   PQNS2 MULTIPLIES (QNS(X/Z)-PQNS0*QNS(X))/(1-Z)  ;PQNS0 = CONST
C
C     (FLORATOS, LACAZE, & KOUNNAS, PHYS.LETT.98B:89 1981, EQ 17
C     SEE ALSO COMMENTS IN ROUTINE FINTGV.)
C
c     21-Nov-95: Since the number of quark flavors varies with
c     Q2, we can't save results of earlier calculations to re-use.
c     Remove the arrays that store values.

#include <CONST.CMN>
c-----------------------------------------------------------------
C
      IF3 = 1
      IF (IPM .EQ. 1) IF3 = 2
C
      ALZ = LOG(Z)
      AL1 = LOG(1D0-Z)
      ZP  = 1D0+Z
      ZM  = 1D0-Z
      Z2 = Z*Z
      ZP2 = 1D0+Z2
      PF1 = -2D0*Z*ALZ-1D0/2D0*ZP*ALZ**2-5D0*ZM
      PF2 = -2D0*ZP2*ALZ*AL1-3D0*ALZ
      PG1 = 2D0*ZP*ALZ+40D0/3D0*ZM
      PG2 = ZP2*(ALZ**2+11D0/3D0*ALZ+67D0/9D0-PI2/3D0)
      PA  = 2D0*ZP2/ZP*AINTG(Z)+2D0*ZP*ALZ+4D0*ZM
      PN1 = -4D0/3D0*ZM
      PN2 = 2D0/3D0*ZP2*(-ALZ-5D0/3D0)
      PQNS1 = CF**2*(PF1+IPM*PA) + .5D0*CF*CA*(PG1-IPM*PA) + CF*TR*PN1
      PQNS2 = CF**2* PF2     + .5D0*CF*CA* PG2     + CF*TR*PN2
C     ZINT = PQNS1*FQNSXZ + (PQNS2*FQNSXZ-PQNS0*FQNSX)/ZM

      RETURN
      END
```

pqs.f

```
      SUBROUTINE PQS(Z,I,J,PQS1,PQS2,PQG)
      IMPLICIT DOUBLE PRECISION (A-H,O-Z)
C     Modified by $BASE/sf/qcdfit/double.sed      12-May-93 WGS
C
C     THIS ROUTINE CALCULATES THE NLO SINGLET SPLITTING FUNCTIONS
```

```
C
C     FOR Q->Q CALLS PQNS WITH IPM = +1
C
C     PQS1 MULTIPLIES QS(X/Z)
C     PQS2 MULTIPLIES (QS(X/Z)-PQS0*QS(X))/(1-Z)   ;PQS0 = CONST
C
C     FOR G->Q CALCULATES PGQ  -- MULTIPLIES G(X/Z)
C
C     (HERROD & WADA, PHYS.LET.96B:195 1980; ALSO SEE COMMENTS IN
C     ROUTINE FINTGS.)
C
c     21-Nov-95: Since the number of quark flavors varies with
c     Q2, we can't save results of earlier calculations to re-use.
c     Remove the arrays that store values.

#include <CONST.CMN>
c-----------------------------------------------------------------
C
C     FIRST GET Q->Q PIECE
C
      ALZ = LOG(Z)
      AL1 = LOG(1D0-Z)
      ZP  = 1D0+Z
      ZM  = 1D0-Z
      Z2 = Z*Z
      ZP2 = 1D0+Z2
      ZI = 1D0/Z
      FQQ = 20D0/9D0*ZI-2D0+6D0*Z-56D0/9.
     .      *Z2+(1D0+5D0*Z+24D0/9D0*Z2)*ALZ
     .      -ZP*ALZ**2
      CALL PQNS(Z,I,J,1,PQS1,PQS2)
      PQS1 = PQS1 + 2D0*CF*TR*FQQ
C
C     NOW GET G->Q PIECE
C
      FQG1 = -40D0/9D0*ZI+4D0-50D0*Z+436D0/9.
     .      *Z2-(2D0+16D0*Z+88D0/3D0*Z2)*ALZ
     .      +(2D0+4D0*Z)*ALZ**2+8D0*Z*ZM*AL1
     .      +(2D0-4D0*Z+4D0*Z2)*(AL1**2-PI2/6D0)
     .      -4D0*(1D0+2D0*Z+2D0*Z2)*BINTG(Z)
      FQG2 = -14D0+29D0*Z-20D0*Z2+(-3D0+4D0*Z-8D0*Z2)*ALZ
     .      -(1D0-2D0*Z+4D0*Z2)*ALZ**2-8.
     .      *Z*ZM*AL1+(2D0-4D0*Z+4D0*Z2)
     .      *(-AL1**2+2D0*ALZ*AL1+PI2/3D0)
      PQG = -1D0*(CA*TR*FQG1+CF*TR*FQG2)
C     ZINT = PQS1*FQSXZ + (PQS2*FQSXZ-PQS0*FQSX)/ZM + PQG*FGXZ

      RETURN
      END
```

pg.f

```
      SUBROUTINE PG(Z,I,J,PGG1,PGQ)
      IMPLICIT DOUBLE PRECISION (A-H,O-Z)
C     Modified by $BASE/sf/qcdfit/double.sed      12-May-93 WGS
C
C     THIS ROUTINE CALCULATES THE NLO GLUON SPLITTING FUNCTIONS
C
C     FOR G->G CALCULATES PGG1 -- MULTIPLIES  G(X/Z)
C
C     FOR Q->G CALCULATES PGQ  -- MULTIPLIES QS(X/Z)
C
C     (HERROD & WADA, PHYS.LET.96B:195 1980; ALSO SEE COMMENTS
C     IN ROUTINE FINTGG).
```

```
C
c     21-Nov-95: Since the number of quark flavors varies with
c     Q2, we can't save results of earlier calculations to re-use.
c     Remove the arrays that store values.

#include <CONST.CMN>
c-----------------------------------------------------------
C
C
C     FIRST GET Q->G PIECE
C
      ALZ = LOG(Z)
      AL1 = LOG(1D0-Z)
      ZP  = 1D0+Z
      ZM  = 1D0-Z
      Z2 = Z*Z
      ZP2 = 1D0+Z2
      ZI = 1D0/Z
      FGQ1 = 5D0/2D0+7D0/2D0*Z-(2D0+7D0/2D0*Z)
     .     *ALZ+(1D0-.5D0*Z)*ALZ**2
     .     +(6D0*ZI-6D0+5D0*Z)*AL1+(2D0*ZI-2D0+Z)*AL1**2
      FGQ2 = -ZI-19D0/9D0-37D0/9D0*Z-44D0/9.
     .     *Z2+(12D0+5D0*Z+8D0/3D0*Z2)*ALZ
     .     -(2D0+Z)*ALZ**2-1D0/3D0*
     .     (22D0*ZI-22D0+17D0*Z)*AL1-(2D0*ZI-2D0+Z)
     .     *(AL1**2-2D0*ALZ*AL1-PI2/6D0)
     .     +(4D0*ZI+4D0+2D0*Z)*BINTG(Z)
      FGQ3 = 40D0/9D0*ZI-40D0/9D0+32D0/9.
     .     *Z+4D0/3D0*(2D0*ZI-2D0+Z)*AL1
      PGQ = -1D0*(CF**2*FGQ1 + CF*CA*FGQ2 + CF*TR*FGQ3)
C
C     NOW GET G->G PIECE
C
      FGG11 = -2D0/9D0*(23D0*ZI-29D0+19D0*Z-23D0*Z2)
     .     -4D0/3D0*ZP*ALZ
      FGG2  = 4D0/3D0*ZI-16D0+8D0*Z+20D0/3.
     .     *Z2-(6D0+10D0*Z)*ALZ-2D0*ZP*ALZ**2
      FGG31 = -8D0/9D0-Z/18D0-(47D0/6D0-25D0/6.
     .     *Z+44D0/3D0*Z2)*ALZ
     .     +(1D0/ZM+1D0/ZP+5D0/4D0+6D0*Z-2D0*Z2)
     .     *ALZ**2+(-11D0/2D0*ZI+7D0/2D0
     .     +13D0/4D0*Z)*AL1+.25D0*(-5D0*ZI+5D0+2D0*Z)*
     .     AL1**2-(4D0/ZM+4D0*ZI
     .     -5D0+7D0*Z-4D0*Z2)*ALZ*AL1+ZP*CINTG(Z)
     .     +4D0*(1D0/ZP-ZI-2D0-Z-Z2)
     .     *BINTG(Z)-PI2/3D0*(ZI-1D0+2D0*Z-Z2)
      PGG1 = CA*TR*FGG11 + CF*TR*FGG2 + CA**2*FGG31
C     ZINT = PGQ*FQSXZ + PGG1*FGXZ + PGG0*(FGXZ-FGX)/ZM

      RETURN
      END
```

C.4 Higher-Twist Calculation

Program `dispow.f`, provided by Bryan Webber, implements the calculation of the higher-twist effect. Note that the central value for the higher-twist effect used in the QCD evolution program is one-half the value from this program (see Section 7.1.6).

dispow.f

```
      Program Dispow
C---  Program to calculate 1/Q^2 and 1/Q^4 corrections to F2,F1,F3.
C     References:
C     Yu.L.Dokshitzer, G.Marchesini and B.R.Webber, CERN-TH/95-281
C      (hep-ph/9512336, to be published in Nucl Phys B);
C     M.Dasgupta and B.R.Webber, Phys.Lett.B382(1996)273.
C
      Implicit none
      Real*8 Q2,x,w,Asum1,Asum2,Asum3,dx,A2p,scale,upv,dnv,dup,ddn,
     & Fval,Dval,Dgauss,eps,F1int2,F2int2,F1int4,F2int4,F3int4,
     & L,Gpow,Cpow1,Cpow2,Cpow3,Fsum1,Fsum2,Fsum3,xvm(11),ex,
     & Cvm(11),Dvm(11),up1,dn1,du1,dd1,up2,dn2,du2,dd2,Eval
      Integer i
      Common/Fcom/x,scale,Fval
      External F1int2,F2int2,F1int4,F2int4,F3int4
C
C--- F2 data from M.Virchaux & A.Milsztajn, PL B274(92)221
C
      Data xvm/0.070d0,0.100d0,0.140d0,0.180d0,0.225d0,0.275d0,
     &         0.350d0,0.450d0,0.550d0,0.650d0,0.750d0/
      Data Cvm/-.100d0,-.077d0,-.052d0,-.043d0,-.046d0,-.048d0,
     &         -.041d0,0.090d0,0.304d0,0.792d0,1.250d0/
      Data Dvm/0.113d0,0.098d0,0.075d0,0.049d0,0.026d0,0.023d0,
     &         0.026d0,0.050d0,0.095d0,0.190d0,0.420d0/
C
C Precision for Dgauss integrations and second derivative
      eps=1d-5
      ex=1d-3
C
    1 Print *,' Q^2?'
      Read *, Q2
      If (Q2.le.0) stop
      scale=sqrt(Q2)
      Print *,' dx?'
      Read *, dx
      If (dx.le.0) stop
C
C 1/Q^2 contributions
C
C NP parameter: A2p = (C_F/2Pi) int dmu^2 delta aeff(mu^2)*log(mu^2)
      A2p=-0.2
C
      Write (9,*) ' new frame'
      Write (9,*) ' set font duplex'
      Write (9,*) ' set limits x 0 0.8 y -.5 2.0'
      Write (9,*) ' title bottom ''x'' size 3'
      Write (9,*) ' title left ''D021(x,Q223) (GeV223)'' size 3'
      Write (9,*) ' case       '' X X    X X      X X'''
C---Plot Virchaux-Milsztajn F2 points
      Write (9,*) ' set symbol 90 size 3'
      Write (9,*) ' set order x y dy'
      Write (9,'(3f10.4)') (xvm(i),Cvm(i),Dvm(i),i=1,11)
      Write (9,*) ' plot'
      Write (9,*) 0.0, 0.0
      Write (9,*) 0.8, 0.0
      Write (9,*) ' join'
      Write (9,*) ' set order x y dummy'
      Write (9,*) ' (Q^2 =',Q2
      Fsum1=0d0
      Fsum2=0d0
      Fsum3=0d0
```

```
      Asum1=0d0
      Asum2=0d0
      Asum3=0d0
      x=.5*dx
      Do while (x.lt.1d0)
        w=1d0-x
        L=Log(w)
        Call Mrsaval(x,scale,upv,dnv,dup,ddn)
C---Valence x*q(x) and its derivative
C   N.B. This is for average of neutrino and antineutrino
        Fval=upv+dnv
        Dval=dup+ddn
C---Contribution to F2
        Gpow=Dgauss(F2int2,x,1d0,eps)-(9d0+4d0*L)*Fval+x*Dval
        Fsum2=Fsum2+Fval*dx/x
        Asum2=Asum2+A2p*Gpow*dx/x
        Cpow2=A2p*Gpow/Fval
C---Contribution to 2xF1 and xF3
        Gpow=Dgauss(F1int2,x,1d0,eps)-(5d0+4d0*L)*Fval+x*Dval
        Fsum1=Fsum1+Fval*dx/x
        Asum1=Asum1+A2p*Gpow*dx/x
        Cpow1=A2p*Gpow/Fval
        Write (9,'(3e15.5)') x,Cpow2,Cpow1
        x=x+dx
      Enddo
      Write (9,*) ' join'
      Print *,' Lowest-order Adler sum =',Fsum2
      Print *,' Coeff of 1/Q^2 contrib =',Asum2/Fsum2
      Print *,' Lowest-order G-LS  sum =',Fsum1
      Print *,' Coeff of 1/Q^2 contrib =',Asum1/Fsum1
C
C 1/Q^4 contributions
C
C NP parameter: A2p = (C_F/2Pi) int dmu^2 delta aeff(mu^2)*log(mu^2)
      A2p=0.04
C
      Write (9,*) ' new frame'
      Write (9,*) ' set font duplex'
      Write (9,*) ' set limits x 0 0.8 y -.5 2.0'
      Write (9,*) ' title bottom ''x'' size 3'
      Write (9,*) ' title left ''D041(x,Q223) (GeV243)'' size 3'
      Write (9,*) ' case       '' X X    X X      X X'''
      Write (9,*) 0.0, 0.0
      Write (9,*) 0.8, 0.0
      Write (9,*) ' join'
      Write (9,*) ' set order x y dummy dummy'
      Write (9,*) ' (Q^2 =',Q2
      Fsum1=0d0
      Fsum2=0d0
      Fsum3=0d0
      Asum1=0d0
      Asum2=0d0
      Asum3=0d0
      x=.5*dx
      Do while (x.lt.1d0)
        w=1d0-x
        L=Log(w)
        Call Mrsaval(x,scale,upv,dnv,dup,ddn)
C---Valence x*q(x) and its derivative
C   N.B. This is for average of neutrino and antineutrino
        Fval=upv+dnv
        Dval=dup+ddn
C---Second derivative
        Call Mrsaval(x+ex,scale,up1,dn1,du1,dd1)
```

```
        Call Mrsaval(x-ex,scale,up2,dn2,du2,dd2)
        Eval=(du1+dd1-du2-dd2)/(2.*ex)
C---Contribution to F2
        Gpow=Dgauss(F2int4,x,1d0,eps)+(15d0+4d0*L)*Fval
     &       +x*Dval+0.5d0*x*x*Eval
        Fsum2=Fsum2+Fval*dx/x
        Asum2=Asum2+A2p*Gpow*dx/x
        Cpow2=A2p*Gpow/Fval
C---Contribution to 2xF1
        Gpow=Dgauss(F1int4,x,1d0,eps)+(11d0+4d0*L)*Fval
     &       -3d0*x*Dval+0.5d0*x*x*Eval
        Fsum1=Fsum1+Fval*dx/x
        Asum1=Asum1+A2p*Gpow*dx/x
        Cpow1=A2p*Gpow/Fval
C---Contribution to xF3
        Gpow=Dgauss(F3int4,x,1d0,eps)+(9d0+4d0*L)*Fval
     &       -3d0*x*Dval+0.5d0*x*x*Eval
        Cpow3=A2p*Gpow/Fval
        Fsum3=Fsum3+Fval*dx/x
        Asum3=Asum3+A2p*Gpow*dx/x
        Write (9,'(4e15.5)') x,Cpow2,Cpow1,Cpow3
        x=x+dx
      Enddo
      Write (9,*) ' join'
      Print *,' Lowest-order Adler sum =',Fsum2
      Print *,' Coeff of 1/Q^4 contrib =',Asum2/Fsum2
      Print *,' Lowest-order 2xF1  sum =',Fsum1
      Print *,' Coeff of 1/Q^4 contrib =',Asum1/Fsum1
      Print *,' Lowest-order G-LS  sum =',Fsum3
      Print *,' Coeff of 1/Q^4 contrib =',Asum3/Fsum3
      Goto 1
      End
C-----------------------------------------------------------------------
      Function Flint2(z)
C---Integrand for 1/Q^2 contribution to F1
      Implicit none
      Real*8 Flint2,z,w,Fz,Fval,x,scale,upv,dnv,dup,ddn
      Common/Fcom/x,scale,Fval
      Call Mrsaval(x/z,scale,upv,dnv,dup,ddn)
      Fz=upv+dnv
      w=1d0-z
      Flint2=-4d0*(Fz-Fval)/w+2d0*(2d0+z+2d0*z**2)*Fz
      End
C-----------------------------------------------------------------------
      Function F2int2(z)
C---Integrand for 1/Q^2 contribution to F2
      Implicit none
      Real*8 F2int2,z,w,Fz,Fval,x,scale,upv,dnv,dup,ddn
      Common/Fcom/x,scale,Fval
      Call Mrsaval(x/z,scale,upv,dnv,dup,ddn)
      Fz=upv+dnv
      w=1d0-z
      F2int2=-4d0*(Fz-Fval)/w+2d0*(2d0+z+6d0*z**2)*Fz
      End
C-----------------------------------------------------------------------
      Function Flint4(z)
C---Integrand for 1/Q^4 contribution to F1
      Implicit none
      Real*8 Flint4,z,w,Fz,Fval,x,scale,upv,dnv,dup,ddn
      Common/Fcom/x,scale,Fval
      Call Mrsaval(x/z,scale,upv,dnv,dup,ddn)
      Fz=upv+dnv
      w=1d0-z
      Flint4=4d0*(Fz-Fval)/w-4d0*(1d0+z+3d0*z**3)*Fz
```

```
      End
C-----------------------------------------------------------------
      Function F2int4(z)
C---Integrand for 1/Q^4 contribution to F2
      Implicit none
      Real*8 F2int4,z,w,Fz,Fval,x,scale,upv,dnv,dup,ddn
      Common/Fcom/x,scale,Fval
      Call Mrsaval(x/z,scale,upv,dnv,dup,ddn)
      Fz=upv+dnv
      w=1d0-z
      F2int4=4d0*(Fz-Fval)/w-4d0*(1d0+z+9d0*z**3)*Fz
      End
C-----------------------------------------------------------------
      Function F3int4(z)
C---Integrand for 1/Q^4 contribution to F3
      Implicit none
      Real*8 F3int4,z,w,Fz,Fval,x,scale,upv,dnv,dup,ddn
      Common/Fcom/x,scale,Fval
      Call Mrsaval(x/z,scale,upv,dnv,dup,ddn)
      Fz=upv+dnv
      w=1d0-z
      F3int4=4d0*(Fz-Fval)/w-4d0*(1d0+z+z**2)*Fz
      End
C-----------------------------------------------------------------
      Subroutine Mrsaval(x,scale,upv,dnv,dup,ddn)
cccccccccccccccccccccccccccccccccccccccccccccccccccccccccccccccccccc
c                                                                  c
c  MRSA valence distributions and their x derivatives              c
c                                                                  c
cccccccccccccccccccccccccccccccccccccccccccccccccccccccccccccccccccc
      implicit real*8(a-h,o-z)
      dimension z(18,8),f(2),g(2)
      data z/
     .2.029386, -1.892760,  0.478114,  0.538000,  0.044742,  0.058742,
     .3.956000, -0.136659, -0.513630, -0.389400,  1.267936,  0.134397,
     .5.132000, -0.235874,  0.939374, -0.008433,  0.833784,  0.376702,

     .0.295255, -0.169615,  0.028711,  0.330000,  0.174503, -0.045713,
     .4.706000, -0.536820,  0.114806,  5.029000, -0.322071,  0.949196,
     .5.561000, -2.161758, -1.334992, -0.002353,  1.134808, -0.156988,

     .0.775400,-0.517656,0.159759,-0.300000,0.049683,-0.098598,
     .5.300000,0.233708,0.282415,0.000000,-1.100596,0.052043,
     .5.200000,-3.232076,0.712254,0.003932,1.625446,-0.699441,

     .0.160750, -0.104311,  0.017157, -0.300000,  0.052451, -0.065844,
     .9.272000, -0.576575,  0.109982, -1.153000,  1.173228,  0.169775,
     .15.600000, -6.054861,  0.267608, -0.002159,  0.919959, -0.153501,

     .0.099280, -0.042174,  0.008380,  0.400000, -0.070009,  0.067714,
     .9.270000,  0.606514, -0.190625,  0.000000,  7.334181, -3.106807,
     .25.000000,-20.291985,  4.165453, -0.005437,  0.080749,  0.256036,

     .0.040260, -0.021695,  0.004481, -0.300000,  0.024073, -0.042711,
     .9.272000, -1.998587,  1.019307, -1.153000,  2.932868, -1.591815,
     .15.600000,-14.772277,  5.885859, -0.003502,  1.155235, -0.269042,

     .0.001753,  0.017854, -0.004894, -0.195549, -0.180373,  0.047210,
     .6.592858,  1.960693, -1.082506,  0.121744, -0.775791,  0.007846,
     .8.249182, -7.279327,  1.702087,  0.928112, -0.034017,  0.084953,

     .-0.004324,  0.012668, -0.001675, -0.276236,  0.090440, -0.112318,
     .2.647901,  3.239016, -0.534956,  1.390272, -2.629704,  0.646575,
     .-3.178775,  4.968992, -1.683463,  1.055388,  0.781798, -0.491059/
```

```
      al=0.23
      q2=scale*scale
      q0=2.
      arg=(dlog(scale/al)/dlog(q0/al))
      s=dlog(arg)

      do 10 j=1,2

      a=z(1,j)+z(2,j)*s+z(3,j)*s*s
      b=z(4,j)+z(5,j)*s+z(6,j)*s*s
      c=z(7,j)+z(8,j)*s+z(9,j)*s*s
      d=z(10,j)+z(11,j)*s+z(12,j)*s*s
      e=z(13,j)+z(14,j)*s+z(15,j)*s*s
      h=z(16,j)+z(17,j)*s+z(18,j)*s*s
      f(j)=a*x**b*(1.-x)**c*(1.+d*sqrt(x)+e*x)*(dlog(1./x))**h
   10 g(j)=f(j)*(b/x-c/(1.-x)+(.5*d/sqrt(x)+e)/(1.+d*sqrt(x)+e*x)
     & -h/(x*dlog(1./x)))
      upv=f(1)
      dnv=f(2)
      dup=g(1)
      ddn=g(2)
      return
      end
C-----------------------------------------------------------------------
      DOUBLE PRECISION FUNCTION DGAUSS(F,A,B,EPS)
      DOUBLE PRECISION W(12),X(12),A,B,EPS,DELTA,CONST,AA,BB,Y,C1,C2,S8,
     1                 S16,U,F
      DATA CONST /1.0D-25/
      DATA W
     1       / 0.10122 85362 90376 25915 25313 543D0,
     2         0.22238 10344 53374 47054 43559 944D0,
     3         0.31370 66458 77887 28733 79622 020D0,
     4         0.36268 37833 78361 98296 51504 493D0,
     5         0.02715 24594 11754 09485 17805 725D0,
     6         0.06225 35239 38647 89286 28438 370D0,
     7         0.09515 85116 82492 78480 99251 076D0,
     8         0.12462 89712 55533 87205 24762 822D0,
     9         0.14959 59888 16576 73208 15017 305D0,
     A         0.16915 65193 95002 53818 93120 790D0,
     B         0.18260 34150 44923 58886 67636 680D0,
     C         0.18945 06104 55068 49628 53967 232D0 /
      DATA X
     1       / 0.96028 98564 97536 23168 35608 686D0,
     2         0.79666 64774 13626 73959 15539 365D0,
     3         0.52553 24099 16328 98581 77390 492D0,
     4         0.18343 46424 95649 80493 94761 424D0,
     5         0.98940 09349 91649 93259 61541 735D0,
     6         0.94457 50230 73232 57607 79884 155D0,
     7         0.86563 12023 87831 74388 04678 977D0,
     8         0.75540 44083 55003 03389 51011 948D0,
     9         0.61787 62444 02643 74844 66717 640D0,
     A         0.45801 67776 57227 38634 24194 430D0,
     B         0.28160 35507 79258 91323 04605 015D0,
     C         0.09501 25098 37637 44018 53193 354D0 /
      DELTA=CONST*DABS(A-B)
      DGAUSS=0.
      AA=A
    5 Y=B-AA
      IF(DABS(Y) .LE. DELTA) RETURN
    2 BB=AA+Y
      C1=0.5D0*(AA+BB)
      C2=C1-AA
      S8=0.
```

```
      S16=0.
      DO 1 I = 1,4
      U=X(I)*C2
    1 S8=S8+W(I)*(F(C1+U)+F(C1-U))
      DO 3 I = 5,12
      U=X(I)*C2
    3 S16=S16+W(I)*(F(C1+U)+F(C1-U))
      S8=S8*C2
      S16=S16*C2
      IF(DABS(S16-S8) .GT. EPS*(1.0D0+DABS(S16))) GO TO 4
      DGAUSS=DGAUSS+S16
      AA=BB
      GO TO 5
    4 Y=0.5D0*Y
      IF(DABS(Y) .GT. DELTA) GO TO 2
      PRINT 7
c      DGAUSS=0.
      RETURN
    7 FORMAT(1X,37HDGAUSS ... TOO HIGH ACCURACY REQUIRED)
      END
```

Appendix D: Structure-Function Tables

This Appendix lists the numerical results from the structure-function analysis described in Chapter 6. See Appendix B of this thesis for instructions on obtaining these tables in machine-readable form.

D.1 Statistical and Systematic Errors

Table D.1 lists the values of F_2, xF_3, and the statistical errors ΔF_2, ΔxF_3, and $\Delta F_2 \Delta xF_3$, as a function of x and Q^2. The point-to-point systematic errors, $\left(+1\delta(k)-\left(-1\delta(k)\right)\right)/2$, are listed as follows:

- The energy-calibration systematic errors for F_2 are listed in Table D.2.
- The energy-calibration systematic errors for xF_3 are listed in Table D.3.
- The flux-extraction systematic errors for F_2 are listed in Table D.4.
- The flux-extraction systematic errors for xF_3 are listed in Table D.5.
- The cross-section systematic errors and the systematic error due to R for F_2 are listed in Table D.6.
- The cross-section systematic errors and the systematic error due to R for xF_3 are listed in Table D.7.
- The physics-model systematic errors for F_2 are listed in Table D.8.
- The physics-model systematic errors for xF_3 are listed in Table D.9.

D.2 Separate E744 and E770 Results

Since experiments E744 and E770 have separate data samples, separate Monte Carlo corrections, and (to some degree) separate systematic errors, it can be useful to examine the structure functions extracted from each experiment as a separate measurement. Table D.10 and D.11 lists the structure functions from experiments E744 and E770, respectively. Table D.12 lists the E744 F_2 with the 1δ variation in those systematic quantities that are independent between the two experiments: C_{HAD}, $\langle B/A \rangle^{\nu}$, and $\langle B/A \rangle^{\bar{\nu}}$. Table D.13 lists the same systematic variations for E770 F_2. Tables D.14 and D.15 list the systematic errors for E744 and E770 xF_3.

D.3 Removing Physics-Model Corrections

This collaboration has received requests for the values of the structure functions *without* one or more of the physics-model corrections described in Section 4.2.2. The corrections are:

- The isoscalar correction adjusts the effective momentum densities of the quark distributions from an iron target to an isoscalar target. This corrects for the 5.67% excess of neutrons versus protons in the CCFR detector.

- The radiative correction adjusts the charged-current differential cross-section for effects such as emission of a photon by the outgoing muon [Bar86].

- The slow-rescaling correction accounts for the effects of charm-production. The leading-order correction used in this analysis assumed $m_c = 1.31\ GeV$ [Rab92].

- The propagator correction redefines the effective Fermi coupling constant to account for the mass of the W-boson propagator. This analysis assumes $m_W = 80\ GeV$.

Tables D.16 (for F_2) and D.17 (for xF_3) give the correction for removing each component of the model described in Section 4.2.2. The correction is given as:

$$\text{correction} = \frac{F(\text{without correction})}{F(\text{with correction})} \tag{D.1}$$

So, for example, if the value of F_2 without the isoscalar and the slow-rescaling correction is desired, the central value of F_2 in Table D.1 should be adjusted:

$$\begin{aligned} &F_2(\text{no charm or isoscalar correction}) \\ &\quad = F_2(\text{extracted}) \\ &\qquad \times \text{slow rescaling column} \times \text{isoscalar column} \\ &\quad = F_2(\text{extracted}) \\ &\qquad \times \frac{F_2(\text{no slow rescaling correction})}{F_2(\text{with slow rescaling correction})} \\ &\qquad \times \frac{F_2(\text{no isoscalar correction})}{F_2(\text{with isoscalar correction})} \end{aligned} \tag{D.2}$$

The final column of these tables contains the correction for removing all of the physics-model corrections described above. Note that the product of the individual physics-model columns does not equal the value of the column with all physics corrections removed. This is because the physics-model corrections are not linear.

D.4 Notes on the Use of the Structure-Function Tables

D.4.1 Using the Physics-Model Correction Tables

It's important to note the difference between Tables D.8-D.9 and Tables D.16-D.17. Tables D.8-D.9 list the *additive* shift in the structure functions due to a 1δ shift in the *error* of a model parameter (for example, the mass of the charm quark). These tables should be used for systematic error studies on the structure function.

Tables D.16-D.17 list the *multiplicative* shift in the structure functions from *omitting* a given physics-model correction entirely (for example, the slow-rescaling correction for charm production). This tables should be used for studies that test the results of using a different physics model than the one described in Section 4.2.2. For example, this table can be used to remove the effects of the leading-order charm-production correction used for this analysis so that a next-to-leading-order slow-rescaling correction can be applied.

D.4.2 Correlated Errors

When applying adjustments or corrections to the structure functions, it is important to adjust the correlated error $\Delta F_2 \Delta x F_3$ so that the correlation coefficient

$$r = \frac{\left(\Delta F_2 \Delta x F_3\right)}{\left(\Delta F_2\right)\left(\Delta x F_3\right)} \tag{D.3}$$

remains constant within each (x, Q^2) bin. Typical transformations made during the course of systematic error studies or QCD fits are of the form

$$F_2{}'(x, Q^2) = c_2(x, Q^2) \times F_2(x, Q^2) \tag{D.4}$$

$$\Delta F_2{}'(x,Q^2) = c_2(x,Q^2) \times \Delta F_2(x,Q^2) \tag{D.5}$$

$$xF_3{}'(x,Q^2) = c_3(x,Q^2) \times xF_3(x,Q^2) \tag{D.6}$$

$$\Delta xF_3{}'(x,Q^2) = c_3(x,Q^2) \times \Delta xF_3(x,Q^2) \tag{D.7}$$

where c_2 and c_3 are some function of (x,Q^2). Then the following relation will keep r constant under the transformation of Equations D.4-D.7:

$$\left(\Delta F_2 \Delta xF_3\right)' = \frac{\left(\Delta F_2\right)'\left(\Delta xF_3\right)'}{\left(\Delta F_2\right)\left(\Delta xF_3\right)}\left(\Delta F_2 \Delta xF_3\right) = c_2 c_3 \left(\Delta F_2 \Delta xF_3\right) \tag{D.8}$$

When performing any simultaneous fits to F_2 and xF_3, it is important to include the correlated statistical error $\Delta F_2 \Delta xF_3$; the χ^2 calculation is described in Section 7.1.7. The reason is that, at high x, F_2 and xF_3 are determined by the same events and are therefore highly correlated.

D.4.3 Correlations Between Point-to-Point Systematic Errors

When incorporating the systematic errors in Table D.2 through D.9 in an analysis, there is a tendency to over-simplify, assume that these errors are uncorrelated from point to point, and add them in quadrature. Indeed, for making plots such as those of Figures 8.6-8.11, there is no alternative to this simple assumption. However, for any other purpose, the analysis must include the correlations between the point-to-point systematic errors.

Section 7.3 describes the procedure for correctly including these correlations in QCD fits. For convenience, the procedure is briefly reproduced here. Define the structure-function vector as

$$\vec{\mathbf{F}} = \begin{pmatrix} F_2(x,Q^2) \\ xF_3(x,Q^2) \end{pmatrix} \tag{7.30}$$

and the structure-function error matrix

$$\hat{\mathbf{V}} = \begin{pmatrix} (\Delta F_2)^2 & \Delta F_2 \Delta x F_3 \\ \Delta F_2 \Delta x F_3 & (\Delta x F_3)^2 \end{pmatrix} \tag{7.31}$$

$$\hat{\mathbf{V}}^{-1} = \begin{bmatrix} v_{22} & v_{32} \\ v_{23} & v_{33} \end{bmatrix} = \frac{1}{\det \hat{\mathbf{V}}} \begin{bmatrix} (\Delta x F_3)^2 & -\Delta F_2 \Delta x F_3 \\ -\Delta F_2 \Delta x F_3 & (\Delta F_2)^2 \end{bmatrix} \tag{7.34}$$

Then the χ^2 is calculated by summing over all the (x,Q^2) bins that pass the cuts:

$$\vec{\mathbf{F}}^{diff} = \vec{\mathbf{F}}^{data} - \vec{\mathbf{F}}^{theory} + \sum_k \delta_k \left(\vec{\mathbf{F}}^k - \vec{\mathbf{F}}^{data} \right) \tag{7.37}$$

$$\chi^2 = \sum_{(x,Q^2)\text{bins}} \left(\vec{\mathbf{F}}^{diff} \right)^{\mathrm{T}} \hat{\mathbf{V}}^{-1} \left(\vec{\mathbf{F}}^{diff} \right) + \sum_k \delta_k^2 \tag{7.38}$$

where k is summed over each of the systematically-varied structure functions.

Table D.1: F_2, xF_3, and their associated statistical errors.

x	Q^2	F_2	ΔF_2	xF_3	ΔxF_3	$\Delta F_2 \Delta xF_3$
0.0075	1.3	1.305	0.2975E-01	0.7632E-01	0.3700E-01	-0.5877E-03
	2.0	1.366	0.3703E-01	0.1821	0.4039E-01	-0.8464E-03
	3.2	1.587	0.6680E-01	0.9905E-01	0.6319E-01	-0.2951E-02
0.0125	1.3	1.237	0.2408E-01	0.2122	0.3417E-01	-0.2950E-03
	2.0	1.335	0.2783E-01	0.2239	0.3512E-01	-0.4043E-03
	3.2	1.525	0.3794E-01	0.1684	0.4290E-01	-0.9122E-03
	5.0	1.675	0.6004E-01	0.2486	0.5783E-01	-0.2127E-02
0.0175	1.3	1.253	0.2421E-01	0.1894	0.4008E-01	-0.3237E-03
	2.0	1.385	0.2596E-01	0.2767	0.3549E-01	-0.3065E-03
	3.2	1.528	0.3118E-01	0.2906	0.3887E-01	-0.4949E-03
	5.0	1.589	0.4313E-01	0.2543	0.4715E-01	-0.1198E-02
	7.9	1.527	0.7152E-01	0.3513	0.6743E-01	-0.2951E-02
0.0250	1.3	1.226	0.1751E-01	0.2339	0.3704E-01	-0.2208E-03
	2.0	1.311	0.1703E-01	0.3517	0.2670E-01	-0.1048E-03
	3.2	1.463	0.1936E-01	0.3298	0.2605E-01	-0.1706E-03
	5.0	1.558	0.2339E-01	0.3732	0.2882E-01	-0.2723E-03
	7.9	1.661	0.3303E-01	0.3555	0.3521E-01	-0.6526E-03
	12.6	1.759	0.6962E-01	0.3551	0.6568E-01	-0.2989E-02
0.0350	1.3	1.193	0.1848E-01	0.4047	0.5474E-01	-0.2911E-03
	2.0	1.330	0.1818E-01	0.4121	0.3500E-01	-0.1773E-03
	3.2	1.412	0.1799E-01	0.4078	0.2699E-01	-0.1216E-03
	5.0	1.551	0.2052E-01	0.4159	0.2706E-01	-0.1623E-03
	7.9	1.598	0.2536E-01	0.4316	0.3064E-01	-0.3353E-03
	12.6	1.734	0.3787E-01	0.4561	0.3901E-01	-0.7614E-03
	20.0	1.779	0.1028	0.5198	0.9575E-01	-0.6347E-02

(continued on next page)

Table D.1 (continued): F_2, xF_3, and their associated statistical errors.

x	Q^2	F_2	ΔF_2	xF_3	ΔxF_3	$\Delta F_2 \Delta xF_3$
0.0500	1.3	1.228	0.1545E-01	0.3967	0.6599E-01	-0.3308E-03
	2.0	1.336	0.1371E-01	0.5068	0.3600E-01	-0.1111E-03
	3.2	1.434	0.1311E-01	0.4822	0.2357E-01	-0.6663E-04
	5.0	1.509	0.1365E-01	0.5058	0.1989E-01	-0.6090E-04
	7.9	1.593	0.1514E-01	0.5800	0.1979E-01	-0.7600E-04
	12.6	1.611	0.1881E-01	0.5615	0.2215E-01	-0.1539E-03
	20.0	1.683	0.2962E-01	0.6184	0.3011E-01	-0.4066E-03
	31.6	1.622	0.9702E-01	0.6167	0.9101E-01	-0.5234E-02
0.0700	2.0	1.322	0.1539E-01	0.5093	0.5839E-01	-0.2616E-03
	3.2	1.393	0.1375E-01	0.6078	0.3228E-01	-0.7956E-04
	5.0	1.482	0.1351E-01	0.6209	0.2280E-01	-0.5123E-04
	7.9	1.532	0.1379E-01	0.6377	0.1946E-01	-0.4001E-04
	12.6	1.548	0.1609E-01	0.6370	0.2080E-01	-0.8229E-04
	20.0	1.598	0.2097E-01	0.6485	0.2391E-01	-0.1815E-03
	31.6	1.591	0.3695E-01	0.6147	0.3683E-01	-0.6546E-03
0.0900	2.0	1.318	0.1821E-01	0.7605	0.9046E-01	-0.4613E-03
	3.2	1.380	0.1504E-01	0.5799	0.4613E-01	-0.1881E-03
	5.0	1.432	0.1368E-01	0.6738	0.2707E-01	-0.5207E-04
	7.9	1.458	0.1331E-01	0.7340	0.2048E-01	-0.1642E-04
	12.6	1.491	0.1463E-01	0.7146	0.1980E-01	-0.3770E-04
	20.0	1.510	0.1750E-01	0.7376	0.2177E-01	-0.8710E-04
	31.6	1.509	0.2384E-01	0.7384	0.2551E-01	-0.1834E-03
	50.1	1.548	0.6295E-01	0.7445	0.6111E-01	-0.1696E-02
0.1100	3.2	1.335	0.1595E-01	0.6630	0.6051E-01	-0.2547E-03
	5.0	1.363	0.1401E-01	0.7350	0.3292E-01	-0.6234E-04
	7.9	1.385	0.1302E-01	0.7624	0.2200E-01	-0.1085E-04
	12.6	1.413	0.1366E-01	0.7658	0.1940E-01	-0.1372E-04
	20.0	1.449	0.1602E-01	0.7653	0.2086E-01	-0.3829E-04
	31.6	1.382	0.1955E-01	0.7374	0.2253E-01	-0.1175E-03
	50.1	1.503	0.3664E-01	0.7596	0.3705E-01	-0.4764E-03

(continued on next page)

Table D.1 (continued): F_2, xF_3, and their associated statistical errors.

x	Q^2	F_2	ΔF_2	xF_3	ΔxF_3	$\Delta F_2 \Delta xF_3$
0.1400	3.2	1.279	0.1297E-01	0.7642	0.6294E-01	-0.2211E-03
	5.0	1.305	0.1043E-01	0.8043	0.3120E-01	-0.5882E-04
	7.9	1.302	0.9231E-02	0.7931	0.1804E-01	-0.2530E-05
	12.6	1.319	0.9062E-02	0.8154	0.1395E-01	0.5936E-05
	20.0	1.312	0.9773E-02	0.8078	0.1328E-01	0.2064E-05
	31.6	1.270	0.1137E-01	0.8071	0.1419E-01	-0.1022E-04
	50.1	1.251	0.1581E-01	0.8139	0.1711E-01	-0.3658E-04
	79.4	1.272	0.4124E-01	0.8476	0.4090E-01	-0.3180E-03
0.1800	5.0	1.185	0.1110E-01	0.9044	0.4342E-01	-0.9647E-04
	7.9	1.177	0.9669E-02	0.8026	0.2349E-01	-0.1973E-04
	12.6	1.184	0.8893E-02	0.8361	0.1532E-01	0.1525E-04
	20.0	1.155	0.8828E-02	0.8247	0.1269E-01	0.1865E-04
	31.6	1.138	0.9901E-02	0.8280	0.1303E-01	0.1349E-04
	50.1	1.088	0.1174E-01	0.8111	0.1379E-01	0.1185E-04
	79.4	1.098	0.2006E-01	0.7814	0.2082E-01	-0.1986E-04
0.2250	5.0	1.097	0.1162E-01	0.7368	0.5772E-01	-0.1981E-03
	7.9	1.053	0.8881E-02	0.7854	0.2710E-01	-0.2999E-04
	12.6	1.028	0.7769E-02	0.7824	0.1539E-01	0.1044E-04
	20.0	1.001	0.7348E-02	0.8027	0.1141E-01	0.1611E-04
	31.6	0.9815	0.7815E-02	0.7763	0.1066E-01	0.2077E-04
	50.1	0.9498	0.8975E-02	0.7413	0.1131E-01	0.1547E-04
	79.4	0.9334	0.1166E-01	0.7731	0.1279E-01	0.3551E-04
0.2750	7.9	0.9039	0.8981E-02	0.7803	0.3387E-01	-0.4604E-04
	12.6	0.8763	0.7741E-02	0.7207	0.1818E-01	0.2181E-05
	20.0	0.8515	0.7008E-02	0.7066	0.1188E-01	0.2011E-04
	31.6	0.8176	0.7141E-02	0.6839	0.1017E-01	0.2385E-04
	50.1	0.7980	0.7945E-02	0.6755	0.1040E-01	0.2577E-04
	79.4	0.7552	0.9086E-02	0.6373	0.1061E-01	0.2754E-04
	125.9	0.7135	0.1561E-01	0.6265	0.1623E-01	0.1087E-03

(continued on next page)

Table D.1 (continued): F_2, xF_3, and their associated statistical errors.

x	Q^2	F_2	ΔF_2	xF_3	ΔxF_3	$\Delta F_2 \Delta xF_3$
0.3500	7.9	0.7049	0.6639E-02	0.6352	0.3202E-01	-0.4172E-04
	12.6	0.6687	0.5275E-02	0.5946	0.1571E-01	-0.5296E-05
	20.0	0.6274	0.4554E-02	0.5742	0.8879E-02	0.9052E-05
	31.6	0.6025	0.4439E-02	0.5490	0.6821E-02	0.1220E-04
	50.1	0.5723	0.4575E-02	0.5240	0.6214E-02	0.1237E-04
	79.4	0.5395	0.5027E-02	0.4881	0.6307E-02	0.1155E-04
	125.9	0.5254	0.6764E-02	0.4831	0.7438E-02	0.2640E-04
0.4500	12.6	0.4087	0.4541E-02	0.3987	0.1766E-01	-0.9467E-05
	20.0	0.3966	0.3972E-02	0.3729	0.9599E-02	0.3334E-05
	31.6	0.3609	0.3548E-02	0.3487	0.6094E-02	0.8461E-05
	50.1	0.3315	0.3520E-02	0.3216	0.5045E-02	0.9189E-05
	79.4	0.3158	0.3754E-02	0.3078	0.4923E-02	0.9917E-05
	125.9	0.2927	0.4230E-02	0.2885	0.4990E-02	0.1284E-04
	199.5	0.2743	0.7832E-02	0.2563	0.8264E-02	0.3786E-04
0.5500	12.6	0.2378	0.3870E-02	0.2731	0.1866E-01	-0.1341E-04
	20.0	0.2136	0.3137E-02	0.1973	0.9353E-02	-0.1823E-05
	31.6	0.1889	0.2658E-02	0.1834	0.5175E-02	0.3644E-05
	50.1	0.1763	0.2629E-02	0.1733	0.4033E-02	0.5088E-05
	79.4	0.1587	0.2621E-02	0.1595	0.3540E-02	0.5745E-05
	125.9	0.1502	0.2885E-02	0.1454	0.3616E-02	0.5315E-05
	199.5	0.1346	0.4046E-02	0.1314	0.4446E-02	0.1212E-04
0.6500	12.6	0.1184	0.3397E-02	0.8328E-01	0.1967E-01	-0.2220E-04
	20.0	0.9990E-01	0.2085E-02	0.1069	0.7406E-02	-0.1670E-05
	31.6	0.8166E-01	0.1669E-02	0.8762E-01	0.3702E-02	0.1292E-05
	50.1	0.7681E-01	0.1600E-02	0.8174E-01	0.2626E-02	0.2078E-05
	79.4	0.6731E-01	0.1600E-02	0.6648E-01	0.2246E-02	0.1922E-05
	125.9	0.6104E-01	0.1732E-02	0.5806E-01	0.2255E-02	0.1821E-05
0.7500	20.0	0.3505E-01	0.1011E-02	0.3791E-01	0.4179E-02	-0.6640E-06
	31.6	0.2838E-01	0.8458E-03	0.2875E-01	0.2163E-02	0.9329E-07
	50.1	0.2529E-01	0.7646E-03	0.2539E-01	0.1359E-02	0.3855E-06
	79.4	0.2135E-01	0.7569E-03	0.1963E-01	0.1112E-02	0.3495E-06
	125.9	0.2014E-01	0.8035E-03	0.1951E-01	0.1072E-02	0.3805E-06

Table D.2: F_2 energy-calibration systematic errors.

x	Q^2	F_2	ΔF_2^{stat}	C_{HAD}^{744}	C_{HAD}^{770}	δE_{HAD}	C_μ	δE_μ
0.0075	1.3	1.305	0.2975E-01	0.7507E-02	0.7412E-02	0.1566E-02	-0.1867E-01	-0.6575E-03
	2.0	1.366	0.3703E-01	0.1154E-01	0.1173E-01	0.5317E-02	-0.3168E-01	-0.4791E-02
	3.2	1.587	0.6680E-01	0.4577E-02	0.3816E-02	0.3371E-02	-0.5255E-01	0.5895E-03
0.0125	1.3	1.237	0.2408E-01	0.1920E-02	0.1828E-02	0.4194E-02	-0.2226E-01	-0.3293E-02
	2.0	1.335	0.2783E-01	0.6728E-02	0.8336E-02	0.4318E-02	-0.3083E-01	0.3697E-02
	3.2	1.525	0.3794E-01	0.1154E-01	0.2029E-01	0.4396E-02	-0.3711E-01	-0.2990E-02
	5.0	1.675	0.6004E-01	0.1157E-01	0.2311E-01	0.9593E-02	-0.6422E-01	-0.4596E-02
0.0175	1.3	1.253	0.2421E-01	0.6231E-02	0.3820E-02	0.3919E-02	-0.2358E-01	-0.4151E-02
	2.0	1.385	0.2596E-01	0.5705E-02	0.5806E-02	0.1338E-02	-0.2206E-01	-0.6158E-02
	3.2	1.528	0.3118E-01	0.1154E-01	0.5997E-02	0.5287E-02	-0.2850E-01	-0.4286E-02
	5.0	1.589	0.4313E-01	0.1480E-01	0.8272E-02	0.5745E-02	-0.3163E-01	0.8553E-02
	7.9	1.527	0.7152E-01	0.9642E-02	0.4770E-01	0.6142E-02	-0.1654E-01	0.1170E-01
0.0250	1.3	1.226	0.1751E-01	0.1175E-03	0.1513E-02	0.3980E-02	-0.1435E-01	-0.3466E-02
	2.0	1.311	0.1703E-01	0.3357E-02	0.5162E-02	0.5120E-02	-0.1753E-01	0.1905E-03
	3.2	1.463	0.1936E-01	0.4791E-02	0.8472E-02	0.4162E-02	-0.2996E-01	-0.3360E-03
	5.0	1.558	0.2339E-01	0.9165E-02	0.1096E-01	0.5282E-02	-0.2552E-01	-0.5685E-03
	7.9	1.661	0.3303E-01	0.1524E-01	0.1564E-01	0.7416E-02	-0.4689E-01	-0.6090E-03
	12.6	1.759	0.6962E-01	0.2537E-01	0.2440E-01	0.9753E-02	-0.7366E-01	-0.1555E-03
0.0350	1.3	1.193	0.1848E-01	0.4940E-03	0.4741E-02	0.7375E-02	-0.1634E-01	-0.5524E-02
	2.0	1.330	0.1818E-01	0.3551E-02	0.7732E-02	0.8201E-02	-0.2227E-01	-0.6026E-02
	3.2	1.412	0.1799E-01	0.6230E-02	0.5298E-02	0.6397E-02	-0.1487E-01	-0.4272E-02
	5.0	1.551	0.2052E-01	0.1001E-01	0.1162E-01	0.5385E-02	-0.3364E-01	-0.3812E-02
	7.9	1.598	0.2536E-01	0.8525E-02	0.8516E-02	0.5050E-02	-0.3983E-01	-0.2188E-02
	12.6	1.734	0.3787E-01	0.7631E-02	0.2497E-01	0.5926E-02	-0.4153E-01	0.3016E-02
	20.0	1.779	0.1028	0.6308E-01	0.1138E-01	0.1965E-01	-0.4316E-01	-0.2787E-02

(continued on next page)

Table D.2 (continued): F_2 energy-calibration systematic errors.

x	Q^2	F_2	ΔF_2^{stat}	C_{HAD}^{744}	C_{HAD}^{770}	ΔE_{HAD}	C_μ	ΔE_μ
0.0500	1.3	1.228	0.1545E-01	0.3568E-02	0.2900E-02	0.1190E-01	-0.1402E-01	-0.3527E-02
	2.0	1.336	0.1371E-01	0.1863E-02	0.1270E-02	0.5966E-02	-0.1166E-01	-0.4298E-02
	3.2	1.434	0.1311E-01	0.3196E-02	0.1976E-02	0.3983E-02	-0.1891E-01	-0.2090E-02
	5.0	1.509	0.1365E-01	0.4727E-02	0.6658E-02	0.6175E-02	-0.2172E-01	-0.2494E-02
	7.9	1.593	0.1514E-01	0.7664E-02	0.8708E-02	0.5929E-02	-0.2466E-01	-0.3413E-02
	12.6	1.611	0.1881E-01	0.1159E-01	0.1170E-01	0.5576E-02	-0.3007E-01	0.1177E-02
	20.0	1.683	0.2962E-01	0.2147E-01	0.2960E-01	0.6936E-02	-0.5068E-01	-0.5123E-02
	31.6	1.622	0.9702E-01	0.2721E-01	0.2965E-01	0.1835E-01	-0.7700E-01	0.1315E-01
0.0700	2.0	1.322	0.1539E-01	0.3080E-02	0.1139E-02	0.9425E-02	-0.1652E-01	-0.2062E-02
	3.2	1.393	0.1375E-01	0.3805E-02	0.3878E-02	0.7856E-02	-0.1522E-01	-0.4720E-02
	5.0	1.482	0.1351E-01	0.2331E-02	0.5857E-02	0.2620E-02	-0.1550E-01	-0.1845E-02
	7.9	1.532	0.1379E-01	0.4689E-02	0.6580E-02	0.3388E-02	-0.2255E-01	0.1271E-02
	12.6	1.548	0.1609E-01	0.1127E-01	0.9355E-02	0.5989E-02	-0.2457E-01	-0.1127E-02
	20.0	1.598	0.2097E-01	0.1103E-01	0.9691E-02	0.4625E-02	-0.2653E-01	0.5387E-02
	31.6	1.591	0.3695E-01	0.1901E-01	0.1709E-01	0.9964E-02	-0.6239E-01	0.5014E-02
0.0900	2.0	1.318	0.1821E-01	0.4890E-03	0.3787E-02	0.1171E-01	-0.1100E-01	-0.1570E-03
	3.2	1.380	0.1504E-01	0.9275E-03	0.3302E-02	0.8112E-02	-0.1332E-01	-0.4157E-02
	5.0	1.432	0.1368E-01	0.3487E-02	0.1492E-02	0.5893E-02	-0.1614E-01	-0.2135E-02
	7.9	1.458	0.1331E-01	0.4269E-02	0.4734E-02	0.3514E-02	-0.1562E-01	-0.1988E-02
	12.6	1.491	0.1463E-01	0.4875E-02	0.8619E-02	0.4484E-02	-0.2046E-01	-0.9751E-04
	20.0	1.510	0.1750E-01	0.1128E-01	0.1241E-01	0.7629E-02	-0.2584E-01	0.2528E-02
	31.6	1.509	0.2384E-01	0.1283E-01	0.1539E-01	0.6752E-02	-0.3494E-01	0.2881E-02
	50.1	1.548	0.6295E-01	0.1730E-01	0.2378E-01	0.7050E-02	-0.6060E-01	-0.1436E-01
0.1100	3.2	1.335	0.1595E-01	0.1160E-03	-0.2030E-02	0.4490E-02	-0.6416E-02	-0.1315E-02
	5.0	1.363	0.1401E-01	0.2375E-02	0.5027E-02	0.7708E-02	-0.1010E-01	-0.4679E-02
	7.9	1.385	0.1302E-01	0.6484E-02	0.6625E-02	0.7721E-02	-0.1865E-01	-0.4818E-02
	12.6	1.413	0.1366E-01	0.6074E-02	0.6513E-02	0.5105E-02	-0.2244E-01	-0.1934E-02
	20.0	1.449	0.1602E-01	0.7141E-02	0.7577E-02	0.4654E-02	-0.1671E-01	0.5347E-04
	31.6	1.382	0.1955E-01	0.8776E-02	0.1193E-01	0.5660E-02	-0.3065E-01	0.2443E-02
	50.1	1.503	0.3664E-01	0.1465E-01	0.2598E-01	0.6700E-02	-0.4380E-01	0.6628E-02

(continued on next page)

Table D.2 (continued): F_2 energy-calibration systematic errors.

x	Q^2	F_2	ΔF_2^{stat}	C_{HAD}^{744}	C_{HAD}^{770}	ΔE_{HAD}	C_μ	ΔE_μ
0.1400	3.2	1.279	0.1297E-01	0.1044E-02	0.5315E-03	0.9338E-02	-0.4336E-02	-0.3795E-03
	5.0	1.305	0.1043E-01	0.1930E-02	0.6920E-03	0.6999E-02	-0.7932E-02	-0.2360E-02
	7.9	1.302	0.9231E-02	0.1038E-02	0.3660E-03	0.3492E-02	-0.4825E-02	0.3110E-03
	12.6	1.319	0.9062E-02	0.4077E-02	0.3989E-02	0.3354E-02	-0.1477E-01	-0.1349E-02
	20.0	1.312	0.9773E-02	0.4987E-02	0.6689E-02	0.4014E-02	-0.1293E-01	0.2536E-02
	31.6	1.270	0.1137E-01	0.7968E-02	0.7541E-02	0.4664E-02	-0.1016E-01	0.1150E-02
	50.1	1.251	0.1581E-01	0.9599E-02	0.1125E-01	0.5429E-02	-0.2459E-01	0.4800E-02
	79.4	1.272	0.4124E-01	0.1736E-01	0.1675E-01	0.5452E-02	-0.5937E-01	-0.6833E-02
0.1800	5.0	1.185	0.1110E-01	-0.4321E-02	0.6985E-03	0.3716E-02	0.2866E-02	0.9665E-03
	7.9	1.177	0.9669E-02	0.1785E-02	0.4595E-03	0.5258E-02	-0.1146E-02	0.1703E-02
	12.6	1.184	0.8893E-02	-0.2155E-03	0.2456E-02	0.3559E-02	-0.7652E-02	-0.1652E-02
	20.0	1.155	0.8828E-02	0.5843E-02	0.3348E-02	0.3884E-02	-0.1280E-01	-0.1928E-02
	31.6	1.138	0.9901E-02	0.5502E-02	0.7281E-02	0.3778E-02	-0.1056E-01	0.4372E-02
	50.1	1.088	0.1174E-01	0.8829E-02	0.7242E-02	0.5089E-02	-0.1424E-01	0.2597E-02
	79.4	1.098	0.2006E-01	0.1281E-01	0.1589E-01	0.3871E-02	-0.2134E-01	0.4596E-02
0.2250	5.0	1.097	0.1162E-01	0.2176E-02	-0.3912E-02	0.5256E-02	0.3649E-02	0.2644E-02
	7.9	1.053	0.8881E-02	-0.2928E-02	0.9185E-03	0.2604E-02	-0.2945E-02	-0.1561E-02
	12.6	1.028	0.7769E-02	0.3275E-03	-0.1637E-02	0.1431E-02	0.4199E-02	0.2679E-02
	20.0	1.001	0.7348E-02	0.1221E-02	0.1094E-02	0.3072E-02	0.7546E-04	0.1758E-02
	31.6	0.9815	0.7815E-02	0.2765E-02	0.4719E-02	0.3006E-02	-0.3659E-02	0.1054E-02
	50.1	0.9498	0.8975E-02	0.6017E-02	0.3447E-02	0.3857E-02	-0.7297E-02	0.2695E-02
	79.4	0.9334	0.1166E-01	0.6613E-02	0.9856E-02	0.3428E-02	-0.1518E-01	0.1708E-02
0.2750	7.9	0.9039	0.8981E-02	-0.7433E-04	-0.3202E-02	0.1031E-02	0.8796E-02	0.2416E-02
	12.6	0.8763	0.7741E-02	-0.1354E-02	-0.1997E-02	0.1575E-02	0.1345E-02	-0.2354E-05
	20.0	0.8515	0.7008E-02	-0.7444E-03	0.9013E-03	0.1716E-02	0.3038E-02	0.1369E-02
	31.6	0.8176	0.7141E-02	0.1040E-02	0.2857E-02	0.2025E-02	-0.7400E-03	0.1636E-02
	50.1	0.7980	0.7945E-02	0.2665E-02	0.1745E-02	0.2641E-02	-0.6956E-03	0.2344E-02
	79.4	0.7552	0.9086E-02	0.2746E-02	0.3825E-02	0.3086E-02	-0.5130E-02	0.2627E-02
	125.9	0.7135	0.1561E-01	0.1008E-01	0.1118E-01	0.2843E-02	-0.2674E-02	0.3167E-02

(continued on next page)

Table D.2 (continued): F_2 energy-calibration systematic errors.

x	Q^2	F_2	ΔF_2^{stat}	C_{HAD}^{744}	C_{HAD}^{770}	ΔE_{HAD}	C_μ	ΔE_μ
0.3500	7.9	0.7049	0.6639E-02	-0.1789E-02	-0.3620E-02	0.3124E-03	0.8697E-02	0.1541E-02
	12.6	0.6687	0.5275E-02	-0.1778E-02	-0.3299E-02	0.5060E-04	0.9954E-02	0.2096E-02
	20.0	0.6274	0.4554E-02	-0.1675E-02	-0.2110E-02	-0.6443E-04	0.9150E-02	0.1550E-02
	31.6	0.6025	0.4439E-02	0.1110E-03	-0.1051E-02	0.1171E-02	0.6178E-02	0.1879E-02
	50.1	0.5723	0.4575E-02	0.2663E-03	0.4988E-03	0.1082E-02	0.6267E-02	0.2415E-02
	79.4	0.5395	0.5027E-02	0.1636E-02	0.1836E-02	0.1990E-02	0.2240E-02	0.2707E-02
	125.9	0.5254	0.6764E-02	0.4475E-02	0.4014E-02	0.2040E-02	-0.6592E-03	0.2427E-02
0.4500	12.6	0.4087	0.4541E-02	-0.2524E-02	-0.2924E-02	-0.1079E-02	0.1410E-01	0.2633E-02
	20.0	0.3966	0.3972E-02	-0.2129E-02	-0.2155E-02	-0.4887E-03	0.1071E-01	0.2490E-02
	31.6	0.3609	0.3548E-02	-0.1946E-02	-0.2877E-02	-0.5087E-03	0.1102E-01	0.2318E-02
	50.1	0.3315	0.3520E-02	-0.8103E-03	-0.9893E-03	0.5084E-03	0.8134E-02	0.9561E-03
	79.4	0.3158	0.3754E-02	-0.5682E-03	-0.1200E-02	0.4975E-03	0.9051E-02	0.1758E-02
	125.9	0.2927	0.4230E-02	0.6631E-03	-0.1550E-03	0.1162E-02	0.2757E-02	0.1686E-02
	199.5	0.2743	0.7832E-02	0.2406E-02	0.3811E-02	0.1251E-02	0.2265E-02	0.2887E-02
0.5500	12.6	0.2378	0.3870E-02	-0.1758E-02	-0.2304E-02	-0.1927E-02	0.7752E-02	0.1645E-02
	20.0	0.2136	0.3137E-02	-0.1577E-02	-0.2259E-02	-0.8636E-03	0.7883E-02	0.1593E-02
	31.6	0.1889	0.2658E-02	-0.1242E-02	-0.1861E-02	-0.6736E-03	0.7471E-02	0.1358E-02
	50.1	0.1763	0.2629E-02	-0.1095E-02	-0.1642E-02	-0.2260E-03	0.7709E-02	0.1484E-02
	79.4	0.1587	0.2621E-02	-0.3655E-04	-0.8417E-03	0.3394E-03	0.3979E-02	0.1050E-02
	125.9	0.1502	0.2885E-02	-0.2631E-03	0.7315E-04	0.2803E-03	0.5839E-02	0.1105E-02
	199.5	0.1346	0.4046E-02	0.4127E-03	-0.1836E-03	0.8332E-03	0.1933E-02	0.1548E-02
0.6500	12.6	0.1184	0.3397E-02	-0.1302E-02	-0.1728E-02	-0.1821E-02	0.5929E-02	0.1368E-02
	20.0	0.9990E-01	0.2085E-02	-0.1426E-02	-0.1860E-02	-0.1532E-02	0.5701E-02	0.1126E-02
	31.6	0.8166E-01	0.1669E-02	-0.9205E-03	-0.1197E-02	-0.4851E-03	0.5428E-02	0.5556E-03
	50.1	0.7681E-01	0.1600E-02	-0.6242E-03	-0.7809E-03	-0.2348E-03	0.4088E-02	0.4319E-03
	79.4	0.6731E-01	0.1600E-02	-0.7943E-03	-0.6571E-03	0.1905E-03	0.4311E-02	0.5748E-03
	125.9	0.6104E-01	0.1732E-02	0.1012E-03	-0.2814E-03	0.1794E-03	0.3502E-02	0.5333E-03
0.7500	20.0	0.3505E-01	0.1011E-02	-0.8030E-04	-0.6160E-03	-0.2617E-03	0.2291E-02	0.2066E-03
	31.6	0.2838E-01	0.8458E-03	-0.1702E-03	-0.2780E-03	-0.1770E-03	0.1234E-02	0.1324E-03
	50.1	0.2529E-01	0.7646E-03	-0.3354E-03	-0.4982E-03	-0.1742E-03	0.1551E-02	0.4137E-03
	79.4	0.2135E-01	0.7569E-03	-0.1581E-03	-0.3688E-03	-0.1256E-03	0.1474E-02	0.2128E-03
	125.9	0.2014E-01	0.8035E-03	-0.2125E-03	-0.7191E-04	0.1273E-04	0.1471E-02	0.1053E-03

Table D.3: xF_3 energy-calibration systematic errors.

x	Q^2	xF_3	ΔxF_3^{stat}	C_{HAD}^{744}	C_{HAD}^{770}	ΔE_{HAD}	C_μ	ΔE_μ
0.0075	1.3	0.7632E-01	0.3700E-01	-0.3463E-02	-0.1638E-02	0.7229E-03	-0.9052E-02	-0.3397E-02
	2.0	0.1821	0.4039E-01	-0.4949E-02	0.2432E-02	0.1297E-02	0.9210E-02	0.8013E-02
	3.2	0.9905E-01	0.6319E-01	0.2334E-02	0.4000E-02	0.3900E-02	0.6453E-02	0.1044E-03
0.0125	1.3	0.2122	0.3417E-01	-0.2215E-02	0.4981E-02	0.4830E-02	0.1308E-01	0.6797E-02
	2.0	0.2239	0.3512E-01	-0.3258E-02	0.2533E-02	0.9215E-03	-0.3520E-02	-0.8040E-02
	3.2	0.1684	0.4290E-01	-0.1966E-02	-0.1185E-01	-0.2141E-02	-0.3718E-02	0.2980E-02
	5.0	0.2486	0.5783E-01	0.9007E-02	-0.4744E-02	0.7824E-03	0.6386E-02	0.9555E-02
0.0175	1.3	0.1894	0.4008E-01	-0.6730E-04	-0.7226E-03	-0.2588E-02	-0.1011E-01	-0.1973E-02
	2.0	0.2767	0.3549E-01	0.3267E-02	-0.3392E-03	0.5749E-03	-0.2457E-02	0.3622E-02
	3.2	0.2906	0.3887E-01	0.3914E-02	0.8582E-02	0.3357E-02	-0.3866E-02	-0.1810E-02
	5.0	0.2543	0.4715E-01	-0.1046E-01	0.1543E-02	0.1501E-02	-0.1221E-03	-0.5597E-02
	7.9	0.3513	0.6743E-01	0.1107E-01	-0.8919E-02	0.1938E-02	-0.3881E-01	-0.8440E-02
0.0250	1.3	0.2339	0.3704E-01	0.2538E-02	-0.4495E-03	-0.3607E-03	0.2113E-02	-0.9437E-03
	2.0	0.3517	0.2670E-01	-0.7369E-03	-0.1873E-02	0.1102E-02	-0.7542E-02	0.1324E-02
	3.2	0.3298	0.2605E-01	-0.2825E-02	-0.3835E-02	0.4955E-04	-0.1296E-02	0.6839E-03
	5.0	0.3732	0.2882E-01	0.1331E-02	0.1449E-02	-0.2201E-03	-0.9658E-02	0.8776E-03
	7.9	0.3555	0.3521E-01	0.1816E-02	-0.3345E-02	0.1467E-02	0.5827E-03	0.8076E-03
	12.6	0.3551	0.6568E-01	-0.3932E-02	0.9974E-02	0.4885E-02	-0.2071E-01	-0.6506E-02
0.0350	1.3	0.4047	0.5474E-01	0.5299E-02	0.4371E-02	0.3562E-02	0.8434E-02	0.5807E-02
	2.0	0.4121	0.3500E-01	0.2730E-02	-0.9577E-02	-0.2718E-02	-0.1543E-01	-0.3136E-02
	3.2	0.4078	0.2699E-01	0.4628E-02	0.9759E-02	0.5362E-02	-0.1604E-01	-0.1753E-02
	5.0	0.4159	0.2706E-01	0.1483E-02	0.4528E-02	-0.8751E-03	-0.5184E-02	-0.1506E-02
	7.9	0.4316	0.3064E-01	0.2269E-03	-0.2765E-02	0.1324E-02	-0.1722E-02	0.4034E-03
	12.6	0.4561	0.3901E-01	0.1044E-02	0.4673E-03	0.3468E-02	-0.6166E-02	-0.1516E-02
	20.0	0.5198	0.9575E-01	-0.2057E-01	0.1356E-01	-0.4716E-02	-0.4920E-01	0.1696E-02

(continued on next page)

Table D.3 (continued): xF_3 energy-calibration systematic errors.

x	Q^2	xF_3	ΔxF_3^{stat}	C_{HAD}^{744}	C_{HAD}^{770}	ΔE_{HAD}	C_μ	ΔE_μ
0.0500	1.3	0.3967	0.6599E-01	-0.8455E-03	0.4992E-02	-0.1237E-02	-0.6632E-02	0.3105E-02
	2.0	0.5068	0.3600E-01	-0.1882E-02	0.8335E-02	0.9836E-02	-0.2198E-01	-0.7724E-02
	3.2	0.4822	0.2357E-01	0.8052E-03	0.2050E-02	0.4164E-02	-0.3418E-02	-0.1826E-03
	5.0	0.5058	0.1989E-01	-0.2504E-02	-0.1025E-02	0.1248E-02	-0.5220E-02	0.9509E-03
	7.9	0.5800	0.1979E-01	-0.9893E-03	0.3412E-02	0.5707E-03	-0.1558E-01	-0.3280E-02
	12.6	0.5615	0.2215E-01	0.1077E-02	0.6021E-02	0.1606E-02	-0.2922E-02	0.2693E-02
	20.0	0.6184	0.3011E-01	0.4646E-03	-0.2950E-02	0.2563E-02	-0.1618E-01	-0.2929E-02
	31.6	0.6167	0.9101E-01	0.7555E-02	0.3047E-02	-0.1054E-02	0.8745E-02	0.7955E-02
0.0700	2.0	0.5093	0.5839E-01	0.2891E-03	-0.1147E-02	-0.3744E-02	0.1458E-01	0.3872E-02
	3.2	0.6078	0.3228E-01	-0.4170E-02	-0.4542E-02	-0.3276E-02	0.1481E-02	0.6451E-02
	5.0	0.6209	0.2280E-01	0.1745E-03	0.3538E-02	0.4450E-02	-0.3049E-02	-0.3725E-02
	7.9	0.6377	0.1946E-01	-0.2417E-02	0.1902E-02	0.2238E-02	-0.1150E-01	-0.4686E-02
	12.6	0.6370	0.2080E-01	0.6813E-03	-0.1512E-02	0.2793E-02	-0.1180E-01	0.3642E-02
	20.0	0.6485	0.2391E-01	0.5503E-02	0.1663E-02	0.3029E-02	-0.3746E-02	0.3096E-02
	31.6	0.6147	0.3683E-01	-0.7038E-03	0.1397E-01	-0.1301E-02	-0.1702E-01	-0.1035E-01
0.0900	2.0	0.7605	0.9046E-01	0.1687E-01	0.1823E-01	0.4478E-01	-0.6613E-02	-0.1437E-01
	3.2	0.5799	0.4613E-01	0.1577E-01	0.5133E-02	0.9025E-02	-0.1897E-01	0.1392E-02
	5.0	0.6738	0.2707E-01	0.1220E-01	0.4025E-02	0.7473E-02	-0.1845E-01	-0.6287E-02
	7.9	0.7340	0.2048E-01	-0.1387E-02	-0.1110E-02	0.1680E-02	-0.1522E-01	-0.4142E-03
	12.6	0.7146	0.1980E-01	0.2723E-02	0.7320E-02	0.9532E-03	-0.7842E-02	-0.4421E-03
	20.0	0.7376	0.2177E-01	0.6866E-03	0.1736E-02	0.2370E-02	-0.1724E-01	-0.1643E-02
	31.6	0.7384	0.2551E-01	-0.1615E-02	0.8220E-02	0.2228E-02	-0.1247E-01	0.1412E-02
	50.1	0.7445	0.6111E-01	0.3370E-01	0.1270E-01	0.3830E-02	-0.5976E-02	0.1747E-02
0.1100	3.2	0.6630	0.6051E-01	0.4288E-02	0.2362E-02	0.7959E-02	-0.3003E-01	-0.1097E-01
	5.0	0.7350	0.3292E-01	-0.9401E-02	-0.7761E-02	-0.3317E-02	0.1223E-01	0.1086E-01
	7.9	0.7624	0.2200E-01	0.6558E-02	0.3892E-02	0.7275E-02	-0.6755E-02	-0.5492E-02
	12.6	0.7658	0.1940E-01	0.1128E-02	-0.4427E-02	-0.5903E-03	-0.2480E-02	-0.2310E-03
	20.0	0.7653	0.2086E-01	-0.7307E-03	0.3473E-02	0.3866E-03	0.3059E-02	0.2980E-02
	31.6	0.7374	0.2253E-01	0.3536E-02	-0.5624E-03	0.2728E-02	-0.1689E-01	0.8349E-03
	50.1	0.7596	0.3705E-01	0.5717E-02	0.1243E-01	0.4113E-02	0.1032E-02	0.6997E-02

(continued on next page)

Table D.3 (continued): xF_3 energy-calibration systematic errors.

x	Q^2	xF_3	ΔxF_3^{stat}	C_{HAD}^{744}	C_{HAD}^{770}	ΔE_{HAD}	C_μ	ΔE_μ
0.1400	3.2	0.7642	0.6294E-01	-0.1416E-01	0.5720E-02	-0.5002E-02	-0.1777E-01	-0.2365E-02
	5.0	0.8043	0.3120E-01	0.4142E-03	0.8920E-02	0.7870E-02	-0.2375E-02	-0.8887E-02
	7.9	0.7931	0.1804E-01	0.5895E-03	0.2643E-03	0.3111E-02	-0.5907E-02	-0.3698E-03
	12.6	0.8154	0.1395E-01	0.2037E-02	0.2420E-02	0.2089E-02	-0.1024E-01	-0.9949E-03
	20.0	0.8078	0.1328E-01	0.1177E-02	0.3294E-02	0.3210E-02	-0.8049E-02	-0.1835E-03
	31.6	0.8071	0.1419E-01	0.4127E-02	0.4352E-02	0.3045E-02	-0.1400E-01	-0.9331E-03
	50.1	0.8139	0.1711E-01	0.4368E-02	0.8214E-02	0.3466E-02	-0.2171E-01	0.3028E-03
	79.4	0.8476	0.4090E-01	0.1037E-01	0.1224E-01	0.3872E-02	-0.1865E-01	-0.3612E-02
0.1800	5.0	0.9044	0.4342E-01	-0.7183E-02	-0.6186E-02	-0.1946E-02	0.5657E-02	0.1726E-04
	7.9	0.8026	0.2349E-01	-0.1128E-02	-0.3923E-02	-0.2341E-02	0.9623E-02	0.7257E-02
	12.6	0.8361	0.1532E-01	-0.1466E-04	0.9094E-03	0.1458E-02	-0.1124E-01	-0.1003E-02
	20.0	0.8247	0.1269E-01	0.2310E-02	0.4365E-02	0.3136E-02	-0.1208E-01	-0.1716E-02
	31.6	0.8280	0.1303E-01	0.8219E-03	0.2581E-02	0.1895E-02	0.8369E-03	0.2580E-02
	50.1	0.8111	0.1379E-01	0.3513E-02	0.1219E-02	0.2770E-02	-0.6897E-02	0.1455E-02
	79.4	0.7814	0.2082E-01	0.6345E-02	0.6307E-02	0.4256E-02	-0.2646E-01	0.2844E-02
0.2250	5.0	0.7368	0.5772E-01	-0.1534E-02	-0.6650E-02	-0.4811E-02	-0.1098E-01	-0.8966E-03
	7.9	0.7854	0.2710E-01	-0.8122E-03	0.5233E-03	0.2368E-02	-0.1947E-02	0.3698E-03
	12.6	0.7824	0.1539E-01	-0.7357E-03	-0.2083E-02	0.9114E-04	0.2870E-03	0.1136E-03
	20.0	0.8027	0.1141E-01	0.1349E-02	0.4310E-03	0.2461E-02	0.6413E-03	0.8347E-03
	31.6	0.7763	0.1066E-01	0.8578E-03	0.1601E-02	0.2299E-02	-0.2237E-02	0.3137E-02
	50.1	0.7413	0.1131E-01	0.1916E-02	0.8316E-03	0.1605E-02	-0.7735E-02	0.2332E-02
	79.4	0.7731	0.1279E-01	0.2674E-02	0.6832E-02	0.2879E-02	-0.6434E-02	0.2981E-02
0.2750	7.9	0.7803	0.3387E-01	0.1103E-02	0.5214E-03	0.2113E-02	-0.2091E-02	-0.1301E-03
	12.6	0.7207	0.1818E-01	-0.4482E-03	-0.3114E-02	0.2206E-02	0.6844E-02	-0.7166E-03
	20.0	0.7066	0.1188E-01	-0.1510E-02	-0.3159E-02	0.3392E-04	0.2798E-02	0.3169E-02
	31.6	0.6839	0.1017E-01	-0.9310E-03	0.1456E-02	0.1632E-02	-0.4367E-03	0.3997E-03
	50.1	0.6755	0.1040E-01	0.9795E-03	0.3934E-04	0.1873E-02	0.9494E-03	0.1353E-02
	79.4	0.6373	0.1061E-01	0.5792E-03	0.7640E-03	0.2326E-02	-0.1868E-02	0.2335E-02
	125.9	0.6265	0.1623E-01	0.8972E-02	0.5827E-02	0.2450E-02	-0.1120E-01	0.1646E-02

(continued on next page)

Table D.3 (continued): xF_3 energy-calibration systematic errors.

x	Q^2	xF_3	ΔxF_3^{stat}	C_{HAD}^{744}	C_{HAD}^{770}	ΔE_{HAD}	C_μ	ΔE_μ
0.3500	7.9	0.6352	0.3202E-01	-0.7971E-02	0.6251E-03	0.1231E-02	0.1130E-01	-0.5497E-02
	12.6	0.5946	0.1571E-01	-0.2861E-02	-0.2593E-02	-0.8329E-03	0.5938E-02	0.2456E-02
	20.0	0.5742	0.8879E-02	-0.3116E-02	-0.1910E-02	-0.6320E-03	0.1017E-01	0.1683E-02
	31.6	0.5490	0.6821E-02	0.6306E-03	-0.7357E-03	0.1954E-02	0.5750E-02	0.2444E-02
	50.1	0.5240	0.6214E-02	-0.1010E-02	-0.5755E-03	0.8863E-03	0.6502E-02	0.1745E-02
	79.4	0.4881	0.6307E-02	0.1154E-02	0.1838E-02	0.1305E-02	0.2398E-02	0.1895E-02
	125.9	0.4831	0.7438E-02	0.1439E-02	0.4367E-02	0.1711E-02	0.1218E-03	0.2565E-02
0.4500	12.6	0.3987	0.1766E-01	0.4390E-03	-0.3848E-02	0.1106E-02	0.3802E-02	-0.2309E-02
	20.0	0.3729	0.9599E-02	-0.1337E-02	-0.2113E-02	-0.1818E-02	0.1212E-01	0.2206E-02
	31.6	0.3487	0.6094E-02	-0.3764E-02	-0.3372E-02	-0.6975E-03	0.1416E-01	0.2929E-02
	50.1	0.3216	0.5045E-02	-0.1007E-02	-0.5872E-03	0.1606E-03	0.5238E-02	0.5943E-03
	79.4	0.3078	0.4923E-02	-0.1050E-02	-0.2886E-02	0.3211E-03	0.9005E-02	0.2315E-02
	125.9	0.2885	0.4990E-02	0.1043E-02	-0.4696E-03	0.1325E-02	0.3714E-02	0.1801E-02
	199.5	0.2563	0.8264E-02	0.1775E-02	0.2611E-02	0.1192E-02	0.2174E-02	0.2514E-02
0.5500	12.6	0.2731	0.1866E-01	-0.8280E-02	-0.6292E-03	-0.4750E-02	0.1578E-01	0.2894E-02
	20.0	0.1973	0.9353E-02	-0.4286E-02	-0.1619E-02	-0.2115E-02	0.7576E-02	0.2022E-02
	31.6	0.1834	0.5175E-02	-0.2876E-03	-0.1325E-02	-0.5042E-03	0.4627E-02	0.7473E-03
	50.1	0.1733	0.4033E-02	-0.1407E-02	-0.2204E-02	-0.3330E-03	0.7264E-02	0.1495E-02
	79.4	0.1595	0.3540E-02	-0.5831E-03	-0.8344E-03	0.2222E-03	0.4193E-02	0.9473E-03
	125.9	0.1454	0.3616E-02	-0.1010E-02	-0.5980E-04	-0.1240E-04	0.6280E-02	0.1352E-02
	199.5	0.1314	0.4446E-02	0.2073E-03	-0.4498E-03	0.5565E-03	0.2688E-02	0.1974E-02
0.6500	12.6	0.8328E-01	0.1967E-01	0.1320E-02	0.1045E-02	-0.1450E-04	0.2446E-02	0.1916E-02
	20.0	0.1069	0.7406E-02	0.8881E-03	-0.3277E-02	-0.1097E-02	0.1054E-02	-0.6314E-03
	31.6	0.8762E-01	0.3702E-02	-0.1574E-02	-0.1317E-02	-0.1725E-03	0.5929E-02	0.8895E-03
	50.1	0.8174E-01	0.2626E-02	-0.1231E-02	-0.1326E-03	-0.3258E-03	0.5105E-02	0.1056E-02
	79.4	0.6648E-01	0.2246E-02	-0.3868E-03	-0.5988E-03	0.1826E-03	0.3979E-02	0.2507E-04
	125.9	0.5806E-01	0.2255E-02	0.3342E-03	-0.5740E-03	0.2958E-03	0.3748E-02	0.4392E-03
0.7500	20.0	0.3791E-01	0.4179E-02	-0.6531E-03	0.2454E-04	-0.1047E-03	0.3937E-03	0.3394E-03
	31.6	0.2875E-01	0.2163E-02	-0.3672E-03	-0.4532E-03	-0.6355E-03	0.2570E-02	0.3712E-03
	50.1	0.2539E-01	0.1359E-02	-0.2674E-03	-0.9231E-03	-0.2030E-03	0.2241E-02	0.2848E-03
	79.4	0.1963E-01	0.1112E-02	-0.2829E-03	-0.4746E-03	-0.8517E-04	0.1742E-02	0.3785E-03
	125.9	0.1951E-01	0.1072E-02	-0.4781E-03	-0.2472E-03	-0.1050E-03	0.1425E-02	0.8192E-04

Table D.4: F_2 flux-extraction systematic errors.

x	Q^2	F_2	ΔF_2^{stat}	$(B/A)^{\nu}_{744}$	$(B/A)^{\bar{\nu}}_{744}$	$(B/A)^{\nu}_{770}$	$(B/A)^{\bar{\nu}}_{770}$
0.0075	1.3	1.305	0.2975E-01	-0.2071E-02	-0.2071E-02	-0.3050E-03	-0.3030E-03
	2.0	1.366	0.3703E-01	-0.3065E-02	-0.3065E-02	-0.1005E-02	-0.9345E-03
	3.2	1.587	0.6680E-01	-0.3022E-02	-0.3022E-02	-0.9125E-03	-0.3134E-02
0.0125	1.3	1.237	0.2408E-01	-0.1419E-02	-0.1419E-02	0.1470E-03	0.3180E-03
	2.0	1.335	0.2783E-01	-0.2310E-02	-0.2310E-02	-0.2935E-03	-0.2170E-03
	3.2	1.525	0.3794E-01	-0.3226E-02	-0.3226E-02	-0.9930E-03	-0.1290E-02
	5.0	1.675	0.6004E-01	-0.4265E-02	-0.4265E-02	-0.1549E-02	-0.2491E-02
0.0175	1.3	1.253	0.2421E-01	-0.1158E-02	-0.1158E-02	0.4050E-03	0.6100E-03
	2.0	1.385	0.2596E-01	-0.1772E-02	-0.1772E-02	0.4750E-04	0.1990E-03
	3.2	1.528	0.3118E-01	-0.2632E-02	-0.2632E-02	-0.5060E-03	-0.4935E-03
	5.0	1.589	0.4313E-01	-0.3587E-02	-0.3587E-02	-0.1137E-02	-0.1501E-02
	7.9	1.527	0.7152E-01	-0.4795E-02	-0.4795E-02	-0.1275E-02	-0.2403E-02
0.0250	1.3	1.226	0.1751E-01	-0.9505E-03	-0.9505E-03	0.5420E-03	0.7820E-03
	2.0	1.311	0.1703E-01	-0.1303E-02	-0.1303E-02	0.3325E-03	0.4375E-03
	3.2	1.463	0.1936E-01	-0.2065E-02	-0.2065E-02	-0.6247E-04	0.3201E-04
	5.0	1.558	0.2339E-01	-0.2849E-02	-0.2849E-02	-0.6545E-03	-0.6075E-03
	7.9	1.661	0.3303E-01	-0.4077E-02	-0.4077E-02	-0.1262E-02	-0.1658E-02
	12.6	1.759	0.6962E-01	-0.5817E-02	-0.5817E-02	-0.3325E-02	-0.1802E-02
0.0350	1.3	1.193	0.1848E-01	-0.6690E-03	-0.6690E-03	0.5290E-03	0.9100E-03
	2.0	1.330	0.1818E-01	-0.1091E-02	-0.1091E-02	0.5020E-03	0.6845E-03
	3.2	1.412	0.1799E-01	-0.1503E-02	-0.1503E-02	0.2420E-03	0.3605E-03
	5.0	1.551	0.2052E-01	-0.2359E-02	-0.2359E-02	-0.1670E-03	-0.1575E-03
	7.9	1.598	0.2536E-01	-0.3329E-02	-0.3329E-02	-0.7640E-03	-0.9440E-03
	12.6	1.734	0.3787E-01	-0.4517E-02	-0.4517E-02	-0.1419E-02	-0.2010E-02
	20.0	1.779	0.1028	-0.5776E-02	-0.5776E-02	-0.2316E-02	-0.2603E-02

(continued on next page)

Table D.4 (continued): F_2 flux-extraction systematic errors.

x	Q^2	F_2	ΔF_2^{stat}	$(B/A)^{\nu}_{744}$	$(B/A)^{\bar{\nu}}_{744}$	$(B/A)^{\nu}_{770}$	$(B/A)^{\bar{\nu}}_{770}$
0.0500	1.3	1.228	0.1545E-01	-0.7570E-03	-0.7570E-03	0.7385E-03	0.1011E-02
	2.0	1.336	0.1371E-01	-0.9400E-03	-0.9400E-03	0.6695E-03	0.8260E-03
	3.2	1.434	0.1311E-01	-0.1161E-02	-0.1161E-02	0.4269E-03	0.6400E-03
	5.0	1.509	0.1365E-01	-0.1696E-02	-0.1696E-02	0.1145E-03	0.2550E-03
	7.9	1.593	0.1514E-01	-0.2550E-02	-0.2550E-02	-0.3220E-03	-0.2990E-03
	12.6	1.611	0.1881E-01	-0.3537E-02	-0.3537E-02	-0.8450E-03	-0.1058E-02
	20.0	1.683	0.2962E-01	-0.5202E-02	-0.5202E-02	-0.1302E-02	-0.1849E-02
	31.6	1.622	0.9702E-01	-0.6601E-02	-0.6601E-02	-0.2475E-02	-0.1832E-02
0.0700	2.0	1.322	0.1539E-01	-0.7705E-03	-0.7705E-03	0.6885E-03	0.1036E-02
	3.2	1.393	0.1375E-01	-0.8980E-03	-0.8980E-03	0.4995E-03	0.8220E-03
	5.0	1.482	0.1351E-01	-0.1234E-02	-0.1234E-02	0.3160E-03	0.5250E-03
	7.9	1.532	0.1379E-01	-0.1953E-02	-0.1953E-02	0.3499E-04	0.9847E-04
	12.6	1.548	0.1609E-01	-0.2959E-02	-0.2959E-02	-0.5295E-03	-0.4575E-03
	20.0	1.598	0.2097E-01	-0.3959E-02	-0.3959E-02	-0.8395E-03	-0.1227E-02
	31.6	1.591	0.3695E-01	-0.5418E-02	-0.5418E-02	-0.1477E-02	-0.1899E-02
0.0900	2.0	1.318	0.1821E-01	-0.6765E-03	-0.6765E-03	0.7050E-03	0.1098E-02
	3.2	1.380	0.1504E-01	-0.8925E-03	-0.8925E-03	0.7010E-03	0.9240E-03
	5.0	1.432	0.1368E-01	-0.1071E-02	-0.1071E-02	0.4370E-03	0.6060E-03
	7.9	1.458	0.1331E-01	-0.1397E-02	-0.1397E-02	0.1355E-03	0.2955E-03
	12.6	1.491	0.1463E-01	-0.2172E-02	-0.2172E-02	-0.1805E-03	-0.1775E-03
	20.0	1.510	0.1750E-01	-0.3307E-02	-0.3307E-02	-0.6600E-03	-0.6575E-03
	31.6	1.509	0.2384E-01	-0.4364E-02	-0.4364E-02	-0.1045E-02	-0.1184E-02
	50.1	1.548	0.6295E-01	-0.6079E-02	-0.6079E-02	-0.1482E-02	-0.1538E-02
0.1100	3.2	1.335	0.1595E-01	-0.7945E-03	-0.7945E-03	0.6765E-03	0.9915E-03
	5.0	1.363	0.1401E-01	-0.8395E-03	-0.8395E-03	0.4365E-03	0.7310E-03
	7.9	1.385	0.1302E-01	-0.1215E-02	-0.1215E-02	0.2390E-03	0.3860E-03
	12.6	1.413	0.1366E-01	-0.1825E-02	-0.1825E-02	-0.4601E-04	0.3147E-04
	20.0	1.449	0.1602E-01	-0.2798E-02	-0.2798E-02	-0.4285E-03	-0.4539E-03
	31.6	1.382	0.1955E-01	-0.3760E-02	-0.3760E-02	-0.7555E-03	-0.8665E-03
	50.1	1.503	0.3664E-01	-0.4956E-02	-0.4956E-02	-0.1503E-02	-0.1335E-02

(continued on next page)

Table D.4 (continued): F_2 flux-extraction systematic errors.

x	Q^2	F_2	ΔF_2^{stat}	$(B/A)^{\nu}_{744}$	$(B/A)^{\bar{\nu}}_{744}$	$(B/A)^{\nu}_{770}$	$(B/A)^{\bar{\nu}}_{770}$
0.1400	3.2	1.279	0.1297E-01	-0.7135E-03	-0.7135E-03	0.6835E-03	0.9789E-03
	5.0	1.305	0.1043E-01	-0.7745E-03	-0.7745E-03	0.5245E-03	0.7655E-03
	7.9	1.302	0.9231E-02	-0.9310E-03	-0.9310E-03	0.3060E-03	0.4825E-03
	12.6	1.319	0.9062E-02	-0.1414E-02	-0.1414E-02	0.8196E-04	0.1335E-03
	20.0	1.312	0.9773E-02	-0.2060E-02	-0.2060E-02	-0.1900E-03	-0.1925E-03
	31.6	1.270	0.1137E-01	-0.2932E-02	-0.2932E-02	-0.5420E-03	-0.5080E-03
	50.1	1.251	0.1581E-01	-0.4005E-02	-0.4005E-02	-0.5925E-03	-0.7990E-03
	79.4	1.272	0.4124E-01	-0.5748E-02	-0.5748E-02	-0.1371E-02	-0.5035E-03
0.1800	5.0	1.185	0.1110E-01	-0.6725E-03	-0.6725E-03	0.5645E-03	0.7205E-03
	7.9	1.177	0.9669E-02	-0.7820E-03	-0.7820E-03	0.4025E-03	0.4925E-03
	12.6	1.184	0.8893E-02	-0.1008E-02	-0.1008E-02	0.1515E-03	0.2530E-03
	20.0	1.155	0.8828E-02	-0.1451E-02	-0.1451E-02	-0.6354E-04	-0.4148E-04
	31.6	1.138	0.9901E-02	-0.2295E-02	-0.2295E-02	-0.2775E-03	-0.3065E-03
	50.1	1.088	0.1174E-01	-0.2972E-02	-0.2972E-02	-0.2935E-03	-0.5885E-03
	79.4	1.098	0.2006E-01	-0.3946E-02	-0.3946E-02	-0.6040E-03	-0.6350E-03
0.2250	5.0	1.097	0.1162E-01	-0.6730E-03	-0.6730E-03	0.6250E-03	0.7805E-03
	7.9	1.053	0.8881E-02	-0.6240E-03	-0.6240E-03	0.3815E-03	0.5500E-03
	12.6	1.028	0.7769E-02	-0.7265E-03	-0.7265E-03	0.1765E-03	0.3145E-03
	20.0	1.001	0.7348E-02	-0.1056E-02	-0.1056E-02	0.2003E-04	0.5853E-04
	31.6	0.9815	0.7815E-02	-0.1700E-02	-0.1700E-02	-0.1625E-03	-0.1458E-03
	50.1	0.9498	0.8975E-02	-0.2251E-02	-0.2251E-02	-0.3166E-03	-0.3270E-03
	79.4	0.9334	0.1166E-01	-0.3017E-02	-0.3017E-02	-0.2795E-03	-0.3805E-03
0.2750	7.9	0.9039	0.8981E-02	-0.5032E-03	-0.5032E-03	0.3651E-03	0.5147E-03
	12.6	0.8763	0.7741E-02	-0.5971E-03	-0.5971E-03	0.2330E-03	0.3002E-03
	20.0	0.8515	0.7008E-02	-0.7406E-03	-0.7406E-03	0.5856E-04	0.1077E-03
	31.6	0.8176	0.7141E-02	-0.1140E-02	-0.1140E-02	-0.6807E-04	-0.4849E-04
	50.1	0.7980	0.7945E-02	-0.1750E-02	-0.1750E-02	-0.1822E-03	-0.2011E-03
	79.4	0.7552	0.9086E-02	-0.2314E-02	-0.2314E-02	-0.2843E-03	-0.2422E-03
	125.9	0.7135	0.1561E-01	-0.3031E-02	-0.3031E-02	-0.9376E-04	-0.3162E-03

(continued on next page)

Table D.4 (continued): F_2 flux-extraction systematic errors.

x	Q^2	F_2	ΔF_2^{stat}	$(B/A)^{\nu}_{744}$	$(B/A)^{\bar{\nu}}_{744}$	$(B/A)^{\nu}_{770}$	$(B/A)^{\bar{\nu}}_{770}$
0.3500	7.9	0.7049	0.6639E-02	-0.3745E-03	-0.3745E-03	0.3221E-03	0.4488E-03
	12.6	0.6687	0.5275E-02	-0.4065E-03	-0.4065E-03	0.2034E-03	0.2983E-03
	20.0	0.6274	0.4554E-02	-0.4791E-03	-0.4791E-03	0.7337E-04	0.1217E-03
	31.6	0.6025	0.4439E-02	-0.7531E-03	-0.7531E-03	-0.1040E-04	-0.7391E-05
	50.1	0.5723	0.4575E-02	-0.1097E-02	-0.1097E-02	-0.9823E-04	-0.9131E-04
	79.4	0.5395	0.5027E-02	-0.1361E-02	-0.1361E-02	-0.1249E-03	-0.1651E-03
	125.9	0.5254	0.6764E-02	-0.1868E-02	-0.1868E-02	-0.1395E-03	-0.1407E-03
0.4500	12.6	0.4087	0.4541E-02	-0.2308E-03	-0.2308E-03	0.1457E-03	0.2082E-03
	20.0	0.3966	0.3972E-02	-0.2881E-03	-0.2881E-03	0.8430E-04	0.1152E-03
	31.6	0.3609	0.3548E-02	-0.3700E-03	-0.3700E-03	0.1015E-04	0.2089E-04
	50.1	0.3315	0.3520E-02	-0.5272E-03	-0.5272E-03	-0.3250E-04	-0.3235E-04
	79.4	0.3158	0.3754E-02	-0.7486E-03	-0.7486E-03	-0.5385E-04	-0.7561E-04
	125.9	0.2927	0.4230E-02	-0.9451E-03	-0.9451E-03	-0.6320E-04	-0.6744E-04
	199.5	0.2743	0.7832E-02	-0.1111E-02	-0.1111E-02	-0.5110E-04	-0.7120E-04
0.5500	12.6	0.2378	0.3870E-02	-0.1357E-03	-0.1357E-03	0.9860E-04	0.1192E-03
	20.0	0.2136	0.3137E-02	-0.1558E-03	-0.1558E-03	0.6260E-04	0.7430E-04
	31.6	0.1889	0.2658E-02	-0.1652E-03	-0.1652E-03	0.1285E-04	0.2755E-04
	50.1	0.1763	0.2629E-02	-0.2466E-03	-0.2466E-03	-0.1205E-04	-0.1240E-04
	79.4	0.1587	0.2621E-02	-0.3125E-03	-0.3125E-03	-0.2440E-04	-0.3105E-04
	125.9	0.1502	0.2885E-02	-0.4190E-03	-0.4190E-03	-0.4070E-04	-0.3670E-04
	199.5	0.1346	0.4046E-02	-0.5110E-03	-0.5110E-03	-0.1930E-04	-0.3375E-04
0.6500	12.6	0.1184	0.3397E-02	-0.8240E-04	-0.8240E-04	0.5735E-04	0.7890E-04
	20.0	0.9990E-01	0.2085E-02	-0.6660E-04	-0.6660E-04	0.2642E-04	0.3811E-04
	31.6	0.8166E-01	0.1669E-02	-0.6064E-04	-0.6064E-04	0.6471E-05	0.1163E-04
	50.1	0.7681E-01	0.1600E-02	-0.9978E-04	-0.9978E-04	-0.5394E-05	-0.4761E-05
	79.4	0.6731E-01	0.1600E-02	-0.1252E-03	-0.1252E-03	-0.8821E-05	-0.1094E-04
	125.9	0.6104E-01	0.1732E-02	-0.1696E-03	-0.1696E-03	-0.1678E-04	-0.1436E-04
0.7500	20.0	0.3505E-01	0.1011E-02	-0.2571E-04	-0.2571E-04	0.1238E-04	0.1407E-04
	31.6	0.2838E-01	0.8458E-03	-0.2541E-04	-0.2541E-04	0.3750E-05	0.7954E-05
	50.1	0.2529E-01	0.7646E-03	-0.3006E-04	-0.3006E-04	-0.7153E-06	0.2198E-06
	79.4	0.2135E-01	0.7569E-03	-0.3743E-04	-0.3743E-04	-0.1725E-05	-0.2210E-05
	125.9	0.2014E-01	0.8035E-03	-0.4272E-04	-0.4272E-04	-0.3195E-05	-0.4265E-05

Table D.5: xF_3 flux-extraction systematic errors.

x	Q^2	xF_3	ΔxF_3^{stat}	$(B/A)^{\nu}_{744}$	$(B/A)^{\bar{\nu}}_{744}$	$(B/A)^{\nu}_{770}$	$(B/A)^{\bar{\nu}}_{770}$
0.0075	1.3	0.7632E-01	0.3700E-01	-0.3599E-03	-0.3599E-03	0.3900E-03	0.3843E-03
0.0075	2.0	0.1821	0.4039E-01	-0.1169E-02	-0.1169E-02	0.1110E-02	0.1037E-02
0.0075	3.2	0.9905E-01	0.6319E-01	-0.1870E-02	-0.1870E-02	0.8690E-03	0.2976E-02
0.0125	1.3	0.2122	0.3417E-01	0.9120E-04	0.9120E-04	-0.2157E-03	-0.4762E-03
0.0125	2.0	0.2239	0.3512E-01	-0.4452E-03	-0.4452E-03	0.3764E-03	0.2924E-03
0.0125	3.2	0.1684	0.4290E-01	-0.1445E-02	-0.1445E-02	0.1142E-02	0.1482E-02
0.0125	5.0	0.2486	0.5783E-01	-0.2345E-02	-0.2345E-02	0.1500E-02	0.2413E-02
0.0175	1.3	0.1894	0.4008E-01	0.5903E-03	0.5903E-03	-0.6941E-03	-0.1054E-02
0.0175	2.0	0.2767	0.3549E-01	-0.8211E-04	-0.8211E-04	-0.6360E-04	-0.2894E-03
0.0175	3.2	0.2906	0.3887E-01	-0.8717E-03	-0.8717E-03	0.6475E-03	0.6373E-03
0.0175	5.0	0.2543	0.4715E-01	-0.1907E-02	-0.1907E-02	0.1260E-02	0.1660E-02
0.0175	7.9	0.3513	0.6743E-01	-0.3280E-02	-0.3280E-02	0.1208E-02	0.2274E-02
0.0250	1.3	0.2339	0.3704E-01	0.1226E-02	0.1226E-02	-0.1179E-02	-0.1739E-02
0.0250	2.0	0.3517	0.2670E-01	0.4600E-03	0.4600E-03	-0.5502E-03	-0.7192E-03
0.0250	3.2	0.3298	0.2605E-01	-0.2465E-03	-0.2465E-03	0.8415E-04	-0.4344E-04
0.0250	5.0	0.3732	0.2882E-01	-0.1153E-02	-0.1153E-02	0.8280E-03	0.7739E-03
0.0250	7.9	0.3555	0.3521E-01	-0.2332E-02	-0.2332E-02	0.1358E-02	0.1786E-02
0.0250	12.6	0.3551	0.6568E-01	-0.2650E-02	-0.2650E-02	0.3143E-02	0.1706E-02
0.0350	1.3	0.4047	0.5474E-01	0.1875E-02	0.1875E-02	-0.1611E-02	-0.2833E-02
0.0350	2.0	0.4121	0.3500E-01	0.1025E-02	0.1025E-02	-0.1005E-02	-0.1388E-02
0.0350	3.2	0.4078	0.2699E-01	0.2327E-03	0.2327E-03	-0.3853E-03	-0.5649E-03
0.0350	5.0	0.4159	0.2706E-01	-0.8873E-03	-0.8873E-03	0.2342E-03	0.2114E-03
0.0350	7.9	0.4316	0.3064E-01	-0.1927E-02	-0.1927E-02	0.9463E-03	0.1168E-02
0.0350	12.6	0.4561	0.3901E-01	-0.2817E-02	-0.2817E-02	0.1474E-02	0.2087E-02
0.0350	20.0	0.5198	0.9575E-01	-0.3719E-02	-0.3719E-02	0.2159E-02	0.2429E-02

(continued on next page)

Table D.5 (continued): xF_3 flux-extraction systematic errors.

x	Q^2	xF_3	ΔxF_3^{stat}	$(B/A)^{\nu}_{744}$	$(B/A)^{\bar{\nu}}_{744}$	$(B/A)^{\nu}_{770}$	$(B/A)^{\bar{\nu}}_{770}$
0.0500	1.3	0.3967	0.6599E-01	0.3532E-02	0.3532E-02	-0.3256E-02	-0.4512E-02
0.0500	2.0	0.5068	0.3600E-01	0.2068E-02	0.2068E-02	-0.1844E-02	-0.2275E-02
0.0500	3.2	0.4822	0.2357E-01	0.7562E-03	0.7562E-03	-0.7954E-03	-0.1219E-02
0.0500	5.0	0.5058	0.1989E-01	-0.1290E-03	-0.1290E-03	-0.1689E-03	-0.3985E-03
0.0500	7.9	0.5800	0.1979E-01	-0.1148E-02	-0.1148E-02	0.4402E-03	0.4068E-03
0.0500	12.6	0.5615	0.2215E-01	-0.2226E-02	-0.2226E-02	0.1017E-02	0.1272E-02
0.0500	20.0	0.6184	0.3011E-01	-0.3779E-02	-0.3779E-02	0.1334E-02	0.1894E-02
0.0500	31.6	0.6167	0.9101E-01	-0.4489E-02	-0.4489E-02	0.2323E-02	0.1721E-02
0.0700	2.0	0.5093	0.5839E-01	0.3038E-02	0.3038E-02	-0.2693E-02	-0.4128E-02
0.0700	3.2	0.6078	0.3228E-01	0.1365E-02	0.1365E-02	-0.1213E-02	-0.2055E-02
0.0700	5.0	0.6209	0.2280E-01	0.3225E-03	0.3225E-03	-0.5490E-03	-0.9449E-03
0.0700	7.9	0.6377	0.1946E-01	-0.4529E-03	-0.4529E-03	-0.5868E-04	-0.1420E-03
0.0700	12.6	0.6370	0.2080E-01	-0.1497E-02	-0.1497E-02	0.6967E-03	0.6256E-03
0.0700	20.0	0.6485	0.2391E-01	-0.2992E-02	-0.2992E-02	0.9752E-03	0.1422E-02
0.0700	31.6	0.6147	0.3683E-01	-0.3980E-02	-0.3980E-02	0.1478E-02	0.1902E-02
0.0900	2.0	0.7605	0.9046E-01	0.4222E-02	0.4222E-02	-0.3606E-02	-0.5722E-02
0.0900	3.2	0.5799	0.4613E-01	0.2575E-02	0.2575E-02	-0.2235E-02	-0.2971E-02
0.0900	5.0	0.6738	0.2707E-01	0.9326E-03	0.9326E-03	-0.9105E-03	-0.1269E-02
0.0900	7.9	0.7340	0.2048E-01	-0.2229E-03	-0.2229E-03	-0.2031E-03	-0.4975E-03
0.0900	12.6	0.7146	0.1980E-01	-0.1201E-02	-0.1201E-02	0.2676E-03	0.2431E-03
0.0900	20.0	0.7376	0.2177E-01	-0.2303E-02	-0.2303E-02	0.8446E-03	0.8456E-03
0.0900	31.6	0.7384	0.2551E-01	-0.3249E-02	-0.3249E-02	0.1128E-02	0.1282E-02
0.0900	50.1	0.7445	0.6111E-01	-0.4786E-02	-0.4786E-02	0.1441E-02	0.1497E-02
0.1100	3.2	0.6630	0.6051E-01	0.3057E-02	0.3057E-02	-0.2653E-02	-0.3946E-02
0.1100	5.0	0.7350	0.3292E-01	0.1175E-02	0.1175E-02	-0.1046E-02	-0.1840E-02
0.1100	7.9	0.7624	0.2200E-01	0.1633E-03	0.1633E-03	-0.4221E-03	-0.6938E-03
0.1100	12.6	0.7658	0.1940E-01	-0.9125E-03	-0.9125E-03	0.7620E-04	-0.5248E-04
0.1100	20.0	0.7653	0.2086E-01	-0.1946E-02	-0.1946E-02	0.5833E-03	0.6227E-03
0.1100	31.6	0.7374	0.2253E-01	-0.2986E-02	-0.2986E-02	0.8862E-03	0.1017E-02
0.1100	50.1	0.7596	0.3705E-01	-0.3590E-02	-0.3590E-02	0.1526E-02	0.1359E-02

(continued on next page)

Table D.5 (continued): xF_3 flux-extraction systematic errors.

x	Q^2	xF_3	ΔxF_3^{stat}	$(B/A)^{\nu}_{744}$	$(B/A)^{\bar{\nu}}_{744}$	$(B/A)^{\nu}_{770}$	$(B/A)^{\bar{\nu}}_{770}$
0.1400	3.2	0.7642	0.6294E-01	0.4034E-02	0.4034E-02	-0.3424E-02	-0.4977E-02
0.1400	5.0	0.8043	0.3120E-01	0.1925E-02	0.1925E-02	-0.1619E-02	-0.2428E-02
0.1400	7.9	0.7931	0.1804E-01	0.5355E-03	0.5355E-03	-0.6193E-03	-0.1019E-02
0.1400	12.6	0.8154	0.1395E-01	-0.2908E-03	-0.2908E-03	-0.1444E-03	-0.2111E-03
0.1400	20.0	0.8078	0.1328E-01	-0.1468E-02	-0.1468E-02	0.2800E-03	0.2713E-03
0.1400	31.6	0.8071	0.1419E-01	-0.2319E-02	-0.2319E-02	0.6945E-03	0.6621E-03
0.1400	50.1	0.8139	0.1711E-01	-0.3562E-02	-0.3562E-02	0.6492E-03	0.8767E-03
0.1400	79.4	0.8476	0.4090E-01	-0.4643E-02	-0.4643E-02	0.1361E-02	0.5018E-03
0.1800	5.0	0.9044	0.4342E-01	0.2846E-02	0.2846E-02	-0.2308E-02	-0.2951E-02
0.1800	7.9	0.8026	0.2349E-01	0.1096E-02	0.1096E-02	-0.1023E-02	-0.1270E-02
0.1800	12.6	0.8361	0.1532E-01	-0.8464E-04	-0.8464E-04	-0.2785E-03	-0.4694E-03
0.1800	20.0	0.8247	0.1269E-01	-0.9018E-03	-0.9018E-03	0.9859E-04	0.6256E-04
0.1800	31.6	0.8280	0.1303E-01	-0.2008E-02	-0.2008E-02	0.3868E-03	0.4258E-03
0.1800	50.1	0.8111	0.1379E-01	-0.2960E-02	-0.2960E-02	0.3592E-03	0.7069E-03
0.1800	79.4	0.7814	0.2082E-01	-0.3512E-02	-0.3512E-02	0.6304E-03	0.6655E-03
0.2250	5.0	0.7368	0.5772E-01	0.3759E-02	0.3759E-02	-0.3213E-02	-0.4053E-02
0.2250	7.9	0.7854	0.2710E-01	0.1477E-02	0.1477E-02	-0.1213E-02	-0.1777E-02
0.2250	12.6	0.7824	0.1539E-01	0.1793E-03	0.1793E-03	-0.3667E-03	-0.6725E-03
0.2250	20.0	0.8027	0.1141E-01	-0.5554E-03	-0.5554E-03	-0.2763E-04	-0.9978E-04
0.2250	31.6	0.7763	0.1066E-01	-0.1440E-02	-0.1440E-02	0.2327E-03	0.2173E-03
0.2250	50.1	0.7413	0.1131E-01	-0.2095E-02	-0.2095E-02	0.4135E-03	0.4324E-03
0.2250	79.4	0.7731	0.1279E-01	-0.2954E-02	-0.2954E-02	0.3118E-03	0.4261E-03
0.2750	7.9	0.7803	0.3387E-01	0.1771E-02	0.1771E-02	-0.1443E-02	-0.2041E-02
0.2750	12.6	0.7207	0.1818E-01	0.5815E-03	0.5815E-03	-0.5789E-03	-0.7524E-03
0.2750	20.0	0.7066	0.1188E-01	-0.2328E-03	-0.2328E-03	-0.1083E-03	-0.1992E-03
0.2750	31.6	0.6839	0.1017E-01	-0.9449E-03	-0.9449E-03	0.1137E-03	0.6562E-04
0.2750	50.1	0.6755	0.1040E-01	-0.1733E-02	-0.1733E-02	0.2567E-03	0.2767E-03
0.2750	79.4	0.6373	0.1061E-01	-0.2244E-02	-0.2244E-02	0.3383E-03	0.2939E-03
0.2750	125.9	0.6265	0.1623E-01	-0.3061E-02	-0.3061E-02	0.9939E-04	0.3321E-03

(continued on next page)

Table D.5 (continued): xF_3 flux-extraction systematic errors.

x	Q^2	xF_3	ΔxF_3^{stat}	$(B/A)^{\nu}_{744}$	$(B/A)^{\bar{\nu}}_{744}$	$(B/A)^{\nu}_{770}$	$(B/A)^{\bar{\nu}}_{770}$
0.3500	7.9	0.6352	0.3202E-01	0.1961E-02	0.1961E-02	-0.1614E-02	-0.2270E-02
0.3500	12.6	0.5946	0.1571E-01	0.7058E-03	0.7058E-03	-0.6362E-03	-0.9420E-03
0.3500	20.0	0.5742	0.8879E-02	-0.6828E-04	-0.6828E-04	-0.1470E-03	-0.2615E-03
0.3500	31.6	0.5490	0.6821E-02	-0.5845E-03	-0.5845E-03	0.1359E-04	0.1225E-04
0.3500	50.1	0.5240	0.6214E-02	-0.1090E-02	-0.1090E-02	0.1461E-03	0.1324E-03
0.3500	79.4	0.4881	0.6307E-02	-0.1440E-02	-0.1440E-02	0.1647E-03	0.2181E-03
0.3500	125.9	0.4831	0.7438E-02	-0.1885E-02	-0.1885E-02	0.1551E-03	0.1586E-03
0.4500	12.6	0.3987	0.1766E-01	0.7333E-03	0.7333E-03	-0.5887E-03	-0.8554E-03
0.4500	20.0	0.3729	0.9599E-02	0.1633E-03	0.1633E-03	-0.2143E-03	-0.3015E-03
0.4500	31.6	0.3487	0.6094E-02	-0.2443E-03	-0.2443E-03	-0.2180E-04	-0.3494E-04
0.4500	50.1	0.3216	0.5045E-02	-0.5343E-03	-0.5343E-03	0.5101E-04	0.5201E-04
0.4500	79.4	0.3078	0.4923E-02	-0.8377E-03	-0.8377E-03	0.7755E-04	0.1063E-03
0.4500	125.9	0.2885	0.4990E-02	-0.1023E-02	-0.1023E-02	0.7616E-04	0.8415E-04
0.4500	199.5	0.2563	0.8264E-02	-0.1123E-02	-0.1123E-02	0.5439E-04	0.7600E-04
0.5500	12.6	0.2731	0.1866E-01	0.6221E-03	0.6221E-03	-0.4969E-03	-0.5998E-03
0.5500	20.0	0.1973	0.9353E-02	0.2036E-03	0.2036E-03	-0.1981E-03	-0.2321E-03
0.5500	31.6	0.1834	0.5175E-02	-0.7685E-04	-0.7685E-04	-0.2375E-04	-0.6080E-04
0.5500	50.1	0.1733	0.4033E-02	-0.2237E-03	-0.2237E-03	0.1760E-04	0.2120E-04
0.5500	79.4	0.1595	0.3540E-02	-0.3479E-03	-0.3479E-03	0.3930E-04	0.4250E-04
0.5500	125.9	0.1454	0.3616E-02	-0.4468E-03	-0.4468E-03	0.5240E-04	0.4945E-04
0.5500	199.5	0.1314	0.4446E-02	-0.5410E-03	-0.5410E-03	0.2190E-04	0.3785E-04
0.6500	12.6	0.8328E-01	0.1967E-01	0.3988E-03	0.3988E-03	-0.3417E-03	-0.4780E-03
0.6500	20.0	0.1069	0.7406E-02	0.1108E-03	0.1108E-03	-0.9645E-04	-0.1457E-03
0.6500	31.6	0.8762E-01	0.3702E-02	-0.1482E-04	-0.1482E-04	-0.1445E-04	-0.2814E-04
0.6500	50.1	0.8174E-01	0.2626E-02	-0.1038E-03	-0.1038E-03	0.9801E-05	0.7816E-05
0.6500	79.4	0.6648E-01	0.2246E-02	-0.1358E-03	-0.1358E-03	0.1374E-04	0.1645E-04
0.6500	125.9	0.5806E-01	0.2255E-02	-0.1832E-03	-0.1832E-03	0.2292E-04	0.2016E-04
0.7500	20.0	0.3791E-01	0.4179E-02	0.5982E-04	0.5982E-04	-0.5387E-04	-0.6104E-04
0.7500	31.6	0.2875E-01	0.2163E-02	-0.5260E-05	-0.5260E-05	-0.9830E-05	-0.2276E-04
0.7500	50.1	0.2539E-01	0.1359E-02	-0.1764E-04	-0.1764E-04	0.5495E-07	0.4154E-06
0.7500	79.4	0.1963E-01	0.1112E-02	-0.3840E-04	-0.3840E-04	0.2770E-05	0.3510E-05
0.7500	125.9	0.1951E-01	0.1072E-02	-0.4802E-04	-0.4802E-04	0.4910E-05	0.5935E-05

Table D.6: F_2 cross-section systematic errors.

x	Q^2	F_2	ΔF_2^{stat}	σ^{ν}/E	$\sigma^{\bar{\nu}}/\sigma^{\nu}$	No Φ Adj	R
0.0075	1.3	1.305	0.2975E-01	0.2698E-01	0.8169E-02	-0.1738E-01	0.1492E-01
	2.0	1.366	0.3703E-01	0.2824E-01	0.8053E-02	0.4106E-02	0.2305E-01
	3.2	1.587	0.6680E-01	0.3282E-01	0.1022E-01	0.8857E-02	0.3338E-01
0.0125	1.3	1.237	0.2408E-01	0.2558E-01	0.7026E-02	-0.1402E-01	0.1215E-01
	2.0	1.335	0.2783E-01	0.2760E-01	0.7511E-02	0.1190E-01	0.1858E-01
	3.2	1.525	0.3794E-01	0.3155E-01	0.9224E-02	-0.3791E-02	0.2325E-01
	5.0	1.675	0.6004E-01	0.3464E-01	0.9736E-02	0.7941E-02	0.3203E-01
0.0175	1.3	1.253	0.2421E-01	0.2591E-01	0.7384E-02	0.1329E-01	0.1017E-01
	2.0	1.385	0.2596E-01	0.2865E-01	0.7629E-02	-0.9427E-02	0.1668E-01
	3.2	1.528	0.3118E-01	0.3161E-01	0.8439E-02	-0.1602E-01	0.2017E-01
	5.0	1.589	0.4313E-01	0.3286E-01	0.9147E-02	-0.1287E-01	0.2356E-01
	7.9	1.527	0.7152E-01	0.3157E-01	0.7956E-02	0.1632E-02	0.2811E-01
0.0250	1.3	1.226	0.1751E-01	0.2535E-01	0.7259E-02	-0.4072E-02	0.6671E-02
	2.0	1.311	0.1703E-01	0.2710E-01	0.6997E-02	-0.2118E-02	0.1235E-01
	3.2	1.463	0.1936E-01	0.3026E-01	0.7859E-02	-0.3976E-02	0.1731E-01
	5.0	1.558	0.2339E-01	0.3222E-01	0.8216E-02	0.7379E-02	0.1934E-01
	7.9	1.661	0.3303E-01	0.3435E-01	0.9005E-02	-0.1742E-01	0.2340E-01
	12.6	1.759	0.6962E-01	0.3637E-01	0.9585E-02	0.9801E-02	0.3001E-01
0.0350	1.3	1.193	0.1848E-01	0.2468E-01	0.6885E-02	0.1278E-01	0.3546E-02
	2.0	1.330	0.1818E-01	0.2750E-01	0.7205E-02	-0.1096E-01	0.8521E-02
	3.2	1.412	0.1799E-01	0.2920E-01	0.7327E-02	-0.7130E-02	0.1348E-01
	5.0	1.551	0.2052E-01	0.3207E-01	0.7967E-02	-0.9143E-02	0.1714E-01
	7.9	1.598	0.2536E-01	0.3304E-01	0.8181E-02	0.6672E-02	0.1818E-01
	12.6	1.734	0.3787E-01	0.3585E-01	0.8807E-02	-0.2080E-01	0.2343E-01
	20.0	1.779	0.1028	0.3679E-01	0.8491E-02	0.4209E-01	0.2903E-01

(continued on next page)

Table D.6 (continued) F_2 cross-section systematic errors.

x	Q^2	F_2	ΔF_2^{stat}	σ^{ν}/E	$\sigma^{\bar{\nu}}/\sigma^{\nu}$	No Φ Adj	R
0.0500	1.3	1.228	0.1545E-01	0.2540E-01	0.7457E-02	-0.1498E-02	0.1563E-02
	2.0	1.336	0.1371E-01	0.2763E-01	0.7429E-02	-0.2651E-02	0.4394E-02
	3.2	1.434	0.1311E-01	0.2966E-01	0.7511E-02	-0.3953E-02	0.9634E-02
	5.0	1.509	0.1365E-01	0.3121E-01	0.7455E-02	-0.8769E-02	0.1361E-01
	7.9	1.593	0.1514E-01	0.3295E-01	0.7389E-02	0.5860E-02	0.1579E-01
	12.6	1.611	0.1881E-01	0.3331E-01	0.7523E-02	-0.7042E-02	0.1649E-01
	20.0	1.683	0.2962E-01	0.3481E-01	0.7357E-02	-0.1534E-01	0.2075E-01
	31.6	1.622	0.9702E-01	0.3355E-01	0.6723E-02	0.1914E-01	0.2317E-01
0.0700	2.0	1.322	0.1539E-01	0.2734E-01	0.7775E-02	-0.9093E-02	0.1465E-02
	3.2	1.393	0.1375E-01	0.2881E-01	0.7331E-02	-0.8574E-02	0.5091E-02
	5.0	1.482	0.1351E-01	0.3066E-01	0.7133E-02	0.5440E-03	0.9732E-02
	7.9	1.532	0.1379E-01	0.3167E-01	0.6891E-02	-0.5863E-02	0.1249E-01
	12.6	1.548	0.1609E-01	0.3201E-01	0.6795E-02	-0.3384E-02	0.1307E-01
	20.0	1.598	0.2097E-01	0.3304E-01	0.6875E-02	0.1117E-01	0.1482E-01
	31.6	1.591	0.3695E-01	0.3289E-01	0.6705E-02	0.1558E-02	0.1788E-01
0.0900	2.0	1.318	0.1821E-01	0.2725E-01	0.7632E-02	-0.8822E-02	0.1500E-03
	3.2	1.380	0.1504E-01	0.2853E-01	0.7756E-02	-0.1705E-02	0.2473E-02
	5.0	1.432	0.1368E-01	0.2961E-01	0.7010E-02	-0.4050E-02	0.6455E-02
	7.9	1.458	0.1331E-01	0.3014E-01	0.6233E-02	-0.3725E-02	0.9426E-02
	12.6	1.491	0.1463E-01	0.3084E-01	0.6126E-02	-0.2792E-02	0.1088E-01
	20.0	1.510	0.1750E-01	0.3123E-01	0.5964E-02	-0.8601E-03	0.1100E-01
	31.6	1.509	0.2384E-01	0.3120E-01	0.5537E-02	-0.2377E-01	0.1295E-01
	50.1	1.548	0.6295E-01	0.3202E-01	0.5425E-02	0.4851E-01	0.1640E-01
0.1100	3.2	1.335	0.1595E-01	0.2760E-01	0.7576E-02	0.2801E-04	0.1096E-02
	5.0	1.363	0.1401E-01	0.2819E-01	0.6762E-02	-0.8650E-03	0.3951E-02
	7.9	1.385	0.1302E-01	0.2865E-01	0.5949E-02	0.1106E-02	0.7021E-02
	12.6	1.413	0.1366E-01	0.2922E-01	0.5529E-02	0.1545E-02	0.8741E-02
	20.0	1.449	0.1602E-01	0.2997E-01	0.5511E-02	0.1322E-01	0.9201E-02
	31.6	1.382	0.1955E-01	0.2858E-01	0.4926E-02	-0.1260E-01	0.9324E-02
	50.1	1.503	0.3664E-01	0.3109E-01	0.5171E-02	0.7472E-02	0.1262E-01

(continued on next page)

Table D.6 (continued) F_2 cross-section systematic errors.

x	Q^2	F_2	ΔF_2^{stat}	σ^{ν}/E	$\sigma^{\bar{\nu}}/\sigma^{\nu}$	No Φ Adj	R
0.1400	3.2	1.279	0.1297E-01	0.2645E-01	0.7344E-02	0.7889E-03	0.1335E-03
	5.0	1.305	0.1043E-01	0.2699E-01	0.6707E-02	-0.7460E-03	0.1864E-02
	7.9	1.302	0.9231E-02	0.2693E-01	0.5726E-02	-0.5997E-02	0.4413E-02
	12.6	1.319	0.9062E-02	0.2728E-01	0.4996E-02	-0.3328E-02	0.6157E-02
	20.0	1.312	0.9773E-02	0.2713E-01	0.4528E-02	0.1529E-02	0.6741E-02
	31.6	1.270	0.1137E-01	0.2627E-01	0.4027E-02	-0.4074E-02	0.6428E-02
	50.1	1.251	0.1581E-01	0.2588E-01	0.3357E-02	-0.3271E-03	0.7580E-02
	79.4	1.272	0.4124E-01	0.2631E-01	0.2896E-02	0.5059E-02	0.9011E-02
0.1800	5.0	1.185	0.1110E-01	0.2451E-01	0.6197E-02	-0.3987E-02	0.6125E-03
	7.9	1.177	0.9669E-02	0.2435E-01	0.5436E-02	-0.1358E-02	0.2165E-02
	12.6	1.184	0.8893E-02	0.2448E-01	0.4422E-02	-0.5265E-02	0.3813E-02
	20.0	1.155	0.8828E-02	0.2389E-01	0.3650E-02	0.3661E-03	0.4486E-02
	31.6	1.138	0.9901E-02	0.2354E-01	0.3202E-02	-0.6640E-03	0.4422E-02
	50.1	1.088	0.1174E-01	0.2250E-01	0.2598E-02	-0.9518E-02	0.4386E-02
	79.4	1.098	0.2006E-01	0.2271E-01	0.2354E-02	0.7578E-02	0.5562E-02
0.2250	5.0	1.097	0.1162E-01	0.2269E-01	0.6211E-02	-0.9888E-02	0.1510E-03
	7.9	1.053	0.8881E-02	0.2178E-01	0.5138E-02	-0.5860E-03	0.9630E-03
	12.6	1.028	0.7769E-02	0.2126E-01	0.4021E-02	-0.2674E-02	0.2193E-02
	20.0	1.001	0.7348E-02	0.2069E-01	0.3026E-02	0.3014E-02	0.2872E-02
	31.6	0.9815	0.7815E-02	0.2030E-01	0.2573E-02	0.2205E-02	0.3006E-02
	50.1	0.9498	0.8975E-02	0.1964E-01	0.2310E-02	-0.5509E-02	0.2767E-02
	79.4	0.9334	0.1166E-01	0.1930E-01	0.1521E-02	0.4816E-02	0.3239E-02
0.2750	7.9	0.9039	0.8981E-02	0.1869E-01	0.4513E-02	-0.4317E-02	0.4340E-03
	12.6	0.8763	0.7741E-02	0.1812E-01	0.3633E-02	-0.4415E-02	0.1149E-02
	20.0	0.8515	0.7008E-02	0.1761E-01	0.2736E-02	-0.4530E-02	0.1785E-02
	31.6	0.8176	0.7141E-02	0.1691E-01	0.2108E-02	-0.1153E-02	0.1952E-02
	50.1	0.7980	0.7945E-02	0.1650E-01	0.1769E-02	-0.4440E-02	0.1819E-02
	79.4	0.7552	0.9086E-02	0.1562E-01	0.1373E-02	-0.2492E-02	0.1828E-02
	125.9	0.7135	0.1561E-01	0.1476E-01	0.7553E-03	0.1658E-01	0.2143E-02

(continued on next page)

Table D.6 (continued) F_2 cross-section systematic errors.

x	Q^2	F_2	ΔF_2^{stat}	σ^{ν}/E	$\sigma^{\bar{\nu}}/\sigma^{\nu}$	No Φ Adj	R
0.3500	7.9	0.7049	0.6639E-02	0.1458E-01	0.3734E-02	0.3024E-02	0.2246E-03
	12.6	0.6687	0.5275E-02	0.1383E-01	0.3011E-02	-0.4491E-03	0.4988E-03
	20.0	0.6274	0.4554E-02	0.1297E-01	0.2102E-02	-0.1339E-02	0.8906E-03
	31.6	0.6025	0.4439E-02	0.1246E-01	0.1537E-02	-0.3932E-02	0.1047E-02
	50.1	0.5723	0.4575E-02	0.1183E-01	0.1160E-02	-0.3385E-03	0.1011E-02
	79.4	0.5395	0.5027E-02	0.1116E-01	0.9561E-03	0.1909E-02	0.8885E-03
	125.9	0.5254	0.6764E-02	0.1087E-01	0.5751E-03	-0.2617E-02	0.1004E-02
0.4500	12.6	0.4087	0.4541E-02	0.8452E-02	0.1980E-02	0.1546E-02	0.1930E-03
	20.0	0.3966	0.3972E-02	0.8201E-02	0.1542E-02	-0.4798E-02	0.3418E-03
	31.6	0.3609	0.3548E-02	0.7463E-02	0.9929E-03	0.2131E-02	0.4583E-03
	50.1	0.3315	0.3520E-02	0.6856E-02	0.6676E-03	0.2640E-03	0.4543E-03
	79.4	0.3158	0.3754E-02	0.6531E-02	0.5069E-03	0.1568E-02	0.3974E-03
	125.9	0.2927	0.4230E-02	0.6053E-02	0.3132E-03	0.1898E-02	0.3722E-03
	199.5	0.2743	0.7832E-02	0.5673E-02	0.2131E-03	-0.5418E-04	0.4380E-03
0.5500	12.6	0.2378	0.3870E-02	0.4917E-02	0.1174E-02	0.1490E-02	0.8730E-04
	20.0	0.2136	0.3137E-02	0.4417E-02	0.9461E-03	-0.8936E-03	0.1252E-03
	31.6	0.1889	0.2658E-02	0.3907E-02	0.5964E-03	0.7585E-03	0.1813E-03
	50.1	0.1763	0.2629E-02	0.3646E-02	0.3958E-03	-0.1538E-02	0.1915E-03
	79.4	0.1587	0.2621E-02	0.3283E-02	0.2538E-03	-0.7244E-03	0.1609E-03
	125.9	0.1502	0.2885E-02	0.3105E-02	0.2173E-03	-0.4147E-03	0.1436E-03
	199.5	0.1346	0.4046E-02	0.2783E-02	0.9960E-04	0.7775E-03	0.1573E-03
0.6500	12.6	0.1184	0.3397E-02	0.2448E-02	0.6821E-03	-0.1965E-02	0.3775E-04
	20.0	0.9990E-01	0.2085E-02	0.2066E-02	0.4484E-03	-0.1108E-02	0.4365E-04
	31.6	0.8166E-01	0.1669E-02	0.1689E-02	0.2652E-03	0.9371E-03	0.6026E-04
	50.1	0.7681E-01	0.1600E-02	0.1588E-02	0.1683E-03	-0.6690E-04	0.7023E-04
	79.4	0.6731E-01	0.1600E-02	0.1392E-02	0.1241E-03	-0.3860E-03	0.5573E-04
	125.9	0.6104E-01	0.1732E-02	0.1262E-02	0.1031E-03	-0.8472E-03	0.5083E-04
0.7500	20.0	0.3505E-01	0.1011E-02	0.7248E-03	0.1673E-03	-0.2276E-03	0.1279E-04
	31.6	0.2838E-01	0.8458E-03	0.5869E-03	0.1088E-03	-0.7798E-03	0.1578E-04
	50.1	0.2529E-01	0.7646E-03	0.5230E-03	0.6928E-04	-0.2349E-03	0.2044E-04
	79.4	0.2135E-01	0.7569E-03	0.4416E-03	0.4993E-04	0.1466E-04	0.1859E-04
	125.9	0.2014E-01	0.8035E-03	0.4165E-03	0.3407E-04	0.3538E-04	0.1629E-04

Table D.7: xF_3 cross-section systematic errors.

x	Q^2	xF_3	ΔxF_3^{stat}	σ^{ν}/E	$\sigma^{\bar{\nu}}/\sigma^{\nu}$	No Φ Adj	R
0.0075	1.3	0.7632E-01	0.3700E-01	0.1578E-02	-0.1044E-01	0.1633E-01	-0.2261E-02
	2.0	0.1821	0.4039E-01	0.3765E-02	-0.8912E-02	-0.1038E-01	-0.1968E-02
	3.2	0.9905E-01	0.6319E-01	0.2048E-02	-0.9707E-02	0.1791E-01	-0.1298E-02
0.0125	1.3	0.2122	0.3417E-01	0.4389E-02	-0.1040E-01	0.7655E-02	-0.2228E-02
	2.0	0.2239	0.3512E-01	0.4631E-02	-0.9821E-02	-0.1382E-01	-0.2860E-02
	3.2	0.1684	0.4290E-01	0.3481E-02	-0.1060E-01	0.9374E-02	-0.2144E-02
	5.0	0.2486	0.5783E-01	0.5141E-02	-0.9432E-02	0.1107E-01	-0.1117E-02
0.0175	1.3	0.1894	0.4008E-01	0.3917E-02	-0.1277E-01	-0.2225E-01	-0.2142E-02
	2.0	0.2767	0.3549E-01	0.5722E-02	-0.1089E-01	0.1860E-02	-0.2751E-02
	3.2	0.2906	0.3887E-01	0.6009E-02	-0.1087E-01	0.2889E-02	-0.2795E-02
	5.0	0.2543	0.4715E-01	0.5258E-02	-0.1012E-01	-0.9193E-02	-0.1667E-02
	7.9	0.3513	0.6743E-01	0.7264E-02	-0.7532E-02	0.1016E-01	-0.6071E-03
0.0250	1.3	0.2339	0.3704E-01	0.4837E-02	-0.1600E-01	0.1068E-01	-0.1956E-02
	2.0	0.3517	0.2670E-01	0.7274E-02	-0.1152E-01	0.5746E-03	-0.2303E-02
	3.2	0.3298	0.2605E-01	0.6819E-02	-0.1102E-01	0.1321E-01	-0.2648E-02
	5.0	0.3732	0.2882E-01	0.7719E-02	-0.1042E-01	-0.9766E-02	-0.2387E-02
	7.9	0.3555	0.3521E-01	0.7351E-02	-0.9699E-02	0.7668E-02	-0.1221E-02
	12.6	0.3551	0.6568E-01	0.7344E-02	-0.9064E-02	0.1130E-01	-0.8546E-03
0.0350	1.3	0.4047	0.5474E-01	0.8370E-02	-0.2129E-01	-0.1568E-01	-0.1559E-02
	2.0	0.4121	0.3500E-01	0.8522E-02	-0.1452E-01	-0.4499E-02	-0.2114E-02
	3.2	0.4078	0.2699E-01	0.8433E-02	-0.1154E-01	-0.5360E-03	-0.2342E-02
	5.0	0.4159	0.2706E-01	0.8601E-02	-0.1097E-01	-0.2877E-03	-0.2508E-02
	7.9	0.4316	0.3064E-01	0.8926E-02	-0.1012E-01	-0.7575E-02	-0.1943E-02
	12.6	0.4561	0.3901E-01	0.9432E-02	-0.9150E-02	0.1682E-01	-0.9027E-03
	20.0	0.5198	0.9575E-01	0.1075E-01	-0.7918E-02	-0.1638E-01	-0.4695E-03

(continued on next page)

Table D.7 (continued) xF_3 cross-section systematic errors.

x	Q^2	xF_3	ΔxF_3^{stat}	σ^{ν}/E	$\sigma^{\bar{\nu}}/\sigma^{\nu}$	No Φ Adj	R
0.0500	1.3	0.3967	0.6599E-01	0.8203E-02	-0.3310E-01	0.3319E-02	-0.1562E-02
	2.0	0.5068	0.3600E-01	0.1048E-01	-0.2043E-01	0.1430E-01	-0.1806E-02
	3.2	0.4822	0.2357E-01	0.9972E-02	-0.1419E-01	-0.1578E-03	-0.2090E-02
	5.0	0.5058	0.1989E-01	0.1046E-01	-0.1140E-01	0.5154E-02	-0.2189E-02
	7.9	0.5800	0.1979E-01	0.1199E-01	-0.1007E-01	-0.2652E-02	-0.2215E-02
	12.6	0.5615	0.2215E-01	0.1161E-01	-0.9052E-02	0.4956E-02	-0.1426E-02
	20.0	0.6184	0.3011E-01	0.1279E-01	-0.7534E-02	0.1429E-01	-0.6090E-03
	31.6	0.6167	0.9101E-01	0.1275E-01	-0.6313E-02	0.2868E-01	-0.4788E-03
0.0700	2.0	0.5093	0.5839E-01	0.1053E-01	-0.3074E-01	0.9304E-02	-0.1556E-02
	3.2	0.6078	0.3228E-01	0.1257E-01	-0.1810E-01	0.2131E-01	-0.1729E-02
	5.0	0.6209	0.2280E-01	0.1284E-01	-0.1269E-01	-0.9710E-02	-0.1953E-02
	7.9	0.6377	0.1946E-01	0.1319E-01	-0.1024E-01	0.2128E-02	-0.1986E-02
	12.6	0.6370	0.2080E-01	0.1317E-01	-0.9128E-02	0.3560E-02	-0.1873E-02
	20.0	0.6485	0.2391E-01	0.1341E-01	-0.7972E-02	-0.1830E-01	-0.1126E-02
	31.6	0.6147	0.3683E-01	0.1271E-01	-0.6714E-02	0.2399E-01	-0.4699E-03
0.0900	2.0	0.7605	0.9046E-01	0.1573E-01	-0.3947E-01	0.2871E-01	-0.1519E-02
	3.2	0.5799	0.4613E-01	0.1199E-01	-0.2483E-01	0.9893E-02	-0.1431E-02
	5.0	0.6738	0.2707E-01	0.1393E-01	-0.1462E-01	0.1009E-01	-0.1677E-02
	7.9	0.7340	0.2048E-01	0.1518E-01	-0.1016E-01	-0.1052E-01	-0.1723E-02
	12.6	0.7146	0.1980E-01	0.1478E-01	-0.8718E-02	-0.9471E-03	-0.1712E-02
	20.0	0.7376	0.2177E-01	0.1525E-01	-0.7653E-02	0.3205E-03	-0.1374E-02
	31.6	0.7384	0.2551E-01	0.1527E-01	-0.5991E-02	0.2073E-01	-0.5843E-03
	50.1	0.7445	0.6111E-01	0.1540E-01	-0.5278E-02	-0.3199E-02	-0.2578E-03
0.1100	3.2	0.6630	0.6051E-01	0.1371E-01	-0.2998E-01	-0.1752E-01	-0.1183E-02
	5.0	0.7350	0.3292E-01	0.1520E-01	-0.1675E-01	-0.9727E-02	-0.1425E-02
	7.9	0.7624	0.2200E-01	0.1577E-01	-0.1067E-01	-0.1733E-01	-0.1519E-02
	12.6	0.7658	0.1940E-01	0.1584E-01	-0.8305E-02	-0.3992E-02	-0.1523E-02
	20.0	0.7653	0.2086E-01	0.1583E-01	-0.7501E-02	-0.1426E-01	-0.1500E-02
	31.6	0.7374	0.2253E-01	0.1525E-01	-0.5782E-02	0.6505E-02	-0.7958E-03
	50.1	0.7596	0.3705E-01	0.1571E-01	-0.5256E-02	0.4177E-01	-0.3192E-03

(continued on next page)

Table D.7 (continued) xF_3 cross-section systematic errors.

x	Q^2	xF_3	ΔxF_3^{stat}	σ^{ν}/E	$\sigma^{\bar{\nu}}/\sigma^{\nu}$	No Φ Adj	R
0.1400	3.2	0.7642	0.6294E-01	0.1580E-01	-0.3710E-01	-0.1316E-02	-0.1036E-02
	5.0	0.8043	0.3120E-01	0.1663E-01	-0.2104E-01	0.6367E-02	-0.1173E-02
	7.9	0.7931	0.1804E-01	0.1640E-01	-0.1188E-01	0.1060E-01	-0.1251E-02
	12.6	0.8154	0.1395E-01	0.1686E-01	-0.8181E-02	0.3332E-02	-0.1256E-02
	20.0	0.8078	0.1328E-01	0.1670E-01	-0.6510E-02	-0.2812E-02	-0.1230E-02
	31.6	0.8071	0.1419E-01	0.1669E-01	-0.5205E-02	-0.1230E-02	-0.9525E-03
	50.1	0.8139	0.1711E-01	0.1683E-01	-0.3682E-02	0.5225E-03	-0.4744E-03
	79.4	0.8476	0.4090E-01	0.1753E-01	-0.2878E-02	0.1274E-01	-0.3285E-03
0.1800	5.0	0.9044	0.4342E-01	0.1870E-01	-0.2535E-01	-0.9168E-02	-0.8754E-03
	7.9	0.8026	0.2349E-01	0.1660E-01	-0.1394E-01	-0.8390E-02	-0.9771E-03
	12.6	0.8361	0.1532E-01	0.1729E-01	-0.8147E-02	-0.2716E-02	-0.9890E-03
	20.0	0.8247	0.1269E-01	0.1705E-01	-0.5612E-02	0.3504E-02	-0.9478E-03
	31.6	0.8280	0.1303E-01	0.1712E-01	-0.4451E-02	-0.5802E-02	-0.8956E-03
	50.1	0.8111	0.1379E-01	0.1677E-01	-0.3139E-02	0.2524E-03	-0.5444E-03
	79.4	0.7814	0.2082E-01	0.1616E-01	-0.2463E-02	0.1339E-01	-0.3085E-03
0.2250	5.0	0.7368	0.5772E-01	0.1524E-01	-0.3206E-01	0.3490E-01	-0.6855E-03
	7.9	0.7854	0.2710E-01	0.1624E-01	-0.1649E-01	-0.1435E-02	-0.7314E-03
	12.6	0.7824	0.1539E-01	0.1618E-01	-0.8502E-02	-0.2781E-02	-0.7689E-03
	20.0	0.8027	0.1141E-01	0.1660E-01	-0.5042E-02	-0.5977E-02	-0.7325E-03
	31.6	0.7763	0.1066E-01	0.1605E-01	-0.3756E-02	0.1208E-02	-0.7162E-03
	50.1	0.7413	0.1131E-01	0.1533E-01	-0.3039E-02	-0.1898E-02	-0.6107E-03
	79.4	0.7731	0.1279E-01	0.1599E-01	-0.1699E-02	-0.2340E-02	-0.3617E-03
0.2750	7.9	0.7803	0.3387E-01	0.1614E-01	-0.1786E-01	-0.8644E-03	-0.5099E-03
	12.6	0.7207	0.1818E-01	0.1490E-01	-0.9060E-02	-0.3884E-02	-0.5415E-03
	20.0	0.7066	0.1188E-01	0.1461E-01	-0.4991E-02	0.3196E-02	-0.5519E-03
	31.6	0.6839	0.1017E-01	0.1414E-01	-0.3238E-02	-0.9727E-04	-0.5357E-03
	50.1	0.6755	0.1040E-01	0.1397E-01	-0.2463E-02	-0.2242E-02	-0.5239E-03
	79.4	0.6373	0.1061E-01	0.1318E-01	-0.1651E-02	0.3156E-02	-0.4078E-03
	125.9	0.6265	0.1623E-01	0.1296E-01	-0.7942E-03	0.9962E-02	-0.1730E-03

(continued on next page)

Table D.7 (continued) xF_3 cross-section systematic errors.

x	Q^2	xF_3	ΔxF_3^{stat}	σ^{ν}/E	$\sigma^{\bar{\nu}}/\sigma^{\nu}$	No Φ Adj	R
0.3500	7.9	0.6352	0.3202E-01	0.1313E-01	-0.1882E-01	-0.1837E-02	-0.3475E-03
	12.6	0.5946	0.1571E-01	0.1230E-01	-0.9464E-02	0.3207E-02	-0.3408E-03
	20.0	0.5742	0.8879E-02	0.1187E-01	-0.4408E-02	-0.2655E-02	-0.3241E-03
	31.6	0.5490	0.6821E-02	0.1135E-01	-0.2559E-02	0.1187E-02	-0.3116E-03
	50.1	0.5240	0.6214E-02	0.1084E-01	-0.1700E-02	-0.1392E-02	-0.3124E-03
	79.4	0.4881	0.6307E-02	0.1009E-01	-0.1259E-02	-0.1440E-02	-0.2785E-03
	125.9	0.4831	0.7438E-02	0.9990E-02	-0.6456E-03	0.2591E-02	-0.1747E-03
0.4500	12.6	0.3987	0.1766E-01	0.8245E-02	-0.8093E-02	-0.5860E-02	-0.1417E-03
	20.0	0.3729	0.9599E-02	0.7712E-02	-0.3971E-02	-0.3496E-02	-0.1577E-03
	31.6	0.3487	0.6094E-02	0.7211E-02	-0.1849E-02	0.7600E-03	-0.1510E-03
	50.1	0.3216	0.5045E-02	0.6651E-02	-0.1042E-02	-0.2612E-02	-0.1590E-03
	79.4	0.3078	0.4923E-02	0.6364E-02	-0.7152E-03	0.2046E-03	-0.1518E-03
	125.9	0.2885	0.4990E-02	0.5966E-02	-0.3840E-03	0.1534E-02	-0.1350E-03
	199.5	0.2563	0.8264E-02	0.5300E-02	-0.2276E-03	0.3723E-02	-0.4479E-04
0.5500	12.6	0.2731	0.1866E-01	0.5648E-02	-0.5919E-02	-0.1851E-02	-0.3590E-04
	20.0	0.1973	0.9353E-02	0.4081E-02	-0.2976E-02	-0.6208E-02	-0.6160E-04
	31.6	0.1834	0.5175E-02	0.3793E-02	-0.1252E-02	0.1309E-02	-0.6405E-04
	50.1	0.1733	0.4033E-02	0.3585E-02	-0.6601E-03	0.6774E-03	-0.6720E-04
	79.4	0.1595	0.3540E-02	0.3298E-02	-0.3732E-03	-0.5315E-03	-0.5790E-04
	125.9	0.1454	0.3616E-02	0.3007E-02	-0.2868E-03	0.5789E-04	-0.6610E-04
	199.5	0.1314	0.4446E-02	0.2718E-02	-0.1120E-03	0.7252E-03	-0.4050E-04
0.6500	12.6	0.8328E-01	0.1967E-01	0.1722E-02	-0.4096E-02	0.4030E-02	-0.2748E-04
	20.0	0.1069	0.7406E-02	0.2211E-02	-0.1676E-02	0.2533E-02	-0.1605E-04
	31.6	0.8762E-01	0.3702E-02	0.1812E-02	-0.6320E-03	0.7559E-03	-0.1923E-04
	50.1	0.8174E-01	0.2626E-02	0.1690E-02	-0.3014E-03	0.7444E-03	-0.2388E-04
	79.4	0.6648E-01	0.2246E-02	0.1375E-02	-0.1896E-03	-0.3913E-03	-0.1483E-04
	125.9	0.5806E-01	0.2255E-02	0.1201E-02	-0.1430E-03	-0.8173E-03	-0.2385E-04
0.7500	20.0	0.3791E-01	0.4179E-02	0.7839E-03	-0.7243E-03	0.1058E-02	-0.8345E-06
	31.6	0.2875E-01	0.2163E-02	0.5946E-03	-0.2960E-03	0.1006E-02	-0.3954E-05
	50.1	0.2539E-01	0.1359E-02	0.5250E-03	-0.1327E-03	0.1033E-03	-0.5340E-05
	79.4	0.1963E-01	0.1112E-02	0.4058E-03	-0.7946E-04	-0.1304E-04	-0.7170E-05
	125.9	0.1951E-01	0.1072E-02	0.4035E-03	-0.4879E-04	-0.2583E-03	-0.6390E-05

Table D.8: F_2 physics-model systematic errors.

x	Q^2	F_2	ΔF_2^{stat}	m_c	κ	α	B_c	Model Par.
0.0075	1.3	1.305	0.2975E-01	0.5713E-02	-0.1550E-01	-0.1543E-01	-0.1569E-01	0.4091E-01
	2.0	1.366	0.3703E-01	0.2915E-01	0.2664E-02	0.4278E-02	0.6279E-02	0.9271E-02
	3.2	1.587	0.6680E-01	0.4324E-01	0.4026E-02	0.7078E-02	0.1162E-01	0.5576E-01
0.0125	1.3	1.237	0.2408E-01	0.8154E-02	-0.1153E-01	-0.1142E-01	-0.1279E-01	0.5927E-01
	2.0	1.335	0.2783E-01	0.3508E-01	0.1152E-01	0.1297E-01	0.1369E-01	0.1750E-01
	3.2	1.525	0.3794E-01	0.2249E-01	-0.7674E-02	-0.4645E-02	-0.1334E-02	-0.2086E-02
	5.0	1.675	0.6004E-01	0.3779E-01	-0.2240E-03	0.5078E-02	0.1102E-01	-0.3491E-01
0.0175	1.3	1.253	0.2421E-01	0.3696E-01	0.1663E-01	0.1660E-01	0.1426E-01	0.6000E-01
	2.0	1.385	0.2596E-01	0.1453E-01	-0.8941E-02	-0.7651E-02	-0.7937E-02	0.1167E-01
	3.2	1.528	0.3118E-01	0.8498E-02	-0.1863E-01	-0.1594E-01	-0.1395E-01	-0.2685E-01
	5.0	1.589	0.4313E-01	0.1141E-01	-0.1926E-01	-0.1467E-01	-0.1024E-01	-0.5728E-01
	7.9	1.527	0.7152E-01	0.2437E-01	-0.7548E-02	-0.1469E-02	0.4557E-02	-0.2121E-01
0.0250	1.3	1.226	0.1751E-01	0.1895E-01	0.1860E-03	-0.2850E-03	-0.3476E-02	0.3483E-01
	2.0	1.311	0.1703E-01	0.2017E-01	-0.7250E-03	0.2780E-03	-0.1083E-02	-0.1081E-01
	3.2	1.463	0.1936E-01	0.1962E-01	-0.5473E-02	-0.3065E-02	-0.2349E-02	-0.1685E-01
	5.0	1.558	0.2339E-01	0.2932E-01	0.2756E-02	0.6774E-02	0.9547E-02	-0.1006E-01
	7.9	1.661	0.3303E-01	0.3693E-02	-0.2570E-01	-0.1958E-01	-0.1468E-01	-0.2173E-01
	12.6	1.759	0.6962E-01	0.2829E-01	-0.2769E-02	0.6479E-02	0.1310E-01	-0.2022E-01
0.0350	1.3	1.193	0.1848E-01	0.3520E-01	0.1819E-01	0.1686E-01	0.1306E-01	0.2460E-01
	2.0	1.330	0.1818E-01	0.1114E-01	-0.8447E-02	-0.7955E-02	-0.1027E-01	-0.2388E-01
	3.2	1.412	0.1799E-01	0.1495E-01	-0.7393E-02	-0.5510E-02	-0.5960E-02	-0.1045E-01
	5.0	1.551	0.2052E-01	0.1271E-01	-0.1225E-01	-0.8836E-02	-0.7364E-02	-0.1865E-01
	7.9	1.598	0.2536E-01	0.2542E-01	0.6150E-03	0.5755E-02	0.8978E-02	-0.3135E-01
	12.6	1.734	0.3787E-01	-0.3137E-02	-0.3044E-01	-0.2289E-01	-0.1798E-01	-0.3655E-01
	20.0	1.779	0.1028	0.5705E-01	0.2914E-01	0.3928E-01	0.4538E-01	-0.1087E-01

(continued on next page)

Table D.8 (continued): F_2 physics-model systematic errors.

x	Q^2	F_2	ΔF_2^{stat}	m_c	κ	α	B_c	Model Par.
0.0500	1.3	1.228	0.1545E-01	0.2018E-01	0.5211E-02	0.2338E-02	-0.1405E-02	0.5284E-02
	2.0	1.336	0.1371E-01	0.1859E-01	0.1148E-02	0.5950E-03	-0.2299E-02	-0.8302E-02
	3.2	1.434	0.1311E-01	0.1745E-01	-0.2846E-02	-0.1775E-02	-0.3184E-02	-0.1730E-01
	5.0	1.509	0.1365E-01	0.1167E-01	-0.1039E-01	-0.7693E-02	-0.7519E-02	-0.2010E-01
	7.9	1.593	0.1514E-01	0.2397E-01	0.1677E-02	0.6016E-02	0.7629E-02	-0.1400E-01
	12.6	1.611	0.1881E-01	0.7551E-02	-0.1356E-01	-0.7677E-02	-0.4862E-02	-0.2663E-01
	20.0	1.683	0.2962E-01	-0.2457E-02	-0.2448E-01	-0.1650E-01	-0.1269E-01	-0.2590E-01
	31.6	1.622	0.9702E-01	0.2846E-01	0.8515E-02	0.1795E-01	0.2195E-01	-0.6300E-01
0.0700	2.0	1.322	0.1539E-01	0.1039E-01	-0.4368E-02	-0.6334E-02	-0.8973E-02	-0.3589E-01
	3.2	1.393	0.1375E-01	0.1028E-01	-0.6304E-02	-0.6423E-02	-0.8183E-02	-0.1519E-01
	5.0	1.482	0.1351E-01	0.1941E-01	0.3880E-03	0.2029E-02	0.1350E-02	-0.2289E-01
	7.9	1.532	0.1379E-01	0.1080E-01	-0.8365E-02	-0.5033E-02	-0.4616E-02	-0.2545E-01
	12.6	1.548	0.1609E-01	0.9845E-02	-0.7831E-02	-0.3058E-02	-0.1718E-02	-0.3021E-01
	20.0	1.598	0.2097E-01	0.2234E-01	0.4540E-02	0.1113E-01	0.1329E-01	-0.3958E-01
	31.6	1.591	0.3695E-01	0.1069E-01	-0.6821E-02	0.1394E-02	0.3985E-02	-0.2159E-01
0.0900	2.0	1.318	0.1821E-01	0.8279E-02	-0.3906E-02	-0.6949E-02	-0.8834E-02	-0.5525E-02
	3.2	1.380	0.1504E-01	0.1571E-01	0.1274E-02	0.3493E-04	-0.1508E-02	-0.1443E-01
	5.0	1.432	0.1368E-01	0.1255E-01	-0.3296E-02	-0.2669E-02	-0.3554E-02	-0.2506E-01
	7.9	1.458	0.1331E-01	0.1114E-01	-0.5019E-02	-0.2699E-02	-0.2867E-02	-0.2449E-01
	12.6	1.491	0.1463E-01	0.9824E-02	-0.5808E-02	-0.2032E-02	-0.1537E-02	-0.2598E-01
	20.0	1.510	0.1750E-01	0.8652E-02	-0.5342E-02	-0.2911E-03	0.7689E-03	-0.2827E-01
	31.6	1.509	0.2384E-01	-0.1613E-01	-0.2966E-01	-0.2325E-01	-0.2192E-01	-0.3235E-01
	50.1	1.548	0.6295E-01	0.5478E-01	0.4070E-01	0.4920E-01	0.5083E-01	-0.2331E-01
0.1100	3.2	1.335	0.1595E-01	0.1536E-01	0.3149E-02	0.1118E-02	0.1030E-03	-0.2117E-01
	5.0	1.363	0.1401E-01	0.1355E-01	0.4109E-03	0.1659E-03	-0.5710E-03	-0.8080E-02
	7.9	1.385	0.1302E-01	0.1426E-01	0.5770E-03	0.2056E-02	0.1716E-02	-0.2014E-01
	12.6	1.413	0.1366E-01	0.1282E-01	-0.4920E-03	0.2439E-02	0.2519E-02	-0.2874E-01
	20.0	1.449	0.1602E-01	0.2213E-01	0.9867E-02	0.1409E-01	0.1455E-01	-0.1447E-01
	31.6	1.382	0.1955E-01	-0.6118E-02	-0.1680E-01	-0.1175E-01	-0.1109E-01	-0.4575E-01
	50.1	1.503	0.3664E-01	0.1315E-01	0.1616E-02	0.8601E-02	0.9326E-02	-0.1747E-01

(continued on next page)

Table D.8 (continued): F_2 physics-model systematic errors.

x	Q^2	F_2	ΔF_2^{stat}	m_c	κ	α	B_c	Model Par.
0.1400	3.2	1.279	0.1297E-01	0.1351E-01	0.3674E-02	0.9879E-03	0.7720E-03	-0.1820E-01
	5.0	1.305	0.1043E-01	0.1127E-01	0.8019E-03	-0.3271E-03	-0.6241E-03	-0.2255E-01
	7.9	1.302	0.9231E-02	0.4823E-02	-0.5851E-02	-0.5403E-02	-0.5648E-02	-0.6751E-02
	12.6	1.319	0.9062E-02	0.5904E-02	-0.4408E-02	-0.2573E-02	-0.2699E-02	-0.1800E-01
	20.0	1.312	0.9773E-02	0.8995E-02	-0.3951E-03	0.2404E-02	0.2446E-02	-0.2839E-01
	31.6	1.270	0.1137E-01	0.1113E-02	-0.6636E-02	-0.3147E-02	-0.2976E-02	-0.2779E-01
	50.1	1.251	0.1581E-01	0.3930E-02	-0.3484E-02	0.7859E-03	0.9719E-03	-0.3261E-01
	79.4	1.272	0.4124E-01	0.7926E-02	0.1379E-02	0.6329E-02	0.6523E-02	0.5490E-03
0.1800	5.0	1.185	0.1110E-01	0.5237E-02	-0.2616E-02	-0.4230E-02	-0.3996E-02	-0.8229E-02
	7.9	1.177	0.9669E-02	0.6949E-02	-0.8740E-03	-0.1268E-02	-0.1202E-02	-0.1769E-01
	12.6	1.184	0.8893E-02	0.1850E-02	-0.5612E-02	-0.4866E-02	-0.4905E-02	-0.1760E-01
	20.0	1.155	0.8828E-02	0.5989E-02	-0.5740E-03	0.9941E-03	0.9360E-03	-0.1031E-01
	31.6	1.138	0.9901E-02	0.3559E-02	-0.1975E-02	0.1011E-03	0.1260E-03	-0.1009E-01
	50.1	1.088	0.1174E-01	-0.6215E-02	-0.1101E-01	-0.8645E-02	-0.8625E-02	-0.1342E-01
	79.4	1.098	0.2006E-01	0.1022E-01	0.5552E-02	0.8726E-02	0.8614E-02	-0.1396E-01
0.2250	5.0	1.097	0.1162E-01	-0.2324E-02	-0.8858E-02	-0.1051E-01	-0.9923E-02	-0.2511E-01
	7.9	1.053	0.8881E-02	0.5763E-02	-0.1260E-03	-0.8631E-03	-0.5391E-03	-0.7124E-02
	12.6	1.028	0.7769E-02	0.2633E-02	-0.2720E-02	-0.2619E-02	-0.2483E-02	-0.1246E-01
	20.0	1.001	0.7348E-02	0.7146E-02	0.2586E-02	0.3322E-02	0.3370E-02	-0.7275E-03
	31.6	0.9815	0.7815E-02	0.5362E-02	0.1572E-02	0.2676E-02	0.2752E-02	-0.6864E-02
	50.1	0.9498	0.8975E-02	-0.3187E-02	-0.6269E-02	-0.4935E-02	-0.4880E-02	-0.1797E-01
	79.4	0.9334	0.1166E-01	0.6730E-02	0.3942E-02	0.5518E-02	0.5543E-02	-0.1402E-01
0.2750	7.9	0.9039	0.8981E-02	0.6116E-03	-0.4038E-02	-0.4713E-02	-0.4332E-02	0.4940E-02
	12.6	0.8763	0.7741E-02	-0.4791E-03	-0.4404E-02	-0.4568E-02	-0.4329E-02	-0.3696E-02
	20.0	0.8515	0.7008E-02	-0.1442E-02	-0.4709E-02	-0.4472E-02	-0.4328E-02	-0.6390E-02
	31.6	0.8176	0.7141E-02	0.1191E-02	-0.1413E-02	-0.9600E-03	-0.8102E-03	-0.4370E-02
	50.1	0.7980	0.7945E-02	-0.2672E-02	-0.4723E-02	-0.4175E-02	-0.3975E-02	-0.5013E-02
	79.4	0.7552	0.9086E-02	-0.1202E-02	-0.2841E-02	-0.2153E-02	-0.1965E-02	0.8073E-03
	125.9	0.7135	0.1561E-01	0.1786E-01	0.1630E-01	0.1697E-01	0.1720E-01	-0.4839E-02

(continued on next page)

Table D.8 (continued): F_2 physics-model systematic errors.

x	Q^2	F_2	ΔF_2^{stat}	m_c	κ	α	B_c	Model Par.
0.3500	7.9	0.7049	0.6639E-02	0.6917E-02	0.3093E-02	0.2726E-02	0.2990E-02	-0.1422E-02
	12.6	0.6687	0.5275E-02	0.2453E-02	-0.4845E-03	-0.6230E-03	-0.4244E-03	-0.5374E-02
	20.0	0.6274	0.4554E-02	0.7791E-03	-0.1430E-02	-0.1407E-02	-0.1238E-02	-0.2693E-02
	31.6	0.6025	0.4439E-02	-0.2369E-02	-0.4028E-02	-0.3929E-02	-0.3733E-02	-0.4725E-02
	50.1	0.5723	0.4575E-02	0.8142E-03	-0.4101E-03	-0.3020E-03	-0.5376E-04	-0.4999E-02
	79.4	0.5395	0.5027E-02	0.2798E-02	0.1865E-02	0.1963E-02	0.2228E-02	-0.9654E-03
	125.9	0.5254	0.6764E-02	-0.1849E-02	-0.2633E-02	-0.2547E-02	-0.2261E-02	-0.1063E-02
0.4500	12.6	0.4087	0.4541E-02	0.3544E-02	0.1470E-02	0.1462E-02	0.1539E-02	-0.2954E-02
	20.0	0.3966	0.3972E-02	-0.3324E-02	-0.4875E-02	-0.4860E-02	-0.4763E-02	-0.1128E-01
	31.6	0.3609	0.3548E-02	0.3167E-02	0.2074E-02	0.2088E-02	0.2220E-02	-0.2133E-02
	50.1	0.3315	0.3520E-02	0.9984E-03	0.2434E-03	0.2291E-03	0.3974E-03	-0.4045E-02
	79.4	0.3158	0.3754E-02	0.2143E-02	0.1584E-02	0.1534E-02	0.1748E-02	-0.4578E-02
	125.9	0.2927	0.4230E-02	0.2329E-02	0.1926E-02	0.1862E-02	0.2093E-02	0.3389E-03
	199.5	0.2743	0.7832E-02	0.3529E-03	-0.1103E-05	-0.8020E-04	0.1346E-03	-0.1654E-02
0.5500	12.6	0.2378	0.3870E-02	0.2882E-02	0.1433E-02	0.1462E-02	0.1478E-02	-0.1644E-02
	20.0	0.2136	0.3137E-02	0.8461E-04	-0.9437E-03	-0.9209E-03	-0.8821E-03	-0.5787E-02
	31.6	0.1889	0.2658E-02	0.1437E-02	0.7230E-03	0.7337E-03	0.7923E-03	-0.3853E-02
	50.1	0.1763	0.2629E-02	-0.1057E-02	-0.1553E-02	-0.1562E-02	-0.1480E-02	-0.5521E-02
	79.4	0.1587	0.2621E-02	-0.3726E-03	-0.7158E-03	-0.7456E-03	-0.6507E-03	-0.1479E-02
	125.9	0.1502	0.2885E-02	-0.1670E-03	-0.4036E-03	-0.4400E-03	-0.3276E-03	-0.5245E-02
	199.5	0.1346	0.4046E-02	0.9942E-03	0.8040E-03	0.7533E-03	0.8707E-03	-0.4990E-02
0.6500	12.6	0.1184	0.3397E-02	-0.1238E-02	-0.1994E-02	-0.1975E-02	-0.1965E-02	-0.7182E-02
	20.0	0.9990E-01	0.2085E-02	-0.5568E-03	-0.1134E-02	-0.1118E-02	-0.1107E-02	-0.4064E-02
	31.6	0.8166E-01	0.1669E-02	0.1313E-02	0.9189E-03	0.9270E-03	0.9466E-03	-0.1337E-02
	50.1	0.7681E-01	0.1600E-02	0.2120E-03	-0.7541E-04	-0.7741E-04	-0.4318E-04	-0.2085E-02
	79.4	0.6731E-01	0.1600E-02	-0.1941E-03	-0.3855E-03	-0.3968E-03	-0.3570E-03	-0.1210E-02
	125.9	0.6104E-01	0.1732E-02	-0.7191E-03	-0.8439E-03	-0.8576E-03	-0.8124E-03	-0.7828E-03
0.7500	20.0	0.3505E-01	0.1011E-02	-0.1359E-04	-0.2366E-03	-0.2310E-03	-0.2272E-03	0.6042E-03
	31.6	0.2838E-01	0.8458E-03	-0.6209E-03	-0.7856E-03	-0.7833E-03	-0.7763E-03	0.1919E-02
	50.1	0.2529E-01	0.7646E-03	-0.1169E-03	-0.2395E-03	-0.2384E-03	-0.2291E-03	0.3366E-02
	79.4	0.2135E-01	0.7569E-03	0.9805E-04	0.1414E-04	0.1125E-04	0.2353E-04	0.3387E-02
	125.9	0.2014E-01	0.8035E-03	0.9812E-04	0.3694E-04	0.3193E-04	0.4494E-04	0.3479E-02

Table D.9: xF_3 physics-model systematic errors.

x	Q^2	xF_3	ΔxF_3^{stat}	m_c	κ	α	B_c	Model Par.
0.0075	1.3	0.7632E-01	0.3700E-01	0.1359E-01	0.1645E-01	0.1628E-01	0.1624E-01	0.5832E-01
	2.0	0.1821	0.4039E-01	-0.9979E-02	-0.9852E-02	-0.1036E-01	-0.1027E-01	0.1902E-01
	3.2	0.9905E-01	0.6319E-01	0.1574E-01	0.1810E-01	0.1797E-01	0.1789E-01	0.2996E-04
0.0125	1.3	0.2122	0.3417E-01	0.5395E-02	0.7867E-02	0.7865E-02	0.7540E-02	0.4650E-01
	2.0	0.2239	0.3512E-01	-0.1497E-01	-0.1325E-01	-0.1370E-01	-0.1379E-01	0.1800E-01
	3.2	0.1684	0.4290E-01	0.7828E-02	0.1003E-01	0.9479E-02	0.9438E-02	0.3154E-02
	5.0	0.2486	0.5783E-01	0.1175E-01	0.1139E-01	0.1103E-01	0.1128E-01	0.1454E-01
0.0175	1.3	0.1894	0.4008E-01	-0.2836E-01	-0.2240E-01	-0.2221E-01	-0.2261E-01	0.1038E-01
	2.0	0.2767	0.3549E-01	-0.3451E-03	0.2224E-02	0.2064E-02	0.1797E-02	0.8623E-02
	3.2	0.2906	0.3887E-01	0.1843E-02	0.3464E-02	0.3032E-02	0.2963E-02	0.2282E-02
	5.0	0.2543	0.4715E-01	-0.9800E-02	-0.8532E-02	-0.9110E-02	-0.9107E-02	0.5958E-01
	7.9	0.3513	0.6743E-01	0.1199E-01	0.9808E-02	0.9939E-02	0.1063E-01	-0.2076E-01
0.0250	1.3	0.2339	0.3704E-01	0.2680E-02	0.1037E-01	0.1083E-01	0.1007E-01	0.4538E-01
	2.0	0.3517	0.2670E-01	-0.2296E-02	0.7999E-03	0.8603E-03	0.3730E-03	0.3579E-02
	3.2	0.3298	0.2605E-01	0.1124E-01	0.1376E-01	0.1338E-01	0.1321E-01	0.2335E-01
	5.0	0.3732	0.2882E-01	-0.9979E-02	-0.9030E-02	-0.9672E-02	-0.9635E-02	0.9812E-03
	7.9	0.3555	0.3521E-01	0.8042E-02	0.8219E-02	0.7691E-02	0.7908E-02	0.2694E-01
	12.6	0.3551	0.6568E-01	0.1386E-01	0.1244E-01	0.1130E-01	0.1154E-01	-0.3338E-01
0.0350	1.3	0.4047	0.5474E-01	-0.2683E-01	-0.1619E-01	-0.1527E-01	-0.1677E-01	0.1975E-01
	2.0	0.4121	0.3500E-01	-0.9801E-02	-0.4510E-02	-0.4215E-02	-0.4962E-02	0.9853E-02
	3.2	0.4078	0.2699E-01	-0.3431E-02	-0.2084E-03	-0.3520E-03	-0.6843E-03	0.9363E-02
	5.0	0.4159	0.2706E-01	-0.2065E-02	0.3323E-03	-0.1530E-03	-0.1969E-03	0.1465E-01
	7.9	0.4316	0.3064E-01	-0.7810E-02	-0.6783E-02	-0.7492E-02	-0.7338E-02	0.1493E-01
	12.6	0.4561	0.3901E-01	0.1763E-01	0.1722E-01	0.1680E-01	0.1716E-01	-0.3182E-02
	20.0	0.5198	0.9575E-01	-0.1400E-01	-0.1585E-01	-0.1646E-01	-0.1603E-01	0.3392E-04

(continued on next page)

Table D.9 (continued): xF_3 physics-model systematic errors.

x	Q^2	xF_3	ΔxF_3^{stat}	m_c	κ	α	B_c	Model Par.
0.0500	1.3	0.3967	0.6599E-01	-0.1656E-01	0.1290E-02	0.3394E-02	0.1423E-02	-0.1857E-01
	2.0	0.5068	0.3600E-01	0.5493E-02	0.1378E-01	0.1463E-01	0.1333E-01	-0.2332E-01
	3.2	0.4822	0.2357E-01	-0.4947E-02	-0.1420E-03	-0.3082E-04	-0.5564E-03	0.8910E-02
	5.0	0.5058	0.1989E-01	0.2903E-02	0.5584E-02	0.5250E-02	0.5105E-02	0.5892E-02
	7.9	0.5800	0.1979E-01	-0.2851E-02	-0.1979E-02	-0.2583E-02	-0.2430E-02	-0.1162E-01
	12.6	0.5615	0.2215E-01	0.5717E-02	0.5482E-02	0.4941E-02	0.5313E-02	0.3017E-02
	20.0	0.6184	0.3011E-01	0.1584E-01	0.1430E-01	0.1419E-01	0.1488E-01	-0.2798E-02
	31.6	0.6167	0.9101E-01	0.3154E-01	0.2877E-01	0.2857E-01	0.2937E-01	-0.1451E-01
0.0700	2.0	0.5093	0.5839E-01	-0.6139E-02	0.7592E-02	0.9356E-02	0.7608E-02	0.3585E-01
	3.2	0.6078	0.3228E-01	0.1531E-01	0.2097E-01	0.2151E-01	0.2055E-01	-0.9517E-02
	5.0	0.6209	0.2280E-01	-0.1303E-01	-0.9601E-02	-0.9654E-02	-0.9962E-02	-0.3236E-02
	7.9	0.6377	0.1946E-01	0.1116E-02	0.2650E-02	0.2155E-02	0.2214E-02	-0.1285E-02
	12.6	0.6370	0.2080E-01	0.3985E-02	0.4428E-02	0.3552E-02	0.3877E-02	0.1333E-01
	20.0	0.6485	0.2391E-01	-0.1765E-01	-0.1752E-01	-0.1835E-01	-0.1789E-01	-0.1368E-01
	31.6	0.6147	0.3683E-01	0.2517E-01	0.2460E-01	0.2393E-01	0.2453E-01	0.1312E-01
0.0900	2.0	0.7605	0.9046E-01	0.1362E-01	0.2694E-01	0.2907E-01	0.2628E-01	-0.7339E-01
	3.2	0.5799	0.4613E-01	-0.7693E-03	0.8624E-02	0.9877E-02	0.8597E-02	0.7118E-02
	5.0	0.6738	0.2707E-01	0.6162E-02	0.9910E-02	0.1011E-01	0.9630E-02	-0.7579E-02
	7.9	0.7340	0.2048E-01	-0.1169E-01	-0.1026E-01	-0.1052E-01	-0.1055E-01	-0.3879E-01
	12.6	0.7146	0.1980E-01	-0.1223E-02	-0.3464E-03	-0.1002E-02	-0.7053E-03	0.1198E-01
	20.0	0.7376	0.2177E-01	0.1382E-02	0.1022E-02	0.2534E-03	0.7723E-03	-0.1251E-01
	31.6	0.7384	0.2551E-01	0.2216E-01	0.2102E-01	0.2066E-01	0.2128E-01	-0.1402E-02
	50.1	0.7445	0.6111E-01	-0.1294E-02	-0.2369E-02	-0.3312E-02	-0.2584E-02	-0.5356E-01
0.1100	3.2	0.6630	0.6051E-01	-0.2939E-01	-0.1933E-01	-0.1748E-01	-0.1923E-01	-0.1661E-01
	5.0	0.7350	0.3292E-01	-0.1437E-01	-0.1020E-01	-0.9719E-02	-0.1043E-01	-0.2193E-01
	7.9	0.7624	0.2200E-01	-0.1897E-01	-0.1722E-01	-0.1737E-01	-0.1747E-01	-0.1693E-01
	12.6	0.7658	0.1940E-01	-0.4319E-02	-0.3537E-02	-0.4092E-02	-0.3789E-02	0.1910E-02
	20.0	0.7653	0.2086E-01	-0.1371E-01	-0.1336E-01	-0.1442E-01	-0.1385E-01	-0.1166E-01
	31.6	0.7374	0.2253E-01	0.7594E-02	0.7087E-02	0.6385E-02	0.7034E-02	-0.4403E-02
	50.1	0.7596	0.3705E-01	0.4334E-01	0.4248E-01	0.4162E-01	0.4233E-01	-0.2438E-02

(continued on next page)

Table D.9 (continued): xF_3 physics-model systematic errors.

x	Q^2	xF_3	ΔxF_3^{stat}	m_c	κ	α	B_c	Model Par.
0.1400	3.2	0.7642	0.6294E-01	-0.1244E-01	-0.3703E-02	-0.1116E-02	-0.3554E-02	0.7017E-02
	5.0	0.8043	0.3120E-01	0.1205E-02	0.5419E-02	0.6438E-02	0.5291E-02	-0.3070E-01
	7.9	0.7931	0.1804E-01	0.8941E-02	0.1040E-01	0.1056E-01	0.1027E-01	-0.7467E-02
	12.6	0.8154	0.1395E-01	0.3284E-02	0.3576E-02	0.3224E-02	0.3410E-02	-0.3084E-02
	20.0	0.8078	0.1328E-01	-0.2351E-02	-0.2314E-02	-0.2985E-02	-0.2466E-02	-0.1365E-01
	31.6	0.8071	0.1419E-01	0.1091E-03	-0.6440E-03	-0.1380E-02	-0.7307E-03	0.1205E-02
	50.1	0.8139	0.1711E-01	0.1818E-02	0.8676E-03	0.4019E-03	0.1142E-02	0.1164E-01
	79.4	0.8476	0.4090E-01	0.1490E-01	0.1317E-01	0.1268E-01	0.1346E-01	-0.3814E-01
0.1800	5.0	0.9044	0.4342E-01	-0.1358E-01	-0.1062E-01	-0.9023E-02	-0.1067E-01	-0.3741E-01
	7.9	0.8026	0.2349E-01	-0.1033E-01	-0.8943E-02	-0.8389E-02	-0.8953E-02	0.8594E-02
	12.6	0.8361	0.1532E-01	-0.2715E-02	-0.2770E-02	-0.2803E-02	-0.2774E-02	-0.2392E-01
	20.0	0.8247	0.1269E-01	0.4271E-02	0.3740E-02	0.3361E-02	0.3748E-02	-0.8863E-02
	31.6	0.8280	0.1303E-01	-0.4652E-02	-0.5368E-02	-0.5976E-02	-0.5324E-02	-0.9266E-02
	50.1	0.8111	0.1379E-01	0.1250E-02	0.4933E-03	0.1168E-03	0.8199E-03	-0.1166E-01
	79.4	0.7814	0.2082E-01	0.1464E-01	0.1387E-01	0.1317E-01	0.1397E-01	-0.2886E-02
0.2250	5.0	0.7368	0.5772E-01	0.3122E-01	0.3286E-01	0.3521E-01	0.3300E-01	0.1125
	7.9	0.7854	0.2710E-01	-0.2730E-02	-0.2260E-02	-0.1329E-02	-0.2261E-02	-0.2038E-01
	12.6	0.7824	0.1539E-01	-0.2621E-02	-0.3026E-02	-0.2822E-02	-0.2977E-02	-0.1195E-01
	20.0	0.8027	0.1141E-01	-0.4997E-02	-0.5900E-02	-0.6083E-02	-0.5841E-02	-0.5803E-02
	31.6	0.7763	0.1066E-01	0.2380E-02	0.1497E-02	0.1047E-02	0.1592E-02	-0.2765E-02
	50.1	0.7413	0.1131E-01	-0.7431E-03	-0.1508E-02	-0.2089E-02	-0.1448E-02	-0.1007E-01
	79.4	0.7731	0.1279E-01	-0.1168E-02	-0.2028E-02	-0.2502E-02	-0.1801E-02	-0.2031E-01
0.2750	7.9	0.7803	0.3387E-01	-0.7844E-03	-0.1917E-02	-0.7044E-03	-0.1871E-02	-0.2596E-01
	12.6	0.7207	0.1818E-01	-0.3216E-02	-0.4275E-02	-0.3847E-02	-0.4217E-02	0.1460E-01
	20.0	0.7066	0.1188E-01	0.4251E-02	0.3128E-02	0.3142E-02	0.3214E-02	-0.5763E-02
	31.6	0.6839	0.1017E-01	0.1021E-02	0.3123E-04	-0.2024E-03	0.1459E-03	-0.5724E-02
	50.1	0.6755	0.1040E-01	-0.1125E-02	-0.1994E-02	-0.2374E-02	-0.1845E-02	-0.9286E-02
	79.4	0.6373	0.1061E-01	0.4203E-02	0.3451E-02	0.2993E-02	0.3604E-02	-0.1273E-01
	125.9	0.6265	0.1623E-01	0.1079E-01	0.1018E-01	0.9811E-02	0.1049E-01	-0.1749E-01

(continued on next page)

Table D.9 (continued): xF_3 physics-model systematic errors.

x	Q^2	xF_3	ΔxF_3^{stat}	m_c	κ	α	B_c	Model Par.
0.3500	7.9	0.6352	0.3202E-01	0.2444E-03	-0.3008E-02	-0.1629E-02	-0.2999E-02	-0.3074E-01
	12.6	0.5946	0.1571E-01	0.4717E-02	0.2735E-02	0.3283E-02	0.2771E-02	-0.1083E-01
	20.0	0.5742	0.8879E-02	-0.1260E-02	-0.2804E-02	-0.2661E-02	-0.2710E-02	-0.1077E-01
	31.6	0.5490	0.6821E-02	0.2409E-02	0.1200E-02	0.1140E-02	0.1337E-02	-0.5734E-02
	50.1	0.5240	0.6214E-02	-0.2977E-03	-0.1260E-02	-0.1464E-02	-0.1121E-02	-0.8678E-02
	79.4	0.4881	0.6307E-02	-0.5783E-03	-0.1275E-02	-0.1531E-02	-0.1137E-02	-0.5843E-02
	125.9	0.4831	0.7438E-02	0.3344E-02	0.2750E-02	0.2494E-02	0.2932E-02	-0.1044E-01
0.4500	12.6	0.3987	0.1766E-01	-0.3502E-02	-0.6275E-02	-0.5783E-02	-0.6293E-02	-0.1202E-02
	20.0	0.3729	0.9599E-02	-0.1978E-02	-0.3650E-02	-0.3480E-02	-0.3616E-02	-0.1079E-01
	31.6	0.3487	0.6094E-02	0.1875E-02	0.7269E-03	0.7439E-03	0.8095E-03	-0.1034E-01
	50.1	0.3216	0.5045E-02	-0.1768E-02	-0.2571E-02	-0.2642E-02	-0.2483E-02	-0.1050E-01
	79.4	0.3078	0.4923E-02	0.8715E-03	0.2783E-03	0.1665E-03	0.3952E-03	-0.7437E-02
	125.9	0.2885	0.4990E-02	0.2061E-02	0.1618E-02	0.1488E-02	0.1739E-02	-0.7703E-02
	199.5	0.2563	0.8264E-02	0.4119E-02	0.3797E-02	0.3669E-02	0.3909E-02	-0.7442E-02
0.5500	12.6	0.2731	0.1866E-01	0.7904E-03	-0.2200E-02	-0.1805E-02	-0.2206E-02	-0.1495E-01
	20.0	0.1973	0.9353E-02	-0.4878E-02	-0.6323E-02	-0.6191E-02	-0.6322E-02	-0.3759E-02
	31.6	0.1834	0.5175E-02	0.2182E-02	0.1280E-02	0.1303E-02	0.1309E-02	-0.2794E-02
	50.1	0.1733	0.4033E-02	0.1293E-02	0.6865E-03	0.6627E-03	0.7309E-03	-0.5648E-02
	79.4	0.1595	0.3540E-02	-0.9270E-04	-0.5026E-03	-0.5527E-03	-0.4530E-03	-0.4670E-02
	125.9	0.1454	0.3616E-02	0.3970E-03	0.1029E-03	0.3619E-04	0.1504E-03	-0.6562E-02
	199.5	0.1314	0.4446E-02	0.9574E-03	0.7606E-03	0.7022E-03	0.8214E-03	-0.5466E-02
0.6500	12.6	0.8328E-01	0.1967E-01	0.5592E-02	0.3875E-02	0.4057E-02	0.3827E-02	0.1661E-01
	20.0	0.1069	0.7406E-02	0.3648E-02	0.2467E-02	0.2541E-02	0.2458E-02	-0.1076E-02
	31.6	0.8762E-01	0.3702E-02	0.1362E-02	0.7360E-03	0.7532E-03	0.7449E-03	0.2487E-03
	50.1	0.8174E-01	0.2626E-02	0.1146E-02	0.7433E-03	0.7376E-03	0.7673E-03	-0.1084E-02
	79.4	0.6648E-01	0.2246E-02	-0.1453E-03	-0.3803E-03	-0.3980E-03	-0.3612E-03	-0.5902E-03
	125.9	0.5806E-01	0.2255E-02	-0.6416E-03	-0.7992E-03	-0.8252E-03	-0.7800E-03	0.1032E-03
0.7500	20.0	0.3791E-01	0.4179E-02	0.1536E-02	0.1026E-02	0.1060E-02	0.1022E-02	0.6503E-03
	31.6	0.2875E-01	0.2163E-02	0.1293E-02	0.9982E-03	0.1005E-02	0.1001E-02	0.3486E-02
	50.1	0.2539E-01	0.1359E-02	0.2873E-03	0.1031E-03	0.1011E-03	0.1069E-03	0.3765E-02
	79.4	0.1963E-01	0.1112E-02	0.9241E-04	-0.1033E-04	-0.1533E-04	-0.4441E-05	0.4297E-02
	125.9	0.1951E-01	0.1072E-02	-0.1804E-03	-0.2534E-03	-0.2609E-03	-0.2484E-03	0.4145E-02

Table D.10: F_2, xF_3, and the associated statistical errors from E744 only.

x	Q^2	F_2^{744}	ΔF_2^{744}	xF_3^{744}	ΔxF_3^{744}	$\Delta F_2 \Delta xF_3$
0.0075	1.3	1.333	0.4603E-01	0.1016	0.5711E-01	-0.1393E-02
	2.0	1.360	0.5504E-01	0.2033	0.5995E-01	-0.1810E-02
	3.2	1.893	0.1211	-0.6454E-01	0.1147	-0.1057E-01
0.0125	1.3	1.247	0.3745E-01	0.2133	0.5330E-01	-0.7966E-03
	2.0	1.305	0.4130E-01	0.2541	0.5196E-01	-0.8537E-03
	3.2	1.530	0.5951E-01	0.1464	0.6728E-01	-0.2363E-02
	5.0	1.738	0.9610E-01	0.2186	0.9269E-01	-0.5692E-02
0.0175	1.3	1.259	0.3784E-01	0.2021	0.6297E-01	-0.9330E-03
	2.0	1.386	0.3968E-01	0.2500	0.5428E-01	-0.7516E-03
	3.2	1.525	0.4829E-01	0.3271	0.6007E-01	-0.1214E-02
	5.0	1.638	0.6715E-01	0.1943	0.7344E-01	-0.3019E-02
	7.9	1.589	0.1141	0.1984	0.1077	-0.8134E-02
0.0250	1.3	1.246	0.2693E-01	0.2371	0.5708E-01	-0.5525E-03
	2.0	1.308	0.2593E-01	0.3904	0.4080E-01	-0.2684E-03
	3.2	1.461	0.2925E-01	0.3553	0.3931E-01	-0.3835E-03
	5.0	1.601	0.3560E-01	0.4376	0.4376E-01	-0.6075E-03
	7.9	1.669	0.5183E-01	0.3455	0.5531E-01	-0.1691E-02
	12.6	1.687	0.9678E-01	0.4512	0.9131E-01	-0.5037E-02
0.0350	1.3	1.219	0.2925E-01	0.3950	0.8704E-01	-0.8824E-03
	2.0	1.328	0.2753E-01	0.4276	0.5319E-01	-0.4411E-03
	3.2	1.384	0.2771E-01	0.4113	0.4175E-01	-0.3274E-03
	5.0	1.554	0.3184E-01	0.3833	0.4210E-01	-0.4819E-03
	7.9	1.609	0.3958E-01	0.3948	0.4783E-01	-0.8954E-03
	12.6	1.787	0.5937E-01	0.4577	0.6124E-01	-0.1978E-02
	20.0	1.814	0.1608	0.5540	0.1498	-0.1545E-01

(continued on next page)

Table D.10 (continued): F_2, xF_3, and the associated statistical errors from E744 only.

x	Q^2	F_2^{744}	ΔF_2^{744}	xF_3^{744}	ΔxF_3^{744}	$\Delta F_2 \Delta xF_3$
0.0500	1.3	1.227	0.2363E-01	0.4097	0.1013	-0.8829E-03
	2.0	1.326	0.2063E-01	0.5850	0.5434E-01	-0.2698E-03
	3.2	1.455	0.2035E-01	0.5083	0.3675E-01	-0.1791E-03
	5.0	1.528	0.2096E-01	0.4971	0.3064E-01	-0.1647E-03
	7.9	1.617	0.2326E-01	0.5933	0.3036E-01	-0.1848E-03
	12.6	1.631	0.2916E-01	0.5596	0.3434E-01	-0.3852E-03
	20.0	1.685	0.4604E-01	0.5455	0.4688E-01	-0.1062E-02
	31.6	1.578	0.1397	0.6437	0.1311	-0.1020E-01
0.0700	2.0	1.320	0.2389E-01	0.4711	0.9112E-01	-0.7757E-03
	3.2	1.389	0.2131E-01	0.5636	0.5040E-01	-0.2745E-03
	5.0	1.493	0.2114E-01	0.6009	0.3596E-01	-0.1808E-03
	7.9	1.511	0.2102E-01	0.6487	0.2968E-01	-0.1025E-03
	12.6	1.523	0.2408E-01	0.7099	0.3106E-01	-0.1782E-03
	20.0	1.628	0.3324E-01	0.5975	0.3797E-01	-0.5386E-03
	31.6	1.560	0.5748E-01	0.5758	0.5736E-01	-0.1685E-02
0.0900	2.0	1.324	0.2828E-01	0.7165	0.1411	-0.1354E-02
	3.2	1.353	0.2300E-01	0.5614	0.7074E-01	-0.4737E-03
	5.0	1.433	0.2104E-01	0.7183	0.4184E-01	-0.1473E-03
	7.9	1.488	0.2054E-01	0.7048	0.3184E-01	-0.8228E-04
	12.6	1.521	0.2272E-01	0.6887	0.3077E-01	-0.1158E-03
	20.0	1.512	0.2646E-01	0.7456	0.3289E-01	-0.1950E-03
	31.6	1.511	0.3626E-01	0.7637	0.3881E-01	-0.4114E-03
	50.1	1.529	0.9833E-01	0.7459	0.9554E-01	-0.4496E-02
0.1100	3.2	1.325	0.2444E-01	0.6099	0.9312E-01	-0.7166E-03
	5.0	1.383	0.2160E-01	0.6748	0.5111E-01	-0.2226E-03
	7.9	1.375	0.1977E-01	0.7458	0.3369E-01	-0.6244E-04
	12.6	1.404	0.2099E-01	0.7159	0.2994E-01	-0.7607E-04
	20.0	1.445	0.2439E-01	0.7578	0.3176E-01	-0.1062E-03
	31.6	1.370	0.2959E-01	0.7131	0.3412E-01	-0.2797E-03
	50.1	1.512	0.5451E-01	0.8450	0.5514E-01	-0.8540E-03

(continued on next page)

Table D.10 (continued): F_2, xF_3, and the associated statistical errors from E744 only.

x	Q^2	F_2^{744}	ΔF_2^{744}	xF_3^{744}	ΔxF_3^{744}	$\Delta F_2 \Delta xF_3$
0.1400	3.2	1.284	0.1991E-01	0.7752	0.9693E-01	-0.5933E-03
	5.0	1.307	0.1588E-01	0.7619	0.4775E-01	-0.1755E-03
	7.9	1.303	0.1423E-01	0.7747	0.2802E-01	-0.2486E-04
	12.6	1.302	0.1365E-01	0.8330	0.2109E-01	0.1091E-04
	20.0	1.324	0.1505E-01	0.7884	0.2049E-01	-0.1013E-04
	31.6	1.268	0.1704E-01	0.8379	0.2124E-01	-0.1123E-04
	50.1	1.250	0.2456E-01	0.7967	0.2663E-01	-0.1241E-03
	79.4	1.206	0.5698E-01	0.8601	0.5651E-01	-0.9716E-04
0.1800	5.0	1.167	0.1679E-01	0.9528	0.6595E-01	-0.2619E-03
	7.9	1.188	0.1463E-01	0.8468	0.3569E-01	-0.5000E-04
	12.6	1.173	0.1357E-01	0.8338	0.2363E-01	0.1234E-04
	20.0	1.161	0.1352E-01	0.8262	0.1949E-01	0.3651E-04
	31.6	1.131	0.1502E-01	0.8103	0.1978E-01	0.2298E-04
	50.1	1.115	0.1873E-01	0.7782	0.2210E-01	-0.2290E-04
	79.4	1.097	0.3084E-01	0.7968	0.3204E-01	-0.3837E-04
0.2250	5.0	1.082	0.1756E-01	0.7287	0.8728E-01	-0.4513E-03
	7.9	1.052	0.1349E-01	0.7930	0.4140E-01	-0.9903E-04
	12.6	1.028	0.1191E-01	0.7820	0.2387E-01	-0.4475E-05
	20.0	0.9941	0.1109E-01	0.7779	0.1734E-01	0.3208E-04
	31.6	0.9707	0.1172E-01	0.7742	0.1599E-01	0.4215E-04
	50.1	0.9574	0.1364E-01	0.7580	0.1719E-01	0.3928E-04
	79.4	0.9443	0.1821E-01	0.7778	0.2001E-01	0.7032E-04
0.2750	7.9	0.8951	0.1378E-01	0.8230	0.5225E-01	-0.1486E-03
	12.6	0.8591	0.1162E-01	0.7038	0.2747E-01	-0.5516E-05
	20.0	0.8508	0.1084E-01	0.7162	0.1854E-01	0.4165E-04
	31.6	0.8265	0.1088E-01	0.6740	0.1553E-01	0.5367E-04
	50.1	0.7962	0.1207E-01	0.6624	0.1581E-01	0.5731E-04
	79.4	0.7385	0.1354E-01	0.6323	0.1582E-01	0.7104E-04
	125.9	0.7192	0.2516E-01	0.5974	0.2624E-01	0.1497E-03

(continued on next page)

Table D.10 (continued): F_2, xF_3, and the associated statistical errors from E744 only.

x	Q^2	F_2^{744}	ΔF_2^{744}	xF_3^{744}	ΔxF_3^{744}	$\Delta F_2 \Delta xF_3$
0.3500	7.9	0.6937	0.1027E-01	0.6197	0.4978E-01	-0.1317E-03
	12.6	0.6608	0.8115E-02	0.5959	0.2433E-01	-0.2433E-04
	20.0	0.6238	0.6940E-02	0.5597	0.1369E-01	0.1458E-04
	31.6	0.5936	0.6589E-02	0.5416	0.1021E-01	0.2454E-04
	50.1	0.5715	0.6835E-02	0.5189	0.9280E-02	0.2761E-04
	79.4	0.5502	0.7810E-02	0.4958	0.9822E-02	0.2527E-04
	125.9	0.5234	0.1024E-01	0.4855	0.1127E-01	0.6371E-04
0.4500	12.6	0.4161	0.6987E-02	0.4254	0.2729E-01	-0.2676E-04
	20.0	0.3928	0.5956E-02	0.3669	0.1449E-01	0.4965E-05
	31.6	0.3575	0.5312E-02	0.3494	0.9237E-02	0.1619E-04
	50.1	0.3313	0.5313E-02	0.3199	0.7648E-02	0.1961E-04
	79.4	0.3175	0.5716E-02	0.3063	0.7524E-02	0.2012E-04
	125.9	0.2900	0.6387E-02	0.2871	0.7552E-02	0.2834E-04
	199.5	0.2785	0.1207E-01	0.2595	0.1275E-01	0.8835E-04
0.5500	12.6	0.2376	0.5867E-02	0.2974	0.2839E-01	-0.3452E-04
	20.0	0.2124	0.4700E-02	0.2080	0.1408E-01	-0.5271E-05
	31.6	0.1923	0.4044E-02	0.1842	0.7958E-02	0.6767E-05
	50.1	0.1738	0.3941E-02	0.1726	0.6087E-02	0.1129E-04
	79.4	0.1619	0.4048E-02	0.1596	0.5468E-02	0.1343E-04
	125.9	0.1522	0.4323E-02	0.1500	0.5420E-02	0.1269E-04
	199.5	0.1356	0.6177E-02	0.1303	0.6804E-02	0.2624E-04
0.6500	12.6	0.1179	0.5130E-02	0.7896E-01	0.2978E-01	-0.5464E-04
	20.0	0.1009	0.3167E-02	0.1049	0.1130E-01	-0.4423E-05
	31.6	0.8366E-01	0.2605E-02	0.9034E-01	0.5833E-02	0.2473E-05
	50.1	0.7493E-01	0.2394E-02	0.7783E-01	0.3984E-02	0.3911E-05
	79.4	0.6864E-01	0.2425E-02	0.6780E-01	0.3415E-02	0.4163E-05
	125.9	0.6081E-01	0.2542E-02	0.5821E-01	0.3311E-02	0.3921E-05
0.7500	20.0	0.3362E-01	0.1506E-02	0.3623E-01	0.6255E-02	-0.1890E-05
	31.6	0.2768E-01	0.1270E-02	0.2630E-01	0.3283E-02	-0.2510E-06
	50.1	0.2526E-01	0.1131E-02	0.2737E-01	0.2022E-02	0.9193E-06
	79.4	0.2137E-01	0.1149E-02	0.1954E-01	0.1699E-02	0.7033E-06
	125.9	0.2127E-01	0.1278E-02	0.2017E-01	0.1707E-02	0.8978E-06

Table D.11: F_2, xF_3, and the associated statistical errors from E770 only.

x	Q^2	F_2^{770}	ΔF_2^{770}	xF_3^{770}	ΔxF_3^{770}	$\Delta F_2 \Delta xF_3$
0.0075	1.3	1.284	0.3899E-01	0.5826E-01	0.4858E-01	-0.1016E-02
	2.0	1.371	0.5008E-01	0.1646	0.5466E-01	-0.1587E-02
	3.2	1.446	0.8036E-01	0.1541	0.7594E-01	-0.4045E-02
0.0125	1.3	1.230	0.3149E-01	0.2107	0.4457E-01	-0.4606E-03
	2.0	1.360	0.3767E-01	0.1979	0.4767E-01	-0.7660E-03
	3.2	1.524	0.4930E-01	0.1839	0.5573E-01	-0.1478E-02
	5.0	1.634	0.7695E-01	0.2658	0.7405E-01	-0.3385E-02
0.0175	1.3	1.248	0.3159E-01	0.1795	0.5208E-01	-0.4774E-03
	2.0	1.386	0.3434E-01	0.2969	0.4691E-01	-0.5156E-03
	3.2	1.531	0.4085E-01	0.2641	0.5097E-01	-0.8345E-03
	5.0	1.556	0.5630E-01	0.2956	0.6153E-01	-0.1980E-02
	7.9	1.499	0.9201E-01	0.4544	0.8666E-01	-0.4573E-02
0.0250	1.3	1.211	0.2306E-01	0.2304	0.4869E-01	-0.3662E-03
	2.0	1.312	0.2260E-01	0.3226	0.3532E-01	-0.1695E-03
	3.2	1.465	0.2582E-01	0.3098	0.3478E-01	-0.3071E-03
	5.0	1.527	0.3103E-01	0.3255	0.3831E-01	-0.4925E-03
	7.9	1.656	0.4289E-01	0.3621	0.4569E-01	-0.1058E-02
	12.6	1.852	0.1012	0.2469	0.9549E-01	-0.6953E-02
0.0350	1.3	1.176	0.2390E-01	0.4058	0.7056E-01	-0.4150E-03
	2.0	1.331	0.2421E-01	0.4002	0.4649E-01	-0.2938E-03
	3.2	1.433	0.2366E-01	0.4071	0.3540E-01	-0.1895E-03
	5.0	1.551	0.2692E-01	0.4398	0.3545E-01	-0.2296E-03
	7.9	1.592	0.3308E-01	0.4576	0.3996E-01	-0.5287E-03
	12.6	1.696	0.4920E-01	0.4524	0.5063E-01	-0.1232E-02
	20.0	1.755	0.1337	0.4966	0.1245	-0.1077E-01

(continued on next page)

Table D.11 (continued): F_2, xF_3, and the associated statistical errors from E770 only.

x	Q^2	F_2^{770}	ΔF_2^{770}	xF_3^{770}	ΔxF_3^{770}	$\Delta F_2 \Delta xF_3$
0.0500	1.3	1.229	0.2044E-01	0.3870	0.8711E-01	-0.5157E-03
	2.0	1.343	0.1835E-01	0.4457	0.4807E-01	-0.1877E-03
	3.2	1.419	0.1714E-01	0.4627	0.3073E-01	-0.1046E-03
	5.0	1.496	0.1799E-01	0.5111	0.2616E-01	-0.9425E-04
	7.9	1.576	0.1994E-01	0.5698	0.2609E-01	-0.1289E-03
	12.6	1.596	0.2462E-01	0.5623	0.2899E-01	-0.2559E-03
	20.0	1.687	0.3872E-01	0.6716	0.3934E-01	-0.6527E-03
	31.6	1.664	0.1351	0.5891	0.1267	-0.1065E-01
0.0700	2.0	1.325	0.2018E-01	0.5381	0.7628E-01	-0.3716E-03
	3.2	1.398	0.1807E-01	0.6409	0.4219E-01	-0.9311E-04
	5.0	1.476	0.1762E-01	0.6333	0.2958E-01	-0.5999E-04
	7.9	1.547	0.1829E-01	0.6300	0.2578E-01	-0.6479E-04
	12.6	1.568	0.2164E-01	0.5776	0.2801E-01	-0.1527E-03
	20.0	1.580	0.2711E-01	0.6810	0.3086E-01	-0.2635E-03
	31.6	1.615	0.4828E-01	0.6446	0.4808E-01	-0.1064E-02
0.0900	2.0	1.314	0.2386E-01	0.7900	0.1181	-0.6639E-03
	3.2	1.400	0.1988E-01	0.5960	0.6087E-01	-0.3096E-03
	5.0	1.430	0.1802E-01	0.6415	0.3553E-01	-0.7735E-04
	7.9	1.437	0.1752E-01	0.7512	0.2681E-01	-0.5826E-05
	12.6	1.471	0.1913E-01	0.7314	0.2588E-01	-0.5181E-04
	20.0	1.509	0.2332E-01	0.7314	0.2904E-01	-0.1573E-03
	31.6	1.507	0.3165E-01	0.7192	0.3384E-01	-0.3304E-03
	50.1	1.562	0.8204E-01	0.7446	0.7960E-01	-0.2694E-02
0.1100	3.2	1.343	0.2109E-01	0.7057	0.7975E-01	-0.3770E-03
	5.0	1.351	0.1846E-01	0.7750	0.4315E-01	-0.6818E-04
	7.9	1.394	0.1733E-01	0.7763	0.2911E-01	0.2410E-05
	12.6	1.423	0.1805E-01	0.8037	0.2554E-01	-0.1016E-06
	20.0	1.452	0.2125E-01	0.7713	0.2768E-01	-0.5725E-04
	31.6	1.392	0.2606E-01	0.7565	0.3001E-01	-0.2023E-03
	50.1	1.505	0.4967E-01	0.6923	0.5021E-01	-0.1001E-02

(continued on next page)

Table D.11 (continued): F_2, xF_3, and the associated statistical errors from E770 only.

x	Q^2	F_2^{770}	ΔF_2^{770}	xF_3^{770}	ΔxF_3^{770}	$\Delta F_2 \Delta xF_3$
0.1400	3.2	1.275	0.1712E-01	0.7546	0.8283E-01	-0.3442E-03
	5.0	1.304	0.1387E-01	0.8362	0.4129E-01	-0.8075E-04
	7.9	1.302	0.1214E-01	0.8063	0.2360E-01	0.5386E-05
	12.6	1.333	0.1212E-01	0.8021	0.1859E-01	0.1218E-04
	20.0	1.303	0.1287E-01	0.8208	0.1747E-01	0.1155E-04
	31.6	1.273	0.1527E-01	0.7821	0.1907E-01	-0.2599E-04
	50.1	1.254	0.2069E-01	0.8264	0.2237E-01	-0.4427E-04
	79.4	1.353	0.6150E-01	0.8086	0.6098E-01	-0.1315E-02
0.1800	5.0	1.198	0.1481E-01	0.8703	0.5774E-01	-0.1465E-03
	7.9	1.169	0.1289E-01	0.7684	0.3121E-01	-0.3217E-04
	12.6	1.192	0.1181E-01	0.8396	0.2020E-01	0.3939E-04
	20.0	1.151	0.1166E-01	0.8232	0.1672E-01	0.3645E-04
	31.6	1.144	0.1318E-01	0.8418	0.1734E-01	0.2861E-04
	50.1	1.073	0.1520E-01	0.8282	0.1781E-01	0.4211E-04
	79.4	1.099	0.2641E-01	0.7702	0.2740E-01	-0.3903E-04
0.2250	5.0	1.110	0.1551E-01	0.7429	0.7695E-01	-0.3531E-03
	7.9	1.054	0.1182E-01	0.7798	0.3591E-01	-0.3546E-04
	12.6	1.028	0.1031E-01	0.7827	0.2026E-01	0.3367E-04
	20.0	1.006	0.9813E-02	0.8219	0.1517E-01	0.3145E-04
	31.6	0.9901	0.1049E-01	0.7786	0.1430E-01	0.4030E-04
	50.1	0.9442	0.1192E-01	0.7287	0.1502E-01	0.2521E-04
	79.4	0.9258	0.1520E-01	0.7692	0.1665E-01	0.6789E-04
0.2750	7.9	0.9096	0.1187E-01	0.7511	0.4457E-01	-0.5797E-04
	12.6	0.8904	0.1039E-01	0.7357	0.2428E-01	0.1043E-04
	20.0	0.8518	0.9193E-02	0.7001	0.1548E-01	0.3776E-04
	31.6	0.8110	0.9468E-02	0.6911	0.1347E-01	0.4287E-04
	50.1	0.7995	0.1055E-01	0.6855	0.1381E-01	0.4672E-04
	79.4	0.7690	0.1227E-01	0.6399	0.1433E-01	0.4327E-04
	125.9	0.7158	0.2031E-01	0.6427	0.2109E-01	0.2265E-03

(continued on next page)

Table D.11 (continued): F_2, xF_3, and the associated statistical errors from E770 only.

x	Q^2	F_2^{770}	ΔF_2^{770}	xF_3^{770}	ΔxF_3^{770}	$\Delta F_2 \Delta xF_3$
0.3500	7.9	0.7135	0.8728E-02	0.6508	0.4192E-01	-0.5492E-04
	12.6	0.6745	0.6957E-02	0.5954	0.2061E-01	-0.2904E-05
	20.0	0.6307	0.6052E-02	0.5853	0.1171E-01	0.1939E-04
	31.6	0.6100	0.6013E-02	0.5557	0.9183E-02	0.2387E-04
	50.1	0.5729	0.6157E-02	0.5283	0.8367E-02	0.2241E-04
	79.4	0.5318	0.6573E-02	0.4822	0.8233E-02	0.2098E-04
	125.9	0.5271	0.9019E-02	0.4810	0.9910E-02	0.4485E-04
0.4500	12.6	0.4031	0.5978E-02	0.3785	0.2318E-01	-0.1408E-04
	20.0	0.3997	0.5333E-02	0.3780	0.1282E-01	0.7586E-05
	31.6	0.3635	0.4779E-02	0.3488	0.8136E-02	0.1694E-04
	50.1	0.3318	0.4704E-02	0.3229	0.6721E-02	0.1715E-04
	79.4	0.3147	0.4995E-02	0.3085	0.6537E-02	0.1897E-04
	125.9	0.2948	0.5649E-02	0.2897	0.6652E-02	0.2341E-04
	199.5	0.2713	0.1030E-01	0.2539	0.1085E-01	0.6620E-04
0.5500	12.6	0.2377	0.5152E-02	0.2545	0.2478E-01	-0.2154E-04
	20.0	0.2145	0.4213E-02	0.1889	0.1252E-01	-0.2537E-05
	31.6	0.1864	0.3533E-02	0.1823	0.6826E-02	0.7329E-05
	50.1	0.1783	0.3529E-02	0.1740	0.5385E-02	0.9257E-05
	79.4	0.1565	0.3441E-02	0.1593	0.4645E-02	0.1003E-04
	125.9	0.1487	0.3878E-02	0.1418	0.4859E-02	0.9075E-05
	199.5	0.1339	0.5367E-02	0.1321	0.5889E-02	0.2227E-04
0.6500	12.6	0.1188	0.4536E-02	0.8680E-01	0.2623E-01	-0.3706E-04
	20.0	0.9914E-01	0.2770E-02	0.1083	0.9810E-02	-0.2617E-05
	31.6	0.8022E-01	0.2177E-02	0.8555E-01	0.4798E-02	0.2506E-05
	50.1	0.7854E-01	0.2162E-02	0.8501E-01	0.3514E-02	0.4185E-05
	79.4	0.6626E-01	0.2130E-02	0.6539E-01	0.2985E-02	0.3546E-05
	125.9	0.6123E-01	0.2367E-02	0.5794E-01	0.3079E-02	0.3399E-05
0.7500	20.0	0.3627E-01	0.1366E-02	0.3968E-01	0.5625E-02	-0.9278E-06
	31.6	0.2911E-01	0.1144E-02	0.3097E-01	0.2901E-02	0.4584E-06
	50.1	0.2539E-01	0.1039E-02	0.2371E-01	0.1836E-02	0.6561E-06
	79.4	0.2134E-01	0.1008E-02	0.1969E-01	0.1475E-02	0.6742E-06
	125.9	0.1941E-01	0.1034E-02	0.1903E-01	0.1378E-02	0.6563E-06

Table D.12: Systematic errors for E744 F_2.

x	Q^2	F_2^{744}	$\Delta F_2^{744,stat}$	C_{HAD}^{744}	$(B/A)_{744}^{\nu}$	$(B/A)_{744}^{\bar{\nu}}$
0.0075	1.3	1.333	0.4603E-01	0.1806E-01	-0.5247E-02	-0.7445E-03
	2.0	1.360	0.5504E-01	0.2479E-01	-0.6934E-02	-0.2110E-02
	3.2	1.893	0.1211	0.1603E-01	-0.1116E-01	-0.6074E-02
0.0125	1.3	1.247	0.3745E-01	0.4786E-02	-0.3439E-02	0.3760E-03
	2.0	1.305	0.4130E-01	0.1453E-01	-0.4917E-02	-0.6085E-03
	3.2	1.530	0.5951E-01	0.2753E-01	-0.7590E-02	-0.2573E-02
	5.0	1.738	0.9610E-01	0.2819E-01	-0.1098E-01	-0.4600E-02
0.0175	1.3	1.259	0.3784E-01	0.1489E-01	-0.2837E-02	0.1027E-02
	2.0	1.386	0.3968E-01	0.1299E-01	-0.4132E-02	0.1350E-03
	3.2	1.525	0.4829E-01	0.2744E-01	-0.6261E-02	-0.1182E-02
	5.0	1.638	0.6715E-01	0.3863E-01	-0.8697E-02	-0.3242E-02
	7.9	1.589	0.1141	0.1984E-01	-0.1075E-01	-0.4957E-02
0.0250	1.3	1.246	0.2693E-01	0.2660E-03	-0.2351E-02	0.1350E-02
	2.0	1.308	0.2593E-01	0.7706E-02	-0.2948E-02	0.7195E-03
	3.2	1.461	0.2925E-01	0.1082E-01	-0.4701E-02	-0.1560E-03
	5.0	1.601	0.3560E-01	0.2212E-01	-0.7157E-02	-0.1496E-02
	7.9	1.669	0.5183E-01	0.3682E-01	-0.9623E-02	-0.3249E-02
	12.6	1.687	0.9678E-01	0.4846E-01	-0.1279E-01	-0.4746E-02
0.0350	1.3	1.219	0.2925E-01	0.9290E-03	-0.1863E-02	0.1482E-02
	2.0	1.328	0.2753E-01	0.8009E-02	-0.2487E-02	0.1144E-02
	3.2	1.384	0.2771E-01	0.1410E-01	-0.3382E-02	0.5465E-03
	5.0	1.554	0.3184E-01	0.2348E-01	-0.5466E-02	-0.4205E-03
	7.9	1.609	0.3958E-01	0.2041E-01	-0.7766E-02	-0.2032E-02
	12.6	1.787	0.5937E-01	0.1912E-01	-0.1125E-01	-0.3851E-02
	20.0	1.814	0.1608	0.1524	-0.1500E-01	-0.5641E-02

(continued on next page)

Table D.12 (continued): Systematic errors for E744 F_2.

x	Q^2	F_2^{744}	$\Delta F_2^{744,stat}$	C_{HAD}^{744}	$(B/A)_{744}^{\nu}$	$(B/A)_{744}^{\bar{\nu}}$
0.0500	1.3	1.227	0.2363E-01	0.8209E-02	-0.1826E-02	0.1774E-02
	2.0	1.326	0.2063E-01	0.4175E-02	-0.2002E-02	0.1395E-02
	3.2	1.455	0.2035E-01	0.7820E-02	-0.2870E-02	0.1054E-02
	5.0	1.528	0.2096E-01	0.1141E-01	-0.4086E-02	0.3040E-03
	7.9	1.617	0.2326E-01	0.1838E-01	-0.6178E-02	-0.7805E-03
	12.6	1.631	0.2916E-01	0.2809E-01	-0.8566E-02	-0.2129E-02
	20.0	1.685	0.4604E-01	0.5110E-01	-0.1155E-01	-0.3692E-02
	31.6	1.578	0.1397	0.5738E-01	-0.1424E-01	-0.4312E-02
0.0700	2.0	1.320	0.2389E-01	0.7306E-02	-0.1988E-02	0.1783E-02
	3.2	1.389	0.2131E-01	0.9382E-02	-0.2286E-02	0.1339E-02
	5.0	1.493	0.2114E-01	0.5652E-02	-0.3106E-02	0.8810E-03
	7.9	1.511	0.2102E-01	0.1063E-01	-0.4368E-02	0.5949E-04
	12.6	1.523	0.2408E-01	0.2454E-01	-0.6506E-02	-0.1063E-02
	20.0	1.628	0.3324E-01	0.2678E-01	-0.9354E-02	-0.2542E-02
	31.6	1.560	0.5748E-01	0.4448E-01	-0.1184E-01	-0.3716E-02
0.0900	2.0	1.324	0.2828E-01	0.6175E-03	-0.1797E-02	0.1845E-02
	3.2	1.353	0.2300E-01	0.1828E-02	-0.2036E-02	0.1610E-02
	5.0	1.433	0.2104E-01	0.8014E-02	-0.2490E-02	0.9910E-03
	7.9	1.488	0.2054E-01	0.1065E-01	-0.3502E-02	0.4245E-03
	12.6	1.521	0.2272E-01	0.1180E-01	-0.5367E-02	-0.4605E-03
	20.0	1.512	0.2646E-01	0.2569E-01	-0.7626E-02	-0.1492E-02
	31.6	1.511	0.3626E-01	0.2935E-01	-0.1033E-01	-0.2280E-02
	50.1	1.529	0.9833E-01	0.4008E-01	-0.1369E-01	-0.3519E-02
0.1100	3.2	1.325	0.2444E-01	0.4798E-04	-0.1961E-02	0.1683E-02
	5.0	1.383	0.2160E-01	0.6594E-02	-0.2231E-02	0.1245E-02
	7.9	1.375	0.1977E-01	0.1429E-01	-0.2784E-02	0.5895E-03
	12.6	1.404	0.2099E-01	0.1413E-01	-0.4162E-02	-0.8655E-04
	20.0	1.445	0.2439E-01	0.1630E-01	-0.6351E-02	-0.1016E-02
	31.6	1.370	0.2959E-01	0.1957E-01	-0.8313E-02	-0.1785E-02
	50.1	1.512	0.5451E-01	0.3388E-01	-0.1250E-01	-0.2589E-02

(continued on next page)

Table D.12 (continued): Systematic errors for E744 F_2.

x	Q^2	F_2^{744}	$\Delta F_2^{744,stat}$	C_{HAD}^{744}	$(B/A)_{744}^{\nu}$	$(B/A)_{744}^{\bar{\nu}}$
0.1400	3.2	1.284	0.1991E-01	0.2738E-02	-0.1752E-02	0.1668E-02
	5.0	1.307	0.1588E-01	0.4422E-02	-0.1917E-02	0.1331E-02
	7.9	1.303	0.1423E-01	0.2431E-02	-0.2274E-02	0.7930E-03
	12.6	1.302	0.1365E-01	0.9010E-02	-0.3083E-02	0.1475E-03
	20.0	1.324	0.1505E-01	0.1193E-01	-0.4862E-02	-0.4835E-03
	31.6	1.268	0.1704E-01	0.1806E-01	-0.6777E-02	-0.1103E-02
	50.1	1.250	0.2456E-01	0.2272E-01	-0.9057E-02	-0.1584E-02
	79.4	1.206	0.5698E-01	0.3569E-01	-0.1192E-01	-0.1553E-02
0.1800	5.0	1.167	0.1679E-01	-0.9530E-02	-0.1477E-02	0.1230E-02
	7.9	1.188	0.1463E-01	0.4102E-02	-0.1785E-02	0.8945E-03
	12.6	1.173	0.1357E-01	-0.5100E-03	-0.2307E-02	0.3675E-03
	20.0	1.161	0.1352E-01	0.1375E-01	-0.3412E-02	-0.1525E-03
	31.6	1.131	0.1502E-01	0.1253E-01	-0.5120E-02	-0.6640E-03
	50.1	1.115	0.1873E-01	0.2296E-01	-0.7006E-02	-0.1092E-02
	79.4	1.097	0.3084E-01	0.3030E-01	-0.9482E-02	-0.1296E-02
0.2250	5.0	1.082	0.1756E-01	0.4842E-02	-0.1482E-02	0.1381E-02
	7.9	1.052	0.1349E-01	-0.6671E-02	-0.1478E-02	0.9125E-03
	12.6	1.028	0.1191E-01	0.8660E-03	-0.1746E-02	0.4650E-03
	20.0	0.9941	0.1109E-01	0.2673E-02	-0.2385E-02	0.6816E-04
	31.6	0.9707	0.1172E-01	0.6139E-02	-0.3702E-02	-0.3703E-03
	50.1	0.9574	0.1364E-01	0.1391E-01	-0.5352E-02	-0.7034E-03
	79.4	0.9443	0.1821E-01	0.1622E-01	-0.7281E-02	-0.7622E-03
0.2750	7.9	0.8951	0.1378E-01	-0.1967E-03	-0.1162E-02	0.8349E-03
	12.6	0.8591	0.1162E-01	-0.3013E-02	-0.1311E-02	0.5229E-03
	20.0	0.8508	0.1084E-01	-0.1720E-02	-0.1759E-02	0.1327E-03
	31.6	0.8265	0.1088E-01	0.2490E-02	-0.2705E-02	-0.1539E-03
	50.1	0.7962	0.1207E-01	0.6181E-02	-0.3986E-02	-0.4403E-03
	79.4	0.7385	0.1354E-01	0.5820E-02	-0.5082E-02	-0.5321E-03
	125.9	0.7192	0.2516E-01	0.2395E-01	-0.6722E-02	-0.5962E-03

(continued on next page)

Table D.12 (continued): Systematic errors for E744 F_2.

x	Q^2	F_2^{744}	$\Delta F_2^{744,stat}$	C_{HAD}^{744}	$(B/A)_{744}^{\nu}$	$(B/A)_{744}^{\bar{\nu}}$
0.3500	7.9	0.6937	0.1027E-01	-0.3922E-02	-0.9174E-03	0.7894E-03
	12.6	0.6608	0.8115E-02	-0.4046E-02	-0.9570E-03	0.4868E-03
	20.0	0.6238	0.6940E-02	-0.3655E-02	-0.1126E-02	0.1990E-03
	31.6	0.5936	0.6589E-02	0.1917E-03	-0.1603E-02	-0.2560E-04
	50.1	0.5715	0.6835E-02	0.5998E-03	-0.2439E-02	-0.2204E-03
	79.4	0.5502	0.7810E-02	0.4003E-02	-0.3352E-02	-0.3336E-03
	125.9	0.5234	0.1024E-01	0.1007E-01	-0.4332E-02	-0.2761E-03
0.4500	12.6	0.4161	0.6987E-02	-0.5988E-02	-0.5601E-03	0.3486E-03
	20.0	0.3928	0.5956E-02	-0.4705E-02	-0.6440E-03	0.1947E-03
	31.6	0.3575	0.5312E-02	-0.4130E-02	-0.8093E-03	0.1936E-04
	50.1	0.3313	0.5313E-02	-0.1818E-02	-0.1189E-02	-0.7875E-04
	79.4	0.3175	0.5716E-02	-0.1196E-02	-0.1698E-02	-0.1485E-03
	125.9	0.2900	0.6387E-02	0.1477E-02	-0.2099E-02	-0.1445E-03
	199.5	0.2785	0.1207E-01	0.5818E-02	-0.2700E-02	-0.1329E-03
0.5500	12.6	0.2376	0.5867E-02	-0.4011E-02	-0.2981E-03	0.2118E-03
	20.0	0.2124	0.4700E-02	-0.3537E-02	-0.3355E-03	0.1284E-03
	31.6	0.1923	0.4044E-02	-0.2964E-02	-0.4006E-03	0.3670E-04
	50.1	0.1738	0.3941E-02	-0.2422E-02	-0.5371E-03	-0.2816E-04
	79.4	0.1619	0.4048E-02	-0.3485E-04	-0.7702E-03	-0.6445E-04
	125.9	0.1522	0.4323E-02	-0.7038E-03	-0.9879E-03	-0.8094E-04
	199.5	0.1356	0.6177E-02	0.1063E-02	-0.1168E-02	-0.6515E-04
0.6500	12.6	0.1179	0.5130E-02	-0.2990E-02	-0.1914E-03	0.1348E-03
	20.0	0.1009	0.3167E-02	-0.3380E-02	-0.1610E-03	0.6620E-04
	31.6	0.8366E-01	0.2605E-02	-0.2241E-02	-0.1556E-03	0.1729E-04
	50.1	0.7493E-01	0.2394E-02	-0.1235E-02	-0.2107E-03	-0.1249E-04
	79.4	0.6864E-01	0.2425E-02	-0.1816E-02	-0.2965E-03	-0.2233E-04
	125.9	0.6081E-01	0.2542E-02	0.2268E-03	-0.3633E-03	-0.3524E-04
0.7500	20.0	0.3362E-01	0.1506E-02	-0.1579E-03	-0.5312E-04	0.2613E-04
	31.6	0.2768E-01	0.1270E-02	-0.3370E-03	-0.5569E-04	0.1067E-04
	50.1	0.2526E-01	0.1131E-02	-0.7247E-03	-0.6369E-04	-0.3136E-05
	79.4	0.2137E-01	0.1149E-02	-0.3441E-03	-0.8485E-04	-0.4324E-05
	125.9	0.2127E-01	0.1278E-02	-0.5192E-03	-0.1185E-03	-0.9570E-05

Table D.13: Systematic errors for E770 F_2.

x	Q^2	F_2^{770}	$\Delta F_2^{770,stat}$	C_{HAD}^{770}	$(B/A)_{770}^{\nu}$	$(B/A)_{770}^{\bar{\nu}}$
0.0075	1.3	1.284	0.3899E-01	0.1204E-01	-0.4662E-02	-0.4855E-03
	2.0	1.371	0.5008E-01	0.2162E-01	-0.6402E-02	-0.1884E-02
	3.2	1.446	0.8036E-01	0.6077E-02	-0.8279E-02	-0.3384E-02
0.0125	1.3	1.230	0.3149E-01	0.3330E-02	-0.3149E-02	0.4985E-03
	2.0	1.360	0.3767E-01	0.1579E-01	-0.5008E-02	-0.4340E-03
	3.2	1.524	0.4930E-01	0.3393E-01	-0.7001E-02	-0.2075E-02
	5.0	1.634	0.7695E-01	0.3806E-01	-0.9586E-02	-0.3762E-02
0.0175	1.3	1.248	0.3159E-01	0.6751E-02	-0.2820E-02	0.1100E-02
	2.0	1.386	0.3434E-01	0.1016E-01	-0.3874E-02	0.3145E-03
	3.2	1.531	0.4085E-01	0.1006E-01	-0.5735E-02	-0.8285E-03
	5.0	1.556	0.5630E-01	0.1363E-01	-0.7659E-02	-0.2297E-02
	7.9	1.499	0.9201E-01	0.7687E-01	-0.9829E-02	-0.3024E-02
0.0250	1.3	1.211	0.2306E-01	0.2558E-02	-0.2208E-02	0.1287E-02
	2.0	1.312	0.2260E-01	0.9193E-02	-0.2905E-02	0.8100E-03
	3.2	1.465	0.2582E-01	0.1494E-01	-0.4416E-02	0.6253E-04
	5.0	1.527	0.3103E-01	0.1902E-01	-0.6332E-02	-0.1119E-02
	7.9	1.656	0.4289E-01	0.2612E-01	-0.8637E-02	-0.2632E-02
	12.6	1.852	0.1012	0.4679E-01	-0.1190E-01	-0.5638E-02
0.0350	1.3	1.176	0.2390E-01	0.8251E-02	-0.1882E-02	0.1497E-02
	2.0	1.331	0.2421E-01	0.1357E-01	-0.2411E-02	0.1204E-02
	3.2	1.433	0.2366E-01	0.9576E-02	-0.3333E-02	0.6360E-03
	5.0	1.551	0.2692E-01	0.2047E-01	-0.5039E-02	-0.2635E-03
	7.9	1.592	0.3308E-01	0.1472E-01	-0.7174E-02	-0.1563E-02
	12.6	1.696	0.4920E-01	0.4070E-01	-0.9604E-02	-0.3016E-02
	20.0	1.755	0.1337	0.1794E-01	-0.1297E-01	-0.5167E-02

(continued on next page)

Table D.13 (continued): Systematic errors for E770 F_2.

x	Q^2	F_2^{770}	$\Delta F_2^{770,stat}$	C_{HAD}^{770}	$(B/A)_{770}^{\nu}$	$(B/A)_{770}^{\bar{\nu}}$
0.0500	1.3	1.229	0.2044E-01	0.5215E-02	-0.1819E-02	0.1724E-02
	2.0	1.343	0.1835E-01	0.2279E-02	-0.2112E-02	0.1550E-02
	3.2	1.419	0.1714E-01	0.3359E-02	-0.2709E-02	0.1079E-02
	5.0	1.496	0.1799E-01	0.1138E-01	-0.3729E-02	0.3990E-03
	7.9	1.576	0.1994E-01	0.1507E-01	-0.5617E-02	-0.5135E-03
	12.6	1.596	0.2462E-01	0.1998E-01	-0.7661E-02	-0.1725E-02
	20.0	1.687	0.3872E-01	0.4937E-01	-0.1049E-01	-0.2685E-02
	31.6	1.664	0.1351	0.5866E-01	-0.1299E-01	-0.4178E-02
0.0700	2.0	1.325	0.2018E-01	0.1950E-02	-0.1906E-02	0.1648E-02
	3.2	1.398	0.1807E-01	0.6496E-02	-0.2131E-02	0.1261E-02
	5.0	1.476	0.1762E-01	0.1024E-01	-0.2897E-02	0.8430E-03
	7.9	1.547	0.1829E-01	0.1170E-01	-0.4180E-02	0.1855E-03
	12.6	1.568	0.2164E-01	0.1728E-01	-0.6117E-02	-0.8825E-03
	20.0	1.580	0.2711E-01	0.1679E-01	-0.8460E-02	-0.1962E-02
	31.6	1.615	0.4828E-01	0.3135E-01	-0.1106E-01	-0.3004E-02
0.0900	2.0	1.314	0.2386E-01	0.6773E-02	-0.1715E-02	0.1717E-02
	3.2	1.400	0.1988E-01	0.5975E-02	-0.2093E-02	0.1624E-02
	5.0	1.430	0.1802E-01	0.2643E-02	-0.2454E-02	0.1061E-02
	7.9	1.437	0.1752E-01	0.7975E-02	-0.3151E-02	0.4445E-03
	12.6	1.471	0.1913E-01	0.1482E-01	-0.4726E-02	-0.2990E-03
	20.0	1.509	0.2332E-01	0.2212E-01	-0.6933E-02	-0.1184E-02
	31.6	1.507	0.3165E-01	0.2618E-01	-0.9034E-02	-0.1913E-02
	50.1	1.562	0.8204E-01	0.4392E-01	-0.1261E-01	-0.3432E-02
0.1100	3.2	1.343	0.2109E-01	-0.3553E-02	-0.1922E-02	0.1692E-02
	5.0	1.351	0.1846E-01	0.8425E-02	-0.2082E-02	0.1141E-02
	7.9	1.394	0.1733E-01	0.1212E-01	-0.2706E-02	0.6935E-03
	12.6	1.423	0.1805E-01	0.1112E-01	-0.3843E-02	0.2950E-04
	20.0	1.452	0.2125E-01	0.1380E-01	-0.5938E-02	-0.8465E-03
	31.6	1.392	0.2606E-01	0.2082E-01	-0.7590E-02	-0.1425E-02
	50.1	1.505	0.4967E-01	0.4427E-01	-0.1070E-01	-0.2528E-02

(continued on next page)

Table D.13 (continued): Systematic errors for E770 F_2.

x	Q^2	F_2^{770}	$\Delta F_2^{770,stat}$	C_{HAD}^{770}	$(B/A)_{770}^{\nu}$	$(B/A)_{770}^{\bar{\nu}}$
0.1400	3.2	1.275	0.1712E-01	0.9770E-03	-0.1758E-02	0.1667E-02
	5.0	1.304	0.1387E-01	0.1533E-02	-0.1817E-02	0.1261E-02
	7.9	1.302	0.1214E-01	0.6505E-03	-0.2103E-02	0.7590E-03
	12.6	1.333	0.1212E-01	0.7244E-02	-0.2991E-02	0.2635E-03
	20.0	1.303	0.1287E-01	0.1171E-01	-0.4359E-02	-0.3240E-03
	31.6	1.273	0.1527E-01	0.1343E-01	-0.6123E-02	-0.9875E-03
	50.1	1.254	0.2069E-01	0.1995E-01	-0.8143E-02	-0.1291E-02
	79.4	1.353	0.6150E-01	0.3260E-01	-0.1100E-01	-0.2003E-02
0.1800	5.0	1.198	0.1481E-01	0.1242E-02	-0.1601E-02	0.1327E-02
	7.9	1.169	0.1289E-01	0.8435E-03	-0.1785E-02	0.9155E-03
	12.6	1.192	0.1181E-01	0.4379E-02	-0.2185E-02	0.4261E-03
	20.0	1.151	0.1166E-01	0.5942E-02	-0.3094E-02	-0.7403E-04
	31.6	1.144	0.1318E-01	0.1304E-01	-0.4694E-02	-0.5360E-03
	50.1	1.073	0.1520E-01	0.1168E-01	-0.6105E-02	-0.7630E-03
	79.4	1.099	0.2641E-01	0.2724E-01	-0.8323E-02	-0.1150E-02
0.2250	5.0	1.110	0.1551E-01	-0.6916E-02	-0.1453E-02	0.1345E-02
	7.9	1.054	0.1182E-01	0.1665E-02	-0.1481E-02	0.9535E-03
	12.6	1.028	0.1031E-01	-0.3004E-02	-0.1671E-02	0.5090E-03
	20.0	1.006	0.9813E-02	0.2017E-02	-0.2253E-02	0.9704E-04
	31.6	0.9901	0.1049E-01	0.8680E-02	-0.3454E-02	-0.2603E-03
	50.1	0.9442	0.1192E-01	0.5982E-02	-0.4728E-02	-0.5848E-03
	79.4	0.9258	0.1520E-01	0.1708E-01	-0.6363E-02	-0.6579E-03
0.2750	7.9	0.9096	0.1187E-01	-0.5619E-02	-0.1196E-02	0.9012E-03
	12.6	0.8904	0.1039E-01	-0.3672E-02	-0.1300E-02	0.5370E-03
	20.0	0.8518	0.9193E-02	0.1431E-02	-0.1649E-02	0.1788E-03
	31.6	0.8110	0.9468E-02	0.4966E-02	-0.2380E-02	-0.9307E-04
	50.1	0.7995	0.1055E-01	0.3020E-02	-0.3572E-02	-0.3378E-03
	79.4	0.7690	0.1227E-01	0.7108E-02	-0.4699E-02	-0.4762E-03
	125.9	0.7158	0.2031E-01	0.1951E-01	-0.6088E-02	-0.3785E-03

(continued on next page)

Table D.13 (continued): Systematic errors for E770 F_2.

x	Q^2	F_2^{770}	$\Delta F_2^{770,stat}$	C_{HAD}^{770}	$(B/A)_{770}^{\nu}$	$(B/A)_{770}^{\bar{\nu}}$
0.3500	7.9	0.7135	0.8728E-02	-0.6461E-02	-0.9477E-03	0.7753E-03
	12.6	0.6745	0.6957E-02	-0.5895E-02	-0.9514E-03	0.5101E-03
	20.0	0.6307	0.6052E-02	-0.3786E-02	-0.1058E-02	0.1946E-03
	31.6	0.6100	0.6013E-02	-0.1916E-02	-0.1494E-02	-0.1526E-04
	50.1	0.5729	0.6157E-02	0.9056E-03	-0.2231E-02	-0.1668E-03
	79.4	0.5318	0.6573E-02	0.3138E-02	-0.2928E-02	-0.2787E-03
	125.9	0.5271	0.9019E-02	0.6966E-02	-0.3806E-02	-0.2394E-03
0.4500	12.6	0.4031	0.5978E-02	-0.5107E-02	-0.5687E-03	0.3739E-03
	20.0	0.3997	0.5333E-02	-0.3860E-02	-0.6092E-03	0.1967E-03
	31.6	0.3635	0.4779E-02	-0.5442E-02	-0.7773E-03	0.4150E-04
	50.1	0.3318	0.4704E-02	-0.1780E-02	-0.1079E-02	-0.5615E-04
	79.4	0.3147	0.4995E-02	-0.2304E-02	-0.1534E-02	-0.1234E-03
	125.9	0.2948	0.5649E-02	-0.2798E-03	-0.1926E-02	-0.1255E-03
	199.5	0.2713	0.1030E-01	0.6268E-02	-0.2270E-02	-0.8990E-04
0.5500	12.6	0.2377	0.5152E-02	-0.4206E-02	-0.3348E-03	0.2325E-03
	20.0	0.2145	0.4213E-02	-0.4097E-02	-0.3494E-03	0.1503E-03
	31.6	0.1864	0.3533E-02	-0.3294E-02	-0.3573E-03	0.4280E-04
	50.1	0.1783	0.3529E-02	-0.2955E-02	-0.5045E-03	-0.2140E-04
	79.4	0.1565	0.3441E-02	-0.1431E-02	-0.6724E-03	-0.4975E-04
	125.9	0.1487	0.3878E-02	0.1379E-03	-0.8524E-03	-0.7115E-04
	199.5	0.1339	0.5367E-02	-0.3456E-03	-0.1031E-02	-0.4829E-04
0.6500	12.6	0.1188	0.4536E-02	-0.2973E-02	-0.1746E-03	0.1283E-03
	20.0	0.9914E-01	0.2770E-02	-0.3267E-02	-0.1445E-03	0.5823E-04
	31.6	0.8022E-01	0.2177E-02	-0.2082E-02	-0.1490E-03	0.1976E-04
	50.1	0.7854E-01	0.2162E-02	-0.1380E-02	-0.1989E-03	-0.9134E-05
	79.4	0.6626E-01	0.2130E-02	-0.1135E-02	-0.2559E-03	-0.1793E-04
	125.9	0.6123E-01	0.2367E-02	-0.5039E-03	-0.3184E-03	-0.2671E-04
0.7500	20.0	0.3627E-01	0.1366E-02	-0.1146E-02	-0.5206E-04	0.2494E-04
	31.6	0.2911E-01	0.1144E-02	-0.5362E-03	-0.4853E-04	0.9905E-05
	50.1	0.2539E-01	0.1039E-02	-0.8772E-03	-0.6033E-04	0.1660E-05
	79.4	0.2134E-01	0.1008E-02	-0.6694E-03	-0.7510E-04	-0.3710E-05
	125.9	0.1941E-01	0.1034E-02	-0.1112E-03	-0.9559E-04	-0.6805E-05

Table D.14: Systematic errors for E744 xF_3.

x	Q^2	xF_3^{744}	$\Delta xF_3^{744,stat}$	C_{HAD}^{744}	$(B/A)_{744}^{\nu}$	$(B/A)_{744}^{\bar{\nu}}$
0.0075	1.3	0.1016	0.5711E-01	-0.7655E-02	-0.1013E-02	0.9480E-03
	2.0	0.2033	0.5995E-01	-0.9226E-02	-0.2964E-02	0.2331E-02
	3.2	-0.6454E-01	0.1147	0.3531E-02	-0.3963E-02	0.5774E-02
0.0125	1.3	0.2133	0.5330E-01	-0.5594E-02	0.4674E-03	-0.5547E-03
	2.0	0.2541	0.5196E-01	-0.6474E-02	-0.1291E-02	0.7931E-03
	3.2	0.1464	0.6728E-01	-0.5967E-02	-0.2903E-02	0.2950E-02
	5.0	0.2186	0.9269E-01	0.2131E-01	-0.5376E-02	0.4458E-02
0.0175	1.3	0.2021	0.6297E-01	-0.1644E-02	0.1721E-02	-0.1764E-02
	2.0	0.2500	0.5428E-01	0.6912E-02	0.3310E-04	-0.1923E-03
	3.2	0.3271	0.6007E-01	0.9422E-02	-0.2207E-02	0.1516E-02
	5.0	0.1943	0.7344E-01	-0.2933E-01	-0.3780E-02	0.3583E-02
	7.9	0.1984	0.1077	0.2380E-01	-0.5509E-02	0.4696E-02
0.0250	1.3	0.2371	0.5708E-01	0.6172E-02	0.3152E-02	-0.2957E-02
	2.0	0.3904	0.4080E-01	-0.1667E-02	0.1033E-02	-0.1180E-02
	3.2	0.3553	0.3931E-01	-0.6072E-02	-0.7263E-03	0.2185E-03
	5.0	0.4376	0.4376E-01	0.4725E-02	-0.3319E-02	0.1891E-02
	7.9	0.3455	0.5531E-01	0.2197E-02	-0.5108E-02	0.3498E-02
	12.6	0.4512	0.9131E-01	0.3084E-02	-0.8008E-02	0.4491E-02
0.0350	1.3	0.3950	0.8704E-01	0.1353E-01	0.5323E-02	-0.4554E-02
	2.0	0.4276	0.5319E-01	0.5997E-02	0.2413E-02	-0.2290E-02
	3.2	0.4113	0.4175E-01	0.1013E-01	0.6125E-03	-0.8572E-03
	5.0	0.3833	0.4210E-01	0.4733E-03	-0.1370E-02	0.5772E-03
	7.9	0.3948	0.4783E-01	-0.1126E-02	-0.3818E-02	0.2506E-02
	12.6	0.4577	0.6124E-01	0.1726E-02	-0.6619E-02	0.4002E-02
	20.0	0.5540	0.1498	-0.4664E-01	-0.9953E-02	0.5262E-02

(continued on next page)

Table D.14 (continued): Systematic errors for E744 xF_3.

x	Q^2	xF_3^{744}	$\Delta xF_3^{744,stat}$	C_{HAD}^{744}	$(B/A)_{744}^{\nu}$	$(B/A)_{744}^{\bar{\nu}}$
0.0500	1.3	0.4097	0.1013	-0.3546E-02	0.8513E-02	-0.7829E-02
	2.0	0.5850	0.5434E-01	-0.3979E-02	0.4494E-02	-0.3814E-02
	3.2	0.5083	0.3675E-01	0.1755E-02	0.1991E-02	-0.1978E-02
	5.0	0.4971	0.3064E-01	-0.6549E-02	-0.1785E-04	-0.4636E-03
	7.9	0.5933	0.3036E-01	-0.2504E-02	-0.2707E-02	0.1060E-02
	12.6	0.5596	0.3434E-01	0.1909E-02	-0.5179E-02	0.2557E-02
	20.0	0.5455	0.4688E-01	-0.3387E-02	-0.7556E-02	0.3783E-02
	31.6	0.6437	0.1311	0.2207E-01	-0.1041E-01	0.4050E-02
0.0700	2.0	0.4711	0.9112E-01	-0.1927E-02	0.7775E-02	-0.7006E-02
	3.2	0.5636	0.5040E-01	-0.1208E-01	0.3753E-02	-0.3288E-02
	5.0	0.6009	0.3596E-01	-0.4098E-03	0.1288E-02	-0.1559E-02
	7.9	0.6487	0.2968E-01	-0.5539E-02	-0.1049E-02	-0.8792E-04
	12.6	0.7099	0.3106E-01	0.3418E-02	-0.3907E-02	0.1422E-02
	20.0	0.5975	0.3797E-01	0.1008E-01	-0.6119E-02	0.2945E-02
	31.6	0.5758	0.5736E-01	-0.4049E-02	-0.8305E-02	0.3723E-02
0.0900	2.0	0.7165	0.1411	0.3977E-01	0.1084E-01	-0.9489E-02
	3.2	0.5614	0.7074E-01	0.3581E-01	0.5850E-02	-0.5123E-02
	5.0	0.7183	0.4184E-01	0.2876E-01	0.2225E-02	-0.2056E-02
	7.9	0.7048	0.3184E-01	-0.4842E-02	0.2617E-04	-0.6891E-03
	12.6	0.6887	0.3077E-01	0.5726E-02	-0.2461E-02	0.6535E-03
	20.0	0.7456	0.3289E-01	0.1990E-02	-0.5379E-02	0.1908E-02
	31.6	0.7637	0.3881E-01	-0.2656E-02	-0.7955E-02	0.2468E-02
	50.1	0.7459	0.9554E-01	0.7628E-01	-0.1067E-01	0.3425E-02
0.1100	3.2	0.6099	0.9312E-01	0.9707E-02	0.7471E-02	-0.6626E-02
	5.0	0.6748	0.5111E-01	-0.2423E-01	0.3456E-02	-0.3065E-02
	7.9	0.7458	0.3369E-01	0.1375E-01	0.6655E-03	-0.1051E-02
	12.6	0.7159	0.2994E-01	0.5928E-03	-0.1496E-02	0.1291E-03
	20.0	0.7578	0.3176E-01	-0.1939E-02	-0.4244E-02	0.1379E-02
	31.6	0.7131	0.3412E-01	0.7598E-02	-0.6431E-02	0.2093E-02
	50.1	0.8450	0.5514E-01	0.1789E-01	-0.1018E-01	0.2633E-02

(continued on next page)

Table D.14 (continued): Systematic errors for E744 xF_3.

x	Q^2	xF_3^{744}	$\Delta xF_3^{744,stat}$	C_{HAD}^{744}	$(B/A)_{744}^{\nu}$	$(B/A)_{744}^{\bar{\nu}}$
0.1400	3.2	0.7752	0.9693E-01	-0.3381E-01	0.9880E-02	-0.8381E-02
	5.0	0.7619	0.4775E-01	0.5490E-04	0.4872E-02	-0.4153E-02
	7.9	0.7747	0.2802E-01	0.1137E-02	0.1562E-02	-0.1635E-02
	12.6	0.8330	0.2109E-01	0.4712E-02	-0.7485E-03	-0.2401E-03
	20.0	0.7884	0.2049E-01	0.1765E-02	-0.3049E-02	0.6927E-03
	31.6	0.8379	0.2124E-01	0.1057E-01	-0.5743E-02	0.1421E-02
	50.1	0.7967	0.2663E-01	0.8564E-02	-0.7780E-02	0.1737E-02
	79.4	0.8601	0.5651E-01	0.2637E-01	-0.1063E-01	0.1544E-02
0.1800	5.0	0.9528	0.6595E-01	-0.1517E-01	0.6345E-02	-0.5005E-02
	7.9	0.8468	0.3569E-01	-0.2427E-02	0.2530E-02	-0.2281E-02
	12.6	0.8338	0.2363E-01	0.9656E-05	0.7057E-04	-0.6736E-03
	20.0	0.8262	0.1949E-01	0.4876E-02	-0.1996E-02	0.2337E-03
	31.6	0.8103	0.1978E-01	0.1279E-02	-0.4300E-02	0.9195E-03
	50.1	0.7782	0.2210E-01	0.4101E-02	-0.6292E-02	0.1319E-02
	79.4	0.7968	0.3204E-01	0.1604E-01	-0.8603E-02	0.1357E-02
0.2250	5.0	0.7287	0.8728E-01	-0.3533E-02	0.8260E-02	-0.7086E-02
	7.9	0.7930	0.4140E-01	-0.8423E-03	0.3629E-02	-0.2913E-02
	12.6	0.7820	0.2387E-01	-0.1952E-02	0.7951E-03	-0.9781E-03
	20.0	0.7779	0.1734E-01	0.2940E-02	-0.1082E-02	-0.1131E-03
	31.6	0.7742	0.1599E-01	0.1700E-02	-0.3107E-02	0.5392E-03
	50.1	0.7580	0.1719E-01	0.5063E-02	-0.5102E-02	0.9229E-03
	79.4	0.7778	0.2001E-01	0.5848E-02	-0.7041E-02	0.8518E-03
	7.9	0.8230	0.5225E-01	0.2551E-02	0.4194E-02	-0.3286E-02
0.2750	12.6	0.7038	0.2747E-01	-0.8360E-03	0.1354E-02	-0.1297E-02
	20.0	0.7162	0.1854E-01	-0.3596E-02	-0.4989E-03	-0.2410E-03
	31.6	0.6740	0.1553E-01	-0.2279E-02	-0.2099E-02	0.2359E-03
	50.1	0.6624	0.1581E-01	0.1951E-02	-0.3840E-02	0.6109E-03
	79.4	0.6323	0.1582E-01	0.1694E-02	-0.5088E-02	0.6397E-03
	125.9	0.5974	0.2624E-01	0.1804E-01	-0.6455E-02	0.6268E-03

(continued on next page)

Table D.14 (continued): Systematic errors for E744 xF_3.

x	Q^2	xF_3^{744}	$\Delta xF_3^{744,stat}$	C_{HAD}^{744}	$(B/A)_{744}^{\nu}$	$(B/A)_{744}^{\bar{\nu}}$
0.3500	7.9	0.6197	0.4978E-01	-0.1756E-01	0.4757E-02	-0.3958E-02
	12.6	0.5959	0.2433E-01	-0.6073E-02	0.1771E-02	-0.1522E-02
	20.0	0.5597	0.1369E-01	-0.6887E-02	0.4292E-04	-0.4151E-03
	31.6	0.5416	0.1021E-01	0.1374E-02	-0.1182E-02	0.4247E-04
	50.1	0.5189	0.9280E-02	-0.2269E-02	-0.2394E-02	0.3222E-03
	79.4	0.4958	0.9822E-02	0.2734E-02	-0.3489E-02	0.4383E-03
	125.9	0.4855	0.1127E-01	0.3774E-02	-0.4435E-02	0.3100E-03
0.4500	12.6	0.4254	0.2729E-01	0.1288E-02	0.1836E-02	-0.1417E-02
	20.0	0.3669	0.1449E-01	-0.2666E-02	0.4161E-03	-0.4986E-03
	31.6	0.3494	0.9237E-02	-0.8254E-02	-0.4786E-03	-0.3590E-04
	50.1	0.3199	0.7648E-02	-0.2243E-02	-0.1161E-02	0.1226E-03
	79.4	0.3063	0.7524E-02	-0.2430E-02	-0.1826E-02	0.2089E-03
	125.9	0.2871	0.7552E-02	0.2332E-02	-0.2275E-02	0.1770E-03
	199.5	0.2595	0.1275E-01	0.4034E-02	-0.2726E-02	0.1421E-03
0.5500	12.6	0.2974	0.2839E-01	-0.1895E-01	0.1406E-02	-0.1062E-02
	20.0	0.2080	0.1408E-01	-0.9528E-02	0.4337E-03	-0.4018E-03
	31.6	0.1842	0.7958E-02	-0.2471E-03	-0.1282E-03	-0.7655E-04
	50.1	0.1726	0.6087E-02	-0.3151E-02	-0.4970E-03	0.4685E-04
	79.4	0.1596	0.5468E-02	-0.1465E-02	-0.8278E-03	0.9455E-04
	125.9	0.1500	0.5420E-02	-0.2220E-02	-0.1087E-02	0.1066E-03
	199.5	0.1303	0.6804E-02	0.3666E-03	-0.1216E-02	0.7325E-04
0.6500	12.6	0.7896E-01	0.2978E-01	0.3881E-02	0.9340E-03	-0.8055E-03
	20.0	0.1049	0.1130E-01	0.2605E-02	0.2840E-03	-0.2460E-03
	31.6	0.9034E-01	0.5833E-02	-0.3790E-02	-0.2094E-04	-0.4093E-04
	50.1	0.7783E-01	0.3984E-02	-0.2642E-02	-0.1889E-03	0.2228E-04
	79.4	0.6780E-01	0.3415E-02	-0.8656E-03	-0.3144E-03	0.3405E-04
	125.9	0.5821E-01	0.3311E-02	0.7324E-03	-0.3955E-03	0.4871E-04
0.7500	20.0	0.3623E-01	0.6255E-02	-0.1398E-02	0.1272E-03	-0.1126E-03
	31.6	0.2630E-01	0.3283E-02	-0.7125E-03	0.9255E-05	-0.2887E-04
	50.1	0.2737E-01	0.2022E-02	-0.7107E-03	-0.5283E-04	0.5989E-05
	79.4	0.1954E-01	0.1699E-02	-0.6443E-03	-0.8271E-04	0.6865E-05
	125.9	0.2017E-01	0.1707E-02	-0.1248E-02	-0.1279E-03	0.1366E-04

Table D.15: Systematic errors for E770 xF_3.

x	Q^2	xF_3^{770}	$\Delta xF_3^{770,stat}$	C_{HAD}^{770}	$(B/A)_{770}^{\nu}$	$(B/A)_{770}^{\bar{\nu}}$
0.0075	1.3	0.5826E-01	0.4858E-01	-0.2570E-02	-0.5952E-03	0.6214E-03
	2.0	0.1646	0.5466E-01	0.3348E-02	-0.2098E-02	0.2087E-02
	3.2	0.1541	0.7594E-01	0.6105E-02	-0.3513E-02	0.3214E-02
0.0125	1.3	0.2107	0.4457E-01	0.8530E-02	0.6340E-03	-0.7401E-03
	2.0	0.1979	0.4767E-01	0.3588E-02	-0.7841E-03	0.5689E-03
	3.2	0.1839	0.5573E-01	-0.1802E-01	-0.2464E-02	0.2389E-02
	5.0	0.2658	0.7405E-01	-0.6240E-02	-0.4525E-02	0.3644E-02
0.0175	1.3	0.1795	0.5208E-01	-0.1144E-02	0.1993E-02	-0.1911E-02
	2.0	0.2969	0.4691E-01	-0.2530E-03	0.1253E-03	-0.4501E-03
	3.2	0.2641	0.5097E-01	0.1454E-01	-0.1482E-02	0.1070E-02
	5.0	0.2956	0.6153E-01	0.3450E-02	-0.3311E-02	0.2543E-02
	7.9	0.4544	0.8666E-01	-0.3456E-02	-0.5853E-02	0.2860E-02
0.0250	1.3	0.2304	0.4869E-01	-0.6711E-03	0.3040E-02	-0.2850E-02
	2.0	0.3226	0.3532E-01	-0.3367E-02	0.1305E-02	-0.1340E-02
	3.2	0.3098	0.3478E-01	-0.6698E-02	-0.3052E-03	-0.8805E-04
	5.0	0.3255	0.3831E-01	0.1219E-02	-0.2151E-02	0.1423E-02
	7.9	0.3621	0.4569E-01	-0.4345E-02	-0.4272E-02	0.2835E-02
	12.6	0.2469	0.9549E-01	0.1073E-01	-0.5815E-02	0.5330E-02
0.0350	1.3	0.4058	0.7056E-01	0.8227E-02	0.4976E-02	-0.4650E-02
	2.0	0.4002	0.4649E-01	-0.1665E-01	0.2498E-02	-0.2439E-02
	3.2	0.4071	0.3540E-01	0.1739E-01	0.8623E-03	-0.1005E-02
	5.0	0.4398	0.3545E-01	0.9432E-02	-0.1120E-02	0.3638E-03
	7.9	0.4576	0.3996E-01	-0.4042E-02	-0.3318E-02	0.1939E-02
	12.6	0.4524	0.5063E-01	0.3110E-02	-0.5401E-02	0.3131E-02
	20.0	0.4966	0.1245	0.2280E-01	-0.7666E-02	0.4818E-02

(continued on next page)

Table D.15 (continued): Systematic errors for E770 xF_3.

x	Q^2	xF_3^{770}	$\Delta xF_3^{770,stat}$	C_{HAD}^{770}	$(B/A)_{770}^{\nu}$	$(B/A)_{770}^{\bar{\nu}}$
0.0500	1.3	0.3870	0.8711E-01	0.9450E-02	0.8359E-02	-0.7692E-02
	2.0	0.4457	0.4807E-01	0.1494E-01	0.4618E-02	-0.4286E-02
	3.2	0.4627	0.3073E-01	0.3466E-02	0.2110E-02	-0.2049E-02
	5.0	0.5111	0.2616E-01	-0.1104E-02	0.1636E-03	-0.6116E-03
	7.9	0.5698	0.2609E-01	0.5871E-02	-0.2057E-02	0.7017E-03
	12.6	0.5623	0.2899E-01	0.1076E-01	-0.4337E-02	0.2079E-02
	20.0	0.6716	0.3934E-01	-0.4990E-03	-0.7046E-02	0.2748E-02
	31.6	0.5891	0.1267	0.1284E-02	-0.8770E-02	0.3923E-02
0.0700	2.0	0.5381	0.7628E-01	-0.1384E-02	0.7458E-02	-0.6545E-02
	3.2	0.6409	0.4219E-01	-0.6386E-02	0.3561E-02	-0.3130E-02
	5.0	0.6333	0.2958E-01	0.6860E-02	0.1403E-02	-0.1507E-02
	7.9	0.6300	0.2578E-01	0.3508E-02	-0.6290E-03	-0.2763E-03
	12.6	0.5776	0.2801E-01	-0.3736E-02	-0.2840E-02	0.1189E-02
	20.0	0.6810	0.3086E-01	0.3907E-02	-0.5395E-02	0.2277E-02
	31.6	0.6446	0.4808E-01	0.2612E-01	-0.7678E-02	0.3006E-02
0.0900	2.0	0.7900	0.1181	0.3242E-01	0.1008E-01	-0.8920E-02
	3.2	0.5960	0.6087E-01	0.9623E-02	0.5781E-02	-0.5223E-02
	5.0	0.6415	0.3553E-01	0.7017E-02	0.2351E-02	-0.2224E-02
	7.9	0.7512	0.2681E-01	-0.1203E-02	0.1108E-03	-0.7268E-03
	12.6	0.7314	0.2588E-01	0.1298E-01	-0.2036E-02	0.4258E-03
	20.0	0.7314	0.2904E-01	0.2787E-02	-0.4501E-02	0.1523E-02
	31.6	0.7192	0.3384E-01	0.1444E-01	-0.6677E-02	0.2070E-02
	50.1	0.7446	0.7960E-01	0.2274E-01	-0.9135E-02	0.3338E-02
0.1100	3.2	0.7057	0.7975E-01	0.3764E-02	0.7395E-02	-0.6728E-02
	5.0	0.7750	0.4315E-01	-0.1218E-01	0.3122E-02	-0.2839E-02
	7.9	0.7763	0.2911E-01	0.7437E-02	0.8431E-03	-0.1249E-02
	12.6	0.8037	0.2554E-01	-0.6525E-02	-0.1253E-02	-0.4399E-04
	20.0	0.7713	0.2768E-01	0.6184E-02	-0.3558E-02	0.1155E-02
	31.6	0.7565	0.3001E-01	0.1808E-03	-0.5767E-02	0.1674E-02
	50.1	0.6923	0.5021E-01	0.1983E-01	-0.8115E-02	0.2569E-02

(continued on next page)

Table D.15 (continued): Systematic errors for E770 xF_3.

x	Q^2	xF_3^{770}	$\Delta xF_3^{770,stat}$	C_{HAD}^{770}	$(B/A)_{770}^{\nu}$	$(B/A)_{770}^{\bar{\nu}}$
0.1400	3.2	0.7546	0.8283E-01	0.1004E-01	0.9520E-02	-0.8464E-02
	5.0	0.8362	0.4129E-01	0.1595E-01	0.4673E-02	-0.3974E-02
	7.9	0.8063	0.2360E-01	0.5636E-03	0.1554E-02	-0.1582E-02
	12.6	0.8021	0.1859E-01	0.4367E-02	-0.4267E-03	-0.4331E-03
	20.0	0.8208	0.1747E-01	0.6360E-02	-0.2585E-02	0.4669E-03
	31.6	0.7821	0.1907E-01	0.7114E-02	-0.4741E-02	0.1279E-02
	50.1	0.8264	0.2237E-01	0.1509E-01	-0.6868E-02	0.1415E-02
	79.4	0.8086	0.6098E-01	0.1880E-01	-0.9089E-02	0.1991E-02
0.1800	5.0	0.8703	0.5774E-01	-0.1117E-01	0.6352E-02	-0.5455E-02
	7.9	0.7684	0.3121E-01	-0.7143E-02	0.2582E-02	-0.2361E-02
	12.6	0.8396	0.2020E-01	0.1964E-02	0.2629E-03	-0.7890E-03
	20.0	0.8232	0.1672E-01	0.7749E-02	-0.1616E-02	0.1142E-03
	31.6	0.8418	0.1734E-01	0.4896E-02	-0.3779E-02	0.7468E-03
	50.1	0.8282	0.1781E-01	0.3771E-02	-0.5629E-02	0.9225E-03
	79.4	0.7702	0.2740E-01	0.1083E-01	-0.7326E-02	0.1203E-02
0.2250	5.0	0.7429	0.7695E-01	-0.1212E-01	0.8074E-02	-0.6973E-02
	7.9	0.7798	0.3591E-01	0.1101E-02	0.3558E-02	-0.3075E-02
	12.6	0.7827	0.2026E-01	-0.4004E-02	0.8494E-03	-0.1081E-02
	20.0	0.8219	0.1517E-01	0.8672E-03	-0.9410E-03	-0.1622E-03
	31.6	0.7786	0.1430E-01	0.3109E-02	-0.2698E-02	0.3807E-03
	50.1	0.7287	0.1502E-01	0.1263E-02	-0.4299E-02	0.7710E-03
	79.4	0.7692	0.1665E-01	0.1181E-01	-0.6023E-02	0.7349E-03
0.2750	7.9	0.7511	0.4457E-01	0.1116E-03	0.4278E-02	-0.3583E-02
	12.6	0.7357	0.2428E-01	-0.5773E-02	0.1399E-02	-0.1346E-02
	20.0	0.7001	0.1548E-01	-0.5204E-02	-0.3630E-03	-0.3277E-03
	31.6	0.6911	0.1347E-01	0.2660E-02	-0.1797E-02	0.1432E-03
	50.1	0.6855	0.1381E-01	0.2114E-03	-0.3395E-02	0.4716E-03
	79.4	0.6399	0.1433E-01	0.1181E-02	-0.4576E-02	0.5732E-03
	125.9	0.6427	0.2109E-01	0.1237E-01	-0.5927E-02	0.3976E-03

(continued on next page)

Table D.15 (continued): Systematic errors for E770 xF_3.

x	Q^2	xF_3^{770}	$\Delta xF_3^{770,stat}$	C_{HAD}^{770}	$(B/A)_{770}^{\nu}$	$(B/A)_{770}^{\bar{\nu}}$
0.3500	7.9	0.6508	0.4192E-01	-0.4843E-04	0.4778E-02	-0.3927E-02
	12.6	0.5954	0.2061E-01	-0.5263E-02	0.1823E-02	-0.1612E-02
	20.0	0.5853	0.1171E-01	-0.3692E-02	0.8160E-04	-0.4103E-03
	31.6	0.5557	0.9183E-02	-0.1452E-02	-0.1040E-02	0.2551E-04
	50.1	0.5283	0.8367E-02	-0.1032E-02	-0.2139E-02	0.2449E-03
	79.4	0.4822	0.8233E-02	0.3149E-02	-0.2967E-02	0.3678E-03
	125.9	0.4810	0.9910E-02	0.7569E-02	-0.3854E-02	0.2687E-03
0.4500	12.6	0.3785	0.2318E-01	-0.6630E-02	0.1812E-02	-0.1536E-02
	20.0	0.3780	0.1282E-01	-0.3910E-02	0.4329E-03	-0.5090E-03
	31.6	0.3488	0.8136E-02	-0.6499E-02	-0.3882E-03	-0.7765E-04
	50.1	0.3229	0.6721E-02	-0.1072E-02	-0.9980E-03	0.8780E-04
	79.4	0.3085	0.6537E-02	-0.5145E-02	-0.1622E-02	0.1746E-03
	125.9	0.2897	0.6652E-02	-0.8540E-03	-0.2051E-02	0.1540E-03
	199.5	0.2539	0.1085E-01	0.4723E-02	-0.2295E-02	0.9601E-04
0.5500	12.6	0.2545	0.2478E-01	-0.7920E-03	0.1408E-02	-0.1178E-02
	20.0	0.1889	0.1252E-01	-0.2710E-02	0.4862E-03	-0.4751E-03
	31.6	0.1823	0.6826E-02	-0.2626E-02	-0.9080E-04	-0.9020E-04
	50.1	0.1740	0.5385E-02	-0.3965E-02	-0.4504E-03	0.3595E-04
	79.4	0.1593	0.4645E-02	-0.1456E-02	-0.7236E-03	0.7325E-04
	125.9	0.1418	0.4859E-02	-0.1345E-03	-0.9072E-03	0.9415E-04
	199.5	0.1321	0.5889E-02	-0.7673E-03	-0.1076E-02	0.5430E-04
0.6500	12.6	0.8680E-01	0.2623E-01	0.7468E-03	0.9049E-03	-0.7736E-03
	20.0	0.1083	0.9810E-02	-0.6102E-02	0.2599E-03	-0.2185E-03
	31.6	0.8555E-01	0.4798E-02	-0.2334E-02	-0.1463E-04	-0.4729E-04
	50.1	0.8501E-01	0.3514E-02	-0.5209E-03	-0.1813E-03	0.1642E-04
	79.4	0.6539E-01	0.2985E-02	-0.1068E-02	-0.2620E-03	0.2744E-04
	125.9	0.5794E-01	0.3079E-02	-0.1041E-02	-0.3357E-03	0.3716E-04
0.7500	20.0	0.3968E-01	0.5625E-02	-0.2348E-03	0.1385E-03	-0.1085E-03
	31.6	0.3097E-01	0.2901E-02	-0.9610E-03	0.4809E-05	-0.2708E-04
	50.1	0.2371E-01	0.1836E-02	-0.1623E-02	-0.3874E-04	-0.3205E-05
	79.4	0.1969E-01	0.1475E-02	-0.8661E-03	-0.6921E-04	0.5915E-05
	125.9	0.1903E-01	0.1378E-02	-0.4085E-03	-0.1009E-03	0.9765E-05

Table D.16: F_2(without model correction) / F_2(with correction).

x	Q^2	Isoscalar	Radiative	Slow-rescaling	Propagator	No model corrections
0.0075	1.3	0.98432	1.1299	0.89158	0.98619	1.0146
	2.0	1.0026	1.1637	0.91860	1.0044	1.0566
	3.2	1.0024	1.1770	0.92240	1.0029	1.0754
0.0125	1.3	0.98649	1.1110	0.90277	0.98918	1.0065
	2.0	1.0057	1.1459	0.93190	1.0078	1.0519
	3.2	0.99801	1.1439	0.93486	0.99888	1.0630
	5.0	1.0019	1.1604	0.94494	1.0024	1.0850
0.0175	1.3	1.0106	1.1194	0.93041	1.0125	1.0220
	2.0	0.99091	1.1116	0.92245	0.99310	1.0248
	3.2	0.98779	1.1130	0.93161	0.98935	1.0399
	5.0	0.99299	1.1236	0.94527	0.99321	1.0609
	7.9	0.99088	1.1330	0.95073	0.99112	1.0756
0.0250	1.3	0.99550	1.0870	0.92416	0.99752	1.0006
	2.0	0.99759	1.1002	0.93480	0.99984	1.0210
	3.2	0.99487	1.1050	0.94033	0.99641	1.0348
	5.0	1.0025	1.1164	0.95972	1.0032	1.0589
	7.9	0.98947	1.1069	0.95492	0.98891	1.0585
	12.6	0.99499	1.1183	0.96617	0.99276	1.0757
0.0350	1.3	1.0089	1.0889	0.94212	1.0110	1.0083
	2.0	0.99102	1.0751	0.93378	0.99293	1.0040
	3.2	0.99401	1.0846	0.94346	0.99546	1.0201
	5.0	0.99122	1.0848	0.95022	0.99186	1.0306
	7.9	1.0032	1.0996	0.97212	1.0026	1.0557
	12.6	0.98709	1.0861	0.96277	0.98503	1.0485
	20.0	1.0032	1.1066	0.98383	0.99906	1.0727

(continued on next page)

Table D.16 (continued): F_2(without model correction) / F_2(with correction).

x	Q^2	Isoscalar	Radiative	Slow-rescaling	Propagator	No model corrections
0.0500	1.3	0.99623	1.0595	0.93161	0.99791	0.98331
	2.0	0.99670	1.0662	0.94512	0.99840	1.0026
	3.2	0.99711	1.0695	0.95081	0.99825	1.0113
	5.0	0.99319	1.0667	0.95445	0.99370	1.0161
	7.9	1.0009	1.0755	0.97149	1.0005	1.0339
	12.6	0.99628	1.0716	0.97519	0.99419	1.0380
	20.0	0.98616	1.0625	0.97045	0.98202	1.0325
	31.6	0.99148	1.0678	0.97997	0.98444	1.0396
0.0700	2.0	0.99154	1.0447	0.94360	0.99277	0.98691
	3.2	0.99332	1.0506	0.95266	0.99433	0.99943
	5.0	1.0005	1.0602	0.96478	1.0007	1.0140
	7.9	0.99485	1.0552	0.96681	0.99409	1.0163
	12.6	0.99627	1.0569	0.97597	0.99389	1.0253
	20.0	1.0080	1.0704	0.99314	1.0028	1.0429
	31.6	0.99358	1.0559	0.98253	0.98513	1.0297
0.0900	2.0	0.99094	1.0318	0.94655	0.99220	0.97833
	3.2	0.99778	1.0427	0.96049	0.99836	0.99656
	5.0	0.99764	1.0460	0.96534	0.99761	1.0043
	7.9	0.99761	1.0476	0.97148	0.99658	1.0116
	12.6	0.99625	1.0469	0.97661	0.99354	1.0168
	20.0	0.99990	1.0513	0.98655	0.99475	1.0258
	31.6	0.98250	1.0347	0.97324	0.97392	1.0104
	50.1	1.0129	1.0664	1.0054	0.99880	1.0402
0.1100	3.2	0.99862	1.0337	0.96454	0.99908	0.99163
	5.0	0.99995	1.0393	0.97084	0.99968	1.0018
	7.9	1.0017	1.0439	0.97717	1.0002	1.0106
	12.6	1.0007	1.0441	0.98196	0.99764	1.0158
	20.0	1.0083	1.0523	0.99489	1.0026	1.0279
	31.6	0.99280	1.0375	0.98386	0.98343	1.0147
	50.1	0.99480	1.0404	0.98798	0.98009	1.0155

(continued on next page)

Table D.16 (continued): F_2(without model correction) / F_2(with correction).

x	Q^2	Isoscalar	Radiative	Slow-rescaling	Propagator	No model corrections
0.1400	3.2	0.99868	1.0210	0.96889	0.99901	0.98408
	5.0	0.99925	1.0266	0.97449	0.99877	0.99446
	7.9	0.99651	1.0279	0.97536	0.99472	0.99915
	12.6	0.99825	1.0318	0.98141	0.99467	1.0067
	20.0	1.0002	1.0346	0.98787	0.99403	1.0125
	31.6	0.99817	1.0332	0.98998	0.98823	1.0123
	50.1	0.99812	1.0347	0.99222	0.98243	1.0113
	79.4	0.98433	1.0208	0.98010	0.96157	0.99285
0.1800	5.0	0.99621	1.0098	0.97600	0.99545	0.98328
	7.9	1.0002	1.0194	0.98292	0.99798	0.99574
	12.6	0.99781	1.0207	0.98345	0.99357	0.99964
	20.0	1.0011	1.0257	0.99007	0.99411	1.0067
	31.6	1.0004	1.0255	0.99261	0.98957	1.0069
	50.1	0.99457	1.0209	0.98910	0.97781	0.99973
	79.4	0.99832	1.0258	0.99353	0.97300	0.99871
0.2250	5.0	0.99000	0.99069	0.97363	0.98903	0.96880
	7.9	1.0006	1.0076	0.98689	0.99811	0.98843
	12.6	1.0005	1.0128	0.98843	0.99561	0.99547
	20.0	1.0059	1.0210	0.99592	0.99791	1.0050
	31.6	1.0041	1.0201	0.99643	0.99206	1.0040
	50.1	0.99787	1.0143	0.99221	0.97996	0.99538
	79.4	1.0060	1.0244	1.0010	0.97870	0.99874
0.2750	7.9	0.99638	0.99128	0.98502	0.99352	0.97539
	12.6	0.99825	0.99946	0.98830	0.99293	0.98537
	20.0	0.99880	1.0043	0.98981	0.99006	0.99108
	31.6	1.0015	1.0086	0.99395	0.98840	0.99485
	50.1	0.99861	1.0061	0.99251	0.97949	0.98931
	79.4	1.0019	1.0108	0.99640	0.97327	0.98698
	125.9	1.0154	1.0263	1.0097	0.97336	0.99129

(continued on next page)

Table D.16 (continued): F_2(without model correction) / F_2(with correction).

x	Q^2	Isoscalar	Radiative	Slow-rescaling	Propagator	No model corrections
0.3500	7.9	1.0053	0.98452	0.99491	1.0021	0.97035
	12.6	1.0027	0.98906	0.99378	0.99687	0.97712
	20.0	1.0033	0.99545	0.99443	0.99344	0.98459
	31.6	0.99902	0.99398	0.99065	0.98432	0.98268
	50.1	1.0047	1.0005	0.99707	0.98355	0.98601
	79.4	1.0114	1.0076	1.0045	0.98072	0.98587
	125.9	0.99754	0.99550	0.99009	0.95300	0.96275
0.4500	12.6	1.0073	0.97502	0.99695	1.0009	0.96289
	20.0	0.99422	0.96935	0.98422	0.98359	0.95917
	31.6	1.0142	0.99347	1.0034	0.99745	0.98338
	50.1	1.0088	0.98991	0.99817	0.98505	0.97737
	79.4	1.0155	0.99641	1.0052	0.98185	0.97734
	125.9	1.0177	0.99959	1.0071	0.96897	0.96858
	199.5	0.99628	0.98079	0.98538	0.92897	0.93319
0.5500	12.6	1.0104	0.95968	0.99537	1.0030	0.94506
	20.0	1.0020	0.96037	0.98952	0.99107	0.94833
	31.6	1.0142	0.97797	1.0001	0.99603	0.96745
	50.1	1.0021	0.96897	0.98760	0.97609	0.95738
	79.4	1.0081	0.97501	0.99363	0.97168	0.95796
	125.9	1.0111	0.97809	0.99758	0.96038	0.94925
	199.5	1.0122	0.98124	0.99744	0.93945	0.93474
0.6500	12.6	0.98618	0.92089	0.96882	0.98002	0.90224
	20.0	0.99712	0.93807	0.97823	0.98455	0.92330
	31.6	1.0236	0.97000	1.0036	1.0033	0.95779
	50.1	1.0138	0.96451	0.99316	0.98451	0.95288
	79.4	1.0093	0.96186	0.99042	0.97038	0.94540
	125.9	1.0032	0.95575	0.98602	0.95070	0.92879
0.7500	20.0	1.0020	0.92349	0.97625	0.98883	0.90352
	31.6	0.98443	0.91462	0.95893	0.96388	0.89888
	50.1	1.0072	0.94152	0.98117	0.97688	0.92706
	79.4	1.0179	0.95412	0.99428	0.97717	0.93600
	125.9	1.0214	0.95579	0.99802	0.96471	0.92929

Table D.17: xF_3(without model correction) / xF_3(with correction).

x	Q^2	Isoscalar	Radiative	Slow-rescaling	Propagator	No model corrections
0.0075	1.3	0.92886	1.4422	1.3339	1.2117	1.2671
	2.0	0.82403	1.1139	0.93081	0.93431	0.98101
	3.2	0.93710	1.5152	1.1792	1.1416	1.3099
0.0125	1.3	0.93418	1.1846	1.0419	1.0402	1.0679
	2.0	0.83375	1.0723	0.94146	0.92973	0.97495
	3.2	0.91332	1.2263	1.0708	1.0432	1.1057
	5.0	0.93972	1.2599	1.0138	1.0224	1.1444
0.0175	1.3	0.74196	0.98138	0.93279	0.88026	0.88986
	2.0	0.92583	1.1339	1.0120	1.0081	1.0441
	3.2	0.92333	1.1350	1.0053	1.0010	1.0480
	5.0	0.87376	1.1085	0.96193	0.95571	1.0159
	7.9	0.96268	1.2078	0.99612	1.0108	1.1238
0.0250	1.3	0.91707	1.1348	1.0820	1.0465	1.0345
	2.0	0.93572	1.1043	0.99995	1.0021	1.0261
	3.2	0.97332	1.1589	1.0462	1.0399	1.0871
	5.0	0.91265	1.0887	0.97161	0.96998	1.0195
	7.9	0.96269	1.1662	1.0167	1.0175	1.0925
	12.6	0.94608	1.1882	0.99742	0.99700	1.1144
0.0350	1.3	0.86008	1.0134	0.97306	0.95525	0.93053
	2.0	0.92520	1.0641	0.99343	0.98923	0.99659
	3.2	0.94952	1.0908	1.0061	1.0026	1.0318
	5.0	0.94664	1.0945	1.0008	0.99629	1.0377
	7.9	0.93039	1.0789	0.97857	0.97561	1.0219
	12.6	0.98661	1.1561	1.0244	1.0245	1.0977
	20.0	0.90302	1.0775	0.93351	0.93266	1.0244

(continued on next page)

Table D.17 (continued): xF_3(without model correction) / xF_3(with correction).

x	Q^2	Isoscalar	Radiative	Slow-rescaling	Propagator	No model corrections
0.0500	1.3	0.87552	1.0403	1.0507	1.0004	0.96047
	2.0	0.96360	1.0802	1.0322	1.0265	1.0157
	3.2	0.95257	1.0628	1.0054	1.0005	1.0116
	5.0	0.97240	1.0834	1.0131	1.0107	1.0372
	7.9	0.96062	1.0696	0.99203	0.99161	1.0260
	12.6	0.97470	1.0889	1.0035	1.0026	1.0442
	20.0	0.98928	1.1103	1.0108	1.0092	1.0673
	31.6	0.98939	1.1154	1.0084	1.0036	1.0731
0.0700	2.0	0.93957	1.0452	1.0348	1.0125	0.98696
	3.2	0.99523	1.0818	1.0349	1.0346	1.0343
	5.0	0.95655	1.0399	0.98733	0.98598	1.0024
	7.9	0.97820	1.0643	1.0031	1.0020	1.0291
	12.6	0.97741	1.0655	1.0014	0.99824	1.0311
	20.0	0.94876	1.0395	0.97098	0.96572	1.0047
	31.6	1.0025	1.1054	1.0225	1.0140	1.0680
0.0900	2.0	0.98131	1.0590	1.0339	1.0323	1.0010
	3.2	0.97340	1.0471	1.0248	1.0163	1.0042
	5.0	0.99124	1.0590	1.0158	1.0157	1.0251
	7.9	0.96905	1.0356	0.98555	0.98601	1.0064
	12.6	0.97902	1.0490	0.99615	0.99341	1.0213
	20.0	0.98086	1.0517	0.99611	0.99140	1.0228
	31.6	1.0114	1.0879	1.0239	1.0158	1.0571
	50.1	0.95395	1.0344	0.96753	0.95422	1.0014
0.1100	3.2	0.93780	0.99327	0.97530	0.97215	0.95327
	5.0	0.96595	1.0180	0.98450	0.98532	0.98853
	7.9	0.96511	1.0192	0.97796	0.97805	0.99466
	12.6	0.98126	1.0381	0.99316	0.99084	1.0151
	20.0	0.96687	1.0251	0.97982	0.97391	1.0017
	31.6	0.99766	1.0593	1.0081	0.99915	1.0328
	50.1	1.0294	1.0986	1.0400	1.0248	1.0675

(continued on next page)

Table D.17 (continued): xF_3(without model correction) / xF_3(with correction).

x	Q^2	Isoscalar	Radiative	Slow-rescaling	Propagator	No model corrections
0.1400	3.2	0.97335	1.0067	0.98527	0.99477	0.96622
	5.0	0.99429	1.0284	1.0009	1.0065	1.0008
	7.9	1.0066	1.0461	1.0116	1.0138	1.0248
	12.6	0.99898	1.0410	1.0041	1.0029	1.0223
	20.0	0.98845	1.0319	0.99431	0.98947	1.0135
	31.6	0.99218	1.0363	0.99747	0.98870	1.0153
	50.1	0.99278	1.0400	0.99745	0.98284	1.0149
	79.4	0.98661	1.0351	0.99063	0.96876	1.0044
0.1800	5.0	0.98577	0.99606	0.97235	0.98659	0.97134
	7.9	0.99007	1.0094	0.98464	0.98964	0.99308
	12.6	0.99781	1.0235	0.99496	0.99560	1.0094
	20.0	1.0033	1.0319	1.0022	0.99862	1.0178
	31.6	0.99016	1.0193	0.99020	0.98182	1.0033
	50.1	0.99976	1.0308	1.0001	0.98529	1.0099
	79.4	1.0036	1.0389	1.0048	0.98113	1.0107
0.2250	5.0	1.0631	1.0441	1.0159	1.0470	1.0182
	7.9	1.0076	1.0055	0.98521	0.99707	0.99220
	12.6	1.0040	1.0137	0.99222	0.99528	1.0037
	20.0	0.99837	1.0132	0.99102	0.98868	1.0030
	31.6	1.0031	1.0199	0.99796	0.99013	1.0078
	50.1	1.0014	1.0188	0.99765	0.98296	1.0021
	79.4	0.99581	1.0165	0.99310	0.96927	0.99170
0.2750	7.9	1.0179	0.99307	0.97439	0.99578	0.98198
	12.6	1.0097	1.0015	0.98545	0.99298	0.99498
	20.0	1.0164	1.0177	1.0015	1.0011	1.0109
	31.6	1.0071	1.0121	0.99638	0.98967	1.0033
	50.1	1.0029	1.0086	0.99446	0.98057	0.99534
	79.4	1.0122	1.0204	1.0056	0.98139	0.99843
	125.9	1.0061	1.0180	1.0008	0.96395	0.98389

(continued on next page)

Table D.17 (continued): xF_3(without model correction) / xF_3(with correction).

x	Q^2	Isoscalar	Radiative	Slow-rescaling	Propagator	No model corrections
0.3500	7.9	1.0391	0.97656	0.95120	0.99384	0.96735
	12.6	1.0339	0.99792	0.98597	1.0031	0.99562
	20.0	1.0160	0.99826	0.98888	0.99263	0.99541
	31.6	1.0165	1.0057	0.99765	0.99309	1.0005
	50.1	1.0084	0.99993	0.99355	0.98093	0.99040
	79.4	1.0100	1.0020	0.99725	0.97415	0.98447
	125.9	1.0093	1.0055	0.99929	0.96178	0.97427
0.4500	12.6	1.0365	0.96073	0.94738	0.98275	0.96311
	20.0	1.0260	0.97862	0.97577	0.98807	0.98151
	31.6	1.0267	0.99479	0.99497	0.99440	0.99412
	50.1	1.0093	0.98341	0.98581	0.97544	0.97798
	79.4	1.0182	0.99337	0.99863	0.97692	0.97995
	125.9	1.0201	0.99792	1.0040	0.96654	0.97036
	199.5	1.0130	0.99486	0.99883	0.94176	0.94844
0.5500	12.6	1.0647	0.95123	0.93404	0.99019	0.95312
	20.0	1.0264	0.94205	0.93872	0.96630	0.95162
	31.6	1.0437	0.98809	0.99419	0.99997	0.99184
	50.1	1.0305	0.98590	0.99637	0.98902	0.98391
	79.4	1.0188	0.97823	0.99189	0.97216	0.96828
	125.9	1.0244	0.98399	1.0005	0.96452	0.96143
	199.5	1.0169	0.98237	0.99745	0.93964	0.93860
0.6500	12.6	1.2312	0.99645	0.90942	1.0550	1.0069
	20.0	1.0965	0.97734	0.97733	1.0208	0.98501
	31.6	1.0564	0.97520	0.98798	1.0021	0.98040
	50.1	1.0424	0.97882	0.99708	0.99421	0.97850
	79.4	1.0233	0.96485	0.98581	0.96928	0.95866
	125.9	1.0162	0.95826	0.98322	0.95008	0.94080
0.7500	20.0	1.1304	0.96369	0.95116	1.0257	0.96840
	31.6	1.1046	0.98688	0.99969	1.0310	0.99233
	50.1	1.0509	0.96122	0.98296	0.98987	0.96331
	79.4	1.0398	0.95763	0.98423	0.97395	0.95557
	125.9	1.0237	0.94652	0.98001	0.95061	0.93215

Appendix E:
Data versus Monte Carlo Plots

Chapter 4 describes the Monte Carlo program used to correct the data to full acceptance. This Appendix contains supplementary plots that document the event-generation process in the Monte Carlo.

Figures E.1 and E.2 compare the length distributions observed in the data with those generated by the structure-function Monte Carlo after cross-section cuts are applied.

Figures E.3 through E.8 show the muon momentum resolution functions used to smear the generated muon momentum at the front face of the toroid spectrometer, *EMUFFG*, as described in Chapter 4.

Figures E.9 through E.30 compare the distributions of kinematic quantities observed in the data and simulated by the Monte Carlo after structure-function cuts. Figures E.9 through E.19 compare the E744 data against the Monte Carlo events generated using the E744 flux files and calibration constants; Figures E.20 through E.30 compare the E770 data against the Monte Carlo events generated using the E770 flux files and calibration constants.

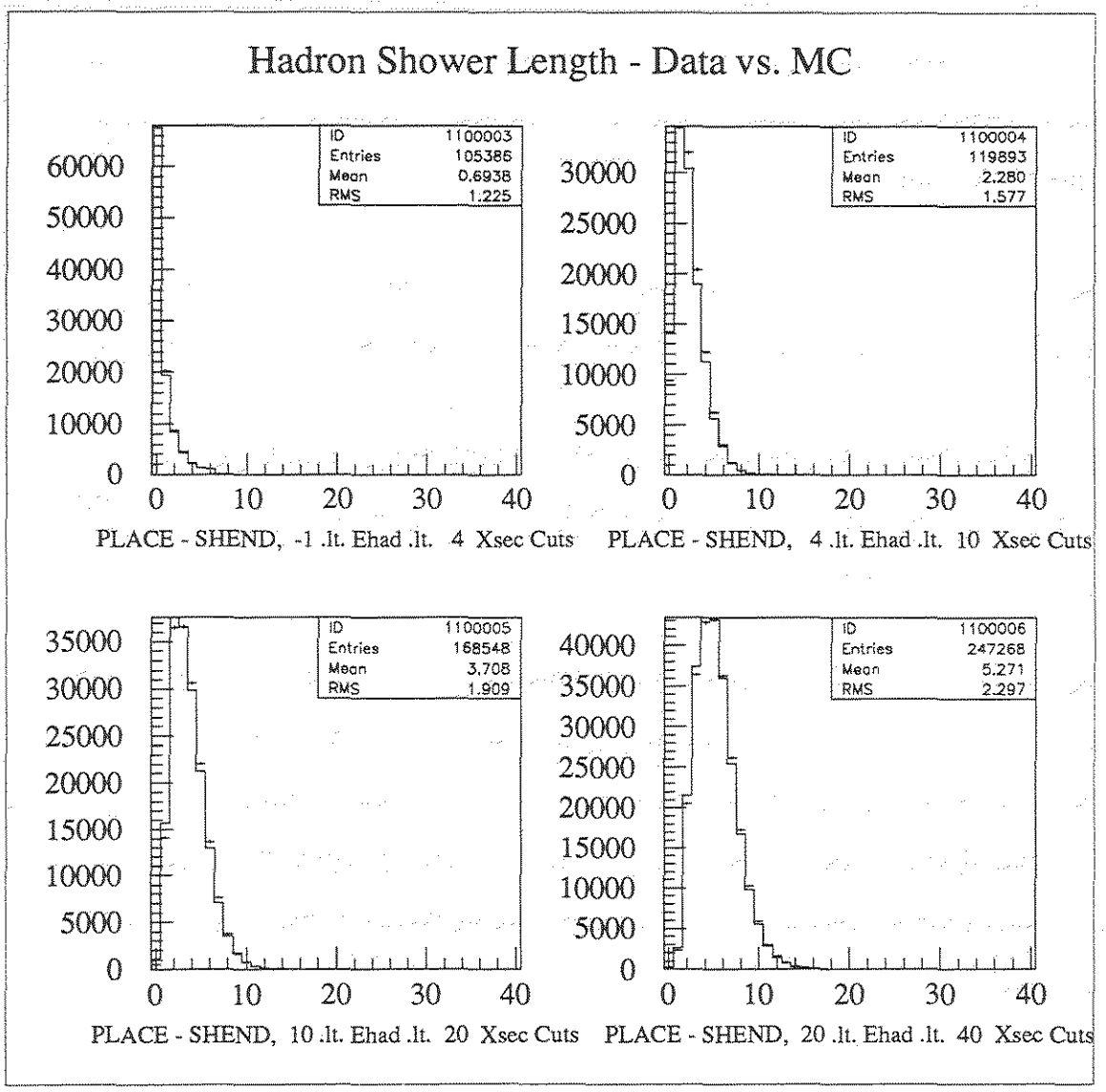

Figure E.1: Data and Monte-Carlo hadron shower length distributions for $-1 < E_{HAD} < 40\ GeV$. It is possible to measure a value of E_{HAD} less than zero due to the muon restricted energy-loss subtraction; see Section 3.?.

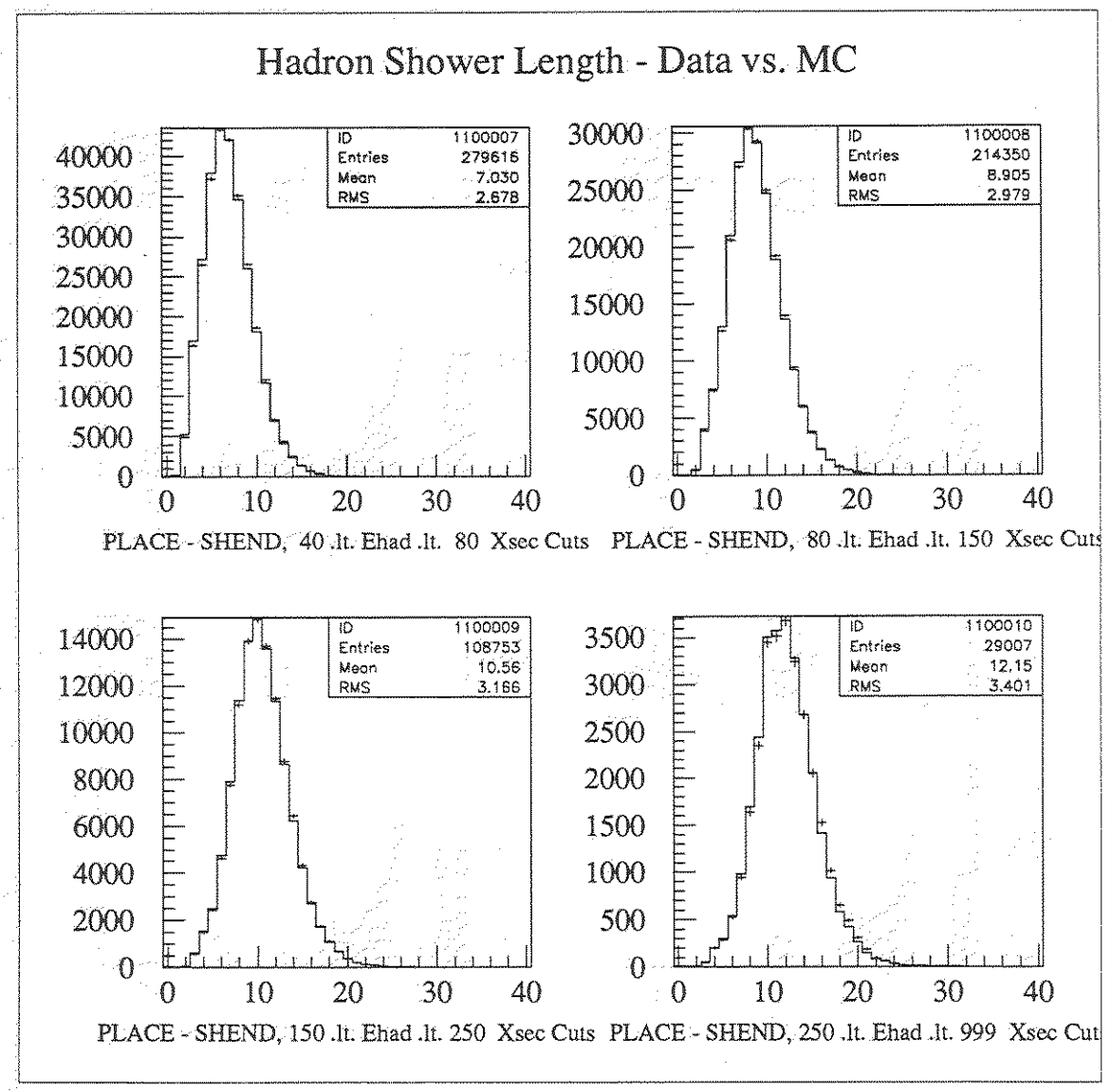

Figure E.2: Data and Monte-Carlo hadron shower length distributions for $E_{HAD} > 40\ GeV$.

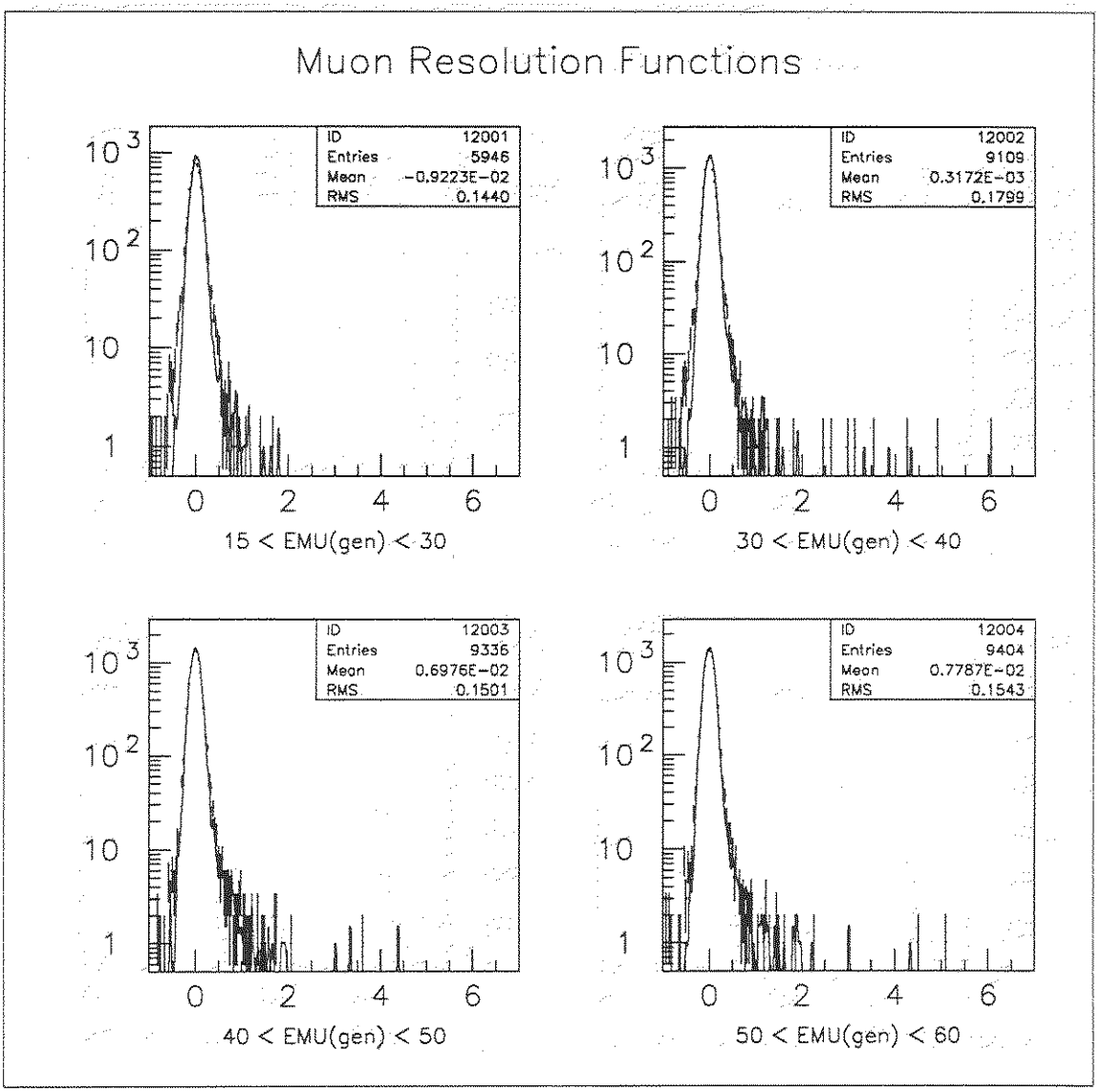

Figure E.3: Resolution functions $\mathcal{F} = \left(1/p_{meas} - 1/p_{gen}\right) / \left(1/p_{gen}\right)$ for $0 < E_{\mu} < 60\ GeV$.

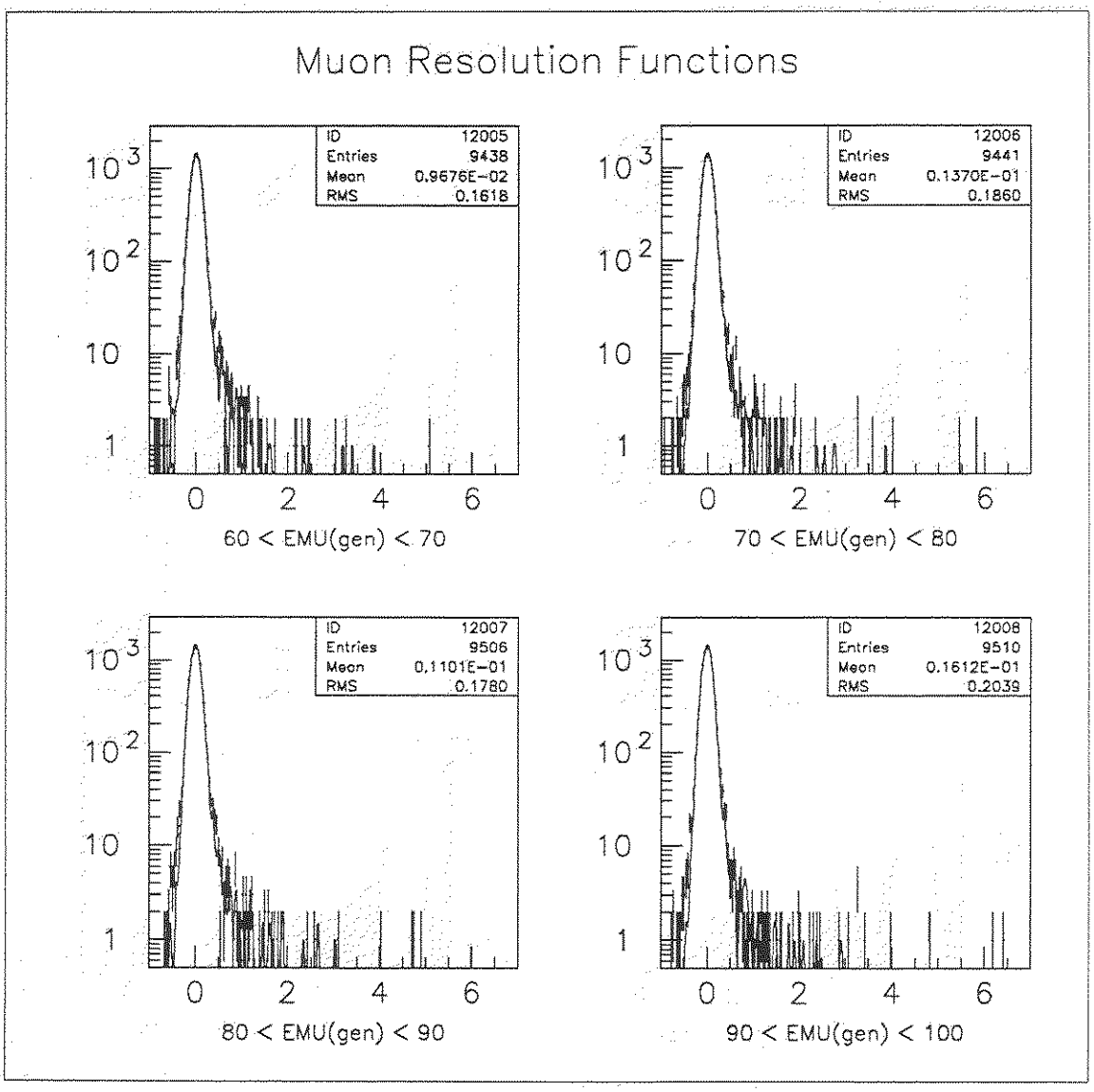

Figure E.4: Resolution functions $\mathcal{F} = \left(1/p_{meas} - 1/p_{gen}\right) / \left(1/p_{gen}\right)$ for $60 < E_{\mu} < 100\ GeV$.

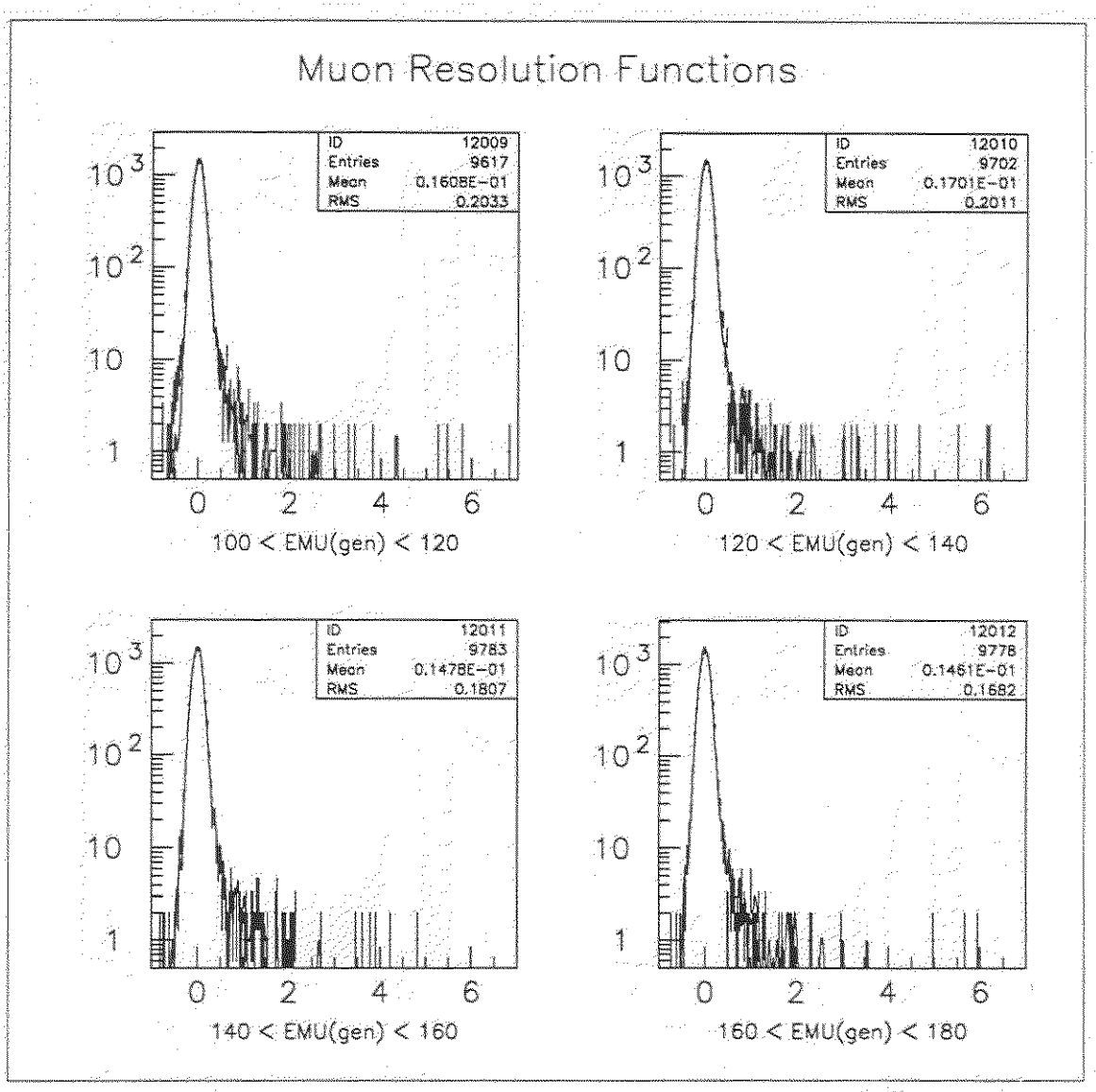

Figure E.5: Resolution functions $\mathcal{F} = \left(1/p_{meas} - 1/p_{gen}\right) / \left(1/p_{gen}\right)$ for $100 < E_{\mu} < 180\ GeV$.

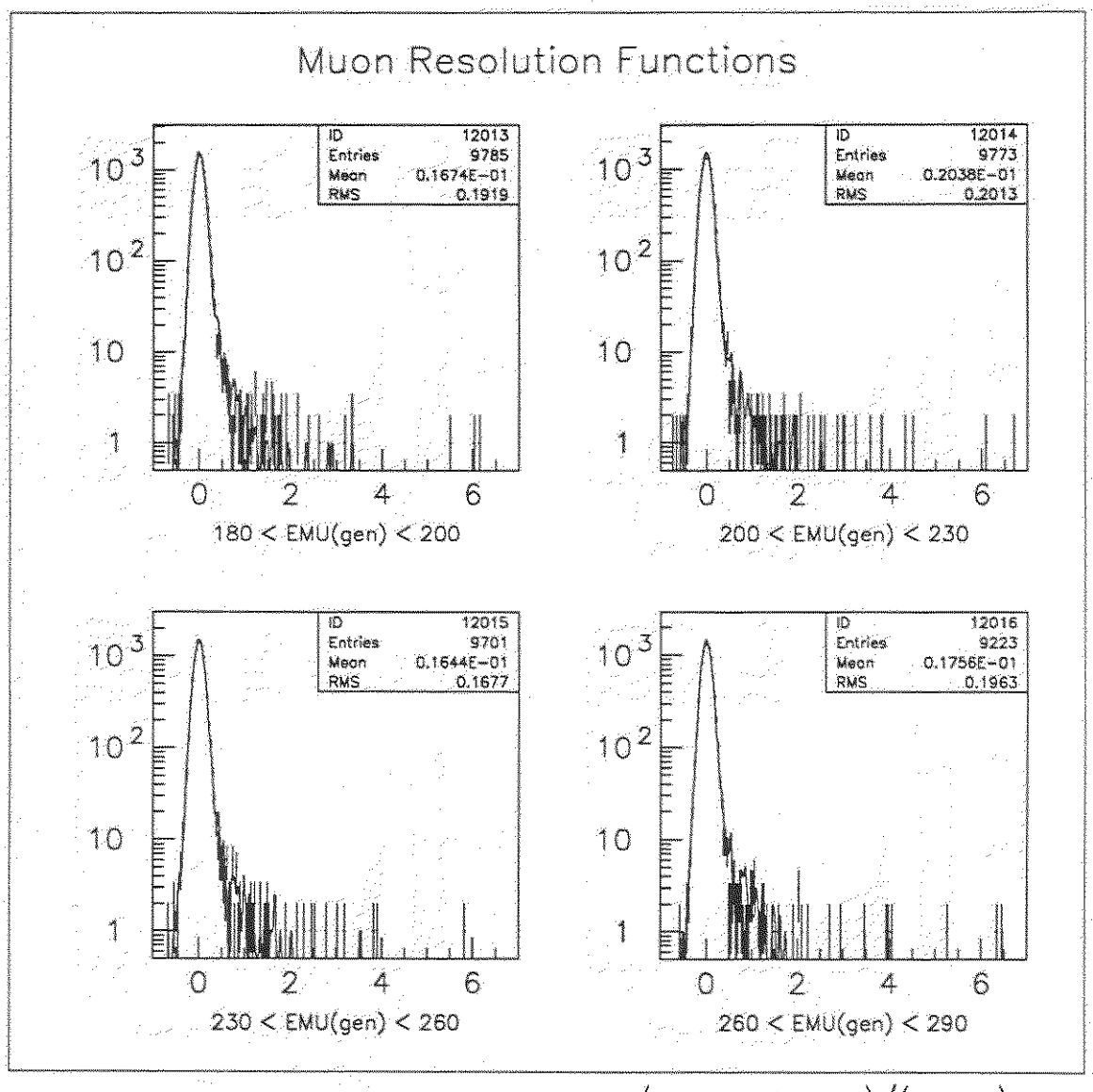

Figure E.6: Resolution functions $\mathcal{F} = \left(1/p_{meas} - 1/p_{gen}\right) / \left(1/p_{gen}\right)$ for $180 < E_{\mu} < 290\ GeV$.

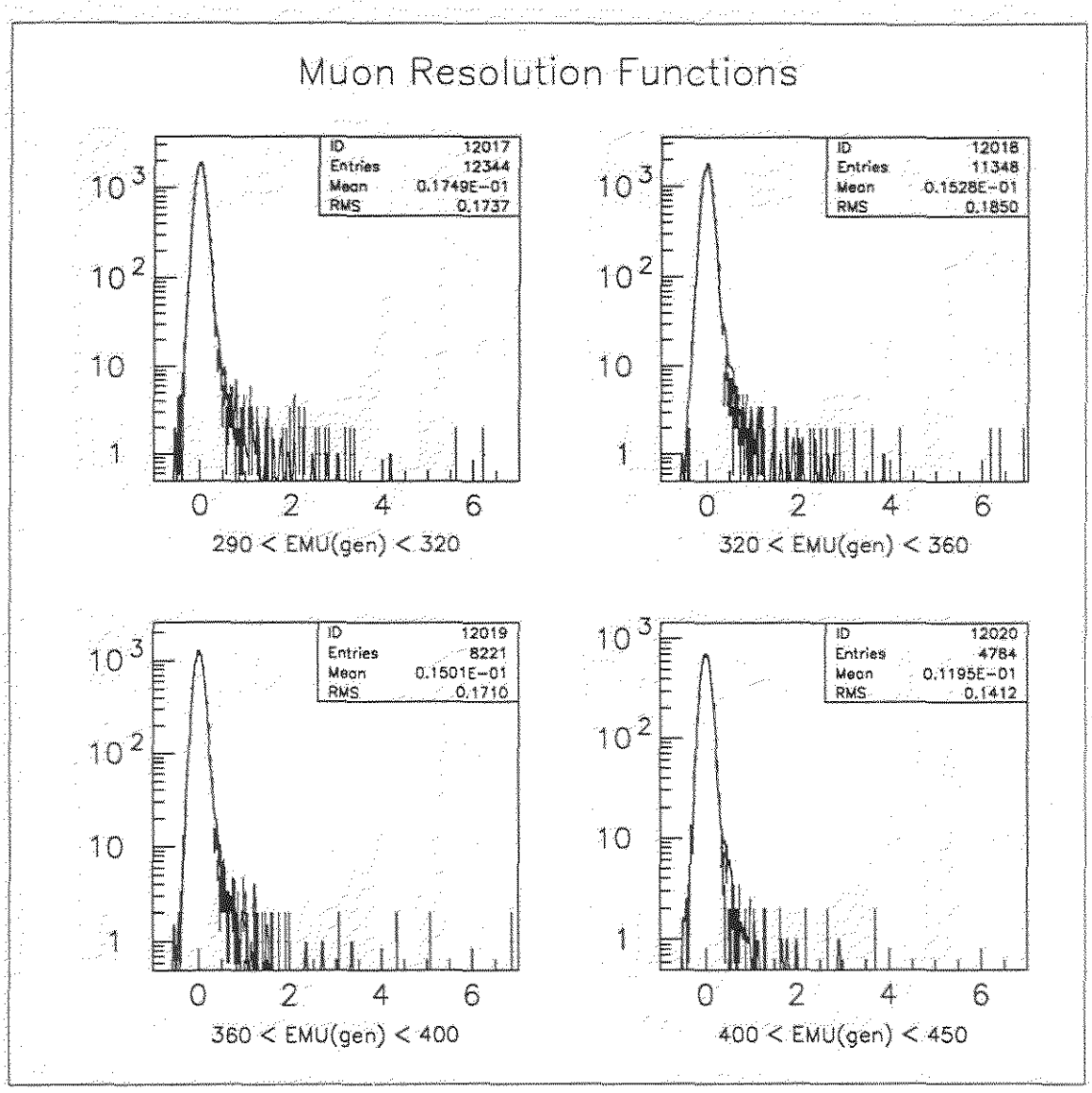

Figure E.7: Resolution function $\mathcal{F} = \left(1/p_{meas} - 1/p_{gen}\right) / \left(1/p_{gen}\right)$ for $290 < E_{\mu} < 450\ GeV$.

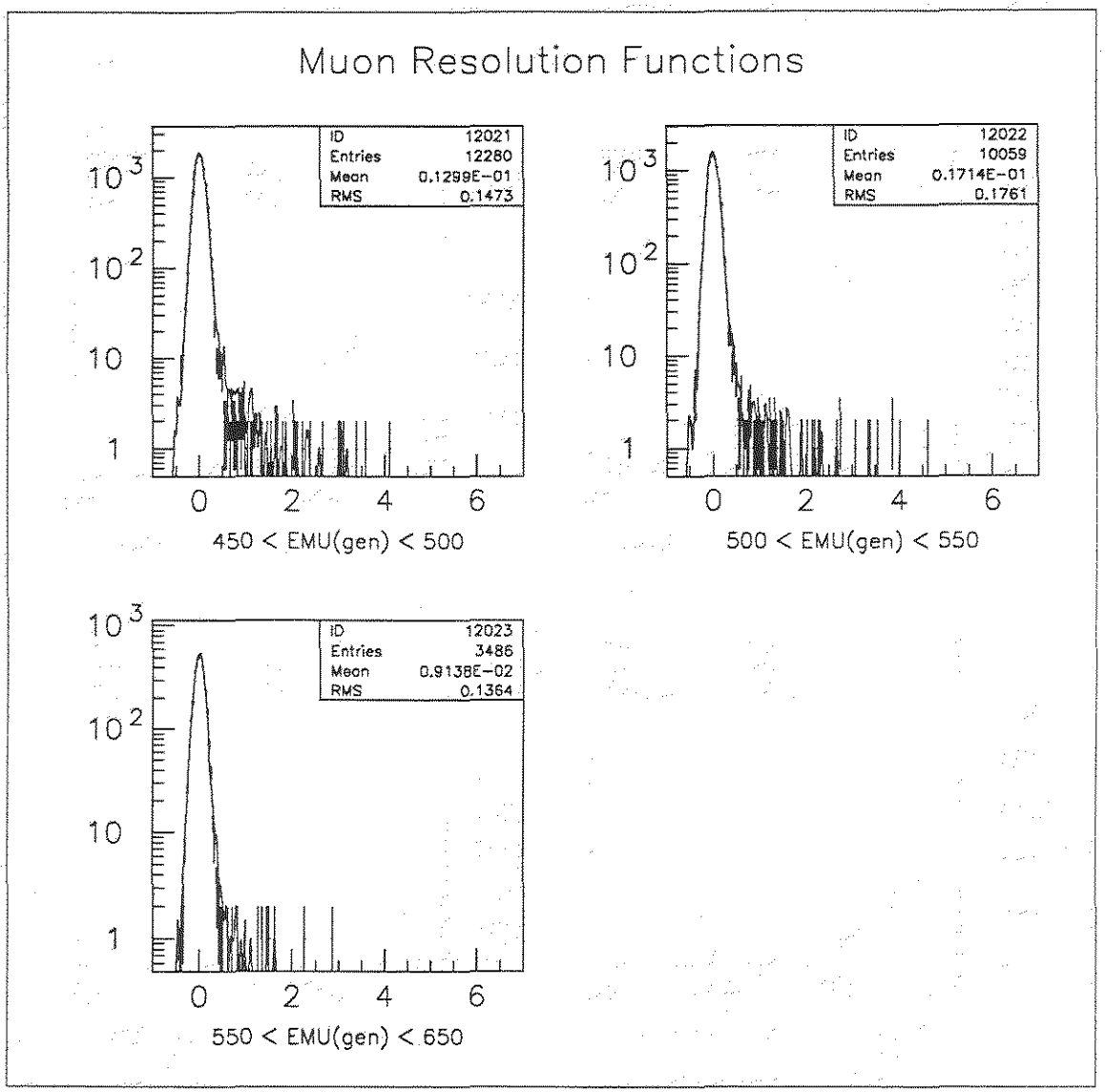

Figure E.8: Resolution functions $\mathcal{F} = \left(1/p_{meas} - 1/p_{gen}\right) / \left(1/p_{gen}\right)$ for $E_\mu > 450\ GeV$.

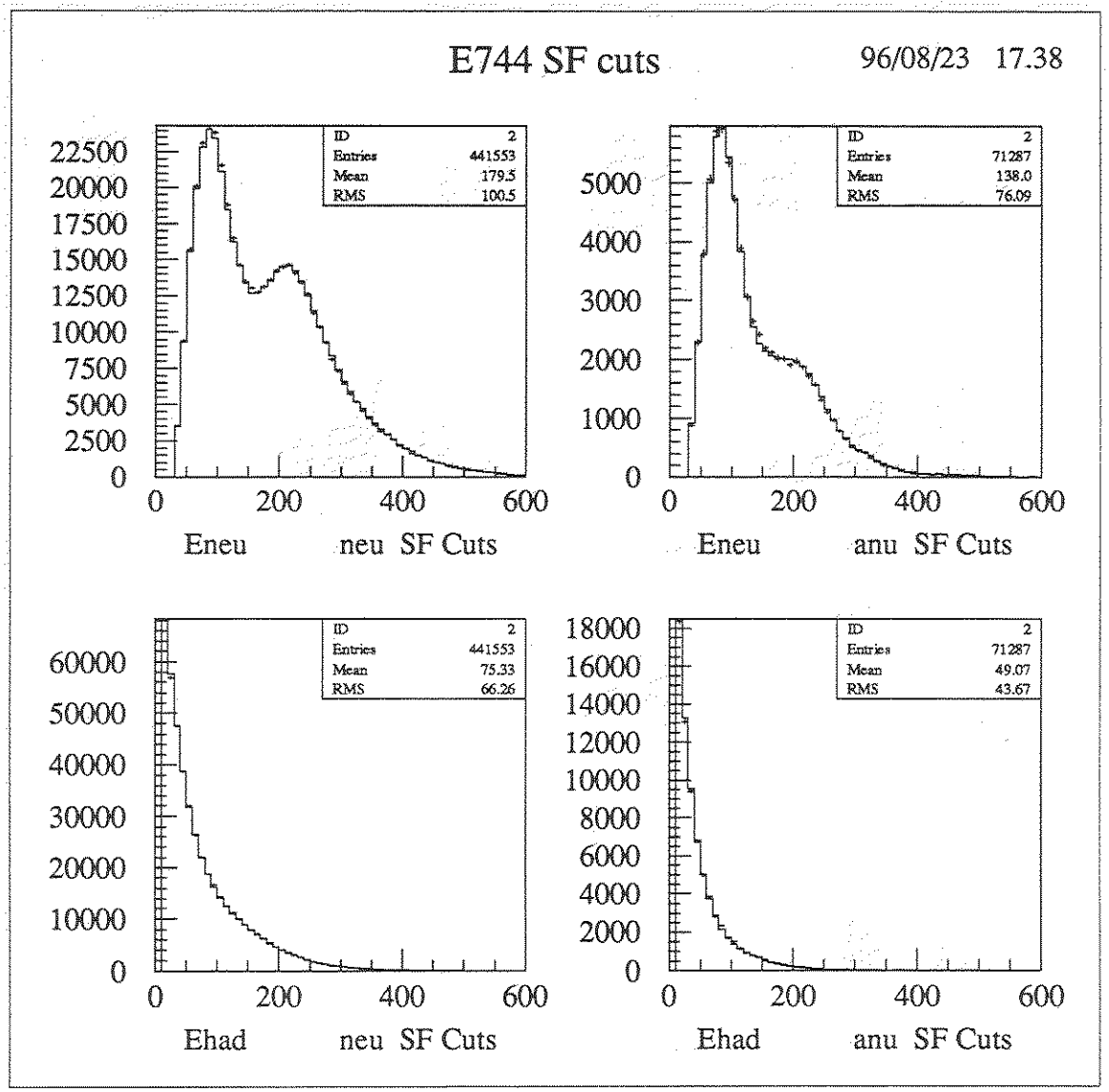

Figure E.9: E744 data versus Monte Carlo for the variables E_ν and E_{HAD}.

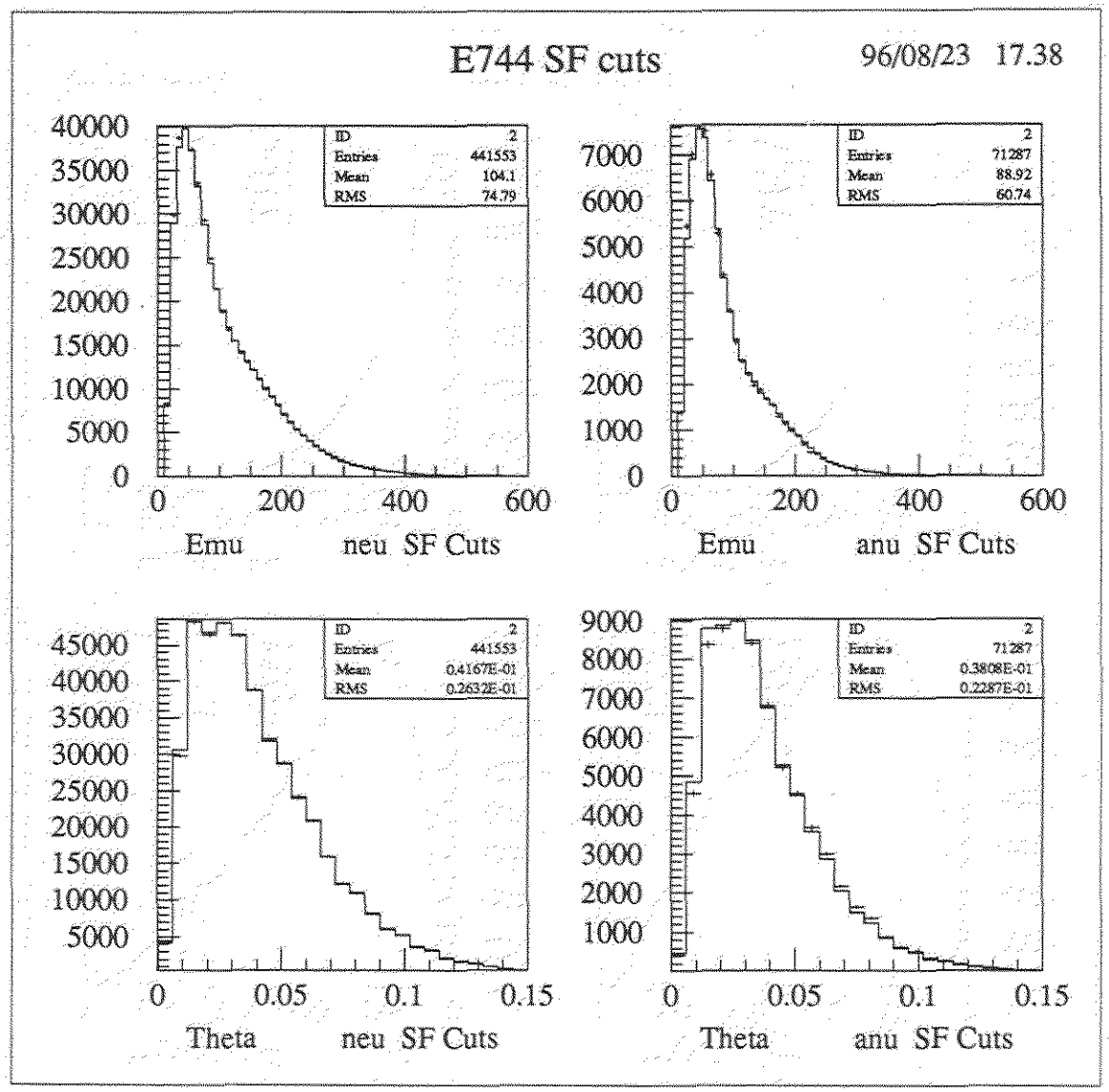

Figure E.10: E744 data versus Monte Carlo for the variables E_μ and θ_μ.

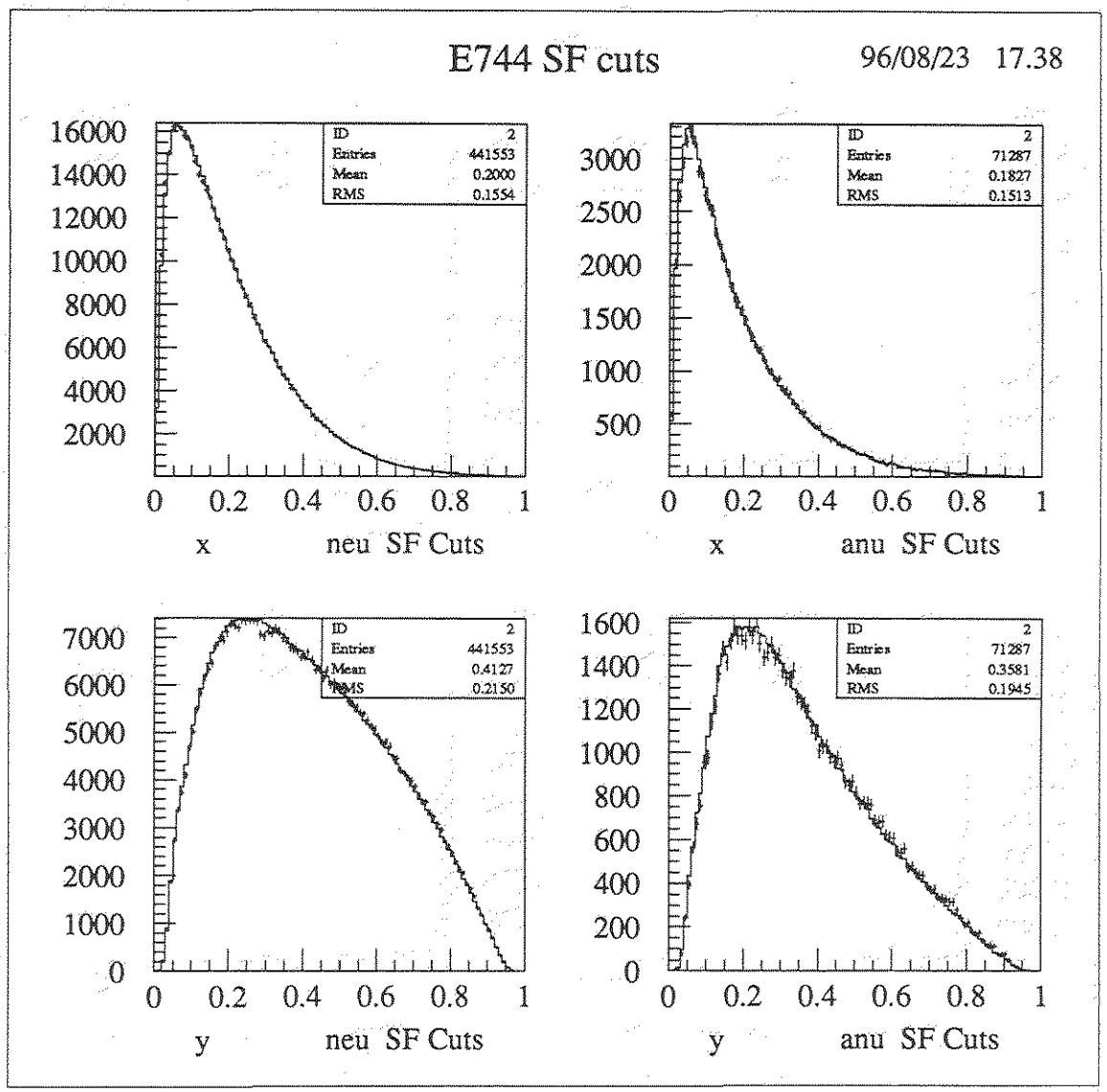

Figure E.11: E744 data versus Monte Carlo for the variables x_{BJ} and y_{BJ}.

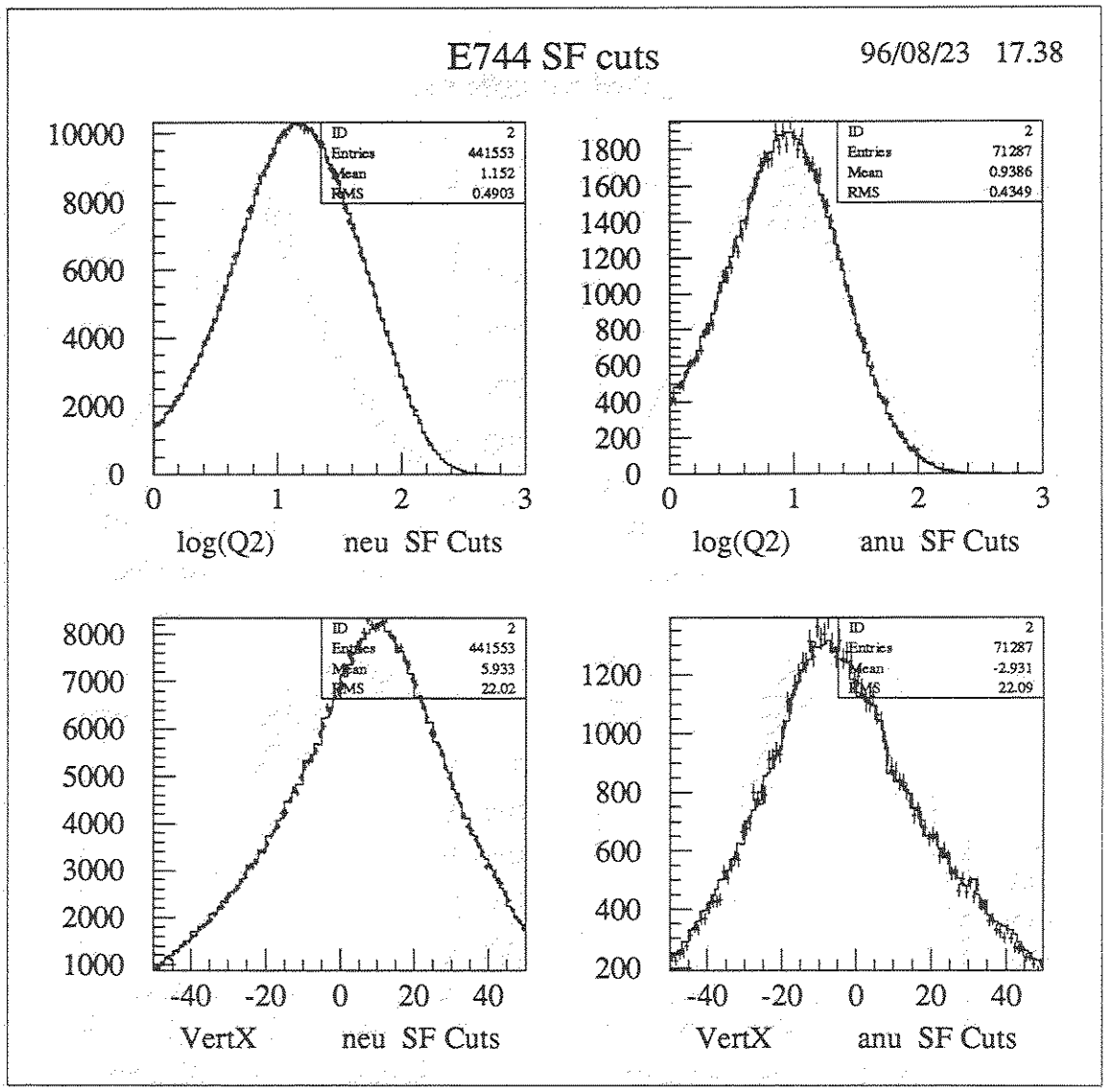

Figure E.12: E744 data versus Monte Carlo for the variables $\log\left(Q^2\right)$ and the x-vertex.

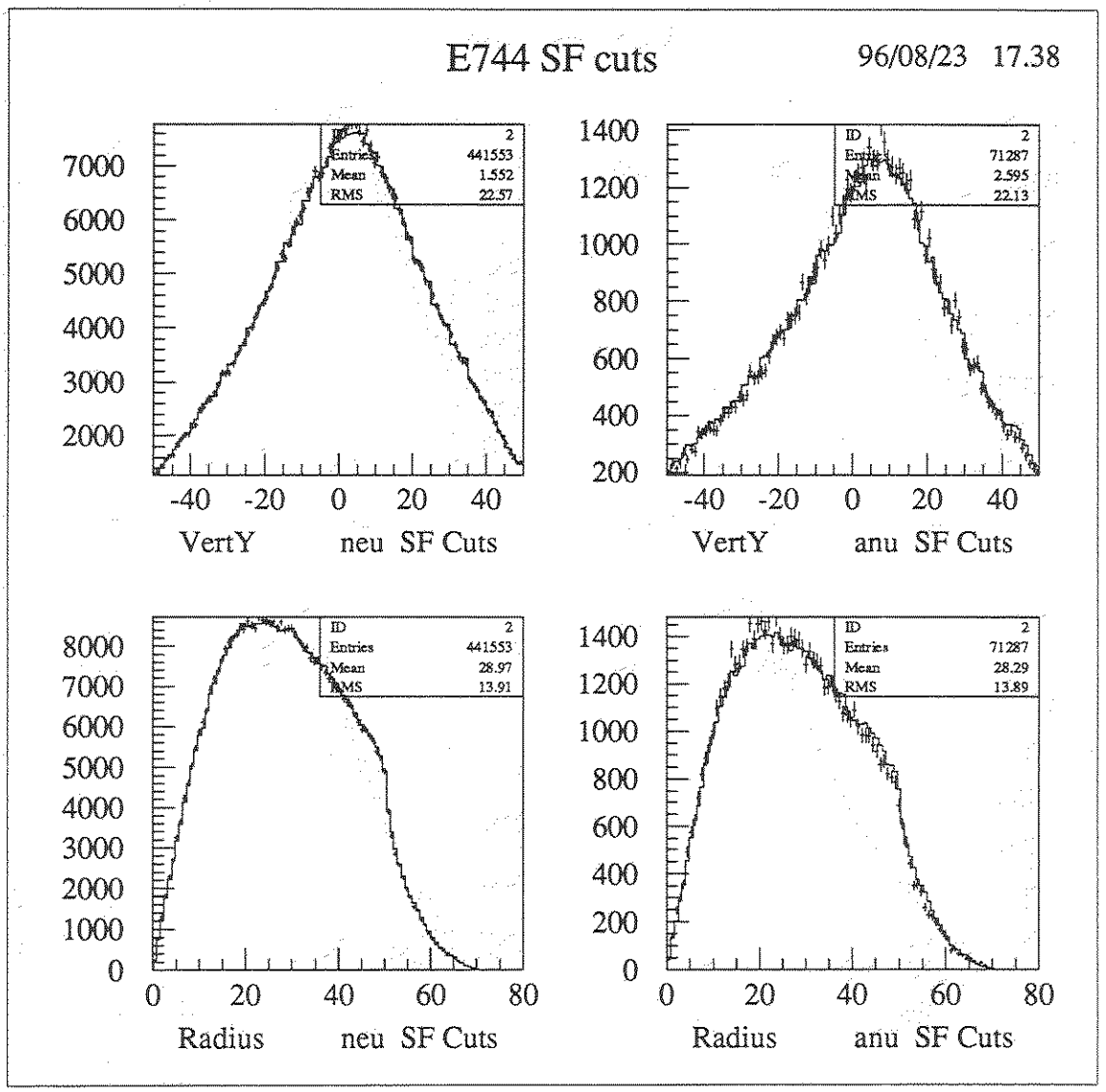

Figure E.13: E744 data versus Monte Carlo for the y-vertex and the vertex radius.

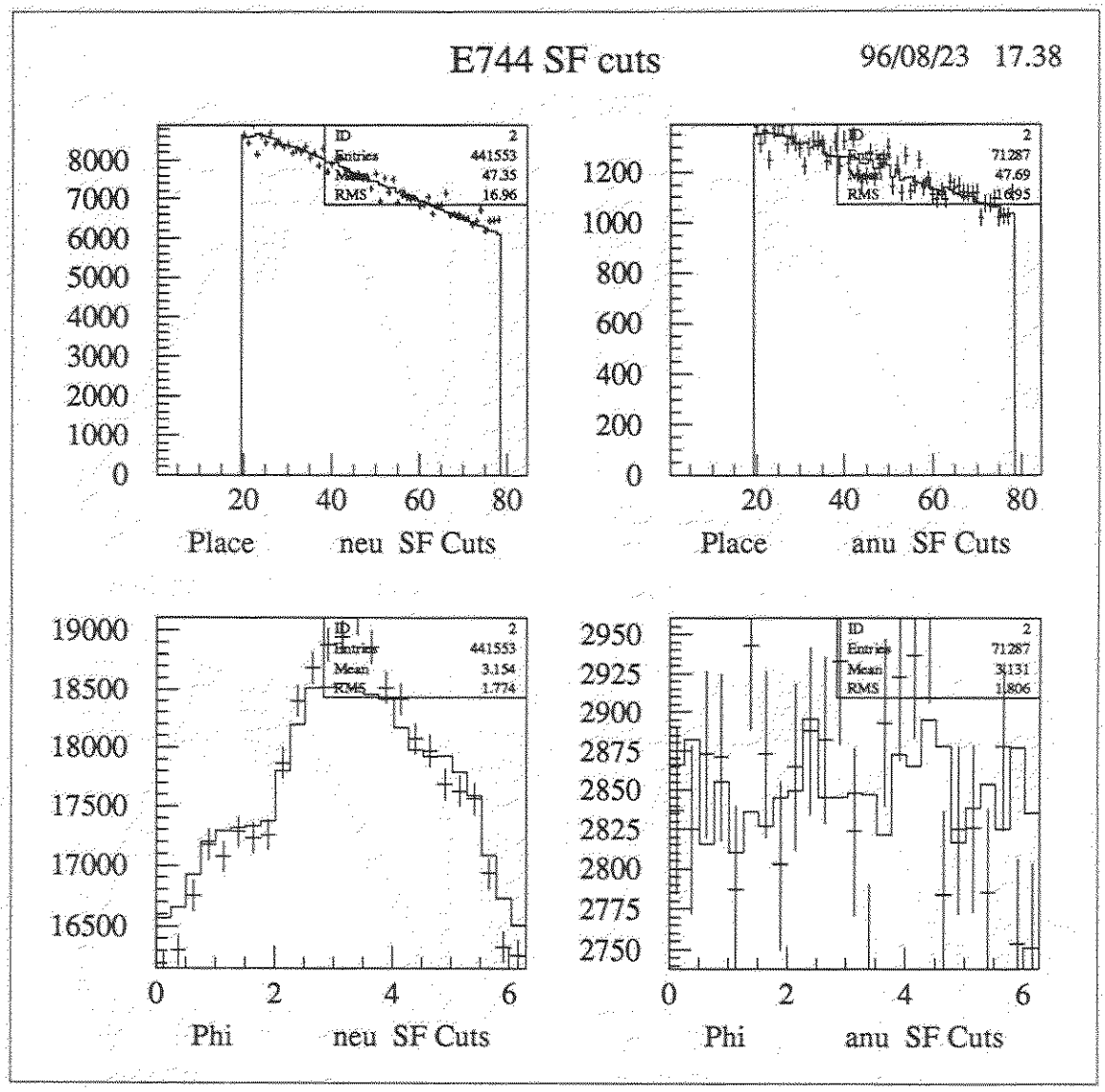

Figure E.14: E744 data versus Monte Carlo for PLACE and ϕ. Note the axes of the ϕ plots are zero-suppressed.

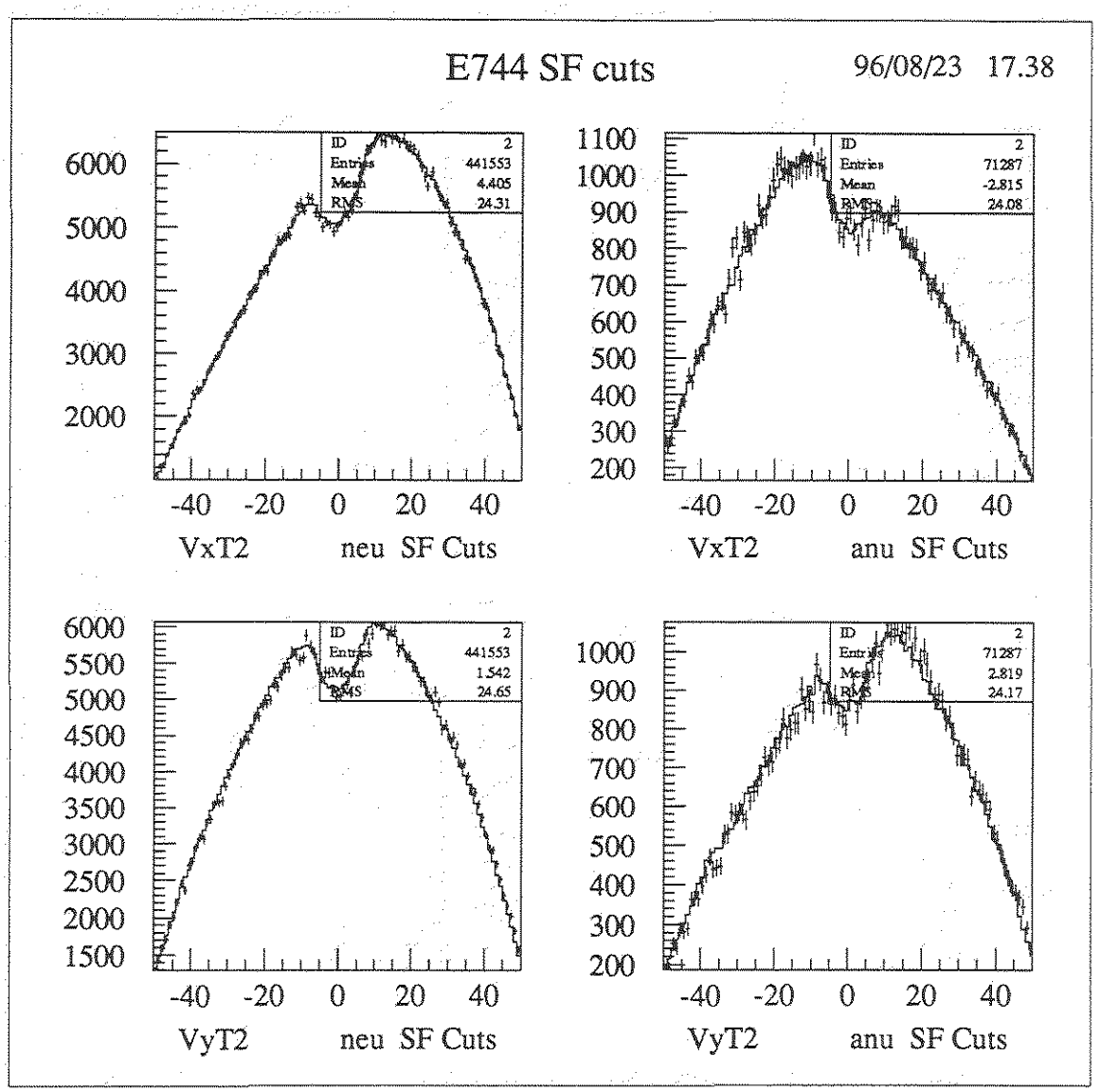

Figure E.15: E744 data versus Monte Carlo for x- and y-vertex at the T2 counter.

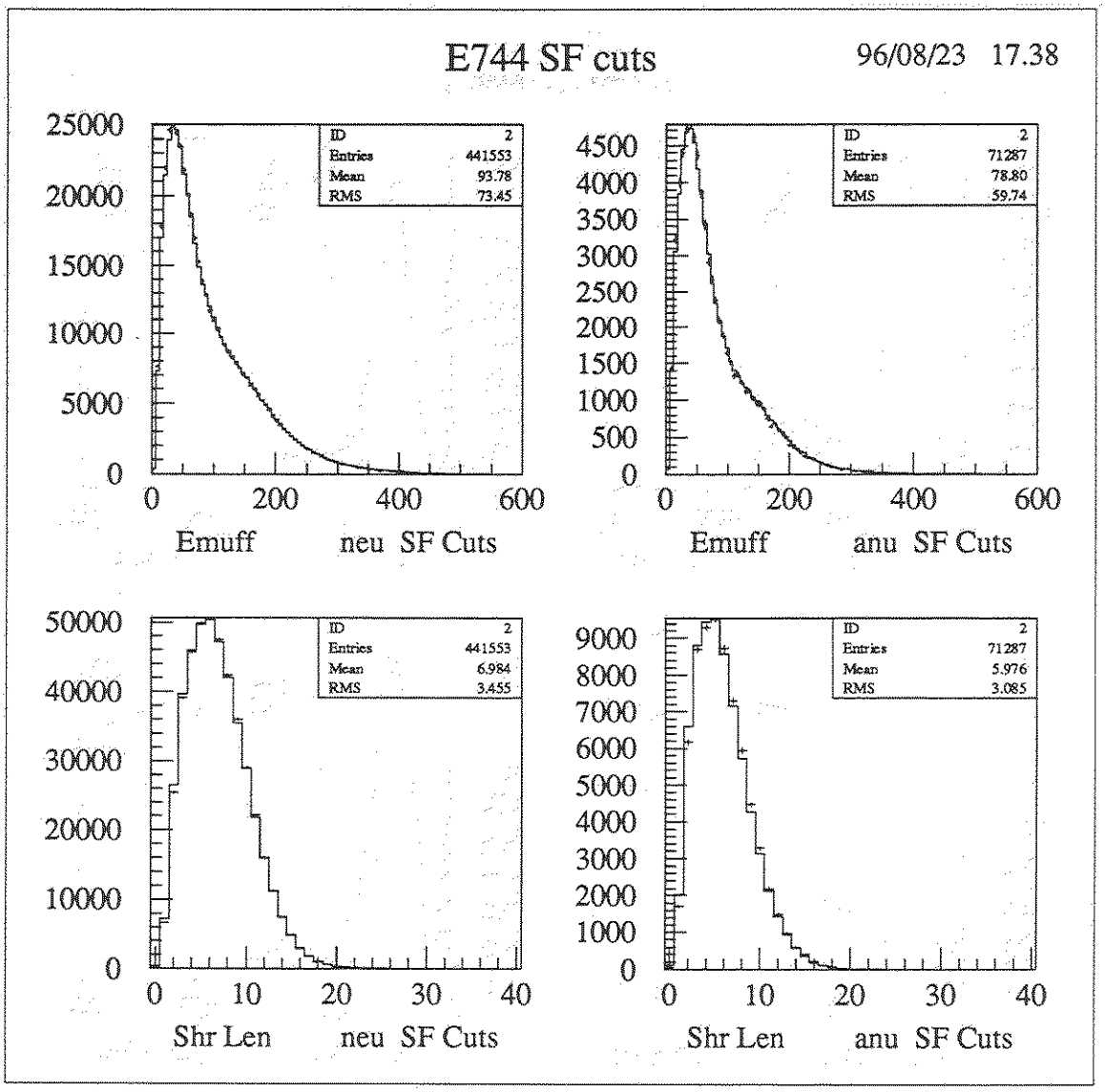

Figure E.16: E744 data versus Monte Carlo for E_{μ}^{FF} and the hadron shower length (*PLACE–SHEND*).

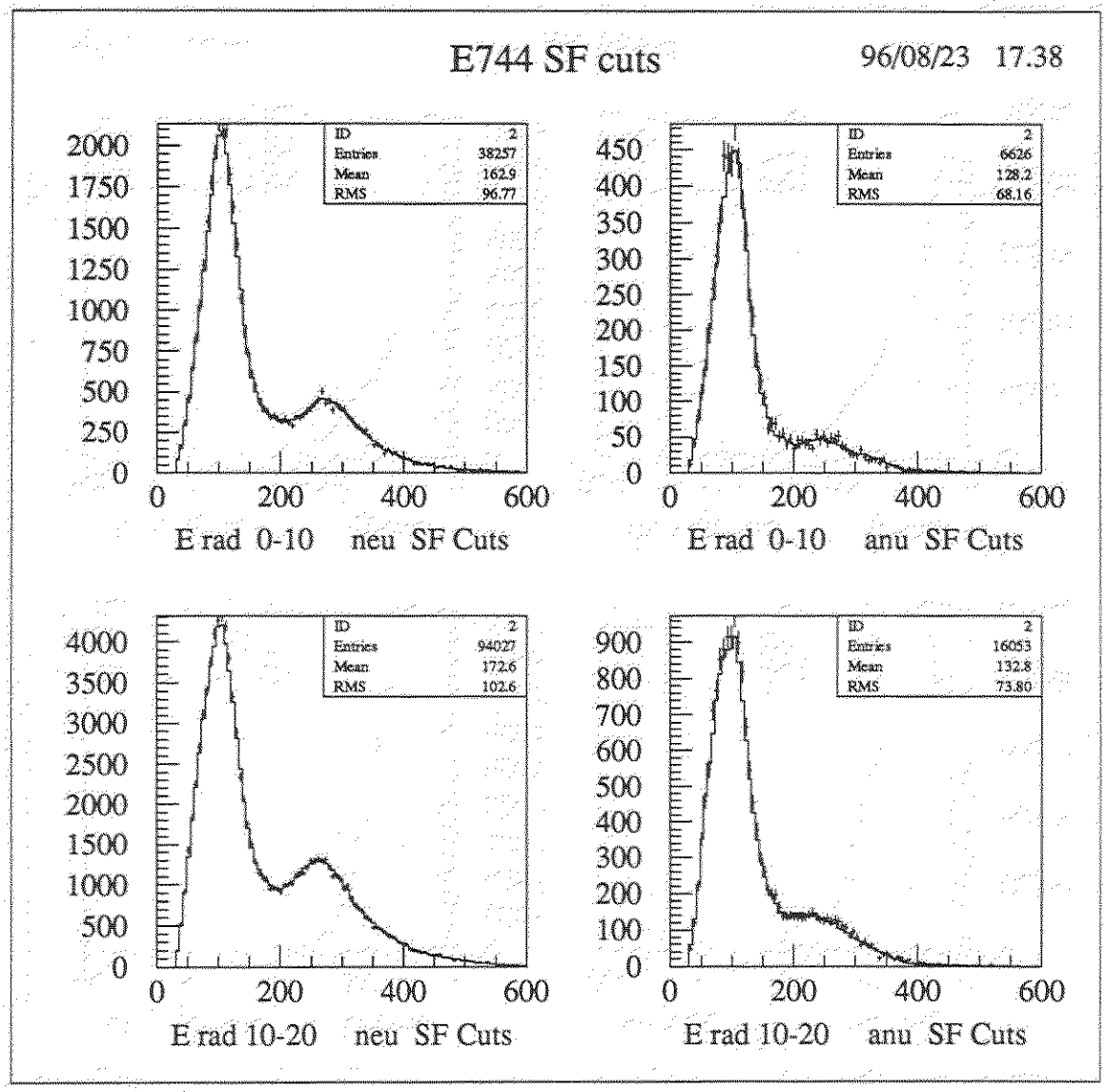

Figure E.17: E744 data versus Monte Carlo for E_ν in the radial bins 0-10 *in* and 10-20 *in*.

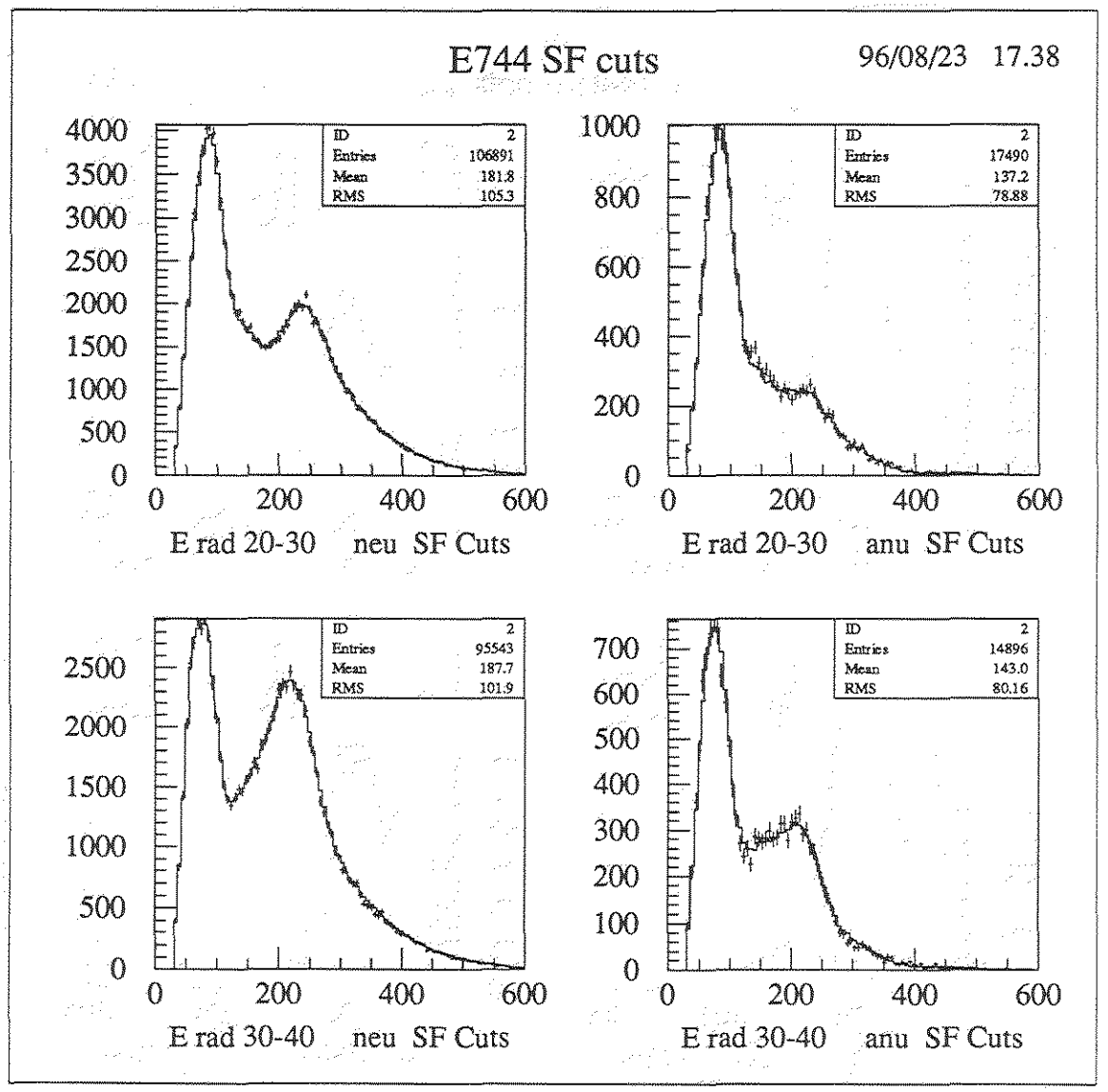

Figure E.18: E744 data versus Monte Carlo for E_ν in the radial bins 20-30 *in* and 30-40 *in*.

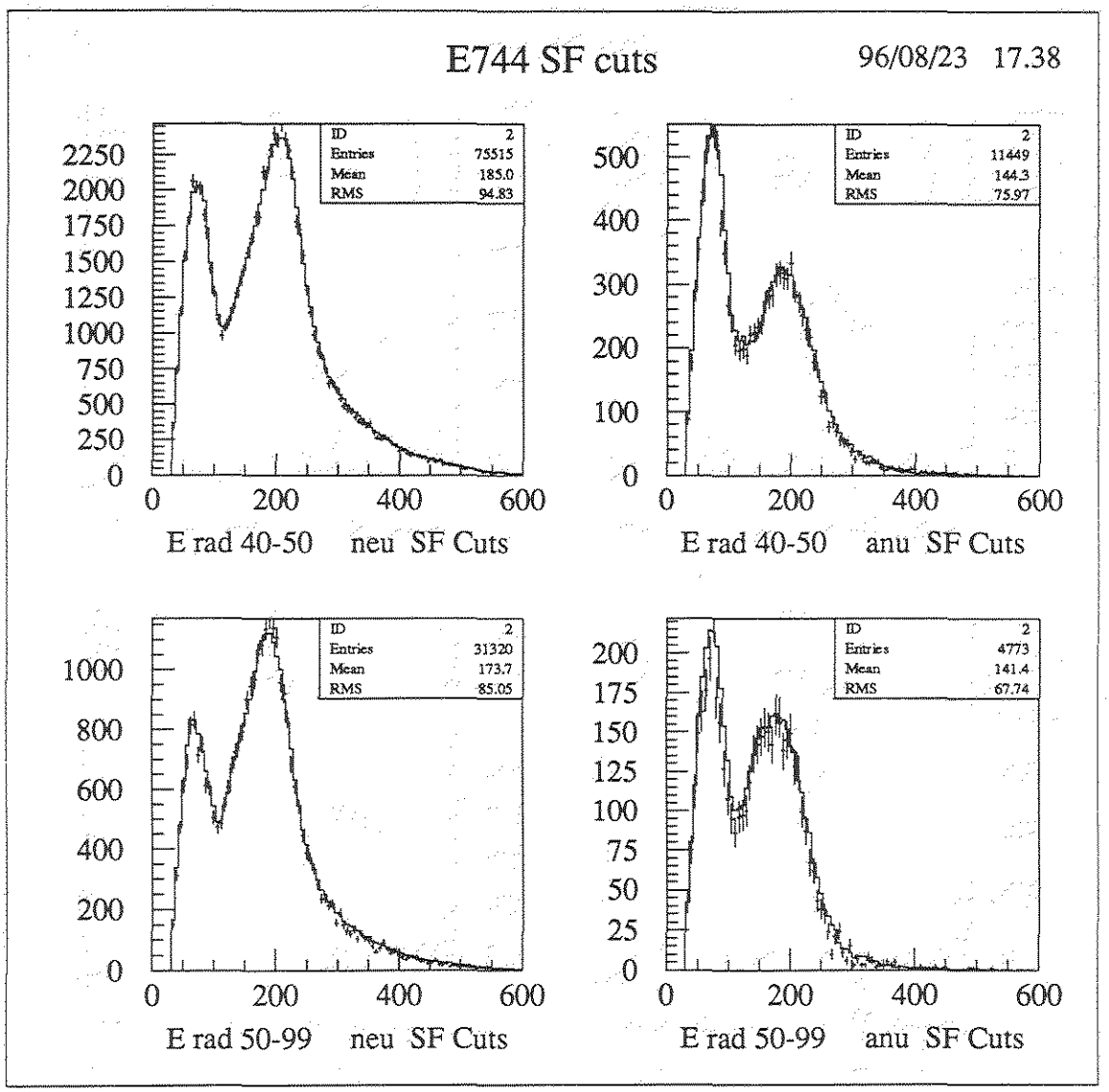

Figure E.19: E744 data versus Monte Carlo for E_ν in the radial bins 40-50 *in* and 50-99 *in*.

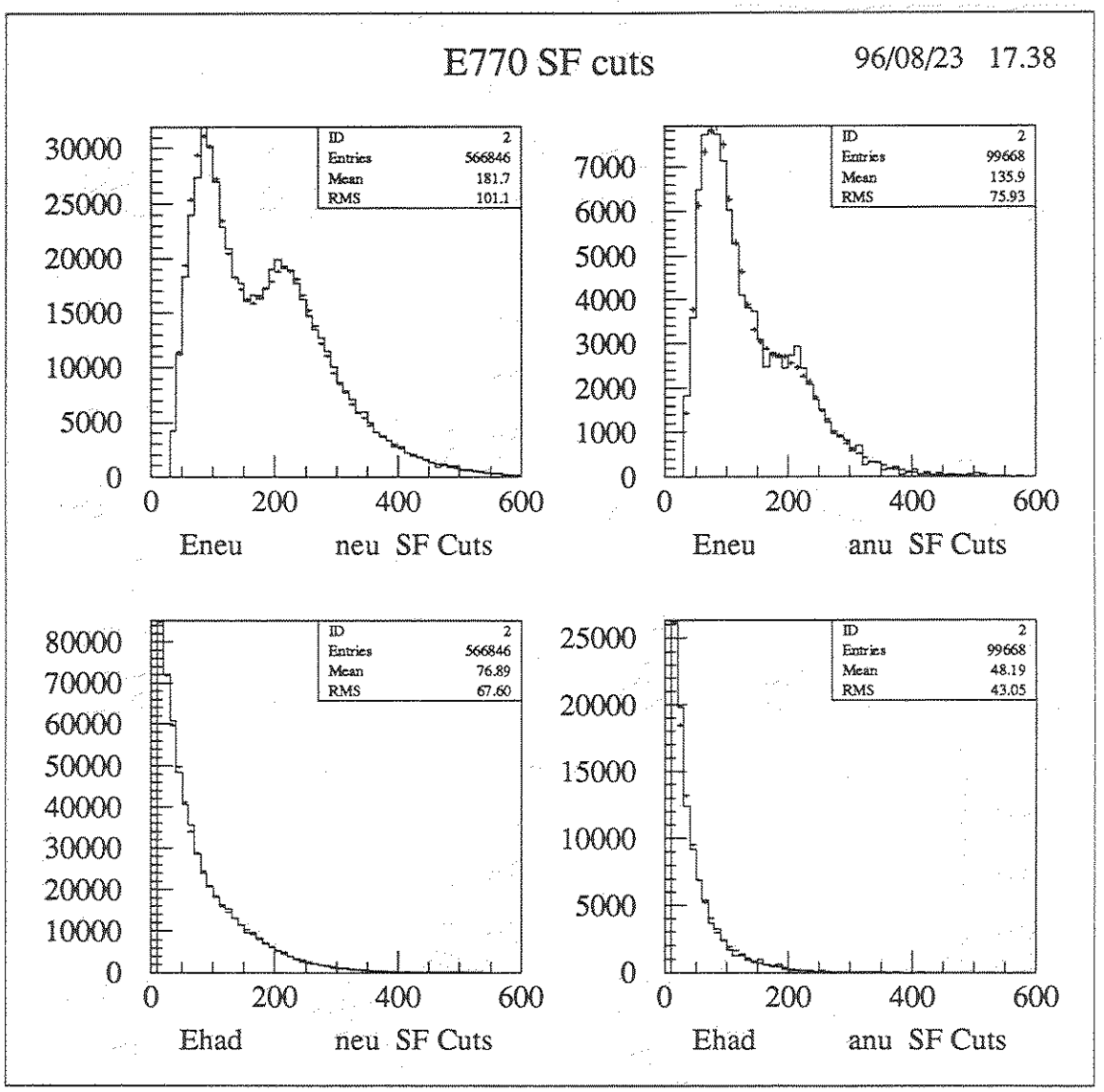

Figure E.20: E770 data versus Monte Carlo for the variables E_ν and E_{HAD}.

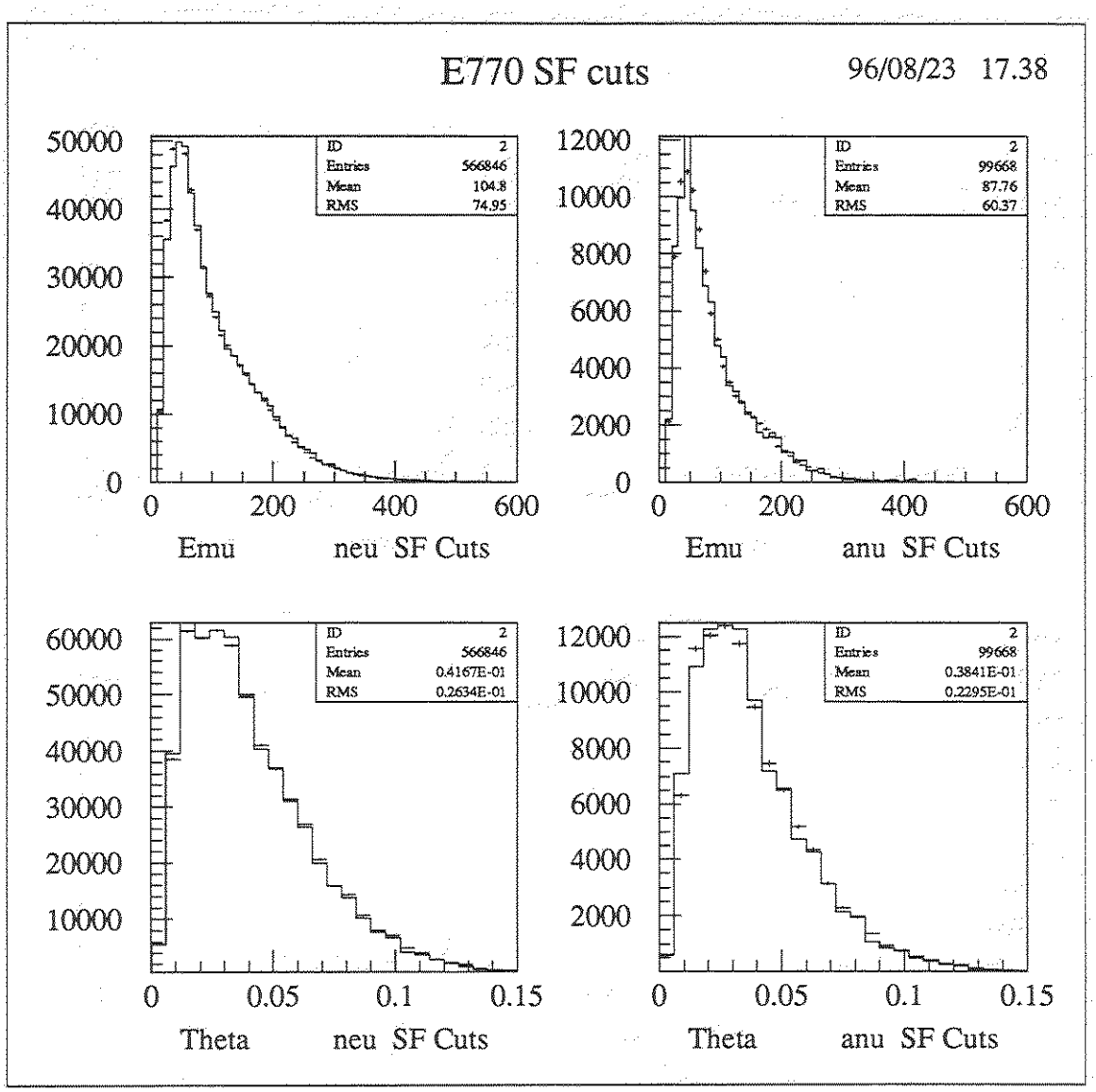

Figure E.21: E770 data versus Monte Carlo for the variables E_μ and θ_μ.

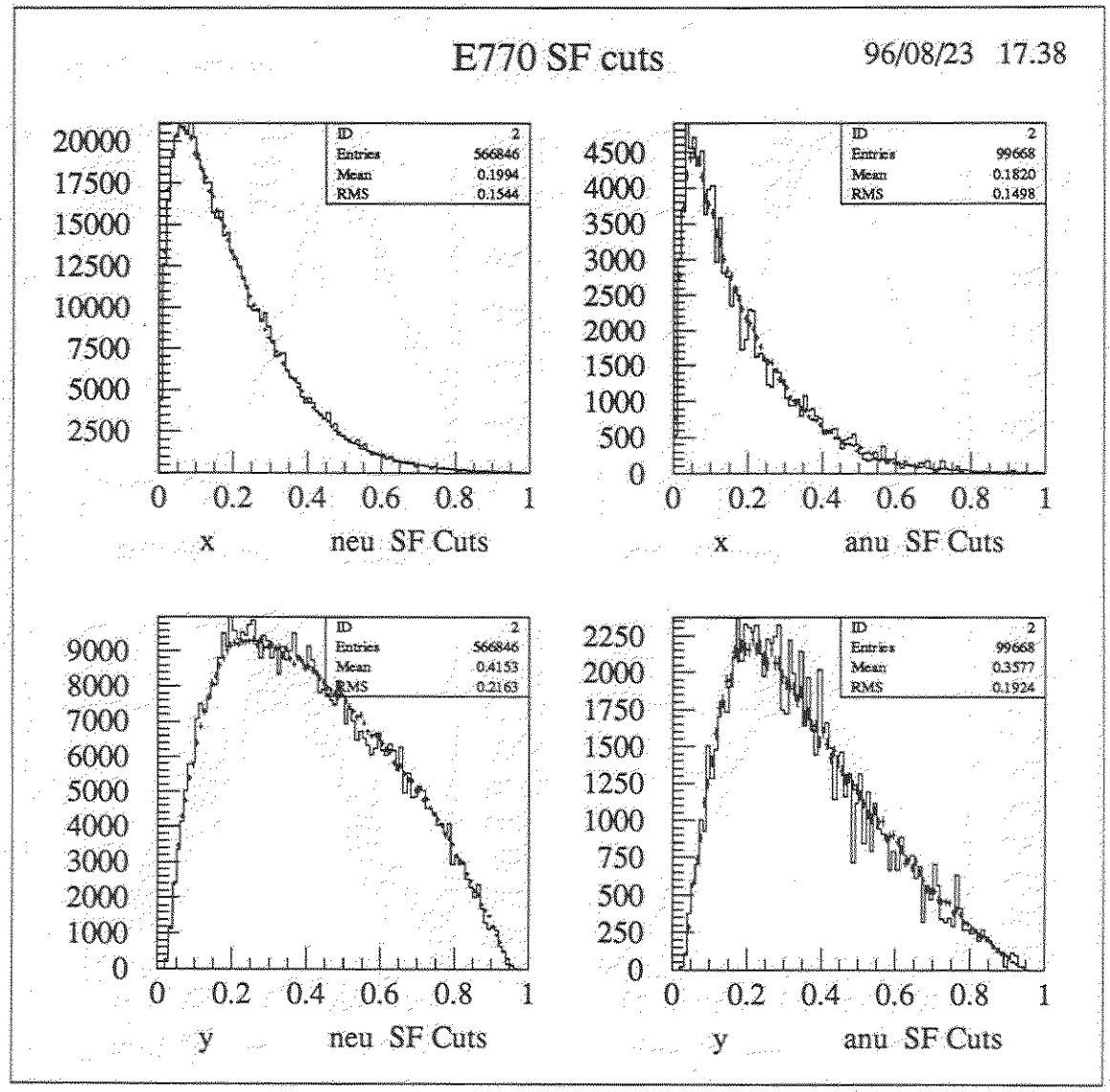

Figure E.22: E770 data versus Monte Carlo for the variables x_{BJ} and y_{BJ}.

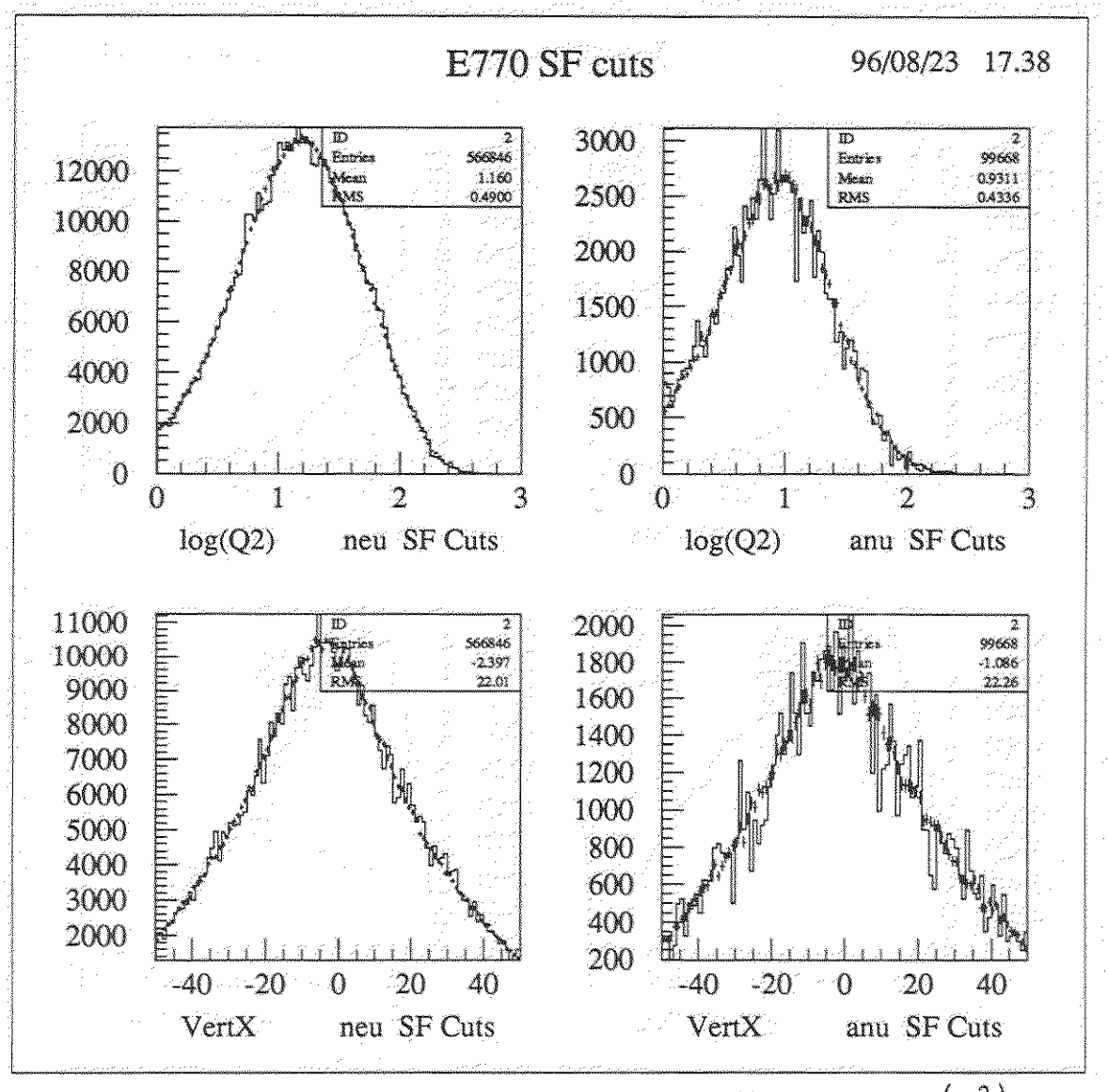

Figure E.23: E770 data versus Monte Carlo for the variables $\log\left(Q^2\right)$ and the x-vertex.

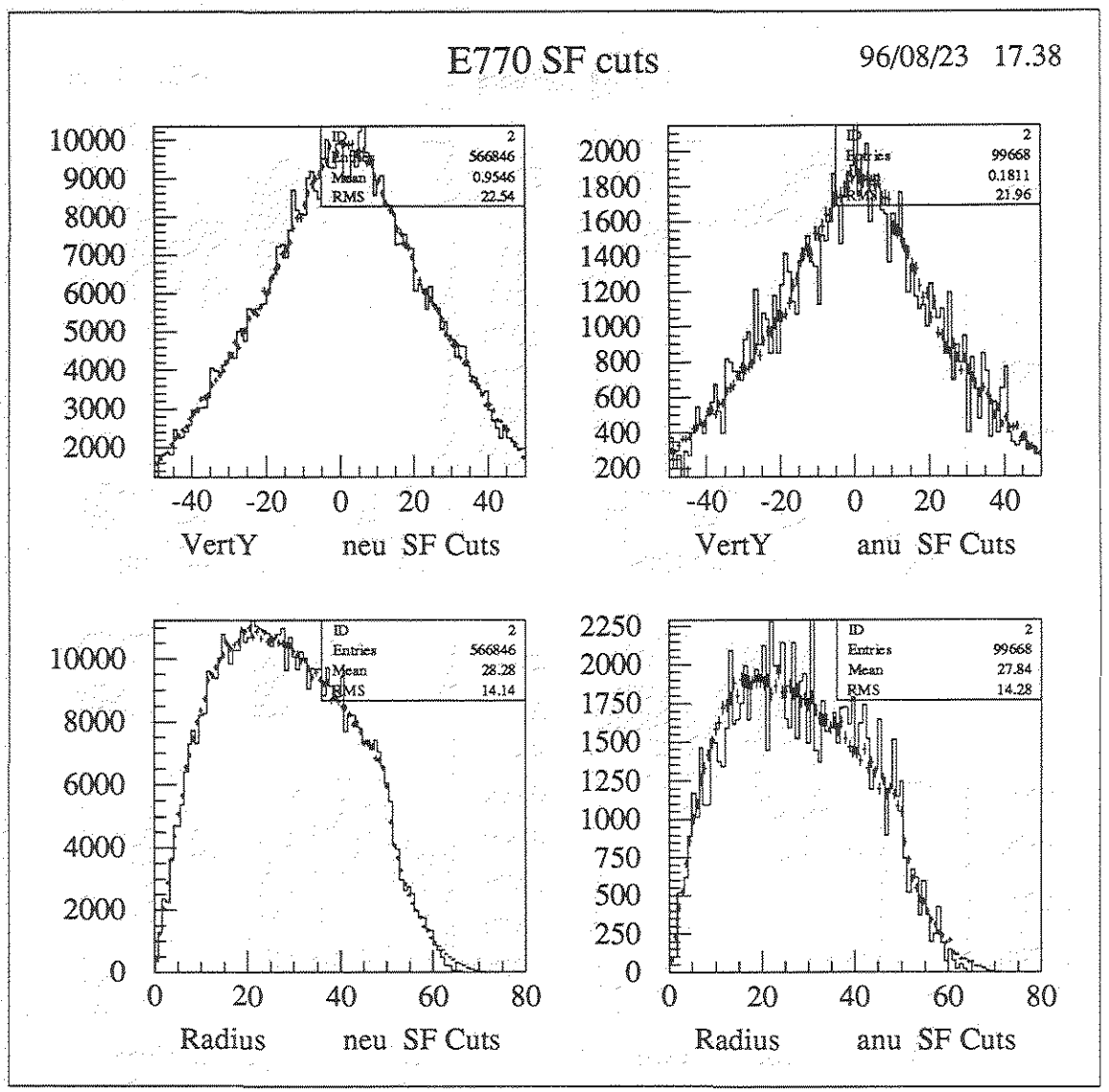

Figure E.24: E770 data versus Monte Carlo for the y-vertex and the vertex radius.

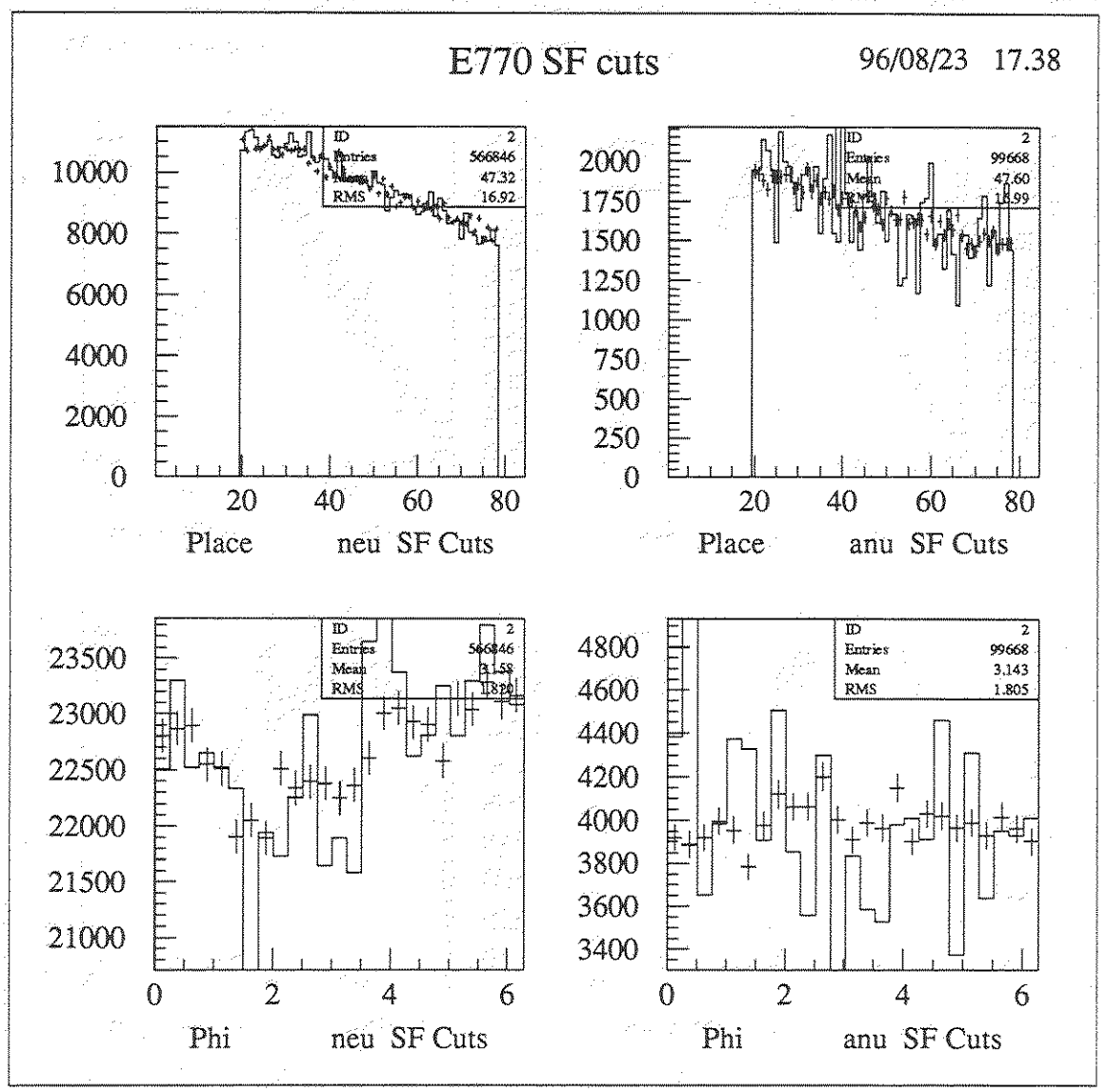

Figure E.25: E770 data versus Monte Carlo for PLACE and ϕ. Note the axes of the ϕ plots are zero-suppressed.

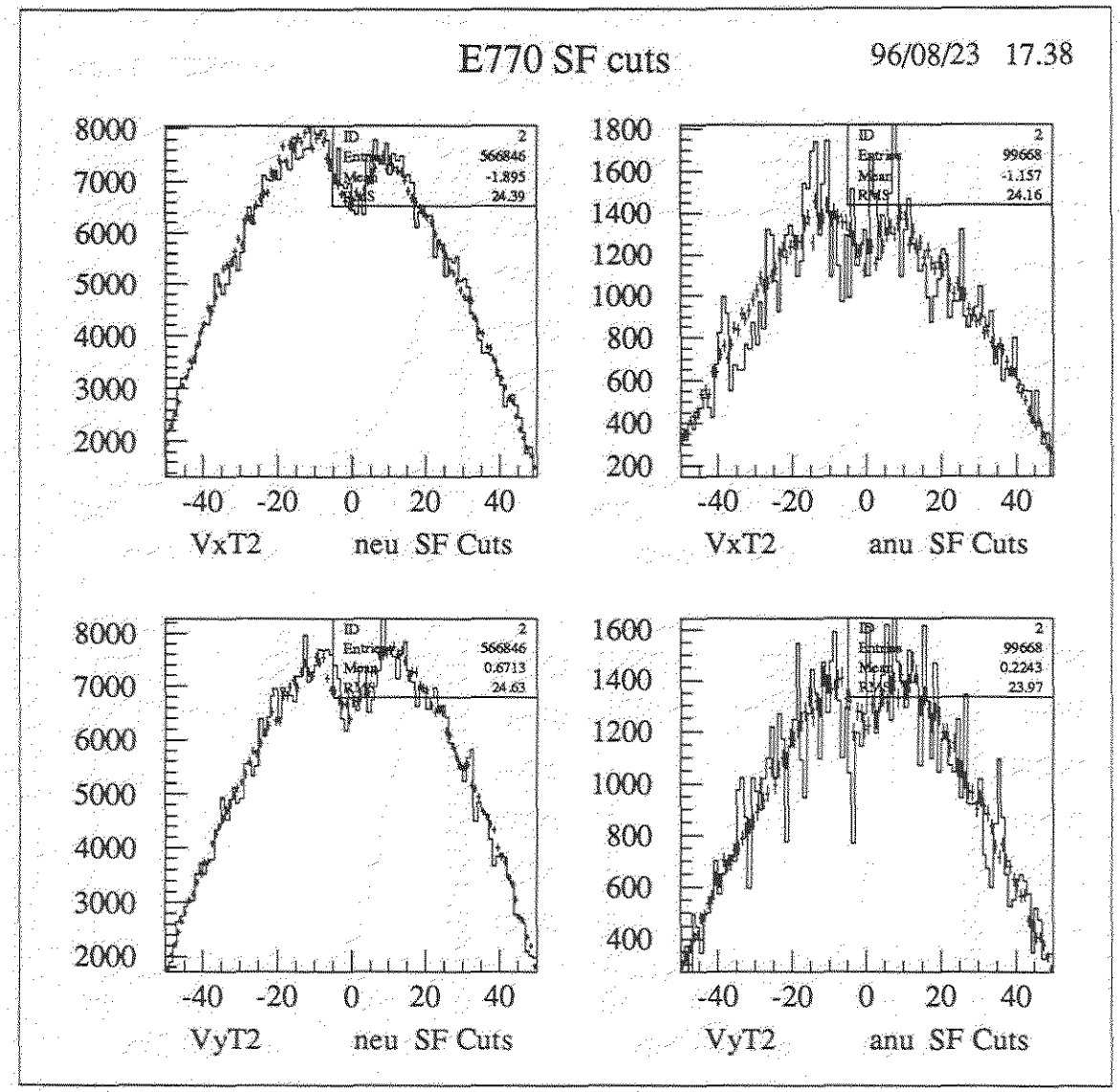

Figure E.26: E770 data versus Monte Carlo for x- and y-vertex at the T2 counter.

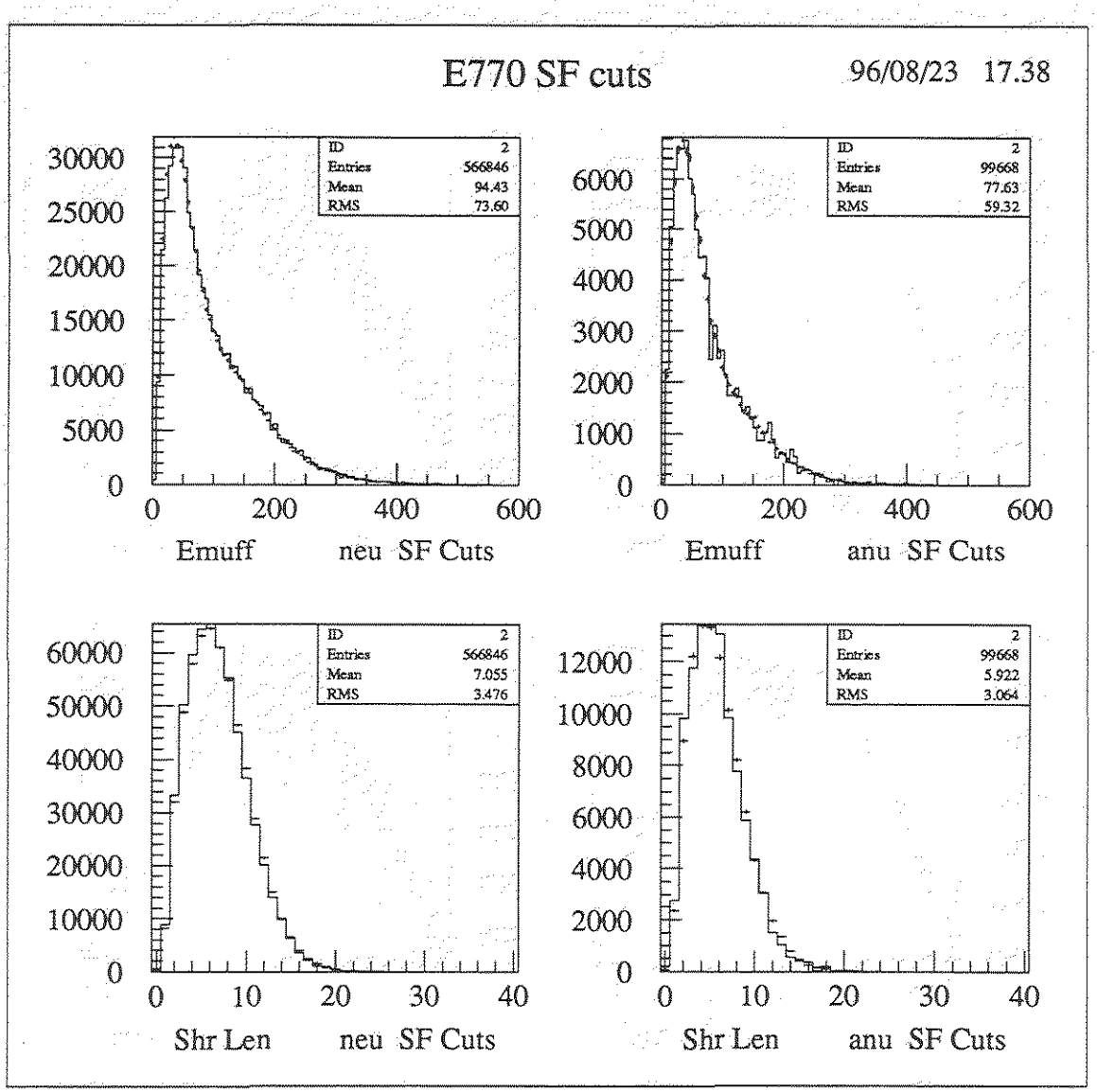

Figure E.27: E770 data versus Monte Carlo for E_{μ}^{FF} and the hadron shower length (*PLACE–SHEND*).

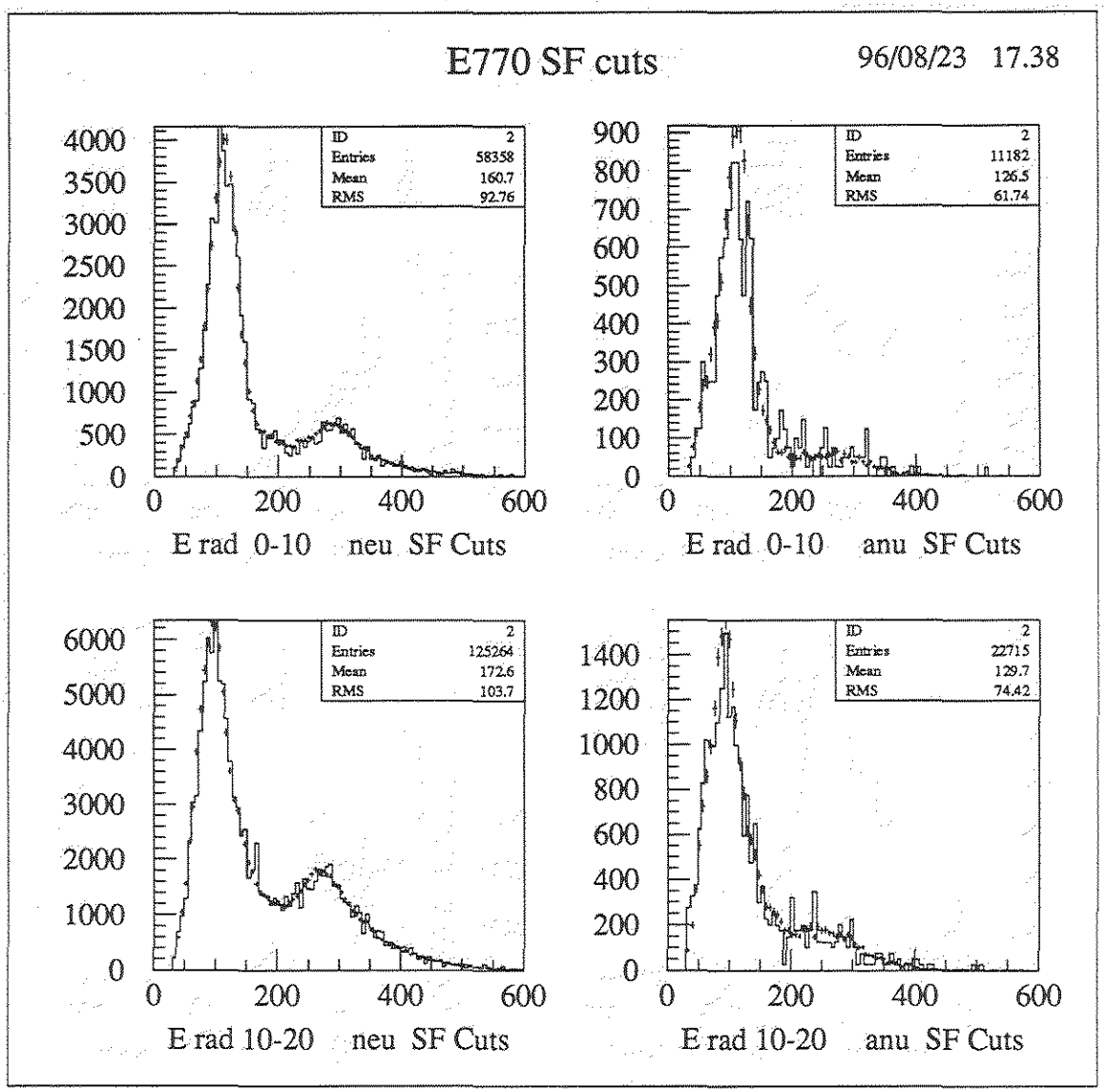

Figure E.28: E770 data versus Monte Carlo for E_ν in the radial bins 0-10 *in* and 10-20 *in*.

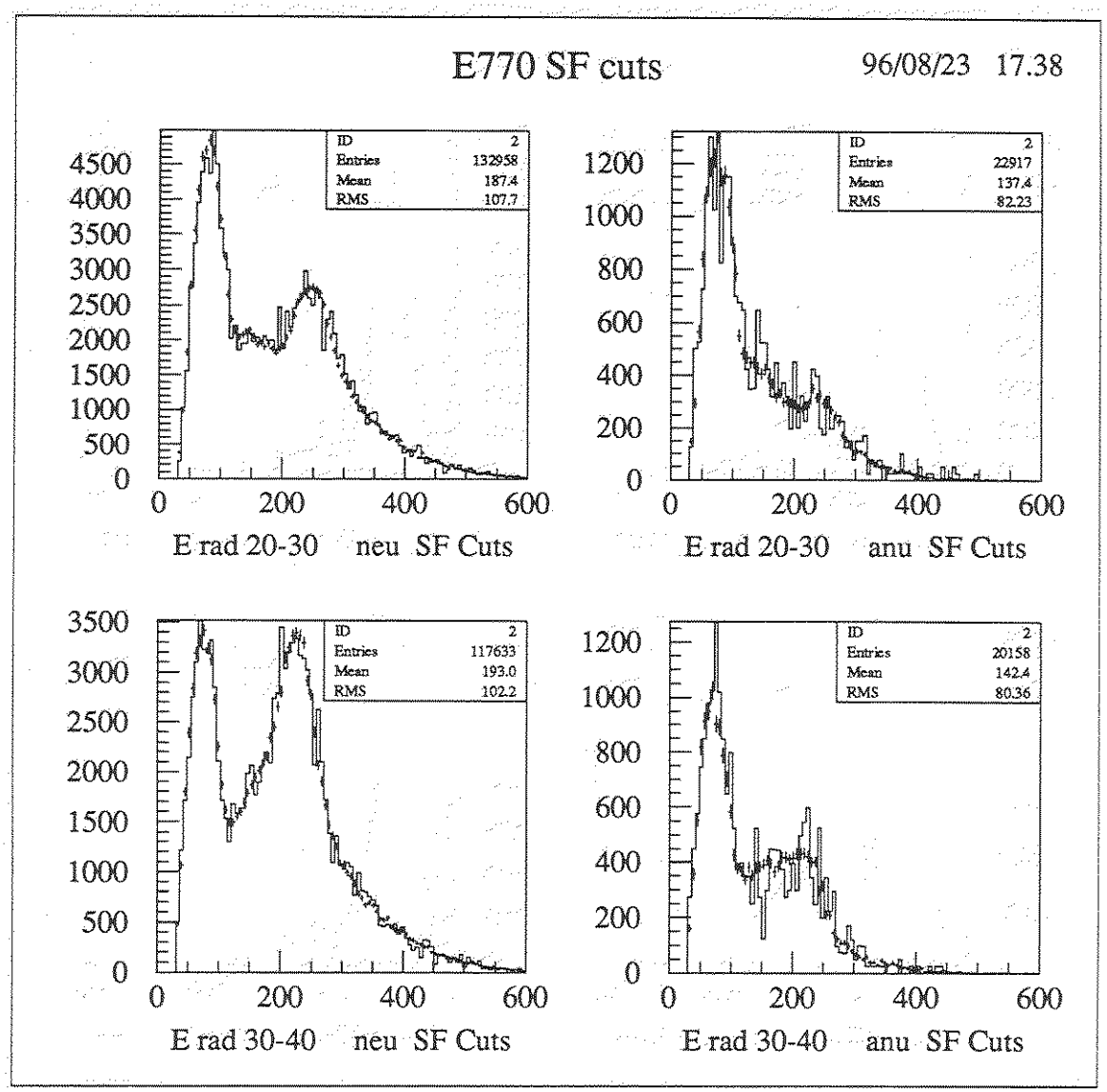

Figure E.29: E770 data versus Monte Carlo for E_ν in the radial bins 20-30 *in* and 30-40 *in*.

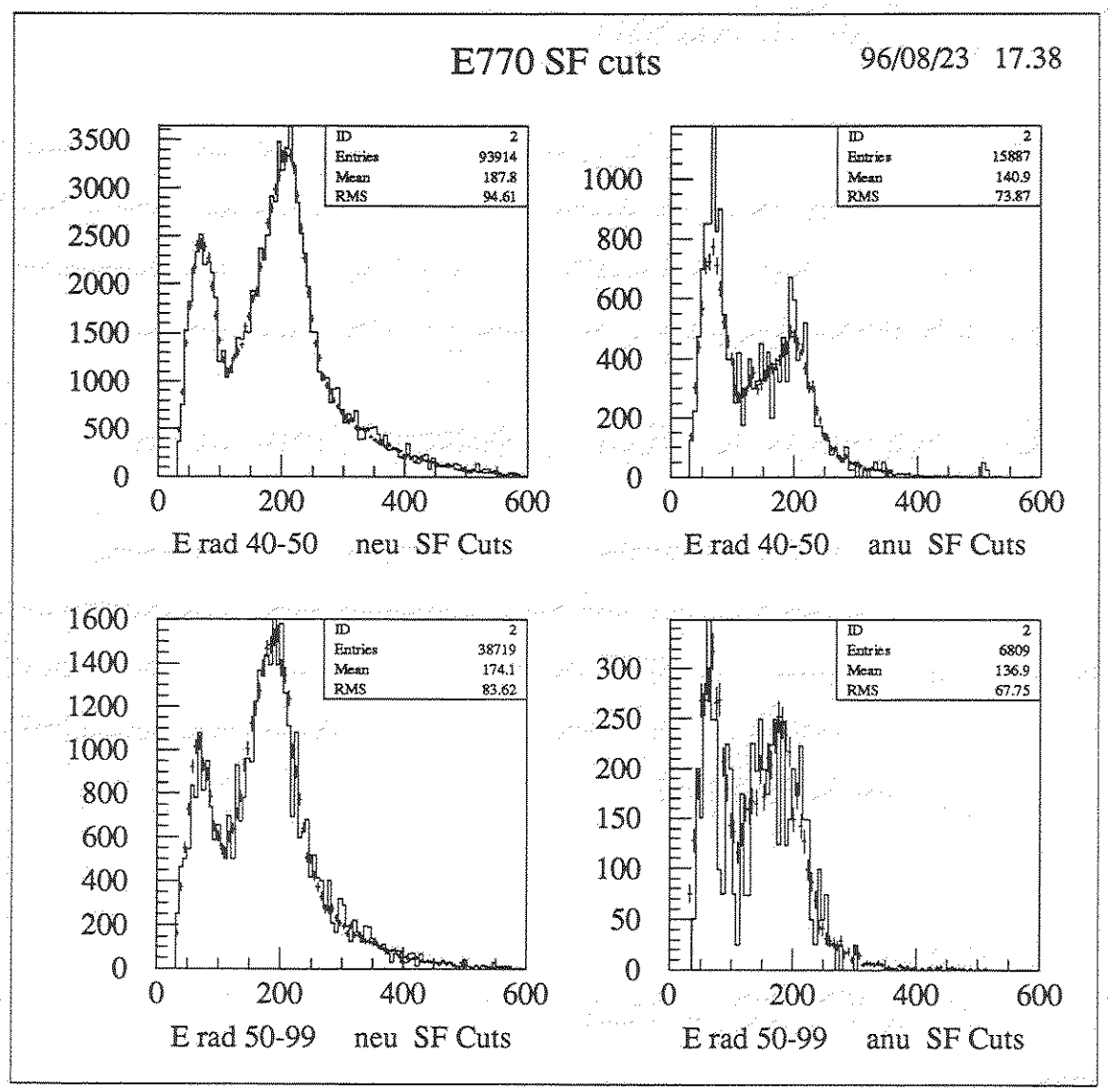

Figure E.30: E770 data versus Monte Carlo for E_ν in the radial bins 40-50 *in* and 50-99 *in*.

Appendix F: Small Corrections to the Energy Calibration

This Appendix is a supplement to Chapter 3 of this thesis, and documents small corrections to the energy calibration. Section F.1 describes a correction to the hadron energy calibration described in Ref. [Sak90]. Section F.2 describes a correction to the counter pulse heights based on hadron shower shape: the "relative gain" correction.

F.1 Corrections to the Hadron Energy Calibration

Apart from this introduction, this Section consists entirely of an internal collaboration memo written by Howard Budd and Arie Bodek concerning small corrections to the hadronic energy calibration of the CCFR detector. It is reproduced here in its original form because the information contained herein was only distributed via electronic mail and has not otherwise been published.

```
To: CCFR/E815 group
From: Howard Budd and A. Bodek
Subject: Pedestal shifts, Hadron energy and muon energy loss
Date: Oct. 6, 1995  Version 3  For Comments

Summary:

It appears that our studies of various effects would
not give a -700 MeV shift. It is only about 130 MeV. A discussion
about the low Ehad near zero case is given in appendix 2.

   1. Revised calibrations for E770 and E744 (from ped shifts in highs)
      Hadron energy for charged current has a shift from pedestal
      shift in the lows.

 E770 measured (Trig 1) CC events
    = Ehad true (1.0039) -0.130 GeV  (For SF analysis asuming 14 counters)
 E744 measured (Trig 1) CC events
     = Ehad true (.9887) -0.071 GeV (For SF analysis assuming 14 counters)

   As described in Appendix 2, for energies above 5 GeV probably
  instead of using the 130 or 71 MeV, one should use a function
  that describes the non linearity of the type (say use 130 MeV)

        Emeasured = Etrue * [T /(T + 0.13)]
```

Where T = Etrue = kinetic energy of the particle in GeV.
probably best to use this for both E770 and E744.

Note that E770 versus E744 has about 1.52% calibration difference.

2. One expects data and MC to agree for muons downstream of the shower, since the calibration for muons was done using the tmaplow (and therefore have the same pedestal shift). This corrects the CC events for the pedestal shift. However, this will yield a difference between the hadron energies for CC and NC events.

   or Ehad(CC)measured (trig 1) -Ehad(NC)measured (trigger 2)
   = 0.338 GeV - 0.0016*Ehad

   For 30 GeV this is 0.338-0.048 = 290 MeV
   (If the CC events was triggered by trigger 2, which comes 3 nsec later, the last term should not be there)

This note discusses:

1. Ped shifts in high yielding difference in hadron calibration between test beam, E744 and E770.
2. Ped shifts in low :
   (a) affect hadron energy and
   (b) affect the calibration of the restricted energy loss for muons. (this yields to some cancelation of the effect of pedestal shift in the lows).
3. Timing shift between trigger 1 and trigger 2 and test beam affecting calibration (order 0.16% for trigger 1 only)
4. Effect of a pion going in for 1 Lambda (20 cm of Fe) before interacting yielding a shift of about 130 MeV in the calibration between neutrino and hadron induced showers (this 2 mips should have the restricted energy loss Caliber, rather then the hadronic caliber.
5. ADC non linearity and phototube non linearity. (small)

Note that the test beam shows that things are linear on the level of 1%. The shifts and our conclusions are within that error.

Introduction:

During the last few days on the Cyber Howard calculated PED shifts for E744, E770 and the testbeam for E770. The PED shift is defined as the PED in either the fast or slow gate minus the PED determined by events in the PED gate. All events had the PED determined from the PED gate subtracted.

To calculated the PED shift for the neutrino events the following procedure was used:

1) NC trigger and only one intime events.
2) The counter that was used had to have counter > PLACE +5 or counter < CEXIT -5
3) No veto hit
4) No DC hits in DC surrounding the counter
5) At most 1 DC hit in sum of planes in the 2 DC upstream and downstream of the counter
6) For Lows ABS(counter ADC - <PED>) < 40
   For Highs ABS(counter ADC - <PED> < 400

For events for the Slow spill PED shift
1) Require trigger for slow PED to fire and no other
2 - 6 same as for fast spill PED

For the data

1) For E744 5 randomly selected tapes were used
2) For E770 we used 5 tapes created by Walter of randomly selected NC events, about 10000. The hadron energy of the event determined which tape the event was on.
3) For slow spill 6 randomly selected tapes were used
   a) 25 GeV cart 2 calibration
   b) 70 GeV Cart 2 calibration
   c) 100 GeV Cart 2 calibration
   d) 100 GeV Cart 3 calibration
   e) 100 GeV Cart 4 calibration
   f) 100 GeV Cart 4 off center calibration run

The Data for these PED shifts are given below:
Note that all counters are averaged over. The PED shift for the low is the sum of the lows.

THIS DATA SET GIVES THE INSPILL PEDS FOR 5 E744 RUNS
(this is from a file in fnalv::usr$root12:[hbudd]pede744.cdc)

RUN =	2133	2117	2188	2225	2235	AVE
AVELOW=	-.6005	-.5633	-.2727	-.7551	-.3672	-.5193
AVEHIG=	.6438	.6552	.7025	.3794	.4415	.5835

THESE ARE PEDS OVER E770, USING RANDOMLY SELECTED NC EVENTS
LIST BELOW SHOWS THE AVERAGE FOR VARIOUS EVERGY BINS THE
ENERGY OF THESE BINS IS LISTED
(this is from a file in fnalv::usr$root12:[hbudd]pede770.cdc)

ENERGY=	000 025	025 075	075 125	125 175	175 225	225 999	ALL
AVELOW=	-.5982	-.6678	-.7050	-.7270	-.7670	-.7922	-.7146
AVECLO=	-.1140	-.1655	-.2286	-.3002	-.3615	-.4546	-.2749
AVEHIG=	.0253	-.4182	-.8460	-1.2086	-1.4879	-1.7846	-.9885

(Note AVECLO is the ped shift of the combination lows.)

THESE RUN ARE SLOW SPILL PEDS FOR THE E770 TEST RUN. THEY ARE
GOTTEN USING TRIG 5. THE AVERAGES FOR THE VARIOUS TAPES ARE LISTED
BELOW.
(this is from a file in fnalv::usr$root12:[hbudd]pedslow.cdc)

TAPE =	2895	2907	2915	2943	2883	2939	AVE
AVELOW=	-.2794	-.3213	-.4712	-.3052	-.5002	-.3003	-.3638
AVECLO=	-.0516	-.0561	-.0801	-.0365	-.0893	-.0293	-.0563
AVEHIG=	.1739	.0524	.0976	.1240	.1321	.0792	.1091

The numbers are the average over all 84 target counters. PED shift for individual target counters are given in the files. (However, for any work that need to be done probably the overall number is fine.) There appears to be some slight run to run dependence, but we will ignore that.

Analysis of HIGHS:

We notice that from the E770 PED shift data, the PED shift for the high ADC's appears to be energy dependent, especially for the highs. We discovered this because the events on the tapes were sorted on the basis of hadron energy, not because the code searched for it. Hence, E744 could have the same effect. We did not determine whether E744 had the same effect. Since the electronics is the same, we assume that E744 has the same effect.

The shift in the high PED as a function of the hadron energy was independent of where in the target cart the hadron shower was. This would say that the was not due to the phototubes or the electronics. The electronics is grouped in units of 12 counters in the nim crates. If the shift is from the electronics there is no way a energy in Counter 10 can

effect the PED in Counter 80. Hence, this shift is most likely due to the ADCs. Counter 10 and counter 80 High ADC are in the same FERA camac crate. For some events the High and Combination Low PED seem to go down together, i.e. they are correlated. The evidence for this was not as compelling as the Ped shift in the highs independent of where the shower was. However, the High and CL FERA are not in the same CAMAC crate. This would argue that the problem was not in the FERA crate. However, this leaves no piece of hardware that can cause the problem. We will assume that the problem is in the ADCs and hence it existed in E744. The FERAs were not changed between E744 and E770.

A change was made in the electronics which did effect the electronics for the highs, the bin oscillation problem was fixed. The bin oscillation problem was due to the sagging of the power supply of the NIM crate from a large pulse going into the *10 amplifier in the nim bin. The sagging on the power supply created an approximately 100 microsecond pulse on the power line. Since the beam for the ping lasted around 1.5 milliseconds, the pulse was long enough to have an effect of succeeding events. The pulse was picked up by the fan-in which created the high and combination lows. Literally, the power supply line acted as an input for the fan-in. The shifting of the ped could be as large as 5 mips, or about 400 counts for the highs. This problem was fixed for E770 by filtering the powerlines of the *10 amplifiers and the fan-ins. Probably, this problem created the difference in the high ped shift between E744 and E770, i.e. high ped shift for E744 = .58 while high ped shift for E770 = -.99.

The PED shift for the 770 highs for 0 < E < 25 GeV = .02. While the PED shift random NC events is -.989. For the neutrino calibration both Trigger 1 and Trigger 6 were used. They both have different PED shifts. For the testbeam only straight through muons were used and so the PED shift is .109. We will now try to get pedshift numbers for both E744 and E770.

From the tables on the previous page we have for the neutrino ped shifts in the HIGHS :

E744 -	Trig 1	.58	
	Trig 6	1.57	(Assuming energy dependence of highs in E744)
E770	Trig 1	-.99	
	Trig 6	.02	

Next we need the ratio of Trigger 1 to Trigger 6 written on tape. These numbers are different in E744 and E770 because we prescaled Trigger 6 in E744.

E744 Trig 1/Trig 6 = 12.28 (gotten from 4 runs)
E770 Trig 1/Trig 6 = 1.725 (gotten from 4 runs)

A Trigger 6 will determine the muon peak for all 84 counters. A Trigger 1 will determine a muon peak for only those counters which are some distance from SHEND. We will assume that Trigger 1 will start measuring muon peaks 20 counters downstream of SHEND. (Willis does not exactly have this number, but this should be close enough.) Trigger 1 can have PLACE anywhere between counter 82 and counter 2 Hence, a Trigger 1 will on the average calibrate only .28 counters for every 1 counter a Trigger 6 will calibrate. We have to scale the ratio of Trigger 1 to Trigger 6 by .28.

E744 HIGH ped shift = .775 * .58 + .225 * 1.57 = .79
E770 HIGH ped shift = .325 *(-.99) + .674 * .02 = -.30

The muon peak from E744 is roughly 70 counts and the muon peak from e770 is roughly 75 counts. Using the high ped shift for

the slow spill of .11 counts we get the following:

Raise E744 hadron energy by |(.79 - .11)|/70 = 0.97%
Lower E770 hadron energy by |(-.30 - .11)|/75 = 0.55%

The PED shift of the lows shows a slight dependence vs hadron energy, but we will assume that there is no dependence.
<low> = -.71 for neutrino for E770
<low> = -.52 for neutrino for E744
<low> = -.36 for calibration for E770 so
<low>neu - <low>test beam = -.35 counts/counter.

For E744 Howard had no file of randomly selected NC events over the entire run. For E770 I compared the PED shift I got using 4 randomly selected tapes with the PED shift using the randomly selected events. They differed by .02 counts. Hence, we will assume the PED shift from E744 of -.52 is correct.

We need to evaluate (sum of lows)/tmaplo. Tmaplo is given on the DST not ADC counts. We measured this ratio for 2 tapes in E770. We imposed the structure function cuts and got 8.63 counts/mip. We did not measure it for E744, (It will probably be slightly different as the voltage of the tubes was slightly higher in E770.). We will use the conversion of 8.63 counts/mip for E744, E770 and the testbeam.

ADC GATE TIMING STUDY

The test beam timing for calibration was set using the NC trigger. Timing for E744 test run and E770 test run is the same. The NC neutrino timing is not quite the same as the NC testbeam timing because the threshold for the NC is different in the neutrino running than the test beam running. (In order to do calibrations, we could not have the NC Trigger impose an energy cut. The NC Trigger was change from 10 GeV threshold to about 4 GeV threshold for the testbeam.) The Trig 2 timing is not the same as Trig 1 timing. This was discovered in the beginning of E744, and the timings were never changed through the entire run. Hence, the trigger timing were never changed since the E744 test beam, with one exception. (Trigger timings were never changed so that trigger timing correction could be imposed through the entire run, without having to worry about where trigger timings shifted.) At the start of E770 we look at all the trigger timings. It appeared that trigger 3 timing had changed from E744. This can happen because Trig 3 timing is determined by penetration > 12 discriminator. This discriminator was set before the start of E744 and E770. Hence, change of this discriminator could change Trig 3 timing. To fix this, We changed trig 3 timing by 4 ns to get its timing the same as E744. Hence the only trigger timing change made during the quad triplet run was designed to try to keep the trigger timing the same for the Quad Triplet Run.

We measured the difference in ADC gate timing between the testbeam and neutrino running with structure function cuts. We used the SBIT timing with no map correction. T1SBIT - ADCGATE = -.0707 TDC counts for neutrino running T1SBIT - ADCGATE = -.715 TDC counts for slow spill runs Hence <ADCGATE>slow - <ADCGATE>neutrino = 2.58 ns. Slow spill ADCGATE is later than fast spill ADCGATE. Next, we need to convert this into a hadron energy shift. During the E770 test beam run, we took a set of 100 GeV hadron in which the ADC gate was delayed by -20, -10, 0, 10, and 20 ns. Using this data we get .0626% shift/ns. (Note this agrees with as data I get for the double vertex analysis done a different way.) Hence the calibration runs had more charge collected so calibr should be reduced by (2.58 ns)*(.0626%) = .16%.

Note that in test beam, the muon calibrations were done using trigger 1. Therefore, trigger 1 timing is the same for test beam and

```
neutrino data, so the highs are not affected.  The hadron calibration
was done using trigger 2. Therefore, NC events have the same time as
in test beam and data. Therefore, this 0.16% is only true for lows in trigger
1 only.

CORRECTIONS (including ped shift from lows)

The overall calibration comes from highs. There is also an absolute
shift from pedestal shifts in the lows.

The muon subraction for charged current events for E770 is correct
in data (in E770) because we are subracting a muon energy calibration for
restricted energy loss which is based on tmap lows, and therefore
includes a wrong mip calibration by  0.08 mips or 8%.
true restricted energy loss should be high by 0.08 mips per counter.
i.e. it should be a calibration of 0.158/1.08 GeV/mip = 0.146 GeV mip
this just compensates for the pedestal shifts.
------------------------

   Now pedetal shifts in lows and other effects.
Trigger 2:
Test beam: Ehad(true)= Ehad measured
                       +0.042mip*0.211x14 (length)/14  (correct for ped shift)
                       -2*(0.211-0.146)        Correct for pion going in
                                                (neutrinos vs pions)
                     = Ehad measured
                       +0.124 GeV * Length/14
                       -0.130 GeV  (correct for pion going in 2 counters)
 So test beam is linear by accident.

Monte Carlo should mimic
 for charged current events (Trigger 1)
For Neutrino:  Ehad measured E770 =
           Ehad  true (1 + 0.55% - 0.16%)  [mips in test beam]
            -0.130 GeV        [neutrinos vs pions]
          -0.08 mips*0.211*14 (Length/14)  [=-0.266 L/14 Gev Ped shift in lows
          +0.08 mips*0.211*14 (Length/14)  (muon subraction has wrong calib)

         = Ehad true (1.0039) -0.130 GeV  (For SF analysis asuming 14 counters)
         = Ehad true (1.0039) -0.130 GeV  (For NC analysis asuming 20 counters)
                                           for CC events trigged by trigger 1
                                           Which is 3 nsec ahead of trigger 2.
For charged current events with exiting muons triggered by
 trigger 2, remove the 0.16% above.
          = Ehad true (1.0055) -0.130 GeV  (For NC analysis asuming 20 counters)
                                       for CC events trigged by trigger 2

-------------------
For neutral current E770:  Ehad measured E770 =
           Ehad  true * (1 + .55%)  [mips in test beam]
            -0.130 GeV        [neutrinos vs pions]
          -0.08 mips*0.211*20 (Length/20)  [=-0.338 L/14 Gev Ped shift in lows]

           = Ehad true (1.0055)  -0.468 GeV.

       or E770 Ehad(CC)measured trig 1 -Ehad(NC)measured trig 2
                                  = 0.338 GeV  - 0.0016 Ehad(true)
   (the last term is not there if the CC events was triggered by
   trigger 2).
--------------------
For Charged current:
For E744: Ehad measured E744 =
           Ehad  true * (1 - 0.97% - 0.16%)  [mips in test beam vs fast spill]
           -0.130 GeV        [neutrinos vs pions]
```

```
          -0.060 mips*0.211*14 (Length/14)
                    [=-0.177 L/14 Gev Ped shift in lows]
          +0.08 mips*0.211*14 (Length/14)
                    [= +0.236 L/14 muon subraction has wrong calib]

         ??   = Ehad true (.9887) -0.071 GeV (For SF analysis assuming 14 count)
            = Ehad true (.9887) -0.046 GeV (For NC analysis assuming 20 count)
                                        for CC events triggered by trig 1
For CC events missing toroid triggered by trigger 2
            = Ehad true (.9903) -0.046 GeV (For NC analysis assuming 20 count)
                                        for CC events triggered by trig 1

-----------------------
For neutral current E744:  Ehad measured E770 =
          Ehad  true * (1 - 0.97% )  [mips in test beam]
           -0.130 GeV        [neutrinos vs pions]
           -0.060 mips*0.211*20 (Length/20)
                                [=-0.253 L/20 Gev Ped shift in lows]

          = Ehad true (.9903)  -0.383 GeV

     or E744 Ehad(CC)measured trigger 1 -Ehad(NC) measured trig 2
                = 0.337 GeV - 0.0016* Ehad true
 (the last term is not there if the CC event was triggered by
   trigger 2, ie it missed the toroid).
```

Appendix 1:

We have looked at the nonlinearity of the electronics. A seperate note will describe the nonlinearity of the electronics, but we will summarize the results. The number of counts of the ADC is about 1800. The nonlinearity study gives a plot of charge into the electronics vs readback pulse height. We put a line on this plot which goes through the point at pulse height = 0 and pulse height = 1800. Points on the plot will deviate from the line. The maximal deviation which is at the center of the plot is the non linearity.

For the lows:
<max deviation> = 4.4 counts
< sigma of max deviation> = 1.27

We tested the superlows from ADC channel 0 to ADC channel 600. The neutrino data did not have any counter with a pulse height of the superlow greater than channel 600.

For the superlow:
< max deviation>= .5 channels
< sigma of max deviation> = .04 counts

We can also experess this as a quadratic term. Let p be the pulse height read back by the ADC and let q be the charge going into the electronics. Let P be the maximum value for the ADC (about 1800) and let Q be the maximum charge for that value of the ADC. Then we can express

$$p=a*q*(1+b*(q/Q))$$

where roughly b = 4*<max deviation>/P

Using the we get for the lows
b = 0098 with sigma of .0028

For the superlows
b = .0033 with a sigma of .00027
None is the above will be included as a correction to the hadron energy.

Note that the above is within the 1% error rms in the hadron energy.
Note that the phototube non-linearity was corrected for (after correction for phototube non-linearity the muon maps and hadron maps were the same). In E815 we will not have the phototube non-linearity.

Appendix 2: Non Linearity

The pedestal shift effects above are all within the quoted 1% systematic error. The non linearity of 130 MeV is comensated by the de/dx of a pion coming in. There may be additional non linearity. The 1984 test beam may indicate an additional non linearity of an extra 100 MeV. (figure 11 in NIm article which goes down to 15 GeV). This is all consistent with the data, since it is 0.5% at 20 GeV. The test beam data at 20 GeV has a scatter of +-1% (from different carts and different times so one cannot see it.

There was data with a small test beam calorimeter that I analyzed (B. Barish et a. NIM 130 (1975)49-60) with 10 cm sampling. In that calorimeter data down to 5 GeV were taken. However, it was unkown at the time, that the calorimeter did not contain the shower transversly. In addition , it was only 1.4 meter long, so the interaction was required to be in the first plate. (it had a beam halo veto also).

At 5 GeV for this calorimeter, the non linearity we 67%+_20% with respect to 50 GeV. Statistics was very poor, and we expect a calorimeter with side leackage to be non linear because of e/pion not equal to 1.0 and also because showers at low energy are wider.

The mean pulse height for that calorimeter was given by

M(in mip) = 5.428 T**2/ (T + 0.721)

The resolutin was 1.105/(SqrtT)

where T is the kinetic energy of the beam particle.
Our calibration is 4.73 mips/GeV. So this calorimeter had a 15% leackage out the sides. For that calorimeter at 50 GeV hadron/electron was 335/269 = 1.25 Versus 1.06+-0.02 for CCFR. If we assume that the non linearity is proportional to e/pi then CCFR's non linerity of 6% is 1/4 to 1/3 of that of this small test beam calorimeter. (i.e 0.721/4 = 180 +-60 MeV)

I would guess that for energies above 5 GeV. The CCFR calorimeter should be represented by

Measured/True = T/ (T + 0.180)

F.2 Relative Gain Correction

After all the corrections to the counter response in the calorimeter described in Chapter 3, there should be no remaining position-dependent effects in the energy response. In particular, the average shape of the hadron shower should not depend on the *z*-vertex

position. We used this property to do a fine-tuning of the energy calibration of the scintillation counters. The goal was to obtain an energy correction factor for each counter:

$$\frac{f_{rel.cal.}(i)\sum_{k=1}^{events}\sum_{j=PLACE}^{j=PLACE-n}\delta_{ikj}\times PH_{kj}}{\sum_{k=1}^{events}\sum_{j=PLACE}^{j=PLACE-n}\delta_{ik}}=\frac{\sum_{k=1}^{events}\sum_{j=PLACE}^{j=PLACE-n}f_{rel.cal.}(i)\times PH_{kj}}{\sum_{k=1}^{events}\sum_{j=PLACE}^{j=PLACE-n}1.0} \tag{F.1}$$

where $f_{rel.cal.}(i)$ is the relative gain calibration for counter i, PH_{kj} is the pulse height of counter j in the event k, n is the number of counters in the shower to average (we set n = 5), and $\delta_{ikj} = 1$ if counter i is the j-th counter in event k (0 otherwise).

Equation F.1 is used to obtain $f_{rel.cal.}(i)$. The right-hand side of the equation is the average pulse height (or energy) per counter in the first n counters of a shower in the sample after the relative-gain correction factors have been applied. The left-hand side is the average of the corrected pulse heights of counter i when it is one of the first n counters of a shower. Note that there are two assumptions in Equation F.1: 1) the average shower longitudinal shape is invariant with respect to z-position in the calorimeter; 2) the number of events is independent of z-position.

Equation F.1 defines the relative gain correction up to an overall multiplicative factor. This factor is then further constrained by the requirement that the sum of all the pulse heights of the hadron showers of all events in the data sample does not change after the relative gain correction:

$$\sum_{k=1}^{events}\sum_{j=PLACE}^{j=PLACE-n}f_{rel.cal.}(i)\times PH_{kj}=\sum_{k=1}^{events}\sum_{j=PLACE}^{j=PLACE-n}PH_{kj} \tag{F.2}$$

This system of equations is solved iteratively. The events included in this study passed cuts of $E_\nu > 30\ GeV$ and radius < 50 inches. The study was repeated for $E_\nu > 0\ GeV$, and for $n = 10$, and for the combination $E_\nu > 0\ GeV$ and $n = 10$; the results were consistent on the 1% level to the results presented here.

The results are shown in Figure F.1. Table F.1 shows the value of $f_{rel.cal.}(i)$ averaged over the counters within a calorimeter cart. Counters 1 through 7 and counters 81 through 84 were not included in this study because their response would be biased by the method. For example, counter 84 cannot be the second counter in a shower because it's the most upstream counter; counter 1 cannot be the first counter in a shower because it's the most downstream counter. Counters 1-7 and 81-84 were assigned $f_{rel.cal.}(i) = 1.0$.

Table F.1: Relative gain averaged over calorimeter carts. Note that the average gain for all counters included in the study is forced to be consistent with 1.0 by Equation F.2.

Cart	Counters i	Average $f_{rel.cal.}(i)$
1	8-14	0.9797 ± 0.0025
2	15-28	0.9880 ± 0.0018
3	29-42	1.0040 ± 0.0018
4	43-56	1.0212 ± 0.0018
5	57-70	1.0027 ± 0.0018
6	71-80	0.9969 ± 0.0057
All	8-80	1.0007 ± 0.0011

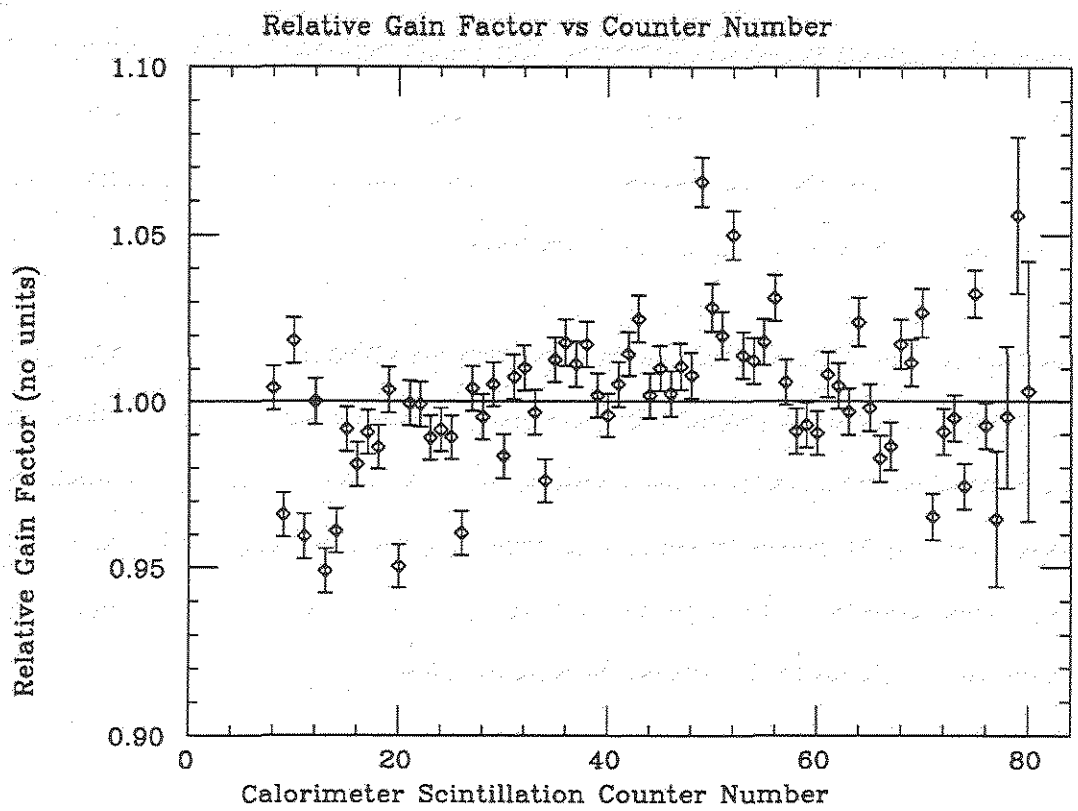

Figure F.1: Relative gain versus counter number. Error bars are statistical only.

Appendix G: Parton Distribution Functions

This Appendix contains plots that compare the parton distributions determined by this experiment and by the global fits [Mar96, Glu95, Lai96]. The Duke and Owens next-to-leading-order QCD fit is described in Chapter 7. The comparison between the partons distributions from the Duke and Owens (D&O) fit to the CCFR data and the global fits to the world's data is one method of comparing the results of different experiments, as discussed in Chapter 8.

The Buras-Gaemers leading-order model is described in Chapter 4. This model is used within the Monte Carlo to generate events for acceptance corrections, and to apply physics-model corrections to the data.

The strange sea is not measured in this analysis. It can be measured in the CCFR experiment from analyzing opposite-sign dimuon events $\left(\nu(\bar{\nu})+N \rightarrow \nu+\bar{\nu}+X\right)$ which arise in part from charged-current neutrino scattering off of s-quarks in the nucleon. The leading-order strange-sea analysis is described in Ref. [Rab93] and the next-to-leading-order analysis is described in Ref. [Baz95]. The strange sea is included in the Figures below because it is used in Equation 8.4 to correct charged-lepton data for comparison to the CCFR result.

The charm sea can be measured in neutrino scattering, but not from the CCFR data. Such an analysis requires a sign-selected beam in order to look for "wrong-sign" muons $\left(\nu(\bar{\nu})+N \rightarrow \mu^{+}\left(\mu^{-}\right)+X\,[\text{observed}]\right)$, which can arise in part from neutral-current scattering off of charm quarks in the proton. Such an analysis was performed on the E616/E701 data [Mis89] and will be performed on the data from the E815 experiment

which uses a sign-selected quadrupole triplet beam. The charm sea from the global-fit analyses is included in the Figures below because, along with the strange sea, it is used in Equation 8.4 to evaluate the "5/18ths rule."

Figure G.1 compares the valence momentum densities $\left(xu_V + xd_V\right)$ from these different fits; Figure G.2 compares the sea distributions $\left(xu_{sea} + x\bar{u} + xd_{sea} + x\bar{d} + xs + x\bar{s}\right)$; and Figure G.3 compares the gluon distributions. Figures G.4 and G.5 compare the strange distributions $(xs + x\bar{s})$ and the charm distributions $(xc + x\bar{c})$, respectively. All distributions are shown at $Q^2 = 5\,GeV^2$.

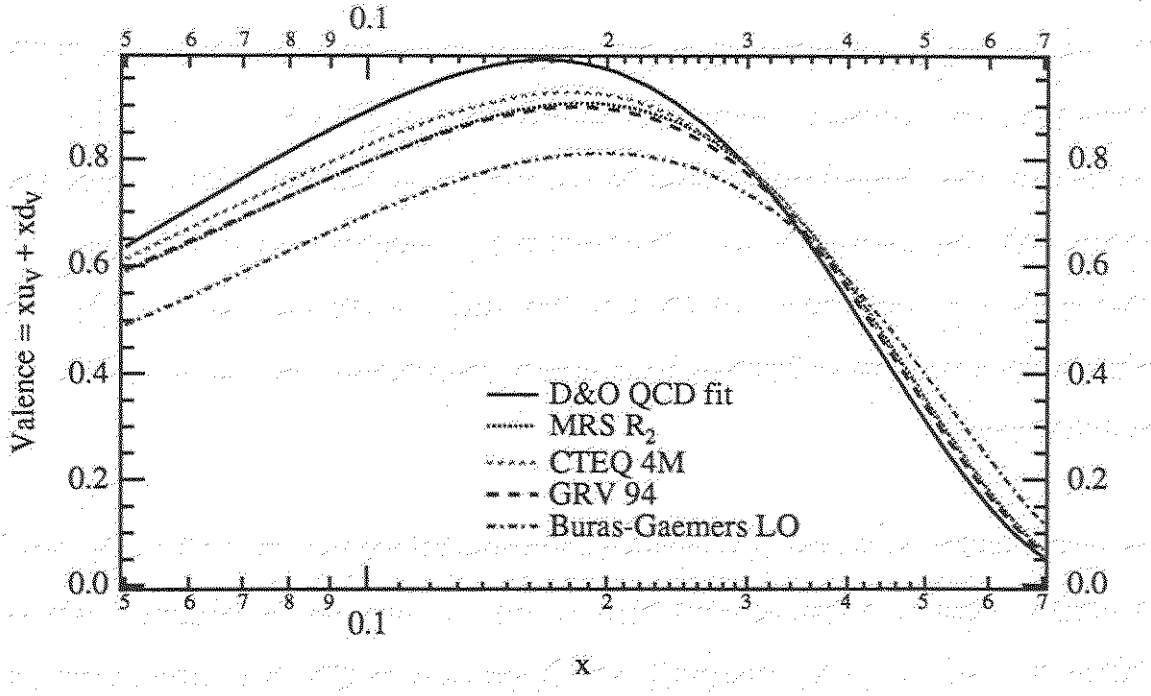

Figure G.1: A comparison of the valence distributions from leading-order, next-to-leading-order, and global fits.

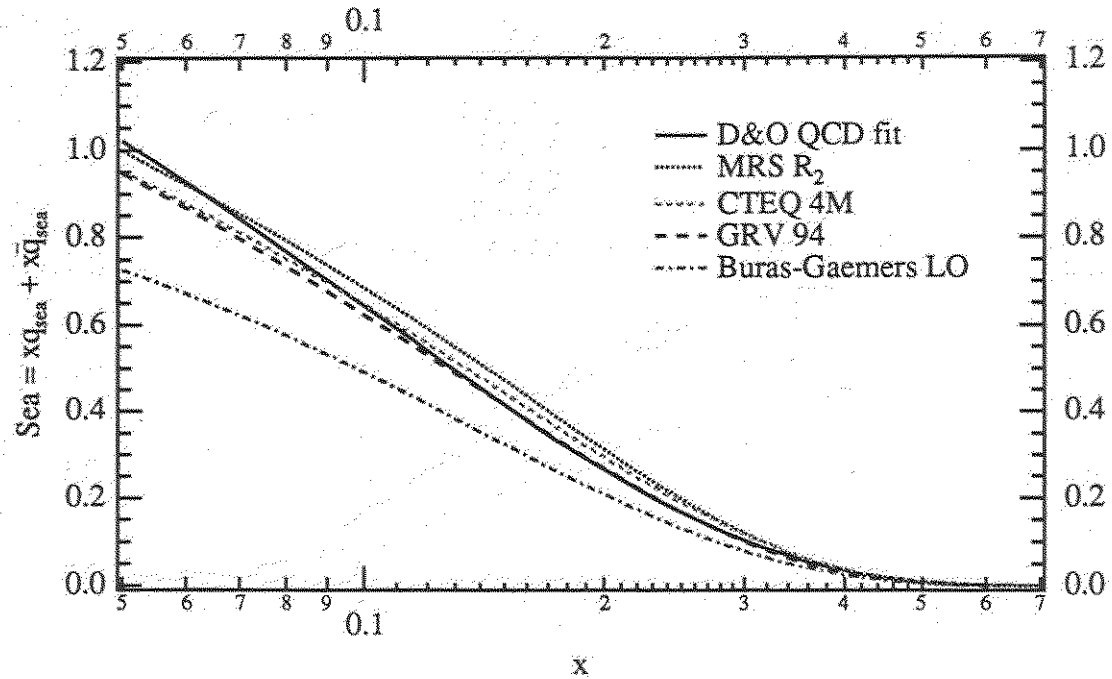

Figure G.2: A comparison of the sea distributions from leading-order, next-to-leading-order, and global fits.

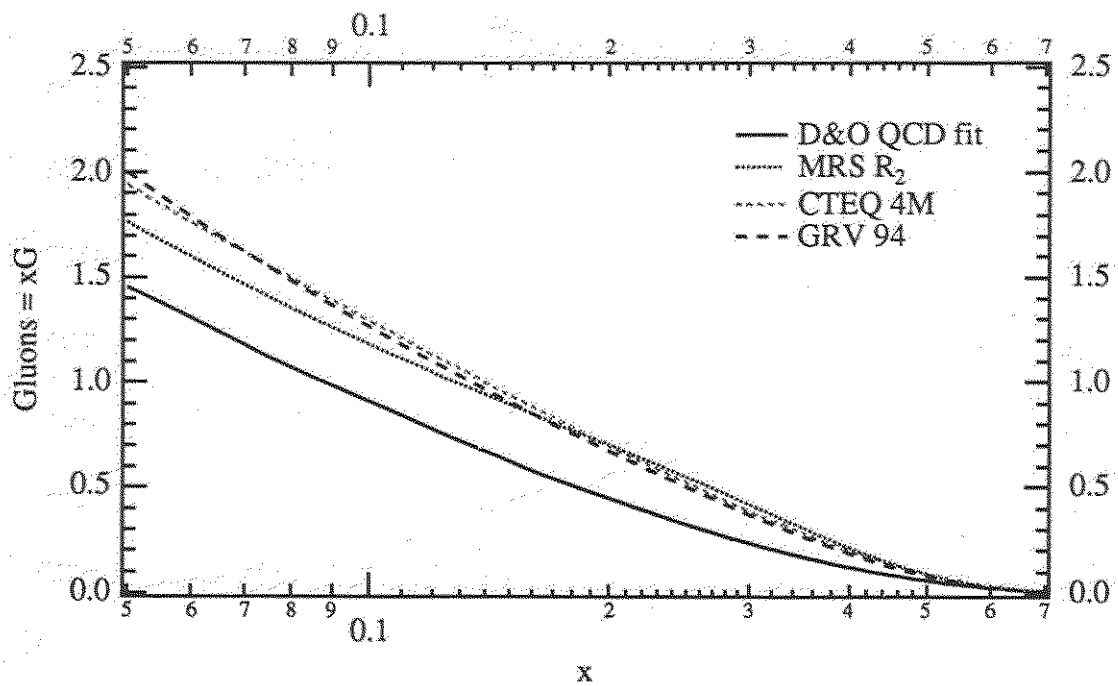

Figure G.3: A comparison of the gluon distributions from next-to-leading-order and global fits.

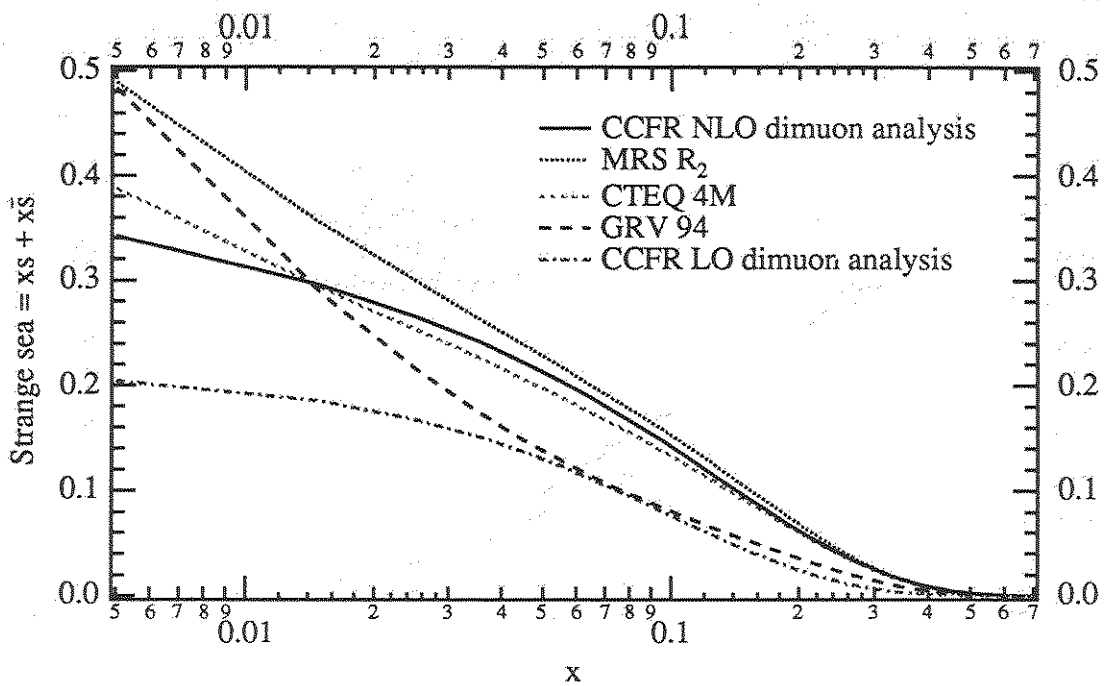

Figure G.4: A comparison of the strange distributions from next-to-leading-order and leading-order analyses, and from global fits.

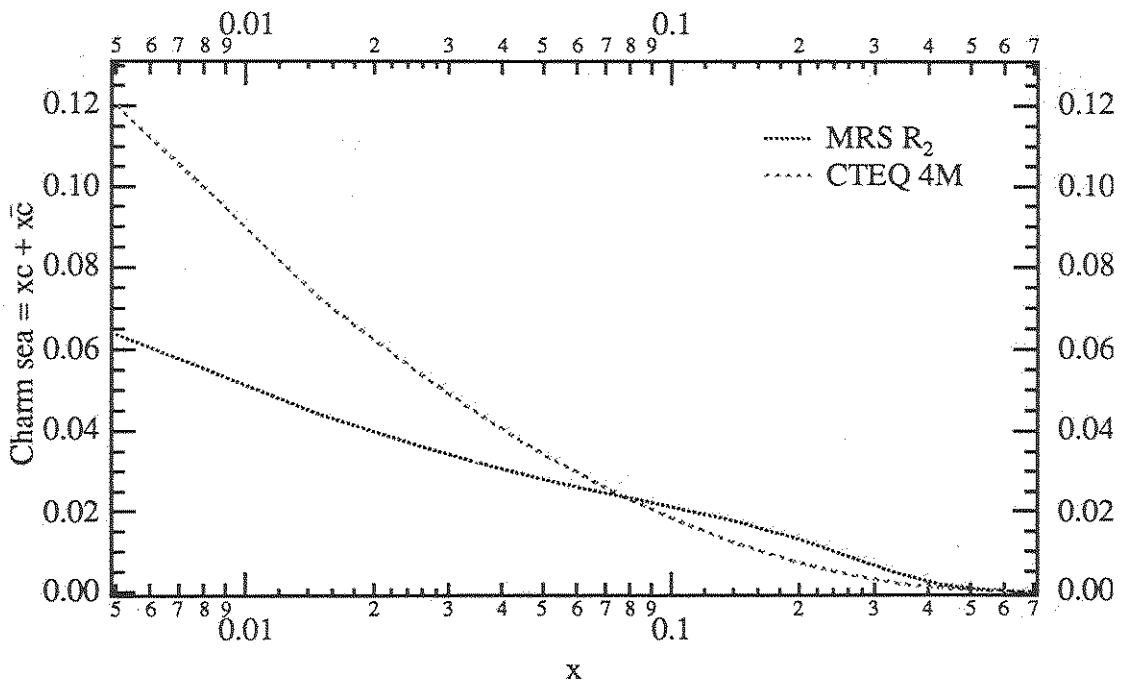

Figure G.5: A comparison of the charm distributions from global fits.

Appendix H: Article Submitted to *Physical Review Letters*

The remainder of this Appendix consists solely of page images of an article written on the analysis presented in this thesis. It was submitted to the journal *Physical Review Letters* on January 30, 1997. The article is available on the Los Alamos National Laboratories on-line e-print archives (URL `http://xxx.lanl.gov`) with the identification number hep-ex/9701017. It is also available by sending a request for Nevis Report 1531 to Anne Therrien, Columbia University, Nevis Labs, P. O. Box 137, Irvington NY 10533 USA.

A New Determination of α_S From Neutrino-Nucleon Scattering

W. G. Seligman,[2] C. G. Arroyo,[2] L. de Barbaro,[5] P. de Barbaro,[6] A. O. Bazarko,[2] R. H. Bernstein,[3] A. Bodek,[6] T. Bolton,[4] H. Budd,[6] J. Conrad,[2] D. A. Harris,[6] R. A. Johnson,[1] J. H. Kim,[2] B. J. King,[2] T. Kinnel,[7] M. J. Lamm,[3] W. C. Lefmann,[2] W. Marsh,[3] K. S. McFarland,[3] C. McNulty,[2] S. R. Mishra,[2] D. Naples,[4] P. Z. Quintas,[2] A. Romosan,[2] W. K. Sakumoto,[6] H. Schellman,[5] F. J. Sciulli,[2] M. H. Shaevitz,[2] W. H. Smith,[7] P. Spentzouris,[2] E. G. Stern,[2] M. Vakili,[1] U. K. Yang,[6] and J. Yu[3]

[1] *University of Cincinnati, Cincinnati, OH 45221*
[2] *Columbia University, New York, NY 10027*
[3] *Fermi National Accelerator Laboratory, Batavia, IL 60510*
[4] *Kansas State University, Manhattan, KS 66506*
[5] *Northwestern University, Evanston, IL 60208*
[6] *University of Rochester, Rochester, NY 14627*
[7] *University of Wisconsin, Madison, WI 53706*

(28 January 1997)

We present a new determination of the proton structure functions F_2 and xF_3 from the CCFR ν-Fe deep inelastic scattering (DIS) experiment. Comparisons to high-statistics charged-lepton scattering results for F_2 from the NMC, E665, SLAC, and BCDMS experiments, after correcting for quark-charge and heavy-target effects, indicate good agreement for $x > 0.1$ but some discrepancy at lower x. The Q^2 evolution of the structure functions yields the quantum chromodynamics (QCD) scale parameter $\Lambda_{\overline{MS}}^{NLO,(4)} = 337 \pm 28(\text{exp.})\ MeV$. This corresponds to a value of the strong coupling constant at the scale of mass of the Z-boson of $\alpha_S(M_Z^2) = 0.119 \pm 0.002(\text{exp.}) \pm 0.004(\text{theory})$ and is one of the most precise measurements of this quantity.

PACS numbers: 13.15.+g, 12.38.Qk, 24.85.+p, 25.30.Pt

High-energy neutrinos are a unique probe for testing QCD and understanding the parton properties of nucleon structure. Combinations of neutrino and antineutrino scattering data are used to determine the F_2 and xF_3 structure functions which determine the valence, sea, and gluon parton distributions in the nucleon [1,2]. The universalities of parton distributions can also be studied by comparing neutrino and charged-lepton scattering data. Past measurements have indicated that F_2^ν differs from $F_2^{e/\mu}$ by 10-20% in the low-x region. These differences are larger than the quoted experimental errors of the measurements and may indicate the need for modifications of the theoretical modeling to include higher-order or new physics contributions. QCD predicts the scaling violations (Q^2 dependence) of F_2 and xF_3 and, experimentally, the observed scaling violations can be tested against those predictions to determine α_S [3] or the related QCD scale parameter, Λ_{QCD}. The α_S determination from neutrino scattering has a small theoretical uncertainty since the electroweak radiative corrections, scale uncertainties, and next-to-leading order (NLO) corrections are well understood.

In this paper, we present an updated analysis of the Columbia-Chicago-Fermilab-Rochester (CCFR) collaboration neutrino scattering data with improved estimates of quark model parameters [4] and systematic uncertainties. The α_S measurement from this analysis is one of the most precise due to the high statistics of the experiment, combined with small theoretical and experimental uncertainties.

The differential cross sections for the ν-N charged-current process $\nu_\mu\,(\overline{\nu}_\mu) + N \to \mu^-\,(\mu^+) + X$, in terms of the Lorentz-invariant structure functions F_2, $2xF_1$, and xF_3 are:

$$\frac{d\sigma^{\nu,\overline{\nu}}}{dx\,dy} = \frac{G_F^2 M E_\nu}{\pi}\left[\left(1 - y - \frac{Mxy}{2E_\nu}\right)F_2\left(x,Q^2\right) + \frac{y^2}{2}2xF_1\left(x,Q^2\right) \pm y\left(1-\frac{y}{2}\right)xF_3\left(x,Q^2\right)\right] \tag{1}$$

where G_F is the weak Fermi coupling constant, M is the nucleon mass, E_ν is the incident neutrino energy, Q^2 is the square of the four-momentum transfer to the nucleon, the scaling variable $y = E_{HAD}/E_\nu$ is the fractional energy transferred to the hadronic vertex with E_{HAD} equal to the measured hadronic energy, and $x = Q^2/2ME_\nu y$, the Bjorken scaling variable, is the fractional momentum carried by the struck quark. The structure function $2xF_1$ is expressed in terms of F_2 by $2xF_1(x,Q^2) = F_2(x,Q^2) \times \frac{1+4M^2x^2}{1+R(x,Q^2)}$, where $R = \frac{\sigma_L}{\sigma_T}$ is the ratio of the cross-section of longitudinally to transversely-polarized W-bosons. In the leading-order quark-parton model, F_2 is the singlet distribution $xq^S = x\sum(q+\overline{q})$, the sum of the momentum densities of all interacting quark constituents, and xF_3 is

the non-singlet distribution $xq^{NS} = x\sum(q-\overline{q}) = xu_V + xd_V$, the valence quark momentum density; these relations are modified by higher-order QCD corrections.

The neutrino DIS data were taken in two high-energy high-statistics runs, FNAL E744 and E770, in the Fermilab Tevatron fixed-target quadrupole triplet beam (QTB) line by the CCFR collaboration. The detector, described in Refs. [5,6], consists of a target calorimeter instrumented with both scintillators and drift chambers for measuring the energy of the hadron shower E_{HAD} and the muon angle θ_μ, followed by a toroid spectrometer for measuring the muon momentum p_μ. There are 950,000 ν_μ events and 170,000 $\overline{\nu}_\mu$ events in the data sample after fiducial-volume cuts, geometric cuts, and kinematic cuts of $p_\mu > 15\ GeV$, $\theta_\mu < 150\ mr$, $E_{HAD} > 10\ GeV$, and $30 < E_\nu < 360\ GeV$, to select regions of high efficiency and small systematic errors in reconstruction.

In order to calculate the structure functions in Eq. (1) from the number of observed ν_μ and $\overline{\nu}_\mu$ events, it is necessary to determine the ν_μ and $\overline{\nu}_\mu$ flux. No direct measurement of the absolute flux was possible in the QTB. The absolute normalization of the ν_μ flux was fixed to the constraint that the neutrino-nucleon total cross-section equaled the world average of the isoscalar-corrected Fe target experiments, $\sigma^{\nu Fe}/E_\nu = (0.677\pm0.014)\times10^{-38}cm^2/GeV$ [7]. The relative flux determination, i.e. the ratio of the flux between different energies and between ν_μ and $\overline{\nu}_\mu$, was determined from the low- E_{HAD} events using a technique described in Ref. [8].

The cross-sections, multiplied by the flux, are compared to the observed number of ν-N and $\overline{\nu}$ -N events in an x and Q^2 bin to extract $F_2(x,Q^2)$ and $xF_3(x,Q^2)$. Structure functions extracted from the CCFR data have been previously presented [9]. This paper presents a re-extraction of the structure functions that includes the following changes: the muon and hadron energy calibrations are determined from a new analysis of test beam data collected during the course of the experiment [5,6]; more complete radiative corrections are applied [10]; the value of R used in the extraction comes from a global fit to the world's measurements [11]. In addition, the estimates of the experimental and theoretical systematic errors in the analysis are improved [8]. The structure functions with statistical errors, along with the QCD fits described below, are shown in Fig. 1.

The structure function F_2 from ν DIS on iron can be compared to F_2 from e and μ DIS on isoscalar targets. To make this comparison, two corrections must be made to the charged-lepton data. For deuterium data, a heavy nuclear target correction must be made to convert $F_2^{\ell D}$ to $F_2^{\ell Fe}$. This correction was made by parameterizing the $F_2^{\ell N}/F_2^{\ell D}$ data from SLAC and NMC [12]. F_2 from electromagnetic interactions couples to the constituent quarks with the square of the quark electric charge. Thus a second correction is necessary:

$$\frac{F_2^\ell}{F_2^\nu} = \frac{5}{18}\left(1 - \frac{3}{5}\frac{(s+\overline{s}-c-\overline{c})}{(q+\overline{q})}\right) \tag{2}$$

This formula is exact to all orders in QCD in the DIS renormalization scheme, so for the purposes of this comparison the charged-lepton structure functions were corrected according to Eq. (2) with quark distributions given by CTEQ4D [2], which parameterizes the parton densities in the DIS scheme. The corrected structure functions from NMC, E665, SLAC, and BCDMS [13,14] for selected x-bins are shown in Fig. 2. There is a 15% discrepancy between the NMC charged-lepton F_2 and the CCFR neutrino F_2 at $x = 0.0125$. As the value of x increases, the discrepancy decreases, until there is agreement between CCFR and the charged-lepton experiments above $x = 0.1$.

The discrepancy between CCFR and NMC at low x is outside the experimental systematic errors quoted by the groups and several suggestions for an explanation have been put forward. One suggestion [15], that the discrepancy can be entirely explained by a large strange sea, is excluded by the CCFR dimuon analysis which directly measures the strange sea [16]. Other suggestions are that the strange sea may have a different distribution than the normally-assumed form [17], or that the heavy nuclear target correction may be different between neutrinos and charged leptons. More experimental data will be necessary to resolve this issue.

According to perturbative QCD (PQCD), the Q^2 dependence of the quark momentum densities is described by "evolution equations" [3]. The evolution of the non-singlet distribution does not depend on assumptions about the gluons, but the singlet distribution co-evolves with the gluon distribution. This analysis takes advantage of the ability of neutrino DIS to measure xF_3, and simultaneously evolves the non-singlet, singlet, and gluon distributions for a precision measurement of Λ_{QCD}.

Systematic uncertainties in the structure function extraction were investigated, leading to correlated errors for each of the data points in Fig. 1. The largest sources of systematic error in the determination of Λ_{QCD} are the muon and hadron absolute energy calibrations. The error in the energy calibration was measured to be 1% for p_μ [6], and 1% for E_{HAD} for the E744 and E770 data separately [5]. Another major source of systematic error is the error in the value of $\sigma^{\overline{\nu}}/\sigma^\nu$, the ratio of the total $\overline{\nu}$ to ν cross-section. The value chosen was the world average of ν-Fe DIS experiments, including this one [7,8], $\sigma^{\overline{\nu}}/\sigma^\nu = 0.499 \pm 0.007$. Other sources of systematic error were investigated, including systematic errors in the flux extraction and variations in the physics model used in the Monte Carlo, but

the effects of these other sources were small [8]. To determine the uncertainty for each source, the structure functions F_2 and xF_3 are extracted with the given systematic quantity changed by one error unit up and down, where an "error unit" is the best estimate of the systematic error prior to the fit described below. The difference of these modified structure functions and the standard ones gives the point-to-point correlated systematic errors in F_2 and xF_3 for each (x, Q^2) bin. Complete tables of errors can be found in Ref. [8].

For the PQCD analysis of the structure functions, we performed a χ^2 fit which minimizes the difference between a theoretical prediction and the measured values of F_2 and xF_3 in each (x, Q^2) bin. The theoretical prediction is obtained using the Duke and Owens NLO QCD evolution program [18,8]. The prediction incorporates a parameterization of the parton distributions for the singlet, non-singlet, and gluon distributions at a reference value $Q_0^2 = 5\,GeV^2$ as shown in Table I and includes Λ_{NLO} as a fit parameter. The prediction is compared to the structure function data using a χ^2 that includes the statistical errors (including the $\Delta F_2 \Delta x F_3$ correlations) and the correlated systematic uncertainties. The systematic errors are included by introducing a parameter $\delta(k)$ for each systematic uncertainty. This parameter controls the amount of systematic deviation added to the structure function and is also included in the χ^2 function (Eq. (4)). For this procedure, we define the structure-function vector $\vec{F} = \left(F_2 \;\; xF_3 \right)^T$ and the structure-function statistical error matrix $\widehat{V} = (\sigma_{ij})$ for $i, j = \{F_2, xF_3\}$. Then the χ^2 for a global fit is given by:

$$\vec{F}^{diff} = \vec{F}^{data} - \vec{F}^{theory} + \sum_k \delta(k) \left(\vec{F}^k - \vec{F}^{data} \right) \tag{3}$$

$$\chi^2 = \left(\vec{F}^{diff} \right)^T \; \widehat{V} \; \left(\vec{F}^{diff} \right) + \sum_k \delta(k)^2 \tag{4}$$

where $\vec{F}^{data}$ are the measured values as shown in Fig. 1, $\vec{F}^{theory}$ are the predictions from the evolution program that depend on fit parameters including $\Lambda_{\overline{MS}}$, and $\vec{F}^k$ are the structure functions measured with the k-th systematic uncertainty changed by one standard error.

The effects of target mass [19] were included in the fit. Calculations of the effects of higher-twist terms (HT) have recently become available [20] and are in agreement with the measurements of the F_2 HT [21]. However, the data in Ref. [21] were analyzed with a value of α_S smaller than our present value which would increase the measurement of HT. An analysis of HT from preliminary CCFR xF_3 data [22] indicates that the calculation of Ref. [20] yields HT that are too large. For this analysis, the values of the F_2 and xF_3 HT corrections were taken to be one-half the values from Ref. [20], with a conservative systematic error given by repeating the fit with no HT correction and with the full HT from Ref. [20].

Cuts of $Q^2 > 5\ GeV^2$ and the invariant mass-squared of the hadronic system $W^2 > 10\ GeV^2$ were applied to the data to include only the perturbative region, and an $x < 0.7$ cut includes the x-bins where the resolution corrections are insensitive to Fermi motion. The $E_\nu < 360\ GeV$ cut implies an effective limit of $Q^2 < 125\ GeV^2$. The best QCD fits to the data are shown in Fig. 1, and the results of the fit are shown in Table I. The $\delta(k)$ values from the fit are all zero within two standard deviations, and have errors that range from 0.12 to 0.98. The fact that these errors are all less than 1.0 indicates that the data coupled with the theory of QCD forms a more restrictive constraint on the systematic error than the variations described above.

From this fit, we obtain a measured value of $\Lambda_{\overline{MS}}$ in NLO QCD for 4 quark flavors of 337 ± 28(exp.)± 13(HT) MeV, which yields $\alpha_S(M_Z^2) = 0.119 \pm 0.002$(exp.)$\pm 0.001(HT)\pm 0.004$(scale), where the error due to the renormalization and factorization scales comes from Ref. [21]. The fit also yields a measurement of the gluon distribution $xG(x, Q_0^2 = 5\ GeV^2) = (2.22 \pm 0.34) \times (1-x)^{4.65 \pm 0.68}$ in the region $0.04 < x < 0.70$ which is consistent with gluon distributions given in Refs. [1,2]. A fit to only the xF_3 data, which is not coupled to the gluon distribution, gives $\Lambda_{\overline{MS}} = 381 \pm 53$(exp.)$\pm 17$(HT) MeV, which is consistent with the result of the combined F_2 and xF_3 fit but has larger errors because effectively only half the data are used. If the systematic uncertainties are not allowed to vary in the F_2 and xF_3 fit and all effects of systematic uncertainties are added in quadrature, the value of $\Lambda_{\overline{MS}}$ is found to be 381 ± 23(stat.)± 58(syst.) MeV.

This result is higher than our previous measurement [9], $\alpha_S(M_Z^2) = 0.111 \pm 0.002$(stat.)$\pm 0.003$(syst.), mainly due to effects of the new energy calibrations. It is also larger than the muon DIS result by the SLAC/BCDMS collaboration [21], $\alpha_S(M_Z^2) = 0.113 \pm 0.003$(exp.)$\pm 0.004$(theory); note that this theoretical error and the CCFR theory error are from the same calculation.

In summary, a comparison of F_2 from ν DIS to that from charged-lepton DIS shows good agreement above $x = 0.1$ but a difference at smaller x that grows to 15% at $x \approx 0.01$. We have presented a new, high-precision measurement

of $\Lambda_{\overline{MS}} = 337 \pm 28\ MeV$ from a fit to the simultaneous Q^2 evolution of F_2 and xF_3. This corresponds to a value of $\alpha_S(M_Z^2) = 0.119 \pm 0.002(\text{exp.}) \pm 0.004(\text{theory})$ and is the most precise DIS measurement of this quantity.

---

[1] M. Glück, E. Reya, A. Vogt, *Z. Phys.* **C67**: 433 (1995); A. D. Martin, R. G. Roberts, W. J. Stirling; DTP/96/44, RAL-TR-96-037 (1996).
[2] H. L. Lai *et al.*, HEP-PH-9610231 (Oct 1996).
[3] G. Altarelli and G. Parisi, *Nucl. Phys.* **B126**: 298 (1977); V. N. Gribov and L. N. Lipatov, *Sov. J. Nucl. Phys.* **15**: 438 (1972); Yu. L. Dokshitzer, *Sov. Phys. JETP* **46**, 641 (1977).
[4] S. A. Rabinowitz *et al.*, *Phys. Rev. Lett.* **70**: 134 (1993).
[5] W. K. Sakumoto *et al.*, *Nucl. Instrum. Meth.* **A294**: 179 (1990).
[6] B. J. King *et al.*, *Nucl. Instrum. Meth.* **A302**: 254 (1991).
[7] R. Blair *et al.*, *Phys. Rev. Lett.* **51**: 343 (1983); P. Berge *et al.*, *Z. Phys.* **C49**: 187 (1991); P. S. Auchincloss *et al.*, *Z. Phys.* **C48**: 411 (1990).
[8] W. G. Seligman, Ph. D. Thesis, Nevis Report 292.
[9] P. Z. Quintas *et al.*, *Phys. Rev. Lett.* **71**: 1307 (1993).
[10] D. Yu. Bardin, V. A. Dokuchaeva, JINR-E2-86-260 (1986).
[11] L. W. Whitlow *et al.*, *Phys. Lett.* **B250**: 193 (1990).
[12] P. Amaudruz *et al.*, *Nucl. Phys.* **B441**: 3 (1995); R. G. Arnold *et al.*, *Phys. Rev. Lett.* **52**: 727 (1984); J. Gomez *et al.*, *Phys. Rev.* **D49**: 4348 (1994); M. R. Adams *et al.*, *Z. Phys.* **C67**: 403 (1995).
[13] M. Arneodo *et al.*, HEP-PH-9610231 (Oct 1996).
[14] M.R. Adams *et al.*, *Phys.Rev.* **D54**: 3006 (1996); L. W. Whitlow, Ph.D. Thesis, SLAC-REPORT-357 (1990); A.C. Benvenuti *et al.*, *Phys. Lett.* **B237**: 592 (1990).
[15] J. Botts *et al.*, *Phys. Lett.* **B304**: 159 (1993).
[16] A. O. Bazarko *et al.*, *Z. Phys.* **65**: 189 (1995).
[17] S. Brodsky and B. Ma, *Phys. Lett.* **B381**: 317 (1996).
[18] S A. Devoto *et al.*, *Phys. Rev.* **D27**: 508 (1983).
[19] H. Georgi and H. D. Politzer, *Phys. Rev.* **D14**: 1829 (1976).
[20] M. Dasgupta and B. R. Webber, HEP-PH-9604388 (Apr 1996).
[21] M. Virchaux and A. Milsztajn, *Phys. Lett.* **B274**: 221 (1992).
[22] A. V. Sidorov, HEP-PH-9607275 (Jul 1996).

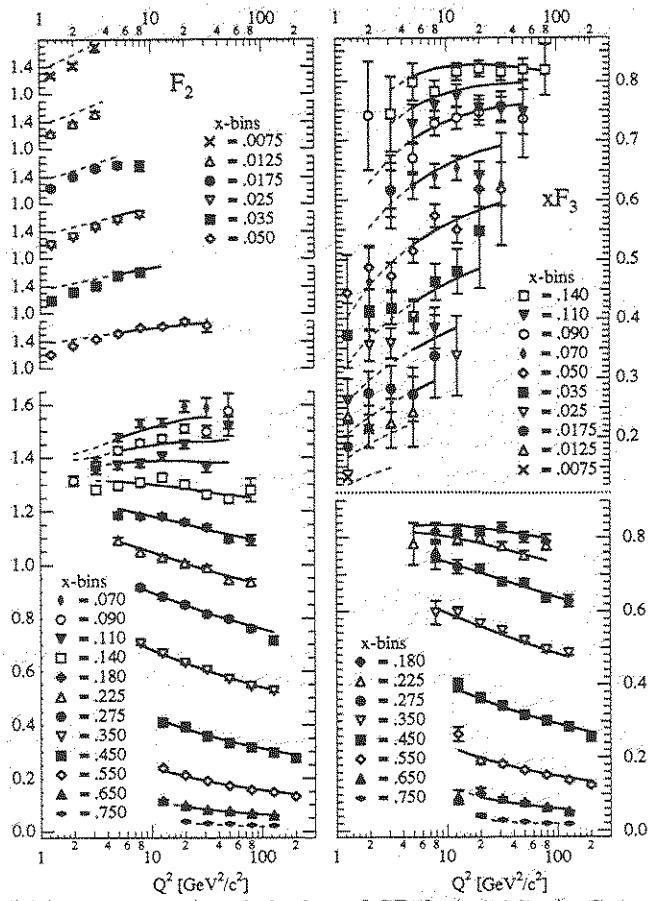

FIG. 1. The F_2 and xF_3 data (statistical errors) and the best QCD fit (solid line). Cuts of $Q^2 > 5\ GeV^2$, $W^2 > 10\ GeV^2$, and $x < 0.7$ were applied for the NLO-QCD fit which include target mass corrections. The dashed line extrapolates the QCD fit into the data regions excluded by the cuts. Deviations of the data from the extrapolated fit are partly due to non-perturbative effects.

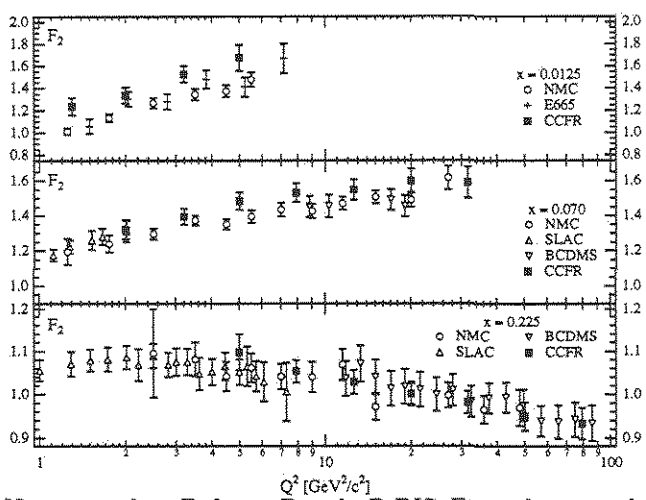

FIG. 2. F_2 from CCFR ν-Fe DIS compared to F_2 from eD and μD DIS. Errors bars are the statistical and systematic errors added in quadrature. The charged-lepton data have been corrected to an isoscalar Fe target, and for quark-charge effects in the DIS scheme which is valid to all orders (see text). The NMC data plotted in the figure were extracted with the same R as used in the CCFR analysis [13].

TABLE I. Results of the global systematic fit to the CCFR data. The parton distributions at $Q_0^2 = 5\ GeV^2$ are parameterized by $xq^{NS}(x) = A_{NS}x^{\eta_1}(1-x)^{\eta_2}$, $xq^S(x) = xq^{NS}(x) + A_S(1-x)^{\eta_S}$, $xG(x) = A_G(1-x)^{\eta_G}$. $\delta(k)$ is the fractional shift for the best value of systematic quantity k as determined by the fit. Only the most important sources of systematic error are shown. $\delta\left(C_{HAD}^{744}\right)$ is the shift for the E744 hadron energy calibration, $\delta\left(C_{HAD}^{770}\right)$ is the shift for the E770 hadron energy calibration, $\delta(C_\mu)$ is the shift for the muon energy calibration, and $\delta\left(\sigma^{\overline{\nu}}/\sigma^{\nu}\right)$ is the shift for the ratio of the total $\overline{\nu}$ to ν cross-section. The χ^2 of the fit is 158 for 164 degrees of freedom.

Parameter	Fit Results	Parameter	Fit Results
$\Lambda_{\overline{MS}}$	$337 \pm 28\ MeV$	A_G	2.22 ± 0.34
η_1	0.805 ± 0.009	η_G	4.65 ± 0.68
η_2	3.94 ± 0.03	$\delta\left(C_{HAD}^{744}\right)$	0.95 ± 0.42
A_{NS}	8.60 ± 0.18	$\delta\left(C_{HAD}^{770}\right)$	0.28 ± 0.27
A_S	1.47 ± 0.04	$\delta(C_\mu)$	0.21 ± 0.18
η_S	7.67 ± 0.13	$\delta\left(\sigma^{\overline{\nu}}/\sigma^{\nu}\right)$	0.04 ± 0.50

Colophon

This thesis was written on a Power Macintosh 7500/100 computer and printed on a LaserWriter II NT. Programs used to generate the contents of the thesis included:

- Microsoft Word 5.1a for word-processing, with MathType 3.1 used to typeset equations;

- Igor Pro 3.0.1 for generating most of the plots; HBOOK and HPLOT were used to generate the calibration plots in Chapter 3 and all the plots in Appendix E;

- Canvas 3.5.1 for creating the diagrams and sketches.

Other programs that were frequently used were Microsoft Excel 5.0 for preparing the contents of some tables, PS2EPS+ for converting Postscript files to Encapsulated Postscript on the Macintosh, and Fetch 3.0.1 for FTP transfer of data from to and from the computers at Nevis Labs.